Université de Liège

Faculté des Sciences
Département d'Astrophysique, de Géophysique et d'Océanographie

---

Astrophysical parameters and multiplicity of massive stars: a mathematical approach

by

Laurent Mahy

Groupe d'Astrophysique des Hautes Energies

– December 2011 –

Supervisor: Dr. Eric Gosset
Co-supervisor: Dr. Yaël Nazé

Dissertation realized for the acquisition of the grade of Doctor of Philosophy in Space Science

Supervisors – Dr. Eric Gosset
Dr. Yaël Nazé

Jury – Pr. Jean Surdej as President
Dr. Eric Gosset
Dr. Yaël Nazé
Dr. Jan Cuypers
Pr. Marc-Antoine Dupret
Pr. Krešimir Pavlovski
Pr. Gregor Rauw

Remerciements

Cette thèse est le point final de quatre années passées dans les étoiles et l'aboutissement d'un rêve vieux de plus de quinze ans. Je voudrais donc en premier lieu adresser mes plus profonds remerciements au Pr. Gregor Rauw pour m'avoir offert la chance de travailler dans son équipe mais aussi pour avoir partagé toutes ses connaissances scientifiques, à travers les cours bien sûr mais aussi au quotidien.

Je voudrais également remercier Dr. Eric Gosset, mon promoteur, pour sa disponibilité et son accueil. En plus de ses qualités humaines précieuses, il m'a aussi permis d'apprendre beaucoup à travers sa riche connaissance scientifique. Merci aussi pour les conseils sans cesse renouvelés (notamment de structures!) et ta façon de rendre les résultats complexes clairs pour tous.

Je suis aussi très reconnaissant au Dr. Yaël Nazé pour sa disponibilité, ses relectures attentionnées et ses conseils avisés. Ma grande gratitude va aussi à tous les membres du "GAPHE" et du "+2" en général pour leur sympathie et leur gentillesse. Vous avez fait de chaque jour passé à cette thèse un moment de plaisir, et pour cela, merci!

Cette thèse n'aurait pas été possible sans l'aide de nombreux observateurs: Pr. Gregor Rauw, Dr. Eric Gosset, Dr. Yaël Nazé, Dr. Michaël De Becker, Dr. Hugues Sana, Dr. Natacha Linder, Dr. Philippe Eenens, Arturo Carlos Flores Hernandez et Dr. Christian Nitschelm. Merci à vous, pour l'acquisition et la réduction des données, ce travail est plus qu'essentiel pour rendre l'astrophysique observationnelle possible. Merci aussi aux Pr. Gregor Rauw, Dr. Eric Gosset, Dr. Yaël Nazé et au Pr. Jean-Pierre Swings pour les relectures attentionnées de ce manuscript. I also want to warmly acknowledge Pr. Jean Surdej to accept to be President of my jury and Pr. Krešimir Pavlovski, Dr. Jan Cuypers and Pr. Marc-Antoine Dupret to be members of my jury.

Ces quatres années auront aussi été marquées par plusieurs voyages et conférences à travers le monde et durant lesquels de nombreuses rencontres et collaborations auront vu le jour. Dès lors un merci spécial est adressé au Dr. Philippe Eenens pour son accueil à Guanajuato et à Arturo pour m'avoir fait découvrir "el Paradisio", son ciel, ses coccinelles, ses abrits de Hobbits et sa nourriture!

Je voudrais aussi chaudement remercier le Dr. Fabrice Martins pour m'avoir initié aux "bases" de CMFGEN mais également pour les nombreuses collaborations. Merci pour sa disponibilité malgré un emploi du temps souvent très chargé. Ce fût un réel plaisir de travailler avec lui! Par ailleurs, je suis aussi reconnaissant au Dr. Hugues Sana pour ses nombreux conseils, et éclaircissements statistiques ainsi qu'au Dr. Mélanie Godart pour la collaboration intensive sur les données CoRoT.

Ces quatres années passées à l'institut m'ont fait découvrir des personnes adorables et at-

tachantes avec qui ce fût un plaisir de manger, de rigoler et de partager une petite "rabrouche" ou une "soyante" tous les midis : Arn, Den, Charles, Davide, Franz, Méla, Oli, Gi,... mais, "last but not least", Nat, pour les moments partagés et Antho pour les nombreuses conversations et les moments CMFGEN!

Enfin, j'aimerais à cet instant exprimer ma plus profonde gratitude à mes parents pour leur éducation, pour avoir toujours cru en moi, pour leurs encouragements, et pour m'avoir toujours laissé libre de mes choix ; à mes grand-parents maternels pour leur gentillesse et l'enfance formidable qu'ils m'ont offerte ; à mes grand-parents paternels qui veillent sur moi depuis les étoiles et à Christine, ma compagne, pour sa patience, sa présence et ses encouragements durant ces derniers mois mais aussi au quotidien.

"*A tous, MERCI du fond du coeur!*".

Enfin pour reprendre une expression de Fabrice : "*Merci aussi à la Nature pour toutes les merveilles qu'elle a créées et pour avoir fait en sorte que les étoiles brillent!*".

Abstract

Often quoted for their crucial role in the ecology of galaxies, massive stars remain mysterious. The exact process leading to their formation, their stability or their stellar winds are so many questions which are still unanswered. Since the lifetime of these objects is too short to allow them to move far away from their birth places, the large majority of massive stars are located in young open clusters or in OB associations. The observations of massive stars in these locations thus provide with promising information on their formation mechanisms. One of the most interesting properties, in this context, is their multiplicity. Indeed, the proportion of multiple systems, the values of orbital periods, of eccentricities, or of mass ratios are parameters directly linked to the formation mechanism and to the dynamical interactions occuring during the earliest stages of their existence. Moreover, constraining this multiplicity with a sufficient accuracy allows to obtain a better determination of the nature and physical parameters of massive stars.

The present work is devoted to the study of the O star populations located in the young open cluster NGC 2244 and in the surrounding Mon OB2 association as well as in several OB associations of the Cygnus complex. We establish not only the multiplicity of about thirty stars but also their fundamental parameters such as their masses or their N content. However, the complexity of observed spectra of multiple systems makes these objects difficult to investigate. Their analysis thus requires the development and the utilization of mathematical tools such as the "disentangling" which allows to separate the spectra of the components from the observed ones or such as the Doppler tomography which aims at mapping the wind interactions seen in some binary systems.

The first part of this dissertation is dedicated to the development and to the characterization of these mathematical methods whilst the second part focuses on the study of populations of massive stars. We refine the orbital and physical parameters of systems already known as multiple. In this context, the analysis of the two components of LZ Cep system reveals modified abundances for the secondary star, confirming a mass transfer from the secondary towards to primary. We also detect for the first time a third star in the HD 150136 system. This object, composed of an O 3, an O 5.5 and an O 6.5, constitutes a new test to apply these mathematical methods and thus to better constrain the physical properties of the system as well as those of each component. Moreover, we find, in the population of NGC 2244, of Mon OB2 and of the Cygnus OB associations, six new binary systems and derive the orbital solutions for five of them. These results show that NGC 2244 hosts only one long-period binary and none with a short period whilst four short-period and no long-period systems are detected in the Cygnus complex. This obvious lack of short-period system in NGC 2244 contrasts with the O star populations in other young open clusters such as NGC 6231 or IC 2944. Besides the multiplicity, the fundamental parameters such as the N content also allows us to, notably, adapt the so-called *Hunter-diagram* to galactic O stars. Moreover, we have obtained photometric data for six O-type stars in NGC 2244 and Mon OB2 with the CoRoT satellite. These data of unprecedented quality allow us to detect the presence, in the O star light curves, of red noise which is supposed to originate from either the sub-surface convection zone, the granulation or an onset of clumping in the winds of the stars. We also highlight the existence of non-radial pulsations in the light curve of Plaskett's Star as well as a hot spot located between the two components of that system. In addition, numerous frequencies, extracted from the CoRoT light curves, reveal, for some of the observed stars, solar-like oscillations or β Cephei-like pulsations. This analysis thus gives a first observational constraint on the bright end of the massive star instability strip.

Résumé

Connues pour leur rôle majeur dans l'écologie des galaxies, les étoiles massives n'en restent pas moins des objets mystérieux. Leur formation, leur stabilité mais aussi leurs vents sont autant de points qui demeurent encore sans claire explication. Comme la durée de vie de ces étoiles est trop courte pour leur permettre de s'éloigner de leur site de formation, la majorité de ces étoiles se situe dans des amas ouverts ou dans des associations OB. L'observation des étoiles massives dans ces environnements peut donc fournir des informations sur leurs mécanismes de formation. Une des propriétés les plus intéressantes dans ce contexte est leur multiplicité. En effet, la proportion de systèmes multiples, les valeurs des périodes orbitales, des excentricités, ou des rapports de masse sont autant de paramètres liés à leur mécanisme de formation et aux interactions dynamiques se passant durant les premières phases de leur existence. De plus, contraindre cette multiplicité permet une estimation plus précise de la nature et des paramètres physiques de ces étoiles.
Cette thèse est dédié à l'étude des populations d'étoiles massives situées dans le jeune amas ouvert NGC 2244 et l'association Mon OB2 qui l'entoure ainsi que dans d'autres associations OB situées dans la constellation du Cygne. Nous établissons non seulement la multiplicité d'une trentaine d'étoiles O provenant de ces sites de formation mais aussi leurs paramètres physiques. Cependant, la complexité des spectres observés pour les systèmes multiples rendent ces objets difficiles à étudier. Leur analyse nécessite donc le développement de méthodes mathématiques comme le "disentangling" qui vise à séparer les composantes individuelles de ces spectres ou la tomographie Doppler dont le but est de cartographier les interactions des vents stellaires se produisant dans certains systèmes binaires.
La première partie de ce travail est consacrée aux développements et à la caractérisation de ces méthodes tandis que la seconde partie se concentre sur les populations d'étoiles massives. Nous affinons les paramètres orbitaux et physiques de systèmes déjà connus comme multiples. Dans ce contexte, l'analyse des deux composantes de LZ Cep montre des abondances de surface modifiées pour l'étoile secondaire, témoignant d'un transfert de matière entre les deux composantes. Nous détectons aussi pour la première fois une troisième étoile dans le système HD 150136. Cette étoile triple se révèle donc comme un nouveau test pour le développement et l'application des méthodes mathématiques visant à contraindre les propriétés physiques individuelles de chaque composante. Par ailleurs, nous trouvons dans la population d'étoiles O de NGC 2244, de Mon OB2 et des associations OB du Cygne, six nouvelles binaires et nous déduisons les solutions orbitales de cinq d'entre elles. Ces résultats montrent que NGC 2244 contient seulement une binaire massive et que sa période est longue alors que les quatres systèmes détectés dans la région du Cygne sont tous des systèmes avec une période courte. Le manque de tels systèmes dans NGC 2244 contraste avec la population d'étoiles O dans d'autres amas ouverts comme NGC 6231. Outre la recherche de multiplicité, les abondances en azote ont permis d'adapter le diagramme d'Hunter aux étoiles galactiques de type O. Nous avons aussi obtenu des données photométriques de six étoiles O de NGC 2244 et de Mon OB2 grâce au satellite CoRoT. Ces données, d'une qualité unique, nous permettent de déceler du bruit rouge dans ces étoiles O. L'origine possible de ce bruit provient soit la zone de convection située sous la surface des étoiles O, de la granulation ou d'un début de "clumping" dans les vents stellaires. Nous soulignons aussi l'existence de pulsations non-radiales dans l'étoile de Plaskett ainsi que d'un point chaud entre les deux composantes de ce système. Les nombreuses fréquences, extraites de ces courbes, révèlent, pour certains objets, des oscillations de type solaire, ou des pulsations de type β Cephéïde. Cette étude apporte donc une première contrainte observationnelle de la fin de la bande d'instabilité des étoiles massives.

Contents

Remerciements iii

Abstract v

Résumé vi

Introduction 1

I Mathematical tools in the analysis of binary or multiple systems 11

1 Determination of the fundamental properties of massive stars 13

1.1 Single stars 13

1.1.1 The CMFGEN atmosphere code for massive stars 13

1.1.2 Main diagnostic lines for the modelling 16

1.2 Spectroscopic binaries 17

1.3 The Roche lobe overflow 19

2 Spectral disentangling 23

2.1 Iterative Doppler differencing 24

2.2 Spectral disentangling in wavelength domain 27

2.3 Application to the evolved binary system LZ Cep 30

3 Doppler Tomography 41

3.1 Fourier-filtered back-projection 42

3.2 Algebraic methods in Doppler tomography 44
3.2.1 The ART method 46
3.2.2 The SIRT method 47
3.3 Applications to evolved binaries 47
3.3.1 Plaskett's Star 47
3.3.2 Cyg OB2#5 49
3.3.3 AO Cas 50
3.3.4 Comparison between analytic and algebraic methods 52

4 The triple system HD 150136 **55**

II Multiplicity of O-type stars in young open clusters and OB associations **71**

5 The young open cluster NGC 2244 and the Mon OB2 association **73**
5.1 The multiplicity in young open clusters 74
5.2 The spectroscopic investigation 76
5.2.1 The binary fraction 76
5.2.2 Observational biases 79
5.3 The determination of the stellar and wind parameters 105
5.4 The CoRoT photometry 111
5.4.1 The CoRoT satellite 111
5.4.2 Analysis processes and frequency determination 112
5.4.3 Significance levels for the CoRoT data 114
5.4.4 Analysis of the photometric CoRoT data 115
5.4.5 Red noise 137
5.5 Conclusions 140

6 The Cygnus associations **147**
6.1 Individual analysis of the sample stars 149

6.1.1 Cygnus OB1 association 149
6.1.2 Cygnus OB3 association 163
6.1.3 Cygnus OB8 association 167
6.1.4 Cygnus OB9 association 170
6.2 Observational biases 177
6.3 Binary fraction in Cygnus associations 177
6.4 Evolutionary status 179
6.5 N content and stellar wind 181
6.6 Conclusions 183

Conclusion **185**

A List of publication **191**

B Frequency lists derived from the CoRoT photometry **223**

C Journal of observations of the Cygnus region **249**

Bibliography **259**

Introduction

A starry sky is one of the most wonderful spectacles a man can see in his life. Beside this beauty, mingle a feeling of vastness and a deep sense of awe. Like in all beautiful spectacles, we have to wait that the first role, the Sun, leaves the stage to appreciate the performances of secondary players. The present dissertation is devoted to these secondary players and in particular to the most spectacular ones among them: the massive stars.

Among the 10^{11} stars estimated in our Galaxy, these massive objects constitute only a small fraction of the stellar population. With masses above 8–10 $M_{\odot}$, they are classified as OB stars and are among the brightest and the hottest objects that we can find in space. However, their life has begun in the darkness and the coolness. Resulting from a collapse of a giant molecular cloud, these stars (or protostars) are, at their birth, surrounded by dust blocking their light and making them difficult to observe. Our limited knowledge of these protostars however tells us that they are dense objects which are still accumulating neighbouring mass. Under the action of the gravity, the molecular cloud contracts, leading to an increase of the temperature in their core. When this temperature reaches 10^7 K, the heat is intense enough to set off the nuclear reactions. The outwards-directed pressure gradient of the radiation, resulting from the hydrogen combustion, halts the core collapse. The star then enters a hydrostatic-equilibrium phase in which it spends the largest part of its life. Its destiny is now set by its initial mass. Once the core's hydrogen is exhausted, the nuclear reactions in the core stop. For stars with a mass smaller than 40 $M_{\odot}$, their core contracts and their enveloppe expands: the stars become Red Supergiants (RSG) and begin to burn hydrogen in a shell whilst their core remains inert and mainly composed of helium. For stars with an initial mass larger than 40 $M_{\odot}$, the stars enter a Luminous Blue Variable (LBV) phase. The exact moment when this phase occurs is not clearly established but is estimated by theory between the end of the core H-burning phase and the beginning of the core He-burning phase. During this very short time ($\sim$ 0.01 Myr), amazing eruptions occur with a strong increase of the mass-loss rate of the stellar wind. After these transitory phases (RSG and LBV), the inert core of helium contracts and the nuclear reactions start again in the core, now burning mainly helium into carbon. The objects with an initial mass greater than 25 $M_{\odot}$ then evolve into Wolf-Rayet (WR) stars. The massive stars are the only ones to go beyond the stage of carbon fusion, by successively igniting hydrogen, helium, carbon, oxygen, neon, magnesium, silicon in their core until reaching iron (as an end product). Once they reach this stage, the core collapses and the star finishes its life in a spectacular supernova. During this extremely short collapse ($\sim$ 1 sec), the star synthetizes elements heavier than iron while releasing them into the interstellar medium.

With such initial masses, the compression due to gravity is also high: the rate of nuclear reactions required for massive stars needs to be huge in comparison to that of low-mass stars. Therefore, the more massive the stars, the faster they burn and the more quickly they consume themselves. These stars have thus shorter lifetimes than their lower-mass counterparts. In general,

they live less than 10 Myrs whilst our Sun has a lifetime estimated to 10 Gyrs, i.e. 10^3 times longer. These stars are thus generally found close to their birth places, often embedded in H II regions that they have themselves excited. Indeed, these stars, with luminosities of $10^5 - 10^6$ $L_\odot$ and effective temperatures of 25–30000 K, are the main sources of ionization of the Universe. In addition, the O stars are also quite rare. For example, for each star with a mass in the range of $60 - 120$ $M_\odot$, there are about 250 stars with masses in the range $1 - 2$ $M_\odot$ and about 640 stars with masses between 0.5 and 1 $M_\odot$.

This scarcity does not prevent these stars to have a deep impact on the ecology of galaxies. Indeed, they do not only burn their combustible, they also spread their material in their surroundings. This injection of mass and energy through their powerful winds and their amazing explosion in supernova shapes the interstellar medium. The compression of the surrounding gases is at the origin of new zones of star formation in their close neighbourhood (see e.g., 30 Dor in the Large Magellanic Cloud – LMC), from which the next generation of stars forms. The matter previously ejected feeds back the new objects by making them more metal rich. Through the ejection of their enriched material, the massive stars lose a significant fraction of their initial mass. For instance, a star of 100 $M_\odot$ can lose up to 90% of its initial mass during its evolution (Maeder 1992). Indeed, the mass-loss rate ($\dot{M}$) of massive stars ranges between 10^{-7} and 10^{-5} $M_\odot$ yr^{-1} and the terminal velocity of the stellar winds (v_∞) is generally between $1500 - 3000$ km s^{-1}, i.e., 1% of the light speed. As a comparison, the Sun has a mass-loss rate and a wind terminal velocity of about 10^{-14} $M_\odot$ yr^{-1} and $400 - 700$ km s^{-1}, respectively. The mass-loss rates change as a function of the age of the stars. The wind is driven through a transfer of momentum from the stellar photons to the material at the stellar surface. As a consequence, this mechanism is dependent on the luminosity of the stars. This interaction between matter and radiation creates a net radiative acceleration sufficient to overcome the gravity (Milne 1926). The mass-loss rates of LBVs and RSG are relatively high with values of about $10^{-5} - 10^{-3}$ $M_\odot$ yr^{-1} whilst the mass-loss rates of WR are of about $10^{-5} - 10^{-4}$ $M_\odot$ yr^{-1}. Such powerful winds constitute the main cause of the ejection of the outer hydrogen envelop of the O stars, thus revealing the inner layers of these stars, more enriched in helium and metals.

In the earliest phases of the Universe, right after the Big Bang, the first generation of stars (so-called Population III stars) formed when there were no metals in the Universe ($Z = 0$). These objects were extremely massive, with average masses of 100 $M_\odot$, whilst current generations of Population I stars have a typical mass of about 1 $M_\odot$and they also had a very strong ionizing power (Schaerer 2002, 2003). Due to their lack of metallicity, their evolution was certainly different from what we know for the populations I and II stars since the mass-loss rates are indeed completely different at zero metallicity. These objects with a larger mass and thus a larger luminosity have therefore greatly contributed to the enrichment of the interstellar medium. Without them, the current chemical composition in the galaxies would be completely different, and life such as we know it in the present day would not have been possible. Furthermore, these stars are assumed to be at the origin of the formation of black holes ($5 - 15$ $M_\odot$) and possibly even of supermassive black holes ($10^6 - 10^9$ $M_\odot$) situated at the centre of many galaxies. They are also thought to be progenitors of long-duration γ-ray bursts. These very intense and luminous explosions detected in the γ-ray domain could indeed be either associated with an unusual explosion of population I and II stars or a supernova explosion of a population III star (Bromm & Larson 2004, and references therein).

Despite the fact that our general knowledge of massive stars was considerably improved over the last decades, our understanding of many crucial aspects is still fragmentary. Different questions, ranging from the exact formation processes of massive stars to their final explosion as

supernovae or their upper-mass limit, the existence and the role of magnetic fields or a detailed comprehension of their stellar winds, remain unanswered. In the next section, we give a brief overview of the remaining questions regarding the massive stars, notably those that are tackled in the present work.

Massive star formation

Describing the formation processes of massive stars and binary systems is currently one of the most challenging questions in astrophysics. Although considerable theoretical progresses in the understanding of their formation were recently made, there is still much confusion on the cause of their formation (Bonnell et al. 2011). The difficulties to understand the earliest stages of their formation are mainly due to the fact that few such objects were seen forming. Several reasons are advanced to explain this obvious lack of observations: the high dust extinction during the earliest phase of their life, the short duration of this evolutionary stage or still their rarity (Zinnecker & Yorke 2007).

Massive stars form deep inside a molecular cloud from a local condensation of the gas and only emerge when they are burning their hydrogen in their core. Those two stages are generally separated by a few 10^5 years. The final product of this formation is often detected in gravitationally bound young open clusters or in non-gravitationally bound OB associations (Lada & Lada 2003). As already mentioned, because of their short life, we can generally assume that the birth place of massive stars nearly corresponds to the place where these stars are currently observed. However, massive stars in isolated parts of the Universe also exist. Some of them were ejected from their birth places, displaying radial velocities larger than 40 km s^{-1} (Blaauw 1961), as a result of tidal interactions or a supernova. $10-25\%$ of massive stars are runaways and only $5-10\%$ of these ejected stars cannot be connected to an OB association or a young open cluster (de Wit et al. 2005). This is the case of HD 93521, located at 1.4 kpc (Irvine 1989) and far away from the Galactic plane ($l = 183.1°$, $b = 62.2°$). Although considered as a possible runaway (Gies 1987a), it is however unlikely that this star was formed in the plane and moved to its current position (Rauw et al. 2008). As a consequence, this object could have been formed in the Galactic halo as few other stars (Heber et al. 1995). The young open clusters and the OB associations are thus of crucial importance to provide observational constraints on the formation models. Despite this mystery, it clearly appears that the formation of massive stars is not just a scaled-up version of the formation mechanism of the lower-mass stars with higher accretion rates (Zinnecker & Yorke 2007).

The stars are thus the final products of a molecular cloud collapse. During this collapse, the cloud passes through different stages. In the first one, the collapse is isothermal until reaching densities of about $10^{-14}-10^{-13}$ g cm^{-3} (Bonnell 2001). The gas then contracts to become optically thick to the infrared radiation, forming the first protostellar core which contracts quasi-statically with the increase of the mass. When the temperature reaches 2000 K, the gas becomes hot enough to dissociate H_2. During this phase, the hydrogen absorbs a part of the thermal energy and a second collapse occurs. When the gas is in atomic form, a second protostellar core is created and continues to contract quasi-statically with the increase of the mass. Kuiper et al. (2010) have shown that the next step in the formation of massive stars can be performed through **accretion**. The matter in the stellar neighbourhood would thus be piled up to create a circumstellar disk around the protostar obtained from the gravitational contraction. This matter would then be slowly accreted, increasing the mass of the emerging star. The gravitation then contracts the protostar until it starts the hydrogen combustion in its core, producing the classical and radiative pressures essential to

avoid the collapse and to keep it "alive". Although this scenario is largely accepted for describing the low-mass star formation, it has been long debated for massive stars. First, a relatively massive protostar would have a luminosity sufficient to generate a radiation pressure able to decrease the accretion rate or even to stop the accretion process. Then, if we assume an accretion rate similar to that of lower-mass stars ($\dot{M}_{\rm accr} \sim 10^{-5} M_{\odot}$ yr^{-1}), this rate would be unable to form a star with a mass of several tens of solar masses in a period of a few 10^5 years. Nevertheless, these barriers have been recently overcome by assuming an anisotropic radiation field. In these new models, the thermal radiation escapes through the optically thin atmosphere, decreasing the radiation pressure feedback onto the accretion flow. Moreover, gravitational torques in the self-gravitating disk allow to accrete enough material to overwhelm the remaining radiation pressure. Simultaneously, most of the radiation pressure would be released through bipolar outflows perpendicular to the disk. Kuiper et al. (2010) have performed simulations of this formation mechanism from which they conclude that a star could grow up to 28.2, 56.5, 92.6, and at least 137.2 $M_{\odot}$, for initial masses of the pre-stellar core of 60, 120, 240, and 480 $M_{\odot}$, respectively. Moreover, we stress that recent mid-infrared observations of the youngest and coldest molecular clouds have been performed by Herschel and seem to corroborate the accretion scenario as formation mechanism for the massive stars (Beuther 2011).

Although this accretion mechanism now appears viable, another scenario was envisaged before: **the stellar collisions and mergers**. This process allowed to overcome the limitation induced by the radiation pressure but required a stellar density higher than 10^6 pc^{-3} (Bonnell & Bate 2005) which is difficult to reach, notably in OB associations. In addition, the collisional time has to be shorter than the timescale for evolution of the most massive stars in the cluster (Zinnecker & Yorke 2007). Therefore, this scenario could thus only occur in the most massive and densest clusters, thereby excluding it of being the first cause of the massive star formation.

Assuming that this accretion mechanism plays the first role in massive star formation does not solve all problems however. Notably the question of how they reach their final mass is still debated (Bonnell & Smith 2011). Two possible processes were envisaged in the literature. **The competitive accretion** scenario highlights the importance of environmental influences and gravitational attractions inside a molecular cloud. In this case, the protostellar objects are assumed to be the results of condensations in the denser parts of the molecular gas cloud. These new bodies keep growing in mass by the accretion of low-density gas reservoirs in their neighbourhood. Consequently, the individual accretion rate strongly depends on the environment. In a molecular cloud hierarchised in subclusters, the material migrates down to the center of the clouds, leading to the formation of lower-mass objects in the surroundings and a higher-mass star in the center. The final mass of the protostar does not only depend on the initial mass of the original clumps but rather on the location of its formation in the molecular cloud. Such a process therefore predicts a direct relationship between the most massive star and the total number of stars in a cluster (Bonnell et al. 2011). However, it requires a slow dispersion of the gas as expected in a turbulent medium. The second mechanism is **the collapse of massive prestellar cores**. However, it is more uncertain than the competitive accretion scenario because the existence of such massive prestellar cores has never been established by observations nor by theoretical predictions. The latter indeed show that such objects should fragment before reaching a condensed high-mass state (Bonnell & Smith 2011). Furthermore, other ingredients such as rotation or magnetic field could impact on the stellar formation and should be taken into account in future investigations.

The veil thus seems to slowly rise on the formation of massive single stars but a non negligible fraction ($\sim 60\%$) of massive stars in young open clusters or OB associations are in fact multiple systems, composed of at least two stars, whose formation mechanism appears to be different from

that of single stars. Until now, three categories of formation processes of multiple systems have been discussed in the literature. The first group contains **the core processes** such as the fission or the fragmentation. The fragmentation process happens when a molecular cloud in non equilibrium breaks up in two or more parts. According to Bonnell (2001), the initial mass of the molecular cloud to create a binary system has to be twice larger than the Jeans mass[1]. This condition implies that each part can gravitationally collapse. As already mentioned, the gravitational contraction occurs in different phases: an initial isothermal phase, a first collapse, an H_2 dissociation phase, and a second collapse. The fragmentation generally happens during the two collapse phases but becomes more difficult when the protostellar cores are formed due to their quasi-sphericity. Moreover, these authors stressed that small perturbations during the second collapse are unlikely to lead to fragmentation. The alternative fission process results in the splitting into two parts of a rapidly rotating protostar. Unlike the fragmentation, it happens when the core is in quasi-equilibrium. The rapid rotation is obtained through angular momentum conservation. With this spin increase, the protostar becomes unstable and deforms until reaching the break up and generating two new protostars.

The second group of formation scenarios gathers **the disk processes**. When a cloud contracts, it generates an accretion disk around the core in formation. If the disk becomes gravitationally unstable and if the gas cools efficiently, the disk can fragment, creating one or more companions which orbit in the same plane as the original disk. These different protostars then continue to accrete matter from the parental cloud. However, the disk fragmentation would produce systems with a typical separation similar to the size of the disk, i.e., several tens of Astronomical Units (AU), leading to the formation of systems with one or more low-mass companions in wide orbits. This scenario does nevertheless not explain the formation of close binary systems with a mass ratio close to unity.

The third category of formation mechanisms groups all the interaction processes. We summarize these processes under the designation of **multiple formation** scenarios. A first kind of scenarios relies on tidal capture. The protostars form as single stars but when two protostars pass close to each other, tidal interaction occurs, leaving both objects gravitationally bound. However, this process requires a high stellar density and can only happen in very dense environments. Another kind of scenarios supposes that the turbulent molecular cloud is split into many parcels that interact together and that continue to store mass from the background cloud. Therefore, the combined actions of gas accretion, interactions with circumbinary disks and dynamical interactions with the other stars in the cluster reduce the separation of wide binaries and favor components with comparable masses (Gies 2008). All the scenarios of this category thus rely on the fact that all forming objects accrete matter through migration over the entire cloud.

Recent works have shown that disk fragmentation requires careful consideration as one of the most viable mechanisms, especially for stars more massive than our Sun (Kratter 2011, and references therein). However, it is difficult to choose a reliable scenario as long as a good knowledge of the distributions in mass ratios, eccentricities and separations of the binary and multiple systems is missing.

Upper-mass limit

Since we still ignore the exact formation process of massive stars, we do not know what are the maximum accretion rates, what is the size of the biggest molecular clouds necessary to form the

[1]The Jeans mass is the minimum mass so that the gas pressure is not sufficient to prevent gravitational collapse.

most massive stars or what are the conditions of stability so that a massive star exists. As a consequence, *"how massive can a massive star be?"* is certainly one of the most popular questions in the astrophysical field. It is also a very good illustration of the lack of knowledge regarding massive stars. Even though we know very well the lower mass limit of the massive stars (8–10 $M_{\odot}$), the upper one is relatively controversial. Nonetheless, we expect to find the answer by observing rich young open clusters or OB associations which are sufficiently young to still have such a star alive... Such very massive stars in the Universe are also expected to be found among the O2-O3 star population or among the WN-Late (WNL[2]) star population (Walborn et al. 2002).

In order to answer this question, numerous ideas have therefore been proposed but, behind this open question, is also hiding the problem of determining reliable stellar masses. For eclipsing binary systems or for systems which show ellipsoidal variations in their light curves (see Chapter 1), this determination is quite reliable because all the orbital parameters and the inclination can be derived by combining photometric light curves and radial velocity curves. It should be noted however that these mass estimates are reliable indicators of the initial masses for young systems, where no interaction has occurred. The Liège group found WR 20a to be the most massive system ever reliably detected by this method. This system is indeed composed of two stars, certainly in transition between the O class and the WR class, with masses of about 82 and 83 $M_{\odot}$ (Rauw et al. 2005a).

For stars not belonging to a binary system, it is however not possible to investigate the orbital motion nor the eclipses. Consequently, the mass-luminosity relation is generally used but the masses estimated by this method have the disadvantage to be approximative and often overestimated. An example of this problem is the determination by Cassinelli et al. (1981) of a mass of $1000 - 2500\ M_{\odot}$ for R 136a in 30 Dor. Further development of the observational instruments invalidated this value by separating R136a in about a dozen of stars (Weigelt et al. 1991), where the most massive one had an initial mass of about $120 M_{\odot}$ at maximum.

With the development of the new generation of atmosphere codes, we can also estimate masses from the positions of stars in the Hertzsprung-Russell (HR) diagram, the so-called *evolutionary masses*, or from the determination of stellar radius and of the stellar gravity, the so-called *spectroscopic masses*, through the expression:

$$M = \frac{gR^2}{G}$$

where M is the mass of the star, g its gravity, R its radius and G is the gravitational constant ($6.67\,10^{-11}\mathrm{m}^3\,\mathrm{kg}^{-1}\,\mathrm{s}^{-2}$). Crowther et al. (2010) have recently reinvestigated the crowded R 136 and NGC 3603 star clusters. Their analysis based on model atmospheres now suggests initial masses in the range $105 - 170\ M_{\odot}$ for three stars in NGC 3603 and between 165 and 320 $M_{\odot}$ for four stars in R 136. All these stars would be in a stage of transition between the O class and the WR class, but their binarity is still unknown and remains to be investigated.

Finally, statistical methods can be used, if sufficiently rich clusters are observed. Figer (2005) investigated the Arches cluster and found that no star with an initial mass higher than 150 $M_{\odot}$ was detected while two or three tens of stars with such a mass were expected. A study of Martins et al. (2008) using model atmospheres confirmed this result by estimating an initial mass of about 120 $M_{\odot}$ for the most massive star in the Arches cluster. Figer's computations and the conclusions of Oey & Clarke (2005) thus suggested a limit of 150 $M_{\odot}$ for massive stars. In the

[2]The WNL stars are extreme O stars which seemingly are still burning hydrogen in their core but appear as WR stars because of their large mass-loss rates.

search of the most massive star, not all estimates agree, and the recent results of Crowther et al. (2010) have raised doubts again on the upper-mass limit of stars, leaving the door widely opened to speculation about this value.

Stellar winds and mass-loss rates

Although the initial mass governs the fate of a star, two other parameters influence the evolution of a massive star: the rotation and the mass-loss rate. Understanding the stellar winds of massive stars is thus a fascinating problem for the observers as well as for the theoreticians. Reviews on stellar winds, their observations and their modelling problems can be found in the following books and papers: Lamers & Cassinelli (1999), Puls et al. (2008), Hillier (2008), Gräfener & Hamann (2008), Blomme (2009), Owocki (2011), Sundqvist et al. (2010, 2011b) and Fullerton (2011). Here we only summarize several important findings and remaining issues concerning the O-type stars.

Determining the mass-loss rate of a massive star relies on different methods based either on the estimate of the excess of infrared and millimeter radiation due to the free-free interactions of electrons in the wind (Lamers & Leitherer 1993) or on fits of several spectral lines affected by the wind properties in the Extreme UV (EUV), UV, Optical and Infrared domains presently by means of atmosphere codes.

As already mentioned, the stellar winds are generated by interactions between matter and radiation. This leads to a net radiative acceleration which is sufficient to overcome the gravity. The theory of stellar winds was introduced by Lucy & Solomon (1970) and developed by Castor et al. (1975, hereafter CAK). In this theory, the transfer of momentum, required to accelerate the material outward, occurs by absorption or scattering in many spectral lines. At the typical density of O star winds, the scattering lines dominate. The main idea of the CAK formalism is that the different scattering lines are almost independent and that their radiative acceleration is proportional to that of the electron scattering cross-section times a multiplicative factor. This factor (or *force multiplier*) was expressed by a power law dependent on a dimensionless optical depth which is proportional to the density and inversely proportional to the local velocity gradient. Therefore, the intensity of the radiative acceleration directly depends on the number of absorption lines which are involved in the transfer of momentum. However, the exact amount of acceleration also depends on the efficiency of the transfer or the opacity of the lines (Martins 2004). Indeed, the more optically thick the lines, the more photons will be absorded and the more momentum will be transferred. This theory was however built from a smooth, stationary and spherically expanding outflow. Although this model could reproduce rather well the observed stellar and wind lines, the assumptions on which it relies are no more exact. More recent investigations indeed showed that the stellar winds are variable and that they contain structures in velocity and in density which were not predicted in the standard model.

The study of stellar wind variability indeed allowed to detect small- as well as large-scale structures in the winds of massive stars. The analysis of unsaturated P Cygni profiles of UV resonance lines have showed the presence of "*narrow absorption components*", or NACs, in the blue edge of absorption lines in O-star IUE spectra. These components are caused by an enhanced optical depth. That implies either an increase of the ion fraction, an increase of the wind density, a decrease of the velocity gradient at the location of the NACs or all three changes together (Fullerton 2011). In addition, the NACs are deep absorption lines, which suggests that the absorbing gas is optically thick and covers a significant fraction of the stellar disk (Fullerton 2011). However, the

NACs are also just the final products of the "*discrete absorption components*", or DACs. In fact, DACs are present in a large majority of O-stars, and are observed to accelerate to the blue wing of the profile over timescales of a few days or less, becoming narrower as they approach an asymptotic velocity. These components are recurrent and seem to move from low outflow velocities to the terminal velocity. Their acceleration timescales seem to be linked to the projected rotational velocity of the star. Therefore, it is supposed that the DACs are due to an outward motion of dense clumps in the stellar atmosphere but relatively close to the photosphere (Kholtygin & Kostenko 2000). Moreover, other structures were also found in the stellar winds, the so-called "*Co-Rotating Interaction Regions*" or CIRs. They are large-scale spiral-shaped structures caused by differences between fast and slow streams emerging from adjacent regions of the stellar surface along nearly radial trajectories very close to the stars (Fullerton 2011). These differences are related to temperature variations (a kind of spot) on or close to the stellar surface. These variations could be due to non-radial pulsations and could be responsible for the DACs observed in the UV part of the stellar spectrum (Blomme 2009). If the former conclusion is correct, almost all the O-type stars should be non-radial pulsators (Fullerton 2011).

In addition to these large-scale variations, direct (Eversberg et al. 1998) and indirect (Bouret et al. 2005) evidence highlighted the presence of outward-moving inhomogeneities in the winds of O-type stars. This result showed that the stellar winds can no longer be considered as smooth, homogeneous medii but are actually composed of clumps. The effects of these clumps are relatively important since they affect the relative strength of lines. Indeed, the clumping differently influences the lines such as Hα in the O stars or the emission lines in the WR stars which are dependent on the density-square of the winds than some UV resonance lines or the X-ray profiles which depend on the density of the winds (Hillier 2008, and references therein). Clumping was thus incorporated in atmosphere codes using a volume filling factor approach. In this approach, the clumps are assumed to be optically thin and small relative to the photon mean-free path. In addition, the interclump medium is supposed to be void. Such atmosphere codes thus ignore the fact that the clump density could be function of radial location, or that the clumps could be (partially) optically thick, which would make the stellar winds porous. The inclusion of clumping often implies a significant reduction of the mass-loss rates, generally by a factor between a few and about ten, in comparison to values obtained from an homogeneous wind. However, this determination is still heavily dependent on the assumptions on which the atmosphere codes are based. For instance, the assumption of an empty interclump medium has recently been questioned by Sundqvist et al. (2010). These authors focused on a tenuous interclump medium to correctly model the intensity of several lines in the UV part of O-star spectra. Moreover, the optical thickness of clumps in the stellar winds is also a concept which is not clearly established. This porosity could indeed exist either spatially or in the velocity space (the so-called *vorosity*) of the winds, thus affecting the wind density structure or the wind velocity structure, respectively. Recent investigations by Sundqvist et al. (2011a) and by Hervé et al. (2011, submitted) seem to indicate that the clumps would be spherical rather than flattened, with a "pancake-like" shape, as it was previously proposed by Feldmeier et al. (2003). However, Cohen et al. (2010) argued that an overall decrease of the mass-loss rates of stellar winds could also be possible without the inclusion of porosity effects. Therefore, to estimate with better accuracy the real mass-loss rates of massive stars, it is crucial to address questions on the shape, size or optical depth of these clumps.

Moreover, not all the spectral lines generated in the wind are formed in the same way and therefore do not yield to same estimates for the mass-loss rate. Indeed, the P Cygni resonance profiles in the UV part of the spectrum, sensitive to the ionization balance and the vorosity, show shapes indicating a more or less spherical outflow of matter and allow us to probe mass-loss rates

as low as 10^{-9} $M_\odot$ yr^{-1}. The recombination lines such as Hα are affected by the clumping factor (Hervé et al., submitted) and are therefore less sensitive, only allowing to derive mass-loss rates of at least 10^{-7} $M_\odot$ yr^{-1}. The theory predicts that the mass-loss rate is proportional to the luminosity but depends also on effective temperature or metallicity. These predictions were confirmed for stars with a luminosity larger than $10^{5.2}$ $L_\odot$. Below this value, there exists a serious discrepancy between the observational and the theoretical mass-loss rates. It is described in the literature as the weak-wind problem (Martins et al. 2005b; Puls et al. 2008; Marcolino et al. 2009). This problem is not completely understood, mainly because the UV P Cygni profiles are less reliable for the determination of the mass-loss rate due to the uncertainties on ionization fraction (see e.g. Lamers & Leitherer 1993) while Hα is not sensitive enough to ionization since hydrogen is almost completely ionized in massive star atmospheres. On the theoretical side, physical possibilities to explain this phenomenon continue to be explored but due to the lack of reliable mass-loss rate estimates, no clear solution is yet found. Martins et al. (2005b) showed however that the inclusion of X-ray emission in model atmospheres is crucial to determine an accurate mass-loss rate from UV lines for the weaker wind stars. Moreover this discrepancy does not appear to be related to the metallicity since the same conclusions were found by Martins et al. (2004, 2005b) for the stars of the Small Magellanic Cloud (SMC) and of the Galaxy, respectively. A possible solution to understand the origin of weak winds could be provided by the investigation of the Brα line at 4.1 μm as primary diagnostic of the mass-loss rate (Puls et al. 2008). However, the confirmation of this line as a reliable indicator of mass-loss rate is still lacking.

To summarize, each wavelength domain thus provides clues to explore the structure of stellar winds but a clear unification among all these phenomena is still missing. This situation directly impacts on the exact determination of mass-loss rates of massive stars. Moreover, other ingredients could also affect our understanding of wind mechanisms such as the rotation or the magnetic field.

The present dissertation

This thesis focuses on the observational study of fundamental properties of massive stars and details some mathematical tools for these studies, especially for massive binary systems. Deriving these properties for a single star is not easy but the complexity of the observed spectra of a multiple system makes the analysis of each component even more difficult. We thus apply mathematical methods to separate the individual contributions of stars in a multiple system in order to treat them as if they were single. That allows us to obtain additional information on each component such as their spectral types, their projected rotational velocities or their surface abundances. We moreover implement alternative techniques to map the interactions between the stellar winds in a binary system. In this way, insight into the nature of these interactions can be provided and a better understanding of the winds and of the global structure of the system can be obtained.

The manuscript is organised as follows. Part I contains Chapters 1, 2, 3, and 4 and tackles mathematical tools applied in the analysis of single stars and multiple systems. Chapter 1 deals with the different ways to determine the fundamental parameters of massive stars, single or not. A short description of the CMFGEN atmosphere code is provided as well as the main diagnostic lines used to constrain the fundamental parameters of massive stars. We also describe the properties of binary/multiple systems as well as their evolution.

Chapter 2 presents two different spectral disentangling methods, those of González & Levato (2006) and of Simon & Sturm (1994). The importance of these methods in the determination of

surface abundances and in the understanding of the mass transfer processes is discussed, notably through the study of the evolved system LZ Cep.

In Chapter 3, we describe the Doppler tomography technique based on the Fourier-filtered back-projection. We also develop two other techniques of Doppler tomography based on algebraic methods to decrease some systematic effects linked to the first technique. A comparison between these three methods is provided after having tested them on three evolved systems.

These mathematical methods are finally applied in Chapter 4 to improve our knowledge on a newly-discovered triple system: HD 150136.

CMFGEN and the disentangling methods are used in Part II to investigate in details several O-star populations. In order to determine the parameters of these stars with a better accuracy, we first establish the multiplicity of stars through a dedicated spectral monitoring. Results for the young open cluster NGC 2244 and for the Mon OB2 association are presented in Chapter 5 whilst a group of nineteen O stars belonging to the Cygnus complex is investigated in Chapter 6. In both chapters, we also revise the spectral classification, the projected rotational velocity, the N content as well as the fundamental parameters for all the studied stars. Such analyses devoted to several young open clusters or OB associations offer important clues about the massive star properties and their formation processes.

Finally, the last chapter concludes this thesis, by recalling the main results and by outlining some future prospects.

This work is using data collected with several ground-based (Observatoire de Haute Provence and Observatoire du Pic du Midi in France, San Pedro Martir in Mexico and La Silla in Chile) and space-borne (CoRoT and IUE) observatories. These data led to the submission and the publication of seven papers as first author and five as co-author in refereed journals as well as two poster proceedings (one as first author, and one as co-author). We note moreover that the papers of Martins et al. (2011) and of Blomme et al. (2011) are displayed in the Appendices.

Part I

Mathematical tools in the analysis of binary or multiple systems

Chapter 1

Determination of the fundamental properties of massive stars

The determination of fundamental parameters of massive single stars such as their masses or their radii requires the utilization of atmosphere codes. In this chapter, we first present how we can determine the stellar and wind parameters of single stars by using the CMFGEN (CoMoving Frame GENeral, Hillier & Miller 1998) atmosphere code. In addition, since a majority of the massive stars is actually constituted of stars belonging to binary or multiple systems, we also introduce the physical properties of these systems and we show how to derive them. In astronomy, the study of the orbital motion of binary stars remains to this day the only secure way giving access to their masses, whilst the study of eclipses provides strong constraints on their radii.

1.1 Single stars

1.1.1 The CMFGEN atmosphere code for massive stars

Single stars do not offer the possibility to constrain directly physical parameters such as their masses or their radii. The quantitative analysis of their properties thus mainly relies on the use of model atmospheres. The comparison between synthetic spectra, generated by means of a model atmosphere code, and observed spectra provides information on the stellar and wind parameters (effective temperature, gravity, surface chemical composition, mass-loss rate,...) of isolated stars.

Modelling a massive star is a complex exercise which requires an elaborated code taking into account a lot of physical phenomena. In this context, CMFGEN is certainly one of the most sophisticated atmosphere codes in the modelling of massive stars. CMFGEN produces non-LTE[3] line-blanketed models including the effects of stellar winds. The inclusion of these three main elements considerably improves the models. Indeed,

- **Non-LTE** is an ingredient required to model the atmosphere of hot stars. For objects like the Sun or other low-mass stars, we can assume to first approximation that LTE holds because collisional processes (ruled by the local temperature) dominate over the radiative processes

[3]LTE = Local Thermodynamical Equilibrium.

(such as photo-excitation or -ionization). However, in more massive stars, the radiation field gets sufficiently strong so that radiative processes introduce severe deviations from LTE.

- **Wind extension**: the strong radiative pressure in the atmosphere of massive stars produces an outward motion, a so-called *stellar wind*, of the material in the external layers. Such powerful winds have two consequences. On the one hand, they make the stellar atmosphere particularly extended in comparison to the stellar radius and on the other hand they maintain the stellar atmosphere in a permanent expansion state. Therefore, the problem of radiative transfer cannot be treated with the plane-parallel approximation for the O-type stars and their evolved descendants. It has to be solved by writing in spherical geometry the equations which are necessary for such spherical atmospheres, and by taking into account the expanding motion.

- **Line-blanketing**: to obtain a reliable synthetic spectrum, the models also have to include the effects of line-blanketing i.e., they account for the overlapping lines of many chemical species and notably the heavy elements. The latter act as a "screen" which blocks the radiation. The photons are then more backscattered towards the inner part of the atmosphere, increasing the temperature and thus the degree of ionization in this region. This effect, called *backwarming*, implies that, for a same spectral classification, the model with metals requires a cooler effective temperature to reach the same ionization. Moreover, this cover created by the inclusion of metal lines also leads, in the outer part of the atmosphere, to the reduction of the ionization which is essentially governed by the Extreme UV (EUV) flux.

Spherically symmetric wind models have thus been generated with the CMFGEN atmosphere code. This code iteratively solves the radiative transfer and statistical equilibrium equations in the co-moving frame, thereby avoiding the approximations needed when we work in the observer's frame. The determinations of the temperature and of the level populations are done iteratively through a linearization technique of the equations. Because of the inclusion of the line-blanketing in the models, the number of statistical equilibrium equations is large. In order to reduce this number, and thus improve the accuracy of the solutions, CMFGEN uses a "superlevel" approach. This approach consists in gathering several levels with similar energies and properties to treat them as a unique level in the statistical equilibrium equations. In this way, detailed and reliable model atmospheres including H, He, C, N, O, Ne, Mg, Si, S, Ar, Fe and Ni can be generated with a reasonable computational cost.

To get models as realistic as possible, it is necessary to inject other ingredients into the code:

- **Temperature structure**: radiative equilibrium has been assumed to determine the temperature structure from the equation of energy conservation throughout the atmosphere.

- **Hydrodynamical structure**: unfortunately, CMFGEN does not allow to compute the hydrodynamical structure, thereby still representing one of its main limitations. Consequently, we use the TLUSTY hydrostatic structures in the photosphere coupled to a classical β-law for the wind velocity structure of the form

$$v = v_\infty \left(1 - \frac{R}{r}\right)^\beta$$

with v_∞ the terminal velocity, R the stellar radius and r the distance from the center of the star. We generally choose $\beta = 0.8$ as default value; this represents the typical value

for O dwarfs (Repolust et al. 2004). The hydrostatic and velocity structures are smoothly connected to give a monotonic function. The TLUSTY structures have been constructed from the OSTAR2002 grid of models generated by Lanz & Hubeny (2003) or have been linearly interpolated from this grid for $T_{\rm eff}$ or $\log g$ not initially included.

- **Microturbulence velocity**, independent on the depth, can be included in the computation of the temperature structure and the individual populations. For the calculation of the emerging spectrum in the observer frame, we adopt a turbulence which is radially dependent and which is expressed by the relation

$$v_{\rm turb}(r) = v_{\rm min} + (v_{\rm max} - v_{\rm min}) \cdot \frac{v(r)}{v_\infty}$$

where $v_{\rm min}$ and $v_{\rm max}$ are the minimum and the maximum microturbulent velocities, respectively. For the synthetic spectra, we generally consider $v_{\rm min} = 5$ km s^{-1} and $v_{\rm max} = 0.1 \times v_\infty$.

- **X-ray** emissions in the wind are included in the CMFGEN atmosphere code since they can affect the ionization balance and the strength of key UV diagnostic lines. In CMFGEN, the X-ray emissions are constrained by two parameters: (1) the shock temperature and (2) the volume filling factor which yields the emission level. In practice, however, the X-ray emitted flux coming out of the atmosphere is derived to match the observed $L_X/L_{\rm bol}$ ratio.

Once the model atmosphere has converged, it is necessary to compare it with the observations. To make this comparison easier, a formal solution of the radiative transfer in the observer frame is computed to provide a detailed synthetic spectrum. In order to represent more realistic line profiles, different effects can be included as e.g., the Stark broadening to better represent the H and He lines. An elaborated description of the conception of the atmosphere code or its physical effects can be found in Hillier & Miller (1998) and Martins (2004).

To conclude the description of this atmosphere code, CMFGEN thus requires as main input data:

- Stellar parameters: Luminosity (L), Radius (R), Mass (M) and the chemical abundances.
- Wind parameters: Mass-loss rate ($\dot{M}$), terminal velocity (v_∞), clumping (f, see later p. 16) and the slope of the velocity field (β).
- "Environment" parameters: the input velocity structure, extension of the atmosphere, the number of depth points, the chemical species and ionization stages, the levels/superlevels for each element.
- Modelling parameters which control the inclusion of physical phenomena (X-rays, adiabatic cooling,...), the convergence,...

and produces as output data:

- the atmospheric structure which provides the temperature structure and the populations as well as other information allowing a complete investigation of the model atmospheres.
- an emerging spectrum for the desired wavelength domain.

1.1.2 Main diagnostic lines for the modelling

The main stellar parameters for the massive stars, analysed in the present work, are derived on the basis of the UV and optical spectra of the stars. However, from a more general point of view, the IR region can also be used to provide such fundamental properties. We consider for the analysis of O-type stars the following indicators to fit the observed spectra[4]:

- **The effective temperature** ($T_{\rm eff}$) is computed from the ratio between the He I 4471 and He II 4542 lines but other lines of helium such as He I 4026, He I 4389, He I 4713, He I 5876, He II 4200 and He II 5412 can also be used. Generally, we can reach an accuracy of about 1000 K on the determination of the $T_{\rm eff}$ in the models.

- **The gravity** ($\log g$) is measured from the Balmer line widths. The larger the $\log g$, the broader the Balmer lines. The main diagnostics are thus the Hδ, Hγ and Hβ lines. We stress that Hα is too heavily affected by the stellar winds to serve as a good indicator of gravity. An accuracy of 0.1 dex is generally reached on the measurement of $\log g$.

- **The luminosity**: the best method to constrain the luminosity and $E(B-V)$ is to reproduce the UV-optical-infrared spectral energy distribution (SED) but requires the spectrophotometry from the UV to the IR to adjust the global flux of the star. For massive stars, the UV data are particularly important because the maximum of intensity of these stars is observed in that region. However, when these data are not available, we determine the luminosity from the absolute V magnitude (M_V) and the $T_{\rm eff}$. The latter indeed allows to compute the adequate bolometric corrections for the stars. The expression of the luminosity is then given by

$$\log\left(\frac{L}{L_\odot}\right) = -0.4 \times (V - (3.1 \times E(B-V)) - (5\log d - 5) + BC - 4.75)$$

  where V is the apparent V magnitude, $E(B-V)$ is the colour excess, d is the distance expressed in parsec and BC is the bolometric correction. The accuracy on the luminosity is directly dependent on the uncertainty on the distance of the object, which is usually not well constrained.

- **The mass-loss rate** ($\dot{M}$): The winds of massive stars are mainly characterized by the UV spectrum of the stars and, especially, by the P-Cygni profiles. As a consequence, the C IV 1548–1550 and N V 1240 lines are the best features to constrain the mass-loss rate. In the optical spectrum, the He II 4686 and Hα lines (Puls et al. 1996) can also be used as diagnostics.

- **The terminal velocity** (v_∞) is the velocity reached by the stellar winds at a very large distance. This parameter can be estimated by the blueshifted absorption part of the P-Cygni profiles in the UV spectrum. As mentioned above, the main diagnostic lines are the C IV 1548–1550 and N V 1240 UV P-Cygni profiles. The CMFGEN uncertainty about the v_∞ parameters is close to 100 km s^{-1} for the O-type stars.

- **The clumping**: several investigations about the stellar winds have shown that the winds of O stars are inhomogeneous (see, e.g., Eversberg et al. 1998 for observational evidence and Bouret et al. 2005 for hints from atmosphere modelling). For that reason, the latest implementation of the CMFGEN code includes the clumping which is expressed by means

[4]Further details concerning the analysis of B-type stars or WR stars are provided by Martins (2011).

of a volume filling factor f and which assumes an empty interclump medium. The filling factor follows the law

$$f = f_\infty + (1 - f_\infty)\, e^{-v/v_{cl}}$$

where f_∞ is the maximum clumping factor at the top of the atmosphere, v the velocity and v_{cl} a parameter indicating the position where the wind starts to be significantly clumped. We used the O V 1371 and N IV 1720 lines to constrain the clumping factor. However, for the mid and late O-type stars, no reliable UV diagnostic line for clumping has been identified, making the determination of this parameter impossible for such stars. Consequently, we assume a homogeneous wind for these categories of stars.

The last step before comparing the synthetic spectrum to the observed one is to include rotation and macroturbulence, by convolving successively the theoretical line profiles by a rotation profile (Gray 2005) and a Gaussian profile representing the macroturbulence (Conti & Ebbets 1977; Ryans et al. 2002). The projected rotational velocity ($v \sin i$) is estimated by using the method of Simón-Díaz & Herrero (2007) and the Gaussian profile is proportional to $\exp(-v^2/2v_{\rm mac}^2)$ with $v_{\rm mac}$ the macroturbulent velocity. For fast rotators, the rotation profiles are sufficient to provide a good match to the observed profiles whilst incorporating some amount of macroturbulence to the rotational profiles allows to obtain a better fit of the wings of the lines for the more slowly rotating objects, even though the origin of this extra broadening is unclear. For the high-resolution spectra investigated in the present work, we finally note that the instrumental resolution can be neglected with respect to the macroturbulence component.

1.2 Spectroscopic binaries

Not all stars are single, about 60% of them are actually binary or multiple systems (Sana et al. 2008). Among these systems, some are detectable by eye or with the help of a telescope (the so-called *visual binaries*) but the majority of binary or multiple systems are too distant to be angularly resolved by the current instruments. In order to study them, we must use alternative techniques of observation such as spectroscopy, photometry or more recently interferometry.

By definition, a spectroscopic binary is a system which presents periodic variations of the wavelengths of spectral lines. We are actually seeing the components of a binary system moving towards us or away from us during their orbital motion. These effects indeed result in a shift, the so-called *Doppler shift*, of the spectral lines. This shift gives access to the radial velocity of the stars, i.e., the velocity of the stars projected on the line-of-sight of the observer. The star which is approaching has its spectrum shifted towards the blue whilst, at the same time, the star which is receding sees its spectral lines red-shifted. The difference between the measured wavelength (λ) and the rest wavelength (λ_0) allows to compute the radial velocity (RV) of each star:

$$\frac{\Delta\lambda}{\lambda_0} = \frac{\lambda - \lambda_0}{\lambda_0} = \frac{RV}{c}$$

where c represents the speed of light.

Binaries detected through such Doppler shifts are classified in several categories:

- the **SB1 binaries** in which only the spectrum of one component is visible. In this group, several situations are possible. In the first one, the system is in fact composed of two stars

but the radial velocity of only one star (the most luminous and often the most massive one) can be measured. The second possibility is that the system hosts a compact object (white dwarf, neutron star or black hole) which is not detectable in the observed wavelength domain. The last possibility is that the binary system might actually be a fake and that the observed recurrent variations of the radial velocity are rather due to radial or non-radial pulsations of a single star or to other types of variations.

- the **SB2 binaries** in which the spectra of each component are clearly visible revealing a system composed of two stars that display either comparable luminosities and/or a close spectral classification.
- the **multiple systems**: these systems are composed of more than two stars gravitationally bound and orbiting around their common centre of mass.

Since only one component is observable in the SB1 systems, the measurements of the Doppler shifts and thus of the radial velocities are possible only on that component. By representing these measurements as a function of the orbital phase, the derived radial-velocity curve provides an idea of the mass function of the system:

$$f(M) = \frac{M_S^3 \sin^3 i}{(M_P + M_S)^2} = \frac{K^3}{2\pi G} P(1 - e^2)^{3/2} \tag{1.1}$$

where M_P and M_S are the masses of the primary and the secondary components, respectively (expressed in $M_\odot$), i represents the inclination of the system (in degree) i.e., the angle between the orbital plane and the plane perpendicular to the observer line-of-sight, K is the semi-amplitude of the radial-velocity curve of the primary (in km s^{-1}), P and e are the orbital period (in days) and the eccentricity of the orbit, respectively, whilst G is the universal constant of gravitation. This expression is however not sufficient to determine the minimal masses ($M_P \sin^3 i$ and $M_S \sin^3 i$) of each component. We have to make further assumptions, either on the mass ratio, or by fixing the mass of one component according to, e.g., its spectral classification. For the double-lined binary systems (SB2), the determination of minimal masses is possible because we can derive the radial-velocity curves of both components. The mass ratio of the system is then expressed by $q = M_P/M_S = K_2/K_1$ and, by combining this ratio with Equation 1.1, we can separately compute $M_P \sin^3 i$ and $M_S \sin^3 i$.

The general appearance of the radial-velocity curves also provides an indication on the shape of the orbit. If the latter is circular, the curve is a sine function. On the contrary, when the eccentricity differs from zero, this curve is more or less distorted depending directly on the value of this parameter and on the orientation of the major axis with respect to the line-of-sight. Obtaining a time series of spectra sampling sufficiently well the orbital cycle is thus particularly important in order to determine as precisely as possible the orbital and physical parameters of a binary system.

For systems where the inclination is sufficiently close to 90° or where both components are relatively close, the stars may eclipse each other during the orbital cycle. These systems, called *eclipsing binaries*, are then investigated on the basis of their spectrum but also of their light curve. In such systems, periodic decreases of the light flux of the entire system as a function of time are observed. These decreases happen because one of the components blocks, as seen from the observer's point of view, the flux coming from the other star, thereby decreasing the total flux emitted by the system in that direction. However, few systems have an inclination close to 90°, and only few systems can thus be fully analyzed on the basis of these variations. When

the separation between both components of a binary system is relatively small, another type of photometric variations can occur because of the tidal interactions that deform these stars. This tidal deformation rather gives to the stars a drop-like shape with the extremities facing each other. As the geometrical surface of the stars, as seen from an observer on Earth, changes as a function of the orbital phase, the amount of light received by the observer undergoes smooth modulations, called *ellipsoidal variations*, that are sometimes superposed for the eclipsing binary systems on top of the eclipses when the inclination is sufficiently close to 90°. Some systems which have an inclination such that the components do not eclipse can still present in their light curve these variations due to the deformation of the stars. These ellipsoidal variations are generally of lower amplitude (few hundredths of magnitude) than the variations due to eclipses (few tenths of magnitude) but both are useful to determine the inclination of the systems which is a mandatory parameter to compute the actual masses of the stars.

The spectroscopic techniques nevertheless do not allow to detect all the binary systems. Indeed, one of the conditions to detect Doppler shifts is that the orbital plane is not perpendicular to the line-of-sight of the observer. Other observational biases such as a rather large mass and/or brightness ratio, or a very wide separation (and thus a very large orbital period or a large eccentricity) could also make us miss the detection of binary systems. Therefore, it is crucial to combine spectroscopy with other methods to improve the detection of companions but we come back on that topic in Chapter 5.

1.3 The Roche lobe overflow

The multiplicity of stars is an important ingredient to determine with accuracy the properties and the evolutionary paths of stars. When two stars are gravitationally bound, their evolutionary schemes can indeed be different and more complex than for a single star. The reason is that the evolution of each component can be influenced by the other star notably through mass transfer episodes. Behind this notion of mass transfer is hiding the notion of the *Roche lobe*. The Roche lobe of a star marks the boundary of the attraction zone of the star accounting for the centrifugal force in the rotating frame of reference of the binary system, i.e., the zone where the material orbiting around a star is gravitationally bound to this star. The Roche lobe equipotential surfaces of both stars meet each other at a contact point of relative equilibrium, called the *Lagrange point* L_1 (see Fig. 1.1). The radius of a sphere having the same volume as the Roche lobe is expressed by:

$$\frac{R_{\rm RL}}{a} = \frac{0.49\,q^{2/3}}{0.6\,q^{2/3} + \ln(1 + q^{1/3})} \tag{1.2}$$

with a the semi-major axis and q the mass ratio (Eggleton 1983).

At the beginning of their life, both stars that form a binary system evolve like single stars until one of the components (generally the most massive one) expands during its evolution. This expansion occurs until the star's volume completely fills the volume of its Roche lobe. When this happens, further expansion of the star leads to a flow of material that crosses the region around L_1 and enters into the sphere of influence of the other star. If the radius of the mass gainer is close to that of the Roche lobe, the matter directly hits the stellar surface. Otherwise, it forms an accretion disk around the companion and then slowly falls down on the mass gainer. In the latter case, the gravitational energy, released during the transfer, is transformed into thermal energy and radiated in the UV or X-ray domain. When the majority of the hydrogen-rich envelop has been transferred, the star contracts, stopping the *Roche lobe overflow* phase. Similar expansions and

mass transfer processes can start again with each ignition of a new element in the stellar core until the star explodes. If the supernova does not disrupt the binary, the resulting system is composed of a massive star and a compact object. The companion in turn expands, and might reach its critical radius, thereby generating a second Roche lobe overflow episode. These processes continue until a second supernova explosion occurs, with the consequence of finally disrupting the system in two single runaway pulsars or creating a binary system composed of two neutron stars (De Loore & van Rensbergen 2005). Depending on the status of the stars with respect to their Roche lobe, the binary system is said *detached*, *semi-detached* or *in contact*, respectively, when no star, one star or both stars completely fill up their Roche lobes.

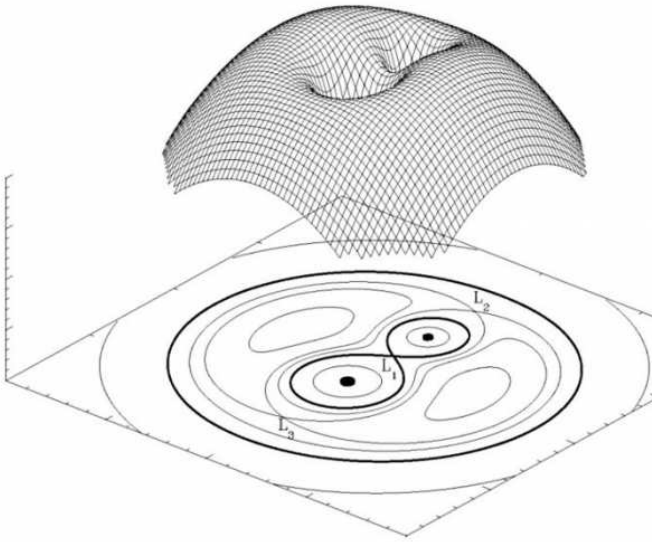

Figure 1.1: 3-D and projected views of theoretical Roche lobes of a binary system. The inner black curve represents the Roche lobes of each star which are in contact at the Lagrange point L_1.

Generally, the Roche lobe overflow can occur at three different evolutionary stages in the life of a star of less than 40 $M_\odot$:

- Case A: The mass transfer begins while the mass loser is still in a core hydrogen burning phase. This situation happens if the star rapidly fills up its critical volume, which implies small Roche lobe volumes. This case mainly occurs when the orbital period ranges between $2-4$ days.
- Case B: The mass loser is in a hydrogen shell burning phase and has not yet ignited helium in its core. The orbital period required to have such a case is estimated between 4 and 1000 days.
- Case C: The mass transfer begins after exhaustion of the helium in the core of the mass loser component. Such a situation requires very large Roche lobes which are only possible for orbital periods of more than 1000 days.

For a star with an initial mass larger than 40 $M_\odot$, the mass decrease is mainly due to its strong LBV-type stellar wind, reducing the importance of Roche lobe overflow as a mass-losing process (Vanbeveren et al. 1998).

The mass transfer processes affect the properties of the stars by changing their masses, their luminosities and their effective temperatures. The exchange of material also modifies the chemical abundances appearing at the surface (hence directly observed in the spectra) as well as the rotational velocity of the gainer and of the loser. Indeed, when a star accretes matter from its companion, the conservation of the total angular momentum implies that its rotational velocity increases and accordingly the rotational mixing in the star increases too. The evolution of the accretor is thus considerably modified (Maeder & Meynet 2000) and can differ from that of the single stars. The analyses of the post Roche lobe overflow binary systems ϕ Per (Bozic et al. 1995) and RY Scuti (Grundstrom et al. 2007) also seemed to reveal the evidence of quasi-conservative processes of mass exchange even though that needs to be confirmed through the analysis of the same kind of systems. As mentioned by Vanbeveren (2011), RY Scuti is composed of an O 9.7I primary and a B 0.5I secondary component. If we referred to the values given by Martins et al. (2005a) of stellar parameters as a function of the spectral classification, we find for the primary a typical mass of about 25 $M_{\odot}$ whilst the secondary's mass should be smaller than 20 $M_{\odot}$. However, the masses derived by Grundstrom et al. (2007) are equal to about 7 $M_{\odot}$ and 30 $M_{\odot}$ for the primary and secondary stars, respectively. The primary star has thus lost about 18 $M_{\odot}$ and, at the same time, the secondary has gained about 10 $M_{\odot}$. After the mass transfer, the total mass of the system has thus decreased by only about 10–20%, revealing a quasi-conservative mass exchange.

Through these examples, we see how it is important to constrain with accuracy the multiplicity as well as the stellar parameters of individual components to understand the evolution processes in the entire binary system. Therefore, we present in the following two mathematical methods to disentangle the spectra of each star in a binary system. In this way, the determination of the individual parameters of each component can be done as if the stars were single. In addition, we apply these techniques on a third example of system in a post Roche lobe overflow phase: LZ Cep.

Chapter 2

Spectral disentangling

Enhancing our understanding beyond the determination of the orbital parameters requires to individually study the spectra of each component of a multiple system. In the last two decades, several methods were thus developed to separate the individual spectral contributions of each star to analyse them as if they were single stars. These techniques enable to determine the physical properties of each component by means of model atmospheres such as CMFGEN. By investigating the effective temperature, the $\log g$, the projected rotational velocity or the surface chemical abundances of these objects, new observational evidence could be brought to characterize the interactions in close binary systems such as the possible mass transfer between the two stars or the existence of rotational mixing.

Even though a variety of different reconstruction techniques exist, they are however not all based on the same concepts. Three categories can be distinguished as mentioned by Pavlovski et al. (2009):

- the **spectral separation** in which the spectrum of each component is reconstructed from a timeseries of observed spectra for corresponding radial velocities and light factors of the components.

- the **spectral disentangling** in which a timeseries of observed spectra provides the individual contributions of the components as well as the orbital elements of the binary systems.

- the **spectroastrometric splitting** that is a technique which uses the spatial information present in a longslit spectrum. It cannot only be applied to detect binary systems, it can also deconvolve the observed spectrum into the individual spectra of its components.

In the frame of the present work, we focus more deeply on the *Iterative Doppler differencing* technique developed by González & Levato (2006) and on the *Spectral disentangling in wavelength domain* technique implemented by Simon & Sturm (1994). The former technique is the most used in this thesis. However, the latter one is applied as a check of the final product obtained by the former method. Therefore, both are consequently described in Section 2.1 and Section 2.2, respectively. It should be noted however that detailed reviews (e.g., Gies 2004; Hensberge & Pavlovski 2007; Hadrava 2009; Pavlovski et al. 2009) exist to describe how other techniques are working.

2.1 Iterative Doppler differencing

To analyse with more details the binaries reported in the next chapters, we thus mainly apply a disentangling program based on the method of González & Levato (2006) and initially introduced by Marchenko et al. (1998). The technique allows not only to compute the spectra of each component, but also to improve the measurements of the radial velocities especially at phases where both stars are heavily blended.

Handling spectra for an easier determination of the radial velocities requires to express them in logarithmic scale, i.e., as a function of $x = \ln \lambda$ rather than λ. The Doppler shift is then given for a line of rest wavelength λ_0 under the following linear form:

$$\begin{aligned} \ln \lambda &= \ln\left[\lambda_0\left(1+\frac{v}{c}\right)\right] \\ &= \ln \lambda_0 + \ln\left(1+\frac{v}{c}\right) \\ &\cong \ln \lambda_0 + \frac{v}{c} \\ \Rightarrow x &\cong x_0 + \frac{v}{c} \end{aligned}$$

We then remove the interstellar lines by setting the wavelength regions where they appear to the continuum (i.e., to unity). Therefore, the observed spectrum of a binary system can be summarized as a sum of the contributions of both stellar components, each one shifted by its own radial velocity. This can be written as:

$$S\,(x) = A\left(x - \frac{v_A(\phi)}{c}\right) + B\left(x - \frac{v_B(\phi)}{c}\right)$$

by assuming that $A(x)$ and $B(x)$ are the spectra of the primary and the secondary stars, respectively, in the heliocentric frame of reference whereas $v_A(\phi)$ and $v_B(\phi)$ are the radial velocities of the primary and secondary stars, respectively, measured at the orbital phase ϕ.

The basic idea to obtain the individual spectra of each component is to use alternatively the spectrum of one component (shifted by its radial velocity) in order to subtract it from the observed spectra so as to calculate the mean spectrum of the other component. In practice, it is however not necessary to know A or B to start the iteration process. An initial approximation associating a flat spectrum to the component B can be applied as starting point for the iterations. In this case, the spectrum A contains at the beginning all the spectral features of the observed spectra. The algorithm then iteratively computes the contributions of each component.

Each iteration is divided in four steps:

1. we first estimate the current best approximation of the spectrum of the secondary star. For this purpose, we sum to the secondary the spectral features of each observed spectrum shifted by the radial velocity of the secondary at the corresponding phase, and weighted by the number of observations in the dataset. Then, we subtract for each observed spectrum the weighted contribution of the primary component shifted by its radial velocity,

2. we then generate temporary templates by removing the freshly calculated secondary spectrum from the observed spectra which means to compute the difference $S_i(x) - B(x - v_B(\phi_i)/c)$. These templates are then used to refine, by means of a cross-correlation technique, the measurements of the Doppler shifts for the primary component,

3. we finally proceed similarly as 1) to calculate the current best approximation of the spectrum of the primary.

4. we compute the radial velocities of the secondary star by a similar technique as 2).

The final spectrum of the primary star is thus built from a series of successive shifts of the observed spectra to which are removed the weighted individual spectrum of the other component. The resulting spectrum is thus summarized as an average of the observed spectra from which the secondary spectrum shifted by the appropriate radial velocity has been eliminated (González & Levato 2006). Its expression is given by

$$A(x) = \frac{1}{n}\sum_{i=1}^{n}\left[S_i\left(x + \frac{v_A(\phi_i)}{c}\right) - B\left(x + \frac{v_A(\phi_i)}{c} - \frac{v_B(\phi_i)}{c}\right)\right]$$

and similarly for the secondary

$$B(x) = \frac{1}{n}\sum_{i=1}^{n}\left[S_i\left(x + \frac{v_B(\phi_i)}{c}\right) - A\left(x + \frac{v_B(\phi_i)}{c} - \frac{v_A(\phi_i)}{c}\right)\right].$$

Through this iterative resolution process, the residuals of the lines of one component that still contaminate the spectrum of the other component are thus at each iteration reduced by a factor of $1/n$ where n represents the number of observations. The convergence and the quality of the disentangled spectra are directly dependent on the quantity of the observed spectra. In general, the signal-to-noise ratio of the primary spectrum is better than those of the observed spectra, the number of input data thus mainly influences the signal-to-noise of the secondary star (Hensberge & Pavlovski 2007). To summarize, the more input data, the better the signal-to-noise of the secondary spectrum relative to those of the observed spectra.

To estimate the radial velocities of each component, we use a cross-correlation technique. This process is based on the construction of a reference spectrum taking into account the characteristic line positions on the wavelength domain taken into account for the disentangling. We investigate a velocity domain going from $-v$ to v with a step Δv. This region is chosen sufficiently large in order not to minimize the effects of the edges. At each step Δv, the reference spectrum is shifted by a Δv velocity and "sliced" on the same velocity domain as the component spectrum (i.e., outside this domain the result of the cross-correlation is equal to zero). A cross-correlation function is then computed between the reference and the component spectra. When many coincidences exist between both spectra, a (very) strong peak results (Hill 1993). The selected final radial velocity thus corresponds to the position, in the velocity domain, of the stronger peak.

In this thesis, we also adapt this method to separate the spectra of either a triple system or a binary system with the interstellar lines as third (non-moving) component. In this context, the observed spectra are described according to

$$S(x) = A\left(x - \frac{v_A(\phi)}{c}\right) + B\left(x - \frac{v_B(\phi)}{c}\right) + C\left(x - \frac{v_C(\phi)}{c}\right).$$

This technique is a priori similar to that for a binary system. We first approximate the third component with a flat spectrum. After this initialisation, we successively use the mean spectrum of one component, shifted by its radial velocity, and the mean spectrum of the second component, also shifted by its own radial velocity, to subtract them from the observed spectra in

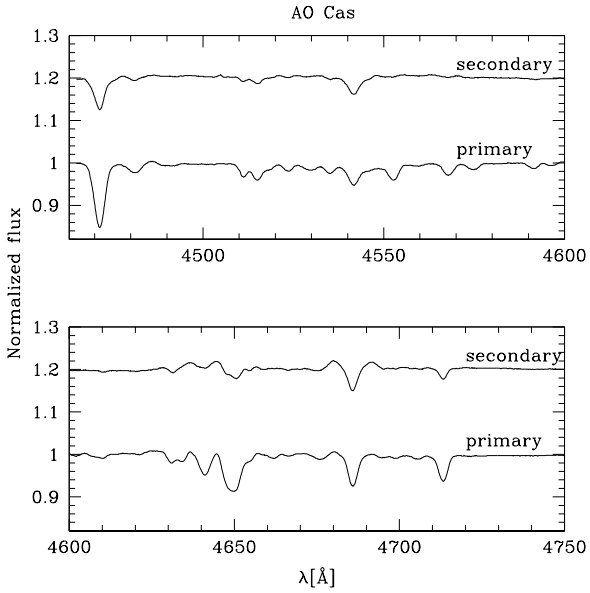

Figure 2.1: Normalized disentangled spectra of AO Cas in the [4465 – 4750]Å wavelength domain. The secondary spectrum is vertically shifted for clarity.

order to compute the mean spectrum of the third component. At each iteration, the temporary templates obtained from the observed spectra at which the contributions of two components have been subtracted are computed. A cross-correlation technique is applied on these templates to improve the determination of the radial velocities of the third object. One iteration is finished when this process is applied for each component of the system.

This iterative algorithm is straightforward, relatively efficient and cheap in CPU time. Generally, less than 10 iterations are sufficient to achieve convergence (González & Levato 2006). It also allows to separate the components on a rather large wavelength domain. At the end of the program, each component is thus computed as a mean spectrum over the orbital cycle and is expressed by

$$A(x) = \frac{1}{n}\sum_{i=1}^{n}\left[S_i\left(x+\frac{v_A(\phi_i)}{c}\right) - B\left(x+\frac{v_A(\phi_i)}{c}-\frac{v_B(\phi_i)}{c}\right) - C\left(x+\frac{v_A(\phi_i)}{c}-\frac{v_C(\phi_i)}{c}\right)\right]$$

$$B(x) = \frac{1}{n}\sum_{i=1}^{n}\left[S_i\left(x+\frac{v_B(\phi_i)}{c}\right) - C\left(x+\frac{v_B(\phi_i)}{c}-\frac{v_C(\phi_i)}{c}\right) - A\left(x+\frac{v_B(\phi_i)}{c}-\frac{v_A(\phi_i)}{c}\right)\right]$$

$$C(x) = \frac{1}{n}\sum_{i=1}^{n}\left[S_i\left(x+\frac{v_C(\phi_i)}{c}\right) - A\left(x+\frac{v_C(\phi_i)}{c}-\frac{v_A(\phi_i)}{c}\right) - B\left(x+\frac{v_C(\phi_i)}{c}-\frac{v_B(\phi_i)}{c}\right)\right]$$

However, this disentangling technique must be considered with caution when we analyse an eclipsing binary. Some observed spectra could indeed be observed during eclipses and the light ratios at these phases would thus be different than those estimated at the other phases (out of eclipses). Therefore, the resulting spectra could be erroneous because they would remove from the observed spectra the secondary (resp. primary) component while its star would be hidden by the primary (resp. secondary) star.

By keeping this restriction in mind, we have applied this method to several binary systems

although, for some of them, no photometric data was available. We analyze later some binary systems such as, for example, LZ Cep (in Section 2.3), HD 48099 (in Section 5.2.1) or some systems in the Cygnus region (in Section 6.1). Other analyses are not presented in the present work such as, for example, 29 CMa or AO Cas (see Fig. 2.1 for AO Cas) since these investigations were already reported in Linder (2008). Furthermore, the modified version of this program is also applied on the triple system, HD 150136, and the full analysis of this system is described in Chapter 4.

2.2 Spectral disentangling in wavelength domain

In order to have an alternative method to compare the obtained results with the *Iterative Doppler differencing* program, we also implement another technique of spectral disentangling. This reconstruction method, called *Spectral disentangling in wavelength domain*, is based on the resolution of the matricial equation $Ax = y$. All the observed spectra (t_k) are concatenated into the vector y whilst the spectra of both components are gathered to form the vector x. The matrix A contains the global information about the Doppler shifts and the light factors[5] of each component. We thus have to know the radial velocities and the light factors of both components with accuracy in order to obtain reliable results. The system can be written as

$$\begin{pmatrix} A_{11} & A_{12} \\ \vdots & \vdots \\ A_{N1} & A_{N2} \end{pmatrix} \cdot \begin{pmatrix} x_1 \\ x_2 \end{pmatrix} = \begin{pmatrix} y_1 \\ \vdots \\ y_N \end{pmatrix}$$

where x_i, y_j are themselves vectors and N corresponds to the number of exposures (generally $N \geq 2$). Moreover, the matrix A is organised in blocks A_{ji}. Their structures are rather simple, each block A_{ji} is built with only one diagonal which is shifted by a number of columns corresponding to the Doppler shift of the component i at the observation t_j and multiplied by its light factor l_{ji}. These submatrices are written under the following form

$$A_{ji} = \begin{matrix} \overleftarrow{\qquad\qquad v_i(t_j) \qquad\qquad} \overrightarrow{\qquad} \end{matrix} \begin{pmatrix} 0 & \dots & 0 & l_{ji} & 0 & \dots & 0 & 0 \\ 0 & \dots & 0 & 0 & l_{ji} & 0 & \dots & 0 \\ 0 & & \dots & 0 & 0 & l_{ji} & \dots & 0 \\ \vdots & \vdots & \vdots & \vdots & \vdots & \ddots & \ddots & 0 \\ 0 & 0 & & \dots & 0 & 0 & 0 & l_{ji} \end{pmatrix}$$

The bins of Doppler shifts are computed by taking the maximum difference between the radial velocities of a same component and by dividing this interval by the step of the observed spectra converted in logarithm of the wavelength (see Section 2.1). The sum of all these bins with the number of points in the spectra defines the number of columns of the matrix A associated to one component. We proceed exactly in the same way for the other star, thereby giving the total number of columns in the matrix A. It thus appears that the vector x_i must be longer than the subvector y_j because the number of columns in the matrix A is larger than the number of points in the observed spectra constituting the vector y.

To obtain the individual spectrum of each component, we have to resolve the linear system by inverting the matrix A. However, for a number of spectra larger than the number of stellar

[5]The light factor of a component is the light contribution of this component relative to the light of the entire system.

components, this matrix is generally huge, sparse, rank deficient and especially over-determined i.e., there exist more equations than unknowns. As a consequence, computing directly its inverse is not possible. To obtain a solution, we hence have to use algebraic methods such as the Singular Value Decomposition (SVD, Simon & Sturm 1994) or, what we have done, the pseudo-inverse expressed by

$$x = \left(A^T A\right)^{-1} A^T y$$

Handling big matrices in computer programs requires a lot of memory but also a lot of CPU time. This technique is thus particularly appropriate for small wavelength domains. Moreover, it is straightforward to generalize it to multiple systems even though this generalization involves an increase of the number of columns in the matrix A, and accordingly, a huge requirement of memory. The disentangling program can also be transformed into an iterative process to determine, in addition to the individual spectra, the orbital parameters of the system. In this case, a least squares solution that minimizes the norm of the residuals $r = ||Ax - y||^2$ is required.

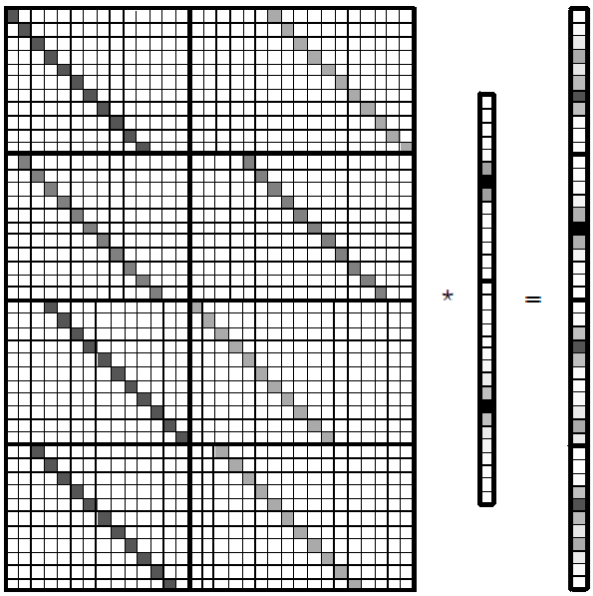

Figure 2.2: Schematic representation of Ilijić (2003) of the linear system $Ax = y$. The different blocks and spectra are separated with a bold face black line. The color scale within the matrix and the vectors is white (black) for zero (unity).

A schematic view given by Ilijić (2003) and shown in Fig. 2.2 exhibits a density plot explaining the structure of the matricial system. This representation is made on the basis of four observed spectra which are concatenated in the right hand term. The Doppler shifts and the light factors used in Fig. 2.2 are respectively

$$RV = \begin{pmatrix} 1 & 0 & -2 & -1 \\ -2 & 0 & 4 & 2 \end{pmatrix} \quad \text{and} \quad l = \begin{pmatrix} \frac{2}{3} & \frac{1}{2} & \frac{2}{3} & \frac{2}{3} \\ \frac{1}{3} & \frac{1}{2} & \frac{2}{3} & \frac{2}{3} \end{pmatrix}$$

This example gives a good representation of the method but also exhibits its limits. Indeed, we clearly see that the observed spectra have to be firstly treated by adjusting their continuum to zero and by transforming the absorption lines into emission ones. In this way, we only take into

account the spectral contributions of both stars and we exclude the possible contamination of the continuum in the determination of the solution. Moreover, in this example, all the observed spectra are resampled to have the same number of pixels. Although this interpolation is not necessary, it avoids a more complex resolution process. We also clearly see in this representation that the shifts due to the radial velocities generate an increase of the number of columns in each block of the matrix A. It implies that the resulting spectra do not have the same size as the observed ones. Finally, the form of the submatrices also implies that, when the radial velocities are not integer values, the Doppler shifts must be rounded to an integer multiple of the sampling step (Hadrava 2009).

The method of *Spectral disentangling in wavelength domain* has been tested on the data of Cyg OB2#9. As an illustration, we present the individual spectra computed by this method in Fig. 2.3 from a timeseries of data collected with different instruments (Nazé et al. 2010). We focus the disentangling on the small [5860 – 5900] Å wavelength region, i.e., on the He I 5876 line. We have also tested the *Iterative Doppler differencing method* on these data, but having only one line to build the cross-correlation mask is not sufficient to obtain an accurate determination of the radial velocities and to allow the program to converge towards a solution. As a consequence, where the technique based on the method of González & Levato (2006) fails, that of Simon & Sturm (1994) can provide promising results.

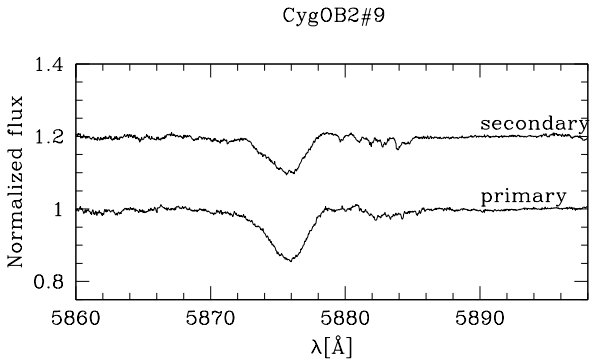

Figure 2.3: Normalized disentangled spectra of Cyg OB2#9 in the [5860 – 5900] Å wavelength domain. The secondary spectrum is vertically shifted for clarity.

Finally, the quality of the individual spectra depends on two conditions, one linked to the observations and one specific to the physics of the studied system. Indeed, obtaining the results as accurate as possible with a disentangling technique requires a rather good sampling of the data on the orbital cycle (i.e., in phase or in radial velocity) but also that the orbital motion of the system produces a large enough Doppler shift to provide a complete view of the width of the lines of both components. In addition, the normalization process of the observed spectra has to be as perfect as possible to limit the creation of oscillations in the continuum of the individual spectra, especially marked around the Balmer lines of the fainter component. That could indeed strongly affect the real determination of the gravity of each component, and at the same time, the determination of the spectroscopic masses i.e., masses generated from the radius and the $\log g$ of the stars.

2.3 Application to the evolved binary system LZ Cep

As shown in the present chapter, the disentangling technique allows to investigate with more precision the individual spectra of each component of a binary system. In this context, a detailed analysis of the two components of LZ Cep is performed. LZ Cep (HD 209481) is a double-lined spectroscopic binary system with a period of 3.070507 days (Kameswara Rao 1972). In addition to the spectroscopic variations due to the orbital motion, this star also presents ellipsoidal variations in its light curve. We have collected a dataset of 10 high-resolution optical spectra of this binary with NARVAL over 15 days in order to constrain the evolutionary status of this system. Moreover, we have retrieved the Hipparcos light curve of this star and we model it by using the NIGHTFALL program[6].

The investigation of the spectroscopic data confirms the previous analyses made by Howarth et al. (1991) and Harries et al. (1998) on the orbital solution. The investigation of the light curve results in an inclination of about 48–50° and confirms the semi-detached configuration of the system. We ignore however whether it is the primary star or the secondary one which fills up its Roche lobe.

The individual spectra of each component are also generated with the disentangling program based on the technique of González & Levato (2006) and we check the resulting spectra by comparing them with those computed from the method of Simon & Sturm (1994). These spectra give us an accurate estimate of the spectral classification of both components, revealing a system composed of an O 9III and of an ON 9.7V for the primary and the secondary star, respectively. The orbital solution and the light curve analysis imply real masses of about 16 $M_{\odot}$ and 6.5 $M_{\odot}$ for the primary and secondary stars, respectively. The models computed with the CMFGEN atmosphere code indicate that the secondary component is strongly enriched in helium and nitrogen and depleted in carbon and oxygen. The surface abundances, the luminosity ($\log(L/L_{\odot}) = 4.69$) and the mass derived for the secondary are typical of Wolf-Rayet stars even though its spectral classification is ON 9.7 V. These properties thus reveal a secondary component on the He-burning sequence which would have lost most of its envelope through a mass transfer between both stars. However, this mass exchange has to be very inefficient to account for the chemical appearance of the primary star. LZ Cep would thus be an example of a post Case A mass transfer.

The determination of the surface abundances for evolved massive systems is rather scarce, but it thus allows to confirm the WR-like appearances of the mass donor (but without the characteristic mass-loss rate of a WR star). Moreover, the analysis of LZ Cep exhibits that both stars have lost mass through the Roche lobe overflow process. Evolved systems such as HD 149404 (Rauw et al. 2001) and LSS 3074 (Gosset et al. 2005) also display the same phenomenon. Nonetheless, the question of the mass conservation through a Case A Roche lobe overflow episode remains unanswered. Indeed, as we already mentioned, other analyses of post Roche lobe overflow systems such as ϕ Per (Bozic et al. 1995) and RY Scuti (Grundstrom et al. 2007) favoured a quasi-conservative mass exchange. Consequently, LZ Cep is a particularly interesting evolved system since it provides additional observational constraints to theoretical binary evolutionary models.

The full analysis of the LZ Cep binary system is published in Mahy et al. (2011b, see paper hereafter).

[6]for more details, see the Nightfall User Manual by Wichmann (1998) available at the URL: `www.hs.uni-hamburg.de/DE/Ins/Per/Wichmann/Nightfall.html`

A&A 533, A9 (2011)
DOI: 10.1051/0004-6361/201116993

Astronomy & Astrophysics

The two components of the evolved massive binary LZ Cephei

Testing the effects of binarity on stellar evolution

L. Mahy[1], F. Martins[2], C. Machado[2], J.-F. Donati[3], and J.-C. Bouret[4,5]

[1] Institut d'Astrophysique et de Géophysique, Université de Liège, Bât. B5C, Allée du 6 Août 17, 4000 Liège, Belgium
e-mail: mahy@astro.ulg.ac.be
[2] LUPM–UMR 5299, CNRS & Université Montpellier II, Place Eugène Bataillon, 34095 Montpellier Cedex 05, France
[3] IRAP–UMR 5277, CNRS & Univ. de Toulouse, 14 Av. E. Belin, 31400 Toulouse, France
[4] LAM–UMR 6110, CNRS & Université de Provence, rue Frédéric Joliot-Curie, 13388 Marseille Cedex 13, France
[5] NASA/GSFC, Code 665, Greenbelt, MD 20771, USA

Received 31 March 2011 / Accepted 29 June 2011

ABSTRACT

Aims. We present an in-depth study of the two components of the binary system LZ Cep to constrain the effects of binarity on the evolution of massive stars.
Methods. We analyzed a set of high-resolution, high signal-to-noise ratio optical spectra obtained over the orbital period of the system to perform a spectroscopic disentangling and derive an orbital solution. We subsequently determine the stellar properties of each component by means of an analysis with the CMFGEN atmosphere code. Finally, with the derived stellar parameters, we model the Hipparcos photometric light curve using the program NIGHTFALL to obtain the orbit inclination and the stellar masses.
Results. LZ Cep is a O 9III+ON 9.7V binary. It is as a semi-detached system in which either the primary or the secondary star almost fills up its Roche lobe. The dynamical masses are about 16.0 $M_{\odot}$ (primary) and 6.5 $M_{\odot}$ (secondary). The latter is lower than the typical mass of late-type O stars. The secondary component is chemically more evolved than the primary (which barely shows any sign of CNO processing), with strong helium and nitrogen enhancements as well as carbon and oxygen depletions. These properties (surface abundances and mass) are typical of Wolf-Rayet stars, although the spectral type is ON 9.7V. The luminosity of the secondary is consistent with that of core He-burning objects. The preferred, tentative evolutionary scenario to explain the observed properties involves mass transfer from the secondary – which was initially more massive- towards the primary. The secondary is now almost a core He-burning object, probably with only a thin envelope of H-rich and CNO processed material. A very inefficient mass transfer is necessary to explain the chemical appearance of the primary. Alternative scenarios are discussed but they are affected by greater uncertainties.

Key words. stars: early-type – binaries: general – stars: fundamental parameters – stars: winds, outflows

1. Introduction

The binary fraction of massive stars is not tightly constrained, but studies of young open clusters indicate that it can easily reach 60% (e.g. Sana et al. 2008). The effects of binarity on stellar evolution depend not only on the properties of the components, but also on the mass ratio, the separation, and the eccentricity. Consequently, their study is complex, requiring the exploration of a large parameter space (de Mink et al. 2011). In the case of young systems with large separations, the components of the binary evolve independently, following single-star evolution (Pavlovski & Hensberge 2005). In evolved binary systems, the evolutionary scheme is completely different. If Roche lobe overflow occurs, the surface chemistry and rotational rate of the components are deeply affected. In particular, the mass gainer is expected to show large nitrogen surface abundance enhancements (Langer et al. 2008). To more clearly understand the physics of binary systems and test the predictions of theoretical models, it is thus important to quantitatively analyze the properties of massive binary systems with well-constrained orbital parameters.

LZ Cep (HD 209481) is a double-lined spectroscopic binary system composed of a primary component with a spectral type O 8.5III and an O 9.5V secondary (Conti & Alschuler 1971). The projected rotational velocities were reported to be close to 155 km s^{-1} and 105 km s^{-1} by Howarth et al. (1991). The period of the system was found to be 3.070508 d by Kameswara Rao (1972), a value that was confirmed by Howarth et al. (1991) and Harries et al. (1998). The eccentricity estimated by Howarth et al. (1991) is about 0.031. Although small, this is significant enough to not be neglected. According to Lucy & Sweeney (1971), the null hypothesis of a circular orbit can be rejected with a significance level of about 0.05. However Harries et al. (1998) determined an orbital eccentricity close to zero in their orbital solution ($e = 0.017 \pm 0.084$), implying that the circularization of the system is not clearly established. From the photometric point of view, LZ Cep is not an eclipsing system but ellipsoidal variations are clearly visible in the light curve. The photometric analysis indicates that this binary is an evolved system (Hill et al. 1976) with a secondary component that fills up its Roche lobe. Hence, the system is most likely to be in a configuration of post case A mass transfer i.e., a system where the mass transfer happened while both components were still in a hydrogen-burning core phase (Howarth et al. 1991).

LZ Cep is thus a target of choice for the study of the effects of binary interactions and their impacts on massive star evolution. The present paper is organized as follows. Section 2 presents the journal of observations and the data-reduction technique. We

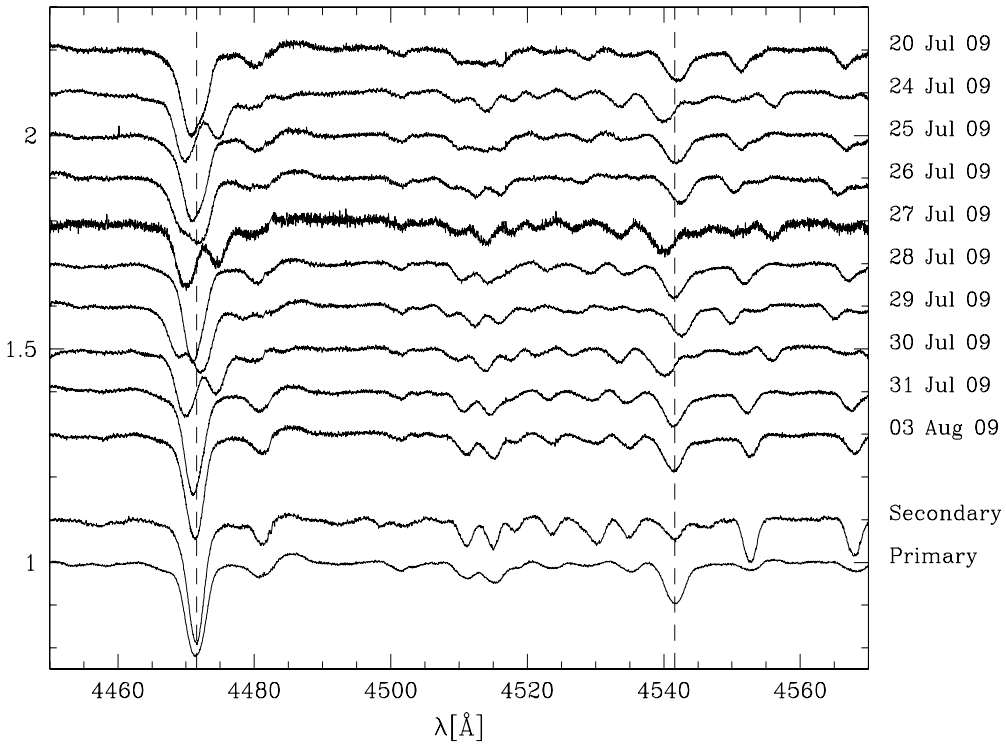

Fig. 1. NARVAL spectra between 4450 and 4570 Å. The upper part of the figure presents the daily spectra. The lower two spectra are the results of the spectral disentangling process. The two vertical dash lines correspond to the rest wavelengths of the He I 4471 and He II 4542 lines.

then devote Sect. 3 to the determination of the orbital solution and the spectroscopic classification. Using the radial velocities obtained from the orbital solution, we apply a disentangling program to separate the individual spectra of both components. In Sect. 4, we apply the CMFGEN atmosphere code on the separated spectra to determine the main stellar and wind parameters as well as the surface abundances of each star. These parameters provide us with information about the stars' evolutionary status. The last step in our investigation is reported in Sect. 5 and consists of the analysis of the Hipparcos light curve, which provides the system inclination and consequently the real masses of the stars. All the parameters and results determined in the present paper are discussed in Sect. 6. Finally, we present our conclusions in Sect. 7.

2. Observations and data reduction

LZ Cep was observed with the spectropolarimeter NARVAL mounted on the Télescope Bernard Lyot (TBL) located at the Pic du Midi observatory in the French Pyrenees. Table 1 gives the journal of observations. A total of ten spectra over a period of 14 d were obtained between 2009 July 20 and 2009 August 3 (Fig. 1). This corresponds to more than four orbital periods of the system. The signal-to-noise ratio (*SNR*) per 2.6 km s^{-1} velocity bin is between 300 and 1300 depending on weather conditions and wavelength. A spectral resolution of 65 000 is achieved. The data were automatically reduced with the Libre ESpRIT package (Donati et al. 1997) installed at TBL. An exhaustive description of the reduction procedure is given in Donati et al. (1997) and we refer to this paper for information.

3. Disentangling and orbital solution

The previous analyses of Howarth et al. (1991) and Harries et al. (1998) focused on the orbital elements of the system. In the present paper, we go one stage further and study the properties of the individual components. The first step is to separate the spectra of each star. We applied an iterative disentangling method consisting of using alternatively the spectrum of one component (shifted by its radial velocity) and subtracting it from the observed spectra to determine the mean spectrum of the other component. The separated spectral components, corrected by the brightness ratio (see below), are shown in Fig. 1 (the two bottom spectra) for the range 4450–4570 Å and in Figs. 3 and 4 (black lines) for a wider spectral band. This disentangling method, inspired by González & Levato (2006), requires the approximative knowledge of the radial velocities as input. We first measured these radial velocities by fitting two Gaussian profiles to the observed spectra. The cross-correlation technique was subsequently used by the disentangling program to refine the radial velocities from the disentangled spectra. This method ensures that radial velocities are obtained at all orbital phases, including those where the lines are heavily blended. The cross-correlation masks were built on a common basis of the Si IV 4089–4116, He I 4388, 4471, 4713, 4921, 5015, 5876, 6678, C IV 5801–5812, O III 5592, and Hα lines. For the primary component, we added the He II 4200, 4542, 5412 lines indicating, by the way, its earlier spectral type (Conti & Alschuler 1971). The list of the radial velocities obtained by cross-correlation is reported in Table 1.

We checked these radial velocities by computing the orbital solution of LZ Cep. For this purpose, we took into account the well-known period of the system ($P_{\rm orb}$ = 3.070507 d, Petrie 1962) and used the Liège Orbital Solution Package (LOSP, Sana & Gosset, A&A, submitted). This software is based on the generalization of the SB1 method of Wolfe et al. (1967) to the SB2 case along the lines described in Rauw et al. (2000) and Sana et al. (2006a). We assigned a weight of 1.0 to all the measurements. Figure 2 represents the fitted radial velocity curves as a function of the phase. We added, for comparison, the radial velocities measured from the *IUE* spectra by Harries et al.

Table 1. Journal of the observations.

Date	HJD [d]	Exposure time [s]	*SNR*	RV_P [km s^{-1}]	RV_S [km s^{-1}]
20 Jul. 2009	2 455 033.48549	2700	330–750	26.7	−100.1
24 Jul. 2009	2 455 037.48790	3300	630–1320	−96.6	211.8
25 Jul. 2009	2 455 038.49492	2700	480–1000	26.3	−95.8
26 Jul. 2009	2 455 039.49494	2700	430–900	45.7	−153.9
27 Jul. 2009	2 455 040.49228	2700	160–350	−98.4	206.6
28 Jul. 2009	2 455 041.48290	2700	550–1180	10.0	−66.0
29 Jul. 2009	2 455 042.49901	2700	640–1330	52.1	−179.1
30 Jul. 2009	2 455 043.47908	2700	560–1150	−95.8	199.2
31 Jul. 2009	2 455 044.49895	2700	570–1230	−4.4	−40.3
03 Aug. 2009	2 455 047.46335	2700	500–1080	−23.8	5.3

Notes. The HJD is measured at mid exposure. The signal-to-noise ratio (*SNR*) is given in the wavelength range 4000–6700 Å and depends on the exact wavelength. Radial velocities are obtained by cross-correlation and have an error of 5 km s^{-1}.

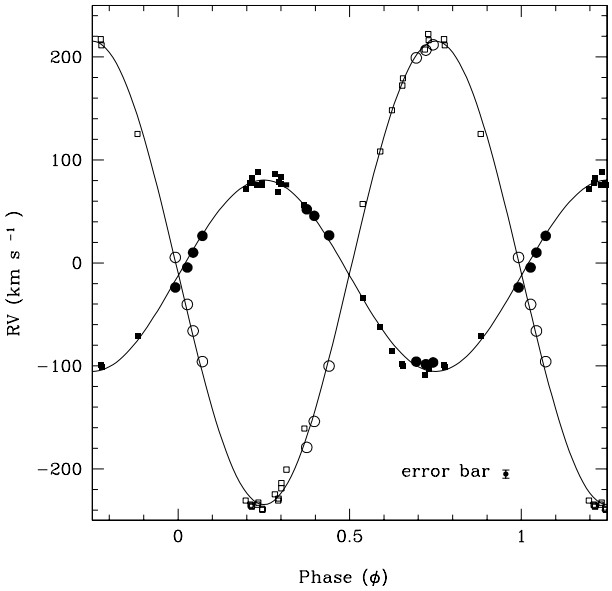

Fig. 2. Radial velocities as a function of orbital phase. The solid (open) symbols are for the primary (secondary). The circles are the data of the present paper, whilst the squares are the data of Harries et al. (1998).

(1998). To compare both datasets, it was necessary to shift the radial velocities of Harries et al. (1998) by −9.4 km s^{-1} to obtain the same systemic velocity as that measured for our dataset. We represent these data by squares in Fig. 2. T_0 is the phase of the conjunction with the primary star in front. We tried to include a non-zero eccentricity in the orbital solution but the fit residuals are smaller for a zero eccentricity, indicating that the system is circularized. Previous studies (Howarth et al. 1991; Harries et al. 1998) have shown that this system could be in a post case A mass transfer phase (see also Sect. 5). It is therefore likely that the tidal interactions have circularized that system. Other differences between our solution and that of Howarth et al. (1991) are notably a smaller value of K_2, lower minimum masses, and a higher mass ratio. The orbital parameters are listed in the upper part of Table 2.

Finally, in the framework of the study of wind parameters (see Sect. 4), we also decided to separate the *IUE* spectra in the range 1200–1800 Å. We thus determined, from the orbital solution, the values of the radial velocities corresponding to the *IUE* spectra. We fixed these radial velocities in the disentangling program to obtain the resulting spectra shown in Fig. 5 (black

Table 2. Orbital solution and stellar parameters.

	Primary	Secondary
P [d]	3.070507 (fixed)	
e	0.0 (fixed)	
T_0 [HJD − 2 450 000]	5032.019 ± 0.002	
$q(M_1/M_2)$	2.53 ± 0.05	
γ [km s^{-1}]	−11.81 ± 0.91	−11.40 ± 1.20
K [km s^{-1}]	88.72 ± 1.02	224.48 ± 2.58
$a \sin i$ [$R_\odot$]	5.38 ± 0.06	13.61 ± 0.16
$M \sin^3 i$ [$M_\odot$]	7.00 ± 0.18	2.77 ± 0.05
rms [km s^{-1}]	2.9198	
$T_{\rm eff}$ [K]	32 000 ± 1000	28 000 ± 1000
$\log \frac{L}{L_\odot}$	$5.11^{+0.19}_{-0.16}$	$4.69^{+0.19}_{-0.16}$
$\log g$	3.5 ± 0.1	3.1 ± 0.1
$M_{\rm spec}$ [$M_\odot$]	$15.9^{+9.8}_{-8.4}$	$4.1^{+2.4}_{-2.1}$
$M_{\rm ev}$ [$M_\odot$]	$25.3^{+6.2}_{-4.0}$	$18.0^{+2.4}_{-2.5}$
radius [$R_\odot$]	$11.7^{+3.3}_{-2.7}$	$9.4^{+2.6}_{-2.2}$
He/H	0.1 ± 0.02	0.4 ± 0.1
C/H [$\times 10^{-4}$]	1.0 ± 0.5	0.3 ± 0.2
N/H [$\times 10^{-4}$]	0.85 ± 0.2	12.0 ± 2.0
O/H [$\times 10^{-4}$]	3.0 ± 0.5	0.5 ± 0.3
$V \sin i$ [km s^{-1}]	130 ± 10	80 ± 10
$v_{\rm mac}$ [km s^{-1}]	40 ± 5	44 ± 5
$\dot{M}$ [$10^{-8} M_\odot$ yr^{-1}]	1.0 ± 0.3	–
v_∞ [km s^{-1}]	1800 ± 100	–

Notes. The given errors correspond to 1-σ. The solar abundances for the chemical elements quoted here are He/H = 0.1, C/H = 2.45×10^{-4}, N/H = 0.60×10^{-4}, and O/H = 4.57×10^{-4}, respectively.

line). Unfortunately, the disentangled spectrum recovered for the secondary is too noisy to help us constrain the wind parameters.

To pinpoint the nature of the components, we determined their spectral types. We measured the equivalent widths by fitting Gaussian functions to the line profiles. We did that for both the most deblended observed spectra and the disentangled spectra. The spectral-type determination is based on the quantitative classification criteria for O-type stars proposed by Conti & Alschuler (1971), Conti (1973), and Mathys (1988, 1989). We derived, from the ratios of the appropriate lines, the spectral classifications O 9III and ON 9.7V for the primary and the secondary star, respectively. The "N" classification of the secondary comes from the strength of the nitrogen lines – e.g. N II 4037–41–43, N II 4601–07–13 and N III 4523–30–34. These results confirm the

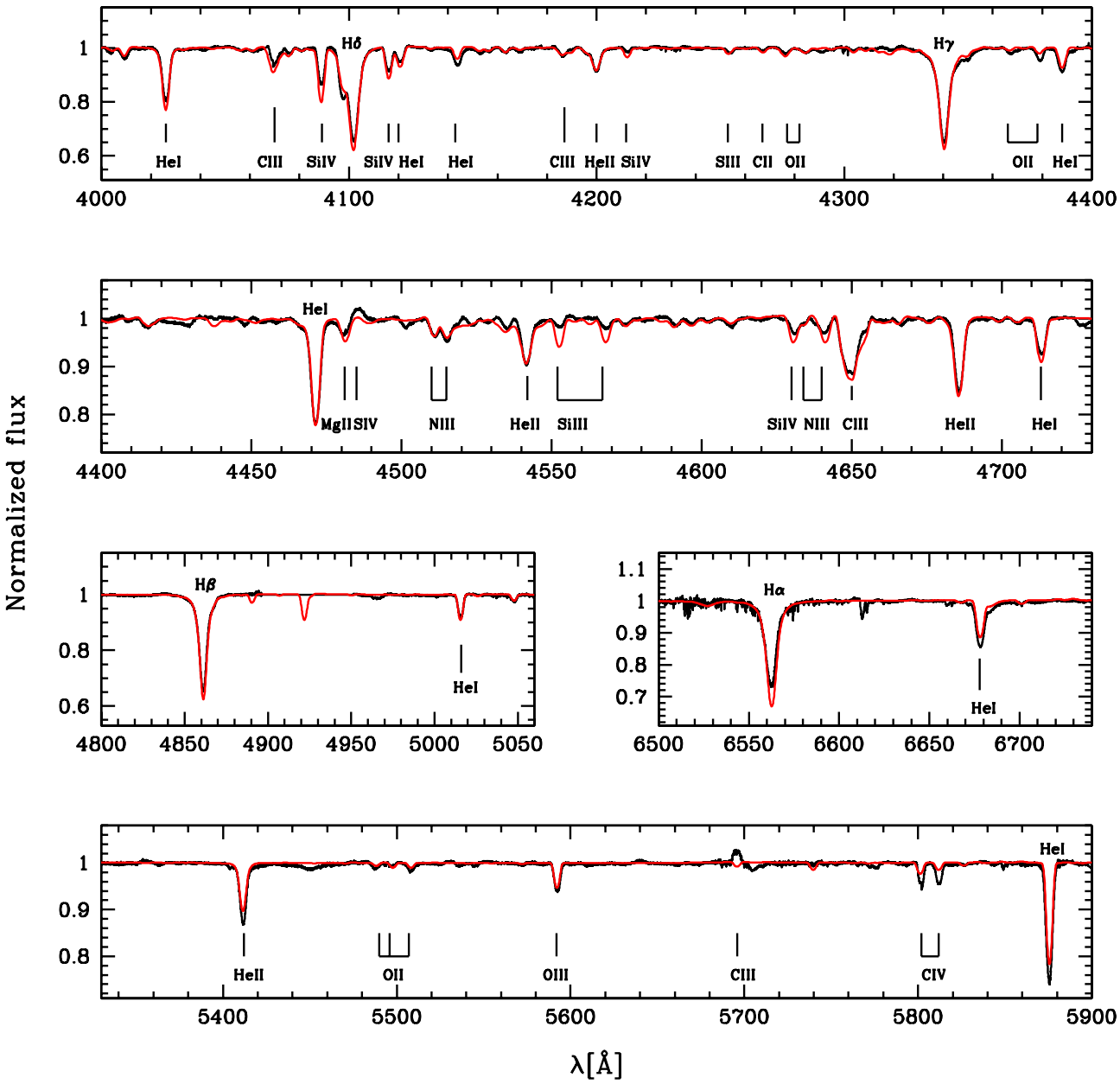

Fig. 3. Best CMFGEN fit (red) of the disentangled optical spectrum (black) of the primary component of LZ Cep. No data are available in the immediate vicinity of He I 4921.

conclusion of Hilditch (1974), who reported that the secondary is of a different luminosity class than the primary component. Otherwise, the spectral types are slightly different from those quoted in the literature. Petrie (1962) quoted LZ Cep as a binary system composed of two O 9.5V stars, whilst Conti & Alschuler (1971) determined a spectral type O 8.5III for the primary and O 9.5V for the secondary component.

In a second stage, we estimated the light ratio. For that purpose, we measured, for both stars, the equivalent widths of the He I 4026, 4143, 4388, 4471, 5876, He II 4200, 4542, Si IV 4089, O III 5592 lines and then computed the ratio of these lines and the corresponding theoretical average values reported in Conti & Alschuler (1971), Conti (1973) and Conti et al. (1977). Owing to the absence of O 9.7 stars in these three papers, we used an O 9.5 star as a reference for the secondary. We find that the primary star is about 1.85 times brighter than the secondary ($l_1/l_2 = 1.85 \pm 0.1$). Alternatively we also measured the equivalent widths of the above-quoted lines in synthetic spectra computed with a similar effective temperature and $\log g$ to those of the primary and secondary components estimated (see Sect. 4). With these synthetic spectra, we obtained a light ratio of about $l_1/l_2 = 1.91$, which is consistent with our previous value ($l_1/l_2 = 1.85 \pm 0.1$). Consequently, we adopt in the following a light ratio of about $l_1/l_2 = 1.85 \pm 0.1$. Petrie (1962) reported a value of $l_2/l_1 = 0.66 \pm 0.1$, which corresponds to $l_1/l_2 = 1.52 \pm 0.3$ (the method they used is not however described). Another estimate was made by Harries et al. (1998). Although their method appears to be relevant, the result seems questionable, probably because of the confusion between the primary and secondary stars. The authors reported a value of about $l_1/l_2 = 0.65 \pm 0.1$. However, when we compare the equivalent widths computed by Harries et al. (1998) with our measurements, no significant difference appears, indicating that the equivalent widths of the primary are larger than those measured for the secondary. We

thus assume that the real determination of Harries et al. (1998) is $l_2/l_1 = 0.65 \pm 0.1$, which corresponds to $l_1/l_2 = 1.54 \pm 0.3$. Consequently, the discrepancy between our measurement and those of Harries et al. (1998) and Petrie (1962) is probably due to the sample of spectral lines that is larger in our analysis, leading to a more accurate determination of the light ratio[1]. As a comparison, if we use a smaller brightness ratio ($l_1/l_2 \sim 1.54$), we obtain absolute luminosities of $\log(L_1/L_\odot) = 5.08$ and $\log(L_2/L_\odot) = 4.74$. The effect on the determination of the abundances is however small and does not exceed the error bars quoted in Sect. 4.

Adopting our brightness ratio, we computed the luminosity of each component. The magnitude and color of the system are $V = 5.55$ and $(B-V) = 0.06$ (Maíz-Apellániz et al. 2004). The visual extinction directly follows from $(B-V)_0 = -0.27$ (appropriate for late O stars, Martins & Plez 2006). With these photometric parameters and assuming a distance modulus for LZ Cep equal to $DM = 10.06^{+0.46}_{-0.38}$ (Sota et al. 2011, and references therein), consistent with the value of 10.12 given by Petrie (1962), we found a visual absolute magnitude of the entire binary system to be equal to $M_V = -5.53^{+0.38}_{-0.46}$. We derived, by using the brightness ratio, $M_{V_P} = -5.06^{+0.38}_{-0.46}$ and $M_{V_S} = -4.39^{+0.38}_{-0.46}$ and with the bolometric corrections corresponding to the spectral types of both components (Martins & Plez 2006), we obtained absolute luminosities of $\log(L_1/L_\odot) = 5.11^{+0.19}_{-0.16}$ and $\log(L_2/L_\odot) = 4.69^{+0.19}_{-0.16}$ (more details about the method are given in Mahy et al. 2010). As a comparison, if we had taken into account a smaller brightness ratio ($l_1/l_2 \sim 1.54$), we would obtain absolute luminosities of $\log(L_1/L_\odot) = 5.08$ and $\log(L_2/L_\odot) = 4.74$. Accordingly, the brightness ratio computed in the present analysis does not significantly affect the determination of the results since these values remain within the measured error bars.

4. Spectroscopic analysis

The disentangled optical spectra of both components were each analyzed with the atmosphere code CMFGEN (Hillier & Miller 1998). The UV spectrum of the primary was also used. CMFGEN produces non-LTE models including the effects of winds and line-blanketing. The rate equations are solved iteratively together with the radiative transfer equation to provide the occupation numbers of energy levels and the radiation field. The computations are done in spherical geometry and in the comoving frame. The temperature structure is a consequence of the radiative equilibrium condition. The velocity structure is an input of the calculation. In our case, we used TLUSTY hydrostatic structures in the photosphere connected to a β-velocity law for the wind part. The OSTAR2002 grid of TLUSTY models was used (Lanz & Hubeny 2003). The density structure directly follows from the mass-conservation equation. Once the atmosphere model is obtained, a formal solution of the radiative transfer equation is performed to yield the synthetic spectrum using an accurate line profile that accounts for both Stark broadening and a variable depth microturbulence. This last quantity varies from 10 km s^{-1} in the photosphere to $0.1 \times v_\infty$ in the outer atmosphere (v_∞ being the terminal velocity). The spectrum is subsequently compared to the observational data to constrain the main parameters. In practice, we determine the following parameters:

- the *effective temperature* $T_{\rm eff}$ is determined from the ionization balance of He. The relative strength of He I and He II directly depends on the temperature. We used He I 4471 and He II 4542 as the main indicators. Other lines were also checked: He I 4026, He I 4389, He I 4713, He I 5876, He II 4200, He II 4686, and He II 5412. An accuracy of $\pm$1000 K in the $T_{\rm eff}$ determination was achieved;
- *gravity* where a larger $\log g$ broadens the width of the Balmer lines wings. We thus used Hβ, Hγ, and Hδ as the main gravity diagnostics. The final $\log g$ are accurate to 0.1 dex;
- *luminosity*: the knowledge of the effective temperature, the absolute V magnitude, and the extinction provides a direct estimate of the luminosity as described in Sect. 3. The uncertainty in the luminosity determination depends mainly in the uncertainty on the distance (see Sect. 3);
- *surface abundances*, which were determined from the strength of the He, C, N, and O lines. The He lines of all ionization states are stronger when the helium content is higher. This effect is different from a change in $T_{\rm eff}$, which changes the relative strengths of lines from successive ionization states. We thus used the same lines as for the effective temperature determination to constrain the He content. For nitrogen, we mainly relied on several N II lines between 4000 Å and 4700 Å, as well as the N III lines in the 4500–4520 Å range. The main carbon indicators were the C III lines around 4070 Å and C III 5696 Å. For oxygen, we relied on the numerous O II lines between 4000 and 4600 Å, as well as on O III 5592 Å. The typical uncertainty in the CNO surface abundance is 50%. To estimate these uncertainties, we ran models with element abundances across a range of values both lower and higher than the preferred value and compared the corresponding spectra to the observed line profiles. When a clear discrepancy was seen between the model and data for all lines of the same element, we adopted the corresponding abundance as the maximum/minimum value of the possible chemical composition. An illustration is shown in Fig. 6. As a test, we conducted the same analysis for the primary with four additional sets of models with the following sets of parameters: $T_{\rm eff} = 31\,000$ K and $\log g = 3.5$; $T_{\rm eff} = 33\,000$ K and $\log g = 3.5$; $T_{\rm eff} = 32\,000$ K and $\log g = 3.4$; $T_{\rm eff} = 32\,000$ K and $\log g = 3.6$. We then estimated the best N/H abundance for each set of models (including also the best-fit combination, $T_{\rm eff} = 32\,000$ K and $\log g = 3.5$) by means of a chi-square method. We then computed the average and 1-σ dispersion of this set of five N/H values and found N/H $= 8.5 \pm 0.18 \times 10^{-5}$. This is perfectly consistent with the value we estimate from Fig. 6. For the other elements and the secondary, we thus proceeded as described above, running models with various abundances for the best-fit model parameters ($T_{\rm eff}$, $\log g$);
- *mass-loss rate*: we used the UV resonance lines of the primary to estimate $\dot{M}$. The C IV 1538–1545 and N V 1240 were the main diagnostics. The uncertainty in $\dot{M}$ is 0.1 dex. For the secondary, the UV spectrum was not good enough to allow this determination but to compute the atmosphere model associated with this star, we took a $\dot{M} = 3 \times 10^{-8}$ $M_\odot$ yr^{-1}. We also used homogeneous models (i.e. no clumping was included), which provided a good fit to the UV lines. As a consequence, our determination should be seen as an upper limit. We also included X-ray emission so as to have a canonical value of $\log \frac{L_X}{L_{\rm bol}} = -7$ (Sana et al. 2006b). This turned out to be a crucial step in reproducing the N V 1240 profile;

[1] If we rely on the same spectral lines as Harries et al. (1998) for the determination, we obtain a brightness ratio that only slightly differs from their estimate.

– *terminal velocity*: the blueward extension of the P-Cygni profiles of the primary UV spectrum are directly related to v_∞. We thus used them to estimate this parameter, where v_∞ is derived to within 100 km s^{-1};
– *rotational and macroturbulent velocity*: we used the Fourier transform formalism (Simón-Díaz & Herrero 2007) to derive the projected rotational velocity ($V \sin i$). The macroturbulent velocity was obtained by convolving the theoretical line profiles with a Gaussian profile in attempt to reproduce the shape of He I 4713.

The best-fits models of both components are shown in Figs. 3 and 4. The fit of the UV spectrum of the primary is shown in Fig. 5. The derived parameters are gathered in Table 2 (bottom part). The quality of the fit is on average very good. Only a few features are not reproduced. This is the case of the Si III lines around 4550 Å. Increasing $T_{\rm eff}$ leads to a better fit, but in that case the other diagnostics are less well reproduced. This problem is frequently observed in our models, and the origin is not known at present. Hence, we decided not to rely on these lines in the present study.

5. Light curve

To more clearly understand the binary system LZ Cep and, in particular, its geometry, we also performed an analysis of the Hipparcos light curve. This investigation was made with the NIGHTFALL program[2]. This software is based on a generalized Wilson-Devinney method assuming a standard Roche geometry. We performed a fit to the light curve by minimizing the free parameters. We fixed the effective temperatures to 32 000 K and 28 000 K for the primary and the secondary star, respectively, as determined by the CMFGEN analysis (see Sect. 4). The mass ratio and the orbital period are those obtained from the orbital solution (see Table 2). We stress that the zero phase of the light curve fit corresponds to the zero phase of the orbital solution.

The light curve (Fig. 7) does not exhibit any eclipses but ellipsoidal variations are clearly visible. The depth of the secondary minimum is very similar to that of the primary minimum. Howarth et al. (1991) considered two different models to explain the geometry of this binary system: a first one where both stars fill their Roche lobe, and a second one with a semi-detached configuration. The emphasis of their analysis was put on the second model with the secondary star filling its Roche lobe.

In our analysis, the NIGHTFALL program also provides two possible solutions that both converge toward a semi-detached system. The first possibility is a situation in which the primary component fills up its Roche lobe (Sol 1 in Table 3). This configuration favors an inclination of about 50.1°. The primary star would fill up its Roche lobe at about 98%, whilst the secondary component would at about 87%. The second possible configuration is a system where the secondary star fills up its Roche lobe (Sol 2 in Table 3). This configuration is closer to that found in the literature. Under this assumption, we found an inclination of about 48.1°. The volumes of the Roche lobes fill up at about 95% and 99% for the primary and the secondary components, respectively. As Howarth et al. (1991) noted and regardless of the chosen configuration, the inclination is well between 45° and 55° but, with the present investigation, we note that we improved to greater accuracy the true value of the inclination. In both configurations, we included the reflection effects, which are not negligible when one star fills out a large fraction of its Roche lobe. We also note that there is no photometric evidence of a non-zero eccentricity.

[2] For more details, see the Nightfall User Manual by Wichmann (1998) available at the URL: http://www.hs.uni-hamburg.de/DE/Ins/Per/Wichmann/Nightfall.html

Table 3. Parameters fitted from the Hipparcos light curve.

Parameters	Sol 1	Sol 2
i [°]	$50.1^{+2.1}_{-1.5}$	$48.1^{+2.0}_{-0.7}$
q [M_1/M_2]	2.53 (fixed)	2.53 (fixed)
Filling factor primary [%]	$98.0^{+1.2}_{-1.0}$	$94.8^{+2.0}_{-3.0}$
Filling factor secondary [%]	$87.0^{+3.0}_{-5.0}$	$98.6^{+0.3}_{-1.5}$
$T_{\rm eff,p}$ [K]	32 000 (fixed)	32 000 (fixed)
$T_{\rm eff,s}$ [K]	28 000 (fixed)	28 000 (fixed)
$M_{\rm p}$ [$M_\odot$]	$15.5^{+1.0}_{-1.0}$	$16.9^{+1.0}_{-1.0}$
$M_{\rm s}$ [$M_\odot$]	$6.1^{+1.0}_{-1.0}$	$6.7^{+1.0}_{-1.0}$
$R_{\rm pole,p}$ [$R_\odot$]	$10.5^{+1.2}_{-1.2}$	$10.5^{+1.2}_{-1.2}$
$R_{\rm pole,s}$ [$R_\odot$]	$6.1^{+1.2}_{-1.2}$	$7.1^{+1.2}_{-1.2}$
$R_{\rm equ,p}$ [$R_\odot$]	$13.1^{+1.2}_{-1.2}$	$12.4^{+1.2}_{-1.2}$
$R_{\rm equ,s}$ [$R_\odot$]	$6.9^{+1.2}_{-1.2}$	$9.3^{+1.2}_{-1.2}$

Notes. The index "p" ("s") refers to the primary (secondary). $R_{\rm pole}$ is the polar radius, and $R_{\rm equ}$ the equatorial radius.

The error bars given in Table 3 are established by exploring the parameter space. We fixed one parameter and allowed the others to vary in order to reach the minimum of the χ^2. The error bars were then determined for a variation in the χ^2 corresponding to a 90% confidence level and the appropriate number of freedom degrees (for more details, see Linder et al. 2009).

Both models are extremely close to each other in terms of parameters values and it is difficult to favor one configuration without any eclipse and based on only the light curve fit. We can only safely conclude that LZ Cep is in a transitory state, where both components are close to entirely filling their Roche lobe. LZ Cep is close to being a contact binary.

6. Stellar evolution and binarity

The position of the two components of the LZ Cep system in the HR diagram is displayed in Fig. 8. The two stars are located significantly away from the zero-age main sequence. The isochrones reveal that the primary would be assigned an age of 4–6 Myr by using single-star evolutionary tracks. The secondary would have an age of 7–9 Myr. This difference in age could be due to a different rotation rate. As demonstrated by Brott et al. (2011), isochrones based on rapidly rotating star evolutionary models tend to be located closer to the ZAMS than isochrones based on tracks with lower rotation rates. This is found for stars with luminosities above 3.0×10^5 $L_\odot$ in the Galaxy. However, this effect is significant only for values of $V \sin i$ larger than ~250 km s^{-1}. Since the projected rotation rates we derive are 130 and 80 km s^{-1} for the primary and secondary components, respectively, we can exclude rotation as an explanation to the age difference between both stars.

We determined various masses for the components of the LZ Cep system. From the orbital solution and the light curve analysis, we derived the true present masses of about 16 $M_\odot$ and 6.5 $M_\odot$ for the primary and the secondary components, respectively. These masses can be compared to the spectroscopic masses obtained from the luminosity, temperature, and gravity. We obtained $15.9^{+9.8}_{-8.4}$ $M_\odot$ for the primary and $4.1^{+2.4}_{-2.1}$ $M_\odot$ for the secondary. Within the error bars, the agreement is very good for the primary, and marginal for the secondary. This could be due to

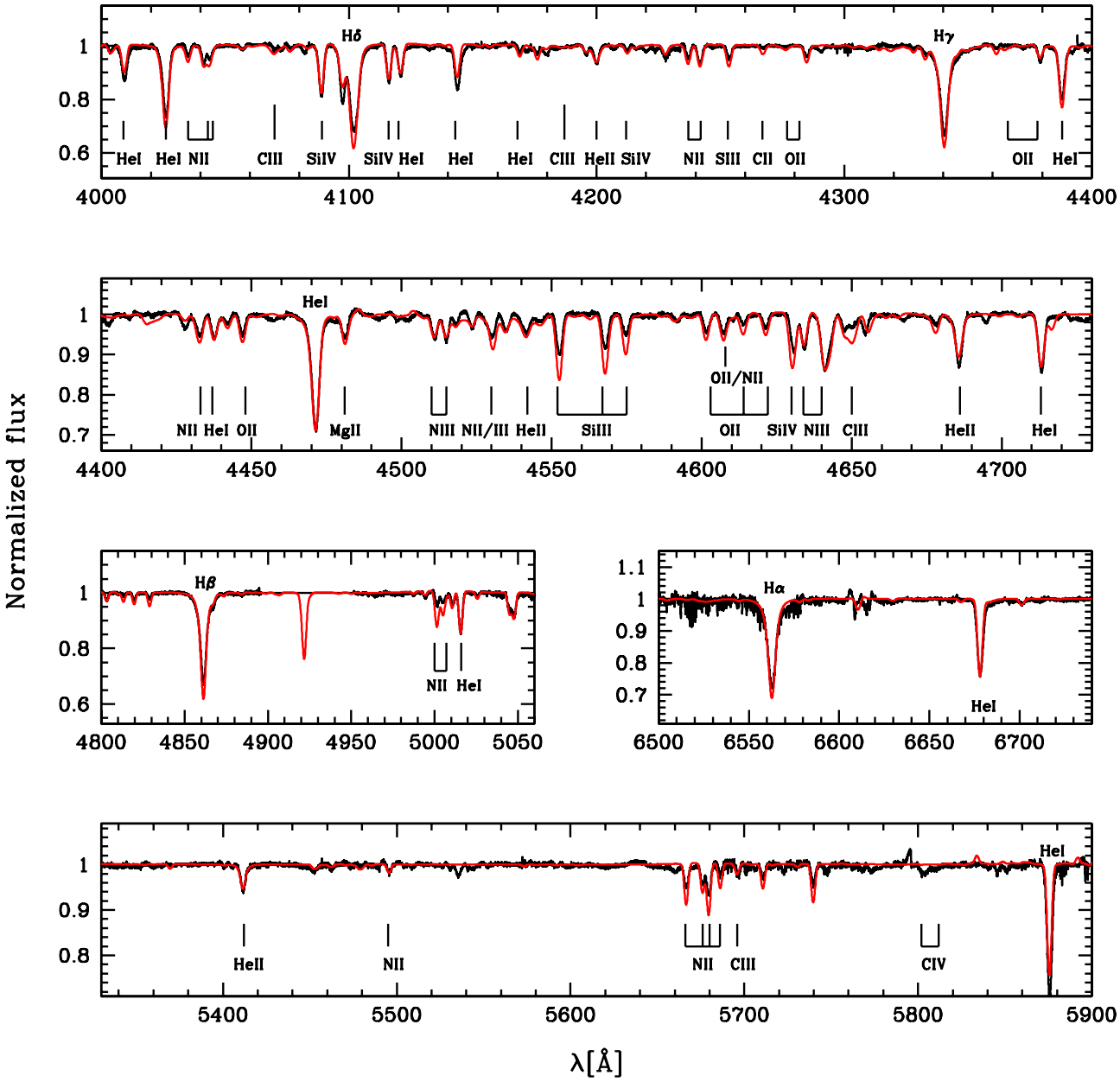

Fig. 4. Same as for Fig. 3 but for the secondary component of LZ Cep. No data are available in the immediate vicinity of He I 4921.

the deformation of the secondary (see Fig. 7) and that we derive only an average gravity. The evolutionary masses derived using single-star evolutionary tracks are respectively $25.3^{+6.2}_{-4.0}$ $M_\odot$ and $18.0^{+2.4}_{-2.5}$ $M_\odot$ for the primary and the secondary. The former masses, estimated from the orbital solution and the inclination, are in strong conflict with the latter ones. Under normal circumstances, a star of initial mass around 25 $M_\odot$ does not lose 10 $M_\odot$ through stellar winds before it enters the Wolf-Rayet phase (e.g. Meynet & Maeder 2000). Hence normal evolution cannot explain the mass discrepancy for the primary. In addition, if the discrepancy in mass concerned only one component, one could argue that mass was lost through Roche-lobe overflow and given to the other component. In our case, both stars however have evolutionary masses much larger than present masses. This is an indirect indication that the system was affected by binary interaction and that single-star evolutionary tracks cannot be used blindly to derive the initial masses of the components of LZ Cep. We also note that the spectroscopic masses we obtained are lower than expected for single-star evolution (see e.g. Martins et al. 2005). This is especially true for the secondary, for which a mass of $4.1^{+2.4}_{-2.1}$ $M_\odot$ is much lower than the 10–15 $M_\odot$ of Martins et al. (2005). Having such a low mass but still the luminosity and effective temperature of an O star imply the occurrence of processes not present in single-star evolution.

Another indication of interaction within the system comes from the analysis of the surface abundances. In Fig. 9, we show the nitrogen to carbon ratio as a function of the nitrogen to oxygen. In addition, single-star evolutionary tracks including rotational mixing from Meynet & Maeder (2003) are shown. We see that the primary, located at the bottom-left corner of Fig. 9, displays surface chemistry consistent with single star evolution. However, the secondary features extreme nitrogen enrichment and carbon/oxygen depletion. Such high N/C and N/O ratios are only reached during the Wolf-Rayet phase of single star evolution (the Wolf-Rayet phase is indicated by bold symbols in Fig. 9). Interestingly, this is consistent with the high helium

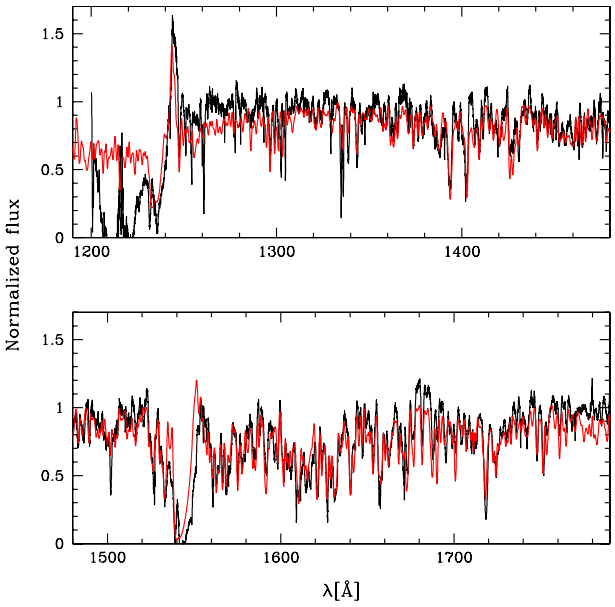

Fig. 5. Best-fit CMFGEN model (red) of the disentangled UV spectrum (black) of the primary component of LZ Cep.

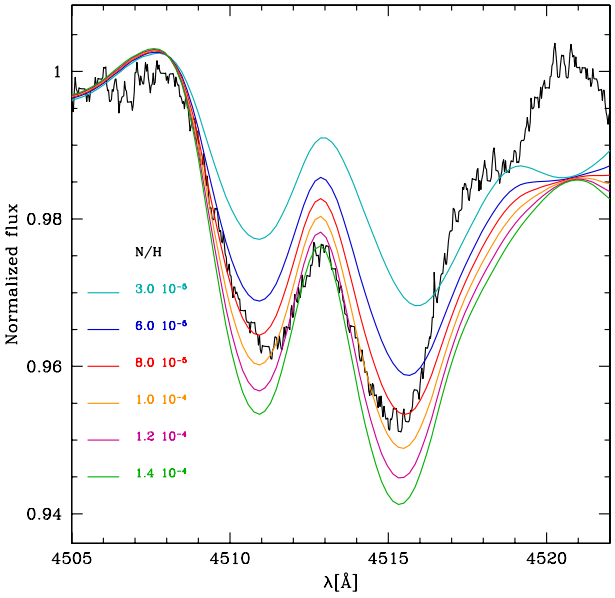

Fig. 6. Illustration of the N/H determination for the primary component of LZ Cep. Colored lines represent the models and the black line is the disentangled spectrum. We estimate that the best-fit model abundance has N/H slightly above 8.0×10^{-5} and that models with N/H = 6.0×10^{-5} and N/H = 1.0×10^{-4} correspond to the extrema of the allowed N/H values.

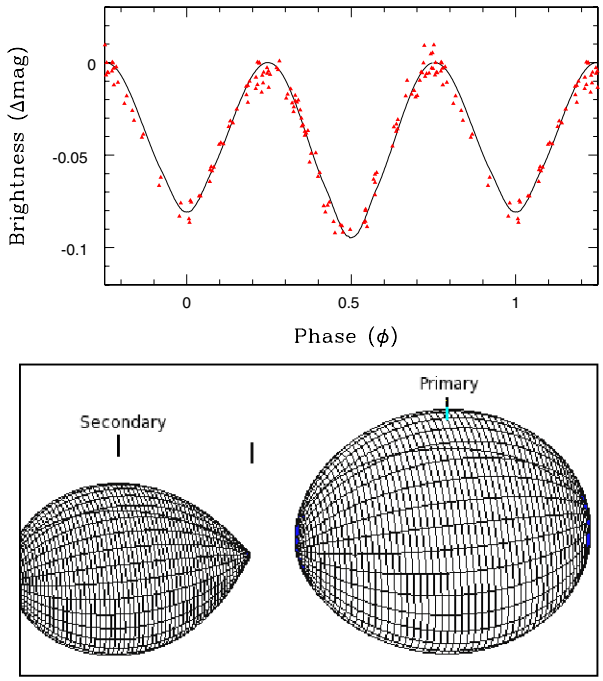

Fig. 7. *Top*: photometry of LZ Cep from Hipparcos satellite. The red triangles are the observational data. A period of ~3.07 d is used. The solid line corresponds to the theoretical light curve fit with the parameters listed in Table 3. *Bottom*: a 3D view of both stars when the secondary star fills up its Roche lobe.

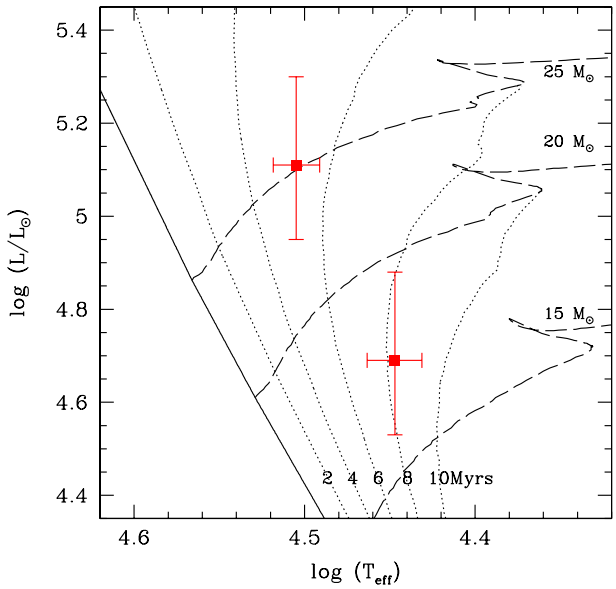

Fig. 8. HR diagram with the position of the two components of the LZ Cep system shown by the red squares. The primary is the most luminous star. The evolutionary tracks computed for an initial rotational velocity of 300 km s^{-1} and the isochrones are from Meynet & Maeder (2003).

content of the secondary He/H = 0.4, corresponding to $Y = 0.6$, which is only observed in advanced stages of evolution in single-star evolutionary tracks with initial masses of about 20 $M_\odot$. This raises the question of whether the secondary is more evolved than the primary and currently in a state of central helium burning. Using the mass-luminosity relation of Schaerer & Maeder (1992) for core H-free stars, we find that a star with a current mass of about 6 $M_\odot$ (resp. 5 $M_\odot$) should have a luminosity $\log \frac{L}{L_\odot} = 4.85$ (resp. 4.69). This is remarkably consistent with the derived luminosity of the secondary ($\log \frac{L}{L_\odot} = 4.69$).

All indications thus favor the scenario in which the secondary was initially more massive, evolved faster, transferred mass to the companion and is now close to being a core He-burning object. This could also explain the rather low gravity and mass of the secondary (if it is truly a main-sequence O star, $\log g$ should be much higher – see also above). However, there are two caveats to this scenario. First, the spectroscopic appearance of the secondary is not that of an evolved massive star. With a spectral type ON 9.7V, it resembles a normal main-sequence

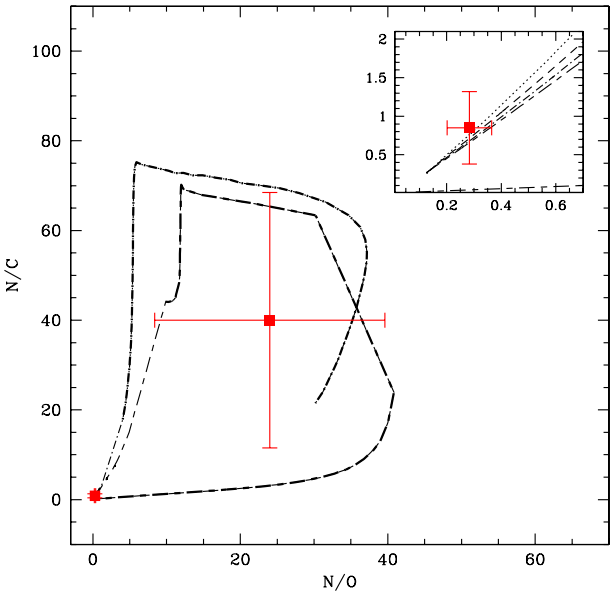

Fig. 9. N/C versus N/O for the components of LZ Cep (red squares). The inset zooms on the primary value. The evolutionary tracks are from Meynet & Maeder (2003). The dotted line (resp. dashed, dot-dashed, short-dash long-dashed lines) are tracks for a 15 $M_{\odot}$ (resp. 20, 25, 40 $M_{\odot}$) star. The bold lines indicate the Wolf-Rayet phase of the evolution according to Meynet & Maeder (2003), i.e. $X(\mathrm{H}) < 0.4$ and $T_{\mathrm{eff}} > 10\,000$ K.

star. Said differently, despite of all the indications, the absence of strong mass loss characterizing evolved massive stars (and affecting spectral types) is challenging. Gräfener & Hamann (2008) demonstrated that the mass loss rate of Wolf-Rayet stars depended on the Eddington factor Γ_{e}. Estimating this factor from the parameters we determined, we obtain $\Gamma_{\mathrm{e}} \sim 0.17$. This is rather low, and much lower than the range of values for which Gräfener & Hamann (2008) provide mass loss prescriptions for Wolf-Rayet stars (their computations are restricted to $\Gamma_e > 0.4$). Hence, the secondary may very well have a rather normal wind. If we use the mass loss recipe of Vink et al. (2001), we obtain $\log \dot{M} \sim -7.0$, which is much more typical of O stars. Consequently, it does not seem impossible that the secondary is an evolved object with a rather normal wind and thus the appearance of an O star.

The second caveat is the chemical composition of the primary. If almost all the envelope of the secondary was dumped onto the primary, the chemical pattern would be different. The primary should then show evidence of N enrichment and CO depletion because material from the secondary would be processed, the secondary being significantly evolved. According to our determinations, there are only weak signatures of CNO processing. This favors a weak accretion of material from the donor. A way out of this puzzle is to invoke a very non-conservative mass transfer, even though this kind of process was not observed in the two post Roche lobe overflow key systems: ϕ Per (Bozic et al. 1995) and RY Scuti (Grundstrom et al. 2007). All in all, the scenario according to which the secondary was initially more massive and evolved more rapidly to the core-He burning phase while filling its Roche lobe and transferring very inefficiently material onto the primary seems a valuable explanation of the system.

However other explanations can be invoked. de Mink et al. (2007) and Langer et al. (2008) argued that strong nitrogen enhancement can be produced in interacting binaries. Two effects are at work: the mass gainer receives N-rich material usually from the inner layers of the donor, and the angular momentum received from the primary triggers rotational mixing, which increases the surface nitrogen content of the secondary. In total, at solar metallicities, the enrichment can be a factor of ten relative to the initial N abundance. According to Table 2, the nitrogen surface abundance of the secondary star in LZ Cep is 25 times the initial value. This is qualitatively consistent with the predictions of binary evolution that depend on the orbital parameters and masses of the components. In contrast to the scenario described above, the primary is then the mass donor. Since rotational mixing is triggered by mass transfer, one also expects helium enrichment in the secondary, which is what we observe in the LZ Cep. However, according to de Mink et al. (2009), a mass fraction of $Y = 0.6$ can be reached only for very short periods and occurs only for stars more massive than $\sim$40 $M_{\odot}$. Another concern is that the rotational velocity of the secondary is not extreme. With $V \sin i = 80$ km s^{-1}, and assuming that the rotation axis is parallel to the orbital axis, this gives a rotation rate of $\sim$100 km s^{-1}. However as shown by Langer et al. (2008), the rotational velocity can reach very large values after mass transfer, and subsequently return to more moderate values. The question is whether rapid mixing can be triggered during this short spin-up phase. It seems unlikely, but further dedicated simulations should be run to help answer this unknown.

For the combination of the inclination, projected rotational velocities, and radius, we can estimate the rotational period of each star and verify whether synchronization has been achieved in the system. Assuming an inclination angle of 49.1° (the average of the two values from Table 3), we obtain a rotational period of 3.09 ± 0.24 d using $R = 10.50\ R_{\odot}$ (average of the polar radii for the primary) and 3.75 ± 0.31 d using $R = 12.75\ R_{\odot}$ (equatorial radius). Similarly, the rotational period of the secondary is 3.15 ± 0.45 d (polar radius) and 4.21 ± 0.60 d (equatorial radius). Compared to the orbital period (3.07 d), the true rotational periods of both components (which are probably in-between the polar and equatorial cases) are thus roughly from 10% to 20% larger, implying that the synchronous co-rotation is not completely established in the system. However, given the small differences and the similarity between the primary and secondary rotational periods, the system is certainly on the verge of achieving this.

All in all, we have thus gathered evidence of mass transfer and tidal interaction in the massive binary system LZ Cep. A scenario in which the secondary was initially the more massive star appears to explain more observational constraints, although it is not free of challenges. What is clear is that single-star evolutionary tracks are certainly not relevant to explaining the position of the two components in the HR diagram. This was highlighted by Wellstein et al. (2001), who computed evolutionary tracks for interacting binaries and showed that as soon as mass transfer occurs, dramatic deviations from single-star evolutionary track happen. Consequently, the evolutionary masses we derived in Table 2 are very uncertain.

7. Conclusion

We have presented a detailed analysis of the binary system LZ Cep. We used high-resolution and high *SNR* spectra collected with the instrument NARVAL on the TBL. We have derived an orbital solution from which we did not find evidence for a non-zero eccentricity. We have applied a spectral disentangling programme to our data set. This gave us the individual spectra of each component of the system. We have determined the

combined spectral type of the system to be O 9III+ON 9.7 V. We have subsequently performed a quantitative spectroscopic analysis with the CMFGEN atmosphere code. Although the secondary star has a main-sequence luminosity class, its surface abundances indicates that the star has experienced significant helium and nitrogen enhancement, as well as carbon and oxygen depletion. The primary barely shows any sign of chemical processing. The analysis of the Hipparcos photometry has revealed ellipsoidal variations that can be explained by two configurations of this system: LZ Cep is a semi-detached system in which either the primary or the secondary almost entirely fills its Roche lobe. The ellipsoidal variations in the light curve correspond to an inclination of about 48°. Together with the spectroscopic orbital solution, this has allowed us to determine the masses of the system of about 16.0 $M_{\odot}$ for the primary and 6.5 $M_{\odot}$ for the secondary. These masses are in good agreement with the spectroscopic masses. The evolutionary masses obtained using single-star evolutionary tracks are higher. Our results indicate that LZ Cep is in a transitory state following mass transfer from the secondary – which was initially the most massive component – to the primary. The secondary is now (close to being) a core He-burning object. The mass transfer must have been very inefficient to account for the weak chemical processing at the surface of the primary. The caveats to this scenario have been discussed. The system is not yet completely synchronized, but the individual rotational periods are only 10 to 20% longer than the orbital period.

Our investigation of the binary system LZ Cep represents a significant improvement to previous studies. We have obtained the individual spectra of each component. This leads to the determination of a number of stellar parameters that could be used to constrain the evolutionary status of the system. This evolved system is thus particularly interesting because it provides observational constraints of theoretical binary evolutionary models. Similar analyses have been performed for B stars (e.g., see Pavlovski et al. 2009) but studies of systems composed of two evolved early-type stars are scarce (e.g., Plaskett's star by Linder et al. 2008). We have emphasized the need for theoretical binary system evolutionary models because our comparison of the stellar properties of the components of evolved binary systems with those of single-star theoretical predictions has revealed discrepancies.

Acknowledgements. We thank the anonymous referee for valuable comments that helped us to improve the presentation of the paper and the discussion of our results. L.M. thanks the PRODEX XMM/Integral contract (Belspo) and the Communauté française de Belgique – Action de recherche concertée – ARC – Académie Wallonie-Europe for their support. We thank John Hillier for making his code CMFGEN available and for constant support with its use.

References

Bozic, H., Harmanec, P., Horn, J., et al. 1995, A&A, 304, 235
Brott, I., de Mink, S. E., Cantiello, M., et al. 2011, A&A, 530, A115
Conti, P. S. 1973, ApJ, 179, 161
Conti, P. S., & Alschuler, W. R. 1971, ApJ, 170, 325
Conti, P. S., Leep, E. M., & Lorre, J. J. 1977, ApJ, 214, 759
de Mink, S. E., Pols, O. R., & Hilditch, R. W. 2007, A&A, 467, 1181
de Mink, S. E., Cantiello, M., Langer, N., et al. 2009, A&A, 497, 243
de Mink, S. E., Langer, N., & Izzard, R. G. 2011, Bulletin de la Société Royale des Sciences de Liège, 80, 543
Donati, J., Semel, M., Carter, B. D., Rees, D. E., & Collier Cameron, A. 1997, MNRAS, 291, 658
González, J. F., & Levato, H. 2006, A&A, 448, 283
Gräfener, G., & Hamann, W.-R. 2008, A&A, 482, 945
Grundstrom, E. D., Gies, D. R., Hillwig, T. C., et al. 2007, ApJ, 667, 505
Harries, T. J., Hilditch, R. W., & Hill, G. 1998, MNRAS, 295, 386
Hilditch, R. W. 1974, MNRAS, 169, 323
Hill, G., Hilditch, R. W., & Pfannenschmidt, E. L. 1976, Publications of the Dominion Astrophysical Observatory Victoria, 15, 1
Hillier, D. J., & Miller, D. L. 1998, ApJ, 496, 407
Howarth, I. D., Stickland, D. J., Prinija, R. K., Koch, R. H., & Pfeiffer, R. J. 1991, The Observatory, 111, 167
Kameswara Rao, N. 1972, PASP, 84, 563
Langer, N., Cantiello, M., Yoon, S., et al. 2008, IAU Symp. 250, ed. F. Bresolin, P. A. Crowther, & J. Puls (Cambridge Univ. Press), 167
Lanz, T., & Hubeny, I. 2003, ApJS, 146, 417
Linder, N., Rauw, G., Martins, F., et al. 2008, A&A, 489, 713
Linder, N., Rauw, G., Manfroid, J., et al. 2009, A&A, 495, 231
Lucy, L. B., & Sweeney, M. A. 1971, AJ, 76, 544
Mahy, L., Rauw, G., Martins, F., et al. 2010, ApJ, 708, 1537
Maíz-Apellániz, J., Walborn, N. R., Galué, H. Á., & Wei, L. H. 2004, ApJS, 151, 103
Martins, F., & Plez, B. 2006, A&A, 457, 637
Martins, F., Schaerer, D., & Hillier, D. J. 2005, A&A, 436, 1049
Mathys, G. 1988, A&AS, 76, 427
Mathys, G. 1989, A&AS, 81, 237
Meynet, G., & Maeder, A. 2000, A&A, 361, 101
Meynet, G., & Maeder, A. 2003, A&A, 404, 975
Pavlovski, K., & Hensberge, H. 2005, A&A, 439, 309
Pavlovski, K., Tamajo, E., Koubský, P., et al. 2009, MNRAS, 400, 791
Petrie, R. M. 1962, AJ, 67, 279
Rauw, G., Sana, H., Gosset, E., et al. 2000, A&A, 360, 1003
Sana, H., Gosset, E., & Rauw, G. 2006a, MNRAS, 371, 67
Sana, H., Rauw, G., Nazé, Y., Gosset, E., & Vreux, J.-M. 2006b, MNRAS, 372, 661
Sana, H., Gosset, E., Nazé, Y., Rauw, G., & Linder, N. 2008, MNRAS, 386, 447
Schaerer, D., & Maeder, A. 1992, A&A, 263, 129
Simón-Díaz, S., & Herrero, A. 2007, A&A, 468, 1063
Sota, A., Maíz Apellániz, J., Walborn, N. R., et al. 2011, ApJS, 193, 24
Vink, J. S., de Koter, A., & Lamers, H. J. G. L. M. 2001, A&A, 369, 574
Wellstein, S., Langer, N., & Braun, H. 2001, A&A, 369, 939
Wichmann, R. 1998, Nightfall User Manual
Wolfe, Jr., R. H., Horak, H. G., & Storer, N. W. 1967, The machine computation of spectroscopic binary elements, ed. M. Hack (New York: Gordon & Breach), 251

Chapter 3

Doppler Tomography

Massive stars release large quantities of material through their stellar winds. When these stars are gravitationally bound in a binary system, the winds interact between each other, thus creating a wind-wind collision zone. The shock-heated plasma in this wind interaction zone can produce optical, UV, IR or even X-, if not γ-ray emission lines. It is however not possible to separate the contributions to the spectrum linked to this region by means of the disentangling programs because these algorithms only provide a mean spectrum of each component over the orbital cycle. That supposes that the line profiles of both components remain rather constant over the orbital period whilst the emission lines formed in the wind interaction zone are characterized by changes in their shape as a function of time. As a consequence, we need other methods to obtain additional information on the interaction zones.

In this context, the Doppler tomography technique was developed to map in velocity space the formation region of an emission line (Marsh & Horne 1988; Horne 1991; Kaitchuck et al. 1994). This method was inspired by medical imaging techniques and is very similar to the X-ray tomography. In the medical domain, tomography allows to reconstruct a three-dimensional distribution of an organism from a series of two-dimensional images. For that purpose, the volume (or the organism) is first "cut" in different slices. An X-ray source and a detector are placed on opposite sides of a slice to observe the organism under different viewing angles. The intensity of the X-ray beam is recorded for each observation as a function of the spatial position. The collection of images is numerically treated to reconstruct the distribution of the internal structure, satisfying the different projections. The process is then repeated on each slice to map the volume in 3D.

In astrophysics, a series of one-dimensional projections (the observed spectra) are used for recreating a two-dimensional map of the emissivity region in velocity space. In this chapter, we present two reconstruction methods: an analytic method based on the Fourier-filtered back-projection technique and an algebraic method based on iterative processes. We then compare the effeciency of these techniques by applying them to the observations of three evolved binary systems.

3.1 Fourier-filtered back-projection

Before introducing the reconstruction methods, it is important to define the frame of reference used in the Doppler tomography (Fig. 3.1). The coordinate system is defined with the center of mass of the system as the origin. The x-axis is located between the two components and points from the primary to the secondary. The y-axis points in the direction of the secondary star's motion whilst the z-axis is perpendicular to the orbital plane of the binary system.

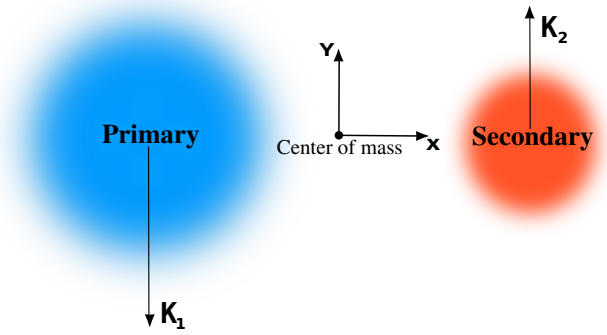

Figure 3.1: Reference frame used for the Doppler tomography.

Let's consider a gas flow that is stationary in the rotating frame of a binary system, i.e., the material rotates with the binary. Each element of this gas can be described by its position (x, y, z) as well as by its velocity (v_x, v_y, v_z). As we already mentioned, the Doppler tomography maps the emissivity of this flow as a function of the velocity coordinates (v_x,v_y). The v_z component, associated to the radial velocity of the center of mass, is fixed for computing the Doppler map. We thus assume that all the emission represented in the tomogram is located in the orbital plane. To compute such a map, we assume that, during the orbital phase, the radial velocity of each particle of material describes, in the frame of reference of the observer, an S-shaped pattern. Therefore, each pixel of the Doppler map, given by a velocity vector (v_x, v_y, v_z), can be associated to a particular component, the so-called *"S-wave" component* (Horne 1991). The radial velocity at the binary phase $v(\phi)$ can hence be depicted by the "S-wave" relation:

$$v(\phi) = -v_x \cos(2\pi\phi) + v_y \sin(2\pi\phi) + v_z \tag{3.1}$$

where ϕ is the orbital phase and (v_x, v_y, v_z) are the velocity coordinates of the gas flow. v_x and v_y thus correspond to the projected velocity components along the x- and y-axes so that $v_x = V_x \sin i$ and $v_y = V_y \sin i$ with i being the inclination of the binary system. Therefore, the Doppler tomogram is defined as the emissivity of a spectral line as a function of the velocity and can be integrated along any line-of-sight to reproduce the line profile seen at a given orbital phase (Kaitchuck et al. 1994). The choice of working in the velocity space appears to be obvious. Indeed, the relationship between the observed spectra and the Doppler map is direct and does not require any a priori knowledge about the precise nature of the velocity field (Horne 1991). However, the resulting disadvantage is that two different elements of gas (with distinct spatial coordinates) can have the same velocity coordinates, which can render the interpretation of such maps quite difficult.

In addition to working in the velocity space, Doppler tomography also relies on several

other assumptions. The description of the reference frame assumes that the binary system has a circular orbit to avoid variations of the velocity between both components. In addition, the emission derived from all the elements of the system has to be visible during the full orbital cycle. Consequently, the eclipsing binaries require a special treatment which aims at removing from the analysis the phases corresponding to the eclipses.

The most common method implemented in astrophysics to produce Doppler maps is the Fourier-filtered back-projection (for further details, see e.g., Marsh & Horne 1988; Horne 1991; Kaitchuck et al. 1994). The back-projection method consists in allocating to each pixel involved in the projection a value corresponding to the observed flux. We suppose that we cannot directly investigate the emissivity of the system, $\epsilon(v_x, v_y)$, but we have information about it from several observed spectra, $I(v, \phi)$, taken over the complete orbital cycle. The observed spectra are then represented by the Radon transform, $R[.]$, of the emissivity such as:

$$I(v,\phi) = R\left[\epsilon(v_x, v_y)\right] = \int_{-\infty}^{+\infty} \epsilon(v\cos(2\pi\phi) - u\sin(2\pi\phi), v\sin(2\pi\phi) + u\cos(2\pi\phi))\, du.$$

where ϕ is the orbital phase and v is the velocity displacement of the rest wavelength of the spectral line, $v = \frac{\lambda-\lambda_0}{\lambda_0}c$.

As a consequence, the inverse of this transform provides the emissivity of the gas:

$$\epsilon(v_x, v_y) = \frac{\int I((v_x, v_y, v_z), \phi)\, w(\phi)\, d\phi}{\int w(\phi)\, d\phi}.$$

where $w(\phi)$ stands for the weight as a function of phase.

However, since the observations form a discrete dataset, the back-projection is obtained by summing the flux density from each observed spectrum at the velocity given by the velocity curve (Horne 1991):

$$\epsilon(v_x, v_y) = \frac{\sum_{j=1}^{n} I((v_x, v_y, v_z), \phi_j)\, w(\phi_j)}{\sum_{j=1}^{n} w(\phi_j)}$$

where n corresponds to the number of observations, $I((v_x, v_y, v_z), \phi_j)$ to the flux at the velocity $v(\phi_j) = -v_x \cos\left(2\pi\phi_j\right) + v_y \sin\left(2\pi\phi_j\right) + v_z$ and $w(\phi_j)$ to the weight allocated to the spectrum j.

The back-projection technique provides the real Doppler tomogram, but convolved with a Point-Spread Function (PSF) in the $v_x - v_y$ plane. This PSF is characterized by a Gaussian core with extended wings having a $1/\sqrt{v_x^2 + v_y^2}$ profile (Horne 1991). Therefore, we apply, as an extension to this method, a Fourier filter to the observed spectra to sharpen the PSF. We first compute the Fourier transform of each observed spectrum and we then multiply the Fourier amplitudes by a filter

$$G(\omega) = \left(\frac{\omega}{\omega_N}\right) \exp\left[\frac{-\omega^2}{2\omega_c^2}\right]$$

where ω_N is the Nyquist frequency and ω_c is the cutoff frequency determined from the spectral resolution of the data. The first factor (ω/ω_N) allows to suppress the $1/\sqrt{v_x^2 + v_y^2}$ tail whilst the second one $(\exp[-\omega^2/2\omega_c^2])$ decreases the amplification of high-frequency noise in the spectra (Kaitchuck et al. 1994). An inverse Fourier transform is then performed on the results to recover the filtered spectra and the back-projection is applied to provide the Doppler map. Even though the application of a filter reduces the noise in the Doppler tomogram, it also affects its resolution. Consequently, a compromise has to be found between a high resolution and a low noise.

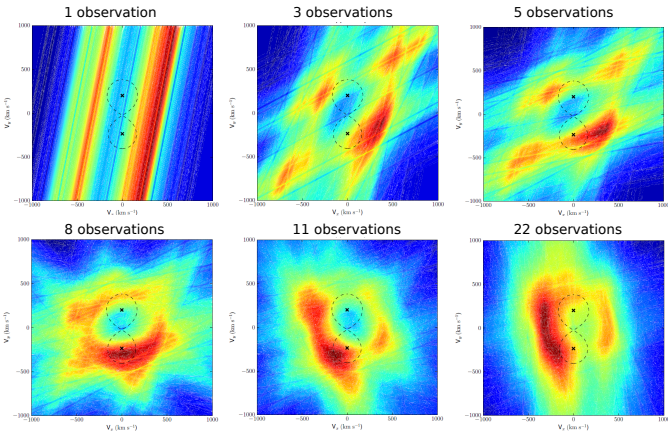

Figure 3.2: Spoke-like effect in the Doppler tomogram built from 1, 3, 5, 8, 11 and 22 observations, respectively.

Although that method is fast and straightforward, it does have the disadvantage of producing "spikes" in the Doppler map at angles corresponding to the binary phases sampled by the data. As we show in Fig. 3.2, these artefacts are particularly visible if the coverage of the orbital cycle is not uniform, and can lead to spurious results. Indeed, among the 6 tomograms shown in Fig. 3.2, only the last one (built from the 22 observations) is computed from data well-sampled over the entire orbital period. The other ones are affected by spikes and/or are totally erroneous.

3.2 Algebraic methods in Doppler tomography

With the current increasingly fast computers, other methods of tomographic reconstruction have been developed in medical imagery to, notably, decrease the effects generating the spikes. By adjusting these methods to the astrophysical field, the emission-line tomography problem is re-written as a system of linear equations. These methods, the so-called *algebraic methods*, serve as an alternative to the Fourier-filtered back-projection and ask to "slice" the Doppler map and the observed spectra in small areas. In order to make the distinction between the elements of the Doppler map and those of the observed spectra, we define the projections (or observed spectra) as composed of areas called "dexels" (detector elements, see Darcourt et al. 1998) whilst the Doppler maps are constituted of "pixels". The values of these "dexels" are given by the flux at each wavelength of the observed spectra. As a consequence, the system of linear combinations is written as

$$I(v_k, \phi_j) = \sum_{i=1}^{n} R_{ji}\, \epsilon_i(v_x, v_y) \qquad \forall k \in [1, m] \text{ and } j \in [1, l]$$

with m the number of "dexels" in each projection, l the number of observed spectra and n the number of pixels in the tomogram. These equations can be expressed under the matricial form $I = R\epsilon$ where

- I is the vector of observations. Each "dexel" is concatenated to form a long vector whose size is equal to the number of observed spectra (l) $\times$ the number of points per observation (m).

- ϵ represents the Doppler map transformed in a vector of size n^2.
- R is the projection matrix or the weighting matrix. This matrix represents the contribution of each pixel to each dexel. This matrix is built as a function of the data acquisition and not of the data themselves. In the simplest case (see Fig. 3.3, left panel), we have:

$$R_{ji} = \begin{cases} 1 & \text{if the pixel } i \text{ is crossed by the projection } j, \\ 0 & \text{otherwise.} \end{cases}$$

  Of course, a more complex form can be envisaged. Indeed, rather than attributing a value equal to unity to the pixels which are involved in a projection, we can calculate, for each element of the matrix R, the surface of the intersection between the projection width and the cell surface, as illustrated in Fig. 3.3 (right panel, for more details, see e.g. Kak & Slaney 2001).

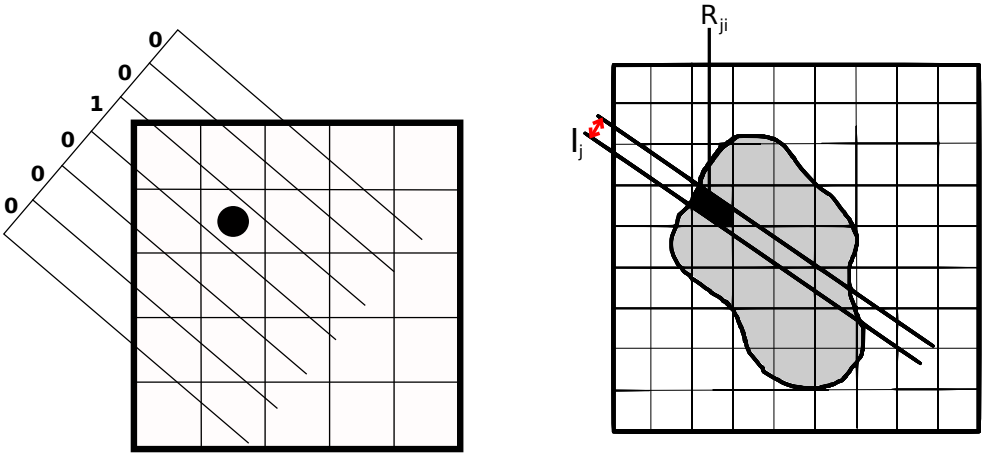

Figure 3.3: Conventions which are adopted for the implementation of the algebraic algorithms used for the Doppler tomography: the *left panel* represents the contribution of each pixel to a given projection whilst the *right panel* exhibits the determination of the contribution of each pixel based on the intersection surface. The red arrow indicates the projection width.

In the algorithms we implement, we chose to assign to each pixel the value 1 or 0 rather than considering the intersection surface. Indeed, because of the huge quantity of memory required for the computation, we have to define a projection width proportional to the pixel size. Consequently, taking into account the intersection surface does not significantly improve the determination of the emissivity level in the tomogram. We have also built the Doppler map so that the maximum radial velocity reached by the material can be represented in the corners of the map, as illustrated in Fig. 3.4. This definition and the requested high accuracy suggest that the weighting matrix is rectangular as well as particularly large and ill-conditioned. Such properties make the matricial equation difficult to invert. Moreover, this matrix is sparse because each dexel allows to see only a small portion of the total number of pixels. Consequently, methods such as the pseudo-inverse or the Singular Value Decomposition (SVD) factorization, as previously described for the disentangling methods, could be used but the large size of the matrix and thus the required CPU time make them unadapted. Therefore, the iterative methods, already applied in medical imagery, are preferred over the inversion methods. These methods consist, from an initialisation of ϵ, to

iteratively correct the estimate of the solution by computing, at the k^{th} iteration, the differences between the estimates of the $(k-1)^{\text{th}}$ iteration and the observed spectra I.

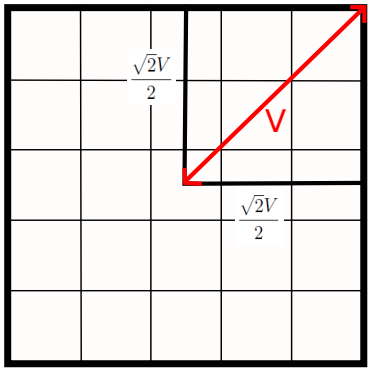

Figure 3.4: Definition of the size of the Doppler map.

3.2.1 The ART method

Among these iterative methods, ART (Algebraic Reconstruction Technique, Buzug 2008 and references therein) is certainly one of the oldest techniques. The latter is an iterative process which consists in correcting at each iteration the old solution by a factor proportional to the error on the real projection. In order to simplify the description of the process, the problem of the resolution of linear systems is summarized to finding a point representing the solution in a space at n dimensions where each equation corresponds to a hyperplane. These hyperplanes are thus a kind of sets of constraint to fullfil. ART starts from a random initialisation of the solution even though we generally affect to the $\epsilon_i^{(0)}$ a zero value. This initial guess is then projected on the first hyperplane, giving a new solution after the first iteration. We use this solution to project it on the second hyperplane to give $\epsilon^{(2)}$. The iterative corrections continue on the basis of all the equations, until obtaining the final solution. Each pixel is thus updated at each iteration, as follows:

$$\epsilon^{(k)} = \epsilon^{(k-1)} + R_j^T \frac{I_j - < R_j, \epsilon^{(k-1)} >}{||R_j||^2}$$

where $< \cdot, \cdot >$ is the scalar product, k the iteration and j the observed spectrum. This process thus uses at each iteration only one projection. As an illustration, Fig. 3.5 describes the resolution process for a system composed of two equations.

At the same time, to obtain unique solution, the system must have idealized physical conditions (Buzug 2008). When the data are too noisy as it can be the case in astrophysics, the iterative algorithm can be affected by an oscillation phenomenon around the real solution, even for a square matrix. If we look closer at Fig. 3.5, we clearly see that the convergence of this method is directly dependent on the angle between two consecutive hyperplanes. Consequently, if this angle is small, the algorithm needs more iterations to reach convergence. However, it is physically unlikely in tomography that two consecutive projections are almost parallel since they are assumed to be taken to cover as uniformely as possible the orbital cycle. For a rectangular projection matrix, i.e., when the system is under-determined (i.e., the size of I is smaller than that of ϵ) or over-determined (i.e., the size of I is larger than that of ϵ), no unique solution is found but the solution determined by

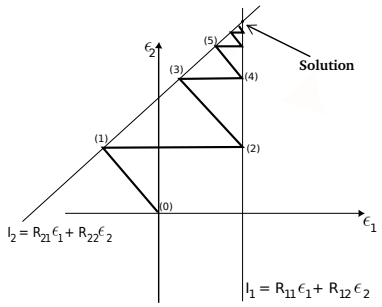

Figure 3.5: Principle of the ART method.

the algorithm is located in the close neighbourhood of the intersection of the hyperplanes. The program thus converges towards a solution so that $||I - R\epsilon^{(k)}||^2$ is minimal.

3.2.2 The SIRT method

The SIRT (Simultaneous Iterative Reconstruction Technique) method uses the same equations as ART but takes into account all the projections at each iteration before computing the new values. The change for each pixel corresponds to the mean value of all the changes computed on that pixel (Kak & Slaney 2001). These new values are obtained from the expression[7]:

$$\epsilon^{(k)} = \epsilon^{(k-1)} + \frac{\Lambda}{||R||^2} \cdot R^T \cdot \left(I - < R, \epsilon^{(k-1)} >\right) \qquad \text{with } 0 < \Lambda < 2.$$

As for ART, this method does not depend on the initialisation of the solution vector. Moreover, accounting for all the information at once implies that the SIRT needs more computational time and more memory than ART. However, it generally requires less iterations than ART to converge towards the real solution, usually leading to better results as we will see in the next section.

3.3 Applications to evolved binaries

We apply the Fourier-filtered back-projection and the algebraic methods on a series of spectra of three evolved binaries: Plaskett's star, Cyg OB2#5 and AO Cas. These stars have already been investigated and the results are given in Linder et al. (2008), Linder et al. (2009) and Linder (2008), respectively. The aim of this section is thus not to re-analyse these binary systems (though a small word on the physics of the systems will be given) but the goal is to compare the Doppler tomograms and to give the advantages/disadvantages of each method.

3.3.1 Plaskett's Star

Plaskett's Star is an O 8I/III+O 7.5III/V binary system which will be presented with more details in Section 5.4. The Doppler maps of the He II 4686 and Hα lines (Figures 3.6 and 3.8, respectively) are computed from a series of eighteen high-resolution spectra taken with FEROS on the 2.2 m

[7] $||\cdot||$ means the matricial norm.

telescope at La Silla (Chile). We fix the systemic velocity (v_z in Eq. 3.1) to a value equal to 0.0 to obtain similar tomograms than those of Linder et al. (2008).

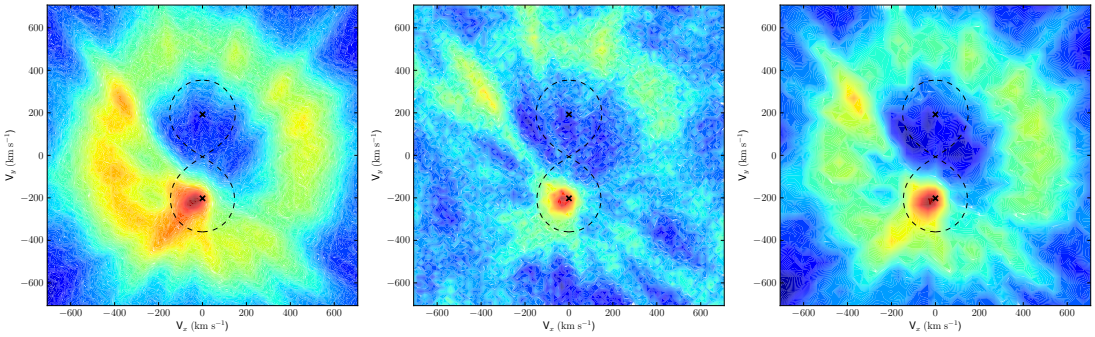

Figure 3.6: Doppler maps of the He II 4686 line of Plaskett's star, computed with the Fourier-filtered back-projection method (left panel), the ART (middle panel) and the SIRT (right panel). The dashed line draws the Roche lobes in velocity space whilst the velocity of the center of mass of the primary (secondary) is represented by a cross in the bottom (top) part of the map.

To illustrate the principles of the Doppler tomography, we show in Fig. 3.7 the observed line profile variations of the He II 4686 line. The S-wave for the highest emission peak is indicated in red, but the other weaker emissions also have their own S-waves, used to build the Doppler map. The He II 4686 line displays three emission peaks, a narrow one moving as a function of the orbital cycle and two broader ones (respectively blue-shifted and red-shifted) that do not present large variations in wavelength. The Doppler tomograms of both the He II 4686 and the Hα lines present their highest emission peak near the center of mass of the primary (v_x = −60 and −68 km s^{-1}, respectively). They also reveal an annular region around the center of mass of the whole system (for more information, see Linder et al. 2008). We stress that this annular region is not due to the tomography method but is real and is generated by the two "stationary" emissions around the rest wavelength.

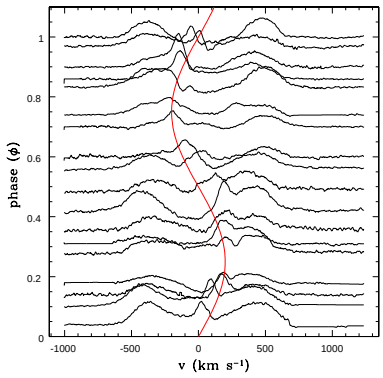

Figure 3.7: Line profile variation of the He II 4686 line as a function of the orbital phase. The S-wave corresponding to the highest peak is shown in red.

Since the Fourier-filtered back-projection is the most commonly used method in astrophysical applications, we consider this technique as the starting point for the comparison. The Doppler maps of the He II 4686 line, produced from the algebraic methods, are computed by using a matrix

composed of 7218×7225 elements to reach a resolution in the $v_x - v_y$ plane of about 23.5 km s^{-1}(as indication the step in the Fourier-filtered back-projection technique is equal to 1 km s^{-1}). The weight attributed to each spectrum is rigorously the same for each method, i.e., unity for all. For the Hα line, a projection matrix of 10818 × 11025 elements is used to construct the tomograms, leading to a step in the Doppler map of about 28.6 km s^{-1}.

For the map computed with the Fourier-filtered back-projection method, the emissivity zone of the He II 4686 line close to the primary star appears to be stretched out toward the bottom-left corner of the map. That is due to the "spike" artefacts, as we have presented in Section 3.1. This effect is clearly less marked on the strongest emission peak of the Doppler maps determined by the algebraic methods even though it remains present in the annular structure. Concerning the annular structure, the ART method can barely reproduce it compared to the two other tomograms while this structure is definitely real.

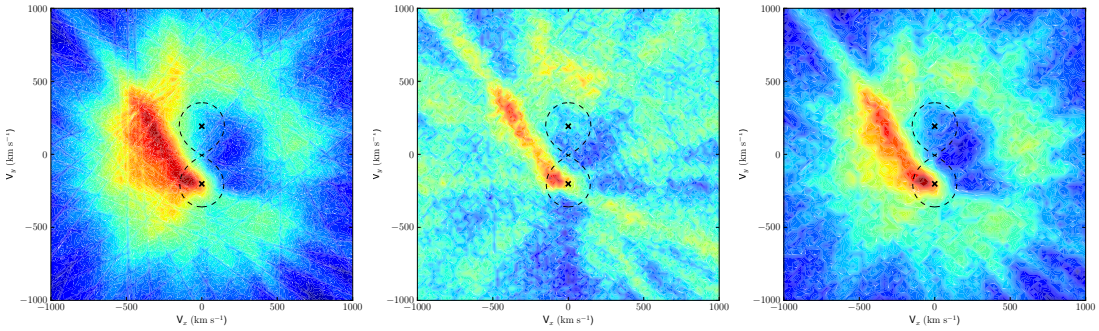

Figure 3.8: Same as for Fig. 3.6 but for the Hα line of Plaskett's star.

To summarize, the highest emission peak, in the He II 4686 and Hα tomograms, is clearly marked, while its "dilution" is less visible in the maps built from the algebraic methods. However, the maps computed from ART appear to be less reliable. Indeed, the annular structures which are clearly detected in the line profiles of the observed spectra are barely reproduced. In addition, we also see that the effects of the spikes seem to be amplified by this method. These conclusions however have to be confirmed through the two other applications.

3.3.2 Cyg OB2#5

Cyg OB2#5 is probably a multiple system composed of three or maybe four components (Kennedy et al. 2011). A first analysis of the two main components (primary and secondary) that form a short-period eclipsing binary was made by Rauw et al. (1999). Spectral types of O 6−7 and of Ofpe/WN9 were assigned to the primary and secondary stars, respectively. Furthermore, these authors computed an orbital solution which provides the position of both components in the Doppler maps. A more recent investigation by Linder et al. (2009) was devoted to the system's light curve, the X-ray observations and the optical spectra. The modelling of the light curve indicated a contact system whilst the X-ray (Linder et al. 2009) and radio (Kennedy et al. 2010) data suggest at least one, maybe two, additional components. We reproduce the Doppler maps for the He II 4686 and Hα lines (Figs. 3.9 and 3.10) with the same parameters as used by Linder et al. (2009), i.e., with a systemic velocity of about −33 km s^{-1} and a mass ratio of 3.31. Weights of 1.0 are given to all the spectra. The projection matrices used in the algebraic algorithms have a size of 4800 × 4900 for both lines, corresponding to a resolution of about 30.3 km s^{-1} in the $v_x - v_y$ map. These matrices

are smaller than for Plaskett's star since the reconstruction technique is only applied to eight observed spectra, well-sampled over the orbital cycle. These data were collected during September 1996 and April 1997, with the 2.1m telescope equipped with the ESPRESSO spectrograph at San Pedro Màrtir observatory (Mexico).

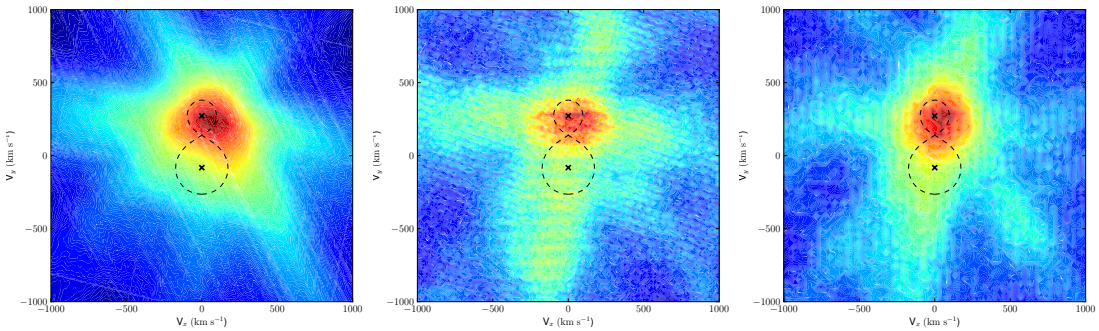

Figure 3.9: Doppler maps of the He II 4686 line of Cyg OB2#5, computed with the Fourier-filtered back-projection method (left panel), the ART (middle panel) and the SIRT (right panel). The dashed line draws the Roche lobes in velocity space whilst the velocity of the center of mass of the primary (secondary) is represented by a cross in the bottom (top) part of the map.

The tomogram, shown in Fig. 3.9, indicates an emission zone close to the velocity of the secondary star. The comparison of the three Doppler maps in Fig. 3.9 reveals the presence of spikes in all three plots. However, we clearly see, for the Fourier-filtered back-projection method, that the emission region "leaks" along all the directions of the spikes whilst this effect is less marked for the algebraic methods, especially the SIRT one. Concerning the formation region of the Hα line (Fig. 3.10), positive velocities are found, for v_x and v_y, which corresponds to material moving from the primary to the secondary and following the orbital motion of the secondary star (Linder et al. 2009). The tomograms are rather comparable, except that the emission zone also appears larger for the Fourier-filtered back-projection. The light-blue zone is extended along the x-axis from -1000 to 1000 km s^{-1} whilst, for the ART and SIRT method, this region covers an interval between -800 and 800 km s^{-1}. This "dilution" is partly explained by the application of the Fourier filter in the back-projection method but the shape of the emission zone is still different from those computed from the other method, even though we do not apply this filter.

The three methods applied on Cyg OB2#5 give rather realistic results even though the emission region still appears slightly different for the ART method, as we already mentioned for Plaskett's Star. In the algebraic techniques, we observe an increase of the spike effect in the bottom-left part of the maps. Though this effect depends on the data sampling, it could also be partly increased because of the lower resolution used to compute the maps of the He I 4686 line (Fig. 3.9).

3.3.3 AO Cas

AO Cas is a semi-detached system where the primary fills up its Roche lobe. Linder (2008) reported a probable inclination of the system of 66° and determined a spectral classification of O 9.5III and O 9V for the primary and secondary components, respectively. She computed the orbital solution of this system, reporting a semi-amplitude of about 230.6 km s^{-1} for the primary and 143.7 km s^{-1} for the secondary.

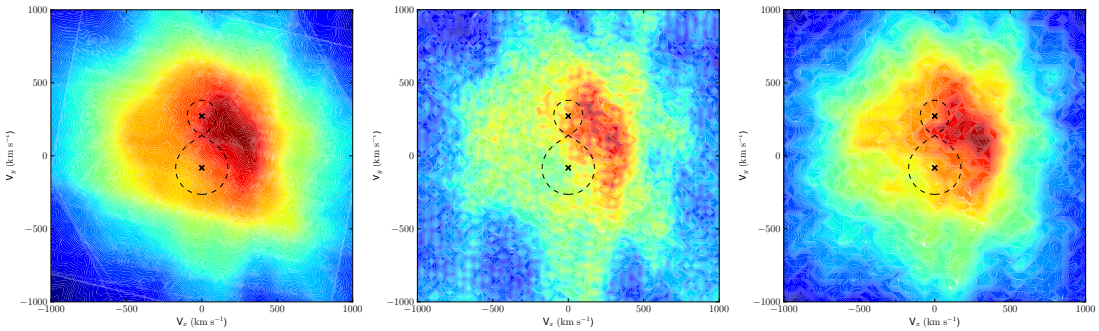

Figure 3.10: Same as for Fig. 3.9 but for the Hα line of Cyg OB2#5.

The computation of the Doppler maps are made from forty-three observed spectra. These data were obtained between 2002 and 2007 with the Aurélie spectrograph on the 1.52m telescope at the Observatoire de Haute-Provence (OHP) in France. However, the wavelength domain covered by the instrument is relatively small and depends on the chosen configuration. For these campaigns, the spectra are focused on the [4450 – 4900] Å wavelength domain. Consequently, the Doppler map of the Hα line is not investigated. The journal of these observations and the complete analysis of this system is given by Linder (2008).

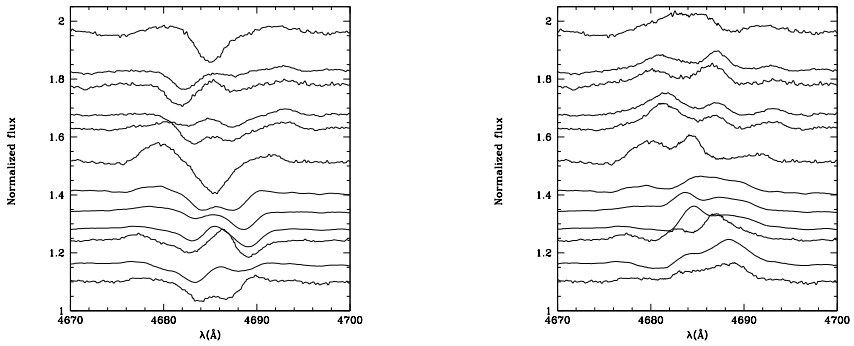

Figure 3.11: He II 4686 line profiles of AO Cas sampled over the orbital cycle. The left panel shows the observed line profiles, whilst the right one displays the restored profiles.

Unlike those of Plaskett's star or Cyg OB2#5, the spectra of AO Cas (Fig. 3.11, left panel) present, in the He II 4686 line, weak emissions coupled with strong absorption profiles bound to both components. The presence of these absorption profiles prevents us to detect the entire emission of the binary system. Indeed, parts of the emissions could be located in the cores of the absorption lines. Therefore, we apply a first-order "cleaning" process by removing the absorption parts of the He II 4686 line. To this end, we use synthetic spectra with the same spectral classification than each component and broadened from the adequate rotational velocity to match the absorption line profiles. The best results are achieved for $v \sin i$ of about 107 and 91 km s^{-1} for the primary and the secondary, respectively. We then shift these data with the radial velocity of the star corresponding to the given orbital phase and we subtract the line profiles from the observed spectra. We however notice that the profile of the He II 4686 line is slightly dependent on the wind parameters even though it is not the best indicator in the optical domain. The spectra resulting from the "restoration" process are shown in the right panel of Fig. 3.11. We first ap-

ply the Fourier-filtered back-projection algorithm on the dataset. We find a maximum emission at $(28, -245)$ km s^{-1}and two other emission zones at $(319, -75)$ and $(52, 99)$ km s^{-1}. The second peak could be reminiscent of systems which present a strong colliding wind region such as systems formed of at least one WR star (see more details in WR20a, Rauw et al. 2005b).

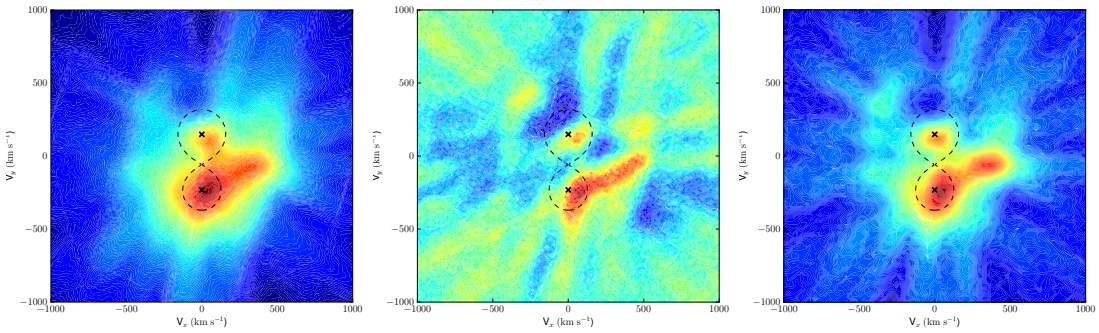

Figure 3.12: Doppler maps of the He II 4686 line of AO Cas, computed with the Fourier-filtered back-projection method (left panel), the ART (middle panel) and the SIRT (right panel).

For the computation of the tomograms with the algebraic methods, we use a resolution of 10 km s^{-1} for the ART method whilst a resolution of 25 km s^{-1} is adopted for the SIRT map (because of expensive CPU time requirement). The three Doppler tomograms are displayed in Fig. 3.12. We clearly see the similarity between the Fourier-filtered back-projection and the SIRT maps. Once again, the dilution is less marked with the SIRT technique, revealing obvious separated emissivity zones. Moreover, as it was the case for the two previous systems (Plaskett's Star and Cyg OB2#5), the tomogram computed by ART shows an overemissivity in the zones affected by the spikes. Even though we detect the maximum of emission in this map, the result is not reliable since it generates emissions which are not observed.

3.3.4 Comparison between analytic and algebraic methods

From a general point of view, the Doppler maps computed with the ART technique are not optimal: the intensity of the emissivity map is generally poorly represented, which distorts the real properties of the colliding-wind interaction zone. Moreover, the convergence is relatively slow compared to the SIRT method as we show in Fig. 3.13 for Plaskett's star. The two other methods (Fourier-filtered back-projection and SIRT) seem to provide equivalent results.

Consequently,

- the models computed with SIRT and the Fourier-filtered back-projection method seem to be more realistic than those generated with ART, as we showed for the three studied systems
- the SIRT technique also looks to be more reliable. Although the results of the Fourier-filtered back-projection are affected by the filter, its effect is not sufficient to produce such differences between the dilutions of both tomograms.
- independently of the spectral resolution of the data given as input, the algebraic methods are clearly dependent on the chosen resolution to build the Doppler map. Even though the reconstruction by SIRT appears more accurate, the choice of this step indeed directly affects

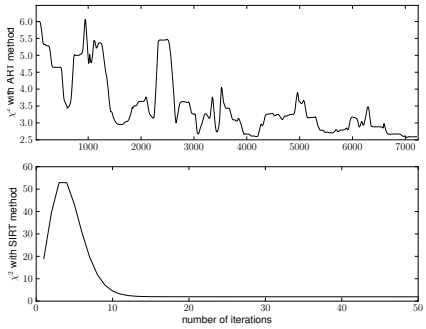

Figure 3.13: Comparison of the convergence between ART and SIRT methods applied to the He II 4686 line of Plaskett's star.

the memory requirement hence the computational time necessary to obtain the tomograms. Therefore, the resolution of the Doppler map cannot be refined indefinitely.

In the next chapter, we apply the disentangling method and the Doppler tomography technique to improve our knowledge of the nature of a newly-detected triple system as well as of its different components.

Chapter 4

The triple system HD 150136

HD 150136 is a bright X-ray source (Skinner et al. 2005), a non-thermal radio emitter (Benaglia et al. 2006) and the nearest system (1.32 ± 0.12 kpc) harbouring an O 3 star. Niemela & Gamen (2005) indeed classified HD 150136 as an O 3+O 6 binary. These authors emphasized the presence in the electromagnetic spectrum of the N IV 5203 and N V 4603–19 absorption lines and the N IV 4058 emission line, typical of the earliest spectral types. But this object was also suspected to be a triple system for several reasons. In the optical domain, Niemela & Gamen (2005) indeed measured on the He I lines radial velocity variations which do not follow the orbital motion of any of the binary components. In the radio domain, Benaglia et al. (2006) detected, in the neighbourhood of HD 150136, a radio source of about 2″, i.e. the resolution limit of the radio data. In X-rays, Skinner et al. (2005) observed an X-ray emission slightly variable that they attributed to an occultation effect due to rotation or to a putative third star. Nevertheless, these different investigations never ascertained the existence of a third star in HD 150136.

In addition, the O 2–O 3 stars are considered, with the WNL stars, as belonging to the most massive objects even though their masses are still poorly constrained. Several methods exist to determine the stellar masses: from their positions in the HR diagram (evolutionary masses), from their radii and gravities (spectroscopic masses) or from their orbital parameters when they form a binary system (dynamical masses). The dynamical masses are more reliable than the other masses but, since the inclinations of the systems are often unknown, these masses represent only "minimum masses".

Finding an O 3 star in a multiple system thus constitutes a rare opportunity to determine with accuracy its minimum mass. Our investigation of HD 150136 is based on seventy-nine high-resolution high signal-to-noise spectra taken from 1999 to 2009 with successively the 1.5m (from 1999 to 2001) and 2.2m (for data between 2002 and 2009) telescopes at La Silla (Chile) equipped with the FEROS spectrograph. These data allow us to confirm, for the first time, the detection of a third component in the HD 150136 system. We also bring the proof that this component is physically bound to the inner system. Its orbit appears to be eccentric with an eccentricity larger than 0.3 and a period between 8 and 15 years. However, with such a period range, our monitoring is not yet sufficient to be more accurate on the determination of these parameters.

We apply the disentangling method (see Chapter 2) to separate the contributions of the three components. To obtain the individual spectra, we have to correct the disentangled spectra by the brightness ratios. To determine these ratios, we compute the equivalent widths of a set of diagnostic lines measured on the most deblended observed spectra and on the disentangled ones.

For each component, the equivalent width of a line corresponds to the ratio between the real flux divided by the sum of the three components' continuum fluxes:

$$EW_{\rm meas} = \frac{F}{F_{C_{\rm P}} + F_{C_{\rm S}} + F_{C_{\rm T}}}$$

Moreover, we estimate the equivalent widths of a single star with the same spectral classification than the studied components either on the basis of the tables reported in Conti & Alschuler (1971), Conti (1973) and Conti (1974) or from CMFGEN synthetic spectra[8] (especially for spectral types earlier than O 4 or later than O 9.5 because those types did not exist in the previous tables). These equivalent widths are the ratios between the real equivalent width of the star and the continuum flux of this star:

$$EW_{\rm single} = \frac{F}{F_C},$$

with F_C correponding to either the primary, the secondary or the tertiary component.
We hence compute the ratios $\frac{EW_{\rm meas}}{EW_{\rm single}}$ for each component such that

$$\left(\frac{EW_{\rm meas}}{EW_{\rm single}}\right)_{\rm P} + \left(\frac{EW_{\rm meas}}{EW_{\rm single}}\right)_{\rm S} + \left(\frac{EW_{\rm meas}}{EW_{\rm single}}\right)_{\rm T} \cong 1$$

The brightness ratios are then estimated from the mean values $\frac{EW_{\rm meas}}{EW_{\rm single}}$ determined on several individual spectral lines of two different components. For HD 150136, we focus on the He I 4471 and 5876 as well as He II 4542 lines, thereby implying $l_{\rm P}/l_{\rm S} \cong 2.5$ and $l_{\rm S}/l_{\rm T} \cong 1.5$. We also revise the spectral classification of the components, yielding an O 3V(f*)–O 3.5V((f$^+$)) primary, an O 5.5–6V((f)) secondary and an O 6.5–7V((f)) tertiary.

We then fit the individual disentangled spectra with the CMFGEN atmosphere code to constrain the stellar parameters of each star. In this context, the luminosities of the three components are measured on the basis of the total absolute V magnitude of the system. This absolute magnitude is estimated from:

$$M_{V_{\rm tot}} = V - (3.1 \times E(B-V)) - ((5 \log d) - 5)$$

with $E(B-V) = (B-V) - (B-V)_0$ where $(B-V)_0$ is taken from the tables of Martins & Plez (2006), $V = 5.5$ (Niemela & Gamen 2005) and $(B-V) = 0.16$ (Reed 2005) whilst the distance d is equal to 1.3 kpc (Herbst & Havlen 1977).
The individual values of the absolute V magnitude for each star are computed from the ratios between the individual flux and the sum of the continuum fluxes of the three components:

$$\begin{aligned}
M_{V_P} &= M_{V_{\rm tot}} + 2.5 \log\left(\frac{F_{C_{\rm P}} + F_{C_{\rm S}} + F_{C_{\rm T}}}{F_{\rm P}}\right) \\
M_{V_S} &= M_{V_{\rm tot}} + 2.5 \log\left(\frac{F_{C_{\rm P}} + F_{C_{\rm S}} + F_{C_{\rm T}}}{F_{\rm S}}\right) \\
M_{V_T} &= M_{V_{\rm tot}} + 2.5 \log\left(\frac{F_{C_{\rm P}} + F_{C_{\rm S}} + F_{C_{\rm T}}}{F_{\rm T}}\right)
\end{aligned}$$

From the bolometric corrections from Martins & Plez (2006), we compute the luminosity of each

[8]The equivalent widths of these spectra were kindly provided by Dr. F. Martins.

star by the expression:

$$\begin{aligned}
\log\left(\frac{L_{\rm P}}{L_\odot}\right) &= -0.4 \times (M_{V_P} + BC_{\rm P} - 4.75) \\
\log\left(\frac{L_{\rm S}}{L_\odot}\right) &= -0.4 \times (M_{V_S} + BC_{\rm S} - 4.75) \\
\log\left(\frac{L_{\rm T}}{L_\odot}\right) &= -0.4 \times (M_{V_T} + BC_{\rm T} - 4.75)
\end{aligned}$$

where BC is the bolometric correction. Therefore, we find, for the three components of HD 150136, $\log(L_{\rm P}/L_\odot) = 5.86^{+0.12}_{-0.11}$, $\log(L_{\rm S}/L_\odot) = 5.32^{+0.12}_{-0.10}$, and $\log(L_{\rm T}/L_\odot) = 5.01^{+0.11}_{-0.10}$.

We further constrain from the disentangled spectra the stellar parameters of the three components by using CMFGEN. We find $T_{\rm eff}$ of 46500 K and $\log g$ of 4.0 for the primary, $T_{\rm eff}$ of 40000 K and $\log g$ of 4.0 for the secondary, and $T_{\rm eff}$ of 36000 K and $\log g$ of 3.5 for the tertiary. However, the small value of $\log g$ seems to be caused by the disentangling program because the widths of Balmer lines (indicator lines of $\log g$, see Chapter 1) are not fully sampled even at phases where the spectral separation is maximum.

The orbit of the third component has a long period that we are not able to constrain with accuracy but that we estimate between 8 and 15 years. In addition, its eccentricity is estimated to at least 0.3. The comparison between the Keplerian and evolutionary masses allows us to determine masses of $64-71$, $36-40$ and $27-36\ M_\odot$ for the primary, the secondary and the tertiary components, respectively. Moreover, the positions of the stars on the HR diagram indicate, for the three components, ages between 1 and 3 Myrs, thus locating them on the main-sequence band.

Since the inner system is composed of two massive stars orbiting around each other with a period of about 2.67 days, the presence of a colliding wind interaction zone is quite likely. We thus apply the Doppler tomography technique (see Chapter 3) to map the stellar winds of the inner components. This investigation shows a large emissivity zone close to the primary component, probably due to its strong wind. Although the wind parameters and the disentangled He II 4686 and Hα line profiles are uncertain, this result could indicate that the wind of the primary is actually stronger than those of usual O 3V stars.

The full analysis of HD 150136 is reported in Mahy et al. (2011, submitted, see pre-print hereafter).

Astronomy & Astrophysics manuscript no. hd150136
October 3, 2011

Evidence for a physically bound third component in HD 150136

L. Mahy[1], E. Gosset[1], H. Sana[2], Y. Damerdji[1], M. De Becker[1], G. Rauw[1], and C. Nitschelm[3]

[1] Institut d'Astrophysique et de Géophysique, Université de Liège, Bât B5C, Allée du 6 Août 17, B-4000, Liège, Belgium
e-mail: mahy@astro.ulg.ac.be
[2] Sterrenkundig Instituut "Anton Pannekoek", University of Amsterdam, Postbus 94249, NL-1090 GE Amsterdam, The Netherlands

[3] Instituto de Astronomía, Universidad Católica del Norte, Avenida Angamos 0610, Antofagasta, Chile

Received ...; accepted ...

ABSTRACT

Context. HD 150136 is one of the nearest system harbouring an O3 star. Long-suspected to be a binary, the possible existence of a third component has not been excluded in earlier investigations.
Aims. We confirm the presence of a tertiary star in the spectrum of HD 150136 that is physically bound to the inner binary system. This discovery makes HD 150136 the first confirmed triple system with an O3 primary star. We present a detailed analysis of the individual components of this newly determined triple system. It currently corresponds to one of the most massive systems in our galaxy.
Methods. We analyze high-resolution high signal-to-noise data collected through multi-epoch runs spread over ten years. We apply a disentangling program to refine the radial velocities and to obtain the individual spectra of each star. With the radial velocities, we compute the orbital solution of the inner system and we describe the main properties of the orbit of the outer star such as the preliminary mass ratio, the eccentricity and the orbital-period range. With the individual spectra, we determine the stellar parameters of each star by means of the CMFGEN atmosphere code.
Results. We bring clear evidence that HD 150136 is a triple system composed of an O3–3.5V((f$^+$)), an O5.5–6V((f)) and an O6.5–7V((f)) star. The three stars are between 0–3 Myrs old. We derive dynamical masses of about 64, 40 and 35 $M_\odot$ for the primary, the secondary and the third components by assuming an inclination of 49°. The inner system displays a clear emission associated to the two stellar winds. The third star moves with a period in the range between 2950 and 5500 d on an outer orbit with an eccentricity of at least 0.3. However, because of the long orbital period, our dataset is not sufficient to constrain the orbital solution of the tertiary component with high accuracy.

Key words. Stars: early-type - Stars: binaries: spectroscopic - Stars: fundamental parameters - Stars: individual: HD 150136

1. Introduction

NGC 6193 is a young open cluster surrounded by an H II region in the Ara OB1 association. The core of the cluster is hosting two bright and massive stars separated by about 10″: HD 150135 and HD 150136.

Several investigations in different wavelength domains (optical, radio and X-rays) allowed to improve the knowledge of HD 150136. In the optical domain, Niemela & Gamen (2005) reported this star as a binary system composed of an O3 primary and an O6 secondary. Indeed, spectral absorption lines of N IV 5203 and N V 4603–19 (wavelength are hereafter expressed in Å) as well as the emission line N IV 4058 were observed in the composite spectra. These lines are considered as the typical features for O2–O3 stars (Walborn et al. 2002a). This is a rather scarce category and only a few of these stars are reported as binary systems. Therefore, even though these objects are considered, with the WNL stars, as possibly belonging to the most massive objects, their actual masses are poorly known.

Located at a distance of 1.32 ± 0.12 kpc (Herbst & Havlen 1977), HD 150136 would thus harbour the nearest O3 star and would constitute a target of choice to investigate the fundamental parameters of such a star. Initially, the orbital period of the system was estimated to about 2.7 d whilst the mass ratio between the primary and the secondary stars was measured to be equal to 1.8 (unpublished, Garmany et al. 1980). The analysis of Niemela & Gamen (2005) allowed the authors to refine these values to 2.662 d for the orbital period and 1.48 for the mass ratio. Moreover, the possibility of a third component bound to the system was envisaged (though no clear pattern was detected) to explain that the He I lines do not follow the orbital motion of any of the binary components.

In the radio domain, HD 150136 was reported as a non-thermal radio emitter (Benaglia et al. 2006; De Becker 2007) which suggests the presence of relativistic electrons accelerated in shocks issued from a wind-collision region. This non-thermal source could be of about 2″ size (i.e., the resolution, Benaglia et al. 2006) and could be associated with a close visual component separated from HD 150136 by about 1.6″ (Mason et al. 1998), i.e., about 0.01 pc if we assume a distance of about 1.3 kpc. So far, there was however no indication that this star is physically bound to the binary system.

The *Chandra* X-ray observations of the young open cluster NGC 6193 revealed that HD 150136 is one of the X-ray brightest O-type stars known ($\log L_X = 33.39$ erg s^{-1} and $L_X/L_{bol} = 10^{-6.4}$, Skinner et al. 2005). Its emission probably results from a radiative colliding wind interaction and appears to be slightly variable on a timescale smaller than one day. According to Skinner et al. (2005), the discrepancy between the

Send offprint requests to: L. Mahy

orbital period and the time-scale of variation of this X-ray emission is probably due to an occultation effect either linked to the stellar rotation or to a putative third star of rather short period.

All these investigations thus suggest that HD 150136 is a multiple system rather than a binary even though evidences are still lacking. In this context, an intense spectroscopic monitoring at high resolution in the optical domain, first initiated to study the binary itself, was performed to bring a new light on this system. We organize the present paper as follows. Section 2 describes the observations and the data reduction technique. Section 3 reveals the existence of a third star in the data of HD 150136 and focuses on the disentangling process in order to compute the individual spectra of the components. A first determination of the orbital solution of the known short-period system and based on a SB2 configuration is presented in Sect. 4. We also demonstrate that these parameters can be optimized by assuming the external influence of a third component. The possible orbit of this third star is addressed in Sect. 5 and an SB3 partial solution is derived. This discovery makes HD 150136 one of the first systems where it is demonstrated that the third component is physically bound to the inner system (see also Tr16-104 Rauw et al. 2001 and HD 167971 Blomme et al. 2007). However, it is the first time that the primary is an O 3 star. We thus use in Section 6 the CMFGEN atmosphere code (Hillier & Miller 1998) to derive the fundamental properties of the stars in order to improve our knowledge on the O 3 star parameters. Otherwise, the configuration of the short-period binary seems to suggest a wind interaction zone detectable through the He II 4686 and Hα lines. We devote Sect. 7 to the analysis of the variability observed in these lines by applying a Doppler tomography technique. Finally, we discuss the implications of our results and we provide the conclusions in Sect. 8 and Sect. 9, respectively.

2. Observations and data reduction

A multi-epoch campaign was devoted to the observation of HD 150136. Between 1999 and 2009, we collected 79 high-resolution high signal-to-noise spectra of this star with the échelle Fiber-fed Extended Range Optical Spectrograph (FEROS) successively mounted at the ESO-1.5m (for spectra taken in 1999 and 2001) and the ESO/MPG-2.2m (for observations between 2002 and 2009) telescopes at La Silla (Chile). This instrument has a resolving power of about 48000 and the detector was a 2k × 4k EEV CCD with a pixel size of 15μm × 15μm. Exposure times were between 2 and 10 min to yield a signal-to-noise ratio, measured in the continuum on the region [4800–4825]Å, greater than 200 (see Table 1). FEROS is providing 39 orders allowing to cover the entire optical wavelength domain going from 3800 to 9200Å. The journal of the observations is listed in Table 1. Concerning the data reduction process, we used an improved version of the FEROS pipeline working under the MIDAS environment (Sana et al. 2006). The data normalization was performed by fitting polynomials of degree 4–5 to carefully chosen continuum windows. We mainly work on the individual orders but the regions around the Si IV 4089, 4116, He II 4686 and Hα emission lines were normalized on the merged spectrum. We also note that the flatfields of the 2009 campaign presented some oscillations of unknown origin. We have applied a filter to smooth these flatfields and thus limited the effects of the undesirable oscillations on the observed spectra.

Equivalent widths (EWs) and the Doppler shifts were estimated on each spectrum by fitting Gaussian profiles on the spectral lines. For the computation of the radial velocities, we adopted the rest wavelengths from Conti et al. (1977), for the lines with a rest wavelength shorter than 5000Å, and Underhill (1994), for the other ones.

3. Third component and disentangling

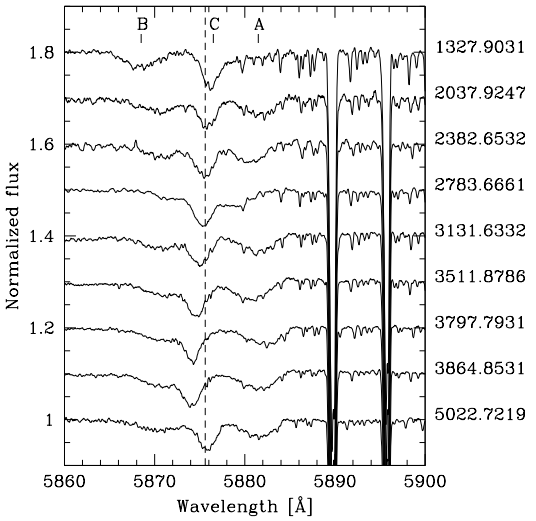

Fig. 1. Normalized spectra of HD 150136 zoomed on the [5860–5900]Å region and vertically shifted for clarity. The He I 5876 line displays a clear SB3 signature. A and B components are quoted only on the older spectrum as indication.

With the high-resolution spectra analysed in the present paper, we report the unambiguous detection of a third star signature for the system HD 150136 (Fig. 1). The data indeed exhibit a clear variation of the C component compared to the rest wavelength (He I 5875.62) shown by the dashed line. Moreover, the last observation confirms the periodicity of the variation, suggesting that the third star is also a member of a binary system. Although several analyses suspected the existence of this component, it has never been unveiled until now.

To separate the contribution of each star in the observed spectra. For that purpose, we applied a modified version of the disentangling program of González & Levato (2006) by adapting it to triple systems. This method consists of an iterative procedure which uses alternatively the spectrum of a first component (shifted by its radial velocity) and then the spectrum of a second component (also shifted by its radial velocity) to remove them from the observed spectra. The obtained result is a mean spectrum of the remaining third star. This program also allows us to re-compute with a cross-correlation technique the radial velocities of each star, even at phases for which the lines are heavily blended. The cross-correlation windows were built on a common basis gathering the He II 4200, He I 4471, He II 4542, He I 4713, He I 4921, O III 5592, C IV 5801–12 and He I 5876 spectral lines. In addition, we added the N V 4603–19 lines for the primary star. The radial velocities obtained from this technique are listed in Table 1. The resulting spectra were disentangled in a [4000–5900]Å wavelength domain and Hα. Though the He II 4686 and Hα lines present particuliar variations along the orbital phase, we included them in the process. However, the assumption of constant lines (on which relies the disentangling method) is no more satisfied, thus making these line profiles unreliable.

To obtain the individual spectra, we correct the disentangled spectra by the brightness ratio. We use the disentangled and the

Table 1. Journal of the observations.

HJD	S/N	RV_P	RV_S	RV_T	HJD	S/N	RV_P	RV_S	RV_T	HJD	S/N	RV_P	RV_S	RV_T
1327.9031	311	173.5	-368.8	25.4	3134.6275	474	-213.7	302.9	-29.4	3798.9088	376	173.4	-302.5	-69.3
2037.7746	214	-234.8	263.1	14.3	3134.9164	295	-138.4	155.4	-34.4	3799.9158	241	-75.4	86.0	-63.2
2037.9247	231	-246.8	292.5	13.2	3134.9183	318	-135.0	146.7	-34.0	3800.7716	262	-163.5	254.6	-71.8
2381.6519	384	167.6	-355.2	-6.4	3135.6251	317	164.2	-329.6	-33.8	3800.7746	308	-163.4	249.1	-70.9
2381.8167	404	156.4	-314.5	0.2	3135.6271	346	164.5	-323.3	-36.7	3800.9192	374	-113.9	156.9	-74.1
2382.6532	346	-184.6	232.9	-2.3	3135.8725	356	190.3	-355.7	-31.9	3861.6554	278	-158.9	239.1	-72.8
2382.7995	380	-222.9	280.8	-0.7	3135.8744	376	189.5	-352.8	-33.3	3861.9066	339	-210.5	324.1	-68.1
2383.6582	339	16.4	-71.8	-3.0	3509.5753	237	-28.0	1.3	-49.2	3862.8769	322	113.4	-171.7	-69.6
2383.8118	434	84.2	-158.7	5.8	3509.5784	220	-31.6	11.2	-48.9	3863.6503	357	147.8	-243.0	-69.2
2782.6246	538	172.7	-332.9	-19.3	3510.7732	273	62.8	-135.0	-50.3	3863.8683	336	51.0	-85.6	-73.6
2783.6661	461	-139.0	152.8	-18.4	3510.7762	263	61.3	-131.0	-51.6	3864.6371	353	-218.1	329.3	-70.8
2784.6897	389	-70.9	35.4	-18.3	3511.5647	306	-229.1	316.3	-45.8	3864.8531	341	-193.5	298.4	-72.6
3130.6387	399	167.7	-329.1	-33.9	3511.5677	316	-229.3	319.7	-45.9	5021.4921	578	172.2	-356.7	10.9
3130.6407	355	169.1	-325.8	-32.5	3511.8786	300	-186.6	249.9	-53.8	5021.5611	527	157.0	-342.4	9.2
3131.6332	374	-216.6	292.9	-28.1	3511.8816	308	-182.1	247.7	-54.6	5021.6147	519	145.3	-315.3	7.9
3131.6351	443	-211.1	296.6	-27.6	3512.5377	243	114.6	-217.9	-48.5	5022.4910	461	-211.5	257.4	9.9
3131.9266	391	-215.6	306.8	-26.3	3512.8633	344	193.7	-344.7	-53.0	5022.7219	548	-252.6	306.6	8.9
3131.9286	396	-223.7	303.3	-28.7	3512.8663	281	193.7	-347.6	-50.6	5023.4973	378	29.2	-117.8	9.1
3132.6081	290	52.3	-110.1	-30.4	3796.7553	210	152.1	-255.5	-70.3	5023.7349	419	118.2	-278.0	9.4
3132.6101	380	53.1	-112.1	-31.2	3796.7576	204	154.0	-251.6	-70.4	5025.5220	386	-236.7	283.7	7.9
3132.8874	460	144.6	-294.1	-32.9	3797.7890	219	-211.3	334.1	-72.4	5025.7098	474	-188.9	211.0	10.4
3132.8893	479	149.8	-287.3	-29.2	3797.7931	207	-212.5	331.3	-72.9	5028.5145	472	-142.5	133.9	3.6
3133.6779	418	48.9	-109.2	-38.2	3797.9131	271	-206.0	318.1	-70.1	5028.7328	342	-57.7	-15.7	8.2
3133.6798	451	52.5	-107.3	-36.1	3797.9161	307	-203.6	317.8	-71.7	5029.4986	455	167.5	-354.3	7.9
3133.9098	376	-73.6	59.9	-30.0	3798.7598	294	131.4	-229.7	-66.2	5029.7368	330	120.2	-269.5	3.5
3134.6256	379	-222.1	304.4	-29.4	3798.7628	243	130.5	-232.6	-68.3	5031.4953	487	10.9	-99.6	12.5
										5031.6685	391	92.6	-228.8	6.0

Notes. HJD is expressed in the format HJD−2 450 000. RV_P, RV_S and RV_T are the radial velocities (in km s^{-1}) measured by cross-correlation and where no correction of the systemic velocities has been applied. We notice that the error bars on these values are of about 5 km s^{-1}.

observed spectra to measure the EWs and constrain the spectral classification of the three components of HD 150136. This determination is based on the quantitative classification criteria presented by Conti & Alschuler (1971) and Conti (1973) which uses the EW ratios of the He I 4471 and He II 4542 lines to define the spectral type. This leads to an O3–O3.5 primary star, an O5.5–O6 secondary star and an O6.5–O7 third star. The weak N III 4634–41 emission and the strong He II 4686 absorption lines of the secondary and the tertiary components suggest to add the ((f)) suffix to their spectral types. In addition, the criterion given by Walborn et al. (2002b) confirms the classification of the primary. Its spectrum is reminiscent of that of HD 64568, i.e., close to an O3V(f*). However, the N IV 4058 line has an intermediate EW (∼ 160 mÅ) between the values measured on the N III 4634 (∼ 140 mÅ) and N III 4641 (∼ 250 mÅ) lines, thereby indicating a spectral type between O3V(f*) and O3.5V((f$^+$)). The (f*) reports a spectrum with the N IV 4058 emission line stronger than the N III 4634–41 lines and a weak He II 4686 absorption line whilst the ((f$^+$)) refers to a spectrum with the medium N III 4634–41 emission lines, the weak He II 4686 line and the Si IV 4089–4116 lines in emission. To compute the different brightness ratios, we compare the absolute EWs measured on the observed spectra with the theoretical values issued from synthetic models and which have the same spectral type as our disentangled data. This comparison was performed on the Helium lines and we obtained $L_P/L_S = 2.54$, $L_S/L_T = 1.53$ and $L_P/L_T = 3.89$ with an error bar at 1–σ of about 0.10. The individual spectra are shown as black lines in Figs. 2, to 4.

With $V = 5.5 \pm 0.12$ (Niemela & Gamen 2005), a mean $(B-V) = 0.16 \pm 0.01$, measured from Reed's catalog (Reed 2005), and a $(B-V)_0 = -0.28$ (Martins & Plez 2006), we computed an absolute V magnitude for the entire system equal to $M_V = -6.47^{+0.34}_{-0.36}$ by assuming a distance of about 1.32 ± 0.12 kpc. From the different brightness ratios, we then obtained $M_{V_P} = -5.91^{+0.34}_{-0.36}$, $M_{V_S} = -4.90^{+0.34}_{-0.36}$ and $M_{V_T} = -4.44^{+0.34}_{-0.36}$ for the primary, the secondary and the tertiary stars, respectively. The bolometric correction was computed on the basis of the expression given by Martins et al. (2005) from a typical effective temperature determined as a function of the spectral type of the three stars. These values coupled with the absolute V magnitude of the three stars yield the bolometric luminosities of about $\log(L_P/L_\odot) = 5.86^{+0.12}_{-0.11}$, $\log(L_S/L_\odot) = 5.32^{+0.12}_{-0.10}$, and $\log(L_T/L_\odot) = 5.01^{+0.11}_{-0.10}$ for the three stars. These luminosities are in good agreement with the ones of main-sequence stars having similar spectral classifications.

4. Inner short-period binary system

With the radial velocities refined by the disentangling program, we computed the orbital solution of the short-period system formed by the A and B components. We have first re-estimated the orbital period of the short-term binary by using the Heck-Manfroid-Mersch technique (hereafter HMM, Heck et al. 1985, and revised by Gosset et al. 2001) on the basis of $RV_S - RV_P$ values. We obtain an orbital period of about 2.67456 ± 0.00001. We then used the Liège Orbital Solution Package (LOSP[1]) to determine the SB2 orbital solution of the inner binary. Fig. 5 displays the radial-velocity curves and Table 2 lists the orbital parame-

[1] LOSP is developed and maintained by H. Sana and is available at http://www.science.uva.nl/ hsana/losp.html. The algorithm is based on the generalization of the SB1 method of Wolfe et al. (1967) to the SB2 case along the lines described in Rauw et al. (2000) and Sana et al. (2006).

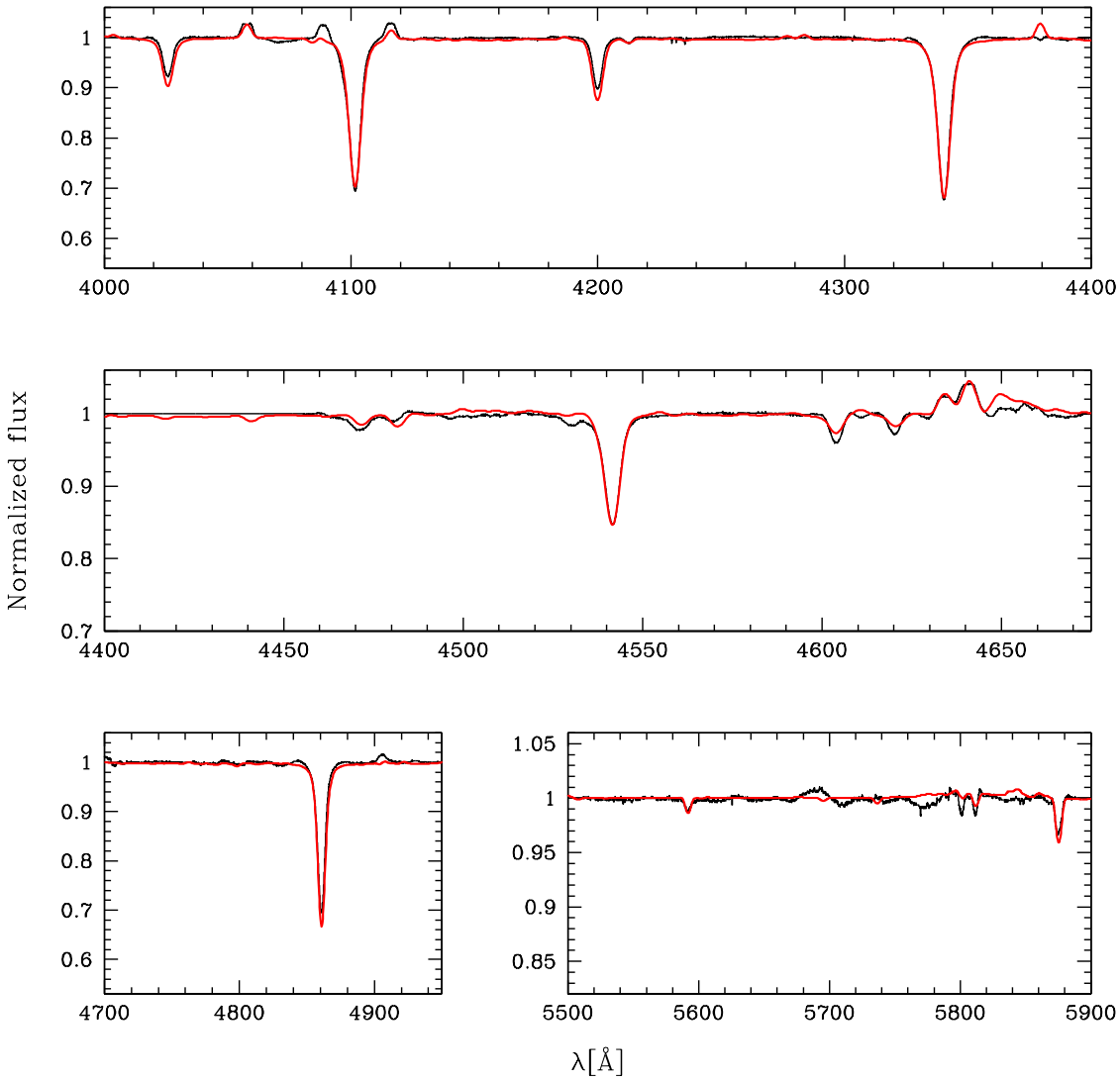

Fig. 2. Best-fit CMFGEN models (red) of the disentangled optical spectrum (black) of the primary component of HD 150136.

ters determined for an SB2 configuration. The system shows no significant deviation (test of Lucy & Sweeney 1971) from circularity and we thus adopt $e = 0$. In consequence, T_0 represents the phase of the conjunction with the primary in front. We however see that the dispersion of some observational points around the theoretical radial-velocity curves is rather large. Such a dispersion is probably due to the influence of the third star.

Consequently, we have computed, for the primary and the secondary stars, the averages on each epoch obtained from the differences between the observations and the radial-velocity curves. We have also removed from these values the systemic velocity quoted in Table 2. Moreover, we have compared these results to the systemic velocities of the primary and the secondary components computed on each individual observing campaign. Both methods report comparable global trends of the velocities for the inner system (see Table 3). By plotting the mean systemic velocities of the inner system and the mean radial velocities of the third component computed on each epoch as a function of time (Fig. 6), we detected a clear trend suggesting a periodical motion, reminiscent of an additional orbit. Therefore, we suggest that HD 150136 is at least an SB3 system.

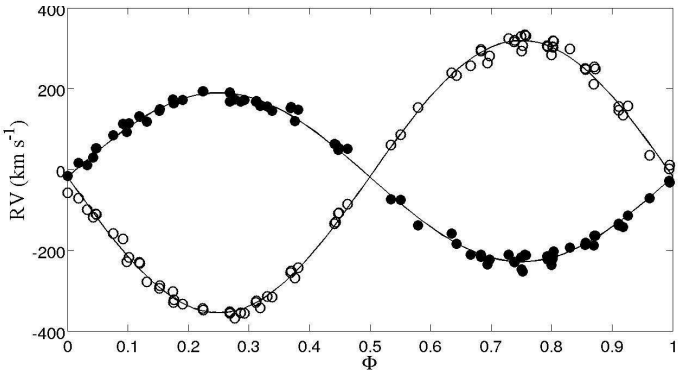

Fig. 5. Radial-velocity curves corresponding to the short-period inner SB2 system as a function of the phase. Filled circles (open) represent the primary (secondary) component.

5. The outer system

5.1. The outer system as an SB2

We used the mean systemic velocities of the inner system determined from each epoch as a primary component and we consider

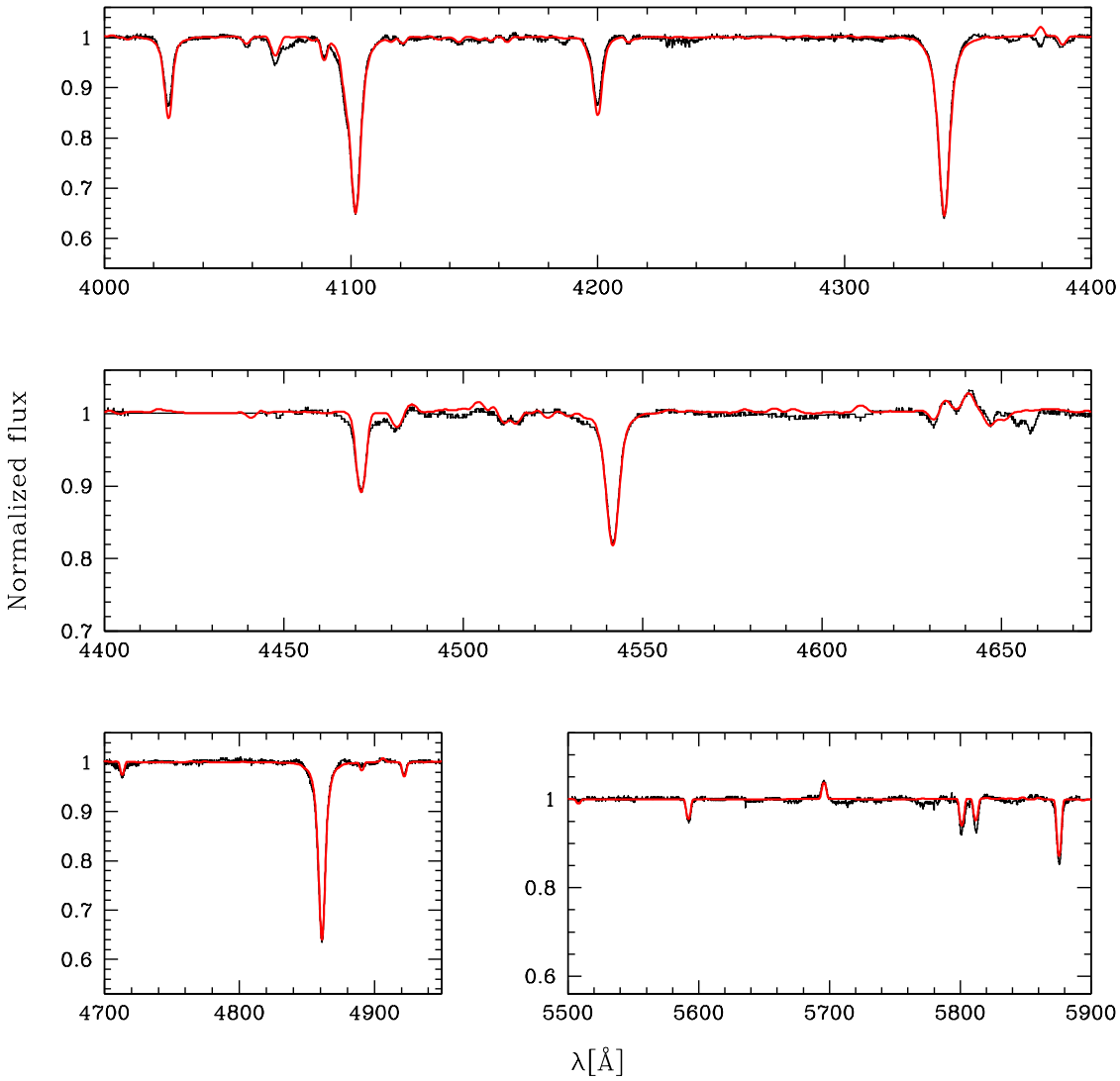

Fig. 3. Same as for Fig. 2 but for the secondary component of HD 150136.

Table 2. Orbital solution of the short-period binary system computed with LOSP and an SB3 program.

	SB2 solution		SB3 solution	
	Primary	Secondary	Primary	Secondary
P [days]	2.67454 ± 0.00001		2.67455 ± 0.00001	
e	0.0 (fixed)		0.0 (fixed)	
T_0 [HJD – 2450000]	1327.164 ± 0.003		1327.161 ± 0.006	
$q(M_1/M_2)$	1.615 ± 0.021		1.586 ± 0.019	
γ [km s^{-1}]	−19.7 ± 1.5	−17.8 ± 1.8	−26.1 ± 2.5	−24.4 ± 2.5
K [km s^{-1}]	208.9 ± 1.7	337.2 ± 2.7	211.2 ± 1.5	335.0 ± 1.5
$a \sin i$ [$R_\odot$]	11.0 ± 0.1	17.8 ± 0.1	11.2 ± 0.1	17.7 ± 0.1
$M \sin^3 i$ [$M_\odot$]	27.9 ± 0.5	17.3 ± 0.3	27.7 ± 0.4	17.5 ± 0.3
rms [km s^{-1}]	13.15		7.95	

Notes. The given errors correspond to 1–σ.

the third component as the secondary companion. These velocities did not allow us to determine with accuracy the real orbital period of the wide outer system. However, we could estimate this value between 2950 and 5500 d, i.e, between 8 and 15 years. Consequently, computing its orbital solution is useless without further high-resolution monitoring of HD 150136. Nonetheless, the measured velocities can provide information about the orbit as well as on the mass ratio between the inner system and the third component. To estimate the mass ratio, we calculated the average between the systemic velocities of the primary and the secondary stars and took these values as radial velocities of the inner system. We focused on the radial velocities of both com-

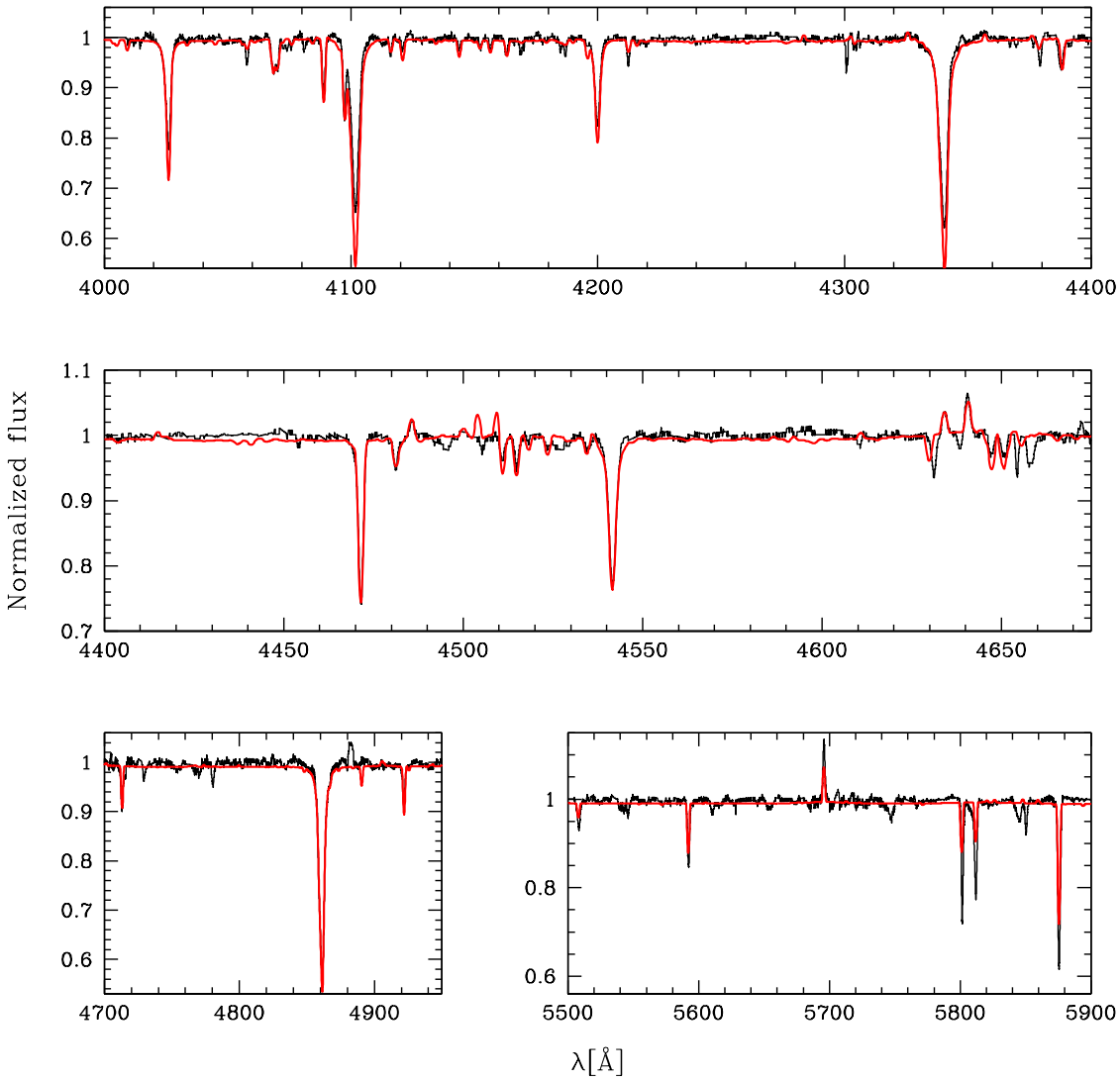

Fig. 4. Same as for Fig. 2 but for the third component of HD 150136.

Table 3. Systemic velocities (in km s^{-1}) of the primary and the secondary components as well as the mean value on each epoch.

HJD−2 450 000	Primary	Secondary	Mean
1327.9031	−32.6	−36.1	−34.4
2037.8496	−38.2	−49.1	−43.7
2382.7319	−22.2	−24.0	−23.1
2783.6601	−27.5	−23.9	−25.7
3133.4644	−20.6	−16.0	−18.3
3511.4421	−16.9	−13.8	−15.4
3798.7490	−8.5	−2.2	−5.4
3863.3497	−2.7	−5.2	−3.9
5025.8661	−32.2	−33.6	−32.9

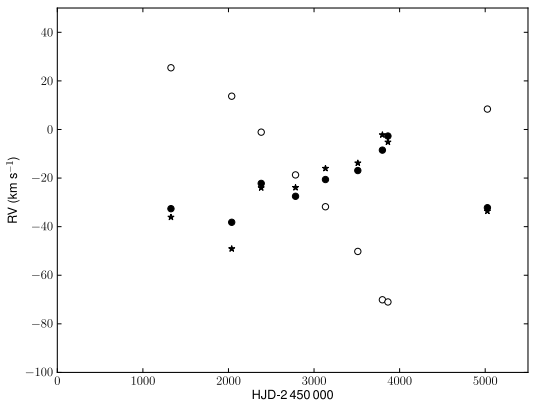

Fig. 6. Radial velocities of the outer system represented as a function of the time. Filled circles/filled stars correspond to the systemic velocities of the primary/secondary component whilst the open circles report the mean radial velocities of the third component.

ponents by fitting by a least-mean-square method the following relation:

$$RV_{\rm T}(\phi) = c_1\, RV_{\rm P+S}(\phi) + c_2$$

where $RV_{\rm P+S}(\phi)$, $RV_{\rm T}(\phi)$ are the systemic radial velocity of the inner system and the radial velocity of the third component, respectively, whereas $c_1 = -\frac{M_{\rm P+S}}{M_{\rm T}}$ with $M_{\rm P+S}$ and $M_{\rm T}$ the masses of the inner system and the third star, respectively. The linear regression gives us values of about $c_1 = -2.60$ and $c_2 = -79.58$ km s^{-1}. From c_2, we deduce $\gamma_{\rm T} \cong -14$ km s^{-1}. To verify the impact of the period on the value of the mass ratio, we

have also computed several orbital solutions assuming different orbital periods sampled between 2950 and 5500 d. All thes solutions led to a mass ratio of about 2.94. However, among the velocities exhibited in Figure 6, the point corresponding to HJD= 2 452 037.8496 (2001) displays a clear deviation probably due to the shortage of observations during this campaign. If we remove this point, we obtain by the linear regression method a mass ratio of about 3.1 and by the other method a mass ratio of about 3.2. We thus conclude to a mass ratio of about 2.9 ± 0.3 between the inner system and the third star. Similarly, from this sample of orbital periods, we derived an eccentricity larger than 0.3 for the outer system.

5.2. HD 150136 as a triple system

To better constrain the orbital parameters of the inner system, we took into account the influence of the third component by fitting all the components together. For that purpose, we determined with another method the orbital parameters of the inner system. This technique provided the approached orbital solutions for the two SB2 systems in HD 150136 i.e., the inner system composed of the primary and the secondary stars and the outer one formed by the mean systemic velocities characterizing the center of mass of the inner system and the radial velocities of the third component. Therefore, we performed on all the three sets of data (P, S and T) a global least square fit with an assumed circular orbit for the inner binary. For both systems, we followed the same procedure. We first deduced the approached orbital solution using the keplerian periodogram introduced by Zechmeister & Kürster (2009). This method consists in a fit of a simple sine function in the true anomaly domain. The approached orbital solution is then globally refined using a Levenberg-Marquardt minimization. We search the period in $[0.6\,T, 2.0\,T]$ for the outer orbit where T is the total time span of the observations. We use a constant step of frequency for both systems equal to $0.01/T$. Figure 7 exhibits the orbital solution for the short-term binary system by taking into account the influence of the third star. Following an F-test on the ratio of the two χ^2 of the fits, we conclude that this solution is clearly improved in comparison with that computed in Section 4 (see Fig. 5). The improvement is sufficiently marked to remain significant even though the F-test is not fully valid due to the non-linearity... We report in Table 2 the refined orbital parameters (see SB3 solution). Among these values, we notably observe a decrease of the error bars and an improvement on the mass ratio and on the systemic velocities.

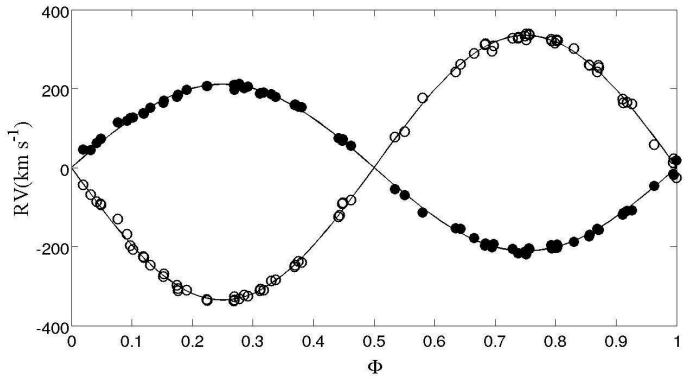

Fig. 7. Radial-velocity curves corresponding to the short-period inner system as a function of the phase according to the SB3 fit. Filled circles (open) represent the primary (secondary) component. The velocities are expressed in the frame of the center of mass of the P+S system.

6. Atmosphere analysis of the three stars

The three components of HD 150136 have been modelled separately by using the CMFGEN atmosphere code (Hillier & Miller 1998). Non-LTE models including winds and line-blanketing have been computed. The computations are done in spherical geometry and in the co-moving frame. A more detailed description of this code is provided in Hillier & Miller (1998). For the velocity structure, we used TLUSTY hydrostatic structures in the photosphere associated with a β-velocity law $v = v_\infty(1 - R/r)^\beta$ for the wind part (v_∞ being the wind terminal velocity). The TLUSTY models were taken from the OSTAR2002 grid of models computed by Lanz & Hubeny (2003) and $\beta = 0.8$, typical for O dwarfs, was adopted (Repolust et al. 2004). The models include the following chemical species: H, He, C, N, O, Ne, Mg, Si, S, Ar, Fe and Ni with the solar composition of Grevesse et al. (2007), except for N. We also used the superlevel approach to limit the required computation memory. When the atmosphere model has converged, the synthetic spectrum was generated through the formal solution of the radiative transfer equation. For that purpose, a microturbulent velocity varying linearly (with velocity) from 10 km s^{-1}, in the photosphere, to 0.1 $\times\, v_\infty$, in the outer boundary, was used. The emerging spectra were compared to the disentangled ones to constrain the main parameters in a more accurate way.

We thus determined the effective temperature ($T_{\rm eff}$), the $\log g$, the luminosity, the N content, the projected rotational velocity and the macroturbulence of each component through the following diagnostics:

- the *effective temperature*: $T_{\rm eff}$ is computed on the basis of the ratio between the He I 4471 and He II 4542 lines. However, other lines of helium such as He I 4026, He II 4200, He I 4388, He I 4713, He I 4921 and He I 5876 are also considered as indicators. Generally, we estimated the error in the models on the determination of that parameter to be equal to 1000 K.

- the *gravity*: we use the wings of the Balmer lines (Hδ, Hγ and Hβ) as main diagnostics to constrain the $\log g$. We refrained from using the Hα line because it forms at least partially in the stellar wind. However, for the tertiary star, the determination of the gravity is more uncertain because of the disentangling process (see Sect. 8). Therefore, the uncertainty on the $\log g$ is equal to 0.1 dex for the primary and the secondary and to 0.25 dex for the third component.

- the *luminosity*: the luminosity was constrained by the V-band magnitude by adopting a distance of about 1.3 kpc and a color excess ($B - V$) of 0.44 as explained in Section 3. The accuracy on the luminosity depends on the uncertainty on the distance of HD 150136 (1.32 ± 0.12 kpc).

- the *surface abundances*: the Nitrogen abundance was determined on the N III triplet in the 4500–4520Å range but also on the N IV 4058 and N III 4634–41 line profiles. The typical uncertainty on the CNO surface abundances is of about 50%. To estimate these uncertainties, we ran models with several different values of N and compared the corresponding spectra to the observed line profiles. When a clear discrepancy was seen on all lines of the same element, we adopted the corresponding abundance as the maximum/minimum value of the possible chemical composition. Carbon abundance was estimated to be solar for the three stars whilst Oxygen abundance was not determined

Table 4. Stellar parameters of the three components.

Parameters	Primary	Secondary	Third
Sp. type	O3V(f*)/ O3.5V((f+))	O5.5–6V((f))	O6.5–7V((f))
$T_{\rm eff}$ [K]	46500 ± 1000	40000 ± 1000	36000 ± 1000
$\log\left(\frac{L}{L_\odot}\right)$	$5.86^{+0.12}_{-0.11}$	$5.32^{+0.12}_{-0.10}$	$5.01^{+0.11}_{-0.10}$
R [$R_\odot$]	$13.14^{+3.62}_{-2.05}$	$9.54^{+1.98}_{-1.45}$	$8.24^{+1.65}_{-1.29}$
$\log g$	4.00 ± 0.10	4.00 ± 0.10	3.50 ± 0.25
M_{spec} [$M_\odot$]	$63.9^{+27.5}_{-27.4}$	$33.2^{+27.7}_{-14.2}$	$7.8^{+12.3}_{-4.7}$
M_{evol} [$M_\odot$]	$70.6^{+11.4}_{-9.1}$	$36.2^{+5.0}_{-1.6}$	$27.0^{+3.0}_{-3.5}$
N/H [$\times 10^{-4}$]	8.0±4.0	3.0±1.5	3.0±2.0
$V \sin i$ [km s^{-1}]	171±20	136±20	72±10
v_{mac} [km s^{-1}]	65±10	41±10	14±5
$\dot{M}$ [$M_\odot$ yr^{-1}]	1.0×10^{-6}	7.0×10^{-8}	3.0×10^{-9}
v_∞ [km s^{-1}]	3500 ± 100	2500 ± 100	1200 ± 100

Notes. The given errors correspond to 1–σ. The solar abundance for Nitrogen is N/H = 0.6×10^{-4}.

because of the lack of diagnostic lines.

– the *rotational and macroturbulent velocity*: the synthetic spectra were successively convolved by a rotational profile and a Gaussian profile representing the macroturbulence. First, the projected rotational velocity was computed with the method of Simón-Díaz & Herrero (2007) based on the Fourier transform. Then, the macroturbulent velocity was determined so that the shape of the He I 4713 line is best reproduced. When the latter line was not visible in the spectrum, we used the He I 5876 and/or the C IV doublet at 5801–12Åas second indicator.

The best-fit models of the three components are displayed in red in Figs. 2, 3 and 4 whilst the derived parameters are given in Table 4. However, the optical spectra do not give us enough information to constrain the wind properties of these components. We accordingly limit our investigation on the stellar parameters. Indeed, the Hα and He II 4686 lines are likely affected (to some extent) by the colliding-wind interaction zone at least for the primary and the secondary components. Since the disentangling generates mean spectra on the entire dataset, the Hα and He II 4686 line profiles could therefore be different from those of single stars with the same spectral classifications. We also investigated the UV domain but the small number of IUE data in the archives does not allow us to separate the individual contributions of the three components. Given the large ionizing flux generated by an O3 star, we have thus assumed that the flux collected in UV was mainly from the primary whilst the He II 4686 and Hα lines in the optical range serve to constrain the wind parameters of the secondary and the third components. Therefore, we caution to consider the wind parameters ($\dot{M}$ and v_∞) listed in Table 4 as preliminary values, useful to compute the atmosphere models.

7. Doppler tomography of the inner system

The O3V(f*)/O3.5V((f+))+ O5.5–6V((f)) inner system with its small separation between both components likely favours interactions between the stellar winds. If we look closer at the observed spectra, we clearly see that HD 150136 displays weak emissions in the He II 4686 and Hα lines. In order to better represent the emissivity of the inner system and notably the possible interactions between the wind of the primary and that of the secondary star, we use a Doppler tomography technique on those line profiles. This technique maps the formation region of these lines in velocity space. The absorption line profiles of the primary and the secondary as well as the presence of the third component in the spectra do not simplify the representation of the emissivity in the inner system (see left panel in Fig. 8). A preliminary treatment to eliminate these contributions in the observed spectra must first be applied. To realize this "cleaning" process, the disentangled spectrum of the third star, shifted by its radial velocity, was subtracted from all the spectra in our dataset. We also took the He II 4686 line profiles of the synthetic spectra of the primary and the secondary obtained with the CMFGEN code (see Sect. 6). We hence subtracted them by shifting them with their respective radial velocities to remove the absorption parts of the lines. The resulting restored line profiles only took into account the emission part of the He II 4686 line (Fig. 8, right panel). However, this process must be used with caution, especially for the Hα line. This line is indeed particularly dependent on the mass-loss rate and on the terminal velocity of the star. Therefore, this cleaning process requires reliable absorption line profiles which is not the case for our three stars. The reconstructed emissions of the He II 4686 and Hα lines are nearly symmetric and follows the orbital motion of the primary component. To analyse its entire profiles, we have applied a Doppler tomography technique on these two lines.

The Doppler tomography technique assumes that the radial velocity of any gas flow is stationary in the rotating frame of reference of the system. The velocity of a gas parcel, as seen by the observer, can be expressed by a so-called "S-wave" function:

$$v(\phi) = -v_x \cos(2\pi\phi) + v_y \sin(2\pi\phi) + v_z$$

where ϕ represents the orbital phase, (v_x, v_y) are the velocity coordinates of the gas flow and v_z is the systemic velocity of the emission line. This relation assumes an x-axis situated between the stars, from the primary to the secondary and a y-axis pointing in the same direction as the orbital motion of the secondary star (see e.g., Rauw et al. 2002; Linder et al. 2008). Usually, the method of the Fourier-filtered back-projection based on Radon's transform is used in astrophysics. However, this technique has the disadvantage of generating "spikes" in the tomogram if the observations do not densely sample the entire orbital cycle. In order to limit these artefacts, we thus applied another Doppler tomography program based on the resolution of the matricial system $Af = g$ where A is the projection matrix, f is the vector of emissivity and g is a vector concatenating the observed spectra. The elements of the projection matrix are equal to 1 if the projection of the S-wave onto the (v_x, v_y) plane is verified or to 0 otherwise. The solutions of the $Af = g$ system were computed from an iterative process called *SIRT* (Simultaneous Iterative Reconstruction Technique, Kak & Slaney 2001). The latter starts from an initialisation of the solution vector and computes at each iteration a correction which improves the solution of the previous iteration. These corrections are given by

$$f^{(n+1)} = f^{(n)} + \frac{\mu}{||A||^2} A^t \left(g - A f^{(n)}\right)$$

with μ a constant so that $0 < \mu < 2$ and $||\cdot||$ the matricial norm. This method converges to a least-square solution but requires more computational time than the Fourier-filtered back-projection.

The tomograms were computed from multi-epoch spectra. Consequently, we had to correct the radial velocities to bring the spectra to the same systemic velocity on the entire campaign. The He II 4686 Doppler map (Fig. 9) exhibits a single

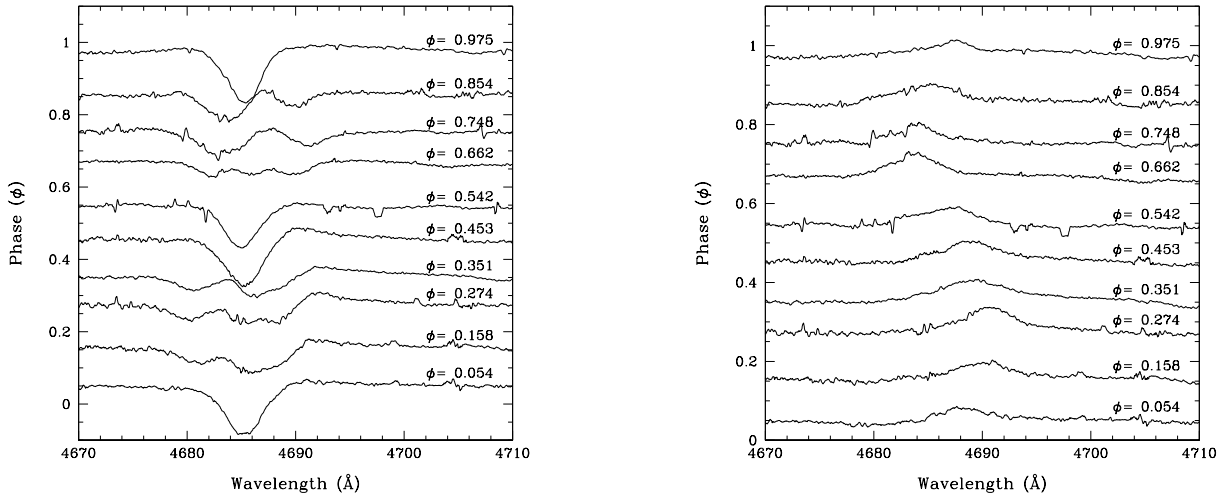

Fig. 8. *Left*: The observed He II 4686 line profiles in the HD 150136 spectrum. *Right*: The restored He II 4686 line profiles in the HD 150136 spectrum corrected for the absorption lines.

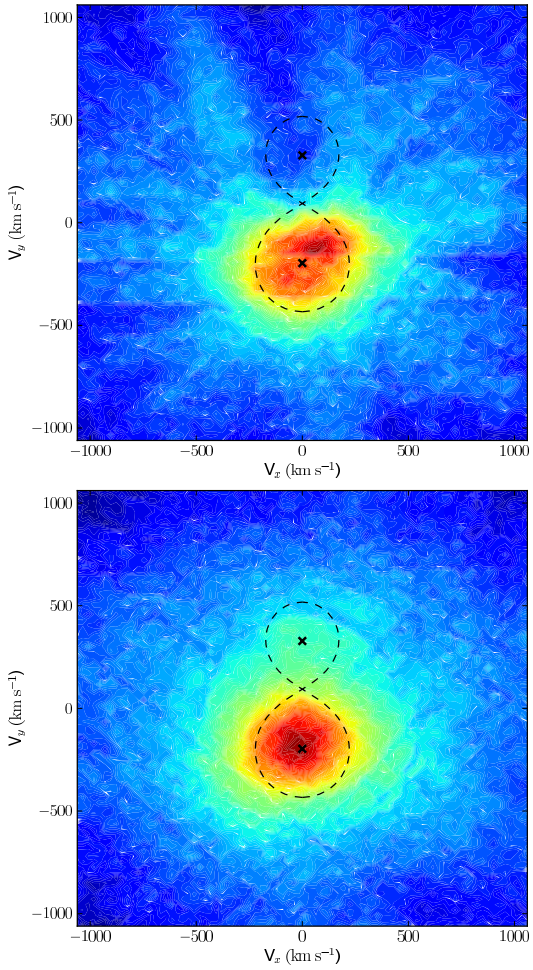

Fig. 9. *Top*: Doppler map of the He II 4686 line of HD 150136 computed after removing the absorption line profiles of the primary and the secondary stars as well as of the third component. The crosses correspond to the radial velocity amplitudes of the primary and secondary stars. The shape of the Roche lobe in velocity-space (thick dashed line) was calculated for a mass ratio (primary/secondary) of 1.59. The Doppler map was computed with $v_z = 0$ km s^{-1}. In the colorscale, red (blue) indicates the maximum (minimum) emissivity. *Bottom*: Same as for the upper panel, but for Hα.

region of emission concentrated near the velocity of the center of mass of the primary star. The maximum of emissivity is located at $(v_x, v_y) \sim (50, -137)$ km s^{-1}. These values imply that the matter flows from the primary to the secondary and moves in the same direction as the primary motion. For the Hα line, we see a similar pattern as for the He II 4686 line. However, the analysis of the S-wave of the highest emission peak reveals a $(v_x, v_y) \sim (-24, -155)$ km s^{-1}. These resulting tomograms do not show any structures reminiscent of a wind-wind interation or of a Roche lobe overflow. The emissions of the He II 4686 and Hα lines appear to be formed in an unperturbed part of the primary wind. We notice that these Doppler maps are close to those computed by Rauw et al. (2002) for HDE 228766.

8. Discussion

8.1. The inner system

The projected rotational velocities and the radii quoted in Table 4 suggest that both components of the inner system of HD 150136 are in synchronous rotation, i.e., the angular velocity is similar for both stars. Moreover, from the minimum and evolutionary masses reported in Tables 2 and 4, we derive an inclination of about $47.2^{\circ}{}^{+2.9}_{-2.5}$ for the primary and of about $51.3^{\circ}{}^{+1.7}_{-3.2}$ for the secondary. Consequently, by assuming that our stellar parameters are close to the reality, we estimate the inclination of the inner system to be about $49^{\circ} \pm 5^{\circ}$. This value favours a non-eclipsing system and agrees with the previous inclination of about 50° given by Niemela & Gamen (2005). We then focus on the possible synchronous co-rotation of the inner system. From the orbital period and the radii, co-rotational velocities of about 276^{+57}_{-42} km s^{-1}and 187^{+36}_{-30} km s^{-1}for the primary and the secondary components, respectively, are found. Such velocities require an inclination of about $38^{\circ}{}^{+16}_{-11}$ and $47^{\circ}{}^{+37}_{-15}$ to be in agreement with the measured $v \sin i$. These inclinations are in agreement with the value estimated from the masses. Therefore, we may conclude that the inner system is probably in synchronous co-rotation.

By adopting a mass ratio of 1.586 and an $a \sin i = 28.9\ R_{\odot}$, we estimate the minimal radii of the Roche lobes of the primary and the secondary from the expression given by Eggleton (1983). We find $(R_{\rm RL} \sin i)_{\rm P} = 12.12\ R_{\odot}$ and $(R_{\rm RL} \sin i)_{\rm S} = 9.82\ R_{\odot}$. If this result confirms that the secondary does not fill its Roche

lobe, the case of the primary depends on the inclination of the system. However, by assuming an inclination of 49° ± 5° and by taking the radius given in Table 4, this component would not fill its Roche lobe either.

8.2. The tertiary component

Previous investigations as e.g., that of Niemela & Gamen (2005) or Benaglia et al. (2006) mentioned the existence of a third component in HD 150136. Sometimes, the close visual companion located at about 1.6″ (Mason et al. 1998) was quoted as this tertiary star. However, from the present analysis, we conclude that this close visual star cannot be this third component revealed by our analysis. First of all, the spectral classification of the close visual companion is estimated to be later than B3 while we clearly reported here an O6.5–7V((f)) classification. Moreover, if we assume an orbital period in the range of 8–15 years for the outer orbit, the possible separation between the third component and the inner system is estimated between 3500 and 9100 $R_\odot$ i.e., between about 16 and 43 AU. With such a separation and assuming a distance of 1.3 kpc for HD 150136, we calculate an angular separation of about 12 and 32 mas, much smaller than 1.6″ as estimated for the close visual companion by Mason et al. (1998). On the basis of the spatial separation associated with a mass ratio between the inner system and the tertiary component of about 2.9, this third component should be detectable by interferometry according to the sketch reported by Sana & Evans (2011). An observation made with SAM/NaCo (Nasmyth Adaptive Optics System, Paranal, Chile) in March 2011 allowed to detect a possible object at the limit of being significant (Sana et al. in preparation). This object would be located below 25 mas. Of course, this information must be taken with great care and needs to be confirmed by future observing campaigns.

Although HD 150136 is now established to be a triple system, this system could still have a higher multiplicity. Indeed, the possible close visual component located at about 1.6″ could be also bound to the system. In order to determine whether HD 150136 is a dynamically stable hierarchical triple system, we use the stability criterion quoted by Tokovinin (2004):

$$P_{\rm out}(1 - e_{\rm out})^3 > 5P_{\rm in}$$

where $P_{\rm in}$ and $P_{\rm out}$ are the orbital periods of the inner and the outer systems respectively and $e_{\rm out}$ is the eccentricity of the outer orbit. Even though we do not know precisely the exact value of the parameters of the external orbit, we can still report, in the worst case, that this criterion is satisfied for the configuration of HD 150136.

8.3. Evolutionary status

The stellar parameters determined with the CMFGEN atmosphere code allow us to give the positions of the three stars in the Hertzsprung-Russell (HR) diagram. As shown in Fig. 10, all these components are located relatively close to the ZAMS. The isochrones reveal an age of about 0–2 Myrs for the primary and the secondary stars whilst the tertiary would be slightly older with an age of about 1–3 Myrs. Even though this discrepancy is barely significant, such a difference in age was already observed in several studies. Indeed, Mahy et al. (2011) reported that a possible reason to see such a difference in the inferred age could be attributed to a different rotational rate between the components (see also Brott et al. 2011). By taking into account an inclination of 49° for the primary and the secondary component and by assuming that the tertiary is in the same orbital plane as the inner binary, we measure rotational velocities of about 227, 180 and 95 km s^{-1} for the primary, the secondary and the tertiary components, respectively. In order to represent them together, we use the evolutionary tracks computed with an initial rotational velocity of 300 km s^{-1} (see Fig. 10). However, evolutionary tracks based on the individual rotational rate were also investigated but this does not change the conclusions, the discrepancy does not seem to come from a different rotational rate. It has to be stressed though that the evolution of the rotational velocity, and hence the efficiency of rotational mixing, is probably quite different in a close binary system when the stars corotate synchronously on the one hand, and in a rather isolated third star on the other hand.

This discrepancy in age is strengthened by the determination of the stellar parameters (see Sect. 6). Even though the parameters of the primary and the secondary stars agree with those of stars on the main sequence, we observe for the third component that its luminosity corresponds to a main-sequence star whilst its gravity is more reminiscent of an evolved star. However, the $\log g$ is determined on the basis of the wings of Balmer lines and its estimate could be wrong if the wings of these lines are poorly reproduced by the disentangling process. In the case of HD 150136, we see that, due to the broadness of the Balmer lines, the spectral separation between the different components is too small to sample the full width of these lines. Therefore, the true value of the $\log g$ could be affected by the disentangling process.

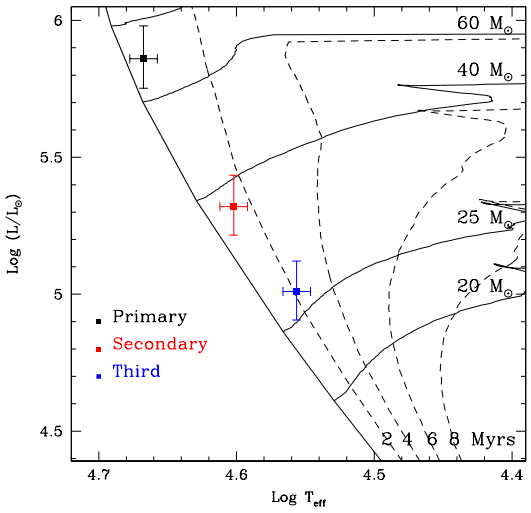

Fig. 10. HR diagram reporting the position of the three components of HD 150136. The evolutionary tracks computed for an initial rotational velocity of about 300 km $s^{-1}$and the isochrones are from Meynet & Maeder (2003).

Moreover, the parameters of the third star also show an evolutionary mass larger than the spectroscopic one even though both values are smaller that what the mass ratio between the inner system and the third star seems to indicate. We notice that the spectroscopic mass is derived from the radius and the $\log g$ of the star. Consequently, a wrong estimate of $\log g$ could affect the determination of the spectroscopic mass. If we consider the evolutionary mass of the inner system (primary and secondary), we find a total mass of about 100 $M_\odot$. By adopting the mass ratio we have derived between the inner system and the third star, we obtain a mass of about 35 $M_\odot$ for the tertiary component. This value is close to the evolutionary mass, which would show that the spectroscopic $\log g$ would be wrong. This dynamical mass

would also lead to a $\log g$ value of about 4.1, which is more reminiscent of a main-sequence star.

Finally, if we assume that the disentangling does not affect the true value of the $\log g$, we have to look at the real phenomena which could explain such a value. From the different evolutionary schemes of Eggleton & Kiseleva (1996), it is however unlikely that the third star has a giant luminosity class. Indeed, according to these authors, a massive triple system such as HD 150136, i.e., with $M_P > M_S > M_T$, should first undergo a Roche lobe overflow in the inner binary. Since the primary star is more massive than the other ones, it should be the first to evolve, thus implying the mass tranfer in the inner system. Therefore, the tertiary component could not be evolved while the primary and the secondary still remain on the main-sequence band. Furthermore, the absence of modified surface chemical abundances and the low $v \sin i$ derived for the third component also do not support an alternative scenario where the third component would have been captured by the inner system after having been ejected by a supernova kick or by dynamical interactions in the neighbourhood of HD 150136. All in all, it thus appears that the tertiary component as well as the two other stars belong to the main sequence and that the most probable cause to have a wrong estimate of $\log g$ is the disentangling process.

8.4. Colliding wind and non-thermal radio emission

The presence of an O3–3.5V star in the inner system seems to be mainly responsable of the variations observed in the He II 4686 and Hα lines. However, the proximity of the O5.5–6V((f)) secondary probably implies a wind-wind interaction zone between the two stars. According to the formalism of Stevens et al. (1992) and the parameters given in Table 4, we expect that the powerful wind of the primary star crashes onto the surface of the secondary star. This scenario is in line with the finding of Skinner et al. (2005). The collision of the primary wind with the secondary surface could generate an extra X-ray emission associated with the secondary inner surface. The short time-scale X-ray variability could then result from occulation effects very much as those observed for CPD−41° 7742 (Sana et al. 2005). Though this scenario seems to agree with the results of the Doppler tomography where we saw that the emission is only due to the primary star, the position of the contact zone remains unreliable because the wind parameters of the secondary are uncertain. Therefore, we used the mass-loss rate of about $\dot{M} = 10^{-6} M_\odot$ yr^{-1} derived by Howarth & Prinja (1996) as a function of stellar luminosity and we assumed an inclination of 49° for the system. These assumptions lead to a probable radiative primary wind, with a cooling parameter $\chi \cong 0.87$. Moreover, on the basis of different values for the fundamental parameters, Skinner et al. (2005) derived $\chi = 0.2$, also in agreement with a non-adiabatic regime for the X-ray emission from the inner wind-wind interaction region. On the other hand, any X-ray contribution coming from the colliding wind region between the inner system and the third star should a priori be produced in the adiabatic regime, at least in a very large fraction of the long eccentric orbit.

Otherwise, the confirmation that HD 150136 includes a third star is worth discussing in the context of its non-thermal radio emission. The stellar wind material is quite opaque to radio photons, that are unlikely to escape if the absorbing column along the line of sight is too thick. The radius of the $\tau = 1$ radio photosphere can be estimated on the basis of the formula given by Wright & Barlow (1975) and Leitherer et al. (1995), following the same approach as De Becker et al. (2004) in the case of the candidate binary system HD 168112. Using the stellar wind parameters given in Table 4, we calculated the radio photosphere radii, respectively for the primary, the secondary and the tertiary components. These radii are plotted as a function of wavelength in Fig. 11. When discussing the radio emission from massive stars, one should have in mind that stellar winds are radio emitters, but in the thermal regime. On the other hand, the wind-wind interaction in massive binaries could produce non-thermal radiation in the form of synchrotron radiation. Benaglia et al. (2006) reported on a clearly non-thermal spectral index between 3.6 and 6 cm, but the spectral index at longer wavelengths (13 and 20 cm) is more typical of a thermal spectrum. We will therefore focus on the values derived at shorter wavelengths. As we are dealing with a triple system, let us separately consider two wind interactions regions: a first one within the short period subsystem (hereafter, SPC for short period collision), and a second one involving the third star (hereafter, LPC for long period collision). We can easily check whether any putative non-thermal radio emission from the SPC could contribute to the measured non-thermal radio flux. The curves in Fig. 11 are dominated by the primary contribution, which is easily explained by its large mass loss rate. The radii at 6 and 3.6 cm are of the order of 260 and 370 $R_\odot$ for the primary. The projected stellar separation ($a_1 \sin i + a_2 \sin i$) is of about 29 $R_\odot$, which translates into stellar separation of the order of 38 $R_\odot$ for an inclination of about 49° (see Sect. 8.1). The radio photospheres at 3.6 and 6 cm overwhelm thus completely the close primary + secondary system, and consequently the SPC is deeply buried in the opaque wind. This fact clearly rejects the possibility that the non-thermal radio photons come from the interaction between the primary and secondary components. Alternatively, they could come from the LPC. The radii of the radio photosphere at 6 cm constitute therefore minimum boundaries for the distance between the LPC and, respectively, the primary (solid curve in Fig. 11) and the tertiary (long-dashed curve). The sum of these two radii (i.e. about 390 $R_\odot$), should be considered as a lower limit for the stellar separation between these two stars. That value is indeed much lower than the stellar separation estimated in Sect. 8.2 on the basis of the probable period of the wide system. A more stringent lower limit could be derived using values at 20 cm, as the free-free absorption increases as a function of wavelength. However, the non-thermal nature of the radio photons at that wavelength is not guaranteed by the spectral index reported by Benaglia et al. (2006). We note that the radio photospheric radii estimated here are intimately dependent on the assumed stellar wind parameters, that should be considered with caution. In particular, the mass loss rate of the primary may be significantly underestimated here. However, our conclusion relies on conservative margins.

9. Conclusion

The analysis of high-resolution high signal-to-noise data, collected on several epochs with FEROS, allowed us to detect for the first time in the spectrum of HD 150136 a third component physically bound to the inner system. In addition, we revised the spectral classification of the three components to an O3–3.5V((f$^+$)) primary, an O5.5–6V((f)) secondary and an O6.5–7((f)) tertiary. We have also estimated the evolutionary masses to be equal to 71, 36, 27 $M_\odot$, respectively.

We have refined the orbital solution of the inner binary system by fitting the radial velocities of the different components of the SB3 system altogether. The results improved the accuracy of the majority of the parameters reported by Niemela & Gamen

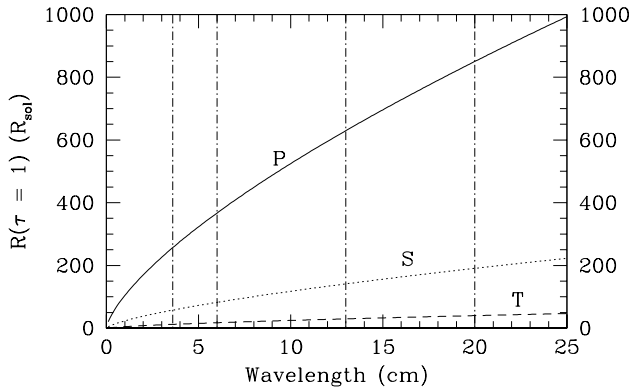

Fig. 11. Dependence of the radius of the $\tau = 1$ radio photosphere as a function of wavelength for the primary (P), the secondary (S) and the tertiary (T) components. The vertical lines are located at 3.6, 6, 13 and 20 cm corresponding to the wavelengths investigated by Benaglia et al. (2006).

(2005). Moreover, we find that the inner system is probably in synchronous co-rotation. The agreement between the evolutionary and the keplerian masses would suggest a probable inclination of about 49°, reporting dynamical masses of about 64, 40 and 35 $M_{\odot}$.

From the systemic velocities measured on every epoch, we estimated that the orbit of the third star should have a period between 2950 and 5500 d and an eccentricity greater than 0.3. More data are necessary to achieve an accurate orbital solution of the outer orbit. A possible alternative would be to observe HD 150136 by interferometry to constrain the missing orbital parameters.

The determination of the individual stellar parameters of the three stars yielded a luminosity and a gravity corresponding to main-sequence stars for the primary and the secondary components but these parameters are more tricky for the third star. Indeed, we observed a clear discrepancy between its luminosity (comparable to main-sequence stars) and its $\log g$ (typical of giant stars). The origin of such a difference is unclear but it seems that it could come from the disentangling program notably because the spectral separation which is not sufficient to see the full width of the broadest lines such as the Balmer lines for the three components. Consequently, HD 150136 is probably composed of at least three O-type stars located on the main sequence and with inferred ages between 0–3 Myrs. Finally, we showed that the non-thermal radio emission should come from the wind-wind interaction region between the third star and the inner short-period system, that should be the site for particule acceleration in this multiple system.

Acknowledgements. This research was supported by the PRODEX XMM/Integral contract (Belspo), the Fonds National de la Recherche Scientifique (F.N.R.S.) and the Communauté française de Belgique – Action de recherche concertée – A.R.C. – Académie Wallonie-Europe. The authors thank Thomas Fauchez for a first detailed look to the data in the framework of a student work. We also thank Dr. F. Martins for his helpful comments and Pr. D.J. Hillier for making his code CMFGEN available. We are also grateful to the staff of La Silla ESO Observatory for their technical support.

References

Benaglia, P., Koribalski, B., & Albacete Colombo, J. F. 2006, PASA, 23, 50
Blomme, R., De Becker, M., Runacres, M. C., van Loo, S., & Setia Gunawan, D. Y. A. 2007, A&A, 464, 701
Brott, I., de Mink, S. E., Cantiello, M., et al. 2011, A&A, 530, A115+
Conti, P. S. 1973, ApJ, 179, 161
Conti, P. S. & Alschuler, W. R. 1971, ApJ, 170, 325
Conti, P. S., Leep, E. M., & Lorre, J. J. 1977, ApJ, 214, 759
De Becker, M. 2007, A&A Rev., 14, 171
De Becker, M., Rauw, G., Blomme, R., et al. 2004, A&A, 420, 1061
Eggleton, P. P. 1983, ApJ, 268, 368
Eggleton, P. P. & Kiseleva, L. G. 1996, in NATO ASIC Proc. 477: Evolutionary Processes in Binary Stars, ed. R. A. M. J. Wijers, M. B. Davies, & C. A. Tout (Kluwer Academic Publishers), 345–+
Garmany, C. D., Conti, P. S., & Massey, P. 1980, ApJ, 242, 1063
González, J. F. & Levato, H. 2006, A&A, 448, 283
Gosset, E., Royer, P., Rauw, G., Manfroid, J., & Vreux, J.-M. 2001, MNRAS, 327, 435
Grevesse, N., Asplund, M., & Sauval, A. J. 2007, Space Science Reviews, 130, 105
Heck, A., Manfroid, J., & Mersch, G. 1985, A&AS, 59, 63
Herbst, W. & Havlen, R. J. 1977, A&AS, 30, 279
Hillier, D. J. & Miller, D. L. 1998, ApJ, 496, 407
Howarth, I. D. & Prinja, R. K. 1996, Ap&SS, 237, 125
Kak, A. C. & Slaney, M. 2001, Principles of Computerized Tomographic Imaging (Classics in Applied Mathematics) (Society of Industrial and Applied Mathematics)
Lanz, T. & Hubeny, I. 2003, ApJS, 146, 417
Leitherer, C., Chapman, J. M., & Koribalski, B. 1995, ApJ, 450, 289
Linder, N., Rauw, G., Martins, F., et al. 2008, A&A, 489, 713
Lucy, L. B. & Sweeney, M. A. 1971, AJ, 76, 544
Mahy, L., Martins, F., Machado, C., Donati, J. ., & Bouret, J. . 2011, ArXiv e-prints
Martins, F. & Plez, B. 2006, A&A, 457, 637
Martins, F., Schaerer, D., & Hillier, D. J. 2005, A&A, 436, 1049
Mason, B. D., Gies, D. R., Hartkopf, W. I., et al. 1998, AJ, 115, 821
Meynet, G. & Maeder, A. 2003, A&A, 404, 975
Niemela, V. S. & Gamen, R. C. 2005, MNRAS, 356, 974
Rauw, G., Crowther, P. A., Eenens, P. R. J., Manfroid, J., & Vreux, J.-M. 2002, A&A, 392, 563
Rauw, G., Sana, H., Antokhin, I. I., et al. 2001, MNRAS, 326, 1149
Rauw, G., Sana, H., Gosset, E., et al. 2000, A&A, 360, 1003
Reed, C. 2005, VizieR Online Data Catalog, 5125, 0
Repolust, T., Puls, J., & Herrero, A. 2004, A&A, 415, 349
Sana, H., Antokhina, E., Royer, P., et al. 2005, A&A, 441, 213
Sana, H. & Evans, C. J. 2011, 272, 474
Sana, H., Gosset, E., & Rauw, G. 2006, MNRAS, 371, 67
Simón-Díaz, S. & Herrero, A. 2007, A&A, 468, 1063
Skinner, S. L., Zhekov, S. A., Palla, F., & Barbosa, C. L. D. R. 2005, MNRAS, 361, 191
Stevens, I. R., Blondin, J. M., & Pollock, A. M. T. 1992, ApJ, 386, 265
Tokovinin, A. 2004, in Revista Mexicana de Astronomia y Astrofisica, vol. 27, Vol. 21, Revista Mexicana de Astronomia y Astrofisica Conference Series, ed. C. Allen & C. Scarfe, 7–14
Underhill, A. B. 1994, ApJ, 420, 869
Walborn, N. R., Howarth, I. D., Lennon, D. J., et al. 2002a, AJ, 123, 2754
Walborn, N. R., Howarth, I. D., Lennon, D. J., et al. 2002b, AJ, 123, 2754
Wolfe, Jr., R. H., Horak, H. G., & Storer, N. W. 1967, The machine computation of spectroscopic binary elements, ed. M. Hack (New York: Gordon & Breach), 251
Wright, A. E. & Barlow, M. J. 1975, MNRAS, 170, 41
Zechmeister, M. & Kürster, M. 2009, A&A, 496, 577

Part II

Multiplicity of O-type stars in young open clusters and OB associations

Chapter 5

The young open cluster NGC 2244 and the Mon OB2 association

The northern Monoceros is a well-known star-forming region in the Milky Way. This area is composed of two distinct regions: the Rosette Nebula containing the Mon OB2 association and the more compact Mon OB1 association, 5° to the North. It is now well-established that both regions are independent from each other. Indeed, the latter is located in the Local Spiral Arm at a distance of 800 pc from the Sun whilst Mon OB2 and the Rosette region are thought to be part of the Perseus spiral arm at about 1600 pc (Turner 1976).

The Rosette nebula region is rich in massive and young OB-type stars, detectable by the large quantity of UV light they emit. This light ionizes and heats the gas surrounding them, thus creating the H II region in which they are embedded. In the core of the Mon OB2 association is located the young open cluster NGC 2244 which is centered at $\alpha(2000) = 06^h31^m55^s$ and $\delta(2000) = +04°56'30''$ (Bonatto & Bica 2009). These authors inferred an age of about 1 – 6 Myrs for that cluster and Hensberge et al. (2000) placed NGC 2244 at a distance of about 1.4 – 1.7 kpc, thus confirming its belonging to the Rosette nebula.

In order to put our studies in context, we first present a general summary on the topic of the multiplicity of massive stars and the importance of such studies for understanding massive star formation processes. Then, we tackle the analysis of the O-type stars in the young open cluster NGC 2244 and the surrounding Mon OB2 association, and establish their multiplicity. The results on multiplicity were published in Mahy et al. (2009) and Mahy et al. (2010, see the end of Section 5.2.1). Since all these stars constitute a homogeneous set of objects, i.e., stars with same age, distance and chemical composition, we present the quantitative study of the stellar and wind parameters obtained by means of the CMFGEN atmosphere code (Hillier & Miller 1998). We present, in Appendix A, the paper (Martins et al. 2011) relative to this analysis. We end this chapter by analyzing the high-quality photometric data of six O-type stars, in NGC 2244 and Mon OB2, acquired with the CoRoT satellite. The Liège contribution is published in Mahy et al. (2011a, Section 5.4.1) and in Blomme et al. (2011) reported in Appendix A. Finally, we present the conclusions and a summary of the different investigations that we present and that we partly published in Mahy et al. (2011c, Section 5.5).

5.1 The multiplicity in young open clusters

A large quantity of massive stars are detected as binary or multiple systems. Even the single field stars are sometimes believed to have been part of a multiple system in the past and then ejected by a supernova kick or by dynamical interactions (Sana & Evans 2011). Recent works, partly performed by the Liège group, led to show that binarity (or multiplicity) in the massive star population is relatively common, and is even dominant over single stars! Consequently, not taking into account the duplicity of a star can lead to a poor estimate of its fundamental properties such as its spectral classification, its mass-loss rate or its actual mass.

Detecting the multiplicity of a star is of a crucial importance to distinguish between the possible formation scenarios of massive stars which may impact on the binary fraction. It is also important to understand the evolution processes which have affected these stars. Because of their mutual influence, the evolutionary paths of components in a binary system are often not comparable with those of a single star. Additional mechanisms such as tidal effects or mass transfers have a deep impact on the evolution of these components. Both phenomena mainly affect the stellar rotational rates, thus modifying the induced rotational mixing of the enriched material into the stellar photosphere (de Mink et al. 2009). In addition, the mass transfer via Roche lobe overflow also changes the surface abundances of the stars, thus modifying their evolutionary paths. Knowing the multiplicity of the stars that we analyse is thus a necessary condition to improve our understanding of their physical properties, but it is not an easy task.

A summary made by Mason et al. (1998) of spectroscopic binary systems quoted in the literature reported a binary fraction of 61, 50 and 20% in open clusters and associations, among field stars and runaways, respectively. But, among the stars studied in that survey, many had still an uncertain binary status. If we exclude these "SB?" systems, the percentages of confirmed binaries decrease to 34, 20 and 5% for open clusters and associations, among field stars and runaways, respectively (Mason et al. 1998). This example is thus a good illustration of the difficulty to constrain with accuracy the real binary fraction of the massive stars. Numerous observational biases can prevent the detection of binary systems, such as for example a low inclination, a small mass ratio, a large eccentricity or a wide separation between the components. Systems where the optical spectrum is the result of a blending of two equal-strength lines can also constitute an additional hurdle in detecting the binarity. Indeed, since the line profiles have the same intensity, it is therefore possible to miss the orbital motion in the spectra (see Sana et al. 2011b, for an example of this bias). In addition, the detections are strongly biased towards systems with short orbital periods. It is indeed easier to unveil such systems because of the larger amplitude of the radial velocity variations but also because the typical length of an observing campaign generally ranges between 3 and 10 days. Therefore, the scarcity of binary systems with a large mass ratio or with a period of the order of a few months does not necessarily mean that these systems are indeed rare (Rauw 2007). To decrease the number of undetected systems, several observational means need to be combined such as spectroscopy, photometry, adaptative optics imagery or speckle interferometry. These different detection techniques allow to probe different mass ratios or different separations. The last two techniques however have to be considered with caution because, on the one hand, the detected "visual" component can be itself a binary system and, on the other hand, nothing ensures that the "visual" component is gravitationnally bound to the star being observed. An overview of the parameter space probed by these techniques is given in Sana & Evans (2011).

Several spectroscopic investigations were made to constrain the binary fraction of O-type stars in nearby young open clusters. García & Mermilliod (2001) reported the binary frequencies

Table 5.1: Spectroscopic binary fraction in young open clusters. The first column lists the name of the cluster, the second column gives the number of O stars observed in the cluster, the third, fourth and fifth columns report the binary fraction determined by a dedicated monitoring, the associated reference and the binary fraction found by García & Mermilliod (2001), respectively.

Clusters	# O stars	Binary frac.	ref.	García & Mermilliod (2001)
NGC 6231	16	63%	1	79%
NGC 6611	9	44%	2	42%
IC 2944	15	57%	3	44%
IC 1805	10	30%	4,5,6	80%
IC 1848	5	40%	6	–
Tr 16	24	48%	7	35%
Tr 14	6	0%	8	14%
Col 228	15	33%	9	24%
Westerlund 1	20	30%	10	–
Westerlund 2	13	15%	11	–
30 Dor	54	45%	12	–
NGC 346	19	21%	13	–
N 11	44	43%	13	–
NGC 2004	4	25%	13	–
NGC 330	6	0%	13	–

Ref.: 1. Sana et al. (2008), 2. Sana et al. (2009), 3. Sana et al. (2011a), 4. Rauw & De Becker (2004), 5. De Becker et al. (2006), 6. Hillwig et al. (2006), 7. Sana & Evans (2011, and references therein), 8. Penny et al. (1993), 9. H. Sana, private comm., 10. Ritchie et al. (2009), 11. Rauw et al. (2011), 12. Bosch et al. (2009) and 13. Evans et al. (2006)

among eight galactic open clusters hosting at least six O-type stars. As a result of their study, these authors (but also other authors before such as Penny et al. 1993) have proposed that the spectroscopic binary fraction increases with the cluster density. However, these investigations of the multiplicity of massive stars in open clusters relied on old, low quality and heterogeneous data, often mainly taken from the literature. Therefore, some stars are quoted to show radial velocity variations (and thus classified as binary systems) while, in fact, they may be single. Consequently, to confirm these results, these young open clusters were re-investigated (mostly by the Liège team) using dedicated intensive monitorings over different epochs sampling several timescales to constrain the short- as well as the long-period binary systems. These analyses have significantly revised the binary fraction in certain clusters, and extended the studies to other regions containing at least four O stars. A list of the different minimum binary fractions in the O-rich clusters (Sana & Evans 2011) is reported in Table 5.1. We also compare the "new" binary fractions to those derived by García & Mermilliod (2001). The values of the binary frequency must however be considered with caution, especially for the distant clusters (lower part of Table 5.1) and Col 228, because the multiplicity of all the O-type stars belonging to those regions has not been fully probed yet or because a sufficiently large time sampling has not been obtained so far. Sana & Evans (2011) derived from these different investigations on the young open clusters an average binary fraction of about 0.44 ± 0.05 and rejected with a very high confidence the null hypothesis that all O stars are spectroscopic binaries. A more recent work (Sana, private comm.) on an extended sample seems to indicate that up to 56% of the O stars, combined over several young open clusters, are detected as binaries. A tentative correction for the biases in the detection process would moreover point to an intrinsic binarity or multiplicity reaching 75%.

5.2 The spectroscopic investigation

5.2.1 The binary fraction

In order to increase the list of young open clusters for which the binary fraction is established, we focus on the young open cluster NGC 2244 and the surrounding Mon OB2 association. This cluster contains a total of seven O-type stars (Fig. 5.1) whose the membership was established by Ogura & Ishida (1981). However, one of them (HD 258691) is relatively faint (V = 9.7) and could not be monitored with the telescopes we used for our observing campaigns. The binary fraction on this cluster was estimated to 50% by García & Mermilliod (2001) by also considering six stars out of the seven (but they instead excluded HD 46485). These authors reported possible radial velocity variations for HD 46056, HD 46150, and HD 46223 on the basis of the open-cluster database compilled by Mermilliod (1995).

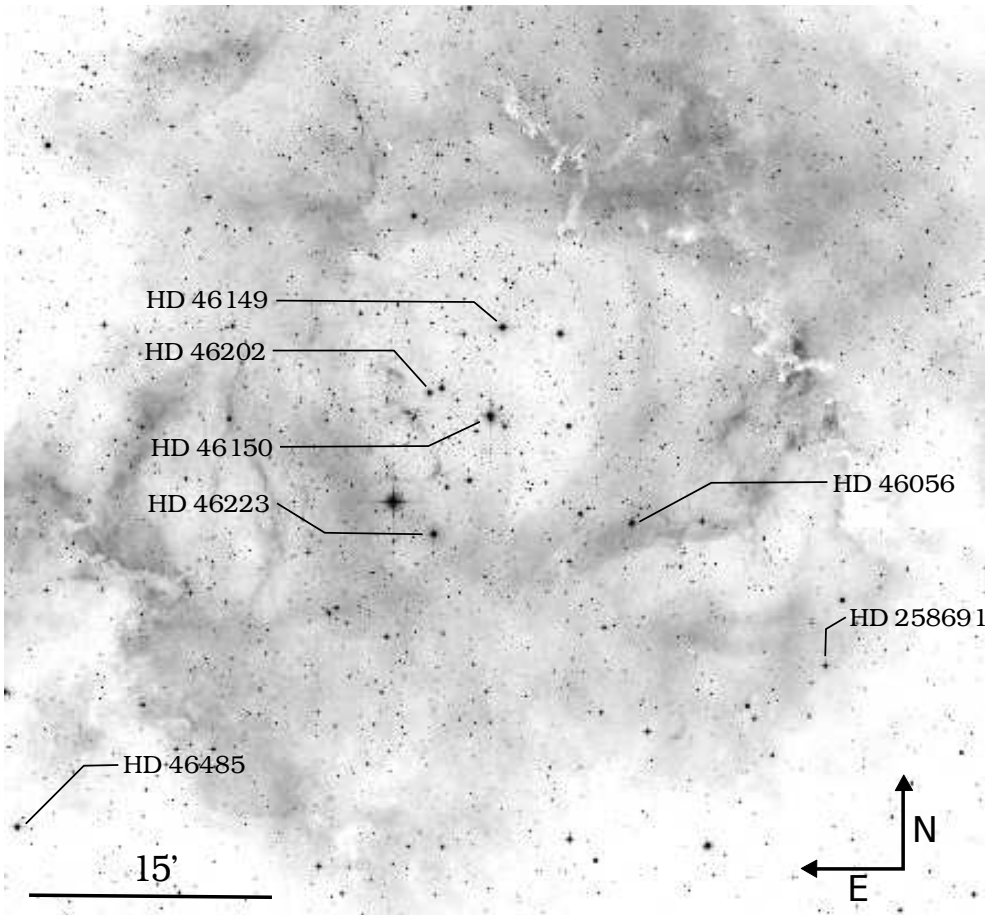

Figure 5.1: O-type stars in the young open cluster NGC 2244.

We have also monitored three O stars belonging to the Mon OB2 association (HD 46573, HD 46966 and HD 48279) which have received little attention in the literature. In addition to these stars, a tenth target has been included in our survey: HD 48099. Also belonging to the Mon OB2 association, this system was already investigated in the past. Indeed, this star was first quoted as a binary 55 years ago by Slettebak (1956). Its orbital period was estimated to 3.1 days by Garmany

et al. (1980) but the first publication on its orbital solution awaited the work of Stickland (1996). In order to complete these investigations, we re-analyze HD 48099 with a disentangling program (see Chapter 2) to constrain the individual parameters of each component and study their evolutionary status. HD 48099 is the only known short-period binary system in Mon OB2. Another system, already known as binary system, is also located in Mon OB2: Plaskett's Star. As we already mentioned in Chapter 3, this star is composed of an O 8I/III primary and an O 7.5III/V secondary and has an orbital period of about 14.39 days. Since this system was investigated in details by Linder et al. (2008), it is not included in our sample. However, we come back later to this system in Section 5.4 since it was recently observed by the CoRoT satellite.

The spectroscopic campaign we analyze is spread over ten years and involves several instruments. The spectra mainly come from the spectrographs Aurélie and Elodie, respectively, attached to the 1.52m and the 1.93m telescopes at Observatoire de Haute Provence in France, the 2.10m equipped with ESPRESSO at San Pedro Màrtir in Mexico and FEROS mounted at the ESO/MPG 2.20m at La Silla in Chile. We have collected about 250 spectra spread among the ten stars, allowing us to investigate the short- as well as the long-term variations for each target. The journal of the observations is summarized in Mahy et al. (2009).

In order to consider the possibility that a star is a binary system, we focus our analysis on the detection of significant periodic variations of the radial velocities (RVs) and/or the signature of a companion whose spectral lines move in anti-phase with those of the main star. If the phase coverage is sufficient to determine the period of the system, a full orbital solution can be computed, leading to the precise determination of the orbital parameters. When the sampling is not sufficient to compute an orbital solution, we only evaluate the spectral type of the two components and their mass ratio, with only loose constraints on the orbital elements. If none of these criteria is fulfilled, but significant radial velocity variations are detected, then the star is considered as "RV variable", and reported as binary candidate. The radial velocity variations are considered as significant if they are larger or equal to three times the average radial velocity measurement error. For all stars except rapid rotators, this error is well represented (as is confirmed by tests on individual data) by the radial velocity dispersion of the narrow Na I interstellar lines at 5890 and 5896 Å and the diffuse interstellar band (DIB) at 5780 Å, which has similar strength and width as the stellar lines. For the rapid rotators, a χ^2 evaluation from shifts of the synthetic line profile shows the radial velocity error to be about 10 km s^{-1}.

The analysis of the radial velocities and of the line profiles by means of the Temporal Variance Spectrum (hereafter TVS, Fullerton et al. 1996) yields the following results:

- **HD 46150**: Located at the center of the cluster, this star is classified as O 5.5V((f)). Our investigation shows that this star could be a binary candidate. Indeed, the TVS exhibits structures with double and triple peaks for all the main characteristic stellar lines in the range [5500 – 5900] Å. In addition, radial velocity variations, at the limit of being significant, are derived for the He II 4542, O III 5592 and C IV 5801–12 lines. Both elements thus suggest that HD 46150 could be a binary system. However, no SB2 signature is observed and no significant radial velocity dispersion is found for the He I 4471 and 5876 lines which renders the true nature of the star questionable.

- **HD 46223**: Classified as an O 4V((f$^+$)), this star does not show any significant variation of its radial velocities. Moreover, the TVS analysis results in no significant line profile variation with a significance level of 0.01. Therefore, this star is considered as a probable single star.

- **HD 46056**: This star is the fastest rotator belonging to the cluster with $v \sin i \sim 355$ km s^{-1}. Classified as an O 8V, this object exhibits variations in the central part of its line profiles. However, these variations are probably due to non-radial pulsations rather than a putative companion since the full widths of the line profiles are unchanged as a function of time. Therefore, we attribute to this star a presumably single status.

- **HD 46485**: This O 8V star is the second fast rotator in our sample with $v \sin i$ of about 300 km s^{-1}. As it is located at about 38′ from HD 46150, its membership to NGC 2244 is uncertain. Its characteristics are similar to those of HD 46056. Consequently, we also consider this star as presumably single.

- **HD 46149**: This star clearly exhibits the signature of a secondary component in its spectrum. The companion moves relatively slowly, indicating a long-period binary. Its radial velocities suggest an orbital period larger than 800 days. We compute a mass- and a flux-ratio of about $M_P/M_S = 1.9$ and $l_P/l_S = 2.3$, respectively. For an O 8V primary, these values therefore result in a companion with a spectral type of B0–1V. From recent additional data obtained with the Coralie spectrograph by the Leuven team and collected by the Liège team with Aurélie, we estimate an orbital period for that system between 720 and 860 days. However, this range is still too large to allow us to determine accurately the orbital solution of this system. By taking into account the refined radial velocities obtained by cross-correlation and by fitting these values by a linear regression technique such as $RV_S = c_1 RV_P + c_2$ with $c_1 = -M_P/M_S$ and c_2 a constant, we compute a mass ratio of about 3.24 ± 0.22. This difference is mainly due to an accurate determination of the radial velocities at phases where the secondary is barely detected, notably when the secondary signature is located in the blue wing of the primary. A better characterization of this binary appears to be necessary but requires an intensive and regular monitoring over more than 2 years.

- **HD 46202**: This target is the latest O-type star in NGC 2244 with a spectral classification of O 9V. It does not show any significant variation in its radial velocities nor in the TVS. Consequently, we consider the star to be presumably single.

The analysis about the multiplicity in NGC 2244, published in Mahy et al. (2009) and Mahy et al. (2011c, see Section 5.5), thus reveals a new binary fraction between 14% (one out of seven) and 43% (three out of seven) in NGC 2244. Indeed, HD 46149 is the only star which clearly exhibits binarity. HD 46150 is a doubtful candidate even though the variations are slightly significant. Lastly, HD 258691 has not been investigated during our study and accordingly, has to be considered as a possible binary. One surprising result in this investigation is the absence of short-period binaries whilst six O-type stars out of sixteen in the young open cluster NGC 6231 were reported to have an orbital period of less than 10 days (Sana et al. 2008). We also see that the current binary fraction in NGC 2244 is significantly reduced compared to the 50% quoted by García & Mermilliod (2001). A similar overestimate was already reported by Rauw & De Becker (2004) and De Becker et al. (2006) for IC 1805. These results thus show that using literature data rather than a dedicated dataset render the binary fraction derived in this kind of studies dubious.

Moreover, previous investigations of the multiplicity of young open clusters (e.g., García & Mermilliod 2001 or Penny et al. 1993) seemed to indicate a possible correlation between the binary fraction and the density of such clusters. After having analyzed the multiplicity in NGC 2244, we estimate the surface density obtained from Tadross et al. (2002) for three clusters: NGC 2244, IC 1805 and NGC 6231. Their binary fractions are then compared on the basis of this surface density, revealing a possible anti-correlation. However, recent investigations performed on other

open clusters (notably NGC 6611, Sana et al. 2009 and Westerlund 2, Rauw et al. 2011) seem to disprove this possible link with the density, even though no complete statistical analysis has yet been made. Sana & Evans (2011) reported that, according to the current investigations, the null hypothesis of a common parent distribution for all the nearby young open clusters could not be rejected. However, another null hypothesis under which all the O-type stars are spectroscopic binaries can this time be rejected with a small significance level (i.e., very significantly).

Concerning the three stars belonging to the Mon OB2 association, our investigation about their multiplicity has revealed that **HD 46573** is an SB1 system with a possible period of about 11 days. The maximum spread in its radial velocity variations is of about $10 - 15$ km s^{-1}. With such low-level variability, it is however unclear whether this star is a real binary or a star showing pulsations. In the absence of a secondary signature, we derived a spectral type of O 7.5V((f)) for this star. The two other stars, **HD 46966** and **HD 48279**, are classified as O 8.5V and ON 7.5V, respectively. The analysis of their radial velocities as well as their TVS does not show any significant variations. Therefore, we consider them as presumably single.

The multiplicity of the last star in our sample, **HD 48099**, was already known but we conduct an in-depth analysis of this object by applying a disentangling method to obtain the individual spectra of both stars. We are able to determine the individual stellar parameters such as their $T_{\rm eff}$, luminosity, and $\log g$. However, the separation between the components is insufficient to allow to sample the full widths of the Balmer lines. Therefore, the determinations of the gravity and of the spectroscopic masses computed from the radii and the gravity have to be considered with caution in this analysis. We also revise the orbital solution of the system, by determining a period of about 3.07806 ± 0.00009 days and a mass ratio of about 1.77 ± 0.03. The minimum masses (0.70 ± 0.02 and 0.39 ± 0.01 for the primary and the secondary, respectively) indicate that the inclination of the system is probably low, close to 16°. Both components are classified as O 5.5V((f)) and O 9V for the primary and the secondary, respectively. This analysis has been reported in Mahy et al. (2010).

5.2.2 Observational biases

As we have often pointed out in this thesis, the sole spectroscopic analysis does not allow to detect all the binary systems. Several natural and "technical" parameters actually affect the detection of such systems, such as e.g., a low inclination, a long orbital period and/or a high mass ratio as well as a poor time sampling of the observations. Therefore, it is important to evaluate the probability we have of missing a binary system in our observing campaign.

Garmany et al. (1980) provided a first statistical approach to estimate the rate of binaries which might remain undetectable. We first use that approach to give a statistical estimate of the number of systems we could have missed. For that purpose, we take a rather conservative assumption that the semi-amplitude of the radial velocity curve K is smaller than $2 \times \sigma_{RV}$.

The mass function of the primary component is given by

$$f(M) = \frac{M_{\rm P} \sin^3 i}{q(1+q)^2} = 1.0355 \times 10^{-7} K^3 P (1-e^2)^{3/2}$$

where the mass ratio $q = M_{\rm P}/M_{\rm S}$ and where $M_{\rm P}$, $M_{\rm S}$, K, P and e are the mass of the primary and the secondary (expressed in $M_\odot$), the semi-amplitude (in km s^{-1}), the orbital period (in days) and the eccentricity of the orbit, respectively. Inserting an upper limit on K and assuming $e = 0$ then

Table 5.2: Probability (%) to have missed a binary system given by the Garmany et al. (1980) approach.

	$P = 5$ days			$P = 14$ days			$P = 28$ days		
	q=1	q=5	q=10	q=1	q=5	q=10	q=1	q=5	q=10
HD 46056	0.4	5.0	19.4	0.8	10.3	44.9	1.2	16.9	–
HD 46150	0.4	4.6	18.1	0.7	9.5	45.5	1.1	15.7	34.7
HD 46202	0.1	0.6	2.2	0.1	1.2	4.3	0.1	1.9	7.0
HD 46223	0.1	0.8	2.9	0.1	1.6	6.0	0.2	2.6	9.7
HD 46485	0.5	6.7	26.6	1.0	13.8	–	1.6	23.1	–
HD 46966	0.1	0.4	1.6	0.1	0.9	3.1	0.1	1.4	5.0
HD 48279	0.1	0.3	1.0	0.1	0.6	2.0	0.1	0.9	3.3

	$P = 60$ days			$P = 300$ days		
	q=1	q=5	q=10	q=1	q=5	q=10
HD 46056	2.1	30.4	–	6.1	–	–
HD 46150	1.9	28.8	78.2	5.7	53.3	
HD 46202	0.3	3.2	12.1	0.7	9.8	51.5
HD 46223	0.3	4.4	17.2	1.0	13.7	19.6
HD 46485	2.7	43.3	–	0.8	–	–
HD 46966	0.2	2.3	8.5	0.5	6.9	29.0
HD 48279	0.1	1.5	5.5	0.4	4.5	17.1

yields an upper limit on $\sin i$:

$$\sin i \leq 9.392 \times 10^{-3} \sigma_{RV} \left(\frac{Pq(1+q)^2}{M_{\rm P}} \right)^{1/3} .$$

We assume for $M_{\rm P}$ the mass associated to the spectral types of the stars (Martins et al. 2005a). By assuming a random distribution of the orbital directions in space, the probability that the orbital inclination is smaller than the value quoted above can be estimated by

$$\int_0^{i_{\rm up}} \sin i \, {\rm d}i = 1 - \cos i_{\rm up}$$

Therefore, we estimate for each of the O stars in NGC 2244 and Mon OB2 the probability that a binary system has been missed, for several values of the orbital period and the mass ratio (see Table 5.2). Though the approach of Garmany et al. (1980) is relevant, it does not take into account the time sampling of the observations. Therefore, to study the impact of the observational biases, we focus on another method in which we perform Monte-Carlo simulations to reproduce binary systems from random orbital parameters and "observed" with the same sampling as our actual data. We then look at the peak-to-peak variations (ΔRV) of these systems to see whether they would have been detected or not. We use as a criterion a ΔRV of 20 km s^{-1} for the stars of NGC 2244 and Mon OB2, except for the two fast rotating stars where we took a ΔRV of 40 km s^{-1} because the measurement errors are larger. We stress that this criterion is comparable to the criterion chosen for the detection of binary systems in NGC 2244 and in Mon OB2. We perform such simulations by generating 10000 binary systems based on the assumptions that 50% of the binaries have an orbital period shorter than 10 days, while the other 50% have $P > 10$ days. Moreover, the periods are uniformly drawn from log P space (between 0.3 and 3.5), the system orientations ($\cos i$) are randomly drawn from a uniform distribution, the mass ratio $q = M_{\rm P}/M_{\rm S}$ is also uniformly distributed between 1.0 and 10.0, and eccentricities are uniformly selected between 0.0 and 0.8. The derived probabilities are given in Table 5.3.

Table 5.3: Probability (%) of missing a significant orbital *RV* variation on the basis of Monte-Carlo simulations. The values of the header of each column (3 – 6) indicate the interval of orbital periods under consideration.

Star	M_1	2 – 10	10 – 365	365 – 3000	2 – 3000
HD 46056	20.8	2.0	17.0	77.0	24.0
HD 46149	20.8	1.0	4.0	31.0	7.0
HD 46150	34.4	1.0	3.0	21.0	5.0
HD 46202	17.1	1.0	9.0	50.0	13.0
HD 46223	46.9	1.0	3.0	22.0	5.0
HD 46485	20.8	1.0	20.0	68.0	20.0
HD 46573	22.9	1.0	6.0	38.0	9.0
HD 46966	18.8	1.0	6.0	34.0	8.0
HD 48279	22.9	1.0	7.0	40.0	10.0

We find that the probability of missing a short-period binary is rather low ($< 20\%$) for all the stars of our sample. However, we clearly see that for long orbital periods, i.e., larger than one year, this probability increases to about 50%. These statistical tests show that it is difficult to constrain with certainty the true binary fraction. In this respect, the phase coverage is very important for this kind of investigation.

A&A 502, 937–950 (2009)
DOI: 10.1051/0004-6361/200911662

Astronomy & Astrophysics

Early-type stars in the young open cluster NGC 2244 and in the Monoceros OB2 association⋆

I. The multiplicity of O-type stars⋆⋆

L. Mahy[1], Y. Nazé[1,⋆⋆⋆], G. Rauw[1,†], E. Gosset[1,‡], M. De Becker[1,⋆⋆], H. Sana[2], and P. Eenens[3]

[1] Astrophysical Institute, Liège University, Bât. B5C, Allée du 6 Août 17, 4000 Liège, Belgium
e-mail: mahy@astro.ulg.ac.be
[2] European Southern Observatory, Alonso de Cordova 1307, Casilla 19001, Santiago 19, Chile
[3] Departamento de Astronomia, Universidad de Guanajuato, Apartado 144, 36000 Guanajuato, GTO, Mexico

Received 14 January 2009 / Accepted 27 April 2009

ABSTRACT

Aims. We present the results obtained from a long-term spectroscopic campaign to study the multiplicity of O-type stars in both the young open cluster NGC 2244 and the Mon OB2 association.
Methods. Our spectroscopic monitoring was performed over several years, allowing us to investigate different timescales. For each star, several spectral diagnostic tools were applied to search for line shifts and profile variations. We also measured the projected rotational velocity and revisited the spectral classification.
Results. Several stars in our sample have been previously considered to be spectroscopic binaries, although only a few scattered observations were available. Our results now have identified a more complex situation for two new spectroscopic binaries (HD 46 149 in NGC 2244 and HD 46 573 in Mon OB2). The first object is a long-period double-lined spectroscopic binary, although the exact value of its period remains uncertain and the second object is classified as an SB1 system with a period of about 10.67 days but the time series of our observations do not enable us to derive a unique orbital solution for this system. We also find another star to be variable in radial velocity (HD 46 150) and detect line profile variations in two rapid rotators (HD 46 056 and HD 46 485).
Conclusions. This spectroscopic investigation places a firm lower limit (17%) on the binary fraction of O-stars in NGC 2244 and reveals the lack of short-period O+OB systems in this cluster. In addition, a comparison of these new results with two other well-studied clusters (NGC 6231 and IC 1805) puts forward possible hints of a relation between stellar density and binarity, which could provide constraints on the theories of the formation and early evolution of hot stars.

Key words. stars: binaries: spectroscopic – stars: early-type – galaxy: open clusters and association: individual: NGC 2244 – galaxy: open clusters and association: individual: Monoceros OB2

1. Introduction

Since O-type stars are preferentially found in either young open clusters or OB associations, these two environments appear to play a key role in massive star formation. Detailed observations could provide interesting constraints on the different formation scenarios proposed by theoreticians (for a summary of these, see e.g., Zinnecker & Yorke 2007). Massive stars in clusters are ideal targets because they represent a homogeneous population (of similar distance, age, and chemical composition). Moreover, the study of O-type stars in open clusters, and in particular their multiplicity, is of major interest for understanding the physical properties of these objects. Other parameters (e.g., orbital period, eccentricity, and mass ratio) of these multiple systems in addition to their binary frequency can provide a unique signature of star formation and dynamical interactions within the cluster during the very early phases of its existence.

Investigations based upon extensive spectroscopic campaigns in some clusters (e.g., NGC 6231, Sana et al. 2008; IC 1805, De Becker et al. 2006) have been performed over several years. These detailed observations led to a serious correction of the results proposed by García & Mermilliod (2001) for O-type star rich clusters, by greatly improving our knowledge of the precise physical parameters of the binaries in these clusters. To extend these studies, we undertook a similar spectroscopic monitoring of the O-type star population in another young open cluster, NGC 2244.

With an inferred age of about 2–3 Myr (Chen et al. 2007) and a radial velocity (RV) of 26.2 ± 3.4 km s^{-1} (Kharchenko et al. 2005), NGC 2244 is inside the Rosetta nebula and forms the core of the Monoceros OB2 association. The cluster is the youngest of two or three subgroups of OB stars and stellar aggregates in this association (Li & Smith 2005).

Some stars in NGC 2244 were observed by Plaskett & Pearce (1931) and reanalyzed by Petrie & Pearce (1961). These authors found that the majority of these objects has quite constant RVs. These results were, however, subsequently challenged by Abt & Biggs (1972) and Liu et al. (1989).

From a compilation of heterogeneous data, García & Mermilliod (2001) estimated the proportion of spectroscopic

⋆ Table 2 is only available in electronic form at the CDS via anonymous ftp to cdsarc.u-strasbg.fr (130.79.128.5) or via http://cdsweb.u-strasbg.fr/cgi-bin/qcat?J/A+A/502/937
⋆⋆ Based on observations collected at Observatoire de Haute-Provence (France), San Pedro Màrtir Observatory (Mexico), La Silla Observatory (European Southern Observatory), and Asiago Observatory (Italy).
⋆⋆⋆ Postdoctoral Researcher F.R.S.-FNRS.
† Research Associate F.R.S.-FNRS.
‡ Senior Research Associate F.R.S.-FNRS.

binaries in NGC 2244 to be about 50% of the O-type stars (three out of six considered as binaries). Such an O-star binary fraction would make this cluster the third binary-rich cluster in their sample after NGC 6231 and IC 1805. As already mentioned above, the figures for these two clusters were subsequently significantly revised (Rauw & De Becker 2004; De Becker et al. 2006; Sana et al. 2008). In addition, until now, only two spectroscopic binaries have been detected with certainty in Mon OB2: HD 47 129 (Plaskett's star, Linder et al. 2008) and HD 48 099 (Stickland 1996; Mahy et al. in preparation) which both lie outside NGC 2244. These conflicting results provide support for a revised, thorough analysis of the binarity in NGC 2244.

Other studies in different wavelength domains have provided additional information about the content and overall organization of the cluster. *Chandra* mosaic observations of NGC 2244 were presented by Wang et al. (2008). The X-ray spectra of the OB-type stars were found to be rather soft and consistent with the standard model of small-scale shocks produced, in the inner regions of the stellar winds, by the line-driving instability (Feldmeier et al. 1997). The X-ray luminosities of these stars follow the canonical L_X/L_{bol} relation (Sana et al. 2006b) rather closely and found no evidence of extra emission caused by wind-wind collisions in binary systems. Wang et al. (2008) found that the fainter X-ray sources are strongly concentrated around HD 46 150 (O5.5 V) whilst no strong clustering of X-ray sources was found around the most massive component HD 46 223 (O4 V). Following these authors, there are two possible explanations of this difference: either HD 46 223 was ejected as a result of dynamical interactions (but it does not display a strong proper motion), or it may actually be younger and would then not be part of the same population as the central part of the cluster.

The present paper, based on a long-term spectroscopic campaign, is organized as follows. Section 2 describes the observing campaign. The properties of the individual objects (spectral classification, projected rotational velocity, and multiplicity) are presented in Sect. 3. The multiplicity and the rotational velocities of massive stars in NGC 2244 are discussed in Sect. 4 while Sect. 5 provides a summary of our results.

2. Observations and data reduction

Our team have collected 207 spectra of 9 stars over 9 years using several different telescopes. This sample has allowed us to investigate the presence of short and long-term variations for each star.

Most of our observations were obtained with the 1.52 m telescope of the Observatoire de Haute-Provence (OHP) equipped with the Aurélie spectrograph. The detector used was a thin back-illuminated CCD with 2048 × 1024 pixels of 13.5 μm^2. The grating #3 (600 lines/mm) allowed us to obtain spectra with a resolving power of 10 000, centered on 5700 Å and covering wavelengths between 5500 Å and 5920 Å. Exposure times were typically 10 to 45 min resulting in signal-to-noise ratios higher than 150. Such high quality observations were needed to search for weak variations or the spectroscopic signature of faint companions. We also collected spectra with the same instrument in the blue domain (centered at 4670 Å and covering the 4450–4900 Å region). These data were acquired during 28 days in November 2007 and 6 days in September and October 2008. The entire dataset was reduced in a classical way (bias and flatfield corrections) using MIDAS software developed at ESO (European Southern Observatory). The spectra were wavelength calibrated using Thorium-Argon comparison spectra obtained immediately before or after the stellar spectrum. The spectra were finally normalized to the continuum by fitting polynomials of degree 4 or 5.

Additional spectra were obtained at Observatorio Astronómico Nacional of San Pedro Màrtir (SPM), in Mexico, with the 2.1 m telescope equipped with Espresso. This échelle spectrograph gives 27 orders in the 3780–6950 Å wavelength domain with a resolving power of $R = 18\,000$. The CCD detector was a SITE 3 optical chip with 1024 × 1024 pixels of 24 μm^2. Typical exposure times ranged from 5 to 15 min. We had to add consecutive spectra of a given night at the expense of time resolution to obtain signal-to-noise ratios close to 300. The data were reduced using the échelle package available within the MIDAS software.

In addition, we gathered spectra from both Elodie and ESO archives. Elodie was an échelle spectrograph giving 67 orders in the 3850–6850 Å spectral range ($R = 42\,000$) mounted at the 1.93 m telescope at OHP. We retrieved 13 spectra acquired between November 1999 and November 2005. The mean signal-to-noise ratio of the data of our targets was 150 for an exposure time ranging from 10 min to 1 h. The ESO archives provided us with 11 spectra taken with FEROS (Fiber-fed Extended Range Optical Spectrograph) mounted at the ESO/MPG 2.20 m telescope at La Silla ($R = 48\,000$). The data reduction was performed using a modified FEROS pipeline working under the MIDAS environment. Beyond the modifications already described in Sana et al. (2006a), several new features were implemented. We used a 2D fit of the order position for improved stability. We also used the wavelength calibration frames obtained with the "new" ThArNe calibration lamp (see e.g., FEROS-II user manual 77.0, Sect. 2.5). The latter however heavily saturates in the red, even on the shortest exposures planned by the calibration plan[1]. Therefore, we computed a master calibration frame for each exposure time. We then proceeded with the extraction of the calibration spectra separately for each master frame. We finally used the detected lines from the 3 s/15 s/30 s master wavelength calibration frames to calibrate the orders 30–39/10–29/1–9 respectively. The saturated lines or the lines outside the linearity range of the detector were rejected from the fit and the detection threshold was optimised for each order. Finally, a 2-iteration 3-σ clipping method was used to discard the very few remaining discordant lines (mostly because of artifacts related to poorly corrected bad column effects). The obtained wavelength calibration residuals were all in the range 2.7–2.9 mÅ.

To increase the dataset of HD 46 149, we retrieved two spectra from Asiago archives of mean signal-to-noise ratio of about 155. These two spectra were taken by the 1.82 m Copernicus telescope equipped with the échelle instrument (R = 28 600). Unfortunately, no flatfields were available and we could only apply an overscan correction. Because of the lack of a well-suited calibration atlas, the spectra were approximatively calibrated in wavelength but this first order calibration was subsequently checked using the interstellar lines. The overview of the observations is given in Table 1 (available electronically).

For most stars in NGC 2244, the radial velocities (RVs) and the equivalent widths (*EW*s) were determined by fitting Gaussians to the line profiles, except for the two rapid rotators. Indeed, Gaussian functions were found to reproduce well the observed profile of moderately rotationally broadened lines in

[1] As a reminder, the latter provides 3 series of two exposures with increasing exposure times of 3 s, 15 s, and 30 s, a scheme that is repeated at the beginning and at the end of the night.

Table 1. Observations used for the study of massive stars in both NGC 2244 and Mon OB2.

Object	Cluster	Obs. run	Telescope/Instrument	Wavelength domain	n# Spectra	ΔT
HD 46 056	NGC 2244	Feb. 2006	OHP – AURELIE/1.52 m	5500–5900 Å	6	5.02
		Apr. 2007	SPM – ESPRESSO/2.20 m		5	6.00
		Nov. 2007	OHP – AURELIE/1.52 m	4450–4900 Å	1	...
		Jan. 2008	OHP – AURELIE/1.52 m	5500–5900 Å	4	3.00
		Mar. 2008	SPM – ESPRESSO/2.20 m		1	...
HD 46 149	NGC 2244	Dec. 1994	Asiago – Echelle/1.82m		1	...
		Dec. 1998	Asiago – Echelle/1.82 m		1	...
		Jan. 2003	OHP – ELODIE/1.93 m		1	...
		Nov. 2005	OHP – ELODIE/1.93 m		1	...
		Jan. 2006	ESO – FEROS/2.20 m		1	...
		Feb. 2006	OHP – AURELIE/1.52 m	5500–5900 Å	6	5.10
		Apr. 2007	SPM – ESPRESSO/2.20 m		3	3.97
		Apr. 2007	OHP – AURELIE/1.52 m	5500–5900 Å	1	...
		Nov. 2007	OHP – AURELIE/1.52 m	4450–4900 Å	6	25.05
		Jan. 2008	OHP – AURELIE/1.52 m	5500–5900 Å	4	5.03
		Mar. 2008	SPM – ESPRESSO/2.20 m		5	4.93
		Sep. 2008	OHP – AURELIE/1.52 m	4450–4900 Å	1	...
		Oct. 2008	OHP – AURELIE/1.52 m	4450–4900 Å	3	4.02
HD 46 150	NGC 2244	Nov. 1999	OHP – ELODIE/1.93 m		1	...
		Jan. 2003	OHP – ELODIE/1.93 m		1	...
		Nov 2004	OHP – ELODIE/1.93 m		1	...
		Jan. 2006	ESO – FEROS/2.20 m		1	...
		Feb. 2006	ESO – FEROS/2.20 m		1	...
		Feb. 2006	OHP – AURELIE/1.52 m	5500–5900 Å	6	5.10
		Apr. 2007	SPM – ESPRESSO/2.20 m		5	5.99
		Nov. 2007	OHP – AURELIE/1.52 m	4450–4900 Å	5	25.07
		Jan. 2008	OHP – AURELIE/1.52 m	5500–5900 Å	4	2.99
		Mar. 2008	SPM – ESPRESSO/2.20 m		5	3.95
		Oct. 2008	OHP – AURELIE/1.52 m	4450–4900 Å	4	4.00
HD 46 202	NGC 2244	Jan. 2006	ESO – FEROS/2.20 m		1	...
		Feb. 2006	OHP – AURELIE/1.52 m	5500–5900 Å	2	1.98
		Apr. 2007	OHP – AURELIE/1.52 m	5500–5900 Å	2	5.00
		Nov. 2007	OHP – AURELIE/1.52 m	4450–4900 Å	4	20.00
		Jan. 2008	OHP – AURELIE/1.52 m	5500–5900 Å	4	3.01
HD 46 223	NGC 2244	Jan. 1999	OHP – ELODIE/1.93m		1	...
		Nov 2005	OHP – ELODIE/1.93 m		1	...
		Jan. 2006	ESO – FEROS/2.20 m		1	...
		Feb. 2006	ESO – FEROS/2.2 0m		1	...
		Feb. 2006	OHP – AURELIE/1.52 m	5500–5900 Å	6	5.03
		Apr. 2007	OHP – AURELIE/1.52 m	5500–5900 Å	3	6.00
		Nov. 2007	OHP – AURELIE/1.52 m	4450–4900 Å	5	21.98
		Jan. 2008	OHP – AURELIE/1.52 m	5500–5900 Å	4	3.06
		Mar. 2008	SPM – ESPRESSO/2.20 m		3	2.01
		Oct. 2008	OHP – AURELIE/1.52 m	4450–4900 Å	1	...
HD 46 485	NGC 2244	Nov. 2005	OHP – ELODIE/1.93 m		1	...
		Jan. 2006	ESO – FEROS/2.20m		1	...
		Nov. 2007	OHP – AURELIE/1.52 m	4450–4900 Å	6	14.99
		Jan. 2008	OHP – AURELIE/1.52 m	5500–5900 Å	4	3.05
		Mar. 2008	SPM – ESPRESSO/2.20 m		5	4.02
HD 46 573	Mon OB2	Jan. 2006	ESO – FEROS/2.20 m		1	...
		Feb. 2006	ESO – FEROS/2.20 m		1	...
		Feb. 2006	OHP – AURELIE/1.52 m	5500–5900 Å	3	2.97
		Apr. 2007	SPM – ESPRESSO/2.20 m		5	5.99
		Nov. 2007	OHP – AURELIE/1.52 m	4450–4900 Å	6	25.98
		Jan. 2008	OHP – AURELIE/1.52 m	5500–5900 Å	5	3.05
		Oct. 2008	OHP – AURELIE/1.52 m	4450–4900 Å	3	3.00
HD 46 966	Mon OB2	Jan. 2003	OHP – ELODIE/1.93m		2	1.76
		Nov 2004	OHP – ELODIE/1.93 m		1	...
		Jan. 2006	ESO – FEROS/2.20 m		2	1.94
		Feb. 2006	OHP – AURELIE/1.52 m	5500–5900 Å	6	5.01
		Feb. 2007	OHP – AURELIE/1.52 m	5500–5900 Å	1	...
		Apr. 2007	OHP – AURELIE/1.52 m	5500–5900 Å	1	...
		Nov. 2007	OHP – AURELIE/1.52 m	4450–4900 Å	5	24.05
		Jan. 2008	OHP – AURELIE/1.52 m	5500–5900 Å	4	3.02
HD 48 279	Mon OB2	Jan. 2000	OHP – ELODIE/1.93m		1	...
		Nov 2004	OHP – ELODIE/1.93 m		1	...
		Nov. 2007	OHP – AURELIE/1.52 m	4450–4900 Å	9	16.02
		Jan. 2008	OHP – AURELIE/1.52 m	5500–5900 Å	4	3.01
		Mar. 2008	SPM – ESPRESSO/2.20 m		4	4.01
		Oct. 2008	OHP – AURELIE/1.52 m	4450–4900 Å	1	...

The first and the second columns give the name of the object and the membership to the cluster or association (Ogura & Ishida 1981). The next columns are the epochs of the campaign, the telescope/instrument used, the observed wavelength domain, the number of spectra obtained and the time elapsed between the first and the last spectrum of the run, expressed in days.

massive stars. To measure the RVs, we fitted the bottom half of the line profiles, while the entire line was used to estimate the *EW*s. For the two rapid rotators, we used a synthetic line profile generated with the projected rotational velocity of the star to determine the Doppler shifts, and we integrated the complete line profiles to measure the *EW*s. We note that we used the same rest wavelengths as Conti et al. (1977) to calculate the RVs.

We inferred the spectral type and the luminosity class of each star by using the classification criteria of Conti & Alschuler (1971), Conti (1973), and Mathys (1988, 1989) hereafter referred to as "Conti's criteria". To support our results, we visually compared the spectra to the atlas of Walborn & Fitzpatrick (1990). We also checked the luminosity class by comparing the computed visual absolute magnitude with the photometric calibration proposed by Martins & Plez (2006). We also needed to assume a value for the distance of the cluster. Massey et al. (1995) derived a spectroscopic parallax to this region of 1.9 ± 0.1 kpc, whereas more recent photometric studies place NGC 2244 at a distance of between 1.4 and 1.7 kpc (Hensberge et al. 2000) in agreement with previous estimates (Ogura & Ishida 1981; Pérez 1991). In the present paper, we adopt a mean distance for NGC 2244 of 1.55 kpc. However, we note that a change of distance by 10% would not modify our conclusions. Finally, we compared our spectral classification with previous results from earlier studies (notably quoted in the Reed catalogue Reed 2005).

3. The O-type star population in NGC 2244 and Mon OB2

Our study of the multiplicity of O-type stars is based on two wavelength domains: a blue region (4450–4900 Å) and a yellow one (5500–5920 Å). In addition to the RV and profile analysis, the former setting provides an accurate determination of the spectral classification of each star; the numerous interstellar features observed in the latter setting enable us to check the quality of the wavelength calibration and RV measurements. We provide, in Table 2 (available electronically at CDS), the heliocentric Julian days (HJD) and the RVs of each spectrum, while Table 3 quotes, object by object, the mean RVs and the 1-σ standard deviation of the different lines.

In the following, an object is considered to be a true spectroscopic binary (Sect. 3.1) if we detect either the presence of significant, periodic RV variations or the signature of a companion whose spectral lines move in anti-phase with those of the main star. If a star fulfills the former criterion, a full orbital solution can be computed, leading to the precise determination of the orbital parameters. When the latter criterion is fulfilled, it only allows us to evaluate the spectral type of the two components and their mass ratio, with only loose constraints on the orbital period. If none of these criteria is fulfilled, but significant RV variations are detected, then the star will be considered to be a "RV variable", and thus a binary *candidate*. The RV variations are considered as significant if they are larger or equal to three times the average RV measurement error. For all stars except the two rapid rotators, this error is well represented (as was confirmed by tests on individual data) by the RV dispersion in the narrow diffuse interstellar band (DIB) at λ 5780, which has similar strength and width to the stellar lines. For the rapid rotators, χ^2 evaluation from shifts of the synthetic line profile showed the RV error to be about 10 km s^{-1}. An object for which significant RV variations are detected is presented in Sect. 3.2. The remaining objects are presented in Sect. 3.3.

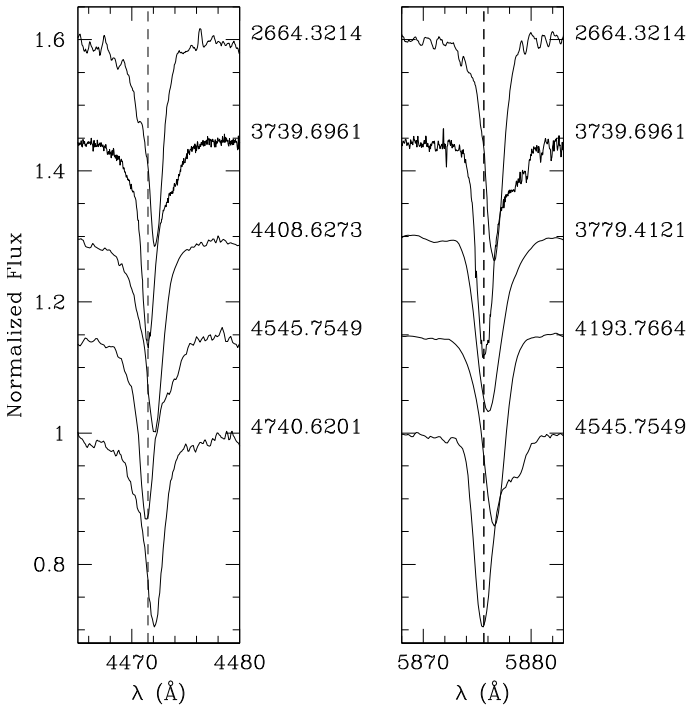

Fig. 1. He I λ 4471 and He I λ 5876 line profiles of HD 46 149 observed during our spectroscopic campaigns. The time is given on the right side of the figure in the format HJD − 2 450 000. All spectra are displayed in the heliocentric frame of reference. The vertical dashed line represents the rest wavelength. The signature of the secondary is clearly seen, in particular at HJD ∼ 2 454 545.

3.1. Spectroscopic binaries

3.1.1. HD 46 149

The first spectroscopic study of HD 46 149 was completed by Plaskett & Pearce (1931), who measured a mean RV of about 45.0 ± 1.5 km s^{-1}. On the basis of new data, Petrie & Pearce (1961) confirmed that the star might be single. They obtained a mean RV of about 38.0 ± 2.1 km s^{-1}. Liu et al. (1989) analyzed three datasets obtained over three different epochs (in November 1987, February 1988, and October 1988). They found a RV dispersion of about 10.2 km s^{-1} and, therefore, considered the star to be a potential binary. Turner et al. (2008) reported some velocity variabilities of HD 46 149 because of the presence of a close spectroscopic companion.

In February 2006, the measurements of RVs obtained for six spectra acquired over six consecutive nights did not find evidence of any significant variation ($\overline{RV}$ = 21.6 ± 2.1 km s^{-1}). Moreover, no variation was detected in the line profiles. However, if we compare these RVs with the April 2007 data (HJD ∼ 2 454 199, in Fig. 1), we obtain a shift close to 25 km s^{-1} for the He I λ 5876 line, and a RV shift of about 40 km s^{-1} for He I λ 4471 is measured between the data taken in January 2006 and in November 2007. Our analysis of the entire spectroscopic campaign for HD 46 149 clearly shows significant RV shifts between the observing runs. The two extreme RV values in our sampling are approximately −5 (Jan. 2006, Mar. 2008) and +50 km s^{-1} (Apr. 2007, Nov. 2007 and Sept.–Oct. 2008). In addition, the FEROS spectrum and the data collected between January and April 2008 allowed us to detect the presence of a companion in the red wing of most of the He I lines (visible in Fig. 1 at, for example, HJD ∼ 2 453 739 and

Table 3. The mean radial velocities[a] and the 1-σ dispersions.

Star	He I λ 4471	He II λ 4542	He II λ 4686	O III λ 5592	DIB λ 5780	C IV λ 5801	C IV λ 5812	He I λ 5876	Na I λ 5890
HD 46056	36.1 ± 6.9	49.6 ± 9.3	30.4 ± 12.1	...	26.0 ± 4.1	...	...	28.7 ± 9.7	23.3 ± 2.0
HD 46149	27.3 ± 21.8	27.6 ± 18.7	28.4 ± 22.0	12.6 ± 21.4	23.5 ± 4.7	24.1 ± 21.3	20.7 ± 20.3	22.3 ± 19.4	21.4 ± 3.0
HD 46150	31.2 ± 4.0	45.3 ± 8.1	44.8 ± 5.0	26.9 ± 7.8	23.8 ± 3.9	48.8 ± 11.7	34.0 ± 12.9	32.6 ± 5.4	20.7 ± 2.4
HD 46202	39.8 ± 3.1	38.8 ± 3.8	38.0 ± 3.2	31.8 ± 1.3	25.4 ± 1.5	40.4 ± 2.2	36.1 ± 2.2	40.0 ± 1.4	23.5 ± 1.2
HD 46223	34.5 ± 6.7	44.5 ± 3.2	47.0 ± 3.3	31.1 ± 7.4	23.8 ± 4.6	50.9 ± 2.9	38.6 ± 6.4	35.6 ± 2.7	23.4 ± 3.4
HD 46485	31.5 ± 7.5	43.5 ± 10.7	34.0 ± 9.4	...	21.8 ± 5.5	...	...	30.8 ± 11.1	21.3 ± 4.0
HD 46573	47.0 ± 6.6	48.4 ± 10.0	50.2 ± 7.6	47.9 ± 8.5	27.6 ± 3.9	59.5 ± 5.7	53.2 ± 6.1	50.3 ± 5.4	26.9 ± 1.4
HD 46966	39.2 ± 1.4	44.9 ± 2.0	45.3 ± 2.0	38.4 ± 2.6	23.4 ± 4.7	47.7 ± 3.0	43.4 ± 3.3	40.8 ± 2.4	20.8 ± 2.2
HD 48279	31.4 ± 3.6	40.6 ± 2.6	38.9 ± 5.1	32.8 ± 11.8	23.1 ± 5.0	43.3 ± 6.0	31.9 ± 7.4	39.5 ± 2.1	20.8 ± 3.3

[a] The data are expressed in km s^{-1}.

HJD ~ 2 454 545). The determination of the individual RVs enables us, in this case, to estimate the mass ratio of the two components. At the largest observed separation (at HJD ~ 2 454 545), the highest precision on the RVs of both stars was obtained from analyzing the He I λ 5876 line, which yields velocities of −5.8 and +143.3 km s^{-1} for the primary and the secondary, respectively. The RV of the blended spectrum, +52.5 km s^{-1} at HJD ~ 2 452 664, was measured from the He I λ 5876 line. From these shifts, we estimate a mass ratio (M_1/M_2) of about 1.6. We nevertheless emphasize that the phases for which we measured the RVs might not be the extreme ones of the orbital cycle. In consequence, our mass ratio computation must be considered preliminary at best. We also estimated the flux ratio between the primary and the secondary. We measured, from the deblended He I λ 5876 line, an *EW* for the primary of 572 mÅ, which we compared with the average *EW* quoted by Conti (1973) for such stars. We obtained an optical flux ratio $L_1/(L_1 + L_2)$ for the primary of about 0.7. In consequence, the flux ratio L_1/L_2 is close to 2.3. The obtained mass and flux ratios thus imply that the secondary is an early B-type (for comparison, from the stellar parameters listed in Martins et al. 2005, a binary system composed of an O8 V and an O9.5 V would have a theoretical mass ratio of M_1/M_2 = 1.3 and a flux ratio L_1/L_2 of about 1.9).

We then applied the Fourier analysis to the time series of the primary RVs of He I λ 4471, He II λ 4542, C IV λ 5812, and He I λ 5876 following the method described by Heck et al. (1985) and revised by Gosset et al. (2001). In all cases, we observed the highest peaks in the periodograms but their positiond varied according to the studied line. For example, the computed periodogram corresponding to He I λ 5876 yields a period of about 47 days while the one corresponding to C IV λ 5812 indicates a 1600 day period. We also performed a period search on the combined RV list of He I λ 4471 and He I λ 5876. Even in this case, the detected peak in the periodogram is not significant enough to infer reliably a particular orbital period. The data sampling is thus too poor at the present time to constrain the period of HD 46 149.

To separate the two components of HD 46 149, we used our disentangling program, based on the method proposed by González & Levato (2006). This consists of an iterative process that uses alternately the spectrum of one component (shifted according to its radial velocity) to remove it from the observed spectra and then to calculate a mean spectrum of the other component. Furthermore, this technique allows us to compute the RVs of each star by cross-correlation even at phases for which the lines are heavily blended. We applied the disentangling algorithm to the wavelength domains 4000–4220 Å and 4450–4730 Å. To create the RV cross-correlation mask, we used the He I λ 4026, Si IV λ 4089, He I λ 4120, He I λ 4143, He I λ 4471, Mg II λ 4481, and He I λ 4713 lines for the secondary, and we added the Si IV λ 4116, He II λ 4200, and He II λ 4542 lines for the primary. The calculated mean spectrum of the secondary star looks similar to that of a B0 V star in the Walborn & Fitzpatrick (1990) atlas. However, because of the poor sampling of the data, this result must be considered very preliminary.

HD 46 149 was classified as an O8.5 V ((f)) star (Massey et al. 1995), but we revise its classification to O8 V. We note that this does not depend on the degree of blending in the spectra. With the mass ratio computed above and a theoretical mass for the primary star close to 22 $M_\odot$ (Martins et al. 2005), we estimate the secondary mass to be approximately 14 $M_\odot$. Therefore, the system probably consists of O8 V + B0–1 V stars: HD 46 149 is the first O+B binary discovered so far in NGC 2244.

3.1.2. HD 46 573

This star is a member of Mon OB2, but does not belong to NGC 2244 (Turner 1976). According to the RV variability criterion, the RV dispersions for the stellar lines of HD 46 573 are at the limit of being considered as significant. However, we computed the Temporal Variance Spectrum (TVS, Fullerton et al. 1996) from the Aurélie spectra for the He I λ 4471, He II λ 4542, C IV $\lambda\lambda$ 5801–12, and He I λ 5876 lines. In each case, we obtained double-peaked profiles (Fig. 2). Together, the RV dispersion and the double-peaked TVS structures lend significant support to the binary nature of the star, first envisaged by Mason et al. (1998).

We performed a Fourier analysis of the RVs. We independently applied this method to three RV time series (He I λ 4471, He II λ 4542, and He I λ 5876) but the semi-amplitude spectra did not allow us to identify any dominant peak likely to be associated with a well-determined period. We then combined the RVs of the He I λ 4471 and He I λ 5876 lines. The highest peak in the resulting semi-amplitude spectrum occurs at a frequency of 0.0937 d^{-1} (Fig. 3), which corresponds to a period of about 10.67 days but this value is still very preliminary since random fluctuations cannot be totally excluded. The SB1 orbital solution of HD 46 573 was calculated with the program LOSP (Liège Orbital Solution Package, Sana & Gosset, A&A submitted) based on the method of Wolfe et al. (1967). We assigned the same weight, i.e., 1.0, to all spectra and fixed the period value to 10.67 days. Table 4 gives the main orbital elements computed for HD 46 573. Folded with this period, our data favored a non-zero eccentricity (Fig. 4, bottom panel). While this is an insufficient number to calculate a full orbital solution, the RVs from He II and C IV lines support the results from the He I lines (Fig. 4). However, there are still some phase intervals without

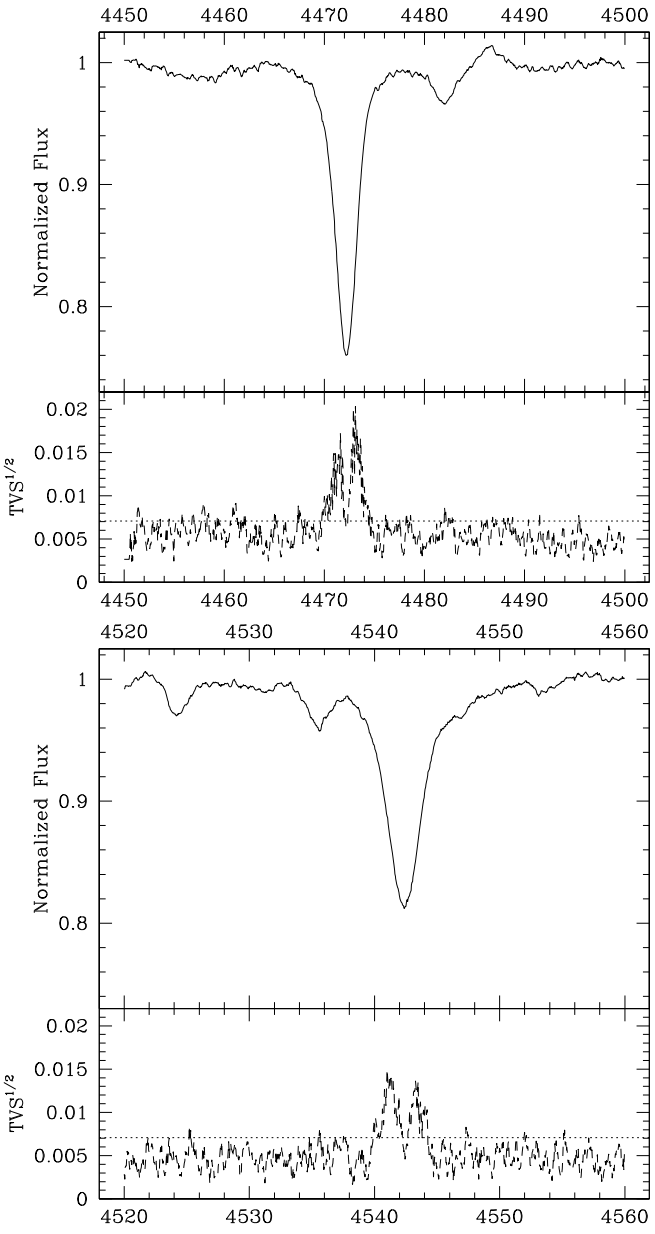

Fig. 2. The mean spectrum and TVS of HD 46 573 computed from the Aurélie spectra for the He I λ 4471 (*top*) and He II λ 4542 lines (*bottom*). In both cases, the double peaked structure is clearly visible. The dotted line illustrates the 99% significance level for the variability evaluated following the approach of Fullerton et al. (1996).

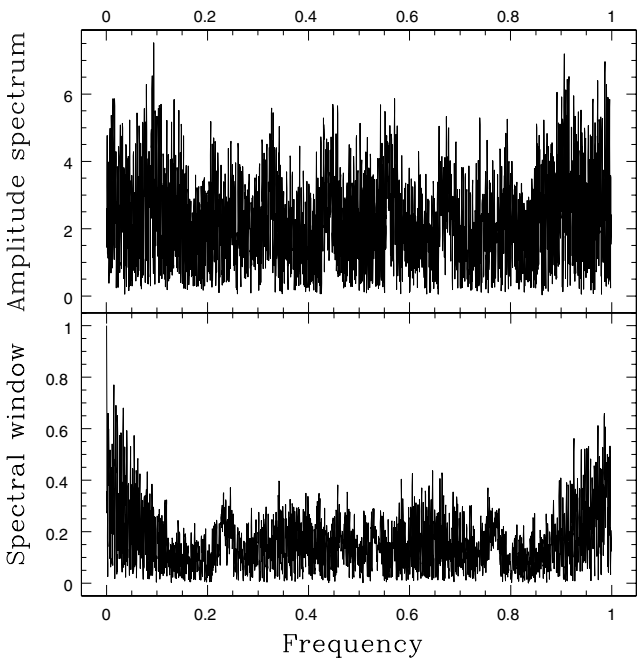

Fig. 3. The square root of the power spectrum (top) and the spectral window (*bottom*) of HD 46 573 computed from RVs of both He I λ 4471 and λ 5876 lines. The y-axis corresponds to the semi-amplitude of the signal. The frequency is expressed in d^{-1}.

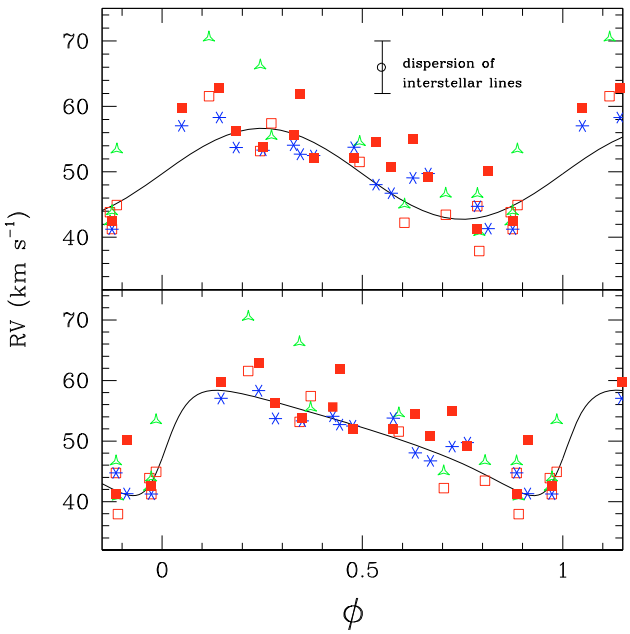

Fig. 4. *Top:* the best-fit circular radial velocity curve for HD 46 573 computed from the RVs of the He I λ 4471 (open squares) and λ 5876 (filled squares) lines for an orbital period of 10.67 days. The open triangles correspond to the RVs of the He II λ 4542 line and the stars to the RVs of the C IV λ 5812 line. The error bar corresponds to the ± 1–σ RV dispersion of the DIB λ 5780. *Bottom*: the best-fit eccentric orbital solution for HD 46 573 computed for the same two lines.

observations and we therefore need more data to secure the period and the orbital parameters.

We then computed, with the Fourier transform method (Simón-Díaz & Herrero 2007), the projected rotational velocity of HD 46 573. Previously estimated to be about 95 km s^{-1} (Conti & Ebbets 1977), we measured, for four lines (He II λ 4686, O III λ 5592, C IV λ 5801, and He I λ 5876), a mean value of about $v \sin i = 110 \pm 18$ km s^{-1}.

The spectral type was previously quoted as O7.5 V ((f)) (Conti & Leep 1974), O7 V (Bisiacchi et al. 1982), or O7 III ((f)) (Walborn 1971). In our data, the He I λ 4471 to He II λ 4542 ratio implies an O7.5 type, while the *EW* ratio between Si IV λ 4088 and He I λ 4143 favors a main-sequence (MS) luminosity class. The visual absolute magnitude is more uncertain since the distance to the star is not exactly known. Assuming that Mon OB2 lies at the same distance as NGC 2244, we estimated M_V for the two extreme values of the distance of NGC 2244 (1.4 kpc and 1.7 kpc). We obtain $M_V = -4.67$ and $M_V = -5.07$, using $V = 7.933$ and $E(B-V) = 0.61$

Table 4. Possible orbital parameters of the SB1 solution of HD 46 573[a].

Parameter	Circular	Eccentric
P(days)	10.67 (fixed)	10.67 (fixed)
e	...	0.47 ± 0.13
ω (degrees)	...	254.63 ± 14.2
T_0	3732.24 ± 0.26	3731.68 ± 0.48
γ (km s^{-1})	49.7 ± 0.7	50.9 ± 0.8
K (km s^{-1})	6.9 ± 0.9	8.5 ± 1.1
$a \sin i$ ($R_\odot$)	1.46 ± 0.19	1.58 ± 0.24
$f(m)$ ($M_\odot$)	0.0003 ± 0.0001	0.0005 ± 0.0002
rms (km s^{-1})	3.5	2.6
Prob (χ^2 >)	78%	99%

[a] T_0 (expressed in HJD−2 450 000) refers to the time of periastron passage for $e \neq 0$ and to the conjunction with the primary star in front for $e = 0$. γ, K, and $a \sin i$ are, respectively, the systemic velocity, the semi-amplitude of the radial velocity curve, and the projected separation between the center of the star and the center of mass of the binary system. The orbital elements are given for a circular and an eccentric orbit, respectively, by the RVs of both He I λ 4471 and λ 5876.

(Maíz-Apellániz et al. 2004). The reported results are closer to a MS star than to a giant (Martins & Plez 2006). The spectrum also exhibits weak N III $\lambda\lambda$ 4634−41 emission lines and strong He II λ 4686 absorption. In Hα, we detect weak emission in the absorption line probably related to the surrounding nebula. Thus, we favor an O7.5 V ((f)) spectral type, for HD 46 573.

In summary, two possible explanations exist for why the secondary component is not detected: a low-mass companion or a low inclination of the orbital plan. However, with such a large $v \sin i$ for the primary, it seems unlikely that the system is observed at such a low inclination angle. In consequence, we assume that HD 46 573 is an O7.5 V ((f)) star, which possesses a lower mass companion.

3.2. Radial velocity variables

3.2.1. HD 46 150

Reported as the second hottest star in NGC 2244, HD 46 150 is also one of the most well studied objects in this cluster. This star was first observed by Plaskett & Pearce (1931), who reported constant RVs. Since the 1970's, many other investigations have been devoted to HD 46 150 (Abt & Biggs 1972; Conti & Ebbets 1977; Garmany et al. 1980), but the interpretations of the multiplicity of the star varied greatly from one author to another. Garmany et al. (1980) considered the changes in the RVs to be a consequence of motions in the stellar atmosphere. Liu et al. (1989) and Underhill & Gilroy (1990) suggested that the star could be a spectroscopic binary, even though the signature of the secondary component had not yet been detected. Fullerton (1990) observed asymmetric line profiles, typical of an SB2.

Between November 1999 and October 2008, we collected 34 spectra spread over different timescales. We observed a slight RV variability in the absorptions (Fig. 5 notably compares the He II λ 4542 line at HJD ~ 2 453 772 and HJD ~ 2 454 397) as well as in the emission lines which is supported by the larger dispersion for stellar lines compared to the interstellar ones. For instance, we noted a RV shift of He II λ 4542 in the blue data by 28 km s^{-1} and of He I λ 5876 in the yellow spectra by 21 km s^{-1}. Moreover, the RV dispersion is smaller for the He I lines than for the He II and metallic lines, which are clearly RV variable. The presence of an unresolved companion could explain this effect. If the secondary is cooler, the He I lines of the primary will indeed be more affected by blends with the lines of the secondary component. The RV variations in lines associated with a stronger ionization (He II, C IV,...) thus reflect the true motion of the primary more accurately, leading to a larger RV dispersion.

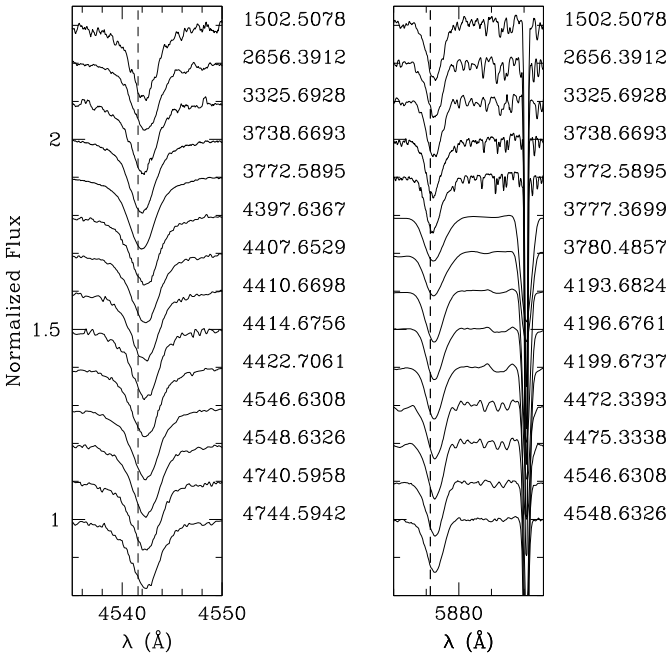

Fig. 5. He II λ 4542 and He I λ 5876 line profiles of HD 46 150 observed during our spectroscopic campaigns.

To compute the TVS from all spectra of HD 46 150, we had to degrade the spectral resolution of the échelle spectra to that of the Aurélie data. We proceeded by convolving the échelle spectra with Gaussians to ensure a homogeneous spectral resolution for all spectra. Variations in double peaks (in the He I λ 4471, He II λ 4542, He II λ 4686, and C IV $\lambda\lambda$ 5801–12 lines) and even variations in triple peaks, shown in Fig. 6, for the He I λ 5876 line, were observed. These features are reminiscent of what is usually found in spectroscopic binaries. However, no obvious signature of a companion could be found. We also note that these variations in double peaks are not visible on short timescales (~7 days), which implies that the system is a rather long-period binary.

To measure the period, we applied the Fourier method to the measured RVs. We used this technique independently for the He I λ 4471, He II λ 4542, C IV λ 5812, and He I λ 5876 lines. For each line, several peaks are present in the periodogram but their semi-amplitude nearly corresponds to the standard deviation in the RVs of the interstellar lines. We also computed the semi-amplitude spectrum by combining the RVs of the He I λ 4471 and the He I λ 5876 lines but, once again, the peak was insignificant to ascertain the period.

Previously estimated to be 118 ± 25 km s^{-1} (Conti & Ebbets 1977) and 86 km s^{-1} (Penny 1996), the projected rotational velocity of HD 46 150 has been determined using the Fourier method for four different lines (He II λ 4686, O III λ 5592, C IV λ 5801, and He I λ 5876). We find a mean value of $v \sin i = 97 \pm 9$ km s^{-1}.

In the literature, the spectral type is quoted to be between O5 V ((f)) (Underhill & Gilroy 1990; Maíz-Apellániz et al. 2004) and O5.5 V ((f)) (Conti & Ebbets 1977; Garmany et al. 1980). From our measurements of the *EW*s, we confirm the

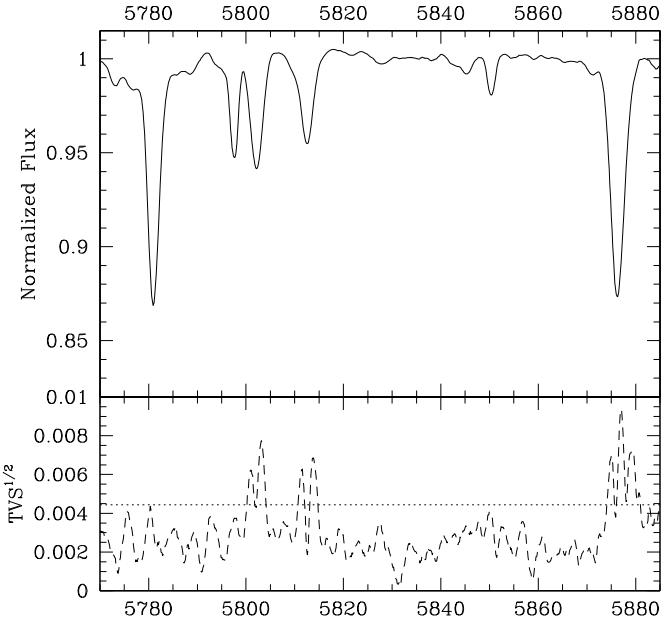

Fig. 6. Mean spectrum and TVS of HD 46 150 for the C IV $\lambda\lambda$ 5801−12 and He I λ 5876 lines. The dotted line illustrates the 99% significance level of the variability evaluated following the approach of Fullerton et al. (1996). We can clearly see the double peaked structure in the stellar lines.

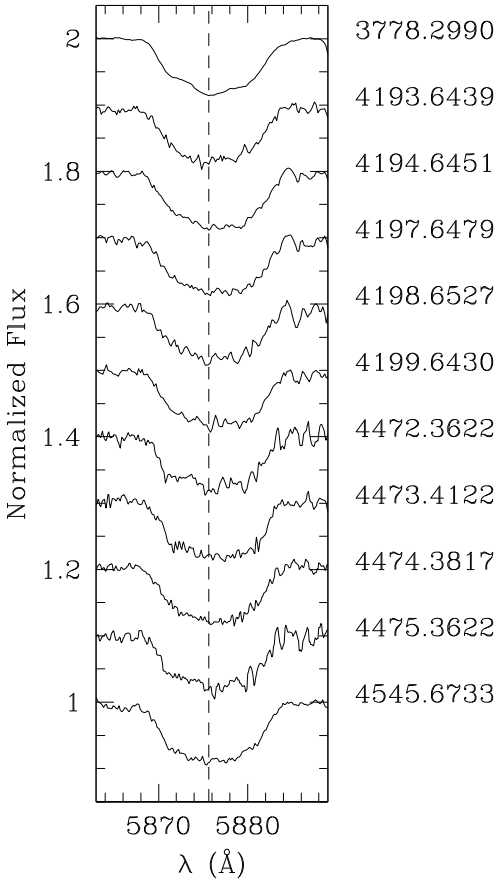

Fig. 7. He I λ 5876 line profiles of HD 46 056 observed from February 2006 to March 2008.

latter spectral type. We observe weak N III $\lambda\lambda$ 4634−41 emission lines and a strong He II λ 4686 absorption line, which verifies the addition of the ((f)) suffix. We compute $M_V = -5.45 \pm 0.22$, from $V = 6.74$ and $E(B-V) = 0.40$, which corresponds to a MS star, although we note that M_V is somewhat brighter than the theoretical value ($M_V^{\rm theo} = -5.12$) of Martins & Plez (2006) for typical O5.5 V stars. The difference could result from the distance taken at 1.55 kpc, or could also reflect the presence of a companion. We conclude that the spectral type of HD 46 150 is O5.5 V ((f)). Despite the lack of a clear periodicity or clear detection of a companion, several pieces of evidence (e.g., double peaked structures in TVS, large ΔRV,...) lead us to consider HD 46 150 as a potential binary.

3.3. Presumably single stars

3.3.1. HD 46 056

In the past, HD 46 056 was generally considered as a spectroscopic binary because of its variable RV (Walborn 1973; Liu et al. 1989; Underhill & Gilroy 1990). The line profiles always appear broad and shallow, suggesting the star is a single rapid rotator rather than a spectroscopic binary. The Helium lines indeed display very broad profiles extending over more than 15 Å with a clearly non-Gaussian shape (see Fig. 7). Furthermore, some metallic lines, such as Mg II λ 4481 or O III λ 5592, are too shallow to allow a measurement of their RVs by Gaussian fits or are too heavily blended to be distinguished as is the case for the C IV $\lambda\lambda$ 5801–12 lines. As a consequence, we adopted a different technique to measure the RVs. We first computed the Fourier transform of different Helium line profiles using our highest quality spectrum of the star, which combines a high signal-to-noise ratio with a high dispersion. We then found the mean projected rotational velocity ($v \sin i$) to be 355 ± 21 km s^{-1}.

Synthetic rotation profiles with $v \sin i = 346$, 350, 358, and 365 km s^{-1} were subsequently used to fit the He I λ 4471, He II λ 4542, He II λ 4686, and He I λ 5876 lines, respectively. For all these lines, the mean of the differences between the two extreme RV values were 28.1 km s^{-1} and the mean 1−σ dispersion is close to 9.5 km s^{-1}. This is close to the adopted measurement error for these broad lines. However, the line profiles appear to vary significantly as confirmed by the TVS analysis. This is reminiscent of HD 326 331 (see Sana et al. 2008) and we therefore conclude that the lines of HD 46 056 display some variations, although these cannot be easily associated with the presence of a companion. For instance, non-radial pulsations could be responsible for changes in the line profiles of HD 46 056, which are also then likely to perturb the measurement of the radial velocities. More spectra and most of all dedicated monitoring (spectroscopic as well as photometric) with a high temporal resolution are necessary to probe the existence of these short-time variations attributable to non-radial pulsations. The detection of these variations in the line profiles of rapid rotators was, for instance, reported by De Becker et al. (2008).

To estimate the spectral classification, since the line profiles are clearly not Gaussian, we measured the *EW*s by integrating the line profiles. Conti's criteria yield a spectral type O8 V. Moreover, the visual absolute magnitude of this object, calculated using $V = 8.16$ and $E(B-V) = 0.47$, is about $M_V = -4.25 \pm 0.21$, which corresponds to a MS star as suggested by the *EW*s of the classification lines. Unlike Frost & Conti (1976) who noticed some sporadic emission in the Hα line and assigned a spectral designation *e* for this star, we report that the narrow emission, visible in the Balmer Hβ and Hα lines,

is probably caused by the presence of nebular material around HD 46 056. This conclusion is supported by the presence of other nebular lines, e.g., the [O III] λ 5007 emission line. Therefore, a spectral type O8 V n is assigned to HD 46 056, in agreement with Walborn (1973) or Underhill & Gilroy (1990).

3.3.2. HD 46 202

Although some authors claim that HD 46 202 may be RV variable (Abt & Biggs 1972; Underhill & Gilroy 1990), we found no variation from our two-year spectroscopic campaign (between January 2006 and January 2008) and we therefore conclude that HD 46 202 is a presumably single star. Indeed, the RV dispersions are similar to those measured for the interstellar lines and the average RVs agree with those reported in the literature. Our results therefore support the previous investigations made by Plaskett & Pearce (1931) and Petrie & Pearce (1961). The projected rotational velocity of HD 46 202, estimated using the Fourier method, amounts on average to $v \sin i = 54 \pm 15\,\mathrm{km\,s^{-1}}$ for the stellar lines. Previous studies reported HD 46 202 as an O9 V star (Morgan et al. 1955, 1965; Walborn 1971; Conti & Leep 1974; Massey et al. 1995). Our data confirm this classification. Moreover, we obtained $M_V = -4.13 \pm 0.21$ from $V = 8.18$ and $E(B-V) = 0.44$, which indeed corresponds to a MS star. As quoted in the literature (Pérez 1991; Massey et al. 1995; Maíz-Apellániz et al. 2004), the visual magnitude seems constant in the range 8.18−8.21, with the exception of Ogura & Ishida (1981) who derived a V magnitude of 8.10.

3.3.3. HD 46 223

HD 46 223 is the hottest member of NGC 2244. The star has been regularly observed by studies of the interstellar medium (e.g., Zagury 2001), but the question of the variability was asked as early as the 1970's. Underhill & Gilroy (1990) concluded on the basis of both published data (Cruz-González et al. 1974; Conti et al. 1977; Gies 1987) and their own observations that the star may vary. The hypothesis of a spectroscopic binary was supported by the study of Liu et al. (1989), who measured a RV dispersion of 10.3 km s^{-1} for three observations. However, these RV changes could also be interpreted as motions in the atmosphere of the star (Underhill & Gilroy 1990).

The dispersions of the RVs of the more intense lines such as He II λ 4542, He II λ 4686, and He I λ 5876 are similar to those of the DIB. These values are slightly smaller than those of the metallic lines and the He I λ 4471 line. In any case, the dispersion is never significantly large even for these metallic lines: indeed, the higher amount of noise in these faint lines might explain their slight larger RV dispersion.

In consequence, we also applied the TVS method to our spectral time series. We performed this test with, on the one hand, only the Aurélie data, and, on the other hand, with all collected spectra (processed to correspond to similar spectral resolution, see Sect. 3.2.1). In both cases, we failed to detect any significant variations around the He I λ 4471, λ 5876, He II λ 4542 and near the C IV $\lambda\lambda$ 5801−12 lines (Fig. 8) and we therefore considered the star to be constant.

To determine the projected rotational velocity of the star, we used the Fourier transform on the same lines as for HD 46 150. We measured a mean projected rotational velocity of about $v \sin i = 100 \pm 17\,\mathrm{km\,s^{-1}}$, while the literature reports a value of $v \sin i = 103\,\mathrm{km\,s^{-1}}$ (Penny 1996). HD 46 223 was previously classified as O5 (Hiltner 1956; Johnson 1962; Bisiacchi et al. 1982), O4 (Morgan et al. 1965), O5 ((f)) (Conti & Leep 1974),

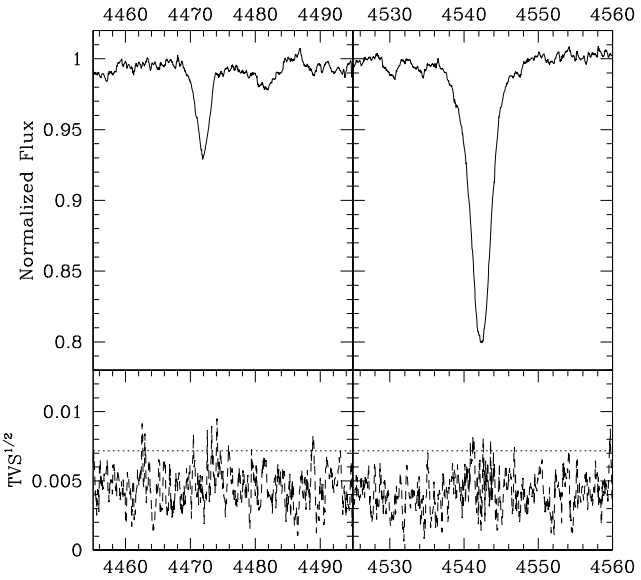

Fig. 8. Mean spectrum and TVS of HD 46 223 computed from the Aurélie data for the He I λ 4471 (on the left) and the He II λ 4542 lines (*on the right*). The dotted line illustrates the 99% significance level for the variability evaluated following the approach of Fullerton et al. (1996).

and, finally, as O4 V ((f)) by Massey et al. (1995). The measured *EW*s correspond to an O4 star. Using $V = 7.27$ and $E(B-V) = 0.50$, we computed a visual absolute magnitude of about $M_V = -5.23 \pm 0.22$, favoring a MS classification even though this value is slightly brighter than the theoretical one (M_V^{theo} = -5.56, Martins & Plez 2006). The spectrum clearly exhibits strong N III $\lambda\lambda$ 4634−41 emission lines accompanied by strong He II λ 4686 absorption. HD 46 223 also displays both the Si IV $\lambda\lambda$ 4088 and 4116 lines in emission. Therefore, we assigned an O4 V ((f$^+$)) spectral type. We also detected weak emission in the Hα line probably due to the nebular material surrounding the star as we already mentioned for HD 46 056.

3.3.4. HD 46 485

In previous works on NGC 2244, little attention was paid to HD 46 485. The literature contains only a few measurements but in no way the results of a dedicated observing run. As for HD 46 056, HD 46 485 presents very broad and moderately deep lines suggesting that this star is a rapid rotator (Fig. 9).

In order to determine the projected rotational velocity of HD 46 485, we independently applied a Fourier transform to three different lines, i.e., He II λ 4686, O III λ 5592, He I λ 5876, and we found a mean value of $301 \pm 25\,\mathrm{km\,s^{-1}}$. Since the line profiles are not Gaussian, we used this measurement to generate several theoretical rotation profiles with $v \sin i = 325$, 318, 291, and 301 km s^{-1}, which we correlated with the observed He I λ 4471, He II λ 4542, He II λ 4686, and He I λ 5876 lines, respectively, to derive the RVs. The 1-σ range of these lines are similar to each other (see Table 3) and, as for HD 46 056, similar to the RV measurement error. However, obvious profile changes are clearly detectable, although they are difficult to attribute to a possible binarity (Fig. 9). They may be due to non-radial pulsations.

Conti & Leep (1974) identified HD 46 485 as an O7.5 star, while Walborn (1971) suggested an O8 V n(e) classification. Using Conti's criteria, we inferred a spectral type of O8 V for

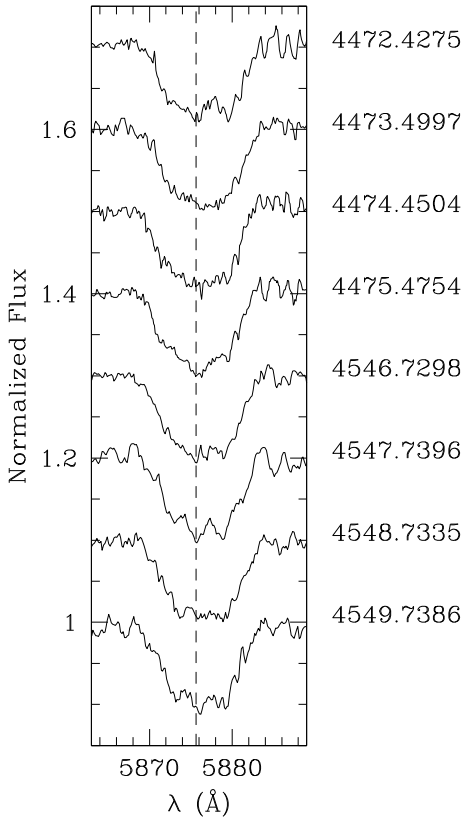

Fig. 9. Same as Fig. 7, but for HD 46 485.

HD 46 485. With $V = 8.20$ and $E(B-V) = 0.58$, we derived a visual absolute magnitude $M_V = -4.68 \pm 0.36$. This value agrees with that of a typical O8 V star (Martins & Plez 2006). In consequence, with its broad diffuse lines, we classify HD 46 485 as an O8 V n star.

3.3.5. HD 46 966

For our study of the variability of HD 46 966, we collected 22 spectra between January 2003 and January 2008. HD 46 966 does not exhibit any significant RV dispersion in neither its metallic nor Helium lines (λ 4471, λ 4542, λ 4686, and λ 5876). Moreover, no significant variation is observed by the TVS method. This suggests that HD 46 966 is a presumably single star.

Penny (1996) estimated the projected rotational velocity of HD 46 966 close to 59 km s^{-1}. Later on, Munari & Tomasella (1999) revised the value to be 90 km s^{-1}. From four different lines (already mentioned for HD 46 573), we measured the $v \sin i$ with the Fourier method and the derived mean value was estimated to be 63 ± 17 km s^{-1} in good agreement with the value given by Penny (1996).

The spectral types quoted in the literature are O8 V (Munari & Tomasella 1999; Maíz-Apellániz et al. 2004) or O8.5 V (Conti et al. 1977; Garmany et al. 1980). Based on the Conti criteria, we derived an O8.5 V spectral type. Although located outside NGC 2244, we assumed that HD 46 966 is situated approximately at the same distance as the open cluster (1.4–1.7 kpc). As before, we computed, for $V = 6.87$ and $E(B-V) = 0.21$, both the minimum visual absolute magnitude $M_V = -4.51$ and its maximum value at about $M_V = -4.93$. These two values are brighter than the theoretical value ($M_V^{\rm theo} = -4.27$, Martins & Plez 2006). However, we consider this difference to be an effect of the uncertain distance rather than a consequence of binarity, and we propose a MS classification for HD 46 966.

3.3.6. HD 48 279

Previous spectroscopic investigations by Petrie & Pearce (1961) reported a mean radial velocity of 31.0 ± 5.1 km s^{-1}. Underhill & Gilroy (1990), on the basis of their measured RV and also those of Petrie & Pearce (1961), Conti et al. (1977) and Sanford & Merrill (1938), proposed that the star was a single-lined spectroscopic binary.

We analyzed 4 spectra in the yellow domain and 10 in the blue region, along with 6 échelle spectra covering the entire visible domain, including the blue and yellow wavebands (see Table 1). The differences between RVs measured for Helium lines are not large enough to support the binary scenario. Although the variations are much stronger in the fainter metallic lines than in the stronger He I λ 4471 and λ 5876 lines, the accuracy in the RV measurements of the more shallow lines is more affected by the noise. In addition, no signature of a companion, such as asymmetries in line profiles, has been found in any spectrum of our time series. The TVS method, first applied to spectra in the blue domain and then to the data in the yellow region, did not show any significant variations in He I λ 4471, He I λ 5876 nor the metallic lines. The likelihood that HD 48 279 is a binary thus remains low.

We estimated the projected rotational velocity from the Fourier method to $v \sin i = 130 \pm 13$ km s^{-1}. This value agrees with that of 123 km s^{-1} determined by Conti & Ebbets (1977) and Penny (1996).

The spectrum of HD 48 279 presents, beside the Balmer lines, deeper He I lines than He II ones, the obvious signature of a late O-type star, and we infer an O7.5 classification from Conti's criteria. We also find that Si IV $\lambda\lambda$ 4088–4116 correspond to a deep absorption. The most remarkable features of the spectrum are the prominent N III absorption lines at 4195, 4634, and 4641 Å, implying an ON spectral designation.

Ogura & Ishida (1981) did not mention that HD 48 279 was a member of NGC 2244 but it still belongs to the Mon OB2 association (de Wit et al. 2004). Without more information, we consider the star to be at the same distance as NGC 2244. Using $V = 7.91$ and $E(B-V) = 0.407$, we compute the two extreme visual absolute magnitudes for a distance between 1.4 and 1.7 kpc. We obtain $M_V = -4.08$ and $M_V = -4.50$, respectively, situating HD 48 279 on the MS band. Accounting for the strength of the nitrogen lines, we hence adopt the ON7.5 V spectral type for HD 48 279, slightly earlier than previous estimates (ON8 V, Conti & Leep 1974; O8 V, Walborn 1973).

3.4. Photometry and close "visual" companions

In addition to our results, it is interesting to consider the photometric variability of each star. From the Hipparcos and the ASAS (All Sky Automated Survey) databases, we thus retrieved data for each studied object. These two datasets were analyzed independently since the instrumentation used in the each survey was quite different.

Table 5 lists the mean V magnitude of each star and the 1-σ standard deviation (on V) of the highest quality data provided for each star in the ASAS catalog. The Fourier transform applied to each studied object reveals no significant periodicity, concluding

Table 5. The mean V magnitude and the 1-σ standard deviation.

Star	Mean V magnitude	1-σ error
HD 46 056	8.132	0.006
HD 46 149	7.598	0.006
HD 46 150	6.720	0.021
HD 46 202	7.946	0.048
HD 46 223	7.270	0.006
HD 46 485	8.255	0.011
HD 46 573	7.925	0.008
HD 46 966	6.854	0.019
HD 48 279	7.596	0.026

therefore that photometric variations in the stars are absent on the observed time series.

The Hipparcos catalog provides us with a sufficient number of data for only four stars of our sample: HD 46 150, HD 46 485, HD 46 573, and HD 46 966. For these objects, we compute a mean magnitude and a corresponding 1-σ standard deviation in the magnitude of 6.787 ± 0.007, 8.342 ± 0.023, 8.030 ± 0.011, and 6.851 ± 0.007, respectively. Once again, these small dispersions do not allow us to conclude anything about the existence of any significant variability in any of studied stars.

The speckle interferometric campaign of Galactic O-type stars with $V \lesssim 8$ undertaken by Mason et al. (1998) revealed that HD 46 150 and HD 48 279 have "visual" companions whose separations range from 2.7″–74.6″ and 4.6″–56.2″, respectively. However, we note that the "visual" companion close to HD 48 279 was quoted as being optical and not physical by Lindroos (1985). In addition, the Washington Visual Double Star (WDS, Mason et al. 2001) catalog also reported a "visual" companion located between 9.6″ and 10.5″ of HD 46 056. However, we emphasize that no evidence exists so far to confirm with any certainty the physical association of these companions, especially with such high angular separations.

Turner et al. (2008) published results of an adaptive optics survey to search for faint companions around Galactic O-star systems (with $V \lesssim 8$). They observed in the I-band to detect companions in the projected separation between 0.5″ and 5.0″. They observed five stars in our sample (HD 46 149, HD 46 150, HD 46 223, HD 46 966, and HD 48 279) but found no companion.

4. Discussion

4.1. Multiplicity of O-type stars

In this paper, we have studied all six O-stars of NGC 2244: HD 46 056, HD 46 149, HD 46150, HD 46 202, HD 46 223, and HD 46 485. HD 46 149 is clearly a long-period SB2, while HD 46 150 is a good binary candidate. The minimum frequency of spectroscopic binaries among O-stars in this cluster is thus at least 17% and could possibly reach 33%.

4.1.1. The detection biases

Because of the spectroscopic approach, a bias exists towards the detection of O+OB binary systems, providing only a lower limit to the true binary fraction. Several observational biases could make us miss a binary system with either a low orbital inclination, a rather large mass and/or brightness ratio, or a very wide separation (and either very long orbital period or a large eccentricity).

We first adopt the approach of Garmany et al. (1980) to estimate the probability that we have missed a binary system because of a low orbital inclination as a function of the assumed mass ratio and orbital period. In this scheme, we consider that the semi-amplitude of the RV curve K should be smaller or equal to twice the RV dispersion (σ_{RV}) of the photospheric lines, i.e., He II λ 4542 in the blue domain and C IV λ 5812 in the yellow region (or He I λ 5876 when this metallic line is not visible). The mass function of the primary component is given by

$$f(m) = \frac{M_1 \sin^3 i}{q\,(1+q)^2} \quad (1)$$

$$= 1.0355 \times 10^{-7}\, K^3\, P\, (1-e^2)^{3/2} \quad (2)$$

where M_1 is the primary mass (in $M_\odot$), K is expressed in km s^{-1}, e represents the orbital eccentricity, $q = M_1/M_2$, and P defines the orbital period (in days).

Equation (2) is transformed to express the orbital inclination as a function of other parameters. To obtain an upper limit to $\sin i$, we insert $2\sigma_{RV}$ as an upper limit to K and assume a zero eccentricity. Therefore, we obtain

$$\sin i \leq 9.392 \times 10^{-3}\, \sigma_{RV} \left(\frac{P\, q\, (1+q)^2}{M_1}\right)^{1/3}. \quad (3)$$

By assuming a random distribution of orbital directions in space, we can write the probability that the orbital inclination is lower than the value obtained from Eq. (3) as

$$\int_0^{i_{\rm up}} \sin i\, {\rm d}i = 1 - \cos i_{\rm up}. \quad (4)$$

The probabilities reported in Table 6 are the mean values computed from the two photospheric lines quoted above and by using as primary masses, the masses listed in Martins et al. (2005).

The probabilities that HD 46 202, HD 46 966, and HD 48 279 ($\simeq 20\, M_\odot$) are binaries with orbital periods of less than 28 days and a companion earlier than A5 ($\simeq 2\, M_\odot$, $q = 10$) are very low (i.e., $\leq$7%). Any missed binary would most probably have to be a system with a rather large mass ratio and a long orbital period.

The same conclusion could be reached for HD 46 223 ($\simeq 47\, M_\odot$). At a period of 28 days, the probability of having an O-type companion is close to zero (~0.2%), and we have only a 3% chance of missing a B3 secondary ($\simeq 8\, M_\odot$, $q = 5$). However, for the same orbital period, there is a 10% chance that the binary signature could have been missed if the spectral type of the second component was B6 or later ($\lesssim 5\, M_\odot$, $q = 10$).

We also perfomed Monte-Carlo simulations following the method of Sana et al. (2009, submitted). The orbital parameters were randomly generated (10 000 trials) based on the assumption that 50% of the binaries have an orbital period of $P \leq 10$ days, while the other 50% have $P > 10$ days. Moreover, the periods are uniformly drawn from log P space (between 0.3 and 3.5), the system orientations ($\cos i$) are randomly drawn from a uniform distribution, the mass ratio $q = M_1/M_2$ is also uniformly distributed between 0.1 and 1.0, and we uniformly selected eccentricities of between 0.0 and 0.8. The simulations show that the probability (Table 7) of have missing, in HD 46 202 and HD 46 223, a peak-to-peak RV variation (ΔRV) larger than the observed value of 20 km s^{-1} is less than 1% for systems with $2 \leq P \leq 10$ days and less than 10% for $10 \leq P \leq 365$ days. For the rapid rotators, the simulations were run for $\Delta RV >$ 40 km s^{-1} since the measurement errors are larger. The probabilities amount to 2% and 20% for HD 46 056 and HD 46 485, respectively. Therefore, it is very unlikely that short-period O+OB

Table 6. Probability to have missed a binary system[a].

	$P = 5$ days			$P = 14$ days			$P = 28$ days		
	$q = 1$	$q = 5$	$q = 10$	$q = 1$	$q = 5$	$q = 10$	$q = 1$	$q = 5$	$q = 10$
HD 46 056	3.9E-3	5.0E-2	19.4E-2	7.8E-3	10.3E-2	44.9E-2	1.2E-2	16.9E-2	...
HD 46 150	3.6E-3	4.6E-2	18.1E-2	7.1E-3	9.5E-2	45.5E-2	1.1E-2	15.7E-2	34.7E-2
HD 46 202	4.7E-4	6.0E-3	2.2E-2	9.4E-4	1.2E-2	4.3E-2	1.5E-3	1.9E-2	7.0E-2
HD 46 223	6.4E-4	8.1E-3	2.9E-2	1.3E-3	1.6E-2	6.0E-2	2.0E-3	2.6E-2	9.7E-2
HD 46 485	5.1E-3	6.7E-2	26.6E-2	1.0E-2	13.8E-2	71.5E-1	1.6E-2	23.1E-2	...
HD 46 966	3.4E-4	4.3E-3	1.6E-2	6.8E-4	8.6E-3	3.1E-2	1.1E-3	1.4E-2	5.0E-2
HD 48 279	2.3E-4	2.9E-3	1.0E-2	4.5E-4	5.7E-3	2.0E-2	7.1E-4	9.0E-3	3.3E-2

	$P = 60$ days			$P = 300$ days		
	$q = 1$	$q = 5$	$q = 10$	$q = 1$	$q = 5$	$q = 10$
HD 46 056	2.1E-2	30.4E-2	...	6.1E-2	...	...
HD 46 150	1.9E-2	28.8E-2	78.2E-2	5.7E-2	53.3E-2	...
HD 46 202	2.5E-3	3.2E-2	12.1E-2	7.3E-3	9.8E-2	51.5E-2
HD 46 223	3.4E-3	4.4E-2	17.2E-2	9.9E-3	13.7E-2	19.6E-2
HD 46 485	2.7E-2	43.3E-2	...	8.2E-3	...	...
HD 46 966	1.8E-3	2.3E-2	8.5E-2	5.3E-3	6.9E-2	29.0E-2
HD 48 279	1.2E-3	1.5E-2	5.5E-2	3.5E-3	4.5E-2	17.1E-2

[a] Table 6 reports the probabilities that a binary system could have been missed for different values of the orbital period P and of the mass ratio $q = M_1/M_2$.

systems were missed by our study, and this result does not depend on the small number of stars in NGC 2244. For long-period (365–3000 days) systems, the probability of missing binaries increases to 50% (70% for rapid rotators). This is expected since our sampling does not permit us to investigate thoroughly this part of the parameter space.

4.1.2. The effects of stellar evolution

We now compare our results with those of other young open clusters studied in a similar way. The minimal binary fraction in NGC 2244 (17%) appears close to that of IC 1805 (20%). However, we note differences in the stellar content of these two clusters. De Becker et al. (2006) found that at least one giant (O III (f)) and one supergiant (O If) belong to IC 1805, while all O-type stars in NGC 2244 are MS objects. Evolution effects (and thus the age of the systems) therefore seem to play no role in the binary properties, although this conclusion should be confirmed by studies of other clusters.

García & Mermilliod (2001) asserted that the orbital periods of spectroscopic binaries in the O-type star rich clusters were around 4–5 days. We emphasize that the absence of short-period binaries in NGC 2244 does not support this conclusion (see previous subsection).

A comparison between NGC 2244, IC 1805, and NGC 6231 (all three now being well-studied) is provided in Table 8. Differences are readily seen in this table. Apart from the already quoted difference in the proportion of short versus long-period binaries, there is also a difference in the nature of the companion. If we consider all O-type stars to be binaries, i.e., those apparently single stars with undetectable low-mass companions, the majority of O-stars in NGC 6231 appears to have OB companions, while the signature of additional early-type objects is found in only a few O-stars of NGC 2244 and IC 1805.

4.1.3. A possible impact of the stellar density

The surface density of a given cluster is evaluated to be the ratio of the number of members of the cluster to the circular area delineated by a typical radius, e.g., the one given by Tadross et al. (2002). Both IC 1805 and NGC 2244 have a rather loose cluster core, whilst the stellar surface density appears much higher in the central part of NGC 6231. With the new binary fraction from De Becker et al. (2006), Sana et al. (2008), and this work, the anticorrelation between the cluster density and its massive star binary fraction proposed by García & Mermilliod (2001) can no longer be supported. In contrast, a possible correlation might reflect the behavior detected in these three clusters more accurately. However, we must remain careful since this assumption is directly linked to the error bars in the binary fraction. If it is confirmed, this would emphasize the important role of dynamical gravitational interactions in the formation of massive binaries (Zinnecker 2003). Confirmation, however, of this relation will require more data. The extreme case of loose OB associations might provide a good testbed for this confirmation.

Table 7. Probability of missing a significant orbital RV variation[a].

Star	M_1	2–10	10–365	365–3000	2–3000
HD 46 056	20.8	0.02	0.17	0.77	0.24
HD 46 149	20.8	0.01	0.04	0.31	0.07
HD 46 150	34.4	0.01	0.03	0.21	0.05
HD 46 202	17.1	0.01	0.09	0.50	0.13
HD 46 223	46.9	0.01	0.03	0.22	0.05
HD 46 485	20.8	0.01	0.20	0.68	0.20
HD 46 573	22.9	0.01	0.06	0.38	0.09
HD 46 966	18.8	0.01	0.06	0.34	0.08
HD 48 279	22.9	0.01	0.07	0.40	0.10

[a] Table 7 lists the probability of missing a significant orbital RV variation ($\Delta RV > 40\,\mathrm{km\,s^{-1}}$ for the two rapid rotators and $\Delta RV > 20\,\mathrm{km\,s^{-1}}$ for the other stars). M_1 represents the primary mass and is expressed in $M_\odot$. The last four columns are classified according to the orbital period of the system (in days).

4.2. Rotational velocities

HD 46 056 and HD 46 485 are two rapid rotators whose lines appear slightly variable. Rapid rotators could either be

- born as such and maintain a rapid rotation over their main-sequence lifetime;

Table 8. Summary of the multiplicity in young open clusters[a].

Cluster	Density (stars/pc^2)	Minimal binary fraction	n# O-stars	Short-period binaries ($P \leq 10$)	Long-period binaries	Variable stars	References
NGC 2244	2.84	17%	6	0	1	3	This paper
IC 1805	1.65	20%	10	1	1	4*	Rauw & De Becker (2004)
							De Becker et al. (2006)
NGC 6231	12.46	63%	16	6**	4	3	Sana et al. (2008)

[a] The first and second columns give the name and the density of the cluster. The third column provides the minimal binary fraction determined after intensive monitoring of the O-type stars. The next columns present the number of O-stars in each cluster, and the number of detected short and long-period binaries and the variable stars (potential binaries and probable intrinsic variables). The last column quotes relevant references. * Notes: four late O-type stars were not studied by the two papers mentioned in the references. We will consider these objects as variable in the absence of a thorough study. ** Notes: we take into account that NGC 6231 also contains a WR+O binary since a WR is an evolved O-star.

- spun-up by transfer of mass and angular momentum during a Roche lobe overflow in a binary system;
- spun-up because of the core contraction at the end of the main-sequence.

For these two rapid rotators, it seems more likely that the first hypothesis is the correct one since we found no clear indication of multiplicity and there is no evidence that these objects are at or near the end of their main-sequence lifetime (for instance, on the basis of their chemical enrichment).

We also compared our distribution of the projected rotational velocities of O-type stars in and around NGC 2244 to the corresponding distribution for B-type stars. Huang & Gies (2006) performed a survey of projected rotational velocities for a large sample of mainly B-type (later than O9.5) main-sequence or giant stars in young open clusters, including NGC 2244. The $v \sin i$ values were derived by comparison between theoretical line profiles and observed profiles of the He I $\lambda\lambda$ 4026, 4387, 4471, and Mg II λ 4481 lines. Huang & Gies (2006) reported the projected rotational velocities of 41 stars in NGC 2244. The average projected rotational velocity of the B-type stars equals to 168 km s^{-1}. The 15 stars that are earlier than B3 show an average $v \sin i$ of 153 km s^{-1}. Five stars out of the total sample (i.e., 12%) were found to display a projected rotational velocity of above 300 km s^{-1}. At first sight, the distribution of the rotational velocities of the O-type stars looks different from that of the B-type stars (see Fig. 10). We performed a two-sample Kolmogorov-Smirnov test to check whether or not the two distributions are significantly different. On the basis of this test and adopting a usual significance level of 0.05, the null hypothesis (both samples are drawn from the same parent distribution) cannot be rejected. This is true for both the full sample and the six O-stars of NGC 2244.

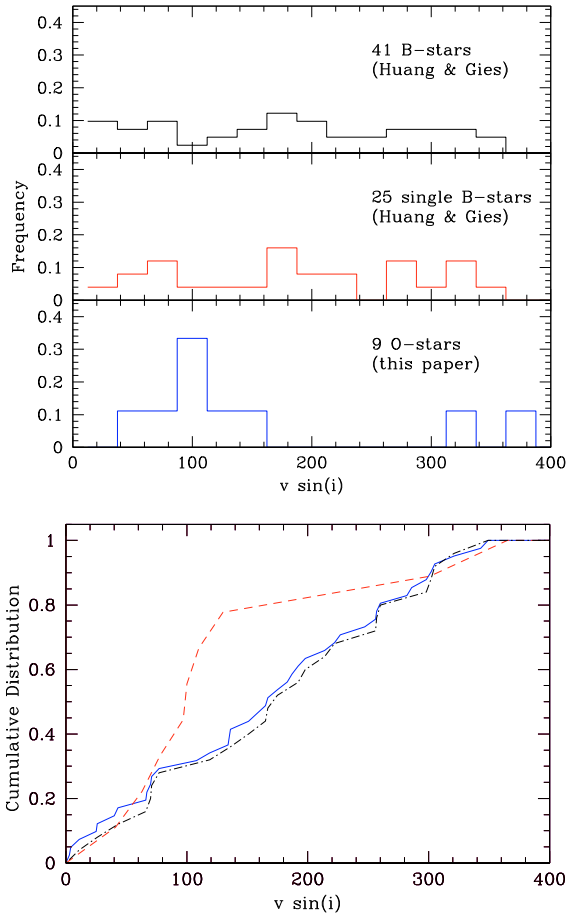

Fig. 10. *Top*: the distribution of projected rotational velocities of (1) the full sample of B stars studied by Huang & Gies (2006, *top panel*), (2) those B stars of Huang & Gies that show a constant radial velocity (*middle panel*), and (3) our sample of O-type stars. *Bottom*: the cumulative distributions of the three samples: all B-stars (solid line), single B stars (dashed-dotted line), and O-stars (dashed line).

5. Summary and conclusions

Our long-term monitoring has shed new light on the multiplicity of six massive O-stars in NGC 2244 plus three in the association Mon OB2. Table 9 summarizes the present knowledge for these stars.

In the association Mon OB2, the current study reveals the detection of a new SB1: HD 46 573. Although we determine a period of 10.67 days and compute the orbital parameters of the system, these results must still be considered as preliminary. Indeed, the accuracy of the RV measurements could strongly influence the orbital solution of the system, considering the low amplitude of the radial velocity variations. The eccentricity of the orbit remains poorly constrained but we note that the eccentric radial velocity curve appears slightly more likely solution than the circular one.

Another interesting result, in NGC 2244, is the detection, for the first time, of a secondary component in HD 46 149. However, for the time being, we can only constrain the period to be at least several tens of days. By virtue of its mass and flux ratios, HD 46 149 is considered to be an O+B binary. An observation campaign should be initiated to monitor the star and constrain the orbital solution of its system more accurately. Finally, we also detect weak variations in the RVs for one star belonging to NGC 2244 (HD 46 150) and variations in the line profiles, most probably unrelated to binarity, in the two rapid

Table 9. Summary[a] of the optical properties of O-stars in NGC 2244 (*top part*) and Mon OB2 (*bottom*).

Name	Spectral type	$v \sin i$	Spectroscopic status
HD 46 056	O8Vn	355 ± 21	C ? (rapid rotator)
HD 46149	O8V+B0–1V	78 ± 11[‡]	SB2
HD 46 150	O5.5V((f))	97 ± 9	Bin?
HD 46 202	O9V	54 ± 15	C
HD 46 223	O4V((f$^+$))	100 ± 17	C
HD 46 485	O8Vn	301 ± 25	C ? (rapid rotator)
HD 46 573	O7.5V((f))	110 ± 18	SB1
HD 46 966	O8.5V	63 ± 17	C
HD 48 279	ON7.5V	130 ± 13	C

[a] The first column provides the name of each star studied in this paper. The next two columns give the spectral classification and the projected rotational velocity (in km s^{-1}) of the O-type stars, while the last column reports the status of the star as derived from our campaign: "C" means that our study did not reveal any indication of RV variability or of binarity, suggesting the star is probably single, "Bin?" indicates a potential binary, "SB1" corresponds to a spectroscopic binary where the second component has not been detected yet but where a period has been determined, whilst "SB2" corresponds to a spectroscopic binary where the two components are visible. [‡] Notes: the reported value for HD 46149 is the projected rotational velocity for the primary.

rotators (HD 46 056 and HD 46 485). The observed binary fraction is thus 17% at minimum.

This work, combined to the results of studies of NGC 6231 and IC 1805, also revealed significant differences between clusters regarding the preference of O+OB systems and the distribution of short versus long-period binaries. These differences cannot be explained by the cluster age but could be linked to density effects. Of course, to confirm such a general conclusion, it is important to rely upon a large sample of well-studied very young open clusters that harbor a significant population of early-type stars. To date however, only a few clusters have been the subject of such an intensive search for binary systems. It is therefore of paramount importance to perform similar studies on a larger sample of clusters, spanning as wide a range of physical properties as possible.

Acknowledgements. This work was supported by the FNRS (Belgium) and by a PRODEX XMM/Integral contract (Belspo) and by the Communauté française de Belgique – Action de recherche concertée (ARC) – Académie Wallonie–Europe. The travels to OHP were supported by the Ministère de l'Enseignement Supérieur et de la Recherche de la Communauté Française. Philippe Eenens acknowledges support through CONACyT grant 67041. We also thank the staff of San Pedro Màrtir Observatory (Mexico) and of Observatoire de Haute-Provence (France) for their technical support. This work made use of the SIMBAD and the ASAS and Hipparcos databases.

References

Abt, H. A., & Biggs, E. S. 1972, Bibliography of stellar radial velocities, ed. H. A. Abt, & E. S. Biggs
Bisiacchi, G. F., Lopez, J. A., & Firmani, C. 1982, A&A, 107, 252
Chen, L., de Grijs, R., & Zhao, J. L. 2007, AJ, 134, 1368
Conti, P. S. 1973, ApJ, 179, 161
Conti, P. S., & Alschuler, W. R. 1971, ApJ, 170, 325
Conti, P. S., & Leep, E. M. 1974, ApJ, 193, 113
Conti, P. S., & Ebbets, D. 1977, ApJ, 213, 438
Conti, P. S., Leep, E. M., & Lorre, J. J. 1977, ApJ, 214, 759
Cruz-González, C., Recillas-Cruz, E., Costero, R., Peimbert, M., & Torres-Peimbert, S. 1974, RMA&A, 1, 211
De Becker, M., Rauw, G., Manfroid, J., & Eenens, P. 2006, A&A, 456, 1121
De Becker, M., Linder, N., & Rauw, G. 2008, Information Bulletin on Variable Stars, 5841, 1
de Wit, W. J., Testi, L., Palla, F., Vanzi, L., & Zinnecker, H. 2004, A&A, 425, 937
Feldmeier, A., Puls, J., & Pauldrach, A. W. A. 1997, A&A, 322, 878
Frost, S. A., & Conti, P. S. 1976, in Be and Shell Stars, ed. A. Slettebak, IAU Symp., 70, 139
Fullerton, A. W. 1990, Ph.D. Thesis, AA(Toronto Univ. (Ontario).)
Fullerton, A. W., Gies, D. R., & Bolton, C. T. 1996, ApJS, 103, 475
García, B., & Mermilliod, J. C. 2001, A&A, 368, 122
Garmany, C. D., Conti, P. S., & Massey, P. 1980, ApJ, 242, 1063
Gies, D. R. 1987, ApJS, 64, 545
González, J. F., & Levato, H. 2006, A&A, 448, 283
Gosset, E., Royer, P., Rauw, G., Manfroid, J., & Vreux, J.-M. 2001, MNRAS, 327, 435
Heck, A., Manfroid, J., & Mersch, G. 1985, A&AS, 59, 63
Hensberge, H., Pavlovski, K., & Verschueren, W. 2000, A&A, 358, 553
Hiltner, W. A. 1956, ApJS, 2, 389
Huang, W., & Gies, D. R. 2006, ApJ, 648, 591
Johnson, H. L. 1962, ApJ, 136, 1135
Kharchenko, N. V., Piskunov, A. E., Röser, S., Schilbach, E., & Scholz, R.-D. 2005, A&A, 440, 403
Li, J. Z., & Smith, M. D. 2005, A&A, 431, 925
Linder, N., Rauw, G., Martins, F., et al. 2008, A&A, 489, 713
Lindroos, K. P. 1985, A&AS, 60, 183
Liu, T., Janes, K. A., & Bania, T. M. 1989, AJ, 98, 626
Maíz-Apellániz, J., Walborn, N. R., Galué, H. Á., & Wei, L. H. 2004, ApJS, 151, 103
Martins, F., & Plez, B. 2006, A&A, 457, 637
Martins, F., Schaerer, D., & Hillier, D. J. 2005, A&A, 436, 1049
Mason, B. D., Gies, D. R., Hartkopf, W. I., et al. 1998, AJ, 115, 821
Mason, B. D., Wycoff, G. L., Hartkopf, W. I., Douglass, G. G., & Worley, C. E. 2001, AJ, 122, 3466
Massey, P., Johnson, K. E., & Degioia-Eastwood, K. 1995, ApJ, 454, 151
Mathys, G. 1988, A&AS, 76, 427
Mathys, G. 1989, A&AS, 81, 237
Morgan, W. W., Code, A. D., & Whitford, A. E. 1955, ApJS, 2, 41
Morgan, W. W., Hiltner, W. A., Neff, J. S., Garrison, R., & Osterbrock, D. E. 1965, ApJ, 142, 974
Munari, U., & Tomasella, L. 1999, A&AS, 137, 521
Ogura, K., & Ishida, K. 1981, PASJ, 33, 149
Penny, L. R. 1996, ApJ, 463, 737
Pérez, M. R. 1991, Revista Mexicana de Astronomia y Astrofisica, 22, 99
Petrie, R. M., & Pearce, J. A. 1961, Publications of the Dominion Astrophysical Observatory Victoria, 12, 1
Plaskett, J. S., & Pearce, J. A. 1931, Publications of the Dominion Astrophysical Observatory Victoria, 5, 1
Rauw, G., & De Becker, M. 2004, A&A, 421, 693
Reed, C. 2005, VizieR Online Data Catalog, 5125, 0
Sana, H., Gosset, E., & Rauw, G. 2006a, MNRAS, 371, 67
Sana, H., Rauw, G., Nazé, Y., Gosset, E., & Vreux, J.-M. 2006b, MNRAS, 372, 661
Sana, H., Gosset, E., Nazé, Y., Rauw, G., & Linder, N. 2008, MNRAS, 386, 447
Sanford, R. F., & Merrill, P. W. 1938, ApJ, 87, 517
Simón-Díaz, S., & Herrero, A. 2007, A&A, 468, 1063
Stickland, D. J. 1996, The Observatory, 116, 294
Tadross, A. L., Werner, P., Osman, A., & Marie, M. 2002, New Astronomy, 7, 553
Turner, D. G. 1976, ApJ, 210, 65
Turner, N. H., ten Brummelaar, T. A., Roberts, L. C., et al. 2008, AJ, 136, 554
Underhill, A. B., & Gilroy, K. K. 1990, ApJ, 364, 626
Walborn, N. R. 1971, ApJS, 23, 257
Walborn, N. R. 1973, AJ, 78, 1067
Walborn, N. R., & Fitzpatrick, E. L. 1990, PASP, 102, 379, erratum: 102, 1094
Wang, J., Townsley, L. K., Feigelson, E. D., et al. 2008, ApJ, 675, 464
Wolfe, Jr., R. H., Horak, H. G., & Storer, N. W. 1967, The machine computation of spectroscopic binary elements, ed. M. Hack, 251
Zagury, F. 2001, New Astron., 6, 403
Zinnecker, H. 2003, in A Massive Star Odyssey: From Main Sequence to Supernova, ed. K. van der Hucht, A. Herrero, & C. Esteban, IAU Symp., 212, 80
Zinnecker, H., & Yorke, H. W. 2007, ARA&A, 45, 481

The Astrophysical Journal, 708:1537–1544, 2010 January 10 doi:10.1088/0004-637X/708/2/1537

A NEW INVESTIGATION OF THE BINARY HD 48099

L. Mahy[1], G. Rauw[1,6], F. Martins[2], Y. Nazé[1,6], E. Gosset[1,7], M. De Becker[1,8], H. Sana[3,4], and P. Eenens[5]
[1] Astrophysical Institute, University of Liège, Bât. B5C, Allée du 6 Août 17, B-4000 Liège, Belgium; mahy@astro.ulg.ac.be
[2] GRAAL, Université Montpellier II, CNRS, Place Eugène Bataillon, 34095 Montpellier, France
[3] European Southern Observatory, Alonso de Cordova 1307, Casilla 19001, Santiago 19, Chile
[4] Sterrenkundig Instituut "Anton Pannekoek," Universiteit van Amsterdam, Postbus 94249, 1090 GE Amsterdam, The Netherlands
[5] Departamento de Astronomia, Universidad de Guanajuato, Apartado 144, 36000 Guanajuato, GTO, Mexico
Received 2009 August 10; accepted 2009 November 25; published 2009 December 22

ABSTRACT

With an orbital period of about 3.078 days, the double-lined spectroscopic binary HD 48099 is, until now, the only short-period O+O system known in the Mon OB2 association. Even though an orbital solution has already been derived for this system, few information are available about the individual stars. We present, in this paper, the results of a long-term spectroscopic campaign. We derive a new orbital solution and apply a disentangling method to recover the mean spectrum of each star. To improve our knowledge concerning both components, we determine their spectral classifications and their projected rotational velocities. We also constrain the main stellar parameters of both stars by using the CMFGEN atmosphere code and provide the wind properties for the primary star through the study of *International Ultraviolet Explorer* spectra. This investigation reveals that HD 48099 is an O5.5 V ((*f*)) + O9 V binary with $M_1 \sin^3 i = 0.70\,M_\odot$ and $M_2 \sin^3 i = 0.39\,M_\odot$, implying a rather low orbital inclination. This result, combined with both a large effective temperature and $\log g$, suggests that the primary star ($v \sin i \simeq 91$ km s^{-1}) is actually a fast rotator with a strongly clumped wind and a nitrogen abundance of about 8 times the solar value.

Key words: binaries: spectroscopic – stars: fundamental parameters – stars: individual (HD 48099)

Online-only material: color figures

1. INTRODUCTION

HD 48099 is a double-lined spectroscopic binary situated near the young open cluster NGC 2244 and embedded in the Monoceros OB2 association in the Rosetta Nebula (Mahy et al. 2009). This star has first been quoted as a binary by Slettebak (1956), and a period of about 3.1 days was derived by Garmany et al. (1980) and Stickland (1996). HD 48099 is, until now, the only short-period O+O system detected in this association (see, e.g., Linder et al. 2008; Mahy et al. 2009).

According to the spectroscopic parallax, HD 48099 is located at a distance of 1829 ± 77 pc (Brown & Bomans 2005), i.e., a distance close to that of NGC 2244 (Hensberge et al. 2000), and seems to be a binary system with a low inclination. Indeed, Garmany et al. (1980) estimated minimum masses of about 0.63 and 0.38 $M_\odot$ and reported the semi-amplitude of the radial velocity (RV) curves to be 55 and 92 km s^{-1} for the primary and secondary stars, respectively. However, there has been no detailed study of each component. Other stellar parameters were reported only for the global system, e.g., a spectral type of O7 V (Walborn 1972; Garmany et al. 1982), $T_{\rm eff} = 30{,}700 \pm 700$ K, and $\log(L/L_\odot) = 5.2 \pm 0.1$ (Levenhagen & Leister 2006).

The present paper is based on the investigation of a series of high-resolution spectra, which help us to improve our knowledge of the main individual stellar parameters of HD 48099. We applied a disentangling method, using an algorithm inspired by the work of González & Levato (2006), to obtain the mean individual spectrum of each star from the observed data of the entire system. We then derived the spectral classification, the $v \sin i$, and the main stellar parameters for each component.

We thus organize this paper as follows. We first describe our entire data set and the data reduction in Section 2. In Section 3, the orbital solution and the properties of the disentangled spectra are presented. Section 4 reports the projected rotational velocities ($v \sin i$) of both components. We give the spectral type of each star of HD 48099 in Section 5, while Section 6 is devoted to the study of the main stellar parameters by using the model atmosphere code CMFGEN (Hillier & Miller 1998). Finally, Section 7 discusses the results and provides the conclusions.

2. OBSERVATIONS AND DATA REDUCTION

The majority of our data were taken with the Aurélie spectrograph mounted on the 1.52 m telescope at the Observatoire de Haute-Provence (OHP). The detector used is a 2048 × 1024 CCD EEV 42–20 #3 with a pixel surface of 13.5 μm^2. The spectra were obtained with a 600 lines mm^{-1} grating, allowing us to reach a resolving power of $R = 8000$ in the blue range (seven spectra centered on 4700 Å in the [4450–4900] Å domain) and $R = 10{,}000$ in the yellow range (15 spectra centered on 5700 Å in the [5500–5900] Å region). Typical exposure times range from 20 to 45 minutes to reach a mean signal-to-noise ratio (S/N) close to 270. The entire data set was reduced using the `MIDAS` software developed at the European Southern Observatory (ESO). The wavelength calibration is based on a series of thorium–argon comparison spectra, immediately taken before and after the stellar spectrum. The normalization of our data was done by fitting polynomials of degree 4 to carefully chosen continuum windows.

Another part of our data was obtained with the Fiber-fed Extended Range Optical Spectrograph (FEROS) échelle spectrometer mounted on the 2.2 m ESO/MPG telescope at ESO (La Silla). We collected four spectra in 2006 March (run ESO 076.D-0294(A)), and we retrieved three other spectra from the ESO archives taken in 2006 January and February

[6] Research Associate F.R.S.-FNRS.
[7] Senior Research Associate F.R.S.-FNRS.
[8] Postdoctoral Researcher F.R.S.-FNRS.

(PI: Casassus, run ESO 076.C-0431(A) and PI: Lo Curto, run ESO 076.C-0164(A)). With a resolving power of $R = 48{,}000$ and typical exposure times ranging from 2.5 to 10 minutes, the spectrograph reaches a mean S/N greater than 300 for our target. The data were reduced with a modified FEROS pipeline working under MIDAS environment. In addition to the modifications already described in Sana et al. (2006), several new features were implemented as mentioned in Sana (2009).

Moreover, the 2.1 m telescope at the Observatorio Astronómico Nacional of San Pedro Mártir (Mexico) equipped with the Espresso spectrograph allowed us to obtain spectra over five nights in 2007 April. This échelle spectrograph covers 27 spectral orders over a wavelength domain equal to [3780–6950] Å with a resolving power of $R = 18{,}000$. This instrument features a SITE 3 optical CCD chip with 1024 × 1024 pixels of 24 μm^2. Consecutive data of a same night, taken with exposure times between 5 and 10 minutes, were added to obtain spectra with a mean S/N close to 250. The data were reduced with the échelle package within the MIDAS software.

Finally, we retrieved two archival Elodie spectra observed by Catala and Bouret in 2003 January and 2005 November, respectively. Elodie was an échelle spectrograph, which gave 67 spectral orders covering the [3850–6850] Å wavelength domain and offering a resolving power of $R = 42{,}000$. This spectrograph was mounted on the 1.93 m telescope at OHP and exposure times of 12 and 33 minutes provided an S/N of about 130 and 100, respectively.

The journal of the observations presenting the 36 spectra is listed in Table 1.

Table 1
Journal of the Observations of HD 48 099

Instrument	HJD − 2 450 000	Φ	RV_P	RV_S
Elodie	2655.3793	0.863	−24.4	84.9
Elodie	3682.5907	0.580	−9.7	54.4
FEROS	3738.7235	0.816	−35.9	99.9
FEROS	3774.5994	0.471	20.8	−3.5
FEROS	3774.6070	0.474	20.6	−2.8
Aurélie	3775.5035	0.765	−40.7	104.8
Aurélie	3775.5146	0.769	−39.2	108.2
Aurélie	3776.5014	0.089	46.5	−34.1
Aurélie	3777.4952	0.412	46.7	−36.4
Aurélie	3778.4762	0.731	−38.7	109.3
Aurélie	3779.2880	0.995	12.6	16.3
Aurélie	3779.3019	0.999	16.1	14.9
Aurélie	3780.3088	0.326	64.8	−74.0
FEROS	3796.5248	0.595	−15.6	64.5
FEROS	3797.5211	0.918	−12.4	59.3
FEROS	3799.5214	0.568	−7.6	51.0
FEROS	3800.5172	0.891	−16.9	72.8
Espresso	4193.7415	0.641	−23.0	94.6
Espresso	4194.7463	0.967	3.8	33.1
Espresso	4197.7630	0.947	−2.8	44.8
Espresso	4198.7354	0.263	69.3	−82.8
Espresso	4199.7469	0.592	−14.7	65.8
Aurélie	4200.3600	0.791	−38.4	106.0
Aurélie	4205.3612	0.416	44.6	−37.0
Aurélie	4205.3793	0.422	42.2	−32.2
Aurélie	4401.6362	0.181	66.9	−75.2
Aurélie	4410.6362	0.105	37.1	−58.1
Aurélie	4411.6912	0.448	32.4	−11.2
Aurélie	4412.6364	0.755	−39.2	118.9
Aurélie	4413.6435	0.081	35.3	−23.1
Aurélie	4414.6915	0.422	35.6	−23.6
Aurélie	4423.6053	0.318	68.1	−78.4
Aurélie	4472.5179	0.209	70.4	−82.3
Aurélie	4473.5943	0.558	−3.5	45.2
Aurélie	4474.4721	0.844	−31.7	92.9
Aurélie	4475.5804	0.204	70.5	−79.2

Notes. The first column gives the name of the instrument with which the spectrum has been acquired. The second one lists the heliocentric Julian date (HJD), and the third provides the phase computed from our orbital solution (see Table 2). The last two columns give the measured radial velocities (in km s^{-1}) of the primary and secondary stars, respectively, at the indicated phase.

3. ORBITAL SOLUTION

The analysis of Garmany et al. (1980), based on an orbital period of about 3.1 days, allowed us to compute, for the first time, the minimum masses and semi-amplitude of the RV curves of HD 48099. However, the first complete orbital solution, available in the literature, was derived by Stickland (1996). He used an orbital period of 3.07809 days and assumed a zero eccentricity to derive, from 23 high-resolution *International Ultraviolet Explorer* (*IUE*) spectra (SWP data), the main orbital parameters of HD 48099.

To determine the orbital motion of the primary and secondary components, we proceed in two steps. To obtain a first approximation of the RVs of both stars, we measured these values by fitting Gaussians to the spectral line profiles of the spectra where the two components were deblended. To this aim, we focus on the Si IV λ4089, He I λ4471, Mg II λ4481, and He I λ5876 lines. We note that the rest wavelengths of these lines were taken from the papers of Conti et al. (1977) and Underhill (1994).

Then, a disentangling method, based on the approach of González & Levato (2006), is applied to separate, in an iterative procedure, the two components of the binary system. This consists of alternately using the spectrum of one component (shifted by its radial velocity) to remove it from the observed spectra in order to calculate a mean spectrum of the other component. Our algorithm also uses the cross-correlation technique to compute the RVs from the disentangled spectra, even at phases for which lines are heavily blended. This method thus allows us to determine RVs for the blended spectra, while the fit with Gaussian functions only allows us to measure the RVs for the deblended spectra. For the purpose of building the RV cross-correlation masks, we used a common basis of spectral lines including the He I λ4471, Mg II λ4481, He I λ4713, O III λ5592, and He I λ5876 lines. We added the He II λ4542, He II λ4686, C IV λ5801, and C IV λ5812 lines for the primary, and N III λ4511 and N III λ4515 for the secondary. The RVs are listed in Table 1. To avoid degrading the best quality data, we have thus interpolated the spectra with a poor resolution to obtain a step similar to the FEROS data. Since the bulk of our data covers the blue and yellow range, we favor the disentangling on two wavelength domains: [4450–4900] Å and [5500–5920] Å. We note that the first region is particularly useful to establish an accurate determination of the spectral classification of each component of the binary system. We also emphasize that the spectra have been disentangled in the [4000–4220] Å wavelength domain but because of the poor time sampling of the data in this domain, the result should only be considered as preliminary.

To compute the improved orbital solution of HD 48099, we first refined the orbital period by combining the RVs of Stickland (1996), after having shifted these values to obtain the same systemic velocity as for our data, with the RVs calculated in

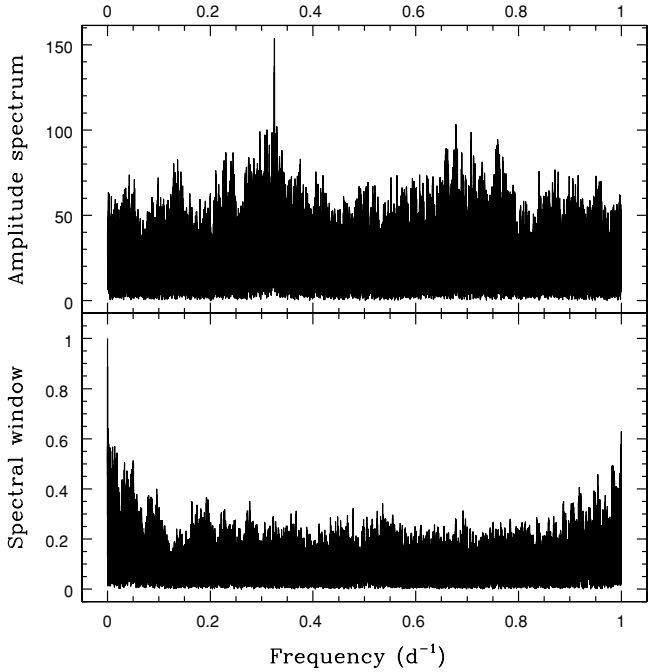

Figure 1. Top: semi-amplitude Fourier spectrum computed from our new RVs along with the RVs measured from the *IUE*-archive spectra by Stickland (1996). Bottom: spectral window corresponding to the sampling of the entire (our + *IUE*) RV data set.

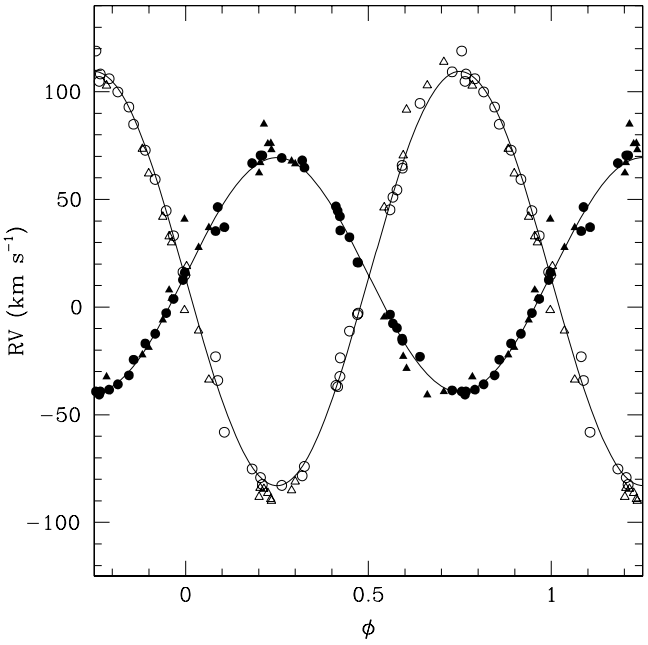

Figure 2. Radial velocity curve of HD 48099 computed only with our RVs measured by fitting Gaussians for the deblended spectra and by cross-correlation for the blended ones. The primary data correspond to the filled symbols and the open ones indicate the radial velocities of the secondary component. Our spectra are represented with circles. We added (by triangles), for comparison, the RVs measured by Stickland (1996) but shifted to obtain the same systemic velocity as for our data.

the present paper. Using these two data sets, we cover a total time interval of $\Delta T = 10684.4$ days, implying a natural peak width in the periodogram equal to $1/\Delta T = 9.359310^{-5}$ day^{-1}. We then apply a Fourier method that is especially designed for astrophysical time series with a highly non-uniform time sampling (see Heck et al. 1985; Gosset et al. 2001) and which was successfully applied to a number of systems studied by our team. The semi-amplitude spectrum (Figure 1), evaluated on the $RV_P - RV_S$ time series by the Fourier analysis, presents a strong peak at the frequency of 0.324880 day^{-1} which corresponds to an orbital period of 3.07806 ± 0.00009 days. The error quoted on the period is assumed to be equal to one-tenth of the width of the peaks of the periodogram. We have rejected the hypothesis that the highest peak is due to white noise, by taking a threshold significance level of 0.01.

Adopting this period, we used the Liège Orbital Solution Package (LOSP) program on our data to compute the orbital solution of HD 48099. This software is based on the generalization of the SB1 method of Wolfe et al. (1967) to the SB2 case along the lines described in Rauw et al. (2000) and Sana et al. (2006); more details as well as the present status of the software can be found in Sana & Gosset (2009). We assigned a weight of 1.0 to all spectra of our data set independently of the primary or secondary star. Figure 2 represents the fitted RV curves as a function of the orbital phase, and Table 2 yields the orbital parameters computed for this star with their corresponding uncertainties. The fit residuals are smaller with a zero eccentricity indicating that the circularization of the orbit is achieved. Although the results obtained are close to those of Stickland (1996), we however underline significant differences notably on the minimal masses of both components. We also emphasize that our orbital solution is subject to smaller uncertainties.

The RVs corresponding to the observed RV curves are then fixed in the input file of the disentangling program to derive

Table 2
Orbital Solution for HD 48099 Computed by Assuming that the Uncertainties on the Secondary RVs are Twice as Large as for the Primary

Parameters	Primary	Secondary
P(days)	3.07806 ± 0.00009	
e	0.0 (fixed)	
T_0 (HJD)	2 452 649.661 ± 0.004	
γ (km s^{-1})	15.0 ± 0.6	13.3 ± 0.8
K (km s^{-1})	54.4 ± 0.7	96.2 ± 1.2
a sin i ($R_\odot$)	3.31 ± 0.04	5.85 ± 0.08
M sin^3 i ($M_\odot$)	0.70 ± 0.02	0.39 ± 0.01
Q (M_1/M_2)	1.77 ± 0.03	
rms (km s^{-1})	2.71	

Notes. T_0 refers to the time of the primary conjunction. γ, K, a sin i correspond to the apparent systemic velocity, the semi-amplitude of the RV curve, and the projected semi-major axis, respectively.

the individual mean spectra presented in Figure 3. Because of some uncertainties on the continuum levels in the observed input spectra, this disentangling technique generates some low-level, low-frequency oscillations (∼5% of the continuum) in the normalization of the disentangled spectra (see, e.g., λ5890 in Figure 3), but such features have no impact on our scientific results.

Finally, we also used the disentangling method to separate the *IUE* spectra. We focus on the [1210–1780] Å wavelength domain. This region features many spectral lines. On the basis of the orbital solution, we determined the phase corresponding to each observed *IUE* spectrum. The theoretical RV curves then gave us the associated RVs for the different phases. As we have done for the optical spectra, we fixed these values in the input file of the program to obtain the mean *IUE* spectrum of both

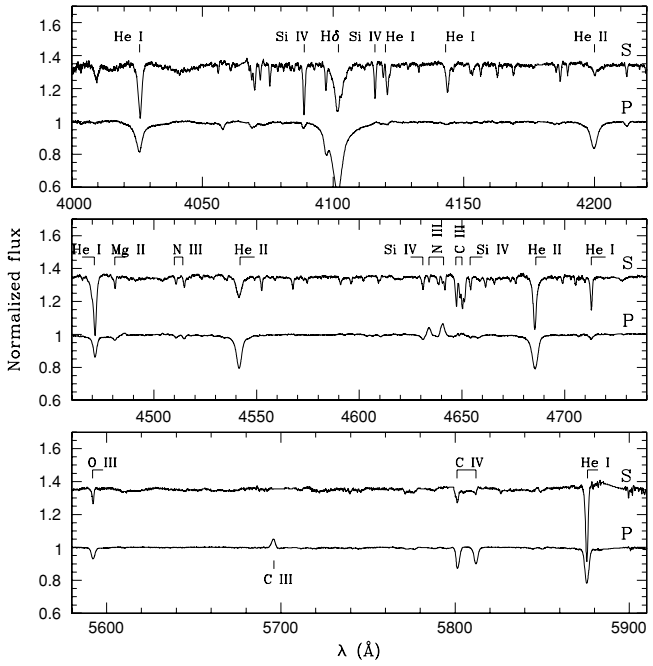

Figure 3. Normalized disentangled spectra of HD 48099 between [4000–4220] Å, [4450–4730] Å, and [5580–5900] Å. In each panel, the lower spectrum is that of the primary. The secondary spectrum is vertically shifted by 0.4 units for clarity.

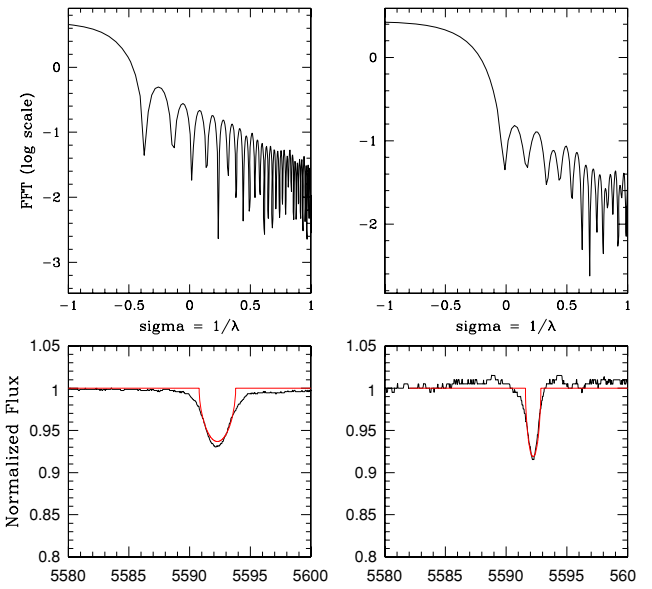

Figure 4. Top: plots of the Fourier transform computed for the O III λ5592 line of the primary star (left) and the secondary component (right). Bottom: synthetic rotational profiles measured for the same lines without taking into account the macroturbulence.

(A color version of this figure is available in the online journal.)

components. However, the disentangled UV spectrum of the secondary is too noisy to allow us to study the wind properties of this star (see Section 6).

4. PROJECTED ROTATIONAL VELOCITIES

A first estimate of the $v \sin i$ was derived by Howarth et al. (1997) to be about 81 and 41 km s^{-1} for the primary and secondary stars, respectively.

The $v \sin i$ is computed for each component by using the Fourier transform method (Simón-Díaz & Herrero 2007) based on a linear limb-darkening law (for detailed explanations and coefficients, see Gray 2005). For the primary, the mean $v \sin i$, computed from the profiles of the He I λ4471, He II λ4542, O III λ5592 (Figure 4, left), C IV λ5812, and He I λ5876 lines, is equal to 91 ± 12 km s^{-1}. For the secondary, we take into account the He I λ4471, He II λ4542, He I λ4713, O III λ5592 (Figure 4, right), and He I λ5876 lines since C IV λ5812 appears very weakly in the mean spectrum. We derive a mean value for $v \sin i$ of 51 ± 17 km s^{-1}.

5. SPECTRAL CLASSIFICATIONS

First, we have measured the equivalent widths (EWs) by fitting two Gaussians to the line profiles of observed spectra corresponding to phases close to the quadratures. The spectral-type determination is based on the quantitative classification criteria for O-type stars of Conti & Alschuler (1971), Conti (1973), and Mathys (1988, 1989). In consequence, we adopt the usual notations: $\log(W') = \log(\text{EW He I } \lambda4471/\text{EW He II } \lambda4542)$, $\log(W'') = \log(\text{EW Si IV } \lambda4089/\text{EW He I } \lambda4143)$, and $\log(W''') = \log(\text{EW He I } \lambda4388) + \log(\text{EW He II } \lambda4686)$. We find $\log(W') = -0.31 \pm 0.02$ and $\log(W') = 0.40 \pm 0.01$ for the primary and the secondary, respectively. We then compared those values to the ones measured on the disentangled spectra, finding that they are in good agreement with each other (see Table 3). On the one hand, the spectral type of the primary star is thus intermediate between two spectral classifications: O5.5 and O6. However, the O5.5 classification is favored after a comparison with the spectra in the atlas of Walborn & Fitzpatrick (1990). Moreover, the mean spectrum of the primary component displays a strong absorption for the He II λ4686 line, whilst the N III λλ4634−4641 lines are in emission, supporting an ((*f*)) tag. On the other hand, the spectrum of the secondary clearly reveals a late O-type star. The value computed from the ratio between He I λ4471 and He II λ4542 corresponds to an O9 star. With $\log(W'') \simeq -0.04$, computed from the échelle spectra, Conti's criteria clearly indicate a main-sequence luminosity (*V*). Furthermore, Mathys O8–O9.7 luminosity criterion confirms that the secondary component lies on the MS band ($\log(W''') \simeq 5.47$). In summary, we assign an O5.5 V ((*f*)) spectral type for the primary and an O9 V one for the secondary.

We then estimated the brightness ratio $l_1/l_2 = 3.96 \pm 0.21$. Indeed, from the Si IV λ4089, He I λ4471, O III λ5592, and He I λ5876 lines, we computed the EW ratio between the primary and secondary, respectively, and the average values calculated from Conti & Alschuler (1971) and Conti (1973) for stars with the same spectral type (for more details, see, e.g., Linder et al. 2008). The primary star is thus about 4 times brighter than the secondary component in the optical domain. This ratio greatly differs from the one computed in the UV domain where Stickland (1996) found a value of 1.8. The discrepancy is surprising since the spectral type that we have found would suggest that the brightness ratio in the UV domain should be even larger than in the optical.

The Reed Catalog (Reed 2005) provides the *UBV* photometry parameters required to compute the bolometric luminosity of each star. We assumed a combined spectral type O7 V for the binary system as already mentioned by Walborn (1972) or Garmany et al. (1982). In consequence, we used $V = 6.37 \pm 0.01$ and $B - V = -0.047 \pm 0.010$. Under this assumption and using $(B - V)_0 = -0.27$ (Martins & Plez 2006), we found $E(B - V) = 0.223 \pm 0.010$.

Table 3
Equivalent Widths Measured Directly from Some Observed Spectra

HJD	Φ	EW_{4471}		EW_{4542}		$\log(W')$		EW_{4089}		EW_{4143}		$\log(W'')$
2450000		P	S	P	S	P	S	P	S	P	S	
2655.3793	0.863	332	600	714	238	−0.33	0.40	...	...	...	...	...
3738.7235	0.816	372	684	740	268	−0.30	0.41	41	322	39	377	−0.07
3796.5248	0.595	379	551	754	208	−0.30	0.42	44	352	36	387	−0.04
3797.5211	0.918	371	600	779	243	−0.32	0.39	39	347	44	427	−0.09
4401.6362	0.181	357	615	773	243	−0.34	0.40	...	...	...	...	...
4412.6364	0.755	351	784	705	312	−0.30	0.40	...	...	...	...	...
4193.7415	0.641	391	625	757	253	−0.29	0.39	...	...	...	...	...
Disentangled	...	338	761	711	322	−0.32	0.37	65	267	70	254	0.02

Notes. The first column represents the HJD−2450000, the second one gives the orbital phase derived from the orbital solution. The next columns report the EWs measured from the data (expressed in mÅ), along with the $\log(W')$ and $\log(W'')$ quantities as defined in the text. The measured EWs were corrected from the brightness ratio ($l_1/l_2 = 3.96$).

Table 4
Summary of the Main Chemical Elements, Super-levels, and Levels Used in the Models

Species	Super-levels	Levels	Species	Super-levels	Levels	Species	Super-levels	Levels
H I	30	30	N IV	44	70	Si IV	66	66
He I	69	69	N V	41	49	Fe III	65	607
He II	30	30	O III	30	75	Fe IV	100	1000
C III	99	243	O IV	30	64	Fe V	139	1000
C IV	64	64	O V	32	56	Fe VI	59	1000
N III	57	287	Si III	50	50	Fe VII	40	245

Note. We also take into account Ne II–IV, S IV–V, Ar III–V, Ca III–IV, and Ni III–VI species.

Assuming that the distance of 1829 ± 77 pc (Brown & Bomans 2005), computed for HD 48099 from the spectroscopic parallax, is correct, the DM (distance modulus) of this star is estimated at 11.31 ± 0.09. The visual absolute magnitude of the entire system would be $M_V = -5.63 \pm 0.11$. We thus derive, from the luminosity ratio, $M_{V_P} = -5.39 \pm 0.12$ and $M_{V_S} = -3.89 \pm 0.06$ for the primary and secondary, respectively. Using the bolometric corrections of Martins & Plez (2006), we inferred a bolometric magnitude of −9.09 ± 0.12 and −7.02 ± 0.06 for the primary and secondary stars, respectively, equivalent to absolute luminosities of $\log(L_1/L_\odot) = 5.54 \pm 0.12$ and $\log(L_2/L_\odot) = 4.71 \pm 0.06$. The luminosities of both stars are in good agreement with our spectral modeling (see Section 6), clearly indicating main-sequence stars.

6. MODELING SPECTRA FOR AN ABUNDANCE STUDY

We have conducted a spectroscopic analysis of the components of HD 48099 using the code CMFGEN (see Hillier & Miller 1998 for details). Non-LTE atmosphere models including winds and line-blanketing have been computed and synthetic spectra have been fitted to the disentangled spectra of HD 48099. We have thus constrained the main stellar parameters of both the primary and the secondary: $T_{\rm eff}$, $\log g$, luminosity, and surface N content. We note that the oscillator strengths for the N III were taken from the atomic data taken from the OPACITY project.[9] The abundances of other chemical elements (see Table 4) have been fixed to solar, since we lack reliable indicators to allow us to change these abundances. The solar abundances of Grevesse et al. (2007) have been used unless stated otherwise. For the primary, we have also fitted the disentangled mean *IUE* spectrum to determine the terminal velocity, mass-loss rate, and clumping factor of the stellar wind. Figures 5 and 6 show the comparison between the disentangled and the theoretical spectra in the optical and UV domains, respectively. The agreement between the model and the observations is rather good for both components of the system. As mentioned in Section 3, the analysis of the individual spectrum of the secondary star in the UV domain is not possible because of its large noise level.

In practice, we have used the He I λ4471 and He II λ4542 lines to estimate $T_{\rm eff}$. The gravity was determined from the Balmer lines Hβ, Hγ, and Hδ. The luminosity was constrained by the *V*-band magnitude: for the adopted distance and extinction (see Section 5), we computed the *V*-band magnitude of our synthetic

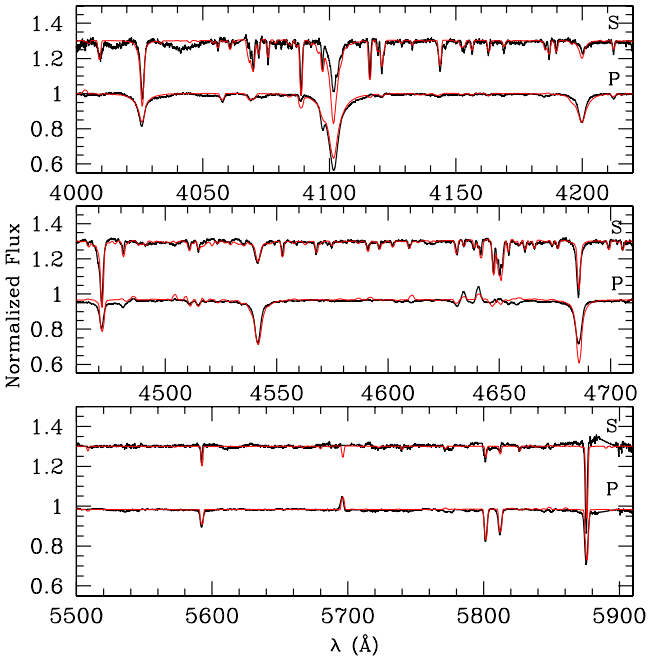

Figure 5. Comparison between the disentangled (black line) and the theoretical (red line) optical spectra of HD 48099. The latter were computed with the CMFGEN atmosphere code. The secondary spectrum was vertically shifted by 0.3 units for clarity.
(A color version of this figure is available in the online journal.)

[9] The oscillator strengths were given in atomic files available at the URL: http://cdsweb.u-strasbg.fr/topbase/op.html. The oscillator strengths (*f*) for the relevant N III lines are: 0.17338 (λ4510.88), 0.21845 (λ4510.96), 0.27716 (λ4514.85), and 0.17310 (λ4518.14).

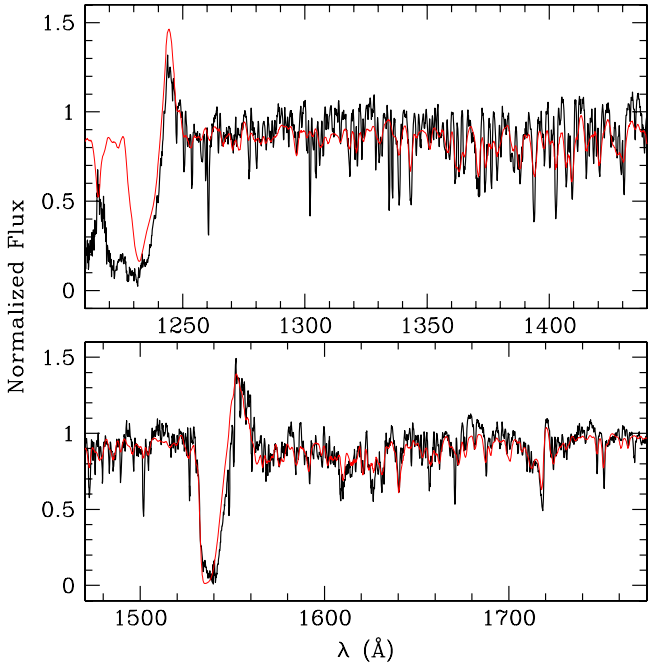

Figure 6. Same as Figure 5 but only for the primary star in the UV domain. The disentangled spectrum was built from the *IUE*-archive spectra of HD 48099.

(A color version of this figure is available in the online journal.)

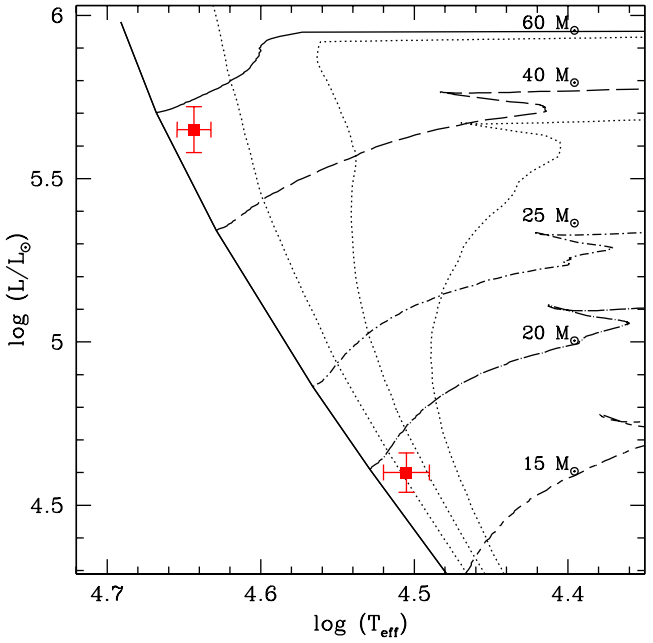

Figure 7. HR diagram with the position of the two components of HD 48099 indicated. Evolutionary tracks are from Meynet & Maeder (2003) for an initial rotational velocity of about 300 km s^{-1}. The isochrones shown by dotted lines are for 2, 4, and 6 Myr.

(A color version of this figure is available in the online journal.)

Table 5
Derived Stellar Parameters for the Two Components of HD 48099

Parameter	Primary	Secondary
$T_{\rm eff}$ (kK)	44 ± 1	32 ± 1
$\log g$	4.5 ± 0.1	3.5 ± 0.1
$\log(\frac{L}{L_\odot})$	5.65 ± 0.07	4.60 ± 0.06
$M_{\rm theo}$ ($M_\odot$)	55 ± 5	19 ± 2
R ($R_\odot$)	11.6 ± 0.1	6.5 ± 0.1
N/H	5×10^{-4}	6×10^{-5}

Note. The masses are from interpolation in the single star evolutionary tracks.

spectra and adjusted the luminosity to correctly reproduce the observed *V*-band magnitude. The results are gathered in Table 5. The primary has a high effective temperature, larger than expected for its spectral type (Martins et al. 2005), but it also has a quite large $\log g$. We will see below that this could mean either that the primary is a very young O star, or that it is a fast rotator. The secondary has $T_{\rm eff}$ and $\log g$ more typical for its spectral type. To obtain a good agreement with the primary spectrum, it is important that the model is enriched in nitrogen. The nitrogen abundance is found to be 5–10 times the solar value, with the best model showing a nitrogen content equal to 8 times this value. However, we note that the nitrogen content is sensitive to the variation of the effective temperature and the microturbulence (equal to 10 km s^{-1} in our model). For example, a variation of 1000 K or 10 km s^{-1} implies a change of about 20% of the nitrogen abundance.

The wind properties of the primary were constrained from the disentangled *IUE* spectrum. The N V λ1240, C IV λ1550, and N IV λ1720 lines were the main indicators. A terminal velocity of 2800 km s^{-1} convincingly reproduced the blueward extension of the main P Cygni profiles. We found that a strongly clumped wind (with a filling factor of 0.01) was necessary to correctly reproduce the N IV λ1720 line (see Bouret et al. 2005). The corresponding mass-loss rate required to fit all P Cygni lines is $2.5 \times 10^{-8} M_\odot$ yr^{-1}.

Figure 7 shows the position of the two components in an HR diagram built with the Geneva single star evolutionary tracks of Meynet & Maeder (2003). Provided that the components of HD 48099 have not gone through an evolutionary phase of mass exchange or mass loss through Roche lobe overflow, the comparison with these evolutionary tracks can provide some indications on the age and absolute parameters of the stars. The secondary appears to be 1–5 Myr old. Its evolutionary mass is $19 \pm 2\ M_\odot$. The primary lies rather close to the main sequence, indicating an age of 0–1 Myr. A mass of $55 \pm 5\ M_\odot$ is derived from interpolation between tracks. Its effective temperature (44 kK) is much hotter than what is expected for a classical main-sequence O5.5 star, but its gravity is also quite high ($\log g > 4.5$ compared to ∼4.0 for class V O stars; see Martins et al. 2005). The star might thus be younger than normal main-sequence stars. Consequently, it might be hotter and more compact, explaining the larger gravity. However, since the secondary appears rather similar to normal late O dwarfs, we might speculate instead that the evolution of the primary was affected by binarity. The rather large surface nitrogen content (about 8 times solar) is also difficult to explain if the star is very young, while it might be more easily accounted for by binarity. In a binary system, the effect of rotation on the evolution is actually enhanced through the exchange of orbital and rotational angular momentum (de Mink et al. 2009). The latter effects have a strong impact on the determination of the stellar parameters, and a comparison with single star tracks might no longer be valid. This idea remains to be tested by theoretical (evolutionary) models of binary evolution. Another possibility of explaining the properties of the primary would be fast rotation. Since the system is seen at low inclination, and assuming that the primary and secondary have their spin axes aligned with the

system's angular momentum vector, we cannot exclude a large rotational velocity for the primary (its $v \sin i$ is $\sim$1.8 times that of the secondary). Fast rotating single stars tend to evolve more "vertically" than normal stars in the early phases of evolution (see a discussion of this effect in Martins et al. 2009). This could explain the larger $T_{\rm eff}$ and enhanced N/H.

7. DISCUSSION AND CONCLUSIONS

Our detailed investigation of the short-period binary HD 48099 revealed a system composed of an O5.5 V ((*f*)) primary and an O9 V secondary. We have studied the main stellar parameters of both stars by using, on the one hand, the CMFGEN code to fit the optical spectra, and, on the other hand, the visual absolute luminosity of both components. These two approaches provided quite similar luminosities. We thus adopt for HD 48099 the values given in Section 6, i.e., $\log(L_1/L_\odot) = 5.65 \pm 0.07$ and $\log(L_2/L_\odot) = 4.60 \pm 0.06$. However, a significant difference remains in the mass ratio of the system. Indeed, the RVs yield a value of about 1.77, while the evolutionary tracks indicate a value close to 2.89. The discrepancy could be seen as an indication that the primary is an evolved star that has lost part of its mass through a Roche lobe overflow or it could again be due to fast rotation (see the discussion in Section 6).

The orbital solution, computed in the present paper, is particularly marked by the very small minimum masses and the low amplitudes of the RV curves. As Stickland (1996) already suggested, the orbit of the binary system should thus be seen under a low inclination angle. From the theoretical estimates proposed by Martins et al. (2005), the gravitational masses of an O5.5 V and an O9 V star correspond to about 34 $M_\odot$ and 18 $M_\odot$, respectively. Under this assumption, we can estimate the inclination of the HD 48099 binary system to be about 16°. We note that a modification of the masses corresponding to ± 1 spectral type alters the inclination of the system by about 1°, whilst the use of evolutionary masses given in Table 5 leads to a change of the inclination by about 2°. However, we must be careful with the comparison between the stellar parameters given in Table 5 for both stars of HD 48099, and the values quoted in Martins et al. (2005) for a same spectral type since the latter were given for $\log g = 3.92$. The $T_{\rm eff}$, L, and the masses could be directly affected by the difference of $\log g$ found for the two stars in the binary system and could explain why the $T_{\rm eff}$ found by CMFGEN is too high compared with the values given in Martins et al. (2005).

By adopting an inclination of 16°, the rotational velocity of both components is close to 330 and 185 km s^{-1} for the primary and secondary, respectively. HD 48099 could thus contain a rapid rotator. Such an assumption could explain why the primary star appears more massive in the evolutionary track than in reality (Meynet & Maeder 2003; Martins et al. 2009). In addition, by assuming that the inclination of the rotation axis of both components is the same as the orbital inclination ($\sim$16°), the stars would essentially be seen pole-on. Since the fast rotation of the primary would make this star hotter near the poles than at the equator, the spectral classification for this star could be biased toward earlier types.

Taking into account the radii of both stars (see Table 5), the rotational velocities suggest that the two components are in synchronous rotation, i.e., the angular velocity is similar for both stars, but exclude a system in synchronous co-rotation, i.e., the orbital period of the system is not the same as the rotation period of both stars. Indeed, to obtain an angular velocity of the system equal to the individual angular rotation velocities of the stars, we must assume that the inclination of the orbit is equal to 28.°5, implying too small masses for such a system. On the basis of an inclination of 16° for both stars, the Roche lobe radii are equal to 14.3 and 11.0 $R_\odot$ for the primary and secondary, respectively. The ratio between the stellar and Roche lobe volumes indicates that the primary star, with a radius of 11.6 $R_\odot$, fills its Roche lobe at 53%, whilst the secondary only occupies 21%. This result thus suggests that, for the young system HD 48099, the fast rotation could be the main factor of evolution. However, we note that a relatively small error on the inclination could have a large impact on the evolutionary status (Roche lobe overflow) of HD 48099 since, by taking an inclination of about 20°, the primary star would fill its Roche lobe.

Finally, we put in perspective the two O+O binary systems known in Mon OB2 association (HD 48099 and Plaskett's star). The comparison shows that the most massive star of both system is affected by nitrogen enrichment. We derived an N overabundance for the fast rotator in HD 48099, while Linder et al. (2008) reported, for Plaskett's star, that the component with the slowest rotation velocity has an N content close to 16 times the solar abundance. However, we emphasize that Plaskett's star is in a post case A Roche lobe overflow stage.

This research is supported by the FNRS (Belgium), by a PRODEX XMM/Integral contract (Belspo) and by the Communauté française de Belgique—Action de recherche concertée (ARC)—Académie Wallonie–Europe. We acknowledge the Ministère de l'Enseignement Supérieur et de la Recherche de la Communauté Française for supporting our travels to O.H.P. We also thank the staff of Observatoire de Haute-Provence and of La Silla ESO Observatory for their technical support. F.M. thanks John Hillier for making his code available and for assistance. P.E. acknowledges support through CONACyT grant 67041.

REFERENCES

Bouret, J.-C., Lanz, T., & Hillier, D. J. 2005, A&A, 438, 301
Brown, D., & Bomans, D. J. 2005, A&A, 439, 183
Conti, P. S. 1973, ApJ, 179, 161
Conti, P. S., & Alschuler, W. R. 1971, ApJ, 170, 325
Conti, P. S., Leep, E. M., & Lorre, J. J. 1977, ApJ, 214, 759
de Mink, S. E., Cantiello, M., Langer, N., Pols, O. R., Brott, I., & Yoon, S.-C. 2009, A&A, 497, 243
Garmany, C. D., Conti, P. S., & Chiosi, C. 1982, ApJ, 263, 777
Garmany, C. D., Conti, P. S., & Massey, P. 1980, ApJ, 242, 1063
González, J. F., & Levato, H. 2006, A&A, 448, 283
Gosset, E., Royer, P., Rauw, G., Manfroid, J., & Vreux, J.-M. 2001, MNRAS, 327, 435
Gray, D. F. 2005, The Observation and Analysis of Stellar Photospheres (3rd ed.; Cambridge: Cambridge Univ. Press)
Grevesse, N., Asplund, M., & Sauval, A. J. 2007, Space Sci. Rev., 130, 105
Heck, A., Manfroid, J., & Mersch, G. 1985, A&AS, 59, 63
Hensberge, H., Pavlovski, K., & Verschueren, W. 2000, A&A, 358, 553
Hillier, D. J., & Miller, D. L. 1998, ApJ, 496, 407
Howarth, I. D., Siebert, K. W., Hussain, G. A. J., & Prinja, R. K. 1997, MNRAS, 284, 265
Levenhagen, R. S., & Leister, N. V. 2006, MNRAS, 371, 252
Linder, N., Rauw, G., Martins, F., Sana, H., De Becker, M., & Gosset, E. 2008, A&A, 489, 713
Mahy, L., Nazé, Y., Rauw, G., Gosset, E., De Becker, M., Sana, H., & Eenens, P. 2009, A&A, 502, 937
Martins, F., Hillier, D. J., Bouret, J. C., Depagne, E., Foellmi, C., Marchenko, S., & Moffat, A. F. 2009, A&A, 495, 257
Martins, F., & Plez, B. 2006, A&A, 457, 637
Martins, F., Schaerer, D., & Hillier, D. J. 2005, A&A, 436, 1049
Mathys, G. 1988, A&AS, 76, 427
Mathys, G. 1989, A&AS, 81, 237

Meynet, G., & Maeder, A. 2003, A&A, 404, 975
Rauw, G., Sana, H., Gosset, E., Vreux, J.-M., Jehin, E., & Parmentier, G. 2000, A&A, 360, 1003
Reed, C. 2005, VizieR Online Data Catalog, 5125, 0
Sana, H. 2009, A&A, 501, 291
Sana, H., & Gosset, E. 2009, A&A, submitted
Sana, H., Gosset, E., & Rauw, G. 2006, MNRAS, 371, 67
Simón-Díaz, S., & Herrero, A. 2007, A&A, 468, 1063
Slettebak, A. 1956, ApJ, 124, 173
Stickland, D. J. 1996, Observatory, 116, 294
Underhill, A. B. 1994, ApJ, 420, 869
Walborn, N. R. 1972, AJ, 77, 312
Walborn, N. R., & Fitzpatrick, E. L. 1990, PASP, 102, 379 (erratum 102, 1094)
Wolfe Jr., R. H., Horak, H. G., & Storer, N. W. 1967, in The Machine Computation of Spectroscopic Binary Elements, ed. M. Hack (New York: Gordon & Breach), 251

5.3 The determination of the stellar and wind parameters

The population of O-type stars in NGC 2244 constitutes a homogeneous set of objects (same distance, age and chemical composition). Therefore, studying the stellar and wind parameters of these stars can provide an insight into the star formation process but also into the evolutionary properties depending on the mass-loss rate or the rotational mixing.

This analysis was performed with the collaboration of Dr. F. Martins from the University of Montpellier. We have taken in charge the treatment of the spectroscopic and IUE data as input of this investigation. Dr. Martins introduced us to the CMFGEN code through the study of the stars of NGC 2244 and Mon OB2. We have made preliminary models to become familiar with CMFGEN and actually did some spadework. However, Dr. Martins' experience with the code allowed him to give to the project its final touch.

We use for this analysis the échelle data with the highest resolution and the highest signal-to-noise ratio. To determine the wind parameters, we combine these data with the *IUE* (International Ultraviolet Explorer) spectra taken between 1979 and 1989 that we have retrieved and normalized. Whenever possible, we apply the disentangling process on the binary systems to separate the individual contributions of each star, thus allowing us to determine the fundamental parameters for each of them. The investigation of the model atmospheres yields the stellar and wind parameters listed in Table 5.4 and published in Martins et al. (2011, see Appendix A). For the stars belonging to NGC 2244 and Mon OB2, the best-fit CMFGEN models (see Figs. 5.2 and 5.3) are of excellent quality and allow an accurate determination of the physical parameters of each object. However, the results obtained by disentangling (see Chapter 2) for HD 46149 are uncertain. On the one hand, the large eccentricity and the long orbital period of the system do not allow us to observe uniformly the orbital cycle (in radial velocity or in phase) of this binary. On the other hand, the spectral separation is insufficient to sample the full width of the broadest lines such as the Balmer lines. As a consequence, the computed parameters for the faintest component, especially its gravity, are unreliable.

From the effective temperature and the luminosity derived in our analysis, we locate the O-type stars on the HR diagram (Fig. 5.4). The inferred age for the O star population of NGC 2244 and Mon OB2 is estimated to be between 0 and 5 Myrs. A trend of lower ages for more massive stars is however detected without knowing whether its origin is real or whether it is due to an artefact of the comparison method. If we believe this trend is real, we may think that the most massive stars form after the lower-mass ones. We can also speculate that, with their high ionizing fluxes and their stronger winds, the early-type stars may emerge faster from their parental cloud. In this case, the late-type O stars would thus remain hidden for a longer time, appearing older on average. However, the latter assumption is unlikely for the stars of NGC 2244 because both categories are assumed to be observable at the same time. Alternatively, different rotational rates could appear as a possible cause of this discrepancy. Indeed, rotation is known to affect the evolutionary tracks and the isochrones in the HR diagram (Meynet & Maeder 2000; Brott et al. 2011a). For stars with masses above 15 $M_{\odot}$, the rotation would actually have similar effects than the overshooting. Consequently, with a faster initial rotational velocity ($v_{\mathrm{rot_{init}}}$), the stars could appear in the HR diagram younger than they are in reality, making the value of $v_{\mathrm{rot_{init}}} = 300$ km s^{-1} inappropriate for the most massive objects in our sample. This hypothesis relies on the assumption that the rotation is however faster for the stars with a larger mass.

When we look closer at the two hottest objects in NGC 2244, we see that both stars have the same age ($\sim 0 - 2$ Myrs). According to Wang et al. (2008), the investigation of the *Chandra*

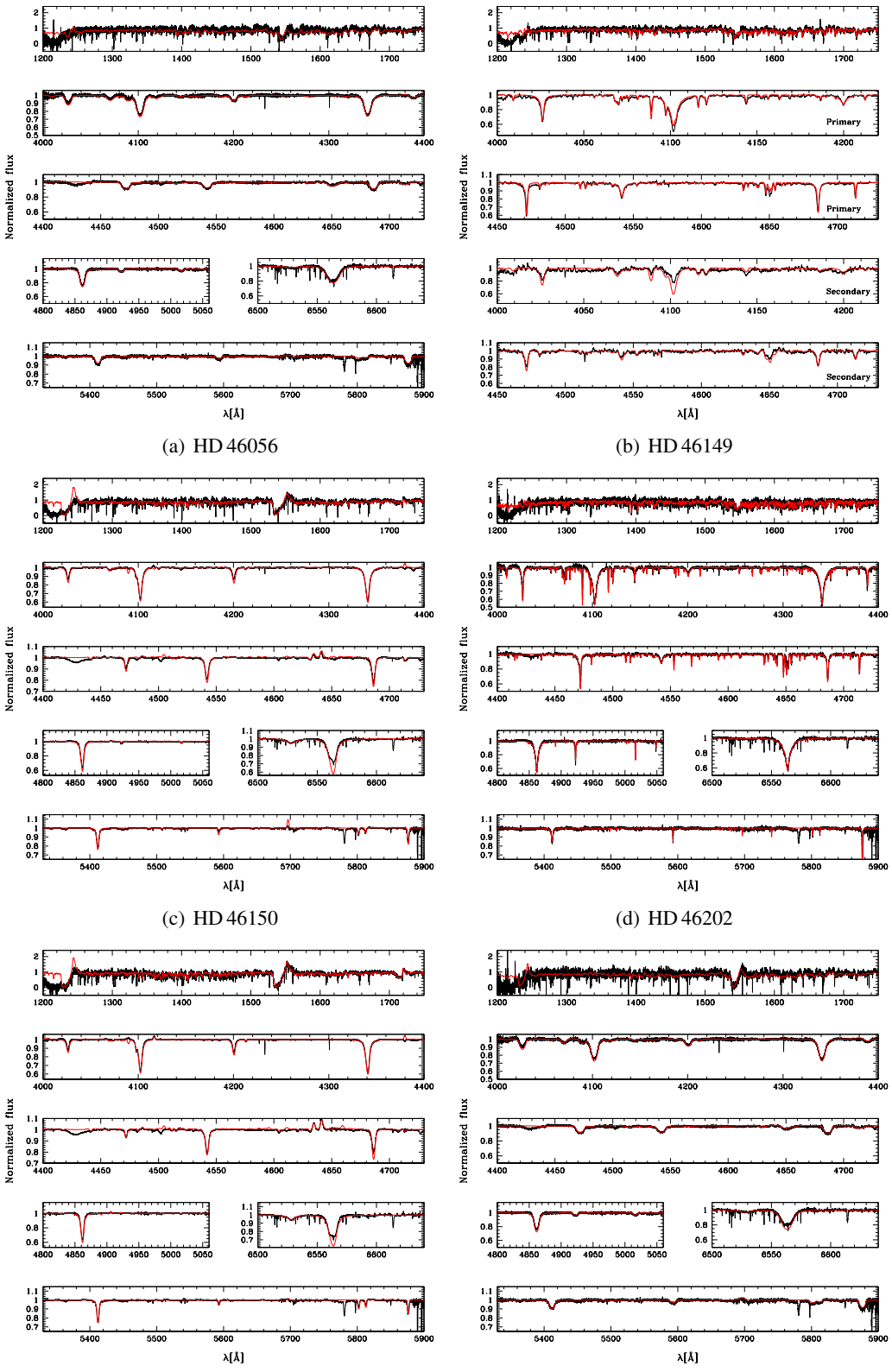

(a) HD 46056 (b) HD 46149

(c) HD 46150 (d) HD 46202

(e) HD 46223 (f) HD 46485

Figure 5.2: Best-fit CMFGEN models for the O-type stars in NGC 2244.

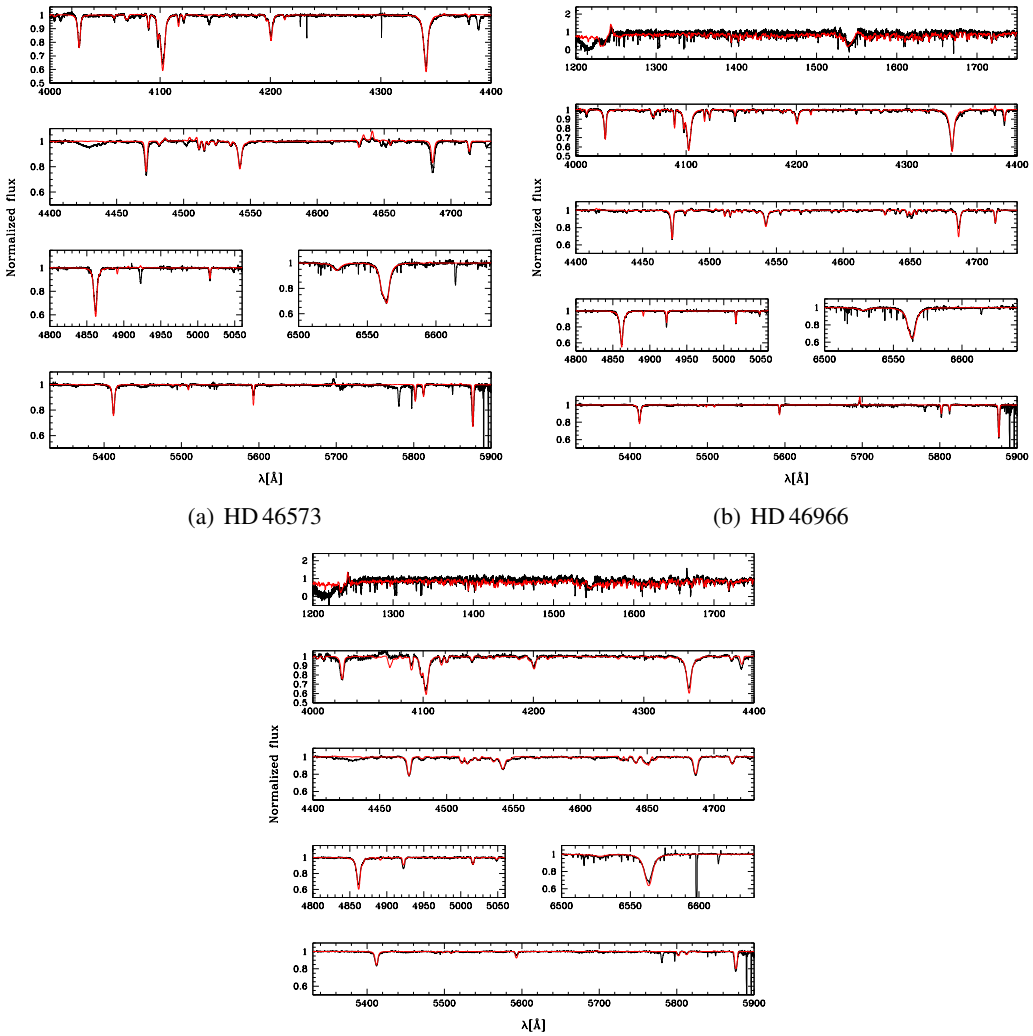

(a) HD 46573

(b) HD 46966

(c) HD 48279

Figure 5.3: Best-fit CMFGEN models for the O-type stars in Mon OB2.

mosaic observations revealed that the fainter X-ray sources, associated to pre-main-sequence stars (PMS), are concentrated around HD 46150 at the center of the cluster (see Fig. 5.1) while no strong clustering of X-ray sources was detected around HD 46223. These authors argued that the possible reason to explain this phenomenon is that either HD 46223 was ejected because of dynamical interactions or that this star might actually be younger and would then not be part of the same population as the central part of the cluster. Our analysis rather indicates that both stars have comparable masses and ages, thereby favoring the dynamical interaction scenario inside NGC 2244.

The study of Martins et al. (2011) also reveals a systematic difference between the mass-loss rates derived from the UV P-Cygni profiles and from the Hα profiles (see Table 5.4). Although our estimates could be biased because of the few available features to constrain this parameter or because of the CMFGEN code itself, a possible physical explanation could be the presence of clumps in the winds of the massive stars (Owocki 2008). Our analysis indeed shows that the

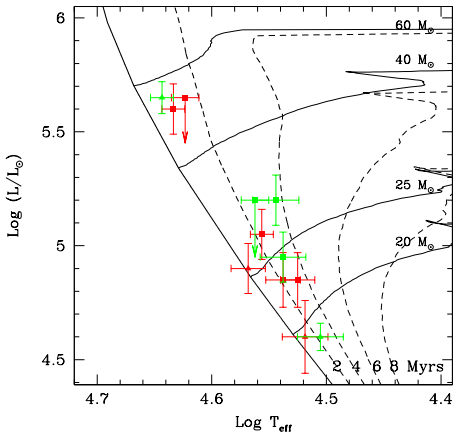

Figure 5.4: HR diagram of the O-type stars in NGC 2244 (in red) and in Mon OB2 (in green). Binaries are displayed with triangles (where the primaries are the most luminous). Evolutionary tracks and isochrones are from Meynet & Maeder (2003) and are computed with $v_{\mathrm{rot_{init}}} = 300$ km s^{-1}.

wind diagnostic lines are not affected at the same way by mass-loss. As we already mentioned in Introduction, the UV resonance lines are dependent on the local wind density (ρ) whilst the $H\alpha$ line depends on ρ^2. Recent simulations made by Sundqvist et al. (2010, 2011b) have shown that optically thick clumps (the so-called *porosity* or *vorosity* in the velocity space) could be important for the line formation. According to these authors, the UV resonance lines will be altered through a strong reduction of their entire profiles whilst the dominant effect of the clumps will be only visible on the emission part of Hα profile i.e., in the line core. However, it is not yet established that the clumps are optically thin or optically thick. What becomes clear is that the spectral mass-loss diagnostics of O stars are affected by wind clumping, even for the weak wind objects. Moreover, in this case (clumped winds), the Hα mass-loss rates derived by using homogeneous models should be considered as upper limits with overestimates by a factor $\sqrt{1/f}$ where f is the clumping volume filling factor (see Chapter 1) if the inter-clump medium is void.

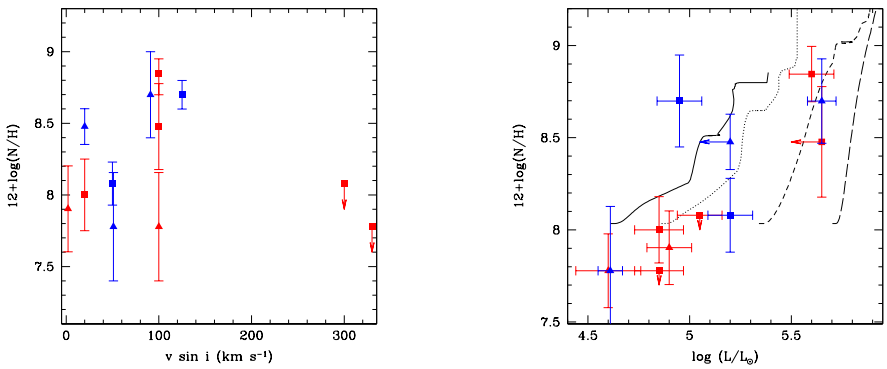

Figure 5.5: N surface abundance (in units of $12 + \log(\mathrm{N/H})$) as a function of $v \sin i$ (left panel) and of luminosity (right panel). Red/blue squares represent the single O stars in NGC 2244/Mon OB2, respectively, whilst the red/blue triangles indicate binaries in NGC 2244/Mon OB2. Evolutionary tracks, shown by solid, dotted, dashed and dot-long dashed lines for M = 20, 25, 40 and 60 $M_{\odot}$, are from Meynet & Maeder (2003) and are computed with $v_{\mathrm{rot_{init}}} = 300$ km s^{-1}.

We also derive the surface nitrogen content for all stars of our sample. The theoretical models notably predict that the chemical abundances are affected by rotation through the internal mixing processes (Meynet & Maeder 2000). This rotation thus increases the N enrichment during the main-sequence phase. At zero rotation, this enrichment does not occur except for stars with a mass above 60 $M_{\odot}$ due to their very high mass-loss rate (Maeder & Meynet 2004). Furthermore, the N content is assumed to become larger when the stellar mass increases. Fig. 5.5 (left panel) shows the N abundances as a function of projected rotational velocity. We observe a clear trend of larger N/H with larger $v \sin i$, except for the two rapid rotators (HD 46056 and HD 46485). When we compare this N content with the luminosity of the stars (Fig. 5.5, right panel), we detect another clear correlation towards a larger enrichment for the more luminous stars (without any exception). We therefore confirm the theoretical predictions about the N content evolution in the massive stars. These results also suggest that the fast rotators are probably too young to have experienced a strong enrichment in spite of their large projected rotational velocities.

Table 5.4: Stellar and wind parameters derived for the O-type stars in NGC 2244 and Mon OB2.

Source	$T_{\rm eff}$ [kK]	$\log\left(\frac{L}{L_\odot}\right)$	$\log g$	$\log(\dot{M}_{UV})$	$\log(\dot{M}_{\rm H\alpha})$	f_∞	v_∞ [km s^{-1}]	$v \sin i$ [km s^{-1}]	$v_{\rm mac}$ [km s^{-1}]	$M_{\rm evol}$ [$M_\odot$]	$M_{\rm spec}$ [$M_\odot$]	N/H [$\times 10^{-4}$]
NGC 2244												
HD 46223	43.0	5.60±0.11	4.01	−7.17	−6.20	0.1	2800	100	32	$52.1^{+6.2}_{-5.9}$	48.3 ± 19.3	7.0±2.0
HD 46150	42.0	<5.65	4.01	−7.30	−6.40	0.1	2800	100	37	< 53.6	59.5 ± 23.7	3.0±2.0
HD 46485	36.0	5.05±0.11	3.85	−7.80	−6.45	1.0	1850	300	–	$28.6^{+3.3}_{-4.3}$	19.5 ± 7.9	≤1.2
HD 46056	34.5	4.85±0.12	3.89	−8.50	–	1.0	1500	330	–	$23.1^{+2.4}_{-1.9}$	15.8 ± 6.7	≤0.6
HD 46149-1	37.0	4.90±0.12	4.25	< −9.0	–		1300	∼0	24	$25.9^{+3.1}_{-3.5}$	30.9 ± 21.6	0.8±0.5
HD 46149-2	33.0	4.60±0.16	3.53	–	–	–	–	100	27	$19.2^{+2.9}_{-2.5}$	4.7 ± 3.6	0.6±0.5
HD 46202	33.5	4.85±0.12	4.10	−9.0	−7.10	1.0	1200	20	17	$22.7^{+2.0}_{-2.4}$	29.0 ± 12.4	1.0±0.5
Mon OB2												
HD 46573	36.5	< 5.20	3.75	–	−6.30	–	–	20	43	< 32.5	20.6 ± 8.3	3.0 ± 1.0
HD 48279	34.5	4.95 ± 0.11	3.77	−8.8	−6.80	1.0	1300	125	22	$24.4^{+2.5}_{-1.9}$	15.2 ± 6.1	5.0 ± 3.0
HD 46966	35.0	5.20 ± 0.11	3.75	−8.0	−6.40	1.0	2300	50	27	$30.9^{+3.8}_{-4.1}$	24.5 ± 9.9	1.2 ± 0.5
HD 48099-P	44.0	5.65 ± 0.07	4.50	−7.6	–	0.01	2800	91	0	$55.3^{+4.3}_{-4.1}$	155.0 ± 50.4	5.0 ± 2.5
HD 48099-S	32.0	4.60 ± 0.06	3.51	–	–	–	–	51	0	$18.5^{+1.5}_{-1.0}$	5.0 ± 1.6	0.6 ± 0.3

Notes: The quoted errors correspond to $1-\sigma$.

5.4 The CoRoT photometry

Despite a number of previous studies, many properties of the O-type stars belonging to NGC 2244 and Mon OB2 remain unrevealed. Fundamental properties such as their age and their position on the HR diagram make these objects interesting candidates for asteroseismology. Following a proposal initiated by our group, certain O-type stars of NGC 2244 and the Mon OB2 association were included among the targets of the CoRoT (Convection, Rotation and planetary Transits, Baglin et al. 2006) satellite. It is thus with the aim of shedding a new light on these objects that the second short run of the CoRoT satellite (SRa02, Baglin et al. 2006) was partly devoted to the observation of six O-type stars in NGC 2244 and Mon OB2 between 2008 Oct 08 and 2008 Nov 12, i.e., over a time span of 34.3 days. The analyses of these six light curves were split between three Belgian groups: the University of Liège received HD 46223, HD 46966 and HD 47129 (Plaskett's Star), the University of Leuven analyzed HD 46149 and HD 46202 and the Royal Observatory of Belgium was in charge of HD 46150. The results of this campaign were published in Mahy et al. (2011a), Degroote et al. (2010), Blomme et al. (2011) and Briquet et al. (2011). However, to ensure a homogeneous comparison and a good concertation, we have analyzed each star in the sample and we present the main results in this section.

5.4.1 The CoRoT satellite

Launched on 2006 Dec 27, the CoRoT satellite[9] was dedicated, on the one hand, to stellar seismology in order to probe the interiors of the stars and, on the other hand, to the search for transiting exoplanets. This satellite was designed for uninterrupted photometric observations during runs from 20 to 160 days. Placed on an eccentric orbit with an inclination close to 90° (90.002°) i.e., almost polar, the satellite travels its orbit in a period of 6184 sec. (i.e., of about 103 min.). Due to its low orbit ($\sim$ 900 km), the satellite undergoes several external perturbations: eclipses due to the light/penumbra/shadow transitions, the gravity and magnetic field changes, as well as the South Atlantic Anomaly (SAA) crossing. Among these sources of perturbations, the passage through the SAA is the main cause of spurious measurements. The percentage of lost datapoints linked to the environmental perturbations amounts to about $7-9\%$ of the observations during a run. Since this crossing occurs twice in a sidereal day, the spectral windows (Fig. 5.6) of the light curves reveal a peak at about 2.007 d^{-1} with a smaller one at about 4.014 d^{-1}. In addition, the orbital period produces other structures with peaks around 13.972 d^{-1} and their harmonics.

We also remove the datapoints affected by other perturbations of an instrumental origin (e.g., the changes of CCD masks or the generation of outliers). These flagged points represent about 5% of the lost datapoints in a light curve. However, they do not constitute the only source of errors. For example, the light curves are also corrupted by jumps or discontinuities caused by a change of the CCD temperature. These effects have been corrected before analyzing the light curves. Table 5.5 summarizes the main properties (starting/ending HJD, duty cycle,...) of the light curves.

The six O-type stars were observed in the same field-of-view between HJD $\cong$ 2 454 748.4 and HJD $\cong$ 2 454 782.9, resulting in a frequency resolution of about $1/\Delta T \cong 0.029$ d^{-1}. The high-precision photometric data were collected every $\sim$ 32 sec. This sampling generates a peak in the spectral window at about 2700 d^{-1}. For Plaskett's Star, this peak is at $f = 2699.764$ d^{-1}, indicating a sampling of 32.003 sec (Fig. 5.6). Consequently, the pseudo-Nyquist frequency for

[9] A complete description of the satellite properties is given in Auvergne et al. (2009).

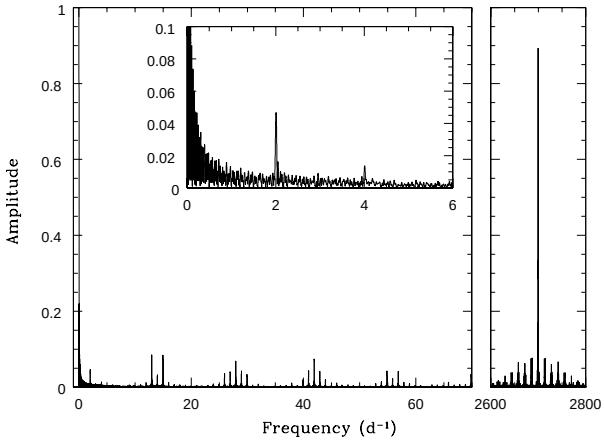

Figure 5.6: Spectral window of the unflagged CoRoT light curve of Plaskett's star.

this star is located at about $f_{\rm Ny}$ = 1349.882 d^{-1}. We notice however that this sampling is not completely regular. That is why the height of the peak only reaches 89% of the total height while it would be 100% if the sampling was regular.

Table 5.5: Parameters of the CoRoT light curves. HJD is in format HJD−2450000

	HD 47129	HD 46223	HD 46150	HD 46966	HD 46149	HD 46202
Light curves						
number of raw data	92696	92687	92695	92688	92687	92287
number of non-flagged data	79895	80403	80282	82273	82281	81777
number of binned data	1700	1702	1702	1706	1706	1697
duty cycle [%]	86.19	86.75	86.61	88.76	88.77	88.91
starting HJD	4748.485467	4748.488547	4748.485591	4748.488454	4748.488556	4748.562629
ending HJD	4782.819956	4782.819650	4782.819657	4782.805898	4782.819660	4782.712238
duration [d]	34.334489	34.331103	34.334066	34.317444	34.331104	34,149609
freq. resolution [d^{-1}]	0.029125	0.029128	0.029126	0.029140	0.029128	0,029283
Spectral window						
window peak [%] at 2.0 d^{-1}	4.6	3.5	3.8	3.9	4.5	3.8
window peak [%] at 4.0 d^{-1}	1.4	1.1	1.0	1.1	1.1	1.0
Significant frequencies						
white noise	174	46	30	31	16	6
red noise	43	15	28	7	14	–

5.4.2 Analysis processes and frequency determination

In our analysis, we choose not to interpolate the points in the flagged zones to avoid introducing systematic effects that could generate erroneous values of the frequencies and affect the scientific results. Moreover, since all the stars observed in the CoRoT field-of-view present a decreasing slope in their raw light curve, probably due to the ageing of the CCDs (Auvergne et al. 2009), we decide to remove this long-term trend by dividing the flux of the light curve by the best linear fit, which appears to be the best among the different possible ones (linear, quadratic, exponential,...).

Once all these pretreatments are done, we apply, to extract the frequencies from the light curves, a Fourier analysis based on the Heck-Manfroid-Mersch technique (hereafter HMM, Heck et al. 1985, revised by Gosset et al. 2001). This technique is comparable to a least-squares fit of a sine function for each individual frequency. It is similar to the method of Ferraz-Mello (1981) and

corrects some deficiencies of other methods such as that of Scargle (1982). Once the periodogram is computed, we iteratively use HMM to prewhiten the signal, frequency by frequency. That treatment assumes that all the frequencies constituting the signal can be represented by a sine function but also that they are independent of each other i.e., for these frequencies no correlation between the respective process exists. Therefore, the flux of the light curve can be written as:

$$F(t_j) = \mu + \sum_{i=1}^{n} A_i \sin((2\pi f_i t_j) + \phi_i)$$

where μ is the observed average, A_i, f_i and ϕ_i are the amplitude, the frequency and the phase of the i^{th} sine function, respectively. At each iteration, the semi-amplitude spectrum is computed for the frequencies situated between 0 and 20.0 d^{-1}. We note that this range is selected because the semi-amplitude spectrum exhibits very little power at higher frequencies. The position of the highest peak is detected, thus giving its frequency, its amplitude and its phase. The sine function characterized by these three values is then subtracted from the data. This process is repeated until reaching the noise level in the observations. In this prewhitening process, we oversample the frequency grid so that its step size is equal to $0.1/T$ d^{-1} in order to be more accurate on the exact value of the frequency.

As we mentioned above, this iterative removal of frequencies is only efficient for independent frequencies because the subtraction of a signal does not affect the other true signals in the light curve. However, because the light curves present gaps due to external and instrumental conditions and also due to the fact that the sampling is irregular, the height of a peak is dependent on the height of other peaks in the periodogram. Therefore, we cannot consider the above-mentioned prewhitening as the final procedure. We have to fit all the frequencies together to improve the accuracy of the real values of the frequencies. For that purpose, we apply an extension of the HMM method made for a multifrequency adjustment. This method was introduced by Gosset et al. (2001, see Eqs A13 to A19). Though this technique is effective for light curves composed of few points ($\sim$ 800 points), it is unsuitable (given the excessive computing time) for the CoRoT light curves with a very large number of datapoints (almost 80000). Consequently, we use this technique to extract blocks of 8 or 10 frequencies at the same time, depending on whether the light curves are binned or not. This multifrequency algorithm thus takes into account the mutual influence of the different frequencies and investigates inside the natural widths of the individual selected peaks several positions, i.e., refined values for each of the frequencies to find the new best fit. The frequencies generated by this method constitute the definitive lists reported in Appendix B. The error estimates for the frequencies were determined on the basis of the expressions given by Lucy & Sweeney (1971) and Montgomery & O'Donoghue (1999):

$$\begin{aligned}
\epsilon(f) &= \frac{\sqrt{6}}{\pi} \frac{\sigma}{A_f \sqrt{N_0}\, \Delta T} \\
\epsilon(A_f) &= \sqrt{\frac{2}{N_0}} \sigma \\
\epsilon(\phi_f) &= \sqrt{\frac{2}{N_0}} \frac{\sigma}{A_f}
\end{aligned}$$

where f, A_f, ϕ_f are the frequency, its amplitude and its phase, respectively, whereas N_0, ΔT and σ are the number of datapoints in the light curve, the run duration, and the standard deviation of the current data, respectively. In addition to the extraction of frequencies, we also search for the potential links between the frequencies. In this context, we examine for each light curve the

possible harmonics and the frequency combinations so that $f_1 + f_2 = f_3$. We also implement, from a backtracking algorithm, a code to find, at each frequency spacing, the larger frequency chain (f_0, $f_0 + \Delta f$, $f_0 + 2\Delta f$, ...). The idea behind the backtracking is the search for solution among all available candidates. Backtracking is a progressing algorithm that keeps track of each new explored frequency. Each element is eliminated as soon as it does not satisfy the criterion to reach the solution. To determine the number of components in a chain at a given frequency, we assume that $f_0 + n\Delta f$ equals a listed frequency if this frequency and $f_0 + n\Delta f$ differ by less than the step size we use in the analysis, i.e., 0.015 d^{-1}. Finally, we also analyze the temporal variations of the detected frequencies. For that purpose, sliding windows, with lengths of 3 and 10 days and shifted with a step of one day, are used on the light curves. Then we apply the HMM method on each frame. All these techniques allow us to deeply investigate the CoRoT light curves in order to extract their frequency content as well as to compare them with theoretical models.

5.4.3 Significance levels for the CoRoT data

Identifying the *significant* frequencies present in the CoRoT data is not an easy task. The evaluation of the absolute significance of a peak in a periodogram of a time series with an uneven sampling is already a controversial problem (Rauw et al. 2008) but, in addition, the expression of the probabilities has never been applied to such large datasets. At last, as we will see later, the semi-amplitude spectra of several stars are affected by red noise[10], thereby making the determination of their significance levels more difficult.

Generally, this determination is established on the basis of a null hypothesis of white noise[11]. For that purpose, we must check whether peaks detected in the semi-amplitude spectrum might result from random variations rather than representing a periodic signal. We thus apply a statistical test to establish whether the frequencies are significant, especially for those with smaller amplitudes. The probability that the power at a preselected frequency exceeds a threshold z is given by

$$\text{Prob}[Z > z] = e^{-z}, \tag{5.1}$$

where $z = P_f/\sigma_0^2$ with P_f the power in the power spectrum at the frequency f which is related to the semi-amplitude periodogram by $P_f = N_0 A_f^2/4$ with N_0, the number of datapoints and A_f the semi-amplitude at the frequency f. Moreover, σ_0^2 represents the variance of the data. This value is estimated from the data before removing a given frequency. The probability that a value larger than z is caused by random noise thus decreases for peaks with a large amplitude in the periodogram (Cuypers 1987).

However, if several frequencies are inspected at the same time for searching the highest peak, a statistical penalty must be paid (Scargle 1982). In the case of an evenly sampled time series, the statistic $Z_{\max} = \max_f Z(f)$ with $f \in f_{\text{Fourier}}$ where the Fourier frequencies $f_{\text{Fourier}} = k/\Delta T$ with $k = 1, \lfloor (N_0 - 1)/2 \rfloor$ ($\lfloor \cdot \rfloor$ corresponding to the integer part) represents the set of independent frequencies to be inspected with N_0 the number of points in the dataset. Then, $Z_{\max}$ obeys to

$$\text{Prob}[Z_{\max} > z] = 1 - (1 - e^{-z})^{\frac{N_0}{2}} \tag{5.2}$$

When the sampling is uneven, periodograms such as those of Scargle (1982), Ferraz-Mello (1981) and HMM preserve Eq. 5.1 but not Eq. 5.2. This is precisely due to the fact that the powers at

[10]The red noise is a random signal whose the power spectrum decreases with the increase of frequencies.

[11]The white noise is a random signal with an uniform power spectrum over a wide range of frequencies.

the different frequencies are no more independent. Horne & Baliunas (1986) thus suggested to modify Eq. 5.2 by substituting $N_0/2$ by the value of $N_{\rm eff}$ which is estimated through simulations. However, in the case of even sampling, they found $N_{\rm eff} \sim N_0$ which contradicts Eq. 5.2. The paper of Horne & Baliunas (1986) contains inaccuracies and errors which were reported in a series of different papers (Cuypers 1987; Schwarzenberg-Czerny 1998; Frescura et al. 2008). In addition, Gosset (2007) presented a counter-indication to the prescription of Horne & Baliunas (1986) of using Eq. 5.2 with the $N_{\rm eff}$ value as a free parameter. Gosset (2007) argued that this formula is not adequate since the widespread practice to oversample the power spectrum in the case of unevenly distributed sampling implies that peaks are statistically larger (see also Frescura et al. 2008).

Therefore, we use the criterion suggested by Gosset (2007):

$$\text{Prob}[Z_{\max} > z] = 1 - e^{-e^{(-\alpha z + \ln(0.8 N_0))}} \tag{5.3}$$

with $\alpha = 0.93$. The α parameter and the value of 0.8 were derived from a series of simulations made on white-noise curves. We note however that Eq. 5.3 is not quite different from Eq. 5.2. Indeed,

$$\begin{aligned} e^{-e^{(-\alpha z + \ln(0.8 N_0))}} &= e^{-e^{(-\alpha z)} 0.8 N_0} \\ &= (e^{-e^{-\alpha z}})^{0.8 N_0} \\ &\cong (1 - e^{-\alpha z})^{0.8 N_0} \end{aligned}$$

Actually, Eq. 5.3 is an asymptotic form of Eq. 5.2 that appears in the expression of the distribution of extreme values over a set of exponentially distributed variables. The new expression given by Eq. 5.3 is thus stricter than Eq. 5.2. Both are perfectly suited only for even sampling but provide a good approximation in cases of gapped data. This is particularly true for the CoRoT sampling which is more reminiscent of a regular sampling with a few gaps. Unfortunately, this formula was determined on the basis of simulated curves having about 1000 datapoints whilst the CoRoT light curves contain about 80000 datapoints, thereby making this criterion untested for such data. When we increase the amount of datapoints, the value of 0.8 possibly becomes unsuitable and should be adapted. That could only be done through heavy additional simulations which are expensive in CPU time. Therefore, we decide to adapt the data by binning the CoRoT light curves with a step of one fiftieth of a day i.e., with a pseudo-Nyquist frequency located at 25 d^{-1}, thereby reducing the number of datapoints to about 1700. We do this process after having checked that no clear signal is present above 25 d^{-1}. In this way, we do not miss any crucial information in our analysis. We note however that for the paper presenting the results of the photometric analysis of Plaskett's Star (Mahy et al. 2011a), we decide to bin with a step of one twentieth of a day, implying a set of 684 points. This choice is made because most of the power is found at low frequencies, as we will see in the next section.

5.4.4 Analysis of the photometric CoRoT data

HD 47129: Plaskett's Star

Plaskett's Star (O 8III/I+O 7.5V/III, Linder et al. 2008) is the most luminous star among the O-type targets observed by CoRoT. This star interests the scientists for a long time since, in spite of numerous investigations, it still hides a part of mystery. This binary system is composed of two very massive and luminous O-type stars with minimum masses, derived by Linder et al. (2008), of about 45.4 and 47.3 $M_\odot$, thus implying a mass ratio $M_{\rm S}/M_{\rm P}$ of about 1.05 ± 0.05. Without

any eclipse or ellipsoidal variations in the light curves obtained from the ground, the real masses are always difficult to constrain. However, Rudy & Herman (1978) estimated an inclination of about $71° \pm 9°$ by using polarimetry. This result implies real masses of about 53.7 and 56.0 $M_\odot$ for the primary and the secondary, respectively. Moreover, the model atmospheres computed by CMFGEN for both components allowed Linder et al. (2008) to derive their wind and photospheric parameters. This analysis confirmed the N overabundance and the C depletion of the primary as well as projected rotational velocities of about 75 and 300 km s^{-1} for the primary and the secondary, respectively. This provides evidence that Plaskett's Star is a binary system in a post Roche lobe overflow evolutionary stage where the matter was transferred from the primary to the secondary component. Even though this analysis allowed to improve the understanding of that system, a discrepancy between the luminosity of both components and their dynamical masses remains unexplained. Linder et al. (2008) argued that these stars have spectral types that are too late for their masses, implying a larger distance than the current one for that system. Therefore, the membership of Plaskett's Star to the Mon OB2 association was questioned. However, if we compare the systemic velocity of Plaskett's Star, estimated to 30.6 ± 1.8 km s^{-1} by Linder et al. (2008), with the radial velocities of other O-type stars situated in Mon OB2 association (Mahy et al. 2009), it appears that these values agree with each other, suggesting that Plaskett's Star belongs to this association. Awaiting a precise parallax determination with the future Gaia mission, only the unprecedented quality of the CoRoT data may bring a new light on the system. The results of this analysis are reported in Mahy et al. (2011a, see the end of this section).

The CoRoT unflagged time series started on HJD = 2 454 748.485467 and ended on HJD = 2 454 782.819956, i.e., a 34.334489-day run. For the analysis described in Mahy et al. (2011a), we have converted the flux in magnitude. However, in the framework of this thesis, we present the results expressed in flux to be consistent with the analyses of the other stars.

The light curve and the semi-amplitude spectrum are displayed in the top and bottom panels of Fig. 5.7, respectively. We detect two main structures in the semi-amplitude spectrum. The first one is composed of the frequencies $f_1 = 0.069$, $f_2 = 0.139$ and $f_3 = 0.208$ d^{-1} and is related to the orbital motion of the system. f_1 is linked to the orbital period ($P_{\rm orb} \sim 14.39625$ days; $f_{\rm orb} \sim 0.06946$ d^{-1}) whilst f_2 and, to a lesser extent, f_3, the two harmonics of f_1, describe small amplitude ellipsoidal variations. On the basis of these three frequencies, we have reconstructed in Mahy et al. (2011a) the information on the ellipsoidal variations and we have fitted it using the NIGHTFALL program. We observe at Fig. 7 in Mahy et al. (2011a) a peak-to-peak variation of about 19 mmag for this recombined signal. Given the absence of grazing eclipses, the inclination is estimated between $i = 30°$ and $i = 80°$ with the current best fit at $i = 67°$. In addition, the presence of a hot spot is needed to correctly reproduce the signal. This spot is either on the rear side of the secondary star (i.e., turned away from the primary) or located on the side of the primary star facing the secondary component. The latter configuration seems more plausible, especially considering the wind interaction model of Linder et al. (2008). The hot spot would be located at a longitude between 345° and 355° (0° corresponding to the direction of the secondary star and 90° indicating the direction of the motion of the primary). Furthermore, this spot would have a temperature ratio of about 1.9 with respect to the surface temperature of the primary. The radius of the spot is found to be about $8° - 10°$ for most solutions, except for those with very high orbital inclinations and low Roche lobe filling factors.

The second significant structure includes seven frequencies: $f_1 = 0.823$, $f_2 = 1.646$, $f_3 = 2.469$, $f_4 = 3.292$, $f_5 = 4.115$, $f_6 = 4.938$ and $f_7 = 5.761$ d^{-1}. The most probable interpretation of these frequencies is that they could correspond to non-radial pulsations (see the full discussion in the paper by Mahy et al. 2011a). Indeed, main-sequence star models with a metallicity of

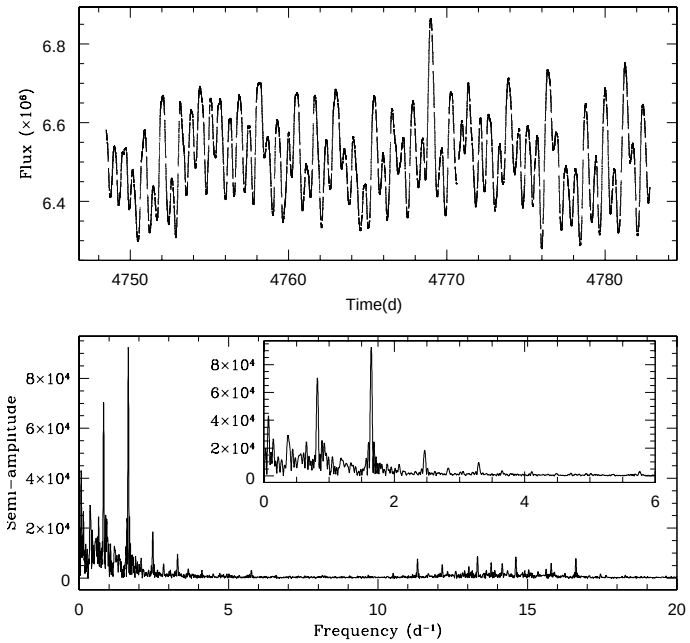

Figure 5.7: *Top*: Unflagged light curve of Plaskett's Star observed with CoRoT during the SRa02 run. *Bottom*: The semi-amplitude spectrum of the light curve of Plaskett's Star computed with the HMM method. The inset shows a zoom-in on the semi-amplitude spectrum in the low-frequency domain.

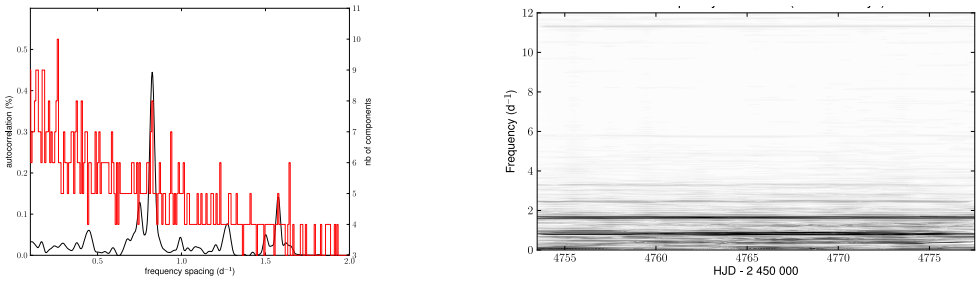

Figure 5.8: *Left*: Autocorrelation functions (black curve) of the semi-amplitude spectrum of Plaskett's Star and number of spectral components in a chain with a given frequency spacing (red curve). *Right*: Time-frequency analysis of Plaskett's Star light curve. The used sliding window has a width of 10 days.

$Z = 0.015$, masses between 30 and 70 $M_{\odot}$ and different mass-loss rates were computed by M. Godart (as part of her PhD thesis at the University of Liège) with the ATON code (Ventura et al. 2008). These models reported possible non-radial pulsations of frequency $f \sim 0.8$ d^{-1} generated by modes with $l = 2,\ 3$ or 4 which can match our observations. Moreover, we investigated the temporal variations of the detected frequencies by computing the time-frequency periodogram in the range of $[0-6]$ d^{-1} (Fig. 5.8, right panel). This analysis shows that the set of seven frequencies are present during the entire observing run which is consistent with possible non-radial pulsations. Both structures are clearly real, but there may be additional real signals. We therefore have to investigate the significance of the other frequencies.

Since no outstanding peak, different from the aliases of the above mentioned structures, is detected in a frequency domain beyond 10 d^{-1}, we bin the light curve with a step of one twentieth of a day, i.e., with a pseudo-Nyquist frequency of $f_{Ny} = 10$ d^{-1}, reducing the CoRoT data into a set of 684 points. Under a null hypothesis of white noise, we detect 79 frequencies at a significance level of 0.01. If we bin the light curve with a step of one fiftieth, we detect this time 174 significant frequencies (given in Appendix B).

We search for frequency combinations of type $f_1 + f_2 = f_3$ and we look at the spacing of these combinations. Among the 174 frequencies judged significant under the null hypothesis of white noise, we find 204 different frequency combinations. We also look at both the autocorrelation function of the power periodogram and the number of components and we find in a chain (f_0, $f_0+\Delta f$, $f_0+2\Delta f$,...) with an assumed frequency spacing Δf. We focus on the $[0-12]$ d^{-1} domain to avoid the effects related to the satellite's orbital period (13.972 d^{-1}) and we only consider for the frequency spacing the range from 0.1 to 2.0 d^{-1}. The left panel of Fig. 5.8 shows that the autocorrelation and the number of components agree at $\Delta f \cong 0.82$d^{-1}. This spacing reveals that an eighth frequency with a value of $f = 6.593$ d^{-1} could be connected to the set of seven harmonics reported above.

By looking closer at the periodogram, we clearly see that the semi-amplitude spectrum is affected by an excess of power at low frequencies. This effect represents either the reality of the underlying deterministic signal or a signal partly made of red noise, i.e. partly stochastic. In the latter case, the null hypothesis of white noise would be no longer appropriate for these data. We come back on this interesting property in Section 5.4.5, after having presented the main results concerning the other stars.

A&A 525, A101 (2011)
DOI: 10.1051/0004-6361/201014777

Astronomy & Astrophysics

Plaskett's star: analysis of the CoRoT photometric data⋆,⋆⋆

L. Mahy[1], E. Gosset[1,⋆⋆⋆], F. Baudin[2], G. Rauw[1,†], M. Godart[1], T. Morel[1], P. Degroote[3], C. Aerts[3,5], R. Blomme[4], J. Cuypers[4], A. Noels[1], E. Michel[6], A. Baglin[7], M. Auvergne[8], C. Catala[8], and R. Samadi[8]

[1] Institut d'Astrophysique et de Géophysique, University of Liège, Bât. B5C, Allée du 6 Août 17, 4000 Liège, Belgium
e-mail: mahy@astro.ulg.ac.be
[2] Institut d'Astrophysique Spatiale (IAS), Bâtiment 121, 91405 Orsay Cedex, France
[3] Instituut voor Sterrenkunde, K.U. Leuven, Celestijnenlaan 200D, 3001 Leuven, Belgium
[4] Royal Observatory of Belgium, Ringlaan 3, 1180 Brussel, Belgium
[5] Department of Astrophysics, IMAPP, University of Nijmegen, PO Box 9010, 6500 GL Nijmegen, The Netherlands
[6] LESIA, CNRS, Université Pierre et Marie Curie, Université Denis Diderot, Observatoire de Paris, 92195 Meudon Cedex, France
[7] Laboratoire AIM, CEA/DSM-CNRS-Université Paris Diderot, CEA, IRFU, SAp, centre de Saclay, 91191 Gif-sur-Yvette, France
[8] LESIA, UMRR8109, Université Pierre et Marie Curie, Université Denis Diderot, Observatoire de Paris, 92195 Meudon Cedex, France

Received 12 April 2010 / Accepted 22 October 2010

ABSTRACT

Context. The second short run (SRa02) of the CoRoT space mission for asteroseismology was partly devoted to stars belonging to the Mon OB2 association. An intense monitoring has been performed on Plaskett's star (HD 47129) and the unprecedented quality of the light curve allows us to shed new light on this very massive, non-eclipsing binary system.
Aims. We particularly aimed at detecting periodic variability that might be associated with pulsations or interactions between both components. We also searched for variations related to the orbital cycle that could help to constrain the inclination and the morphology of the binary system.
Methods. We applied an iterative Fourier-based prewhitening and a multiperiodic fitting procedure to analyse the time series and extract the frequencies of variations from the CoRoT light curve. We describe the noise properties to tentatively define an appropriate significance criterion and, in consequence, to only point out the peaks at a certain significance level. We also detect the variations related to the orbital motion and study them with the NIGHTFALL programme.
Results. The periodogram computed from Plaskett's star CoRoT light curve mainly exhibits a majority of peaks at low frequencies. Among these peaks, we highlight a list of 43 values, notably including two different sets of harmonic frequencies whose fundamental peaks are located at about 0.07 and 0.82 d^{-1}. The former represents the orbital frequency of the binary system, whilst the latter could probably be associated with non-radial pulsations. The study of the 0.07 d^{-1} variations reveals a hot spot most probably situated on the primary star and facing the secondary.
Conclusions. The investigation of this unique dataset constitutes a further step in the understanding of Plaskett's star. These results provide a first basis for future seismic modelling and put forward the probable existence of non-radial pulsations in Plaskett's star. Moreover, the fit of the orbital variations confirms the problem of the distance of this system which was already mentioned in previous works. A hot region between both components renders the determination of the inclination ambiguous.

Key words. stars: early-type – stars: oscillations – stars: individual: HD 47129 – binaries: general

1. Introduction

Plaskett's star, or HD 47129, has long been considered as one of the most massive binary systems in our Galaxy. For nine decades, this star has not stopped to fascinate by its complexity. It has been the subject of several investigations in different wavelength domains, but despite these efforts, the system is still not fully understood.

Plaskett's star is a non-eclipsing binary (Morrison 1978) composed of two very massive and luminous O-type stars. The secondary component features broad and shallow stellar lines, suggesting that this star rotates rapidly. Its projected rotational velocity has been estimated to be close to 300 km s^{-1}, while that of the primary has been measured at about 75 km s^{-1} (Linder et al. 2008). As a consequence of this high rotation speed, the secondary star probably presents a temperature gradient between the poles and equator that could bias the determination of its spectral type, but most importantly, the secondary has a rotationally flattened wind. This configuration probably accounts for several properties of the wind interaction zone. The study of the Hα region by Wiggs & Gies (1992) and Linder et al. (2008) as well as the analysis of Linder et al. (2006) in the X-ray domain have confirmed this assumption.

Bagnuolo et al. (1992) applied a tomographic technique to the International Ultraviolet Explorer (IUE) data to separate the contribution of the secondary star from the primary's spectrum. Their investigation of the individual spectral components has

⋆ The CoRoT space mission was developed and is operated by the French space agency CNES, with participation of ESA's RSSD and Science Programmes, Austria, Belgium, Brazil, Germany and Spain.
⋆⋆ Table 2 is only available in electronic form at http://www.aanda.org
⋆⋆⋆ Senior Research Associate FRS-FNRS.
† Research Associate FRS-FNRS.

provided the spectral types of O7.5 I and O6 I for the primary and secondary stars, respectively, and a mass ratio of $M_2/M_1 = 1.18 \pm 0.12$. Assuming an inclination of $71 \pm 9°$ as estimated by Rudy & Herman (1978) from polarimetry, they found masses equal to 42.5 $M_\odot$ for the primary and 51.6 $M_\odot$ for the secondary.

Linder et al. (2008) found from high-resolution optical spectra minimum masses of 45.4 and 47.3 $M_\odot$ for the primary and secondary, respectively, implying a mass ratio of about 1.05 ± 0.05. They also disentangled the spectra by using an algorithm based on the method of González & Levato (2006). The individual spectra indicated an O8 III/I+O7.5 V/III binary system. In addition, these authors used the model atmosphere code CMFGEN (Hillier & Miller 1998) to derive the wind and the photospheric properties of both components. The major point of their study is the confirmation of an N overabundance and a C depletion of the primary star, which provides additional proof for a binary system in a post-Roche lobe overflow evolutionary stage where matter has been transferred from the primary to the secondary star.

The most disturbing point concerning Plaskett's star however is the discrepancy between the luminosity of both components and their dynamical masses. Linder et al. (2008) explained that these stars have spectral types that are too late for their masses. A solution to this problem is to assume a larger distance of the star, although this would imply that Plaskett's star does not belong to the Mon OB2 association. Despite the numerous investigations undertaken to probe the physics of this binary system and its components, Plaskett's star still hides part of a mystery.

Even though Reese et al. (2009) have emphasized the difficulty to detect pulsation modes in rapidly rotating stars, there are some examples of rapidly rotating O stars (ζ Oph, Kambe et al. 1997; HD 93521, Howarth & Reid 1993; Rauw et al. 2008) where spectroscopic and photometric variability, which are probably related to non-radial pulsation modes with periods of a few hours, have been identified. These rapid rotators have properties quite reminiscent of those of the secondary component in Plaskett's star, which also displays line profile variability (Linder et al. 2008), although the existing spectroscopic data of the system are too scarce to characterize these variations properly. Asteroseismology could therefore provide new insight into the properties of the components of Plaskett's star.

For this purpose, but also to further constrain the binary system itself, Plaskett's star has been chosen as one of the CoRoT (Convection, Rotation and planetary Transits, Baglin et al. 2006; Auvergne et al. 2009) satellite targets in the Asteroseismology field. The unprecedented quality of the CoRoT light curve clearly allows us to search for variations linked to the orbital period of the system and to determine the possible existence of very low-amplitude variations caused by the presence of radial and non-radial pulsation modes for instance.

The present paper describes a complete and detailed analysis of the light curve of Plaskett's star observed by the CoRoT satellite. We organize it as follows. In Sect. 2 we present the CoRoT data. Section 3 is devoted to the frequency analysis and to a study of the noise properties of the data. In Sect. 4 we discuss the inclination of the binary system and some other results obtained from the analysis of the light curve. Finally, we set forth our conclusions in Sect. 5.

2. The CoRoT data

Plaskett's star was observed during the second CoRoT short run SRa02 pointing towards the anticentre of the Galaxy. The observations were made between 2008 October 08 (HJD = 2 454 748.485467) and 2008 November 12 (HJD = 2 454 782.819956). Hereafter, we will express the date as HJD – 2 450 000. The time series obtained is spread over $\Delta T = 34.334489$ days, with a sampling of one point every 32 s. This involves a frequency resolution of $1/\Delta T = 0.029125\ \mathrm{d}^{-1}$.

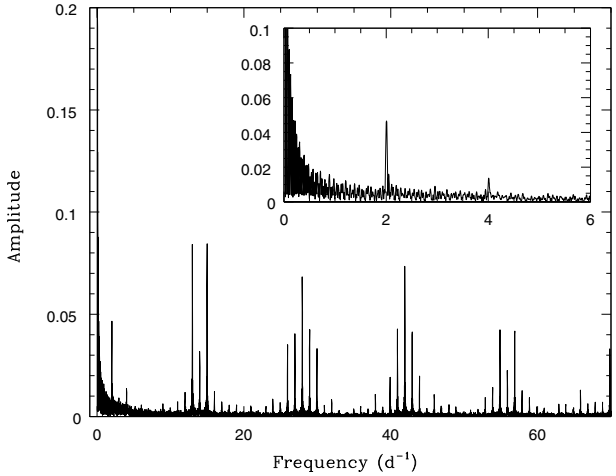

Fig. 1. Spectral window of the final version of the Plaskett's star light curve, observed during the second short run of the mission.

The raw light curve of Plaskett's star contains 92 696 points. At first, we discarded flagged points potentially corrupted by the instrumental conditions (e.g., the changes of CCD masks or the generation of outliers). These observations represent about 4.2% of the datapoints of the CoRoT light curve of Plaskett's star. In addition, we searched the CoRoT light curve for possible jumps or discontinuities caused by a change of the CCD temperature and corrected all of them. Secondly, we also discarded the flagged points associated with the environmental perturbations of the satellite that are mainly due to the regular passage through the South Atlantic Anomaly (SAA) and other Earth orbit perturbations (Auvergne et al. 2009). Because this passage occurs twice in a sidereal day, the spectral window (see the inset in Fig. 1) presents a structure composed of a first peak (4.6% of the amplitude) close to $2.007\ \mathrm{d}^{-1}$ and a second one (1.4% of the amplitude) close to $4.014\ \mathrm{d}^{-1}$. Moreover, gaps owing to the orbital period of the satellite (6184 s) produce other structures with peaks around $13.972\ \mathrm{d}^{-1}$ and their harmonics (Fig. 1). The percentage of lost datapoints because of environmental conditions is only 9.6% for HD 47129. In addition, the spectral window exhibits a 89.0% peak at $f = 2699.764\ \mathrm{d}^{-1}$. This corresponds to the sampling regularity with the highest frequency. Consequently, a pseudo-Nyquist frequency can be located at $f_{\mathrm{Ny}} = 1349.882\ \mathrm{d}^{-1}$ (leading to a step of 32.003 s). We use the word "pseudo" to point out that the aliasing is not pure.

An interpolation of all flagged points of the light curve to fill the gaps cleans the spectral windows of all these peaks, but this process introduces systematic effects that could generate erroneous values of the frequencies and affect the scientific results. Accordingly, we decided not to interpolate among the remaining points of the light curve.

All stars observed in the CoRoT field of view present a global slope in their light curve with probably an instrumental origin (Auvergne et al. 2009, attributed this drift to the ageing of the CCDs). Even though the light curve of Plaskett's star does not seem to be affected by it, maybe because of its high flux variability, we decided to remove this long-term trend. In order not to bias the possible orbital or long-term variations present

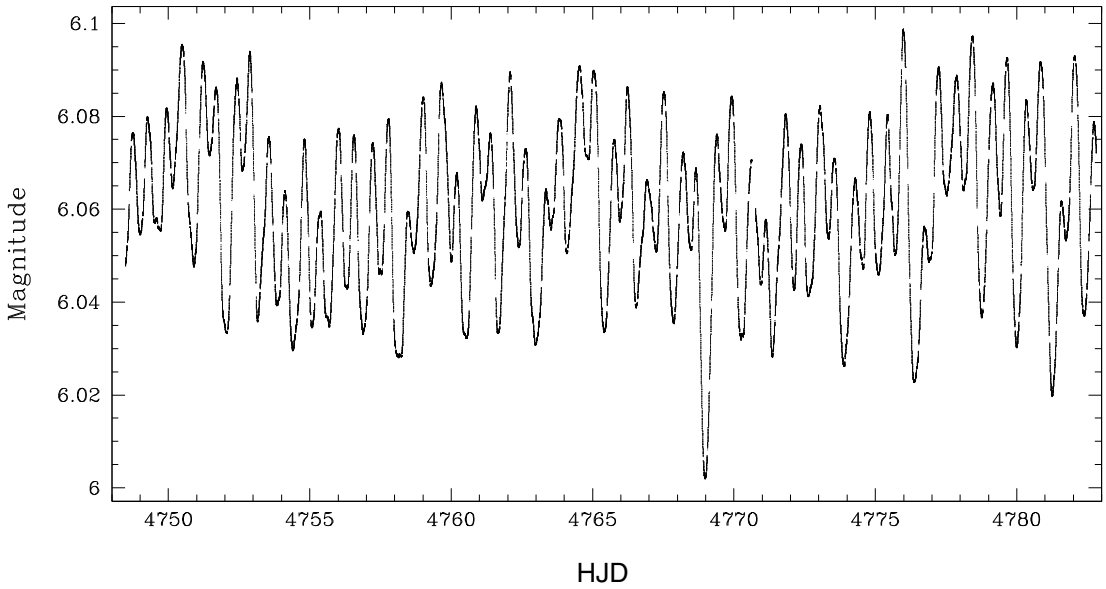

Fig. 2. Full detrended CoRoT light curve of Plaskett's star, containing 79 896 points, observed over about 34.33 days and converted to magnitude. All gaps present in the data are due to the flagged points described in Sect. 2.

in the light curve, the strictly linear trend appears to be the best choice among the different possible trends. However, as we will show in Sect. 3, the low frequencies close to 0 still appear in the semi-amplitude spectrum after removing the trend.

Finally, the CoRoT light curve has also been converted to magnitude from the expression $m = -2.5\log(F) + C$ where F gives the CoRoT flux expressed in $e^- s^{-1}$ and C represents a calibration constant. We estimated this constant at a value of 23.09 ± 0.01 mag after comparing the CoRoT magnitude to that in the V-band quoted by Linder et al. (2008). We note that this conversion in magnitude does not change the decomposition in frequencies reported below. The final version of Plaskett's star light curve (Fig. 2) is composed of 79 896 points.

3. Analysis of Plaskett's star CoRoT light curve

3.1. Looking for periodic structures

The CoRoT light curve confirms that Plaskett's star is not an eclipsing binary although we detect variations that could be linked to the orbital motion of the binary system ($P_{\rm orb}$ = 14.39625 days, see Linder et al. 2008). The light curve also presents large amplitude peak-to-peak variations on shorter time scales. In order to perform a complete investigation of the frequencies present in the CoRoT light curve, we applied a Fourier analysis based on the Heck et al. (hereafter HMM) technique (Heck et al. 1985; revised by Gosset et al. 2001). We emphasize that this method is comparable to the Ferraz-Mello one (Ferraz-Mello 1981) and is especially designed to handle time series with unevenly spaced data. Moreover, its mathematical expression for the power spectrum has the advantage of correcting some deficiencies of other methods such as the one of Scargle (1982). The Fourier technique of HMM used here is equivalent at each individual frequency to a least-squares fit of a sine function (Gosset et al. 2001). In the present paper we will actually use the semi-amplitude spectrum instead of the classical power spectrum, which means that the ordinates represent the amplitude term in front of the sine function.

The semi-amplitude spectrum (Fig. 3) clearly shows that most of the power is concentrated in the $f \leq 6.0$ d^{-1} frequency domain and that aliases generated by the satellite orbital cycle are present between 11.0 and 17.0 d^{-1}. Although we removed the linear trend from the dataset, the signal remains close to the frequency 0.0 d^{-1}. The spectrum is dominated by a set of frequencies distributed according to a regular pattern including the fundamental frequency at about 0.82 d^{-1} and its possible harmonics at about 1.64 d^{-1}, 2.46 d^{-1}, 3.28 d^{-1} and 4.10 d^{-1}. The 2.007 d^{-1} aliases of the two first (main) frequencies are also visible at f = 2.83 d^{-1} and 3.65 d^{-1}. Besides these frequencies, the semi-amplitude spectrum confirms the presence of f = 0.07 d^{-1}, f = 0.14 d^{-1} and probably f = 0.21 d^{-1}, i.e., the orbital frequency and its harmonics, which constitute a second set of frequencies. Further outstanding peaks are also present at $f \sim 0.35$ d^{-1}, $f \sim 0.65$ d^{-1} and $f \sim 0.95$ d^{-1}. The first one has a wider peak that expected from the time basis, it could actually be a blend of several frequencies (at least two, or one plus an alias of f = 1.64 d^{-1}).

In order to analyse the time series in a more systematic way, the in-depth determination of the different frequencies was done in two steps. First, we proceeded to a classical iterative prewhitening of the signal, frequency by frequency. At each step, the semi-amplitude spectrum is computed and the frequency value is selected by the position of the highest peak in the spectrum. The amplitude and the phase, corresponding to this frequency, are directly computed from the Fourier function. We however initiated the process by removing the set of five frequencies composed, notably, of the two highest peaks found in the periodogram (f = 0.82 and f = 1.64 d^{-1}) and the frequencies belonging to this set. Since the frequency f = 0.82 d^{-1} presents possible harmonics, we decided to perform the fit on all of them together, taking into account the existing correlation between the power at the different frequencies. We thus designed a generalized periodogram that gives at each frequency the power included in a frequency and *its harmonics*. The method is based on a particular case of the extension of the HMM method proposed by Gosset et al. (2001). The generalized periodogram exhibits the f = 0.82 d^{-1} peak characterized by the natural width, thus further confirming that this sequence of peaks are indeed true harmonics. These frequencies were removed altogether from the data. Next, the semi-amplitude spectrum has

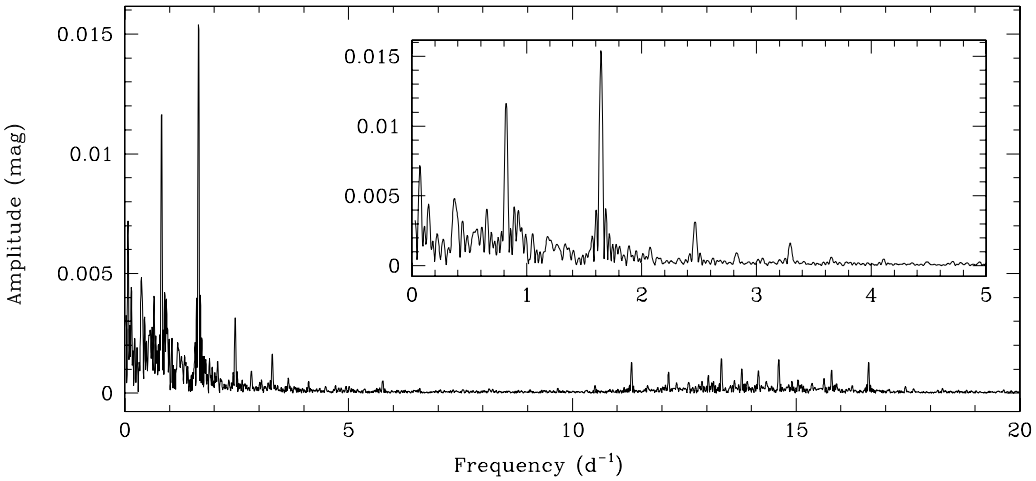

Fig. 3. Semi-amplitude spectrum of the light curve of Plaskett's star computed by the HMM method from the unflagged CoRoT data. We clearly see the aliases due to the orbital period of the satellite near 11–17 d^{-1}. The inset shows a zoom-in on the semi-amplitude spectrum in the low-frequency domain.

been computed again to detect the new highest peak to remove. The analysed data are prewhitened for this frequency and we repeated this process until reaching the noise level of the data. Figure 4 compares the semi-amplitude spectra of the data and of the data prewhitened for the first 20, the first 40 and the first 60 frequencies.

Although efficient, the iterative removing of several frequencies one by one by using the basic HMM method cannot be the final procedure. Because the light curve presents gaps and the sampling is irregular, the height of a peak is dependent on the height of other peaks in the periodogram. Therefore, we need to fit all the listed frequencies together. For this purpose, we used the extension of the HMM Fourier method to the multifrequency adjustment, a high-order Fourier method introduced by Gosset et al. (2001, their Eqs. (A13) to (A19)). Because of an excessive computation time, we applied the multifrequency analysis to binned data to be able to deal with some amount of frequencies at the same time. Indeed, since no peak is clearly dominant above 10 d^{-1}, we binned the data with a step of one twentieth of a day, i.e., with a pseudo-Nyquist frequency of $f_{\rm Ny} = 10$ d^{-1}, reducing the CoRoT light curve into a set of 684 points. The multifrequency algorithm thus takes into account the mutual influence of the different frequencies and investigates inside the natural widths of the individual selected peaks several positions, i.e., refined values for each of the frequencies to find the current best fit.

The results obtained by both methods confirm the detection in the semi-amplitude spectrum of a first structure composed of a main frequency and six harmonics. The fundamental peak is situated around 0.823 d^{-1} and its harmonics around 1.646 d^{-1}, 2.469 d^{-1}, 3.292 d^{-1}, 4.115 d^{-1}, 4.938 d^{-1}, and 5.761 d^{-1}, respectively. Furthermore, we also clearly detect the peak corresponding to the orbital period of Plaskett's star ($f \sim 0.069$ d^{-1}) as well as two harmonics of this frequency. We also report the detection of two frequencies, actually unresolved, at $f = 0.368$ d^{-1} and $f = 0.399$ d^{-1}.

The set of frequencies computed in this way represents the final set (listed in Appendix). We stopped the iterative multifrequency procedure when the noise level was reached (statistically). This critical level is particularly difficult to estimate and constitutes the main topic of the next section.

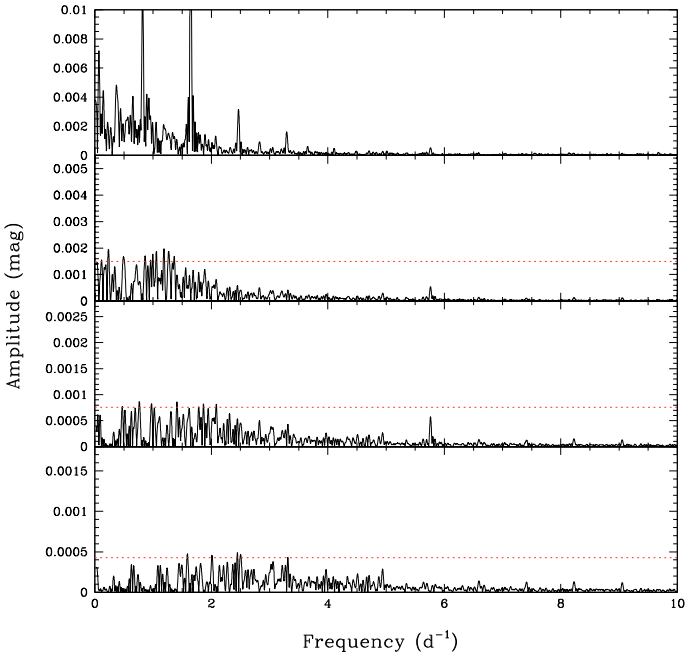

Fig. 4. For comparison, the top panel shows the semi-amplitude spectrum before prewhitening, the subsequent panels represent the semi-amplitude spectrum after prewhitening 20, 40, and 60 frequencies, respectively. The red lines exhibit the critical level at the significance level of 0.01 under a null hypothesis of white noise.

3.2. The noise properties and significant frequencies

From the analysis of the time series illustrated in Figs. 3 and 4 we conclude that there is a clear excess of power at low frequencies. It represents either the reality of the underlying deterministic signal or that the signal is partly made of red noise, i.e., is partly stochastic. Visible on the log-log plot (Fig. 5) of the periodogram of Plaskett's star, this excess of power at low frequencies ($\log f \leq 0.6$) can be described for example as suggested by Stanishev et al. (2002), by using a function of the form

$$P(f) = \frac{C}{1 + (2\pi\tau f)^{\gamma}}, \quad (1)$$

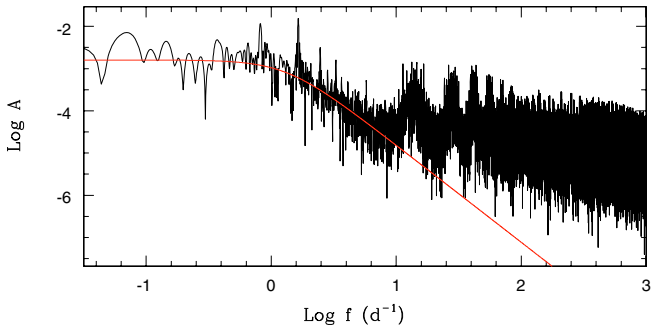

Fig. 5. Log-log plot of the semi-amplitude spectrum of Plaskett's star. The red curve represents the fitted function (Eq. (1)).

with γ related to the slope of the linear part and τ an estimation of the mean duration of the dominant transient structures in the light curve. A least-square fit of the semi-amplitude spectrum in the low-frequency domain yields the parameters $\gamma = 2.3$ and $\tau = 0.12$ d^{-1}. Assuming an origin at least partly intrinsic to the star, several processes could explain the behaviour of the stochastic component of the signal. It could be either due to an onset of clumping at the stellar photosphere or, if we make the parallelism with the works of Harvey (1985) and Aigrain et al. (2004) in helioseismology, to some kind of granulation. Indeed, Cantiello et al. (2009) suggested that the convection zone induced by the iron opacity bump can have an impact on the stellar surface behaviour and thus could be responsible for the existence of red noise. Belkacem et al. (2010) further suggested that this iron convection zone could generate stochastically excited modes in massive stars. Finally, other alternatives are also mentioned to explain this origin as the non-linearity (for more details, see e.g., Perdang 2009).

Despite the possible presence of red noise, it is therefore important to check whether peaks detected in the semi-amplitude spectrum could result from random variations rather than representing a periodic signal. However, the evaluation of the absolute significance of a peak in a periodogram of a time series with an uneven sampling is a controversial problem (e.g., Rauw et al. 2008; Frescura et al. 2008). Furthermore, the detection threshold level will be affected by this assumption of coloured noise, making its estimate more difficult. As a first order indication, we therefore applied a statistical test to establish whether the frequencies are significant, especially for those with smaller amplitudes. The probability that the power at several inspected frequencies exceeds a threshold z under the null hypothesis of a stochastic process of variance σ_f^2 (function of frequencies) is given by the empirical formula of Gosset (2007):

$$\mathrm{Prob}[Z_{\max} > z] = 1 - \left(\mathrm{e}^{-\mathrm{e}^{-0.93z + \ln(0.8N_0)}}\right), \quad (2)$$

where $Z_{\max} = \max_{0<f<f_{\mathrm{Ny}}} Z(f)$, $z = P_f/\sigma_f^2$ with P_f the power in the power spectrum at the frequency f, which is related to the semi-amplitude by $P_f = N_0 A_f^2/4$ and N_0 represents the number of datapoints. Although this expression is only adapted to even sampling, it remains a good approximation (since no better alternative exists) for uneven ones, especially for the CoRoT sampling, which is more reminiscent of a regular but gapped one. We adopted the number of datapoints in the binned light curve, i.e., $N_0 = 684$. A first estimation of the significance level can be made by adopting a null hypothesis of white noise (i.e., σ_f^2 not depending on f). In this case, we detect 79 frequencies (60 frequencies) at a significance level of 0.01 (0.001) or lower.

Table 1. Table of main frequencies.

n	Freq. (d^{-1})	Semi-Ampl. (mmag)	SL$_{\mathrm{White}}$	SL$_{\mathrm{red}}$	Comments
2	1.646	15.413	0.000	0.000	$2f_2$
1	0.823	11.373	0.000	0.000	
8	0.069	6.660	0.000	0.000	
11	0.368	5.026	0.000	0.000	
12	0.650	3.732	0.000	0.000	
9	0.139	3.410	0.000	0.000	$2f_3$
3	2.469	3.124	0.002	0.000	$3f_2$
15	0.932	3.121	0.000	0.000	
16	0.441	3.099	0.000	0.000	
14	0.888	3.069	0.000	0.000	
13	0.399	3.007	0.000	0.000	
17	0.542	2.620	0.000	0.000	
18	0.799	2.567	0.000	0.000	
21	0.572	2.524	0.000	0.000	
20	0.607	2.406	0.000	0.000	
22	1.212	2.042	0.000	0.000	
23	1.185	1.904	0.000	0.000	
28	1.264	1.877	0.000	0.000	
24	1.056	1.864	0.000	0.000	
30	1.334	1.786	0.000	0.000	
27	1.000	1.616	0.000	0.007	
32	1.359	1.598	0.000	0.000	
4	3.292	1.533	1.000	0.000	$4f_2$
33	1.558	1.362	0.000	0.000	
37	1.890	1.124	0.000	0.000	
38	1.686	1.079	0.000	0.000	
46	1.865	0.860	0.000	0.000	
47	2.085	0.834	0.000	0.000	
63	2.312	0.576	0.001	0.001	
7	5.761	0.525	1.000	0.000	$7f_2$
68	2.825	0.510	0.001	0.000	Alias + f_2?
69	2.446	0.496	0.001	0.004	
71	2.503	0.463	0.002	0.009	
74	3.314	0.425	0.004	0.000	
76	3.061	0.386	0.013	0.000	
5	4.115	0.350	1.000	0.000	$5f_2$
6	4.938	0.275	1.000	0.000	$6f_2$
95	3.969	0.256	0.110	0.000	
102	4.508	0.225	0.197	0.000	
106	4.709	0.204	0.366	0.000	
115	4.881	0.182	0.411	0.000	
148	5.646	0.133	0.298	0.000	
150	5.698	0.127	0.412	0.001	

A second approach is to adopt a more complex stochastic process as null hypothesis. In this case, we defined a stochastic distribution law by assuming an empirical function based on white noise above $f = 6.3$ d^{-1} and on red noise defined by the continuum in the power spectrum below $f = 6.3$ d^{-1}. We normalized the above fitted function in order to define a properly scaled σ_f^2 function. Under this refined null hypothesis of red noise, the number of significant frequencies decreases to about 43 (38) at a significance level of 0.01 (0.001). Table 1 exhibits the details of the significant frequencies detected under the null hypothesis of red noise. The columns represent the sequence number of the frequency, the frequency itself, its amplitude, the significance level under the null-hypothesis of white and red noise and some comments, respectively.

If we look at the evolution of the data variance with the iterative prewhitening process (Fig. 6), we note that there is no jump in the curve, which underlines the difficulty to define a threshold. Indeed, both structures formed by the fundamental peaks at

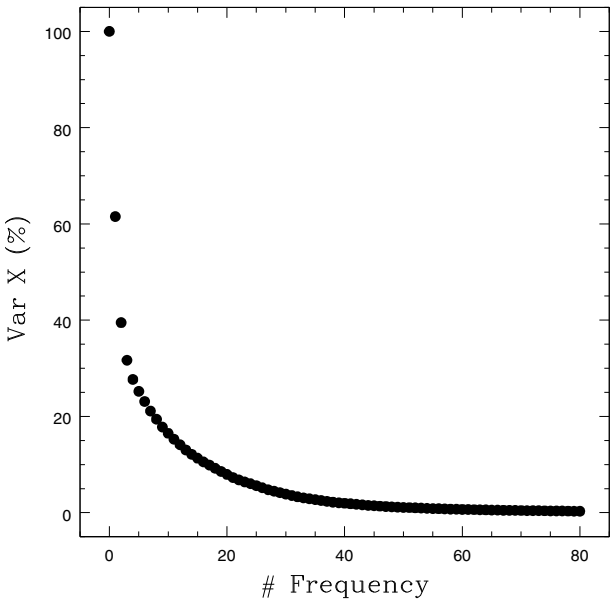

Fig. 6. Evolution of the relative variance of the prewhitened data as a function of the number of frequencies already detected by the multi-periodic algorithm.

$f = 0.823$ and $f = 0.069$ d^{-1} already explain 72% of the variance of the CoRoT light curve and, after 20 frequencies, the total variance of the prewhitened observations strongly decreased.

The decomposition of the signal into frequencies is a formal process that does not necessarily represent the physical truth. Moreover, it neglects non-linearities and complex phenomena. It is thus impossible to derive a list of frequencies free of contaminations. However, the truly existing frequencies (orbit, possible pulsations,...) should be part of this derived list (reported in the appendix). We also decided to use an additional method to contribute to the determination of the reliable frequencies, although this method is not perfect either. We split the data into two halves: a first one gathering the observations taken between HJD = 4 748.48 and 4 765.63 and a second one taking into account the data collected between HJD = 4 765.63 and 4 782.82. We applied the frequency research on each sample separately by using the same technique as above and we directly compared both frequency lists. This method allowed us to put forward a list of 30 frequencies common to both dataset.

The error estimate for the frequencies (listed in the appendix) is obtained from the expression given by Lucy & Sweeney (1971) and Montgomery & O'Donoghue (1999):

$$\epsilon(f) = \frac{\sqrt{6}}{\pi} \cdot \frac{\sigma}{\sqrt{N_0}\Delta T} \cdot \frac{1}{A}, \quad (3)$$

where σ is the standard deviation of the residuals, A expresses the semi-amplitude associated to the frequency, ΔT represents the observation span of time and N_0, the number of points of the binned sample (684). However, these formal errors are often underestimated compared to the actual ones (Degroote et al. 2009). The list of frequencies given in the Appendix contains 150 values and was stopped at the last significant (<0.01) frequency. The first 19 frequencies are highly significant against both null hypotheses (white and red noise), but are also present in both partitional datasets.

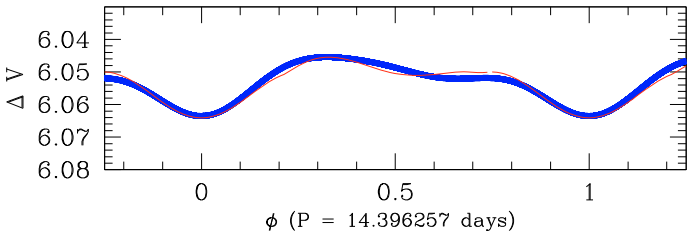

Fig. 7. Example of a model fit of the orbital part of the light curve of Plaskett's star. The parameters of the model (red thin curve) are $i = 67°$, $\text{fill}_P = 0.54$, $\text{fill}_S = 0.450$, longitude of the spot = 350°, radius of the spot = 7° and temperature ratio (spot/primary star) = 1.97.

4. Discussion

4.1. The inclination of the orbit of Plaskett's star

Even though the variations between the maximum and minimum observed in the entire run are close to ~0.1 mag, the unprecedented quality of the CoRoT light curve gives us enough information to attempt a study of the inclination of Plaskett's star. For this purpose, we use the NIGHTFALL programme[1] to fit the variations due to the orbital motion. This programme is based on a generalized Wilson-Devinney method assuming a standard Roche geometry.

We used the information from our Fourier analysis by combining the amplitudes and phases of the peaks detected at the orbital frequency and its first two harmonics ($f = 0.139$ and $f = 0.208$ d^{-1}). The photometric variations of HD 47129 tied to the orbital cycle have a peak-to-peak amplitude of about 19 mmag. The orbital light curve displays a broad minimum roughly centred on phase 0.0 (the conjunction with the primary star is in front)[2]. This is followed by a broad maximum around phase 0.3, whilst there is no clear secondary minimum, but rather a kind of plateau before the brightness decreases towards phase 0.0. These variations are clearly not due to grazing eclipses and cannot be explained by the sole effect of ellipsoidal variations either. Indeed, pure ellipsoidal variations in a system with a circular orbit, such as Plaskett's star, would produce a light curve with two equally deep minima centred on phases 0.0 and 0.5. We note that ellipsoidal variations in an eccentric binary could potentially account for the observed light curve (see e.g. the case of Tr 16-112, Rauw et al. 2009). However, the radial velocity curves of Plaskett's star (Linder et al. 2008, and references therein) provide no evidence whatsoever for a non-zero eccentricity. An alternative possibility to account for the shape of the orbital light curve of Plaskett's star is to assume a configuration where one of the stars has a hot spot on its surface. Indeed, the presence of such a hot, and hence bright, region could counterbalance the small ellipsoidal variations. We fitted the light curve of Plaskett's star with the following assumptions: the mass ratio as well as the temperatures of the stars are fixed according to the results of Linder et al. (2008). A priori, the hot spot could be located on the surface of either star. However, to fit the observed light curve, a spot on the secondary would have to be on the rear side of the

[1] For details, see the NIGHTFALL User Manual by Wichmann (1998) available at the URL: http://www.hs.uni-hambourg.de/DE/Ins/Per/Wichmann/Nightfall.html

[2] With respect to the time of phase 0.0 defined in Linder et al. (2008), the minimum of the light curve is shifted by about 0.03 in phase. This is somewhat larger than what can be accounted for by the uncertainty on the orbital period quoted by Linder et al. Here we have chosen to take phase 0.0 at the time of the minimum of the light curve.

star (i.e. turned away from the primary), whilst a spot on the primary star would be located on the side of the star facing the secondary. The latter configuration seems more plausible, especially in comparison with the wind interaction model of Linder et al. (2008). We therefore assume that the hot spot lies on the surface of the primary. The secondary is taken to rotate asynchronously with a rotation period one quarter of the orbital period, although we stress that this assumption has little impact on our results. At first, the inclination, the Roche lobe filling factors of both stars, the longitude of the hot spot, its radius and temperature ratio are taken as free parameters. The small amplitude of the light curve prevents us, however, from deriving strong constraints on the values of all these parameters. This dilemma can be illustrated by considering for instance the orbital inclination. As a matter of fact, when systematically exploring the parameter space, we find equally good fits for values of i ranging from 30° to 80°. Obviously to reproduce the observed light curve with $i = 80°$ requires extremely low filling factors of at least one of the stars, and this is unlikely because the spectroscopic investigation revealed a luminosity ratio of about 1.9 for stars with essentially identical temperatures (see Linder et al. 2008). Conversely, the lower inclination solutions yield unrealistically large masses. When we constrain the filling factors in a way as to reproduce the spectroscopic luminosity ratio, we find the best fit for an inclination of about 67°. Whilst this number seems quite "reasonable", we stress that it must be taken with caution. We also attempt to fit the ellipsoidal variations individually (i.e., limiting ourselves to the double of the orbital frequency and not accounting for a spot) but, once again, no exact determination of the inclination has been possible. Indeed, the fit of this parameter is directly dependent on the filling factor of both stars.

For all solutions that we find, the longitude of the bright spot is found between 345° and 355° (0° corresponding to the direction of the secondary star and 90° indicating the direction of the motion of the primary). Furthermore, this spot has a temperature ratio of about 1.9 with respect to the surface temperature of the primary. The radius of the spot is found to be about 8°–10° for most solutions, except for those with very high orbital inclinations and low filling factors.

A major problem concerning Plaskett's star remains the distance at which the binary system is situated. Indeed, whatever the configuration used to fit the light curve, the parameters used by `NIGHTFALL` indicate that the star should be located between 2.0 and 2.2 kpc. The increase of the distance would imply that Plaskett's star does not belong to the Mon OB2 association, as was already suspected by Linder et al. (2008). These authors indeed found a discrepancy between the spectral types of both stars and their dynamical masses. If we compare the systemic velocity of Plaskett's star, estimated at 30.6 ± 1.8 km s^{-1} by Linder et al. (2008), with the radial velocities of other O-type stars situated in Mon OB2 association (Mahy et al. 2009), it appears that these values agree between each other and that Plaskett's star would belong to this association. However, this assumption will can only be checked with measurements from the future Gaia mission.

In summary, whilst the light curve does not allow us to establish the inclination of the orbit, we find that its shape is consistent with moderate ellipsoidal variations altered by the presence of a rather bright spot on the primary star, facing the secondary. This spot is very probably related to the wind interaction between the two stars and could actually be due to shock-heated material that is cooling whilst it flows away from the stagnation point.

4.2. Structures present in the light curve

The multiperiodic analysis of the CoRoT light curve allowed us to detect a significant structure composed of a fundamental frequency ($f = 0.823$ d^{-1}) and its six harmonics, but the nature of this signal is not yet established.

In a binary system such as Plaskett's star, a possible cause of spectroscopic or photometric variability could be the asynchronous rotation. Indeed, a binary system is in synchronous rotation when the angular rotation velocity ω and the angular velocity of orbital motion Ω are equal. In HD 47129, this is clearly not the case: adopting the projected rotational velocities and stellar radii from Linder et al. (2008), we estimate rotational periods of about 10.3 (0.1 d^{-1}) and 1.7 days (0.6 d^{-1}) for the primary and secondary, respectively. As a result of asynchronous rotation, tidal interactions may create non-radial oscillations (Willems & Aerts 2002; Moreno et al. 2005; Koenigsberger et al. 2010). These oscillations produce a pattern of azimuthal velocity perturbations superposed on the unperturbed stellar rotation field. These tidal flows lead to the dissipation of energy owing to the viscous shear, thereby impacting on the surface temperature (and hence brightness) distribution. The azimuthal velocity components of tidal interactions are expected to produce a strong line profile variability that resembles the typical signature of non-radial pulsations (bumps in the line profile that migrate from the blue wing of the spectral lines to the red wing). The most spectacular effects are expected in eccentric binary systems, and this model was successfully used to explain the line profile variability of the eccentric B-type binary α Virginis (Moreno et al. 2005; Koenigsberger et al. 2010). Simulations of the influence of the tidal effects on the radial velocities were shown by Willems & Aerts (2002).

In a binary system with a circular orbit, the non-synchronous rotation induces variations of the radius of the non-synchronous rotating component with a super-orbital period that is longer than both the orbital and the rotational period (Moreno et al. 2005). Whilst these super-periods could leave a photometric signature, they should not be visible in the line profile variability, which is mostly dominated by the azimuthal velocity component. Moreno et al. (2005) found that in the circular non-synchronous case, the line profiles should only display a few rather broad bumps. The skewness of the line profile and its radial velocity (compared to the unperturbed profile) should display two maxima and minima per orbital cycle. The corresponding frequency should thus be twice the orbital frequency which is different from $f = 0.823$ d^{-1}.

We then consider that the structure composed of seven frequencies could be due to the rotation of one component of the binary system. In this context, we clearly see by adopting the rotational periods from Linder et al. (2008) that this set of frequencies is unlikely to correspond to the rotation of one star. A similar conclusion is expected if we take into account the projected rotational velocity evaluated by Linder et al. (2008) for both stars at about 75 km s^{-1} and 310 km s^{-1} for the primary and secondary component, respectively. Indeed, Bagnuolo et al. (1992) derived the radii from the luminosities and the effective temperatures of both stars. They found values close to 14.7 $R_\odot$ and 9.7 $R_\odot$ for the primary and secondary stars, respectively. We estimate a rotational period of about 9.9 days and 1.6 days for the primary and secondary stars, respectively, corresponding to rotational frequencies of about 0.1 d^{-1} and 0.6 d^{-1}. Alternatively, if we adopt the theoretical values of the radii quoted by Martins et al. (2005) as a function of the spectral type of each component, we obtain 21.1 $R_\odot$ and 14.2 $R_\odot$ for the primary and secondary

stars, respectively, by assuming that the system is composed of an O8 I and an O7.5 III star. These values yield a rotational period of 14.2 days for the primary and 2.4 days for the secondary. These results suggest that the primary could be in synchronous rotation, while this is clearly not the case for the secondary, which would have a rotational frequency of about 0.42 d^{-1}. In both cases, it appears therefore that the fundamental frequency found in the Fourier analysis is not representative of a rotational motion, except if we could invoke a spotted surface for the secondary. But, in this case, the lack of odd multiples of the rotation frequency would be surprising. By assuming a rotational frequency of $f = 0.823$ d^{-1}, we would obtain a radius of about 7.2 $R_\odot$ for the secondary star, which seems unrealistic for these stars. However, it is possible that the frequency at $f = 0.368$ d^{-1} or $f = 0.399$ d^{-1} is representative of the rotational period of the secondary component. In the latter case, the equatorial radius of the secondary star could be estimated close to 16.7 $R_\odot$ or 15.4 $R_\odot$, respectively.

Next, we suppose that this group of frequencies could arise from wind interactions. Wiggs & Gies (1992) reported on variations of the strength of the high-velocity wings of the Hα and He I λ 6678 emission line profiles. The total equivalent width of the blue and red wings of Hα was found to display a roughly recurrent modulation with a time scale of 2.82 days (0.35 d^{-1}), although the sampling of the spectra of Wiggs & Gies (1992) is admittedly not sufficient to characterize such rapid variations. These authors attributed the variations to instabilities of a radiatively cooling wind-wind interaction. It is interesting to note that this frequency is very close to the "broad peak" detected in the analysis of our photometric data (Sect. 3.1). It has to be stressed though that the *XMM-Newton* observations of Linder et al. (2006) did not reveal any indication of X-ray variability that could be related to the existence of such instabilities in the wind interaction zone.

Finally, we consider that these frequencies could be generated by non-radial pulsations. Indeed, massive stars are composed of a convective core and a radiative envelope, and gravity as well as acoustic modes can be excited (Aerts et al. 2010). Generally, for massive stars situated on the main-sequence band, the p-modes propagate with periods of a few hours while the g-modes have longer periods, of the order of days. However, for Plaskett's star, Linder et al. (2008) concluded that it is an evolved system in a post-Roche lobe overflow evolutionary stage. The inner structure of these stars is different from main-sequence stars, which decreases the g-modes periods and at the same time increases the p-modes periods (Handler 2005). Another family of modes, the strange modes (Saio et al. 1998), could also play a role in the interpretation of this structure of frequencies. These modes are known to have a propagation zone near the surface of massive stars. The exact determination of these modes requires theoretical models to predict variations produced by non-radial pulsations in a rapidly rotating massive star as well as an intense spectroscopic monitoring to characterize the variability of the line profiles. However, for Plaskett's star, massive main-sequence star models computed with ATON (Ventura et al. 2008) and an initial metallicity of 0.015, a range of mass between 30 and 70 $M_\odot$, and different mass-loss rates show that non-radial pulsations with frequency of the order of 0.8 d^{-1} can indeed be found. This frequency could be generated by modes with $l = 2, 3$, or 4.

In summary, we conclude that the alternative scenarios linked to rotation or to winds in both stars fail to explain the structure of the Fourier spectrum, especially the dominant frequency and its set of harmonics. The assumption of multiperiodic non-radial pulsations remains the most plausible one to understand the low-frequency variability detected in the CoRoT light curve of Plaskett's star.

5. Conclusions

We presented the photometric analysis of the very massive binary system HD 47129 observed by CoRoT during the second run SRa02 (~34.33 days). The light curve shows indications of intrinsic variations of the stars, providing evidence of a large number of frequencies. We extracted a total of about 43 frequencies (Table 1), significant under a null hypothesis of red noise, by using two different techniques based on a standard prewhitening and a multiperiodic algorithm. We emphasize that all the frequencies, reported in the present paper, have not necessarily a physical meaning.

This analysis highlighted a group consisting of one fundamental frequency (0.823 d^{-1}) and its six harmonics. In addition, a second structure formed by the orbital frequency (0.069 d^{-1}) and its two harmonics allowed us to investigate the light variation due to orbital effects. This analysis revealed the presence of a hot spot, probably located near the primary star, facing the secondary component and having an origin in the colliding wind interaction zone. However, the determination of the exact value of the system inclination turned out to be ambiguous. A third structure, formed by a much wider peak and thus certainly composed of two frequencies at 0.368 d^{-1} and 0.399 d^{-1}, has also been detected. One of these frequencies could be related to the rotation of the secondary even though Wiggs & Gies (1992) rather suggested an origin in the winds of the stars.

The future work will be devoted to the interpretation of these frequencies in terms of asteroseismology in order to remove an additional part of mystery concerning Plaskett's star. Moreover, a study of the line profiles either of the secondary or of the primary component, obtained from an intense high-resolution spectroscopic campaign, could provide further constraints on the properties of the pulsation modes. Indeed, the broad and shallow line profiles of the secondary star favour this detection, although the orbital motion and the presence of the primary star will certainly render this task more difficult.

Acknowledgements. We thank the CoRoT team for the acquisition and the reduction of the CoRoT data. This present work was supported by the FNRS (Belgium), the PRODEX XMM/Integral contract (Belspo), Gaia DPAC Prodex and the Communauté française de Belgique – Action de recherche concertée – ARC – Académie Wallonie-Europe. The research leading to these results has also received funding from the European Research Council under the European Community's Seventh Framework Programme (FP7/2007–2013)/ERC grant agreement No. 227224 (PROSPERITY), from the Research Council of K.U. Leuven (GOA/2008/04), and from the Belgian federal science policy office (C90309: CoRoT Data Exploitation). M.G. and A.N. thank J. Montalban and P. Ventura for help in computation aspects of massive stars.

References

Aerts, C., Christensen-Dalsgaard, J., & Kurtz, D. W. 2010, Asteroseismology (Springer)
Aigrain, S., Favata, F., & Gilmore, G. 2004, A&A, 414, 1139
Auvergne, M., Bodin, P., Boisnard, L., et al. 2009, A&A, 506, 411
Baglin, A., Auvergne, M., Barge, P., et al. 2006, in ESA SP, ed. M. Fridlund, A. Baglin, J. Lochard, & L. Conroy, 1306, 33
Bagnuolo, Jr., W. G., Gies, D. R., & Wiggs, M. S. 1992, ApJ, 385, 708
Belkacem, K., Dupret, M. A., & Noels, A. 2010, A&A, 510, A6
Cantiello, M., Langer, N., Brott, I., et al. 2009, A&A, 499, 279
Degroote, P., Aerts, C., Ollivier, M., et al. 2009, A&A, 506, 471
Ferraz-Mello, S. 1981, AJ, 86, 619
Frescura, F. A. M., Engelbrecht, C. A., & Frank, B. S. 2008, MNRAS, 388, 1693
González, J. F., & Levato, H. 2006, A&A, 448, 283

Gosset, E. 2007, Le calcul du niveau de signification du plus haut pic dans les périodogrammes de type Fourier par la formule de Horne-Baliunas est contre-indiqué, Thèse d'Agrégation de l'Enseignement Supérieur, Seconde Thèse Annexe, University of Liège
Gosset, E., Royer, P., Rauw, G., Manfroid, J., & Vreux, J.-M. 2001, MNRAS, 327, 435
Handler, G. 2005, JApA, 26, 241
Harvey, J. 1985, in Future Missions in Solar, Heliospheric & Space Plasma Physics, ed. E. Rolfe, & B. Battrick, ESA SP, 235, 199
Heck, A., Manfroid, J., & Mersch, G. 1985, A&AS, 59, 63
Hillier, D. J., & Miller, D. L. 1998, ApJ, 496, 407
Howarth, I. D., & Reid, A. H. N. 1993, A&A, 279, 148
Kambe, E., Hirata, R., Ando, H., et al. 1997, ApJ, 481, 406
Koenigsberger, G., Moreno, E., & Harrington, D. M. 2010, 425, 209
Linder, N., Rauw, G., Pollock, A. M. T., & Stevens, I. R. 2006, MNRAS, 370, 1623
Linder, N., Rauw, G., Martins, F., et al. 2008, A&A, 489, 713
Lucy, L. B., & Sweeney, M. A. 1971, AJ, 76, 544
Mahy, L., Nazé, Y., Rauw, G., et al. 2009, A&A, 502, 937
Martins, F., Schaerer, D., & Hillier, D. J. 2005, A&A, 436, 1049
Montgomery, M. H., & O'Donoghue, D. 1999, Delta Scuti Star Newsletter, 13, 28
Moreno, E., Koenigsberger, G., & Toledano, O. 2005, A&A, 437, 641
Morrison, N. D. 1978, PASP, 90, 493
Perdang, J. 2009, in EAS PS, ed. M. Goupil, Z. Koláth, N. Nardetto, & P. Kervella, 38, 43
Rauw, G., De Becker, M., van Winckel, H., et al. 2008, A&A, 487, 659
Rauw, G., Nazé, Y., Fernández Lajús, E., et al. 2009, MNRAS, 398, 1582
Reese, D. R., Thompson, M. J., MacGregor, K. B., et al. 2009, A&A, 506, 183
Rudy, R. J., & Herman, L. C. 1978, PASP, 90, 163
Saio, H., Baker, N. H., & Gautschy, A. 1998, MNRAS, 294, 622
Scargle, J. D. 1982, ApJ, 263, 835
Stanishev, V., Kraicheva, Z., Boffin, H. M. J., & Genkov, V. 2002, A&A, 394, 625
Ventura, P., D'Antona, F., & Mazzitelli, I. 2008, Ap&SS, 316, 93
Wichmann, R. 1998, Nightfall User Manual
Wiggs, M. S., & Gies, D. R. 1992, ApJ, 396, 238
Willems, B., & Aerts, C. 2002, A&A, 384, 441

Pages 10 to 12 are available in the electronic edition of the journal at http://www.aanda.org

HD 46223

The analysis of HD 46223, HD 46150 and HD 46966 was performed in parallel with our collaborator Dr. R. Blomme from Royal Observatory of Belgium and constitutes the core of the study reported in Blomme et al. (2011). However, both analyses were made independently, using different approaches. First of all, Dr. Blomme used particular stopping criteria to determine the number of significant frequencies for the CoRoT light curves. These criteria were already discussed in the literature and are based on a function partly similar to a χ^2 technique but coupled with a term which corrects for the improvement of the model fit with an increasing number of parameters. In parallel, we use Eq. 5.3 as statistical criterion that we apply on the binned light curves constituted of about 1700 points. Then, we focus the search for frequency spacing on the $[0-12]$ d^{-1} domain while Dr. Blomme only took into account the $[3-12]$ d^{-1} domain. We have also provided for the paper the temporal frequency plots of the three stars and the statistical criterion adapted to the red noise (see Section 5.4.5). Finally, we have computed in parallel with Dr. Blomme the significant frequencies under the null hypothesis of red noise for the three stars. In the following sections, we describe the main results of these analyses.

The observations of HD 46223 started on HJD = 2 454 748.488547 and ended on HJD = 2 454 782.819650, i.e., a 34.331103-day run. The semi-amplitude spectrum (Fig. 5.9) is slightly dominated by the frequencies $f_1 = 0.754$ d^{-1}, $f_2 = 0.248$ d^{-1} and $f_3 = 0.506$ d^{-1}. These three frequencies represent an obvious combination of frequencies since $f_2 + f_3 = f_1$. The shortest of these frequencies, $f = 0.248$ d^{-1}, corresponds to 4.02 days and could be associated with the rotational frequency of the star. Indeed, this frequency and the stellar radius derived from the CMFGEN analysis of HD 46223 (see Table 5.4) allow us to calculate, from the expression $v_{\rm eq} = 2\pi R_* f$, an equatorial velocity of about 140 km s^{-1}. Given that the $v \sin i$ value for HD 46223 is estimated to 100 km s^{-1}, the frequency $f = 0.248$ d^{-1} could therefore be associated with the rotational cycle of the star, if the inclination is of about $43-45°$.

Blomme et al. (2011) detected 500 significant frequencies from the BIC stopping criterion (see the paper in Appendix B). We apply the statistical criterion given in Eq. 5.3 on the binned light curves with $N_0 = 1702$, reporting 46 significant frequencies under the null hypothesis of white noise and a significance level of 0.01. However, these frequencies have to be taken with caution because the periodogram is also clearly biased towards the low frequencies, thereby indicating the presence of red noise in the light curve.

For the detection of the frequency spacing, we decide to increase our set of significant frequencies by probing a part of the frequencies which are judged non-significant on the basis of our statistical criterion. For this purpose, we thus increase the significance level so that the sample of significant frequencies is multiplied by a factor 5. If the additional frequencies indeed correspond to noise, they will be randomly attributed to the different frequency chain, thereby will not significantly affect the results. However, if we add a number too large of non-significant frequencies, the spacing histograms will be too noisy to detect the real chains of frequencies. Therefore, increasing our dataset by a factor 5 appears to be a good compromise for the search of frequency spacing. We proceed in the same way for establishing the frequency spacing of the four remaining CoRoT light curves. In this way, the sample of 46 frequencies we detect for HD 46223 is increased to reach 230 frequencies located between 0 and 12 d^{-1}. The spacing detection is displayed in the left panel of Fig. 5.10. We clearly see that the autocorrelation spectrum does not agree with the number of components found in a chain. We also perform this test on the $[3-12]$ d^{-1} frequency domain to compare our results with those of Blomme et al. (2011). Once again, we do not detect any clear similarity between the autocorrelation test and that of the spacing.

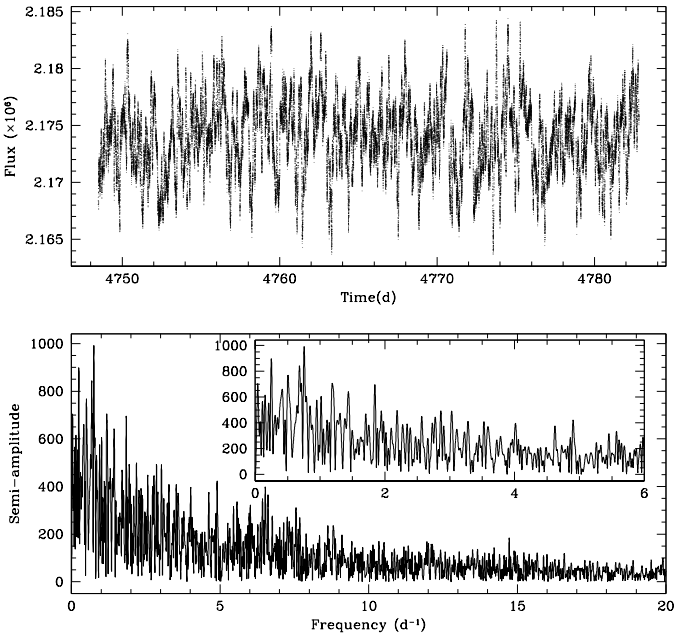

Figure 5.9: Same as Fig. 5.7, but for HD 46223.

The time-frequency analysis (Fig. 5.10, right panel) made on a $[0 - 12]$ d^{-1} frequency region shows that the lifetime of the frequencies in the semi-amplitude spectrum is rather short, indicating that the variations are not stable over the duration of the CoRoT campaign. Pulsations are generally more long-lived and would thus not explain such a result. Therefore, an alternative explanation would be that these variations are due to a non-sustained process or arise from the red noise detected in the light curve of HD 46223 (see Section 5.4.5).

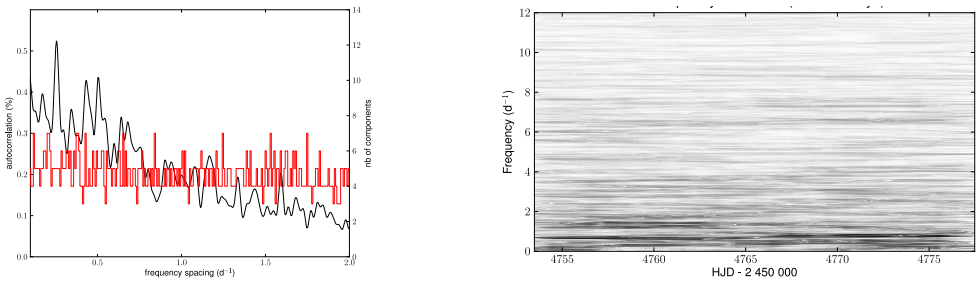

Figure 5.10: *Left:* Same as left panel of Fig. 5.8, but for HD 46223. *Right*: Same as right panel of Fig. 5.8, but for HD 46223.

The lack of oustanding peaks in the semi-amplitude spectrum of HD 46223 does not indeed imply a total absence of excited modes. Theoretical models (Fig. 5.11) were computed by M. Godart (see Plaskett's Star in Section 5.4.4) on the basis of the preliminary parameters derived by Martins et al. (2011). These models theoretically predict frequencies excited by the κ-mechanism and spanned in the range of $[2 - 5]$ d^{-1} for $l = 0$ to $l = 4$. In addition, a non-radial strange mode also exists around 10 d^{-1}. We find frequencies in this range among our significant frequency list but the accuracy on the theoretical frequencies does not allow us to directly relate them to those

derived in the frequency list. The predicted frequencies are definitely not standing out. Moreover, we clearly see that the frequencies f_1, f_2 and f_3, which display the larger amplitudes, cannot be associated with theoretical predictions because they are located in a lower frequency range. As a consequence, they could represent a phenomenon bound to the rotation of the star or to a more complex phenomenon, including effects not predicted by present-day theoretical models.

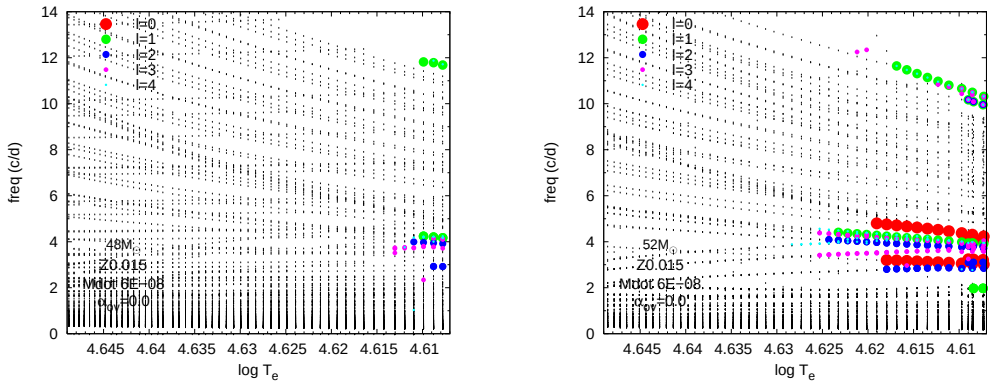

Figure 5.11: Frequency spectra for the theoretical models computed from parameters similar to those of HD 46223 and HD 46150. The models have an initial mass of 48 and 52 $M_{\odot}$ (indicated on each graph) and are computed without overshooting and rotation. The black dots indicate models that do not show pulsations whilst the coloured circles correspond to the excited frequencies: the largest red circles are the radial modes and the size of the circles decreases then from $l = 1$ to $l = 4$, according to the legend (Godart 2011).

HD 46150

The analysis of this star is made in a similar way as for HD 46223 and the results are published in Blomme et al. (2011). The stellar and wind parameters derived by Martins et al. (2011) for HD 46150 are reminiscent of those of HD 46223. Therefore, the theoretical frequencies introduced in the previous section are still valid for this object. As for HD 46223, the range of variations in the CoRoT light curve (Fig. 5.12) of HD 46150 is of the order of 8 mmag (16000 counts). Furthermore, the light curve presents a strong variation on a timescale of about 20 days. This variation is reported in the semi-amplitude spectrum by a dominant peak at the frequency $f_1 = 0.057$ d^{-1} (i.e., about 17.5 days). The next highest peaks are located at $f_2 = 0.146$ and $f_3 = 1.341$ d^{-1}. The general appearance of the light curve and, in particular, of the semi-amplitude spectrum are relatively similar to those of HD 46223 (see Fig. 5.9), i.e., both can be described by red noise. This similarity suggests that stars with almost identical physical parameters have similar internal mechanisms, as one would expect. This remark could indeed be interesting in the framework of the investigation of the possible origin of the red noise (see Section 5.4.5 for more discussion on that subject).

Blomme et al. (2011) reported a list of 500 significant frequencies whilst, from the 1702 datapoints of the binned light curve, we detect 30 significant frequencies under the null hypothesis of white noise and at a significance level of 0.01. As mentioned for the spacing analysis of

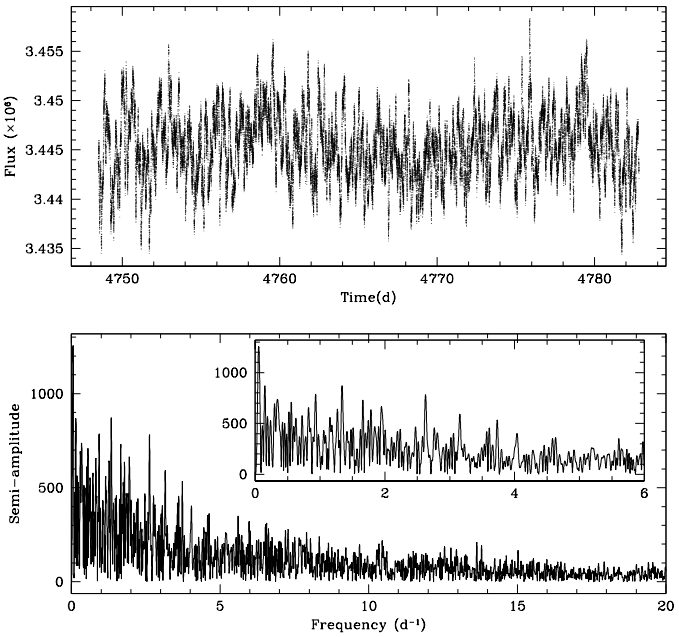

Figure 5.12: Same as Fig. 5.7, but for HD 46150.

HD 46223, we increase by a factor 5 our frequency dataset to reach 150 frequencies. The results of the spacing detections are displayed in the left panel of Fig.5.13 and show that both the chain and the autocorrelation tests are not in agreement with each other, thereby confirming the absence of a regular spacing in the frequency list of HD 46150.

Moreover the time-frequency analysis (Fig. 5.13, right panel), computed on the $[0-12]$ d^{-1} frequency domain, reveals, as it was the case for HD 46223, that the lifetime of the frequencies is short (less than the duration of the observing run). That seems to indicate that these frequencies are linked to a stochastic process, corresponding to the red noise, rather than genuine regular pulsations. Nonetheless, some frequencies located between $f = 2.5$ and $f = 4.0$ d^{-1} may correspond (see right panel in Fig. 5.11) to possible excited modes with $l = 2$ or $l = 3$ but this assumption remains purely speculative as long as we do not have a definitive list of the significant frequencies detected in the light curve.

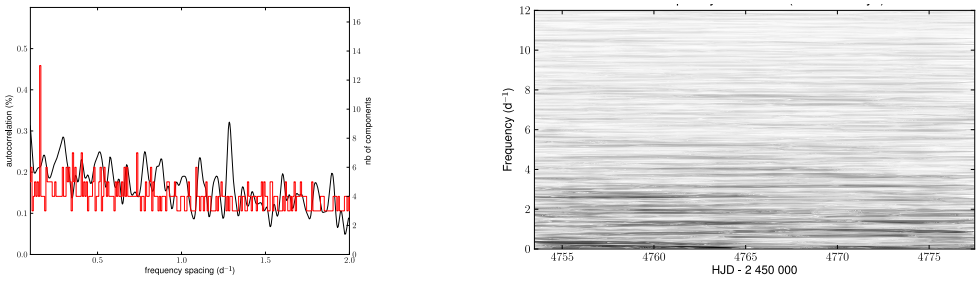

Figure 5.13: *Left:* Same as left panel of Fig. 5.8, but for HD 46150. *Right*: Same as right panel of Fig. 5.8, but for HD 46150.

HD 46150 was reported as a binary candidate (see Mahy et al. 2009). If this star is indeed a real binary, the 18-day oscillation could correspond to the orbital period or ellipsoidal variations of this system. The analysis of its multiplicity does not allow us to find, for HD 46150, a clear period in the small variations of radial velocities but we think that such a period would have been detected on the basis of our spectroscopic dataset. Therefore, the variation at $f = 0.057$ d^{-1} observed in the CoRoT light curve could also be related to the rotational frequency of the object. Nevertheless, this frequency would provide a rotational velocity of about 35 km s^{-1} which is too low in comparison to the projected rotational velocity derived in the previous analyses (Mahy et al. 2009 and Martins et al. 2011). If we rather consider the frequency $f = 0.146$ d^{-1}, we then determine a rotational velocity of about 100 km s^{-1}, which matches the measured $v \sin i$ for an inclination of 90°.

HD 46966

HD 46966 was the last star studied in Blomme et al. (2011, see Appendix A). The contributions of the Liège team and of the Royal Observatory of Belgium were similar as for HD 46223 and HD 46150.

The light curve of this object (Fig. 5.14) clearly shows a variation with a period slightly longer than 10 days. Such a value is rather typical of a short-period massive binary. However, the spectroscopic campaign performed on this star (Mahy et al. 2009) revealed that this object is most probably single. Therefore, possible sources to explain the existence of such a 10-day variation would be either pulsations or the presence of a hot spot on the stellar surface producing a rotational modulation of the light curve.

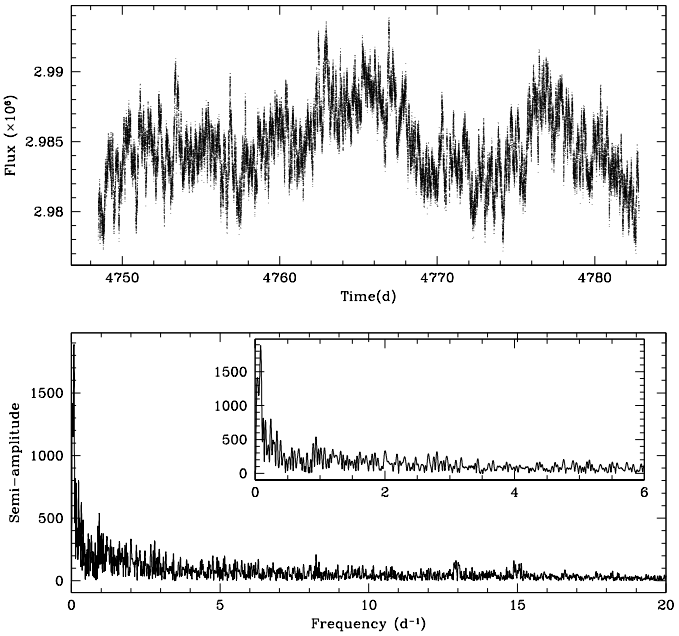

Figure 5.14: Same as Fig. 5.7, but for HD 46966.

This variation is reported in the semi-amplitude spectrum by the highest peak at $f = 0.085$ d^{-1} and a second frequency is detected at $f = 0.040$ d^{-1}. Beside these two frequencies, no outstanding peak appears in the semi-amplitude spectrum. Blomme et al. (2011) found about

300 significant frequencies in this light curve. From the binned light curve, we reduce this number to reach 31 significant frequencies. The spacing research on the [0−12] d^{-1} frequency domain, taking into account an increased dataset (as we did for HD 46223 and HD 46150) of 155 frequencies, reveals on the basis of the autocorrelation and frequency chain tests, a possible spacing at about $\Delta f = 0.215$ (Fig 5.15, left panel). The chain starts at $f = 0.126$ d^{-1} and ends at $f = 1.422$ d^{-1}. However, from the significant frequencies located in the [3−12] d^{-1} domain, no significant spacing is observed neither in our analysis nor in Blomme et al. (2011).

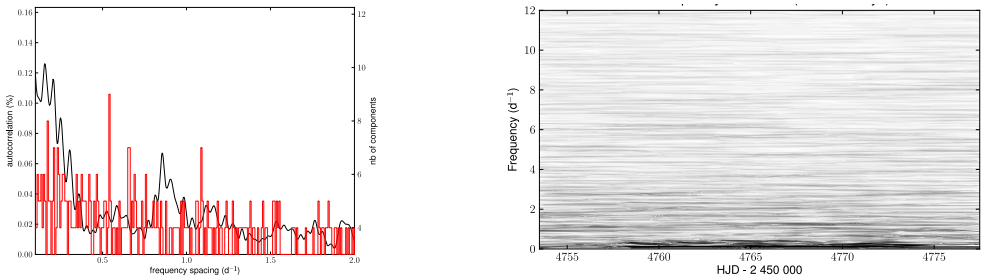

Figure 5.15: *Left:* Same as left panel of Fig. 5.8, but for HD 46966. *Right*: Same as right panel of Fig. 5.8, but for HD 46966.

We continue our investigation by computing the time-frequency diagram. The temporal periodogram shows that the two highest peaks at $f = 0.040$ and $f = 0.085$ d^{-1} are detected during the entire run but that the other frequencies have a rather limited lifetime. This excludes sustained pulsations for these other frequencies. In addition, the positions of the excited models on the HR diagram do not identify HD 46966 as a suitable candidate for pulsations (Fig 5.16, left panel). However, these other frequencies could be generated by a stochastic component or by red noise. The theoretical models computed with ATON show that excited frequencies are found from 2.5 to 4 d^{-1}, i.e., with periods around 6 to 9 hours for the upper masses of the error box (Fig 5.16, right panel) but no outstanding peak in the semi-amplitude spectrum can firmly confirm the existence of such excited modes in HD 46966.

Therefore, the frequency $f = 0.085$ d^{-1} could rather be associated to the rotational period of the star. Such a variation may indeed come from a hot spot on the surface of the star. Using the stellar parameters of Table 5.4 (Martins et al. 2011), we estimate an equatorial velocity of about 44 km s^{-1}, which could be compatible with the $v \sin i$ of about 50 km s^{-1}determined by Mahy et al. (2009) and Martins et al. (2011) from the Fourier transform method of Simón-Díaz & Herrero (2007). However, it would imply as for HD 46150 that the inclination of the star would be close to 90°.

The main results concerning HD 46966, and also HD 46150 and HD 46223 are reported in the paper of Blomme et al. (2011, see Appendix A).

HD 46149

As we already mentioned in Section 5.2.1 and in Mahy et al. (2009), HD 46149 is a binary system composed of an O 8V and an OB companion (probably B0–1V). The CoRoT light curve of this system was investigated by Degroote et al. (2010) and we participated to this paper by providing preliminary individual spectra of each component as well as by giving the radial velocities measured during our spectroscopic campaign. In parallel, we also perform our own analysis, which is

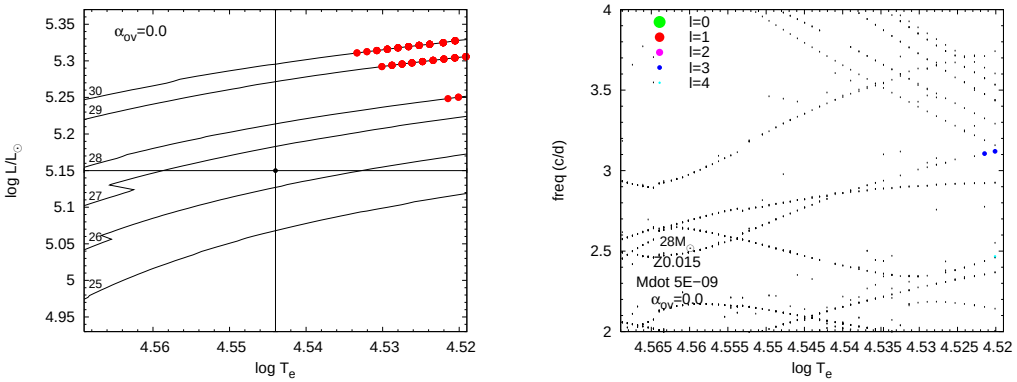

Figure 5.16: *Left*: Evolutionary tracks with 25 to 30 $M_\odot$ computed from a $\dot{M} = 5 \times 10^{-9}\ M_\odot\ \mathrm{yr}^{-1}$ and no overshooting. The error box is shown. These evolutionary tracks do not take into account the rotation. The filled circles stand for models presenting excited modes. *Right*: Same as for Fig. 5.11, but for HD 46966 (Godart 2011).

reported below. We notice that the stellar parameters determined by Degroote et al. (2010) must be taken with caution, for two reasons:

- the orbit of the system is poorly sampled, thereby implying that the semi-amplitude of the radial velocity curves could be underestimated (see Section 5.2.1),
- their fundamental values were determined on observed spectra in which the secondary component is barely visible, making the secondary parameters dubious.

The light curve observed by CoRoT reveals quite similar structures separated by about 11 days (see Fig. 5.17 at HJD $\sim$ 2 454 756, 2 454 767 and 2 454 778). By computing the semi-amplitude spectrum associated to this system, we detect four main frequencies at $f_1 = 0.083$, $f_2 = 0.173$, $f_3 = 0.480$ and $f_4 = 0.521$ d^{-1}. The statistical criterion applied to the binned light curve reveals 13 additional significant frequencies under the null hypothesis of white noise and at a significance level of 0.01. We also see that the semi-amplitude spectrum is affected by red noise as for HD 46966 and to a lesser extent as for HD 46223, HD 46150 and Plaskett's Star.

Degroote et al. (2010) reported the detection of about 10 solar-like oscillations spaced by about $\Delta f = 0.48 \pm 0.02$ d^{-1}. These oscillations begin at $f \sim 3.0$ d^{-1} and finish at $f \sim 7.8$ d^{-1}. The origin of such frequencies could be related, according to these authors, to the stochastically excited (solar-like) oscillations created by the sub-surface convection zone induced by the iron opacity bump (Cantiello et al. 2009; Belkacem et al. 2010). However, it is not obvious whether these frequencies are generated by the primary or the secondary component of the binary system! Our analysis of the frequency spacing (Fig. 5.18, left panel) computed from an increased sample of 80 frequencies (as we already mentioned above) and spread over $[0-12]$ d^{-1} does not confirm the results of Degroote et al. (2010). However, the semi-amplitude spectrum of HD 46149 is clearly affected by red noise. Therefore, some frequencies with small amplitudes could be entangled among the frequencies with highest peaks located between $[0-2]$ d^{-1}. We thus decide to restrict our analysis to the $[3-12]$ d^{-1} domain to be consistent with the investigation of Degroote et al.

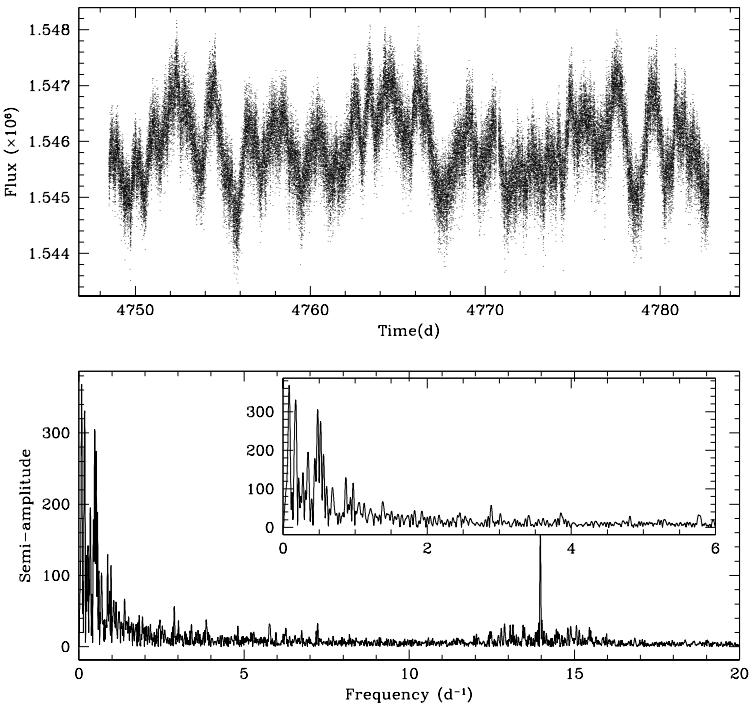

Figure 5.17: Same as Fig. 5.7, but for HD 46149.

(2010). We do detect a chain of 4 components spaced with $\Delta f = 0.48$ (see Fig. 5.18, left panel), including the frequencies $f = 5.785$, $f = 6.266$, $f = 6.744$ and $f = 7.229$ d^{-1}.

The time-frequency analysis is computed between 0.0 and 12.0 d^{-1} and clearly exhibits frequencies with such a spacing ($\Delta f = 0.48 \pm 0.02$ d^{-1}). However, the lifetime of these frequencies is once again rather short. Accordingly, it is unlikely that they originate in long-lived pulsations, which would confirm their stochastic nature.

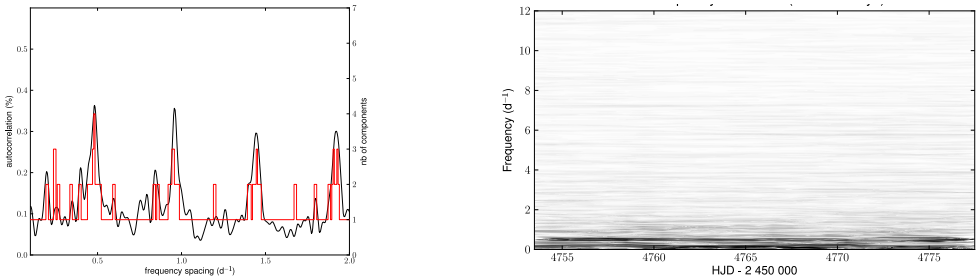

Figure 5.18: *Left:* Spacing detection performed on the [3 – 12] d^{-1} frequency domain. *Right*: Same as Fig. 5.8, but for HD 46149.

We may wonder whether the two frequencies recorded with the highest amplitudes are not due to the rotation of one or both components. If we assume that $f = 0.083$ d^{-1} represents the rotation frequency of the primary star and that $f = 0.173$ d^{-1} is that of the secondary, we derive on the basis of the stellar parameters of Martins et al. (2011) equatorial velocities of about 28.9

and 53.5 km s^{-1} for the primary and the secondary stars, respectively. By inverting the frequency identification, we rather obtain $v_{\rm eq}$ = 60.1 km s^{-1} for the primary and $v_{\rm eq}$ = 25.1 km s^{-1} for the secondary. Even though the parameters of Martins et al. (2011) are uncertain for these objects, we however see from the disentangled spectra that the $v \sin i$ of the secondary ($\sim$ 100 km s^{-1}, see Table 5.4) is much larger than that of the primary. As a consequence, the first identification could be representative of the rotational period of both components. However, that means that the $v \sin i$ quoted in Table 5.4 would be underestimated for the primary and overestimated for the secondary. That would confirm the uncertain nature of these values derived for both stars. This analysis shows once more the clear requirement of an intense and regular monitoring of HD 46149 to cover its entire orbital cycle.

HD 46202

An analysis made solely by the Leuven group on HD 46202 has been published by Briquet et al. (2011). Before starting our analysis, we had to perform a pretreatment to straighten out the raw light curve especially after HJD = 2 454 778. The resulting light curve is displayed in Fig. 5.19. Its semi-amplitude spectrum reveals 6 main frequencies: f_1 = 0.509, f_2 = 2.289, f_3 = 2.643, f_4 = 3.005, f_5 = 4.857 and f_6 = 4.691 d^{-1}. We readily see that f_2, f_3 and f_4 have the same spacing (Δf = 0.36 d^{-1}). These variations can be associated to β Cep–like pulsation frequencies.

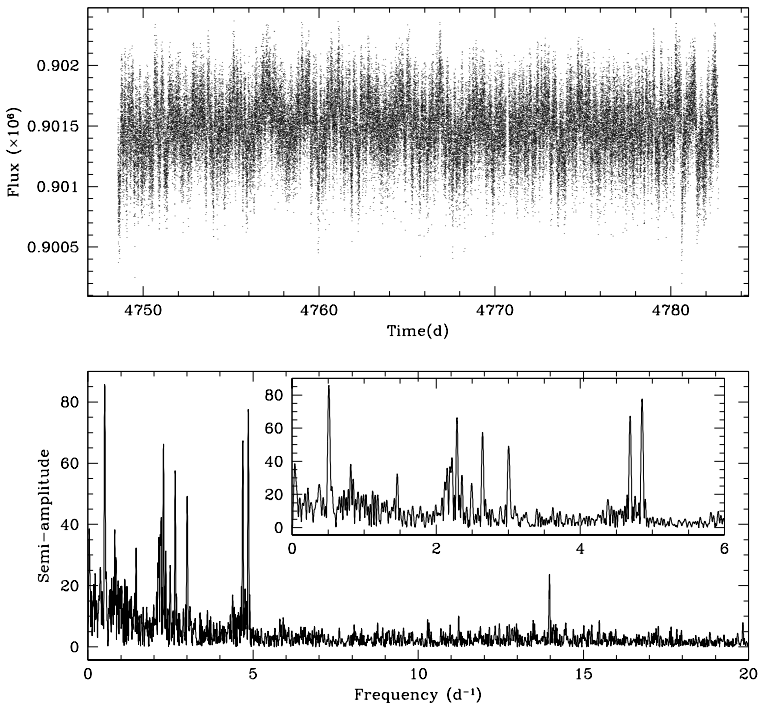

Figure 5.19: Same as Fig. 5.7, but for HD 46202.

To be complete, we independently investigate the CoRoT light curve. With 1697 datapoints, the analysis of the binned light curve yields the same 6 frequencies as significant under the null hypothesis of white noise and at a significance level of 0.01. The semi-amplitude spectrum of HD 46202 is less affected by red noise as for the other stars of our sample. Consequently, we

consider that the null hypothesis of white noise is appropriate to determine the list of significant frequencies.

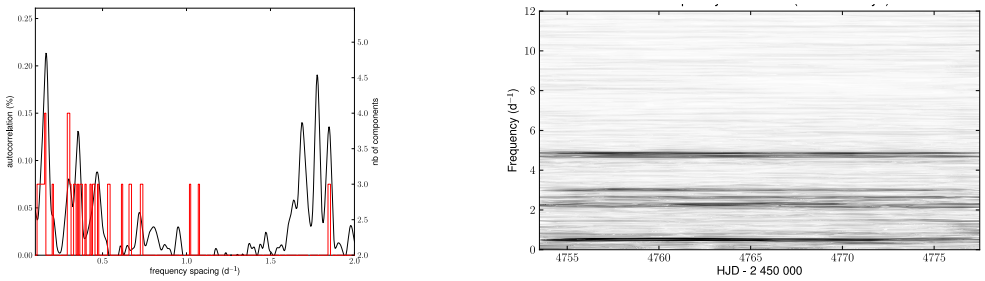

Figure 5.20: *Left:* Same as left panel of Fig. 5.8, but for HD 46202. *Right*: Same as right panel of Fig. 5.8, but for HD 46202.

As we did for the other stars, we increase for the spacing study the number of frequencies by a factor of 5, reaching 30 frequencies. This investigation (Fig. 5.20, left panel) indicates two additional regular spacings of about $\Delta f = 0.16$ and $\Delta f = 0.30$ d^{-1}, both constituting a chain of 4 frequencies. If we take into account the 67 frequencies judged significant by Briquet et al. (2011), we confirm the $\Delta f = 0.16$ d^{-1} spacing and we add four new frequencies to this chain.

The time-frequency analysis (Fig. 5.20, right panel) indicates that the 6 frequencies of the highest peaks are present over the totality of the run, thereby indicating that this set of frequencies could be associated to pulsations driven by the opacity mechanism. Briquet et al. (2011) also suggested that the frequency $f_5 = 4.857$ d^{-1} could be identified as a fundamental radial mode.

5.4.5 Red noise

Despite the care we took in the selection of a statistical criterion, the results reported in Section 5.4.4 have to be considered with caution. Indeed, we have shown that five semi-amplitude spectra are affected to various degrees by red noise rather than white noise. Therefore, the derived significance level could be irrelevant. Furthermore, the presence of red noise would lead to favour the detection of a majority of low frequencies under the null hypothesis of white noise, while, in fact, some of these low frequencies would likely be non-significant under a null hypothesis of red noise.

We thus define another criterion to test the significance of the frequencies under a null hypothesis of red noise. We first have to "quantify" the level of red noise in the periodogram. To that effect, we thus describe the "continuum" of the power spectrum as suggested by Stanishev et al. (2002) through the following function:

$$P(f) = \frac{\alpha_0}{1 + (2\pi\tau f)^\gamma} \tag{5.4}$$

where α_0 is the scaling factor, τ is an estimate of the mean duration of the dominant structures in the light curve and γ represents the slope of the linear part (in the log-log plot). We fit this profile by least-squares to the semi-amplitude and power spectra of all the stars. The values of the different parameters determined for the semi-amplitude spectra are quoted in Table 5.6.

We then integrate Eq. 5.4 to determine the area under the curve and compare this estimation to the variance of the data. This enables us to reach an "equivalent white noise situation". Indeed,

Table 5.6: Parameters of the function describing the red noise (Eq. 5.4). The fits were performed on the semi-amplitude spectra. However, to determine the significance level we have to use the parameters obtained from the power spectra.

Parameters	HD 47129[a]	HD 46223	HD 46150	HD 46966	HD 46149[a]
α_0	12423	524	539	518	155
τ	0.12	0.08	0.09	0.21	0.23
γ	2.3	0.95	0.96	0.93	1.78

[a]: The least-mean square fit is performed on the $[0-6]$ d^{-1} frequency domain. Beyond this range, the noise can be considered as white noise.

in a power spectrum only affected by white noise, the area contained under the white noise level is proportional to the variance of the data times the Nyquist frequency. Therefore, since the variance of the data remains unchanged whatever the red or white nature of the noise, we have to derive a scaling value δ to adjust the area computed under the red noise curve to that measured under the white noise. This can be summarized by:

$$\begin{aligned} \delta \int_0^{f_{\rm Ny}} P(f)\, df &= \int_0^{f_{\rm Ny}} \sigma_0^2\, df \\ &= f_{\rm Ny}\, \sigma_0^2 \end{aligned}$$

with δ a scaling parameter, σ_0^2 the variance of the data and $f_{\rm Ny}$ the Nyquist frequency.
We thus estimate:

$$\sigma_f^2 = \delta P(f)$$

where σ_f^2 is the variance of the frequency f under the hypothesis of red noise.
The statistical criterion (Eq. 5.3 in Section 5.4.3) then becomes:

$$\text{Prob}[Z_{\rm max} > z] = 1 - e^{-e^{(-\alpha z + \ln(0.8 N_0))}}$$

with $z = N_0 A_f^2 / 4\sigma_f^2$ and N_0 is the number of points in the dataset. With this criterion, the number of significant frequencies is considerably decreased, revealing 43, 15, 28, 7 and 14 frequencies for HD 47129, HD 46223, HD 46150, HD 46966 and HD 46149, respectively.

From the τ and γ values listed in Table 5.6, we can assume that the existence of the red noise is at least partly intrinsic to the stars themselves. Indeed, if the red noise was instrumental in origin, all the O-type stars gathered in the same field-of-view of the satellite would have the same τ and γ parameters and would be affected in a similar way by the instrumental problems, which is clearly not the case in the O-type stars observed by CoRoT. We can then wonder where this red noise comes from. The answer to that question is unclear, and mainly speculative. In fact, three physical properties could create red noise: a sub-surface convection, granulation, and/or inhomogeneities in the stellar winds. Cantiello et al. (2009) suggested that the convection zone, induced by the iron opacity bump, can be responsible for the existence of red noise. This zone located very close to the stellar surface would have an impact on the stellar surface behaviour, and could be at the origin of several physical phenomena such as the microturbulence, wind clumping and line profile variability. Moreover, Belkacem et al. (2010) suggested that this iron convection zone could also generate stochastically excited modes in massive stars such as the solar-like oscillations that are detected in HD 46149. All the O-type stars observed by CoRoT are indeed assumed to present such a sub-surface convection zone (see Fig. 9 in Cantiello et al. 2009). Another process that could explain the existence of red noise would be granulation. Kallinger & Matthews (2010) showed that in the two δ Scuti stars they studied, the many hundreds of peaks in the semi-amplitude

spectrum could also be interpreted as being caused by granulation. This idea could be relevant if we could establish a parallelism between the massive stars and the works of Harvey (1985) and Aigrain et al. (2004) in helioseismology, While this could be the case for the A-type stars, its extrapolation to much more massive stars, as those studied here, is however very uncertain. Finally, the last possible origin could be the wind clumping. Puls et al. (2006) suggested that the onset of clumping could happen very close to the stellar surface, thus generating the red noise. If we compare the stellar and wind parameters derived for the O stars belonging to NGC 2244 (Table 5.4) with the results obtained from the CoRoT photometry, we clearly see that the two light curves which present a high level of red noise are those of the two stars which also present clumping in their wind. However, the sample of studied stars is not sufficient to assess whether all the stars that have inhomogeneities in their winds are also affected by red noise. The wind clumping could thus be an interesting origin to explain the red noise, especially for HD 46223 and HD 46150. The analysis of the wind properties performed in Section 5.3 has suggested the presence of optically thick clumps, i.e., porosity/vorosity, as a possible source of the discrepancy observed between the UV and Hα mass-loss rates. That would imply the existence of clumped winds for all the stars of NGC 2244 and Mon OB2. Therefore, assuming the existence of porosity would increase the chances that the clumping sparks off red noise. However, before confirming this hypothesis, we need to improve our knowledge of the wind mechanisms in the massive stars.

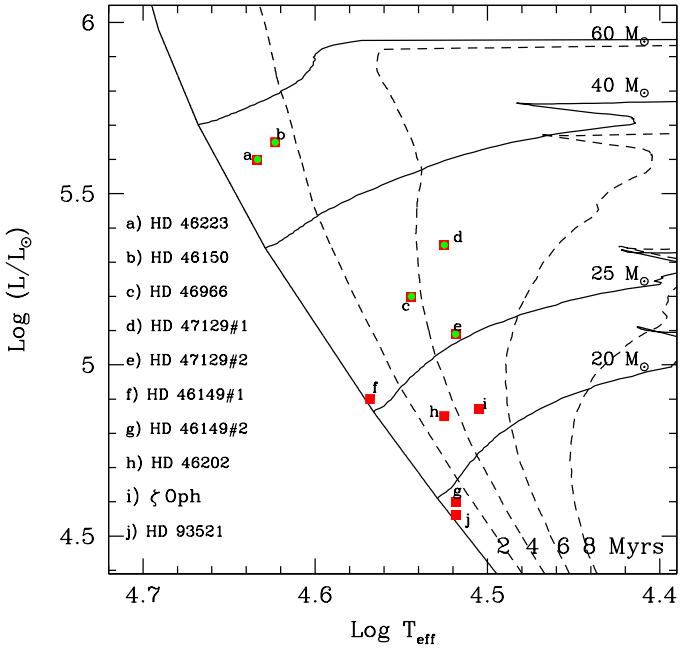

Figure 5.21: Locations on a HR diagram of the stars observed by CoRoT and two others O-type stars which are repertoried as pulsating. Red plus green label represent the stars whose light curve is affected by red noise. A red label characterizes the pulsating stars or those presenting solar-like oscillations.

We represent, in Fig. 5.21, the positions of the stars on the HR diagram by including two other O-type objects in which pulsations were found (ζ Oph, Kambe et al. 1997, and HD 93521, Howarth & Reid 1993; Rauw et al. 2008). The values of $T_{\rm eff}$ and $\log(L/L_\odot)$ mainly come from the CMFGEN investigation (Section 5.3), those of Plaskett's Star, ζ Oph and HD 93521 were given by Linder et al. (2008), Repolust et al. (2004) and Hohle et al. (2010), respectively. The

locations of the stars are particularly interesting and we see that two groups can be identified, the red–green one and the red one. The former contain all the stars for which the semi-amplitude spectrum is affected by red noise whilst the latter contain only the pulsating targets. However, the components of Plaskett's Star have to be considered carefully because their nature and their internal structure are likely partly different from the other stars due to the post Roche lobe overflow episode they have undergone and their giant luminosity class. Therefore, they probably do not lie in the instability strip in the same way as the other sample stars which are clearly on the main-sequence band. The absence of pulsating star in the upper part of the HR diagram could also be the first observational evidence for the end of the instability region.

5.5 Conclusions

This complete investigation of the O-type star population in the open cluster NGC 2244 and in the Mon OB2 association allows us to considerably improve our understanding of their fundamental properties. The multiplicity is now relatively well constrained and gives us a more precise idea of the stars we analyzed (Mahy et al. 2009, 2010). We have shown that the minimal binary fraction in NGC 2244 was only of about 14% and that no short-period (P < 10 days) system was detected among the O stars. However, this binary fraction is flawed by the small size of our sample, and it does not allow us to reject the null hypothesis according to which the parent population is the same for all the O stars. The lack of obvious correlations between the binary fraction and the properties of the clusters points out the crucial need of additional studies, especially for the early-type stars whose formation and evolution are still not completely understood.

Knowing the multiplicity of O-type stars in NGC 2244 and Mon OB2 also gives us important information to determine with more accuracy their stellar and wind parameters (Martins et al. 2011). From the location of the stars on the HR diagram, we have deduced that these stars have an age of about $0 - 5$ Myrs. With such an age and the known distance of $1.4 - 1.7$ kpc, these objects are perfect targets for an asteroseismological analysis. That is why six stars were observed by the CoRoT satellite during the second short run oriented towards the anti-center of the Galaxy. These light curves of an unprecedented quality (Mahy et al. 2011a; Blomme et al. 2011; Degroote et al. 2010; Briquet et al. 2011) gave us the opportunity to probe the physics of those stars as it has never been done before, highlighting an interesting observation: the red noise present in most of the light curves. However, its origin remains currently unclear. Does it come from the sub-surface convection zone, does it come from granulation or does it come from clumping? The answer to this question will require an increase in the size of the sample to obtain a better understanding of these stars, both observationally and theoretically.

The multiplicity of O-type stars in NGC 2244

L. Mahy[1], G. Rauw[1], F. Martins[2], E. Gosset[1], Y. Nazé[1], M. Godart[1], H.Sana[3], M. De Becker[1] and P. Eenens[4]

[1] Institute of Astrophysics and Geophysics, University of Liège, Belgium
[2] GRAAL, Université Montpellier II, CNRS, France
[3] Sterrenkundig Instituut "Anton Pannekoek", Universiteit van Amsterdam, The Netherlands
[4] Departamento de Astronomía, Universidad de Guanajuato, Mexico

Abstract: The investigation of the multiplicity of massive stars is crucial to determine a robust binary fraction but also for understanding the physical properties of these objects. In this contribution, we will present the main results from our long-term spectroscopic survey devoted to the young open cluster NGC 2244. We discuss the spectral classification, the projected rotational velocity (v sin i) and the multiplicity of O-stars. The stellar and wind parameters of each star, obtained using the CMFGEN atmosphere code, help us to better constrain the individual properties of these objects. Several of these stars were observed by the CoRoT satellite (SRa02) in the Asteroseismology channel. This intensive monitoring and the unprecedented quality of the light curves allow us to shed a new light on these objects.

1 Introduction

O-type stars play a key role in the ecology of galaxies but the knowledge of their formation is still fragmented. In this context, the study of massive stars in clusters is interesting in order to discriminate between the different formation scenarios since they constitute a homogeneous population (same age, distance and chemical composition).

The study of the multiplicity of early-type stars in galactic young open clusters through extensive spectroscopic campaigns unveils an average binary fraction of 0.44±0.05 (Sana & Evans 2010, in press). These investigations led to serious corrections of the binary fractions in the rich-open clusters quoted by Garcìa & Mermilliod (2001). However, numerous observational biases prevent the detection of all spectroscopic binaries such as e.g., a very long-term period, a large mass ratio or too low an inclination (for details, see Sana & Evans 2010, in press, Sana et al. 2009 or Mahy et al. 2009).

In order to extend these studies, we have undertaken a detailed investigation of the young open cluster NGC 2244, situated in the core of the Rosette Nebula and aged between 2 and 3 Myr (c.f. Chen et al. 2007, and references therein). We establish the binary fraction of O-type stars in the cluster, present the preliminary wind and stellar parameters of all these stars and summarise the preliminary results of the analysis of the CoRoT data devoted to 4 O-stars in NGC 2244.

2 Spectroscopic campaign

Garcia & Mermilliod (2001) listed 6 O-type stars as belonging to NGC 2244 whilst Ogura & Ishida (1981) reported a seventh O star (HD 258691), fainter than the others ones, and which is located outside of the field of view used by Wang et al. (2008). The question of the membership of this latter is thus opened. As a consequence, our multiplicity investigation focused on the same stars that those taken into account by Garcia & Mermilliod (2001) to establish their binary fraction.

Our spectroscopic dataset thus contains a total of 136 spectra for 6 O-type stars. These spectra were taken with different instruments which implies different resolutions. The data were spread over a timescale of 9 years, allowing us to search for the short as well as the long-period binaries. The details and results of the spectroscopic investigation of O-type stars are reported in Mahy et al. (2009).

Among the 6 O-type stars in NGC 2244, only one has been detected, for the first time, as a spectroscopic binary: HD 46149. The signature of the secondary component is clearly visible (see Mahy et al. 2009) and we have estimated its orbital period to be close to 800 days. However, it is difficult to be more accurate because our data do not cover the entire orbital cycle. From the least blended spectrum, we estimated spectral types of O8V and early B (B0–1) for the primary and the secondary, respectively. We also classified HD 46150 as a binary candidate since small variations, at the limit of being significant, have been detected and the Temporal Variance Spectrum (TVS, Fullerton 1996) exhibited profiles with double or triple peaks. Although HD 46056 and HD 46485 present broad and shallow lines, their line widths did not change as a function of time, supporting the idea that both stars are fast rotators rather than binary systems. In general, the 4 remaining stars, HD 46056, HD 46202, HD 46223 and HD 46485, did not show any significant variations in their radial velocities and were, accordingly, classified as presumably single stars.

The spectroscopic investigation thus reveals a binary fraction of O-type stars in NGC 2244 in the range of 17–33% while the previous estimate (Garcìa & Mermilliod 2001) put this value at 50%, based on a very heterogeneous dataset i.e., radial velocities taken from the literature.

3 Determination of stellar and wind parameters

We have used the CMFGEN atmosphere code (Hillier & Miller 1998) for the analysis of the optical and UV spectra of the 6 O-type stars in NGC 2244. The luminosity was computed by supposing a distance of 1.55 kpc for the young open cluster, i.e., the mean value in the range estimated by Hensberge et al. (2000). On the one hand, the stellar parameters such as the surface gravity ($\log g$) or the effective temperature ($T_{\rm eff}$) were determined from the optical domain. We used the wings of Balmer absorption lines H_β, H_γ and H_δ as indicators of $\log g$ whilst the classical ratio between the equivalent widths of the He I λ 4471 and He II λ 4542 lines provided a good estimate of the $T_{\rm eff}$. Other lines of He I and He II, such as He I λ 4026, He I λ 5876, He II λ 4200 and He II λ 5412 were used as additional diagnostics to determine $T_{\rm eff}$.

On the other hand, the wind parameters were derived from the IUE spectra. The wind terminal velocity (v_∞) was estimated from the absorption part of the P Cygni lines observed in the UV domain. The UV P Cygni and emission lines also served as main indicators of the mass-loss rate ($\dot{M}$).

The $v \sin i$ were directly estimated by comparison of our synthetic spectra to the observed line profiles. A macroturbulence component has to be introduced to correctly reproduce the line profiles (e.g., for the He I λ 4713, C IV λ 5812 and He I λ 5876 lines).

The preliminary wind and stellar parameters of the 6 O-type stars (Martins et al., in prep) are reported in Table 1. However, the results concerning the secondary component of HD 46149 are uncertain. Indeed, our sample of spectra does not cover the entire orbital cycle, it is thus difficult to correctly disentangle the individual spectra of both components of HD 46149. From these parameters,

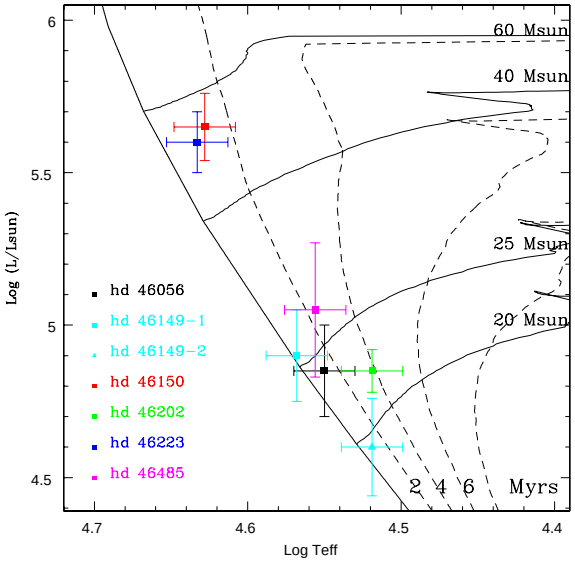

Figure 1: HR diagram showing the position of the O-type stars in NGC 2244. Evolutionary tracks are from Meynet & Maeder (2003) computed with an initial rotational velocity of about 300 km s^{-1}. The dotted lines indicate the isochrones of 2, 4, 6 and 8 Myr.

we put all the stars on a HR diagram (Fig. 1), implying an age of less than 5 Myr for all the O-type stars investigated in Sect. 2. The two hottest stars, HD 46150 and HD 46223, are found to be at the same age (i.e., 0–2 Myr old). A previous study of NGC 2244, by Wang et al. (2008) in the X-ray domain, revealed the existence of X-ray sources, associated to PMS stars, around HD 46150 but not around HD 46223. Two explanations were advanced by these authors. The first one assumes that dynamical interactions are present in NGC 2244, interactions which would be responsible for the ejection of HD 46223 from the central part of the cluster. The second scenario considers that HD 46223 might actually be younger than HD 46150 and would not be part of the same population as the core of the cluster. Our results favor the former explanation based on dynamical interactions inside the cluster since the two hottest stars appear to have a similar age.

Table 1: Preliminary stellar and wind parameters of the 5 O-type stars and both components of HD 46149. The different columns indicate the stars, the spectral type (derived in Mahy et al. 2009), the effective temperature, the luminosity, the surface gravity, the mass-loss rate, the terminal velocity, the projected rotational velocity and the macroturbulence velocity, respectively.

Target	Spectral type	$T_{\rm eff}$ (kK)	$\log(\frac{L}{L_\odot})$	$\log g$	$\log(\dot{M})$ ($M_\odot$ yr^{-1})	v_∞ (km s^{-1})	$v \sin i$ (km s^{-1})	$v_{\rm mac}$ (km s^{-1})
HD 46056	O8V	35.5±2.0	4.85	3.75±0.10	–9.0	1500±100	330	0
HD 46149-A	O8V	37.0±2.0	4.90	4.25±0.10	≤–9.0	1800±100	∼0	24
HD 46149-B	B0–1	33.0±2.0	4.60	3.50±0.10	–	–	100	27
HD 46150	O5.5V	42.5±2.0	5.65	4.00±0.10	–7.2	2800±100	100	37
HD 46202	O9V	33.0±2.0	4.85	4.00±0.10	–8.9	1200±100	20	17
HD 46223	O4((f$^+$)) V	43.0±2.0	5.60	4.00±0.10	–7.2	2800±100	100	32
HD 46485	O8V	36.0±2.0	5.05	3.75±0.10	–8.1	1700±100	300	0

4 The CoRoT photometric data

The CoRoT satellite (Auvergne et al. 2009) has observed 4 O-type stars in NGC 2244 (HD 46149, HD 46150, HD 46202 and HD 46223) during the second short run (SRa02, ∼34 days) with the Asteroseismology channel. The sampling of the obtained data is of one point every 32 s, providing light curves of an unprecedented quality.

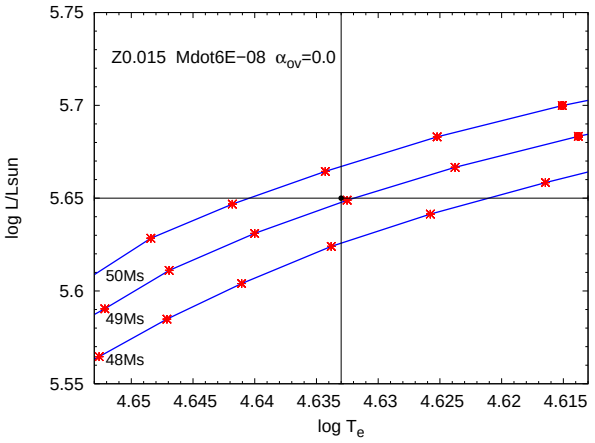

Figure 2: Evolutionary tracks of HD 46223 in the error box computed from the parameters estimated by CMFGEN (Table 1). The red crosses correspond to models computed with ATON and red points correspond to models with excited modes. No overshooting is included in the models.

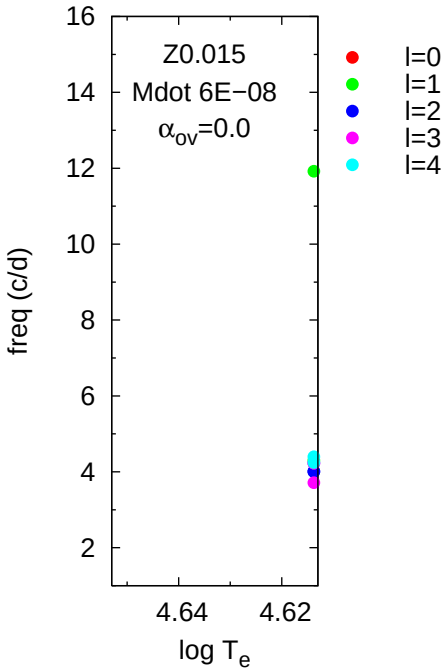

Figure 3: Frequencies computed for the models with excited modes (l) on the tracks of 49 $M_{\odot}$.

Degroote et al. (2010) claimed the presence of solar-like oscillations in the CoRoT light curve of HD 46149. However, it is currently not possible to attribute these oscillations to the late O-type primary or to the early B-type secondary star of the binary system. Another intensive asteroseismological activity is also detected from the CoRoT light curve of HD 46202 (Briquet et al., in prep).

However, from a general point of view, all O-type stars in the sample observed by CoRoT are affected by the presence of red noise. The parallelism with the helioseismology could indicate that this red noise is linked to something similar to granulation. The work of Cantiello et al. (2009) suggested that a sub-surface convection zone, induced by the iron opacity bump, could affect the stellar surface behaviour through, e.g., the microturbulence or the clumping and could be responsible for the red noise. Furthermore, Belkacem et al. (2010) suggested that this convection zone could generate stochastically excited oscillations in massive stars.

We have established a first preliminary theoretical asteroseismological analysis of HD 46223. We have determined an error box (Fig. 2) on the HR diagram from the stellar parameters derived with the CMFGEN code (Hillier & Miller 1998, Table 1). Several models have been computed using the ATON evolution code (Ventura et al. 2008) to determine the possible existence of excited modes in this star. Among the 17 different models (red crosses in Fig. 2), computed in the error box, only two present excited modes. If we consider the associated frequencies (Fig. 3), we should detect frequencies close to 4 d^{-1} and 12 d^{-1}. However, no outstanding peak is visible around these frequencies in the semi-amplitude spectrum (Fig. 4) of HD 46223, which implies that this star would only be affected

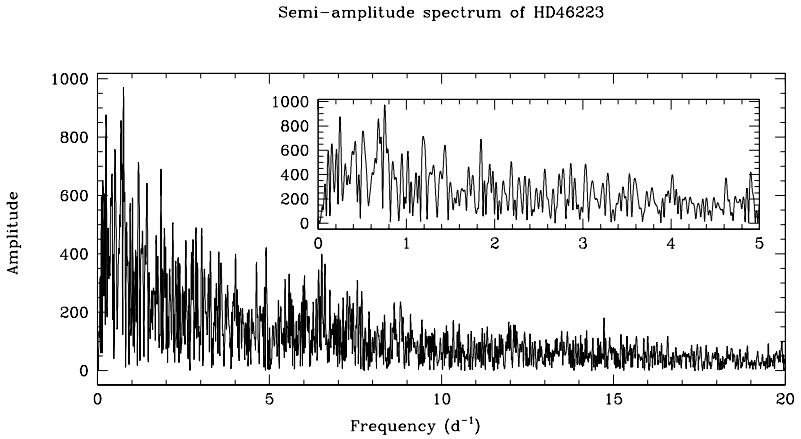

Figure 4: Semi-Amplitude spectrum of the CoRoT light curve of HD 46223 computed with the Heck, Manfroid & Mersch method (Heck et al. 1985; revised by Gosset et al. 2001). The inset shows a zoom-in on the low-frequency domain.

by red noise. However, we present here only preliminary results of the analysis of these CoRoT data. A more detailed analysis will be presented in a forthcoming paper (Blomme et al., in prep).

Acknowledgements

This research is supported by the FNRS (Belgium), by a PRODEX XMM/Integral contract (Belspo) and by the Communauté Française de Belgique-Action de Recherche Concertée (ARC)-Académie Wallonie-Europe. We acknowledge the Ministère de l'Enseignement Supérieur et de la Recherche de la Communauté Française for supporting our travels to O.H.P. We also thank the staff of Observatoire de Haute-Provence and of La Silla ESO Observatory for their technical support. F.M. thanks John Hillier for making his code available and for assistance. P.E. acknowledges support through CONACyT grant 67041.

References

Auvergne, M., Bodin, P., Boisnard, L., et al., 2009, A&A, 506, 411
Belkacem, K., Dupret, M. A., & Noels, A., 2010, A&A, 510, A6
Cantiello, M., Langer, N., Brott, I., et al., 2009, A&A, 499, 279
Chen, L., de Grijs, R., & Zhao, J. L., 2007, AJ, 134, 1368
Degroote, P., Briquet, M., Auvergne, M., et al., 2010, A&A, 519, A38
Fullerton, A. W., Gies, D. R., & Bolton, C. T., 1996, ApJS, 103, 475
Garcìa, B., & Mermilliod, J. C., 2001, A&A, 368, 122
Gosset, E., Royer, P., Rauw, G., et al., 2001, MNRAS, 327, 435
Heck, A., Manfroid, J., & Mersch, G., 1985, A&AS, 59, 63
Hensberge, H., Pavlovski, K., & Verschueren W., 2000, A&A, 358, 553
Hillier, D. J., & Miller, D. L., 1998, ApJ, 496, 407
Mahy, L., Nazé, Y., Rauw, G., et al., 2009, A&A, 502, 937
Meynet, G., & Maeder, A., 2003, A&A, 404, 975
Ogura, K., & Ishida, K., 1981, PASJ, 33, 149
Sana, H. & Evans, C. J., 2010, IAUS272, in press (arXiv:1009.4197)
Sana, H., Gosset, E. & Evans, C. J., 2009, MNRAS 400, 1479
Ventura, P., D'Antona, F., & Mazzitelli, I., 2008, Ap&SS, 316, 93
Wang, J., Townsley, L. K., Feigelson, E. D., et al., 2008, ApJ, 675, 464

Chapter 6

The Cygnus associations

The Cygnus area is an active star-forming region in the Milky Way. Its relative proximity (1 − 2 kpc, Le Duigou & Knödlseder 2002) makes this region suitable for studying the formation processes as well as the interactions between the massive stars and the interstellar medium. Though this region is rich in massive stars, its heavy absorption prevents one from obtaining an accurate estimate of the stellar population. Moreover, the membership of certain stars to a given cluster or an association is sometimes not clearly defined due to the complexity of this area.

The Cygnus constellation (Fig. 6.1) indeed harbours nine OB associations and, at least, a small dozen of young open clusters. The central association Cyg OB2 is one of the youngest of the area (1 − 4 Myrs, Knödlseder et al. 2002) whilst in its surroundings, the associations Cyg OB1, Cyg OB3, Cyg OB7 and Cyg OB9 are older. Therefore, the idea of a formation triggered by Cyg OB2 is unlikely. In the framework of this thesis, we have monitored nineteen O-type stars located in four different associations (Cyg OB1, Cyg OB3, Cyg OB8 and Cyg OB9) or in young open clusters belonging to these associations.

Located at 1.8 kpc according to Humphreys (1978), the Cyg OB1 association contains three nuclei in its core. NGC 6913 has an age estimated to about 4 − 6 Myrs (Massey et al. 1995) and, according to Wang & Hu (2000) a mean distance of about 2.2 kpc. However, a significant number of field stars along the line-of-sight could blur the age and distance indicators that were used (Malchenko & Tarasov 2009). A second cluster, Berkeley 86, seems located in the Orion spiral feature at a distance of about 1.8 kpc with a reddening of $E(B-V) = 0.96 \pm 0.07$ mag (Bhavya et al. 2007). Massey et al. (1995) and Bhavya et al. (2007) estimated the age of this cluster to be close to 5 or 6 Myrs. Finally, IC 4996, the third central cluster in Cyg OB1, is surrounded by a dusty shell. Its reddening is estimated to about $E(B-V) = 0.71 \pm 0.08$ mag and its distance to 2.3 kpc (Delgado et al. 1998). This cluster also seems older than the other two, with an age of 7 Myrs.

To the West of Cyg OB1 lies the Cyg OB3 association whose distance, around 2.4 kpc, was measured by Humphreys (1978). Part of this association, NGC 6871 has been relatively well studied photometrically. Massey et al. (1995) derived from the isochrone fitting ages of 2 − 5 Myrs for the stars with M > 25 $M_\odot$ whilst Reimann (1989) estimated an age of 10 − 20 $M_\odot$ for the stars with M > 4 $M_\odot$. This discrepancy suggests a contamination from nearby objects from the local spiral arm (Slesnick et al. 2002). However, the presence of O-type stars in that cluster puts an upper limit on its real age (∼ 6 − 8 Myrs). This star formation area is however embedded in dark clouds. Therefore, numerous faint young massive stars could still be undetected (Malchenko &

Tarasov 2009).

To the North-East of Cyg OB1, the Cyg OB8 association was not much investigated in the past years, and there exist only few references in the literature. It appears that this association is the youngest among those of the Cygnus complex (~ 3 Myrs, Uyanıker et al. 2001 and references therein). Its distance was estimated by Humphreys (1978) to be about 2.3 kpc.

Finally, Cyg OB9 lies between the well-known Cyg OB2 association, to the East, and Cyg OB1, to the West. This association seems about 8.0 Myrs old and located at a distance of about 1.2 kpc (Uyanıker et al. 2001). Belonging to this association, the NGC 6910 cluster is surrounded by a series of gaseous emission nebulae (Bhavya et al. 2007). Moreover, the extinction in this region is high ($E(B-V)$ of about 1.2 mag) which renders its population hard to observe and poorly known. However, from the few bright massive stars observed, the age of this cluster is estimated at about $6-8$ Myrs, in agreement with the age of the association.

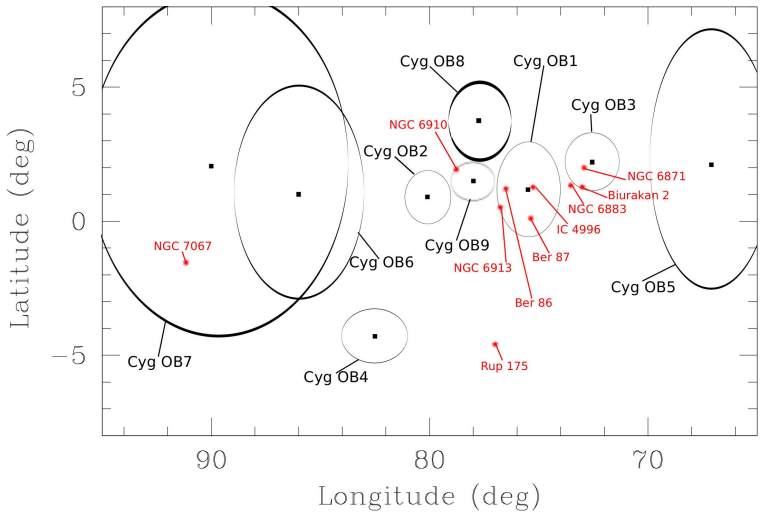

Figure 6.1: Schematic view of the different OB associations and young open clusters in the Cygnus region.

In this chapter, we analyse the multiplicity of nineteen O-type stars in the Cygnus region (with $7 > V > 10$) as well as their fundamental parameters. Their membership to a given association is established on the basis of Humphreys (1978). Thanks to a regular monitoring spread over three years (from 2008 to 2011), we study the radial velocity and line profile variations in the observed spectra over short- and long-term timescales. We have collected 273 spectra by using two different instruments: the Aurélie spectrograph at the 1.52m telescope at OHP and the ESPRESSO spectrograph mounted on the 2.10m telescope at San Pedro Màrtir in Mexico. The details of these instruments have been given in Section 5.2. We have also retrieved 9 spectra from the Elodie archives to complete our dataset. The journal of observations of all the stars is provided in Appendix C. In these tables as in the following, HJD is expressed in format HJD − 2450000 for readability. Moreover, five targets were observed by the *IUE* satellite between 1979 and 1987. We have used these additional data to constrain the wind parameters of these objects on the basis of their UV P Cygni profiles.

As we mentioned in Section 5.2, a star is considered as binary either if significant and periodic variations are detected in its radial velocities or if the signature of a companion whose spectral lines move in anti-phase with those of the main star is observed. If the orbital period is sufficiently

well constrained, we compute a full orbital solution, leading to an accurate determination of the orbital parameters. If not, we only derive the mass and flux ratios between both components as well as their spectral type classification. In the case where significant variations of the radial velocities are measured on all the spectral lines, without any periodic motion nor a secondary signature, the object is considered as a "binary candidate". We will consider the radial velocity changes as significant when the variations reach at least $7 - 8$ km s^{-1}. The common wavelength region between OHP and SPM data is [4450 – 4900] Å. In this spectral band, some interstellar lines exist but they are not sufficiently strong and narrow to use them as indicators of the radial velocity errors. However, our previous experience with the same spectrographs showed us that an accuracy of about $7 - 8$ km s^{-1} is commonly achieved with these spectra (see Section 5.2.1). For rapid rotators, we consider them as variable if radial velocity variations of at least 15 km s^{-1} are detected. For each star, we perform an analysis of the radial velocities by taking the rest wavelengths quoted by Conti et al. (1977) and Underhill (1995). In addition, we calculate the TVS (Fullerton et al. 1996) to search for line-profile variations. When such variations are detected for all the line profiles, the TVS is considered as an additional clue of multiplicity.

Moreover, if the star is presumably single, we estimate its stellar and wind parameters by using the atmosphere code CMFGEN (Hillier & Miller 1998, see Section 1.1.1). If the star is a binary system, we first disentangle the spectra to obtain the individual contributions and to refine the radial velocity measurements. We then correct these spectra for the respective brightness factor (examples of this process are notably available in the LZ Cep or HD 48099 papers in Section 2.3 and in Section 5.2, respectively). We also estimate the orbital period of the system by using the HMM method (Heck et al. 1985; Gosset et al. 2001). When the period is well established, we compute the orbital solution of the system with the LOSP software (Liège Orbital Solution Package, Sana & Gosset, private communication). The latter program is based on the generalization of the SB1 method of Wolfe et al. (1967) to the SB2 case along the lines described in Rauw et al. (2000) and Sana et al. (2006). Finally, we determine the spectral type of each star from Conti's criteria (Conti & Alschuler 1971; Conti 1973) and from those of Mathys (1988, 1989). These criteria are based on the equivalent widths of specific lines. We adopt the usual notations: $\log W' = \log W(4471) - \log W(4542)$, $\log W'' = \log W(4089) - \log W(4143)$, and $\log W''' = \log W(4388) + \log W(4686)$ as well as those of Walborn (1971, and the subsequent papers). We however emphasize that Mathys's criterion requires single stars or binaries where the light ratio is sufficiently well determined and where variations as a function of time due to the stellar winds or wind interactions are not observed.

6.1 Individual analysis of the sample stars

6.1.1 Cygnus OB1 association

HD 193443

Reported as binary by Muller (1954), this star has never been the target of an intense spectroscopic monitoring. Therefore, no orbital solution is known for that system nor are the spectral classifications for both components.

We have acquired thirty-seven spectra of HD 193443 from Aug 2004 (HJD = 3246.4777) to Dec 2010 (HJD = 5543.2387). These data reveal a periodic variation of the line profiles, clearly visible in the He I 4471 and He II 4542 lines (Fig. 6.2). Even though the signature of the secondary

is detected, the small radial velocity separation between both components does not allow us to observe the full widths of lines throughout the orbit, leading to possible problems in disentangling (see Chapter 2). We measure the radial velocities of the primary at the bottom of the absorption lines. At maximum of separation, we also fit a second Gaussian profile to determine the radial velocity of the secondary.

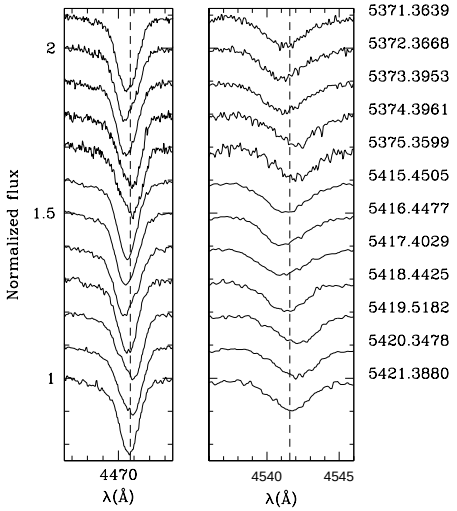

Figure 6.2: He I 4471 and He II 4542 line profiles of HD 193443 at various epochs

Table 6.1: Orbital solution for HD 193443 computed by assuming that the uncertainties on the secondary RVs are three times as large as for the primary.

Parameters	Primary	Secondary
P [d]	7.467 ± 0.001	
e	0.315 ± 0.024	
T_0 (HJD)	3246.120 ± 0.106	
γ [km s^{-1}]	-10.0 ± 1.2	-16.6 ± 2.0
K [km s^{-1}]	38.8 ± 1.5	91.3 ± 3.4
$a \sin i$ [$R_\odot$]	5.4 ± 0.2	12.8 ± 0.5
$M \sin^3 i$ [$M_\odot$]	1.0 ± 0.1	0.4 ± 0.1
Q (M_1/M_2)	2.35 ± 0.11	
rms [km s^{-1}]	5.08	

Before computing the orbital solution of HD 193443, we separate the individual contributions of both stars by applying the disentangling program based on the González & Levato (2006) technique (see Chapter 2). The resulting spectra cover the [4460 − 4890] Å spectral band but remain uncertain because of the small spectral separation between the stars. However, we use this technique to refine by cross-correlation the radial velocities of each component. The cross-correlation window gathers the He I 4471, 4713 and He I 4542, 4686 lines, for both stars. The journal of observations of HD 193443 is provided is Table C.2 in Appendix C.

We compute the periodogram (Fig. 6.3, left panel) from the refined radial velocities of the primary but also from the $RV_S - RV_P$. The highest peak agrees in both methods and corresponds to a period of 7.467 ± 0.001 days. By adopting this period, we are able to fit the radial velocities with an eccentric orbital solution. Table 6.1 and the right panel of Fig. 6.3 respectively provide the best-fitting orbital parameters and the radial-velocity curves.

The He II 4542 line is present but is faint for both stars, indicating two late O-type stars. We compute, from the disentangled and the observed spectra, $\log W' = 0.321$ and $\log W' = 0.483$ for the primary and the secondary, respectively, corresponding to respective spectral types of O 9 and of O 9.5. However, our dataset does not allow us to constrain the luminosity classes of these components.

To determine the brightness ratio, we measure the equivalent widths on the He I 4471, 4713 and on the He II 4542 lines of the disentangled and observed spectra and we compare these values with those of Conti & Alschuler (1971) for stars of the same spectral types as both components. Moreover, we also measure the equivalent widths of the above-quoted lines on CMFGEN synthetic

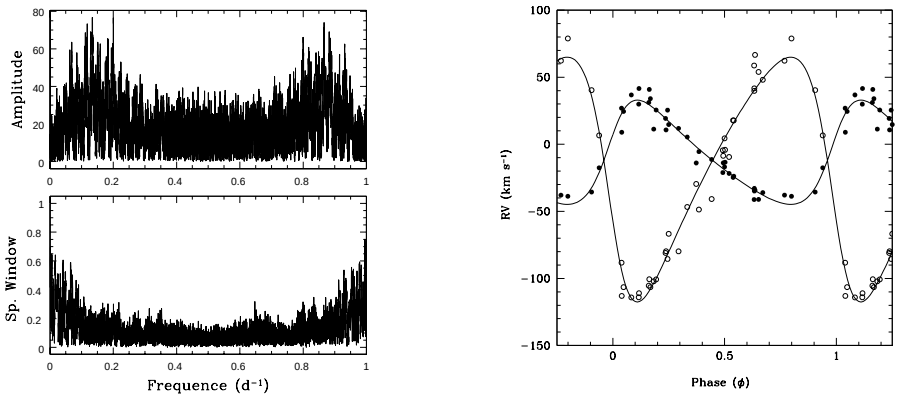

Figure 6.3: *Left*: Semi-amplitude spectrum (upper-left panel) and spectral window (lower-left panel) of HD 193443 computed from the refined radial velocities $RV_S - RV_P$. *Right*: Radial velocity curves of HD 193443. Filled circles represent the primary radial velocities whilst the open circles correspond to the secondary.

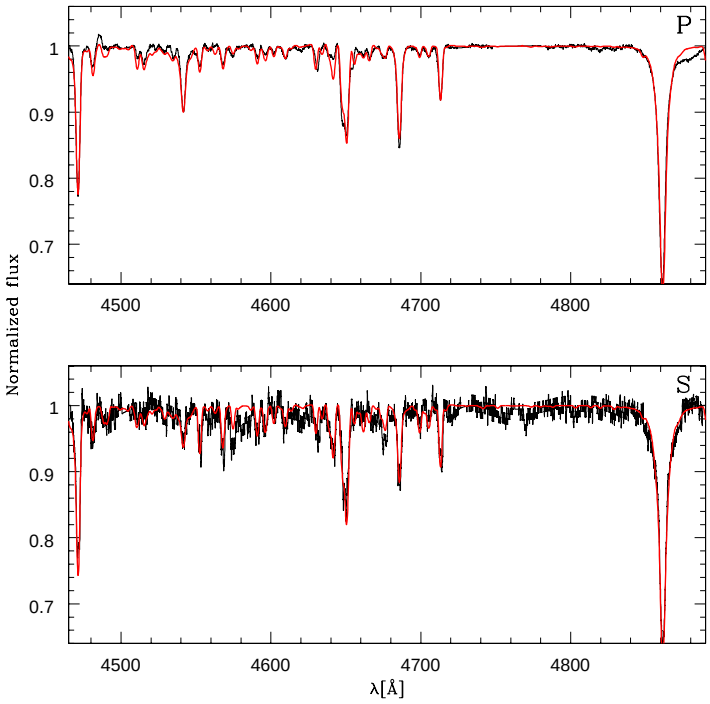

Figure 6.4: Best-fit CMFGEN models for the primary (top) and the secondary (bottom) components of HD 193443.

spectra corresponding to the same spectral classifications. The ratios of these values provide a brightness ratio of about 3.9 between the primary and the secondary components. With $V = 7.25$ and $(B - V) = 0.38$ (Høg et al. 2000), $(B - V)_0 = -0.26$ (corresponding to the spectral type O 9III for the entire system Martins & Plez 2006) and an assumed distance modulus of about 11.31 (Humphreys 1978), we derive an absolute V magnitude for the entire system of about $M_V = -6.04$. By taking into account the relative brightness of each component, we compute an $M_{V_P} = -5.79$ and an $M_{V_S} = -4.33$ for the primary and the secondary, respectively. After having corrected these values by the adequate bolometric corrections, we obtain absolute luminosities of about $\log(L_P/L_\odot) = 5.40 \pm 0.06$ and $\log(L_S/L_\odot) = 4.82 \pm 0.06$.

We then model with CMFGEN both disentangled spectra (corrected by the dilution factor) to derive the stellar properties of each component. Fig. 6.4 exhibits the best-fit CMFGEN models whilst Table 6.5 reports the values of these parameters (see p. 176). The quality of the fit for both stars is rather good. The luminosities and $\log g$ are reminiscent of luminosity classes of giant and main-sequence stars for the primary and the secondary, respectively. Therefore, we classify these respective components of HD 193443 as O 9III and O 9.5V. However, we stress that the disentangled spectra have to be taken with caution since we are not able to sample the full width of the spectral lines, even for the helium ones, because of the small radial velocity separation between both components.

HD 193514

This star was classified as an O 7Ib(f) by Repolust et al. (2004) with $T_{\rm eff}$ of about 34500 K, $\log g$ of 3.55 and a mass-loss rate of $3.48\ 10^{-6} M_\odot$ yr^{-1}. These authors also reported a weak emission in the He II 4686 line profile. Changes from day to day were already observed by Underhill (1995) in the Hα profile, implying that the physical state of the wind changes daily. However, none of these authors did attribute these variations to a binary nature.

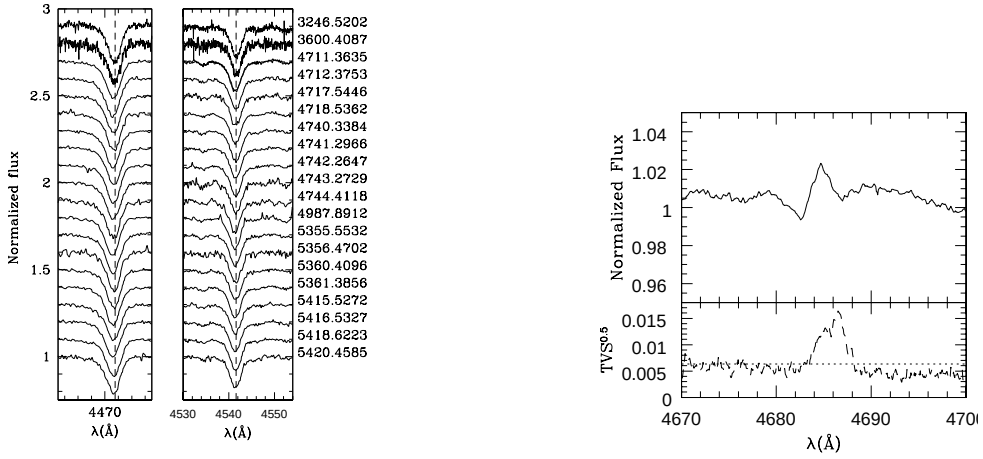

Figure 6.5: *Left*: He I 4471 and He II 4542 line profiles of HD 193514. *Right*: Mean spectrum and TVS of HD 193514 computed from the Aurélie data for the He II 4686 line. The dotted line illustrates the 1% significance level for the variability evaluated following the approach of Fullerton et al. (1996).

The twenty-two spectra of HD 193514 taken from Aug 2004 (HJD = 3246.5202) to Aug

2010 (HJD = 5420.4585) confirm its probable single status (Fig. 6.5, left panel). Indeed, we determine mean radial velocities ($\overline{RV}$) for He I 4471, He II 4542 and He I 4713 of about $\overline{RV}$ = -18.0 ± 5.2, -7.0 ± 5.0 and -15.6 ± 5.0 km s^{-1} where the $1-\sigma$ error is computed from the radial velocities. In addition, the TVS of the He II 4542 and the He I 4713 line profiles do not show any substantial variations, though the He I 4471 and especially the He II 4686 lines do (Fig. 6.5, right panel). The latter lines present a strong variability but since this variability is not detected on all the line profiles, we conclude that it is not due to binarity. We also stress that we do not have enough échelle spectra to characterize the changes reported by Underhill (1995) in the line profile of Hα. In spite of the line profile variations observed in the He I 4471 and He II 4686 lines, we therefore consider HD 193514 as a presumably single star with a relatively variable wind. From the échelle spectra, we determine $\log W' = 0.014$ and $\log W'' = 0.096$, yielding for HD 193514 a spectral classification O 7–O 7.5 and a luminosity class between a giant (III) and a main-sequence star (V). In addition, the strong N III 4634–41 lines coupled with a small He II 4686 emission suggest to complement this spectral classification with an f suffix.

We estimate the stellar and wind parameters from an Elodie spectrum and from an *IUE* spectrum. We compute for this star an absolute V magnitude of about $M_V = -6.18$ from $V = 7.41$ and $(B-V) = 0.44$ (Høg et al. 2000) and by assuming a distance modulus of 11.39 (Humphreys 1978). We then apply the bolometric correction of Martins & Plez (2006) relative to the spectral classification of HD 193514 and we obtain a luminosity of about $\log(L/L_\odot) = 5.71 \pm 0.06$. The best-fit CMFGEN model is displayed in Fig. 6.6 and the derived parameters are listed in Table 6.5. The optical spectrum is affected by strong emissions, notably in the cores of the Balmer lines. Furthermore, the fitted N III 4634–41, C IV 5801–12 and He I 5876 lines are fainter than in the observations. This is a rather common feature in the CMFGEN models (F. Martins, priv. communication) but its origin is still unclear (level population/depopulation, blanketing,...). These lines are indeed dependent on the wind of the star but are also formed near the stellar photosphere. By comparing the stellar parameters with those of Martins et al. (2005a), we see that $T_{\rm eff}$ and $\log g$ are reminiscent of a giant star. However, this object appears overluminous for this luminosity class, which could imply that HD 193514 is in a transitory stage between the giant and the supergiant branch. We adopt for HD 193514 a spectral classification of O 7–7.5IIIf.

HD 193595

HD 193595 is located in the young open cluster Berkeley 86 (Massey et al. 1995). Classified as an O 6V (Garmany & Vacca 1991), this object was poorly investigated in terms of its radial velocity but its photometric properties were reported in several studies (Reed 2005; Høg et al. 2000, for example).

We measure the radial velocities on nine spectra taken at different epochs, between Sep 2008 (HJD = 4711.3816) and Aug 2010 (HJD = 5421.4977). These data reveal rather constant radial velocities for the star: $\overline{RV} = -13.7 \pm 2.2$, -8.1 ± 2.8, -4.5 ± 2.6 and -12.5 ± 1.7 km s^{-1} for the He I 4471, He II 4542, He II 4686 and He I 4713 lines, respectively. We however detect clear variations (at a significance level of 1%) in the line profiles of He I 4471. The results of the TVS associated to the radial velocity measurements seem to imply that the observed variations are probably not due to binarity. Therefore, we classify this target as presumably single. Our revised spectral type for this star is O 7V ($\log W' = -0.036$ and $\log W'' = 0.052$). We determine an absolute V magnitude of about $M_V = -4.41$ from $V = 8.76$, $(B-V) = 0.33$ and by taking the mean value of Cyg OB1 (11.31) as distance modulus (Humphreys 1978). By applying the bolometric

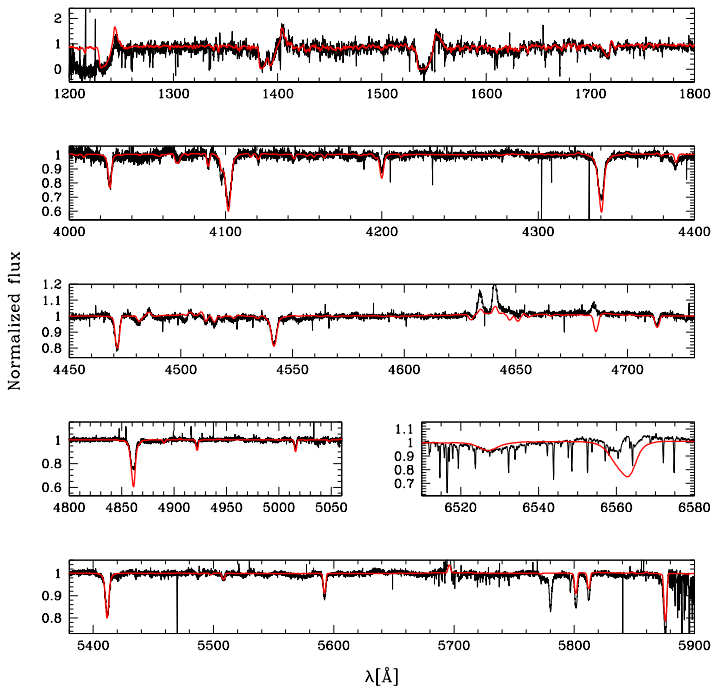

Figure 6.6: Best-fit CMFGEN model for HD 193514.

correction of −3.40 given in the tables of Martins & Plez (2006), we obtain a luminosity of about $\log(L/L_\odot) = 5.02 \pm 0.06$. The parameters derived for this star using CMFGEN (see Table 6.5) are in good agreement with those listed by Martins et al. (2005a) for a star with the same spectral classification.

HD 193682

This star is the hottest object in our sample. Though reported as an O 4III(f) (Garmany & Vacca 1991), HD 193682 suffered from a clear lack of interest in the past years.

We have obtained eleven spectra of this star (Fig. 6.8) between Sep 2008 (HJD = 4711.4038) and Aug 2010 (HJD = 5418.5280). These data show broad line profiles, indicating a rather large projected rotational velocity. From the method of Simón-Díaz & Herrero (2007) based on the Fourier transform, we derive $v \sin i$ of about 150 km s^{-1}. In consequence, the accuracy achieved on the radial velocity measurements is not comparable to that of the other stars. We determine $\overline{RV}$ of about −48.6±11.3, −39.7±7.7 and −55.1±11.1 km s^{-1} for the He I 4471 and He II 4542 and 4686 lines, respectively. Such a high $1-\sigma$ dispersion is probably due to the high projected rotational velocity of the star rather than to binary motions. To confirm our conclusions, we compute the TVS for these lines. We find a significant variation in the line profiles of He II 4686 and Hβ but we cannot consider these changes as due to a binarity because they are not detected in all the lines, notably in the He I 4471 and the He II 4542 lines. Therefore, these variations probably reveal a variable stellar wind rather than a putative companion.

Repolust et al. (2004) determined the stellar and wind parameters of this star: they found $T_{\rm eff}$ of 40000 K, $\log g$ of 3.60, $\dot{M} = 1.73\,10^{-6} M_\odot$ yr^{-1} and a terminal velocity of about 2800 km s^{-1}.

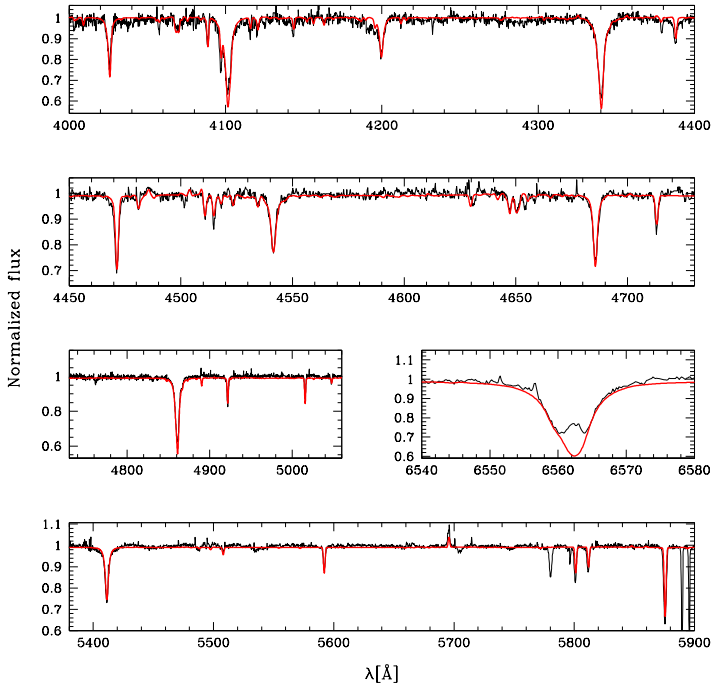

Figure 6.7: Best-fit CMFGEN model for HD 193595.

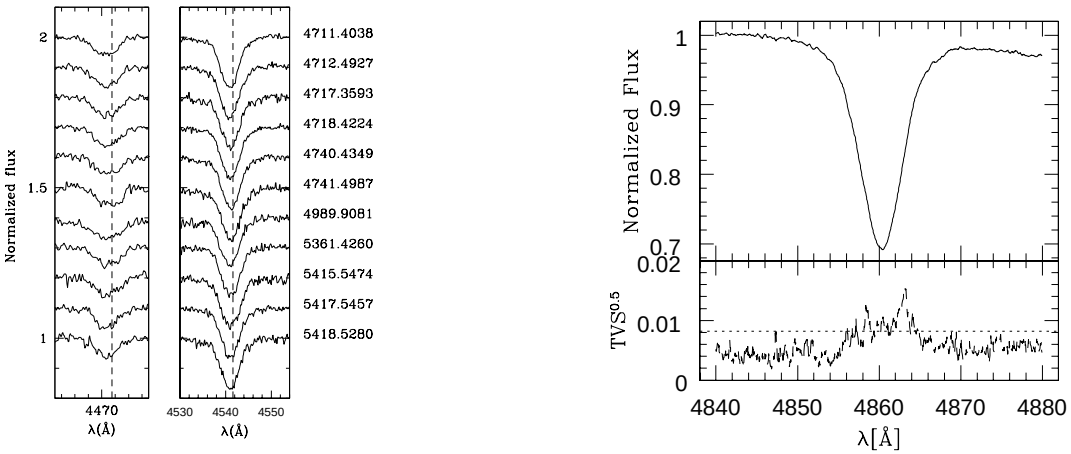

Figure 6.8: *Left*: He I 4471 and He II 4542 line profiles of HD 193682. *Right*: Mean spectrum and TVS of HD 193682 computed from the Aurélie data for the Hβ line. The dotted line illustrates the 1% significance level for the variability evaluated following the approach of Fullerton et al. (1996).

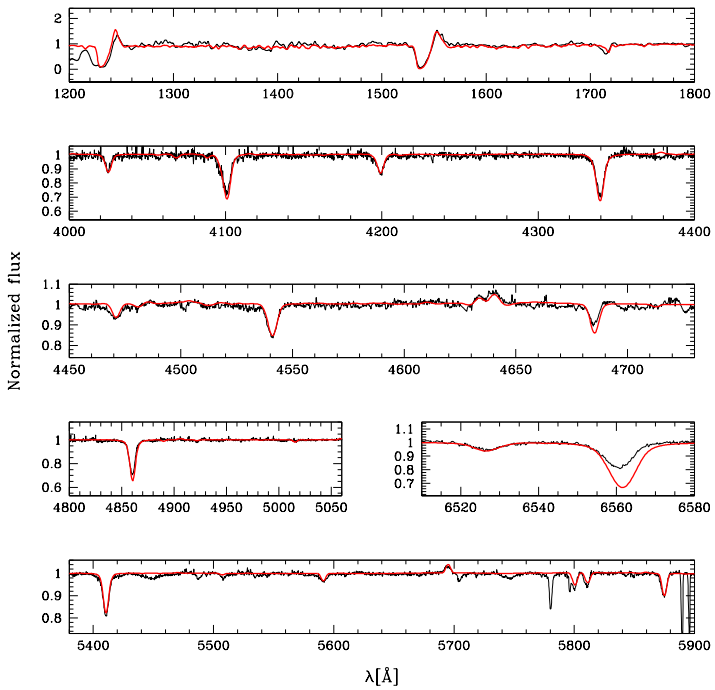

Figure 6.9: Best-fit CMFGEN model for HD 193682.

We use *IUE* spectra to constrain the wind parameters (see Table 6.5). Our model is of excellent quality. However, we observe that the lines affected by the wind in the optical domain (He II 4686 and Hα) are poorly reproduced while the UV profiles are well fitted. As Repolust et al. (2004) already mentioned, the red wings of these lines do not fit the observations perfectly. We calculate, from the He I 4471–He II 4542 ratio, $\log W' = -0.514$, corresponding to an O 5 spectral type. We note that the criteria based on the computation of $\log W''$ and $\log W'''$ are applicable to stars with a spectral type later than O 7 but Walborn's criterion suggests to add a (f) suffix, indicating a medium emission for the N III 4634-41 lines and a medium absorption for the He II 4686 line. We then compute an absolute V magnitude of $M_V = -5.31$ determined from $V = 8.39$, $(B-V) = 0.49$ and a distance modulus of 11.31. By applying the bolometric correction of Martins & Plez (2006) associated to an O 5 spectral classification to the absolute V magnitude, we obtain $\log(L/L_\odot) = 5.49 \pm 0.06$. This luminosity but also $T_{\rm eff}$ and $\log g$ are reminiscent of those of an O 5III star by comparing with the tables of Martins et al. (2005a). We thus revise the spectral classification of HD 193682 to O 5III(f).

HD 194094

This target is rather faint ($V = 9.03$), thereby explaining the little attention paid to it. During our spectroscopic campaign, HD 194094 was observed five times, twice in Jun 2009, twice in Aug 2010 and once in Sep 2011. These five spectra do not exhibit any evidence of a putative companion. We measure the radial velocities on the He I 4471, He II 4542, He II 4686 and He I 4713 lines, reporting mean values of about $\overline{RV} = -18.2 \pm 3.9$, -11.3 ± 3.8, -9.7 ± 8.9 and -13.9 ± 6.1 km s^{-1}, respectively. The $1-\sigma$ errors on these measurements indicate that HD 194094 is probably single and that the radial velocity variations detected on the He II 4686 line are likely due

to a variable stellar wind. We stress however that, unlike the stars previously analysed, the Aurélie data for HD 194094 are not sufficiently numerous nor sufficiently spread over the entire campaign to compute the TVS. Therefore, if we want to include the SPM data in the computation of the TVS, we have to convolve the data so that they reach all the same resolution. Though this process was already used for HD 46150 (see Mahy et al. 2009), we do not have in the [4450 – 4900] Å wavelength domain diagnostic lines similar to the interstellar Na I lines at 5889 and 5896 Å to compare the convolved spectra.

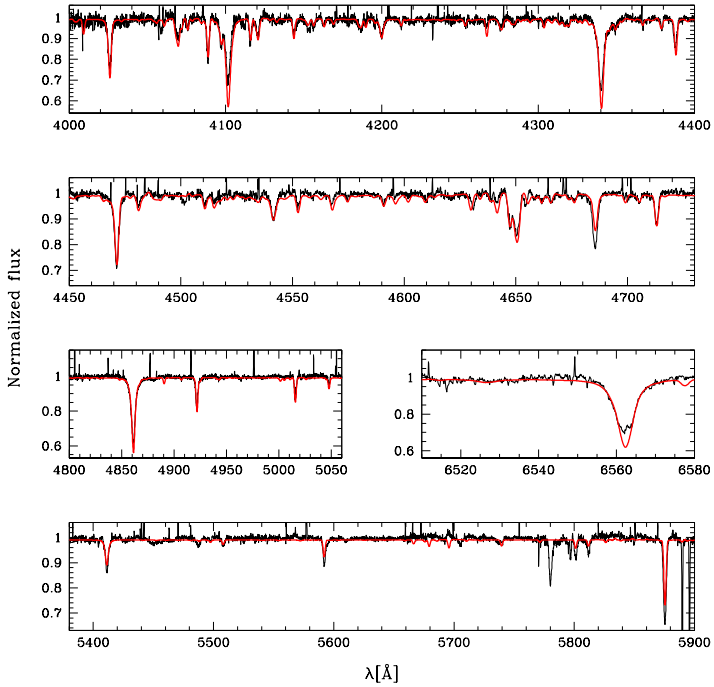

Figure 6.10: Best-fit CMFGEN model for HD 194094.

From an échelle spectrum of HD 194094, we compute $\log W' = 0.232$, $\log W'' = 0.174$ and $\log W''' = 5.204$. These values yield an O 8.5III spectral type. In addition, from $V = 9.03$, $(B-V) = 0.57$ (Høg et al. 2000) and a distance modulus of 11.92 (Humphreys 1978), we determine $M_V = -5.49$. By applying a bolometric correction of -3.06 given by the tables of Martins & Plez (2006) for a spectral type of O 8.5III, we obtain $\log (L/L_\odot) = 5.32 \pm 0.07$ for HD 194094. After comparing it to that quoted in the tables of Martins et al. (2005a), $\log g$ that we have determined is closer to that of a supergiant star. However, this luminosity and the lack of a clear emission in the He II 4686 and in the Hα lines seem to suggest that this star is rather a giant star. Therefore this star could be in a transitory stage between these two luminosity classes. Fig. 6.10 displays the best-fit model for HD 194094 whilst the stellar parameters are listed in Table 6.5.

HD 194280

Presented as a prototype of the OC 9.7Iab class, HD 194280 appears to be a Carbon-rich star with a depletion in Nitrogen (Goy 1973; Walborn & Howarth 2000). According to these authors, the profiles of He I 5876 and Hα indicate that the stellar wind is weak, which would rather be consistent with an earlier evolutionary stage. If this star belongs to a binary system, a mass transfer

could explain its C overabundance and its N depletion.

We have obtained forty-two spectra of this target in the [4460 – 4900] Å wavelength domain spread between Oct 2004 (HJD = 3286.3646) and Nov 2007 (HJD = 4423.2513). The mean radial velocity of the He I 4471, He II 4542, He II 4686 and He I 4713 lines are of $\overline{RV} = -24.9 \pm 4.2$, -11.6 ± 7.6, -5.4 ± 5.0 and -17.1 ± 4.8 km s^{-1}, respectively. These values suggest that this star is presumably single. However, the object presents strong line-profile variations notably in the He I 4471, C III 4650 and Hβ lines, thereby suggesting that its wind could be relatively strong as it is usually observed for stars with an O 9.7I spectral classification.

From the best-fit CMFGEN model, we find an C overabundance and an N depletion, estimated to about 3.3 and 0.2 times the solar abundances[12], respectively. To obtain a fit of good quality, we also need to increase the He abundance to (He/H) = 0.18 i.e., about twice the solar value.

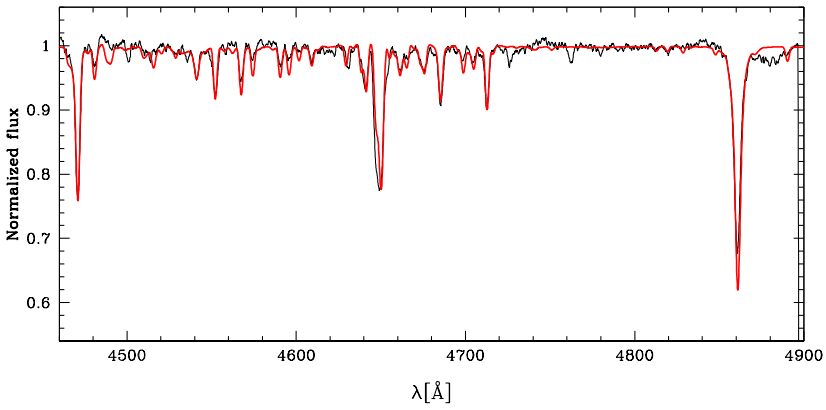

Figure 6.11: Best-fit CMFGEN model for HD 194280.

From the He I 4471–He II 4542 ratio, we obtain $\log W' = 0.742$, which corresponds to an O 9.7 spectral classification. From $V = 8.40$, $(B - V) = 0.71$ (Høg et al. 2000) and by assuming a distance modulus of 11.71 (Humphreys 1978), we computed $M_V = -6.32$, which gives, after having corrected by the bolometric correction, $\log(L/L_\odot) = 5.55 \pm 0.07$. The stellar parameters derived by CMFGEN and listed in Table 6.5 are reminiscent of an OC 9.7Iab star according to the tables of Martins et al. (2005a). Given the spectral range of our data, we are not able to determine $\log W''$, $\log W'''$ nor the wind parameters of this star.

HD 228841

Massey et al. (1995) located this object in the open cluster Berkeley 86, along with HD 193595. This star was successively classified as an O 7V((f)) and an O 6.5Vn((f)) by Massey et al. (1995) and Sota et al. (2011, and references therein).

Eight optical spectra have been collected from Sep 2008 (HJD = 4712.3982) to Aug 2010 (HJD = 5418.5980), mainly in the [4460 – 4490] Å range. The spectra show broad lines which means that HD 228841 is a rapid rotator. We determine from the Fourier transform method of Simón-Díaz & Herrero (2007) a projected rotational velocity of 317 km s^{-1}. Given the broadness

[12] $(C/H)_\odot = 2.45\,10^{-4}$ and $(N/H)_\odot = 6.02\,10^{-5}$ (expressed by number, Grevesse et al. 2007)

of the lines, we adjust by least squares a rotation profile to the spectral lines to determine the radial velocities. The mean values measured on these data amount to $\overline{RV} = -48.4 \pm 8.9$, -25.5 ± 6.5 and -44.9 ± 25.3 km s^{-1} for the He I 4471, He II 4542 and He I 4713 lines, respectively. Given the $v \sin i$, the accuracy obtained on the measurements favours a single status for this star. In addition, the variations in the line profiles computed with the TVS are not significant under a significance level of 1%, which confirms that HD 228841 is probably single.

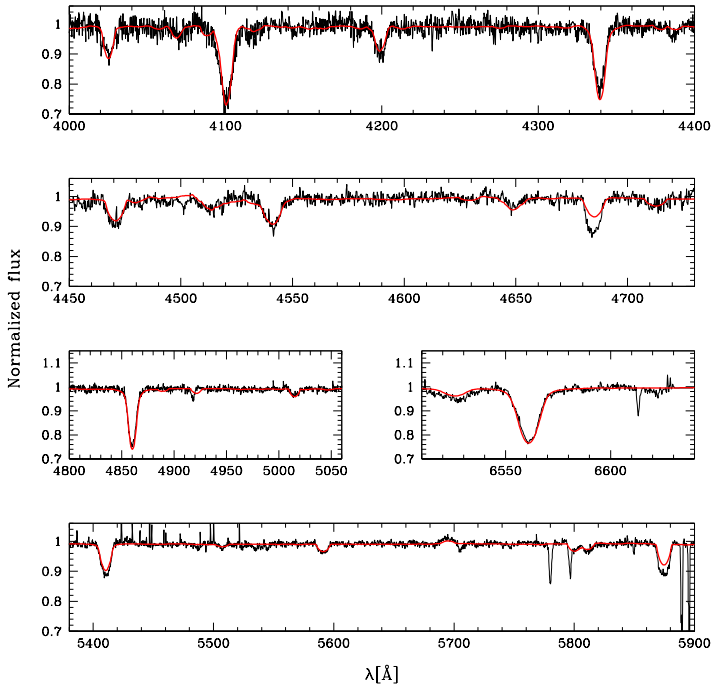

Figure 6.12: Best-fit CMFGEN model for HD 228841.

The synthetic spectrum computed with CMFGEN allows us to derive the stellar and wind parameters listed in Table 6.5. The luminosity of $\log(L/L_\odot) = 5.27 \pm 0.06$ was computed by assuming a distance modulus of 11.60 as quoted by Humphreys (1978). The fit (Fig. 6.12) shows that the synthetic He II 4686 and He I 5876 lines are slightly fainter than in the observed spectrum. Moreover, Conti's criterion indicates an O 7 star ($\log W' = -0.011$) whilst the stellar parameters derived with CMFGEN suggest a luminosity class close to that of a giant star (III). We note that $\log W''$ could not be estimated given the broadness of the lines and thus the severe blend of the Si IV 4089 line with Hδ. We also add an n suffix to the spectral type, meaning that the lines are broad. We thus revise the spectral classification of HD 228841 to O 7IIIn.

HD 228989

Located also in the Berkeley 86 young open cluster (Forbes 1981), this star was quoted as an O 9.5+O 9.5 binary system by Massey et al. (1995). However, no orbital solution was obtained probably because of the faintness of HD 228989 ($V = 9.82$).

We have collected eighteen observations of this object between Aug 2009 (HJD = 5049.9519) and Sep 2011 (HJD = 5815.6460). The journal of observations of HD 228989 is given in Table C.3

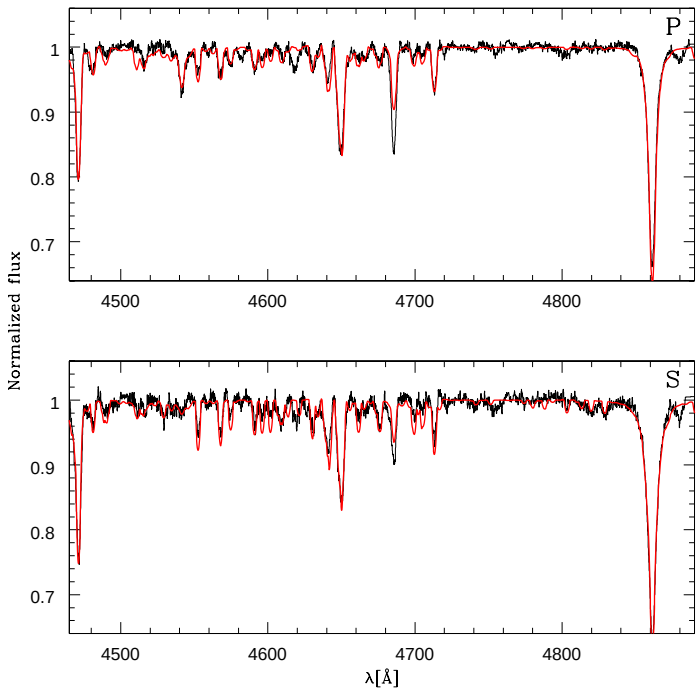

Figure 6.13: Best-fit CMFGEN models for HD 228989.

in Appendix C. These data clearly reveal a binary system composed of two stars with rather similar spectral classifications. We apply the disentangling program to separate the contributions of each star and also to refine their radial velocities. The disentangled spectra corrected for the relative brightness are displayed as black lines in Fig. 6.13. From the disentangled and observed spectra, we determine a spectral type of O 8.5 ($\log W' = 0.238$) and O 9.7 ($\log W' = 0.791$) for the primary and the secondary components, respectively. In addition, we compute for the primary $\log W'' = 0.027$ and for the secondary $\log W'' = 0.206$, suggesting a main-sequence luminosity class for the primary and a giant star for the secondary. Moreover, we estimate the brightness ratio in the same way as for HD 193443. The mean ratio between the observed EWs and those of Conti & Alschuler (1971) and Conti (1973) or those measured on synthetic spectra yields a brightness ratio of about 1.2. From $V = 9.82$ and $(B-V) = 0.71$ (Høg et al. 2000) and by assuming a distance modulus of 10.78, we determine an absolute V magnitude of about $M_V = -3.967$ for the entire system, inferring individual absolute V magnitudes of about $M_{V_\mathrm{P}} = -3.968$ and $M_{V_\mathrm{S}} = -3.502$ for the primary and the secondary components, respectively. By taking into account the bolometric corrections given by Martins et al. (2005a) for the individual spectral types, we calculate bolometric luminosities of about $\log(L_\mathrm{P}/L_\odot) = 4.747 \pm 0.07$ and $\log(L_\mathrm{S}/L_\odot) = 4.489 \pm 0.07$ for the primary and the secondary, respectively.

The computation by the HMM method of the periodogram from the refined radial velocities yields a highest frequency at about 0.56385 d^{-1}, corresponding to an orbital period of 1.773521 days (Fig. 6.14, left panel). Therefore, we compute the orbital solution (Fig. 6.14, right panel and Table 6.2) for the system with the LOSP software (Sana & Gosset, priv. communication).

Using the disentangled spectra, we compute a model atmosphere for each component (see

red lines in Fig. 6.13). The fit is centered on the [4460 – 4900] Å wavelength domain, providing the main stellar parameters for both components (Table 6.5). Comparing with the tables of Martins et al. (2005a), the primary star has a radius, a luminosity and an effective temperature reminiscent of a main-sequence star but with a log g of a giant whilst the secondary is clearly a main-sequence star.

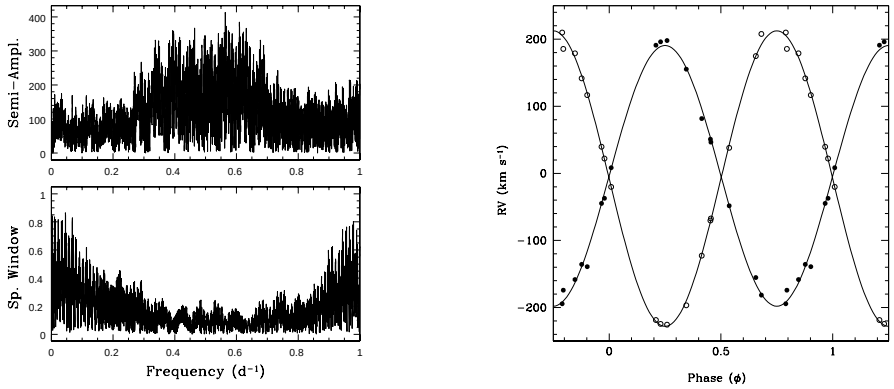

Figure 6.14: *Left*: Semi-amplitude spectrum (upper panel) and spectral window (lower panel) of the He I 4471 radial velocity measurements of HD 228989. *Right*: Radial velocity curves of HD 228989 computed from a $P_{\rm orb}$ = 1.773 days. Full circles represent the primary whilst the open circles correspond to the secondary.

Table 6.2: Orbital solution for HD 228989.

Parameters	Primary	Secondary
P [d]	1.773521 ± 0.000032	
e	0.0 (fixed)	
T_0 (HJD)	5047.771 ± 0.003	
γ [km s^{-1}]	−3.7 ± 1.8	−7.8 ± 1.9
K [km s^{-1}]	194.3 ± 2.5	220.3 ± 2.9
a sin i [$R_\odot$]	6.8 ± 0.1	7.7 ± 0.1
M sin^3 i [$M_\odot$]	7.0 ± 0.2	6.1 ± 0.2
Q (M_1/M_2)	1.133 ± 0.02	
rms [km s^{-1}]	8.37	

HD 229234

Quoted as belonging to NGC 6913 (Humphreys 1978), HD 229234 was classified as an O 9If star by Massey et al. (1995) whilst Negueruela (2004) reported an O 9II spectral type. Previous investigations of Liu et al. (1989) and Boeche et al. (2004) proposed this star to be a binary system with an orbital period of 3.5105 days. This result was confirmed by a recent analysis of Malchenko & Tarasov (2009) made from four spectra.

We have obtained nineteen spectra of HD 229234 between Sep 2008 (HJD = 4717.3892) and Aug 2010 (HJD = 5421.4347). This object obviously displays significant variations in its radial velocities on a short time scale. Our measurements indicate peak-to-peak amplitudes of about 109 km s^{-1} and mean radial velocities of $\overline{RV}$ = −8.7 ± 33.8, 4.9 ± 34.4, 1.7 ± 36.5 and

-6.5 ± 34.0 km s^{-1} for the He I 4471, He II 4542, He II 4686 and He I 4713 lines, respectively. However, no SB2 signature was found in the optical data. We determine on the basis of the HMM technique an orbital period of 3.510595 ± 0.000245 days, confirming the previous estimates of Liu et al. (1989) and Boeche et al. (2004). The parameters of the SB1 orbital solution are listed in Table 6.3. We also derive an O 9III spectral type ($\log W' = 0.372$, $\log W'' = 0.280$ and $\log W''' = 5.325$).

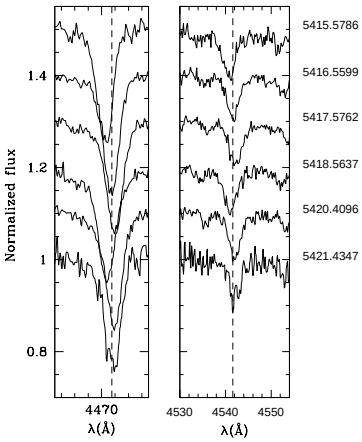

Figure 6.15: A selection of He I 4471 and He II 4542 line profiles of HD 229234.

Table 6.3: SB1 orbital solution for HD 229234.

Parameters	HD 229234
P [d]	3.51059 ± 0.00001
e	0.0 (fixed)
T_0 (HJD)	4714.326 ± 0.011
γ [km s^{-1}]	-16.3 ± 0.8
K [km s^{-1}]	48.5 ± 1.1
$a \sin i$ [$R_\odot$]	3.4 ± 0.1
$f_{\rm mass}$ [$M_\odot$]	0.042 ± 0.003
rms [km s^{-1}]	3.04

Since the contribution of a putative companion is not detectable in the observed spectra, we computed the model atmosphere as if HD 229234 was single. From $V = 8.94$, $(B - V) = 0.71$ (Høg et al. 2000) and a distance modulus of 11.01, we determine an absolute V magnitude of $M_V = -5.08$ and by taking into account the bolometric correction suggested by Martins & Plez (2006) for an O 9III star, we obtain for HD 229234 a luminosity of $\log (L/L_\odot) = 5.11 \pm 0.07$. The best-fit CMFGEN model is displayed in Fig. 6.16 and the stellar parameters are given in Table 6.5.

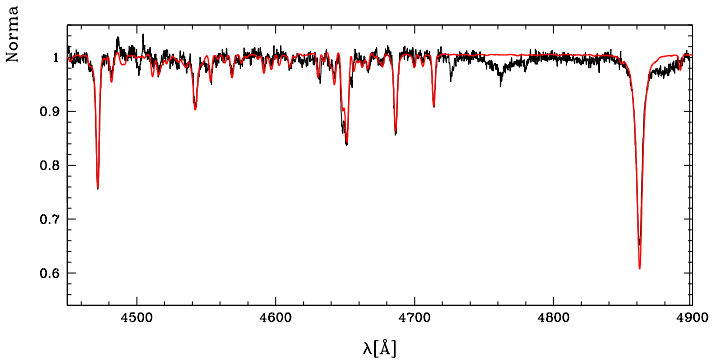

Figure 6.16: Best-fit CMFGEN model for HD 229234.

6.1.2 Cygnus OB3 association

HD 190864

Quoted as belonging to NGC 6871 (Humphreys 1978), HD 190864 is one of the brightest O-type star of Cyg OB3. The spectral classifications derived for this object oscillate between O 6 and O 7 but agree with a giant luminosity class. This star was reported as a possible SB1 system by Mason et al. (1998) and Gies (1987b) whilst a spectral type of B 1II+O 6.5III(f) was attributed to HD 190864 by Garmany & Stencel (1992), assigning it on SB2 status. Moreover, Herrero et al. (1992) and Conti & Ebbets (1977) investigated the line profiles of the star and found scattered values of the projected rotational velocity. Therefore, Herrero et al. (1992) suggested that this difference could be due to a possible varying blend of the profiles of two putative components.

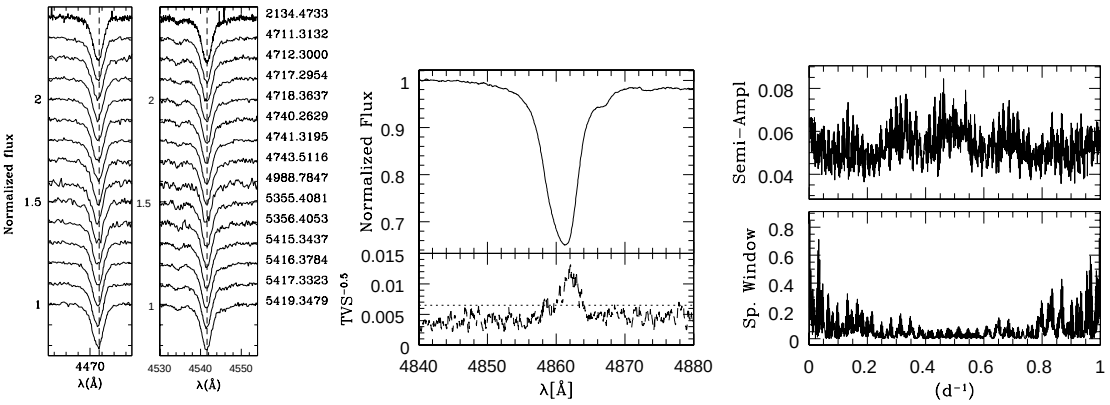

Figure 6.17: *Left*: He I 4471 and He II 4542 line profiles of HD 190864. *Middle*: Mean spectrum and TVS of HD 190864 computed from the Aurélie data for the Hβ line. The dotted line illustrates the 1% significance level for the variability evaluated following the approach of Fullerton et al. (1996). *Right*: The upper panel displays the semi-amplitude spectrum of the line profile variations detected in Hβ whilst the lower one shows the corresponding spectral window.

We have obtained seventeen spectra between Aug 2001 (HJD = 2134.4733) and Aug 2010 (HJD = 5419.3479). This dataset does not show any significant radial velocity changes, except for the He II 4686 line. The mean radial velocity measured on this line is indeed of $\overline{RV} = 4.6 \pm 11.5$ km s^{-1} whilst the other ones derived on He I 4471, He II 4542 and He I 4713 amount to $\overline{RV} = -15.5 \pm 2.5$, -6.3 ± 2.4 and -16.5 ± 3.8 km s^{-1}, respectively. Since our observations cover both short and long time scales, we can exclude that HD 190864 is a binary system with an orbital period shorter than about 3000 days. Therefore, we classify this object as presumably single.

Though no signature of a secondary companion is found in the HD 190864 spectrum, the TVS analysis reveals significant variations of some line profiles. These variations mainly occur in the red wings of the He I 4471, He II 4686 and Hβ lines (Fig. 6.17, right panel). From the HMM method applied on these variations (see the semi-amplitude spectrum in Fig. 6.17), we determine a mean period of these variations of 2.215 ± 0.228 days. Even though this period could be associated to binarity, it is however unlikely that these variations are due to the existence of a secondary star. If that was the case, the TVS pattern should be observed in all the spectral lines which is clearly not the case.

Since no clear evidence exists for HD 190864 being a binary system, we perform the CM-

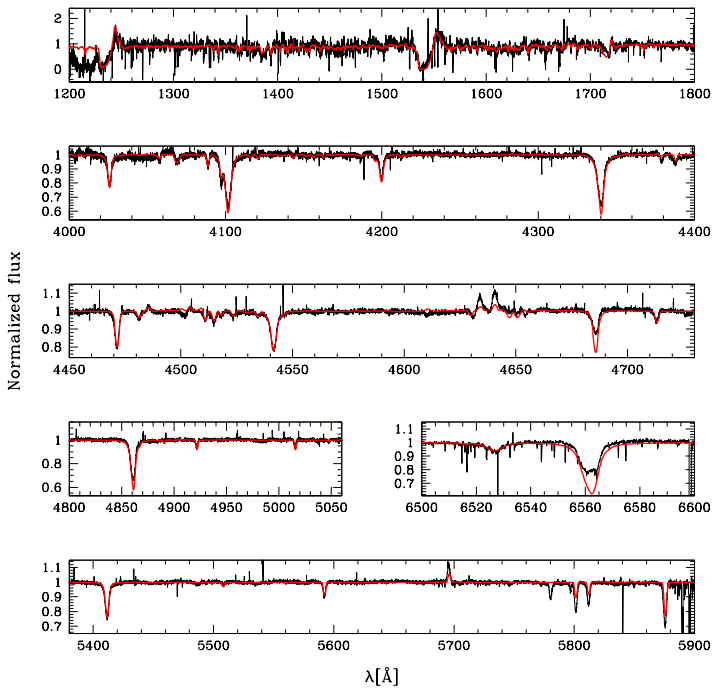

Figure 6.18: Best-fit CMFGEN model for HD 190864.

FGEN analysis on the observed spectrum as if the star was single. A similar investigation was previously reported by Repolust et al. (2004). These authors found $T_{\rm eff}$ of 37000 K, $\log g$ of 3.55, a mass-loss rate of $1.39\,10^{-6} M_{\odot}$ yr^{-1} and a terminal velocity of 2500 km s^{-1}. The parameters we derive (Table 6.5) indicate $T_{\rm eff}$ and $\log g$ larger than those values whilst the mass-loss rate and the terminal velocity are smaller. However, both parameters are determined on the basis of the UV P Cygni profiles whilst the value of Repolust et al. (2004) was estimated from Hα. However, if we look closer at our fit, we see that, by focusing on Hα, our value is underestimated. Similar conclusions reporting a discrepancy between the mass-loss rate estimated from Hα and that estimated from the UV profiles were already drawn from the O-type stars in NGC 2244 but also for HD 193514 and HD 193682. We come back to this topic in Section 6.5. In addition, our model (Fig. 6.18) exhibits some problems in the N IV 1718 line and in the N III doublet at 4634–41 Å. Using $V = 7.77$, $(B - V) = 0.17$ (Høg et al. 2000) and on the basis of the distance modulus of 11.80 given by Humphreys (1978), we determine $M_V = -5.39$ and after applying the bolometric correction, we obtain $\log (L/L_{\odot}) = 5.43 \pm 0.10$. In addition, we derive from Conti's criterion a spectral classification of O 6.5 ($\log W' = -0.193$), consistent with the previous estimates and the stellar parameters we have estimated are reminiscent of a giant star (III). The presence of medium N III 4634–41 lines and a rather weak He II 4686 line suggest to add the (f) suffix. Therefore, the revised spectral type for HD 190864 is O 6.5III(f).

HD 227018

Located at about 1.2° South-West of HD 190864, HD 227018 is rather faint ($V = 8.98$) and therefore not often observed until now. While its spectral type is rather well known (O 6.5–O 7), its luminosity class is poorly constrained. Indeed, Herrero et al. (1992) quoted this star as an O 6.5III

while Massey et al. (1995) attributed it an O 7V((f)) type.

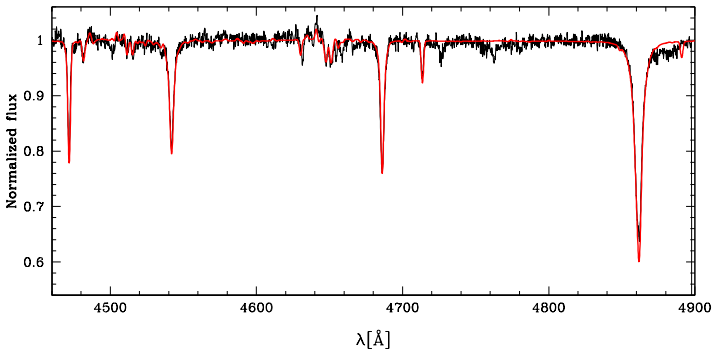

Figure 6.19: Best-fit CMFGEN model for HD 227018.

Between Sep and Oct 2008, we have collected eight spectra with the Aurélie spectrograph and we have increased our dataset with 2 additional spectra taken in August 2010 with the same instrument. The measurements of the radial velocities reveal a rather constant star with mean values of $\overline{RV} = 15.6 \pm 3.4$, 21.7 ± 4.0, 23.8 ± 3.3 and 16.6 ± 3.9 km s^{-1} for the He I 4471, He II 4542, He II 4686 and He I 4713 lines, respectively. Moreover, the TVS spectrum only exhibits a small variation in the He I 4471 line at the limit of being significant while the other lines are relatively stable, thereby indicating that HD 227018 is presumably single.

The absolute V magnitude of this star is computed on the basis of $V = 8.98$, $(B - V) = 0.39$ (Høg et al. 2000) and a distance modulus of 12.49 (Humphreys 1978) and is equal to $M_V = -5.56$. In order to refine the spectral type of this star, we compute, from the He I–He II ratio, $\log W' = -0.201$ which corresponds to an O 6.5 star. Therefore, we determine from the adequate bolometric correction, a luminosity of $\log(L/L_\odot) = 5.51 \pm 0.11$. The CMFGEN analysis of this star shows that HD 227018 is reminiscent of HD 190864. The best-fit model (Fig. 6.19 and Table 6.5) is of good quality in the [4450 – 4900] Å wavelength domain. However, this domain allows us to only derive the stellar parameters. No information can be obtained on the wind parameters. The model parameters indicate that this star still lies on the main-sequence band. Therefore, we attribute to this star a luminosity class V, yielding the spectral classification of O 6.5V((f)). We add the ((f)) suffix because the star shows weak N III 4634–41 emissions and strong He II 4686 absorption lines.

HD 227245

HD 227245 is known as an O 7V (Garmany & Vacca 1991) but because of its faintness ($V = 9.66$) no additional information is available. From five observations taken between Aug 2009 (HJD = 5049.8148) and Jun 2011 (HJD = 5727.7497), we determine mean radial velocities of $\overline{RV} = 5.9 \pm 5.4$, 9.8 ± 3.9, 10.8 ± 6.2 and 6.0 ± 7.3 for the He I 4471, He II 4542, He II 4686 and He I 4713 lines, respectively. The variations of radial velocities are not considered as significant, and HD 227245 is thus probably single.

The spectrum of HD 227245 exhibits He II barely fainter than He I, indicating a mid O-type star. We obtain $\log W' = -0.034$ and $\log W'' = 0.294$, corresponding to a spectral type O 7III. From $V = 9.66$, $(B - V) = 0.60$ (Høg et al. 2000) and a distance modulus of 11.87 (the mean value for the association; Humphreys 1978), we find $M_V = -4.91$ and by taking the bolometric

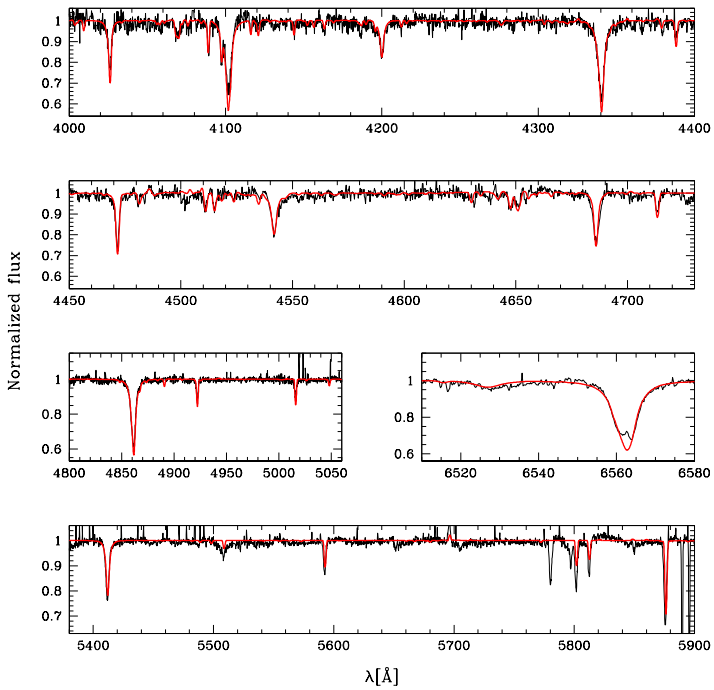

Figure 6.20: Best-fit CMFGEN models for HD 227245.

correction of Martins & Plez (2006), we obtain a luminosity of $\log(L/L_\odot) = 5.20 \pm 0.10$. The best-fit CMFGEN model provides stellar parameters (Table 6.5) similar to those of a star intermediate between the main-sequence and the giant branch. The fit is rather good even though C III 5696, C IV 5801–12 and He I 5876 are less well reproduced. These lines do however not affect the accurate determination of the main stellar parameters.

HD 227757

HD 227757 was reported by Garmany & Stencel (1992) and Herrero et al. (1992) to be an O 9.5V star. This star is relatively faint with $V = 9.25$ and, accordingly, has never been the subject of any spectroscopic monitoring. From five spectra taken between Jun 2009 (HJD = 4988.8797) and Jun 2011 (HJD = 5728.7408), we do not observe significant variations in the radial velocities of HD 227757. Moreover, the three observations made in July 2011 do not show any variations on short time scales. We measure mean radial velocities of $\overline{RV} = -26.8 \pm 4.6$, -26.2 ± 4.5, -28.7 ± 2.9 and -30.0 ± 4.3 km s^{-1} for the He I 4471, He II 4542, He II 4686 and He I 4713 lines, respectively. The spectral line profiles are rather narrow, indicating a small $v \sin i$ (~ 45 km s^{-1}). No signature of a secondary companion is observed despite the narrowness of the lines. We thus consider the star as probably single.

The spectrum of HD 227757 displays a stronger He I 4471 line than the He II 4542 line, indicating a late spectral type. Due to this late type, the blue wing of the He I 4471 line is blended with an O II line. By removing the contribution of the latter line, we measure $\log W' = 0.332$, corresponding to an O 9 star. We also obtain $\log W'' = 0.081$ and $\log W''' = 5.485$ which indicate a main-sequence luminosity class. Therefore, we classified HD 227757 as an O 9V star. From

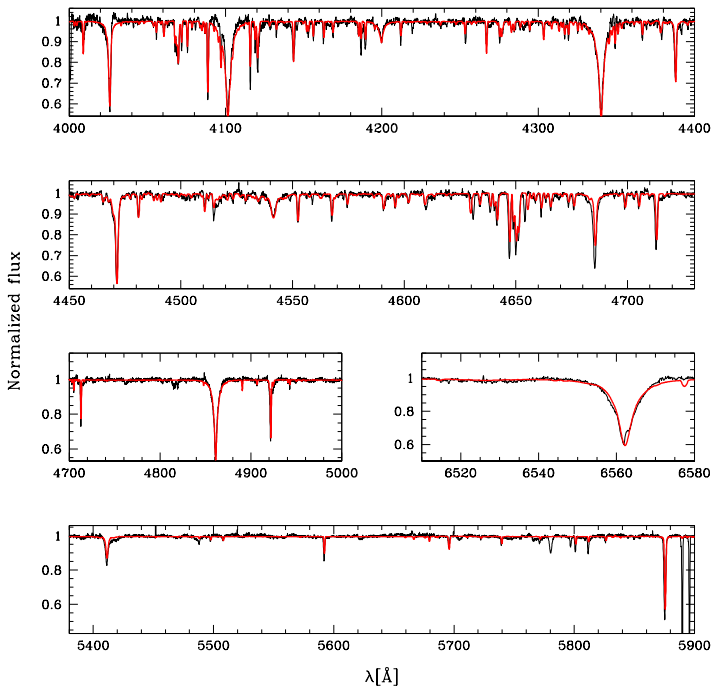

Figure 6.21: Best-fit CMFGEN model for HD 227757.

$V = 9.25$, $(B - V) = 0.16$ and a distance modulus of 11.86 (Humphreys 1978), we determine an absolute V magnitude of $M_V = -3.94$ and by taking into account the bolometric correction of Martins & Plez (2006), we find $\log(L/L_\odot) = 4.70 \pm 0.09$. With such a luminosity, this star could be a weak wind star. However, this property has to be considered as preliminary in the absence of a UV spectrum.

6.1.3 Cygnus OB8 association

HD 191423

Better known under the name of Howarth's Star, HD 191423 is the fastest rotator known until now and it was quoted as the prototype of the ONn stars (nitrogen-rich O star with broad diffuse lines Walborn 2003). Its projected rotational velocity was estimated to be around 400 km s^{-1}. Penny & Gies (2009) computed a $v \sin i$ in the range of [336 – 436] km s^{-1}. Moreover, this star may have a really low terminal velocity ($\sim$ 740 km s^{-1}, Howarth et al. 1997) which could be dependent of the latitude.

We have obtained eight spectra of this star, mainly with the Aurélie spectrograph between Sep 2008 (HJD = 4711.4958) and Aug 2010 (HJD = 5421.5876). From the Fourier transform method of Simón-Díaz & Herrero (2007), we determine $v \sin i = 410$ km s^{-1}, in good agreement with previous estimates. Given the broadness of the lines, we adjust by least squares a rotation profile to the spectral lines to determine the radial velocities. We find mean radial velocities of $\overline{RV} = -44.0 \pm 3.2$, -58.2 ± 19.5 and -56.4 ± 5.13 km s^{-1} for the He I 4471, He II 4542 and He I 4713 lines, respectively. Determining the radial velocities on such a rapid rotator is not an

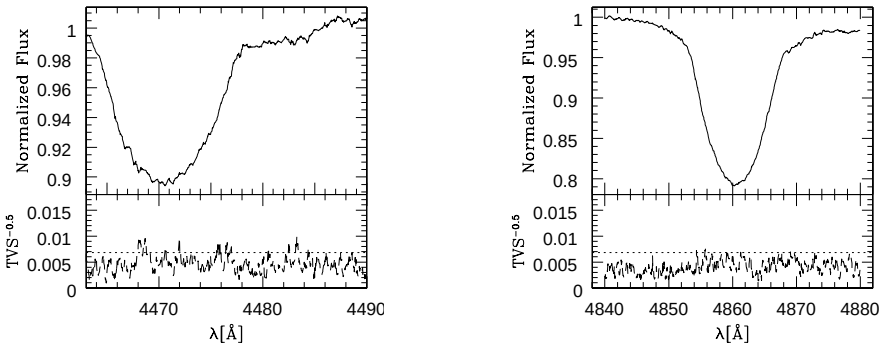

Figure 6.22: Mean spectrum and TVS of HD 191423 computed from the Aurélie data for the He I 4471 and Hβ line. The dotted line illustrates the 1% significance level for the variability evaluated following the approach of Fullerton et al. (1996).

easy task and the measurement errors are generally large because the centroids of the lines are not well defined. This could explain the large deviation observed for the He II 4542 line. The other lines are rather stable in radial velocity, thereby indicating a presumably single star. Moreover, after having computed the TVS spectra for these characteristic lines, we detect no significant variation of line profiles (Fig. 6.22), which confirms the likely single nature of HD 191423. We compute $\log W' = 0.396$ and $\log W''' = 5.187$, giving to this star an O 9III type. We are not able to estimate $\log W''$ given the blend of the Si IV 4089 line with Hδ.

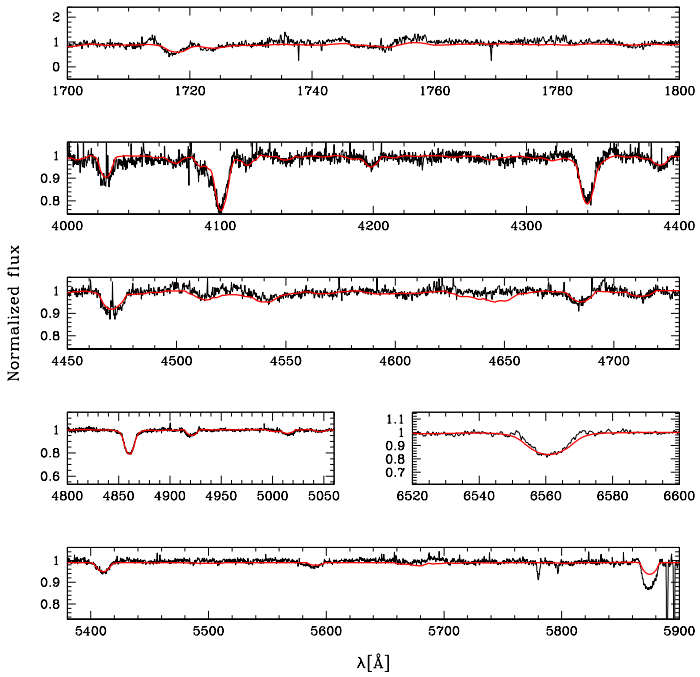

Figure 6.23: Best-fit CMFGEN model for HD 191423.

From $V = 8.05$, $(B - V) = 0.13$ (Høg et al. 2000) and a distance modulus of 12.25 (Humphreys 1978), we find $M_V = -5.41$, which gives $\log(L/L_\odot) = 5.25 \pm 0.12$ by applying

the bolometric correction of Martins & Plez (2006) for the corresponding spectral type. The stellar and wind parameters (Table 6.5) derived from the optical and UV spectra confirm the spectral classification and the small terminal velocity of this star. The model (Fig. 6.23) also yields through the adjustment of the carbon lines at 4070 and 4650 Å a large depletion in C (about 0.1 times the solar abundance) and an enrichment in N (about 9 times the solar abundance). The broadness of the lines and the N content (listed in Table 6.5) suggest to add the suffixes *n* and *N*, thereby giving an ON 9IIIn spectral classification for HD 191423.

HD 191978

HD 191978 was classified as an O 8 star by Goy (1973). The investigation of its radial velocities by Abt & Biggs (1972) did not reveal any significant variations.

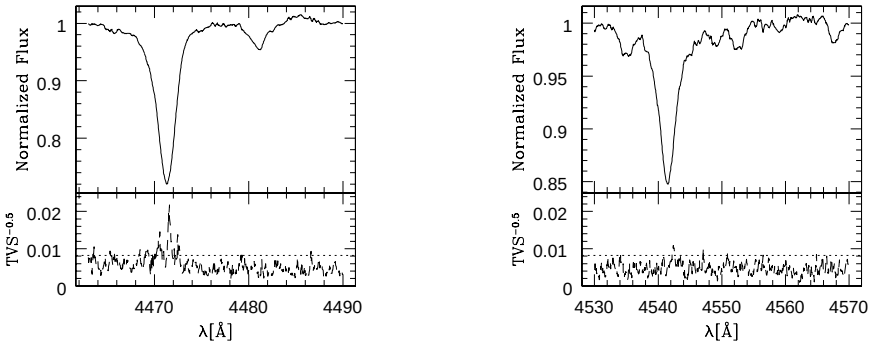

Figure 6.24: Mean spectrum and TVS of HD 191978 computed from the Aurélie data for the He I 4471 and He II 4542 line. The dotted line illustrates the 1% significance level for the variability evaluated following the approach of Fullerton et al. (1996).

We have collected eleven spectra of HD 191978 over a time scale of about 2170 days between Aug 2004 (HJD = 3247.4196) and Aug 2010 (HJD = 5419.4729). The measurements made on these data show relatively constant radial velocities. We obtain mean radial velocities of $\overline{RV} = -18.1 \pm 3.9$ km s^{-1} for the He I 4471 line, $\overline{RV} = -10.4 \pm 5.3$ km s^{-1} for the He II 4542 line, $\overline{RV} = -9.5 \pm 5.0$ km s^{-1} for the He II 4686 line, and $\overline{RV} = -11.8 \pm 6.2$ km s^{-1} for the He I 4713 line. However, the TVS spectra exhibit clearly significant line-profile variations for the He I 4471, He II 4686 and Hβ lines whilst unsignificant line-profile variations are found for the He II 4542 and He I 4713 lines (Fig. 6.24). Since these variations are not detected in all the line profiles, it is difficult to believe that they are linked to binarity. Therefore, we consider this star as presumably single. The determinations of the equivalent widths for the diagnostic lines yield $\log W' = 0.120$, $\log W'' = 0.227$ and $\log W''' = 5.398$, which correspond to an O 8III star. We determine, from $V = 8.04$, $(B-V) = 0.13$ (Høg et al. 2000) and a distance modulus of 12.27 (Humphreys 1978), an absolute V magnitude of $M_V = -5.47$. This value, corrected by the bolometric correction, gives a luminosity of $\log(L/L_\odot) = 5.35 \pm 0.11$ for HD 191978.

The best-fit CMFGEN model (Fig. 6.25 and Table 6.5) is of excellent quality, except for the He II 4686 line which is too weak compared to the observations. The associated stellar parameters are reminiscent of those of an O 8III star on the basis of the tables of Martins et al. (2005a), confirming the O 8III spectral classification.

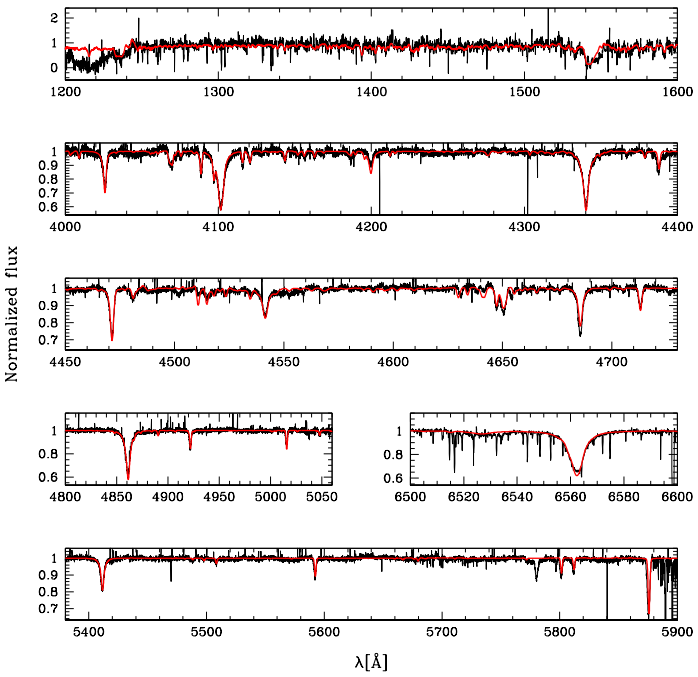

Figure 6.25: Best-fit CMFGEN model for HD 191978.

HD 193117

As several O stars in our sample, HD 193117 has received little attention in the past years. We have obtained eight spectra between Sep 2008 (HJD = 4711.5245) and Aug 2010 (HJD = 5420.6211). Quoted as an O 9.5II by Goy (1973), this star does not present any significant variations in its radial velocities. We indeed measure mean radial velocities of $\overline{RV} = -29.1 \pm 2.4$, -16.6 ± 7.1, -13.5 ± 4.8 and -26.0 ± 4.7 km s^{-1} for the He I 4471, He II 4542, He II 4686 and He I 4713 lines, respectively. In addition to these results, the TVS spectra show no significant change in the line profiles of the star. Since we find no direct evidence of variations in the spectrum of HD 193117, we classify this star as probably single.

The diagnostic line ratios, He I 4471–He II 4542 and Si IV 4089–He I 4143, give $\log W' = 0.343$ and $\log W'' = 0.256$. Furthermore, we computed $\log W''' = 5.155$. These results correspond to an O 9III star. By assuming a distance modulus of 11.87 (Humphreys 1978) and V and $(B-V)$ of 8.73 and 0.56 (Høg et al. 2000), respectively, we determine an absolute V magnitude of $M_V = -5.68$ and from the bolometric correction of Martins & Plez (2006), we obtain a luminosity of $\log(L/L_\odot) = 5.36 \pm 0.09$. The best-fit CMFGEN model (Fig. 6.26 and Table 6.5) is globally in agreement with the observation, except for the C IV 5801–12 and He I 5876 lines.

6.1.4 Cygnus OB9 association

HD 194334

HD 194334 was classified as an O 7.5V star by Goy (1973). We have collected eleven spectra between Sep 2008 (HJD = 4711.5581) and Aug 2010 (HJD = 5420.4943). We compute mean

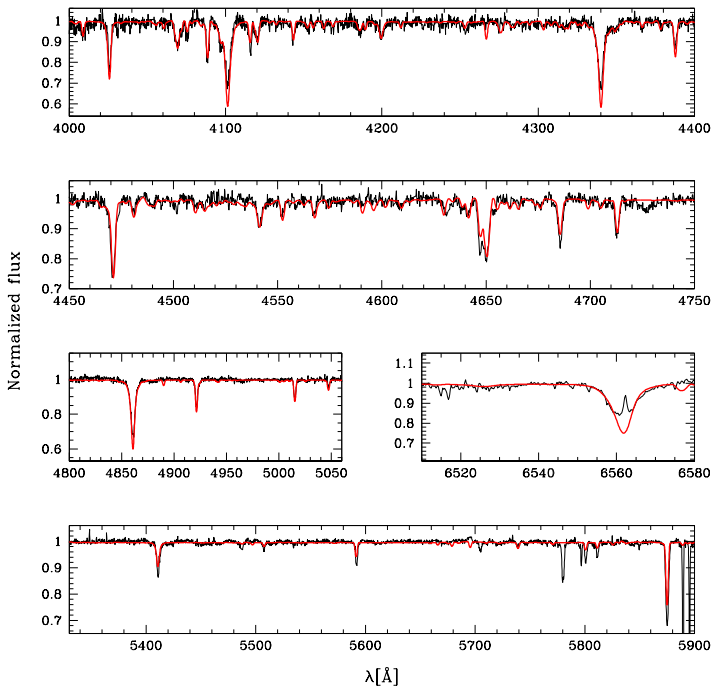

Figure 6.26: Best-fit CMFGEN model for HD 193117.

radial velocities of $\overline{RV} = -15.3 \pm 4.6$, -3.8 ± 5.2, 23.1 ± 12.7 and -15.6 ± 5.3 km s^{-1}, for the He I 4471, He II 4542, He II 4686 and He I 4713 lines, respectively. These velocities reveal a significant variability in the He II 4686 line while the other lines are rather constant. Moreover, changes are also detected in some TVS spectra (Fig. 6.27). We clearly see variations in the He I 4471, He II 4686 and Hβ lines. However, no similar change is observed in the He II 4542 and He I 4713 lines, suggesting that these variations are likely produced in the stellar wind and that the star is probably single.

We determine $\log W' = -0.002$ and $\log W'' = 0.294$ which corresponds to an O 7–7.5III/I star. The distance modulus of 10.09 quoted by Humphreys (1978), $V = 8.79$ and $(B - V) = 0.78$ (Høg et al. 2000) provide us with an absolute V magnitude of $M_V = -4.56$. In addition, by applying the bolometric correction given by Martins & Plez (2006), we find a luminosity of $\log(L/L_\odot) = 5.05 \pm 0.13$. The comparison of $T_{\rm eff}$ and of $\log g$ of the star derived by CMFGEN with the values of Martins et al. (2005a) yields a star with a luminosity class intermediate between giant and supergiant. However, the luminosity of the star we compute is not in agreement with that of an evolved star. This can be explained by the fact that the distance of HD 194334 may be wrong.

HD 194649

Often quoted as an O 6.5 star, HD 194649 was suggested from the UBV photometry of Hiltner (1956) to be a binary system. However, no confirmation is mentioned in the literature.

Our dataset is composed of seventeen spectra taken between Jun 2009 (HJD = 4992.8930) and Sep 2011 (HJD = 5820.6424). The journal of observations of HD 194649 is provided in Ta-

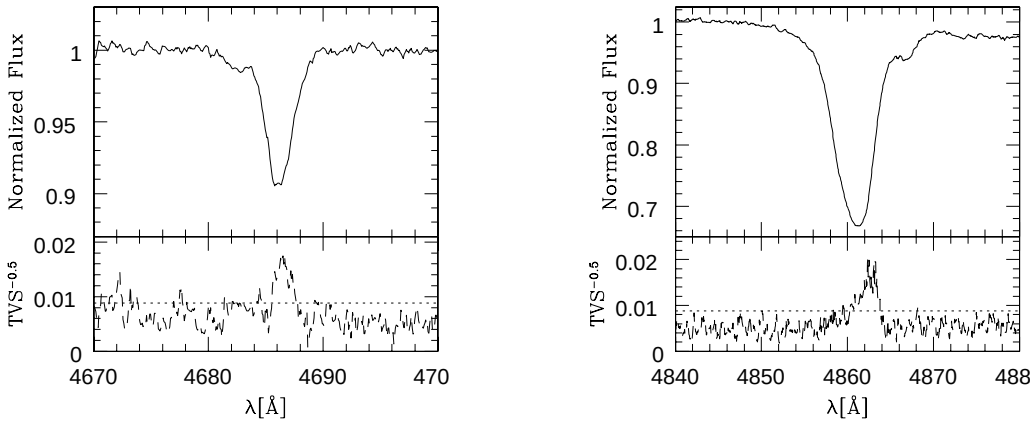

Figure 6.27: Mean spectrum and TVS of HD 194334 computed from the Aurélie data for the He I 4686 and Hβ line. The dotted line illustrates the 1% significance level for the variability evaluated following the approach of Fullerton et al. (1996).

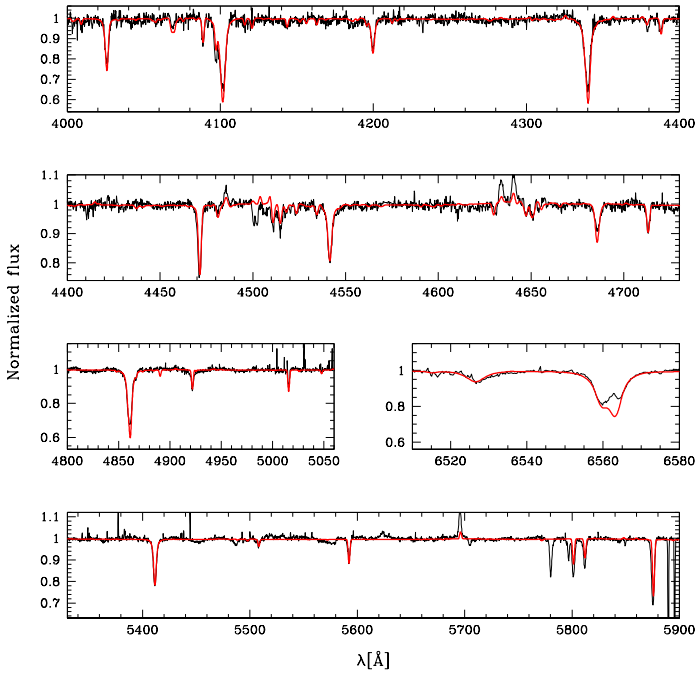

Figure 6.28: Best-fit CMFGEN model for HD 194334.

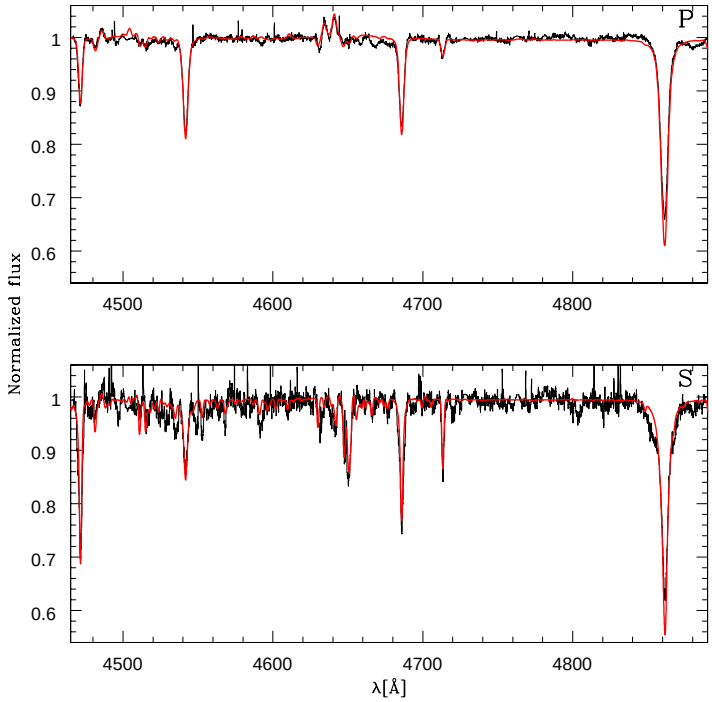

Figure 6.29: Best-fit CMFGEN models for the primary (top) and the secondary (bottom) components of HD 194649.

ble C.4 of Appendix C. These data reveal the obvious signature of a secondary component, moving in anti-phase with the primary. This motion is clearly observed over two consecutive nights, indicating a short-period binary system. From the radial velocities measured on these spectra, we apply the disentangling program to refine these values but also to extract the individual spectra of both components. We use the HMM method to determine from the refined radial velocities the period of the system. We obtain a value of $P_{\rm orb} = 3.39328 \pm 0.00012$ days (Fig. 6.30, left panel). We computed with LOSP the orbital solution (Table 6.4 and Fig. 6.30, right panel) of this system.

We measure the equivalent widths to determine the spectral classification on the disentangled and observed spectra. We find $\log W' = -0.267$ and $\log W' = 0.124$ for the primary and secondary components, respectively, corresponding to O 6 and O 8 types. After comparing the equivalent widths measured on the observed spectra to the values of Conti & Alschuler (1971) and Conti (1973) as well as to values determined from the CMFGEN synthetic spectra with the same spectral classifications, we derived a brightness ratio of about 4.7, indicating a surprisingly faint companion. The spectra of these stars corrected for the brightness ratio are displayed as a black line in Fig. 6.29. Therefore, with $V = 9.02$ and $(B-V) = 0.94$ and assuming $(B-V)_0 = -0.27$ and a distance modulus of 10.40 (Humphreys 1978), we determine an absolute V magnitude of about $M_V = -5.13$. From this value and the relative brightness of each component, we find $M_{V_{\rm P}} = -4.93$ and $M_{V_{\rm S}} = -3.24$ for the primary and secondary components, respectively. By applying the adequate bolometric corrections (Martins & Plez 2006), we derive $\log(L_{\rm P}/L_\odot) = 5.30 \pm 0.12$ and $\log(L_{\rm S}/L_\odot) = 4.49 \pm 0.13$. Moreover, the N III 4634–41–He II 4686 ratio give a (f) suffix to the primary, assuming a giant luminosity class. For the secondary, we determine $\log W'' = -0.03$, corresponding to a main-sequence star. We conclude that the spectral classifications for both stars are O 6III(f) and O 8V for the primary and the secondary, respectively. Therefore, the luminosities

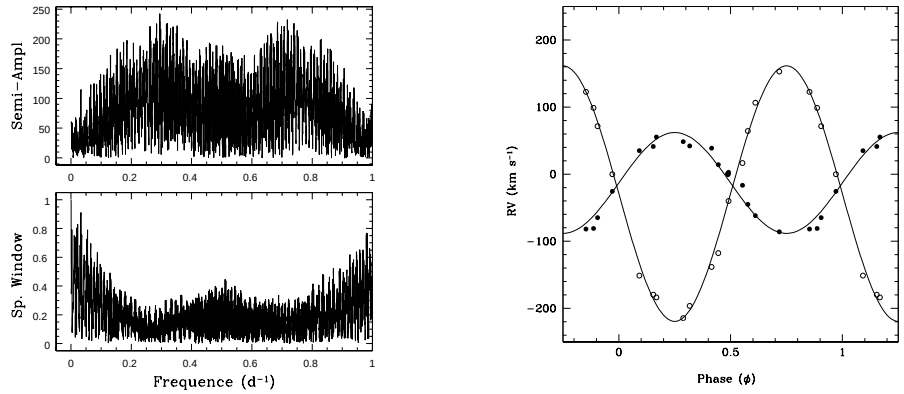

Figure 6.30: *Left*: Semi-amplitude spectrum (upper panel) and spectral window (lower panel) computed from the He I 4471 radial velocity measurements of HD 194649. *Right*: Radial velocity curves of HD 194649. Full circles represent the primary whilst the open circles correspond to the secondary.

suggest that both components are relatively faint for their spectral type in comparison to the values of Martins et al. (2005a). That could mean that the distance of this star is larger than that given by Humphreys (1978). By assuming that the secondary has a luminosity similar to that quoted in the tables of Martins et al. (2005a), we find a distance modulus for the system of 11.57 and in this case, the luminosity of the primary component would be equal to $\log(L_{\rm P}/L_{\odot}) = 5.74$, i.e., a intermediate value between the giant and the supergiant branch.

Table 6.4: Orbital solution for HD 194649.

Parameters	Primary	Secondary
P [d]	3.39328 ± 0.00012	
e	0.0 (fixed)	
T_0 (HJD)	4987.623 ± 0.012	
γ [km s^{-1}]	-13.1 ± 2.5	-28.9 ± 3.8
K [km s^{-1}]	75.2 ± 2.9	190.6 ± 7.4
$a \sin i$ [$R_{\odot}$]	5.0 ± 0.2	12.8 ± 0.5
$M \sin^3 i$ [$M_{\odot}$]	4.7 ± 0.4	1.9 ± 0.1
Q (M_1/M_2)	2.54 ± 0.15	
rms [km s^{-1}]	13.85	

We have fitted the disentangled spectra of both components with CMFGEN on the [4450 – 4900] Å wavelength domain. As we already mentioned, this domain only allows us to derive the stellar parameters of both components. The best-fit models are displayed in Fig. 6.29 whilst the list of stellar parameters is reported in Table 6.5. The stellar parameters of the primary star indicate that this component is reminiscent of a giant star whilst the secondary is more similar to a star between the main sequence and the giant branch.

HD 195213

Reported as an O 7 star by Goy (1973), HD 195213 has been observed ten times in our campaign between Sep 2008 (HJD = 4711.5962) and Aug 2010 (HJD = 5420.5309). Our data do not reveal

any significant variations for the main lines. We indeed compute mean radial velocities of $\overline{RV}$ = 2.1 ± 4.5, 9.6 ± 4.6 and −2.0 ± 4.2 km s^{-1} for the He I 4471, He II 4542 and He I 4713 lines, respectively. The He II 4686 line exhibits a pattern with an emission comparable to the absorption, probably indicating that the stellar wind of the star is relatively strong. We have thus investigated the TVS of these lines. We detect significant variations in the He I 4471, He II 4686 and Hβ lines. Since the TVS variations do not affect all the lines and since the radial velocity variations are not significant, we assume that the observed variability is likely due to the stellar wind rather than to a putative companion.

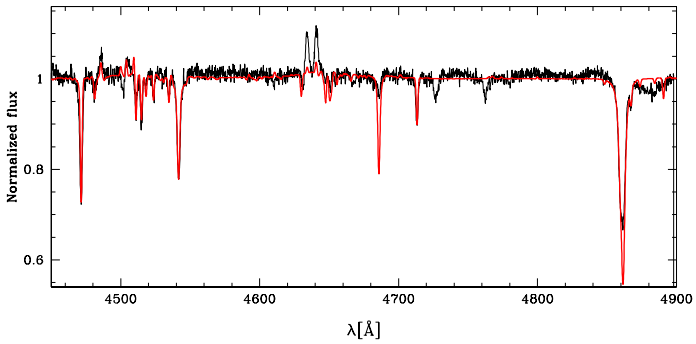

Figure 6.31: Best-fit CMFGEN model for HD 195213.

From the échelle spectrum, we measure $\log W' = -0.026$, corresponding to an O 7 star and $\log W'' = 0.264$, indicating a giant luminosity class. Moreover, we add the (f) suffix to the spectral type because the N III lines at 4634 and 4641 Å emissions are strong whilst the He II 4686 absorption is rather weak. We thus revise the spectral classification of the star to O 7III(f). From $V = 8.78$, $(B-V) = 0.80$ and assuming a distance modulus of 10.40 (the mean distance of Cyg OB9 as reported by Humphreys 1978), we computed an absolute V magnitude of $M_V = -4.94$ and a luminosity of $\log(L/L_\odot) = 5.23 \pm 0.12$, after accounting for the bolometric correction. The stellar parameters, in particular $T_{\rm eff}$ and $\log g$ are more reminiscent of a star located between the giant and the supergiant branchs. It is thus likely that the distance of the star mentioned by Humphreys (1978) is not the real one.

Finally, we stress that the luminosities of all the stars belonging to Cyg OB9 are not in agreement with the other stellar parameters according to the tables of Martins et al. (2005a). By assuming a distance modulus of 11.57 (as we think for HD 194649), we would obtain luminosities of $\log(L/L_\odot) = 5.61$ and $\log(L/L_\odot) = 5.68$ for HD 194334 and HD 195213, respectively. These values are more in agreement with the luminosities of giant stars.

Table 6.5: Stellar and wind parameters derived for the O-type stars in the Cygnus associations.

Source	SpT	$T_{\rm eff}$ [kK]	$\log\left(\frac{L}{L_\odot}\right)$	$\log g$	$\log(\dot{M}_{UV})$	f_∞	v_∞ [km s^{-1}]	$v \sin i$ [km s^{-1}]	$v_{\rm mac}$ [km s^{-1}]	$M_{\rm evol}$ [$M_\odot$]	$M_{\rm spec}$ [$M_\odot$]	N/H [$\times 10^{-4}$]
HD 193443 P	O 9III	31.5	5.40	3.65	–	–	–	105	38	$30.2^{+2.0}_{-1.9}$	46.5 ± 10.3	0.6 ± 0.3
HD 193443 S	O 9.5V	30.0	4.82	3.75	–	–	–	100	27	$17.0^{+2.1}_{-1.8}$	18.6 ± 3.2	0.6 ± 0.3
HD 193514	O 7–7.5IIIf	33.5	5.71	3.50	−5.6	0.01	2350	90	25	$38.5^{+2.0}_{-2.1}$	52.1 ± 10.9	2.0 ± 1.0
HD 193595	O 7V	36.0	5.02	3.75	–	1.0	1800	65	15	$27.2^{+2.0}_{-2.6}$	14.4 ± 3.2	3.0 ± 2.0
HD 193682	O 5III(f)	40.0	5.49	3.75	−6.7	0.01	2800	150	73	$40.6^{+4.6}_{-2.6}$	27.6 ± 5.9	4.0 ± 2.0
HD 194094	O 8.5III	30.0	5.32	3.25	–	–	–	65	32	$27.5^{+2.1}_{-1.9}$	18.7 ± 4.8	1.0 ± 0.5
HD 194280	OC 9.7I	27.5	5.55	3.10	–	–	–	92	41	$31.2^{+1.9}_{-1.8}$	31.5 ± 8.5	0.1 ± 0.1
HD 228841	O 7IIIn	35.0	5.27	3.75	–	–	–	317	0	$30.8^{+2.3}_{-2.4}$	28.2 ± 6.5	3.0 ± 1.5
HD 228989 P	O 8.5V	30.0	4.75	3.50	–	–	–	150	5	$15.5^{+2.4}_{-1.8}$	8.9 ± 2.3	1.0 ± 0.5
HD 228989 S	O 9.7III/V	28.0	4.49	3.80	–	–	–	120	5	$15.6^{+1.3}_{-1.4}$	12.9 ± 4.6	3.0 ± 1.5
HD 229234	O 9III	31.5	5.12	3.60	–	–	–	85	37	$24.4^{+2.3}_{-2.2}$	21.4 ± 5.3	0.6 ± 0.4
HD 190864	O 6.5III(f)	37.5	5.43	3.75	−7.0	0.1	2250	80	43	$36.5^{+2.5}_{-2.7}$	30.8 ± 10.4	5.0 ± 3.0
HD 227018	O 6.5V((f))	37.5	5.51	4.00	–	–	–	70	35	$37.9^{+2.6}_{-2.8}$	67.1 ± 18.7	1.0 ± 0.4
HD 227245	O 7III	35.0	5.20	3.75	–	1.0	–	65	19	$29.4^{+3.1}_{-3.2}$	24.0 ± 7.0	3.0 ± 2.0
HD 227757	O 9V	31.0	4.70	3.75	–	1.0	–	45	5	$18.3^{+2.1}_{-2.1}$	12.4 ± 3.8	0.6 ± 0.3
HD 191423	ON 9IIIn	31.0	5.25	3.50	−7.3	0.01	600	410	0	$26.7^{+3.2}_{-3.2}$	24.6 ± 11.5	5.4 ± 2.5
HD 191978	O 8III	33.5	5.35	3.75	−8.7	1.0	1600	40	32	$30.8^{+3.3}_{-3.1}$	40.8 ± 18.5	3.0 ± 1.5
HD 193117	O 9III	30.0	5.38	3.30	–	1.0	–	80	28	$28.8^{+2.5}_{-2.3}$	22.7 ± 11.1	0.6 ± 0.3
HD 194334	O 7–7.5III/I	35.0	5.05	3.50	–	1.0	–	62	32	$26.4^{+3.9}_{-3.9}$	9.6 ± 3.6	3.0 ± 2.0
HD 194649 P	O 6III(f)	39.0	5.30	3.75	–	–	–	60	68	$35.8^{+3.0}_{-2.6}$	19.7 ± 4.6	3.0 ± 2.0
HD 194649 S	O 8V	34.0	4.49	3.75	–	–	–	60	27	$13.7^{+4.1}_{-3.6}$	5.3 ± 2.4	1.0 ± 0.5
HD 195213	O 7III(f)	35.0	5.24	3.50	–	–	–	60	26	$30.2^{+3.5}_{-3.6}$	12.4 ± 4.7	6.0 ± 2.0

6.2 Observational biases

We perform Monte-Carlo simulations to estimate the probability of having missed binary systems on the basis of our temporal sampling. For that purpose, we randomly draw the orbital parameters of 100000 binary systems. We consider that these systems are not detected if the radial velocity variations are smaller than $7 - 8$ km s^{-1} to be consistent with our binarity criterion. For the fast rotators, we request radial velocity variations of 15 km s^{-1}. Among the parameters, we assume that 60% of the binaries have an orbital period smaller than 10 days. These periods are uniformly drawn in the $[0.3 - 3.5]$ $\log P$ domain. The eccentricities are selected between 0.0 and 0.9 with all systems with orbital periods shorter than 4 days taken to have circular orbits. The mass ratio (M_P/M_S) is uniformly distributed between 1.0 and 10.0 and the system orientations are randomly drawn according to $\cos i \in [-1; 1]$ from a uniform distribution.

Table 6.6: Binary detection probability (%) for the time sampling associated to the different stars in our sample and various period ranges.

Stars	Short [2 – 10]d	Intermed. [10 – 365]d	Long [365 – 3165]d	All [2 – 3165]d
HD 190864	99.9	94.5	76.0	91.2
HD 227018	99.8	82.9	57.1	84.0
HD 193514	99.8	96.0	84.1	94.1
HD 193595	99.7	86.6	64.5	86.6
HD 193682	99.8	92.4	73.6	90.2
HD 191978	99.8	94.1	79.5	92.4
HD 191423	98.8	72.3	36.5	75.6
HD 193117	99.8	91.0	72.1	89.5
HD 194334	99.7	91.3	63.3	86.4
HD 195213	99.7	89.2	67.9	88.0
HD 227757	99.5	82.4	63.3	86.0
HD 194094	99.2	87.0	68.8	87.8
HD 227245	99.5	68.3	59.5	83.9
HD 194280	99.9	96.0	85.1	94.5
HD 228841	99.0	81.4	44.3	78.8

The results of these simulations are listed in Table 6.6. They reveal that at least 70% of the systems with periods smaller than one year should have been detected whilst between 36 and 89% of the systems with an orbital period larger than one year yield significant radial velocity variations to be detected as binaries. Therefore, the detection efficiency is rather good even though we do not exclude to have missed some (long-period) binary systems.

6.3 Binary fraction in Cygnus associations

The spectroscopic analysis made on the Cygnus region includes O-type stars coming from different environments. Therefore, considering them altogether boils down to study a random sample of O-stars. It is also possible to focus on each association or even on young open clusters belonging to these associations. However, in the latter case, we would deal with small number statistics which is not advisable for that approach. Therefore, the binary fraction will be constrained on the entire region and on each OB association.

As we already mentioned, deriving the binary fraction of a given population of stars is far

from being an easy task. It first requires an intense monitoring devoted to the stars but also a good time sampling to constrain the short- as well as the long-period systems. As we saw in Section 5.2.1, this monitoring has to be as homogeneous as possible because combining data from the literature generally provides erroneous results. Moreover, it is important to keep in mind the possible observational biases. Indeed, stars for which no evidence of binarity is found can never be definitely considered as single. Even if no RV shift is detected, the system could be seen under a particular orientation, have a very long period or perhaps a large eccentricity, thereby making the radial velocity variations not significant over a long time scale.

We have observed nineteen stars or multiple systems containing at least one O-type object. Among this sample, four stars (HD 193443, HD 194649, HD 228989 and HD 229234) display clear radial velocity variations and even a companion signature for three of them. Therefore, no doubt remains on the binary status of these objects. Unlike the stars in NGC 2244 (Section 5.2.1), all the binaries of our sample detected in the Cygnus region have periods shorter than 10 days. Moreover, no star seems to show variations on a time scale larger than one year. In addition to these radial velocity variations, several objects show significant variations of some of their line profiles. Since not all the lines are affected, this implies that these variations are probably not due to binarity but rather to a strong stellar wind or perhaps even to non-radial pulsations. Therefore, we find a minimum binary fraction of about 21% among the 19 sample stars (4 out of 19). This global value is however not significantly different of the binary fraction derived for the O stars in NGC 2244 nor of the average value computed for the nearby young open clusters (44 ± 5%). Furthermore, if we take into account the systems containing at least one O-type star, quoted as belonging to the Cygnus region by Humphreys (1978) and already reported as binary systems in the literature, we obtain a minimal binary fraction of 25% (8 stars out of 32). Of course, this value was determined by focusing only on the Cyg OB1, Cyg OB3, Cyg OB8 and Cyg OB9 associations and is not representative of the entire Cygnus region.

We now focus on each individual OB association by first including only our sample stars. In Cyg OB1, the minimal binary fraction is of 33% (3 stars out of 9). In Cyg OB3, we find no star in a binary system out of 4, i.e., 0% whilst in Cyg OB8 and Cyg OB9, we obtain 0% (0 out of 3) and 33% (1 out of 3), respectively. However, if we take into account all the stars mentioned by Humphreys (1978), the minimum O-type star binary fractions become equal to 25% (3 out of 12), 33% (3 out of 9), 0% (0 out of 4) and 29% (2 out of 7) for the Cyg OB1, Cyg OB3, Cyg OB8 and Cyg OB9 associations, respectively. Even though these values are slightly smaller than the average calculated among the O-type star population in the nearby clusters (44 ± 5%, Sana & Evans 2011), they are however not significantly different and could be affected by small number statistics.

Moreover, in the framework of this thesis, the binary fraction is constrained from a spectroscopic point of view. If we take into account the revised results of our campaign, the non-investigated stars which are reported as binaries in the literature, i.e., the results of Turner et al. (2008) from adaptive optics and those of Mason et al. (1998, 2009) from their speckle interferometric survey, the binary fraction among the four OB associations is estimated to 28%. That reminds us that the spectroscopic binary fraction determined in the present work has to be considered as a lower limit.

To bring additional constraints in this work in a larger frame, we have selected SB2 systems (including at least one O star) detected in multiplicity studies (Sana et al. 2008, 2009, 2011a; Rauw & De Becker 2004; De Becker et al. 2006; Hillwig et al. 2006; Rauw et al. 2009) as well as in numerous papers (see, e.g., "spectroscopic" references in Mason et al. 1998). Orbital solutions are known for these 70 systems which are mainly located in young open clusters or OB associations.

We present in Fig. 6.32 the corresponding P vs. e, P vs. q (= M_1/M_2) and q vs. e diagrams. In order not to affect the readibility of these diagrams and because some are missing, we do not include the error bars on these measurements.

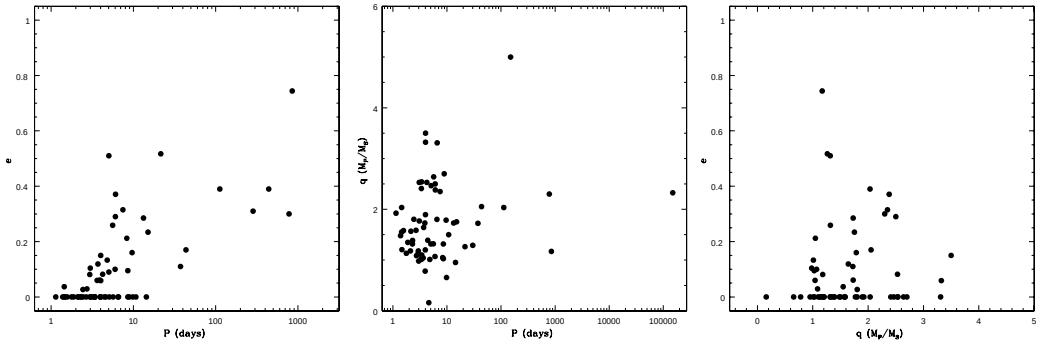

Figure 6.32: Distributions of orbital parameters (period, eccentricity, mass ratio) of binary systems located in young open clusters or OB associations.

From the period-eccentricity diagram, we detect a trend of smaller orbital period with the smaller eccentricity, confirming the lack of highly eccentric short period systems as well as almost circular long period systems. The P vs. q diagram is affected by the difficulty of detecting systems with large mass ratios and/or with long orbital periods. The q vs. e diagram also shows the difficulty of detecting systems with large eccentricities. We stress however that this sample constitutes a small sample of binary systems in comparison with the overall population of binaries among massive stars.

6.4 Evolutionary status

The stellar parameters derived in Section 6.1 provide the positions of the stars in the HR diagram. However, these locations are dependent on the real distances of the stars, which are still uncertain (see Section 6.1). The luminosities have been computed on the basis of the distance modulus given by Humphreys (1978). When no value was available for the stars, we have taken the mean value of the corresponding OB association. The observed V and $(B - V)$ values are from Høg et al. (2000) whilst the bolometric corrections were taken from Martins & Plez (2006) as a function of the spectral classification of the star. The error bars on the luminosities of the presumably single stars are mainly determined by the uncertainties on the distances whilst for the binaries this uncertainty comes also from the brightness ratio between both components. Moreover, the effective temperature is estimated at ±1000 K (see Section 1.1.1).

For this analysis, we use the evolutionary tracks of Meynet & Maeder (2003) computed for single stars with initial rotational velocities of about 300 km s^{-1}. Given the unknown inclination of each star, this rotational velocity represents a "standard" value for the massive stars. Moreover, we do not investigate all the sample stars together. Indeed, it is important to make the difference between the different formation regions because these regions were not formed at the same time and accordingly their O-type star populations are not the same.

The evolutionary ages are indeed clearly different from one association to another. For Cyg OB1, the ages of all the stars are between 1 and 8 Myrs. Despite the fact that the exact membership of the studied stars is unknown, most of them correspond to an age, between 4 and

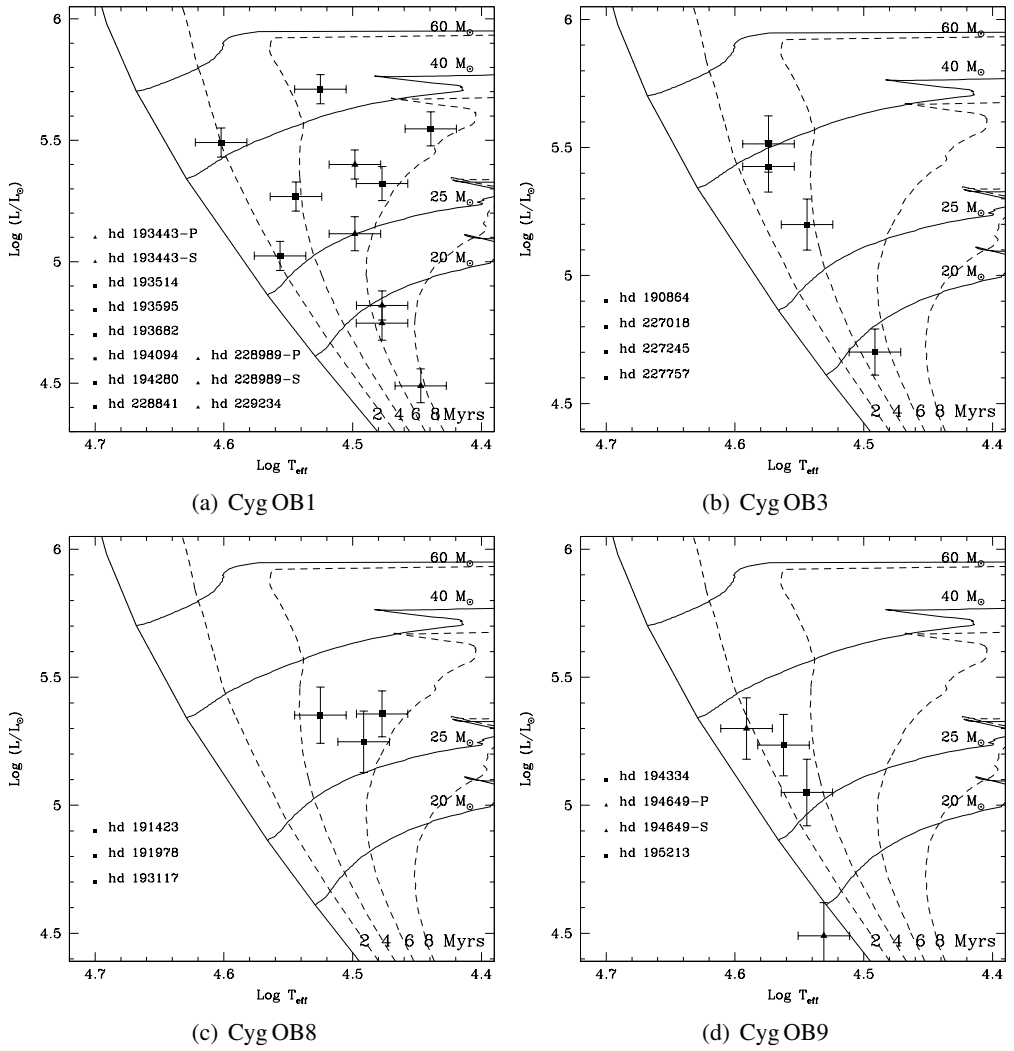

(a) Cyg OB1 (b) Cyg OB3

(c) Cyg OB8 (d) Cyg OB9

Figure 6.33: Positions of the Cygnus O-type stars in the HR diagram. Evolutionary tracks and isochrones are from Meynet & Maeder (2003) and were computed for $v_{\mathrm{rot_{init}}} = 300$ km s^{-1}. Isochrones, represented by dashed lines, correspond to ages ranging from 2 to 8 Myrs with a step of 2 Myrs.

8 Myrs, which agrees with that derived for the clusters of this association. However, three stars (HD 193595, HD 228841 and HD 193682) are clearly younger with an age between 2 and 4 Myrs. Moreover, the positions of the binary components belonging to this association seem to indicate that no interaction has yet occurred in the past evolution of these systems.

The stars in Cyg OB3 appear to be aged between 2 and 6 Myrs. The isochrones show two distinct epochs of 2 – 5 Myrs for the stars with a mass larger than 25 $M_{\odot}$ and from 4 to 7 Myrs for the lower-mass stars. This result coincides with the estimates of Massey et al. (1995) for the most massive stars and of Reimann (1989) for the lower-mass stars (see the beginning of Chapter 6). It also shows that the formation of the early-type stars could occur later than that of the late-type ones or that the lower-mass stars remain hidden for a longer time in their parental clouds than the most massive stars. This trend could confirm the speculative conclusions reported in Section 5.3 and in Martins et al. (2011) for the NGC 2244 stars.

The evolutionary ages in Cyg OB8 are between 4 and 6 Myrs. The ages of the stars in Cyg OB8 do not confirm the estimates of ~ 3 Myrs presented by Uyanıker et al. (2001). Moreover, binarity has played no role in the evolution of three stars belonging to Cyg OB8 because they are all classified as presumably single.

The evolutionary ages in Cyg OB9 show that three stars of this association are 2 – 4 Myrs old. This would mean that the peak of formation would have begun 4 Myrs after the formation of the OB association itself. However, the position on the HR diagram of the secondary component of HD 194649 seems to confirm a poorly constrained distance for this system. If we assume for all the stars of Cyg OB9 a mean distance modulus similar to that suggested for HD 194649, i.e., 11.57, rather than that of 10.40 given by Humphreys (1978), we obtain luminosities of about 5.61, 5.75, 4.96 and 5.68 for HD 194334, for the primary component of HD 194649 and its secondary component as well as for HD 195213, respectively. From these values, the "new" locations of these stars in the HR diagram would reveal ages between 2 and 4 Myrs. However, such a distance would locate these stars outside the commonly adopted association.

6.5 N content and stellar wind

The previous analyses of the O-type stars in NGC 2244 and Mon OB2 (see Section 5.3) yielded a trend of larger N/H with larger $v \sin i$, for all the stars except for the fast rotators. We represent in the left panel of Fig. 6.34 the so-called *"Hunter diagram"* where the stars of the Cygnus region are plotted with black dots whilst the stars of NGC 2244 and Mon OB2 are in red. We note that the "Hunter-diagram" was initially applied to B stars of the Large Magellanic Cloud (LMC) by Hunter et al. (2008). Brott et al. (2011b) described five different regions on this diagram which are reported in their Fig. 10:

- Box 1: is a region of the diagram which is predicted by the theoretical models to be empty
- Box 2: is a region where few stars are predicted but a group of enriched, slow rotators is found
- Box 3: contains the stars which are clearly enhanced in Nitrogen due to rotational mixing
- Box 4: is a region where neither B stars are observed nor where a significant number of them is predicted.

- Box 5: is a region where the un-enriched stars are located.

We see however that these groups are no longer consistent with the O stars in the Milky Way. That is mainly due to their larger metallicity than in the LMC. Indeed, the LMC nitrogen baseline abundance is of 6.9 in units of $12+\log(N/H)$ whilst in the Milky Way, it is 7.8. Therefore, we expect to see the Hunter-diagram vertically shifted for the O stars of our sample. However, Fig. 6.34 does not confirm this shift. We see that the problem linked to the slow rotators with large enrichment is still more severe than for B stars. We distinguish four or five different groups (see left panel of Fig. 6.34):

- Group 1 which takes into account the stars with a low $v \sin i$ (< 160 km s^{-1}) and an N abundance approximately solar ($7.7 < 12 + \log(N/H) < 8.1$). We note that these objects are thus located at positions predicted by the theory.

- Group 2 collects the stars with a low $v \sin i$ (< 160 km s^{-1}) and enhanced nitrogen abundance ($12 + \log(N/H) > 8.1$. This group extends the "Box 2" region (quoted above for the B stars) where the theoretical predictions announced almost no star.

- Group 3 takes into account all the fast rotators ($v \sin i > 280$ km s^{-1}) whatever their N content. However, this group could be split in two different groups, to be similar to the Hunter-plot, with the N-richer fast rotators on one side and N-solar fast rotators on the other side.

- Group 4 represents the N-rich stars with an intermediate projected rotational velocity. In the present work as it was the case in the initial "Hunter-diagram", this group remains empty.

A recent analysis of surface Nitrogen abundances for O stars in the LMC performed by Rivero Gonzalez et al. (2011) confirmed the extension of the "Box 2" region but also the three other groups. However, more stars are needed to redefine precisely the number and the shape of the different groups.

The "luminosity vs N content" plot (right panel of Fig. 6.34) shows three stars which are either too enriched or too depleted for their luminosity. Moreover, the trend detected for the O stars in NGC 2244 and Mon OB2 is not confirmed for the stars in the Cygnus complex. That could be due to their inhomogeneity. Indeed, since they are not located in the same region, the Cygnus stars do not form a set of stars with the same age, distance and chemical composition. Therefore, their respective evolution could be different unlike the O stars in NGC 2244. We however refrain from doing a statistical analysis of the N content given the small number of investigated objects.

Concerning the stellar winds, our investigation of the mass-loss rates performed on five stars on the basis of UV and optical data allows us to show that $\dot{M}_{\rm UV}$ is in general smaller than $\dot{M}_{\rm H_\alpha}$. Though we cannot determine the real value of $\dot{M}_{\rm H_\alpha}$ for these stars[13], we see however that the models of Hα line profiles are generally deeper when the UV P Cygni profiles are well reproduced, except for HD 191423. This analysis confirms the conclusions established for the O-type stars in NGC 2244 and Mon OB2, which suggests that the stellar winds of all the O stars are likely to be clumped (Section 5.3).

[13]This operation is very CPU time consuming

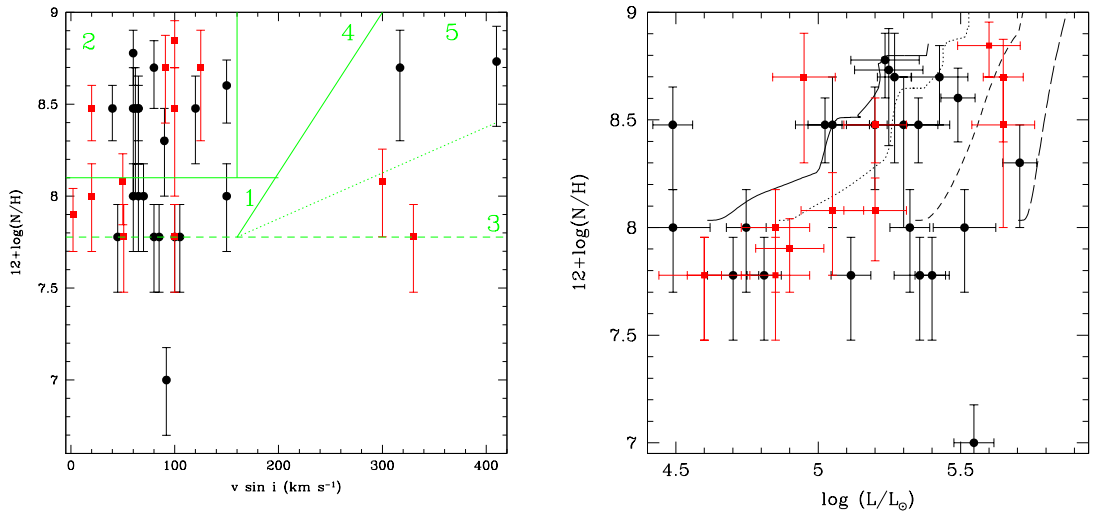

Figure 6.34: *Left*: Nitrogen surface abundance (in units of 12+log(N/H)) as a function of projected rotational velocity. The green dotted lines represent the egdes of the "new" groups whilst the dashed line displays the solar abundance. The black circles indicate the Cygnus stars whilst the red squares are for the stars of NGC 2244 and Mon OB2. *Right*: Nitrogen surface abundance (in units of 12 + log(N/H)) as a function of luminosity. Evolutionary tracks – shown by solid, dotted, dashed and dot-long dashed lines for M = 20, 25, 40 and 60 $M_{\odot}$ – are from Meynet & Maeder (2003) and were computed with $v_{\mathrm{rot_{init}}}$ = 300 km s^{-1}.

6.6 Conclusions

We have undertaken a detailed analysis of nineteen O-type stars belonging to several OB associations in the Cygnus region. We have, on the one hand, investigated the multiplicity of these stars from a dataset of 273 spectra covering the short- and the long-term time scales (see Section 6.1). We have detected four binary systems and provided for the first time their orbital solutions. These four systems have a short period (P < 10 days), which is clearly different from what we found for the O-type stars in NGC 2244 and Mon OB2. The minimal binary fraction in our sample was estimated at 21%, but probably does not reflect the true binary fraction in the Cygnus region. Indeed, this star-forming region contains far more than the nineteen stars studied here. Although the minimum binary fraction is also not the same in all the OB associations, and the derived values are smaller than the average value derived by Sana & Evans (2011) for the O-type star population in the nearby young open clusters, these results are not statistically different, and could be due to a small number effect.

On the other hand, we have computed model atmospheres for all the stars in our sample in order to determine their stellar and wind parameters. These parameters allow us to obtain evolutionary ages for these stars, corresponding to the ages of their home associations at least for Cyg OB1 and Cyg OB3. However, these estimates have shown that Cyg OB8 is certainly older than what is quoted in the literature (∼ 3 Myrs) and that the stars reported by Humphreys (1978) as belonging to Cyg OB9 might well be located outside.

Furthermore, the N content of O stars investigated in the present chapter increases the number of O stars whose surface N abundance is not in agreement with the predictions of single star

evolution models accounting for rotational mixing. Moreover, we emphasize the presence of four or five different groups of stars depending on their N abundances and their projected rotational velocity. The investigation of the mass-loss rates from the UV line profiles and the Hα line profiles clearly exhibits a discrepancy between both values, thereby confirming the previous results obtained for the O-type stars in NGC 2244 and Mon OB2.

Conclusion

Summary

In this thesis, we have analyzed the physical properties of about thirty massive stars through spectroscopy and photometry. We have established their multiplicity, discovering several new binary systems for which we computed for the first time the orbital solutions. The main results obtained in the present work are described below, and we end this dissertation by some future prospects.

Mathematical tools

To determine the stellar and wind parameters of massive stars, we have used the CMFGEN atmosphere code. This code, though extremely powerful, is designed to obtain the stellar and wind parameters of single stars. Nonetheless, almost 60% of the massive star population is composed of binary or multiple systems. Therefore, we had to apply disentangling techniques to separate the individual contributions of each component belonging to those systems. We have presented two different methods based on the works of González & Levato (2006) and Simon & Sturm (1994). Even though these methods generally provide similar results, the former does not take into account the possible changes of luminosity in the eclipsing binaries whilst the latter only gives the opportunity to handle a small wavelength domain because it is expensive in CPU time. To show the utility of these techniques, we have applied our code based on González & Levato (2006) to analyze the two components of the evolved system LZ Cep. The results were presented in Mahy et al. (2011b).

Another property of massive stars is their strong wind. When two stars are gravitationally bound, their winds may interact. To better constrain the interaction regions, we have implemented three methods of Doppler tomography which map in velocity space the emissivity observed in these regions: the Fourier-filtered back-projection (FFBP), the Algebraic Reconstruction Technique (ART) and the Simultaneous Iterative Reconstruction Technique (SIRT). Among these methods, two had never been used in astrophysics: ART and SIRT. We have compared all these techniques by applying them on three evolved systems (Plaskett's Star, Cyg OB2#5, and AO Cas). These applications showed that the results obtained by ART are often unreliable whilst FFBP and SIRT have provided relatively promising results, each with their advantages and their disadvantages. The former technique is fast and not expensive in memory storage but the data have to be pre-treated by a Fourier filter, which influences the resolution of the Doppler maps; the latter technique is relatively slow and expensive in CPU time, which requires a decrease of the resolution to avoid an excess of memory, however, the tomograms computed from this technique turns out to be more accurate than those computed from ART and FFBP.

The disentangling and Doppler tomography techniques have then been used to investigate a newly-discovered triple system: HD 150136. The analysis of this system has been reported in Mahy et al. (submitted to A&A). We have shown that HD 150136 is formed by an inner system orbiting with a 2.67-day period and composed of an O 3V(f*)–O 3.5((f$^+$)) primary and an O 5.5–6((f)) secondary. The variations observed in the He II 4686 and Hα line profiles have been analysed with the SIRT Doppler tomography program. In addition, a third star, gravitationally bound to the inner system and classified as an O 6.5–7((f)), has been detected in the observed spectra, necessitating the use of a three-component disentangling method. This outer star has an orbital period larger than 8 years and an orbit more eccentric than 0.3. The total mass of the system has been estimated to about 140 $M_\odot$, making HD 150136 one of the most massive and close-by system, known to date.

Multiplicity

This dissertation has also been devoted to the study of the multiplicity of massive stars. Knowing the binary status of stars is the first step to determine with accuracy their physical parameters. We first focused on the O-type stars of the young open cluster NGC 2244 and the Mon OB2 association. Located in the Rosette Nebula at a distance of about 1.4 − 1.7 kpc from the Sun, NGC 2244 hosts seven O stars. Among these stars, only one (HD 258691) has not been analyzed in the present work because of its faintness, all others are on the main-sequence branch and have been classified as stars with spectral types going from O 4V((f$^+$)) to O 9V. In this sample, the binary fraction was estimated between 14 and 43%. Only HD 46149 has been for the first time detected as a binary. This system is composed of an O 8V primary and an O 9–B1V secondary system. Because of its long period ($\sim$ 720 − 860 days), the orbital parameters of this system could only be poorly constrained. To this object, we have added HD 46150 and HD 258691 as binary candidates. The former object presented slightly significant variations in its radial velocities even though no companion has been found in the spectral lines. These variations could be due to motions in the stellar atmosphere or be artefacts of the fits with Gaussian profiles. The latter star has not been studied, and without further information we consider it as a potential binary system.

We have also established the multiplicity of some stars located in the surrounding Mon OB2 association. Only one star, HD 46573, displayed variations in its radial velocity which are similar to those detected in SB1 systems. Beside this object, two other systems were already known as binaries: HD 48099 and HD 47129 (Plaskett's Star). The two remaining stars of our sample are considered as presumably single. Therefore, the minimum binary fraction among the stars of Mon OB2 is of 60%. If we put together all the stars of NGC 2244 and Mon OB2, we have a binary fraction between 33% and 50%. These results on the study of multiplicity in NGC 2244 and Mon OB2 have been published in Mahy et al. (2009) whilst the in-depth analysis of the HD 48099 binary system was presented in Mahy et al. (2010).

We then focused on the multiplicity of nineteen O-type stars located in the Cygnus complex. The Cygnus star-forming region is divided in nine OB associations and among these associations are embedded several young open clusters. We have limited our study to massive stars located in four OB associations: Cyg OB1, Cyg OB3, Cyg OB8 and Cyg OB9. Four objects among the stars in our sample have been detected as binaries (HD 193443, HD 194649, HD 228989 and HD 229234). All have short periods ($P < 10$ days), unlike the situation in NGC 2244 where the only star detected as binary (HD 46149) has a long period. We have been able to compute for the first time their orbital solutions. The multiplicity analysis thus led to minimum binary

fractions of about 33%, 0%, 0% and 33% for Cyg OB1, Cyg OB3, Cyg OB8 and Cyg OB9, respectively. Moreover, when we add the other stars quoted by Humphreys (1978) as belonging to those associations, these minimum binary fractions become 25%, 33%, 0%, and 33%, for the same associations. These results will be published in Mahy et al. (2012, in prep.).

Stellar and wind parameters

The study of the physical parameters of O-type stars of the present work has provided us with numerous constraints on the nitrogen contents and the mass-loss rates of these objects. The estimates of the N surface abundances has allowed us to refine the "Hunter-diagram" for the Galactic O-type stars separating it in four or five groups. As it was already observed for B-type stars, a group of slow rotating N-rich stars has been detected. However, we have extended the slow rotator zone to projected rotational velocities smaller than 150 km s^{-1} (compared to about 50 km s^{-1}for B stars). These stars are not explained by the theoretical predictions which foresee that the N enrichment is mainly due to rotational mixing. Moreover, the group of O-type fast rotators in the "Hunter-diagram" can be split in two different parts, one including the highly N enriched stars and one with solar N abundances. As for the B stars, we have detected a zone between intermediate projected rotational velocities ($150 < v \sin i < 250$ km s^{-1} and large N enrichment ($8.1 < 12+\log(N/H) < 9$) where no star is located. We stress however that the "Hunter-diagram" presented for O-stars in the present work is only a first study and must be confirmed through additional investigations of the N content of other O-type stars.

For almost all the O-type stars in NGC 2244 and Mon OB2 and for five O stars in the Cygnus region, we have determined the mass-loss rates from UV P Cygni profiles and from Hα profiles. Both profiles do not depend in the same way on the wind density. Indeed, Hα is a recombination line which depends on the density squared whilst the UV resonance lines only depend on the density. We have seen that the mass-loss rates we have derived are indeed different when they have been determined from one line or the other. We have obtained for all the stars in NGC 2244 and Mon OB2 $\dot{M}_{\rm UV}$ smaller than $\dot{M}_{\rm H\alpha}$. We could see from the CMFGEN synthetic spectra that Hα is generally not well reproduced when the UV lines are. These results would thus indicate that the stellar winds of all the O-type stars are clumped, as it is now expected. It has however not been possible to constrain the properties of those clumps in the present dissertation. Moreover, the derived $\dot{M}$ are lower than the theoretical predictions of Vink et al. (2000) by at least a factor 2. To conclude, the origin and the properties of the winds remains a crucial question since we have seen that two stars with very similar effective temperatures and gravities can have very different wind properties with only a small difference in luminosity. These results confirm that without a clear understanding of the exact nature of the stellar winds, the values of the mass-loss rates must be considered with caution.

The paper on the quantitative analysis of the stellar and wind parameters of O-type stars in NGC 2244 and Mon OB2 have been recently accepted and will be published in Martins et al. (2011, in press). Moreover, the results on the O stars in the Cygnus regions will be soon submitted for publication (Mahy et al. 2012b, in prep.).

CoRoT photometry and red noise

In this thesis, we have also analysed the CoRoT photometric data obtained during the second short run devoted partly to O-type stars in NGC 2244 and Mon OB2. Although these data were

investigated by three different groups (the University of Liège, the University of Leuven and the Royal Observatory of Belgium), we have treated all of them to ensure a homogeneous comparison between the different teams. These data, of unprecedented quality, have revealed solar-like oscillations in the light curve of HD 46149 with a frequency spacing of about 0.48 d^{-1}. It is however not obvious whether these oscillations arise in the primary or the secondary component. Moreover, at least six β Cep-like oscillation frequencies have been detected in the light curve of HD 46202 and a set of 8 harmonics (with frequencies of f = 0.823, 1.646, 2.469, 3.292, 4.115, 4.938, 5.761, 6.585 d^{-1}) associated to non-radial pulsations has been observed in the light curve of Plaskett's Star. In addition, in the latter case, the frequencies linked to the orbital period and to the ellipsoidal variations have allowed us to conclude to the presence of a hot spot most probably situated on the primary star and facing the secondary. This feature is most likely related to the wind interaction or mutual heating between the stars. The results concerning Plaskett's Star have been published in Mahy et al. (2011a).

Besides these three stars, we have also highlighted the presence of red noise in almost all the O-type stars observed by CoRoT even though the most affected objects are HD 46223 and HD 46150. This red noise could have three different origins: either the sub-surface convection zone induced by the iron-opacity bump which would already be responsible for solar-like oscillations detected in HD 46149, or a granulation similar to that detected in helioseismology, or the onset of clumping close to the stellar photosphere. If the last case is corroborated, that would mean that almost all the O stars would have clumped winds. The analysis of red noise and the three remaining O-type stars observed by CoRoT have been presented in Blomme, Mahy et al. (2011). Finally, the observed stars have been located in the HR diagram to which we have added ζ Ori and HD 93521 already known as pulsating O stars. This plot (see Fig. 5.21) displayed two distinct groups of stars; one is situated in the upper part of the diagram and gathers the stars affected by red noise; another one is located in the lower part of the diagram and harbours all the pulsating stars. This result could be the first observational clue for the possible end of the classical instability band of massive stars.

Perspective

Given the numerous question marks mentioned in the introduction that remain for massive stars, it would be optimistic to pretend that all the solutions have been brought by the present dissertation. A research work is never fully achieved and we have only provided a modest contribution to the field. As long as not all the questions have been answered, we will be full of projects for the future.

- As we have seen in this thesis, in most cases, the disentangling programs fail to reproduce with accuracy the exact width of the Balmer lines. Therefore, it could be interesting to investigate how one could recover the information on the Balmer line profiles and to develop a new method of disentangling to decrease the impact of this effect.
- Two techniques of Doppler tomography that we have mentioned yield relatively similar results: though some methods decrease the effects of the "spike" artefacts, they never erase them completely. Therefore, we could envisage to test the method of the maximum of entropy and compare it to Fourier-filtered back-projection or SIRT techniques.
- With the upcoming Gaia astrometrical mission, the real distances at which many of the stars discussed in this thesis are located will be much better known. We will then have more

accurate luminosities of these stars and thus know their real positions in the HR diagram. That will allow us to bring a new light on Plaskett's Star as well as on most of the other stars analysed until now.

- It is also important to establish the multiplicity of massive stars located in regions poorly observed until now. Numerous young open clusters or OB associations still remain to be observed. A first insight into their multiplicity should be established thanks to the Gaia–ESO survey which will begin soon. This survey foresees a total of 300 nights of observations spread over five years. Of course, this survey will not solve all the questions about the multiplicity of massive stars but it could be a first step. Other observations will be still needed to derive the orbital parameters such as the eccentricity, the orbital period or the mass ratio and then bring some strong constraints on the formation processes for close binary systems.

Furthermore, it would be interesting to adapt the development of the CMFGEN atmosphere code to allow a coherent treatment of the transfer but also of the hydrodynamics in order to improve the determinations of physical parameters of stars. Moreover, an adaptation of the atmosphere codes to model in 2D or even in 3D the stellar atmospheres would be interesting to constrain the stellar winds and their 3D structure. Finally, these codes also require a more physical description of micro- and macro-turbulences as well as of effects of the rotation and the magnetic field on the radiative transfert.

To conclude this thesis, we can say that an important amount of work is still awaiting us to answer the remaining questions. But obtaining new data to find answers will certainly raise new questions... Science is like Universe, it has no end!

Appendix A

List of publication

Publications with a peer review

Papers in first author

- **Early-type stars in the young open cluster NGC 2244 and in the Monoceros OB2 association. I. The multiplicity of O-type stars**,
Mahy, L., Nazé, Y., Rauw, G., Gosset, E., De Becker, M., Sana, H., Eenens, P. 2009,
A&A, **502**, 937–950

- **A New Investigation of the Binary HD 48099**,
Mahy, L., Rauw, G., Martins, F., Nazé, Y., Gosset, E., De Becker, M., Sana, H., Eenens, P. 2010,
ApJ, **708**, 1537–1544

- **Plaskett's star: analysis of the CoRoT photometric data**
Mahy, L., Gosset, E., Baudin, F., Rauw, G., Godart, M., Morel, T., Degroote, P., Aerts, C., Blomme, R., Cuypers, J., Noels, A., Michel, E., Baglin, A., Auvergne, M., Catala, C., Samadi, R. 2011,
A&A, **525**, 101–112

- **The multiplicity of O-type stars in NGC 2244**
Mahy, L., Rauw, G., Martins, F., Gosset, E., Nazé, Y., Godart, M., Sana, H., De Becker, M., Eenens, P. 2011,
BSRSL, **80**, 622–627

- **The two components of the evolved massive binary LZ Cephei. Testing the effects of binarity on stellar evolution**
Mahy, L., Martins, F., Machado, C., Donati, J.-F., Bouret, J.-C. 2011,
A&A, **533**, 9–18

- **A quantitative study of O stars in NGC 2244**,
Mahy, L.; Martins, F.; Hillier, D. J.; Rauw, G. 2011,
JPCS, in press.

- **Evidence for a physically bound third component in HD 150136**
Mahy, L., Gosset, E., Sana, H., Damerdji, Y., De Becker, M., Rauw, G., Nitschelm, C. submitted

Papers as co-authors

- **First Orbital Solution for the Non-thermal Emitter Cyg OB2 No. 9**,
  Nazé, Y., Damerdji, Y., Rauw, G., Kiminki, D. C., **Mahy, L.**, Kobulnicky, H. A., Morel, T., De Becker, M., Eenens, P., Barbieri, C. 2010,
  ApJ, **719**, 634–641.

- **Detection of frequency spacings in the young O-type binary HD 46149 from CoRoT photometry**,
  Degroote, P., Briquet, M., Auvergne, M., Sim'on-Díaz, S., Aerts, C., Noels, A., Rainer, M., Hareter, M., Poretti, E., **Mahy, L.**, Oreiro, R., Vučković, M., Smolders, K., Baglin, A., Baudin, F., Catala, C., Michel, E., Samadi, R. 2010,
  A&A, **519**, 38–47.

- **A first orbital solution for the non-thermal radio emitter Cyg OB2 #9**,
  Nazé, Y.; Damerdji, Y.; Rauw, G.; Kiminki, D. C.; **Mahy, L.**; Kobulnicky, H. A.; Morel, T.; De Becker, M.; Eenens, P.; Barbieri, C. 2011,
  BSRSL, **80**, 709–713.

- **Variability in the CoRoT photometry of three hot O-type stars. HD 46223, HD 46150, and HD 46966**,
  Blomme, R., **Mahy, L.**, Catala, C., Cuypers, J., Gosset, E., Godart, M., Montalban, J., Ventura, P., Rauw, G., Morel, T., Degroote, P., Aerts, C., Noels, A., Michel, E., Baudin, F., Baglin, A., Auvergne, M., Samadi, R. 2011,
  A&A 533, 4–16.

- **A quantitative study of O stars in NGC 2244 and the Mon OB2 association**,
  Martins, F.; **Mahy, L.**; Hillier, D. J.; Rauw, G. 2011,
  A&A, in press.

Publications without a peer review

- **HD 150136: towards one of the most massive systems?**,
  Mahy, L., Gosset, E., Sana, H., Rauw, G., Fauchez, T., Nitschelm, C. 2011,
  IAUS, **272**, 521–522.

- **CoRoT observations of O stars: diverse origins of variability**,
  Blomme, R., Briquet, M., Degroote, P., **Mahy, L.**, Aerts, C., Cuypers, J., Godart, M., Gosset, E., Hareter, M., Montalban, J., Morel, T., Nieva, M. F., Noels, A., Oreiro, R., Poretti, E., Przybilla, N., Rainer, M., Rauw, G., Schiller, F., Simón-Díaz, S., Smolders, K., Ventura, P., Vučković, M., Auvergne, M., Baglin, A., Baudin, F., Catala, C., Michel, E., Samadi, R. 2011,
  ASPE, in press.

Astronomy & Astrophysics manuscript no. ngc2244˙rereresubmitted
October 12, 2011

A quantitative study of O stars in NGC2244 and the Mon OB2 association

F. Martins[1], L. Mahy[2], D.J. Hillier[3], and G. Rauw[2]

[1] LUPM–UMR 5299, CNRS & Université Montpellier II, Place Eugène Bataillon, F-34095, Montpellier Cedex 05, France
e-mail: fabrice.martins AT univ-montp2.fr
[2] Institut d'Astrophysique et de Géophysique, Université de Liège, Bât B5C, Allée du 6 Août 17, B-4000, Liége, Belgium

[3] Department of Physics and Astronomy, University of Pittsburgh, 3941 O'Hara street, Pittsburgh, PA 15260, USA

Received ...; accepted ...

ABSTRACT

Aims. Our goal is to determine the stellar and wind properties of seven O stars in the cluster NGC2244 and three O stars in the OB association MonOB2. These properties give us insight into the mass loss rates of O stars, allow us to check the validity of rotational mixing in massive stars, and to better understand the effects of the ionizing flux and wind mechanical energy release on the surrounding interstellar medium and its influence on triggered star formation.
Methods. We collect optical and UV spectra of the target stars which are analyzed by means of atmosphere models computed with the code CMFGEN. The spectra of binary stars are disentangled and the components are studied separately.
Results. All stars have an evolutionary age less than 5 million years, with the most massive stars being among the youngest. Nitrogen surface abundances show no clear relation with projected rotational velocities. Binaries and single stars show the same range of enrichment. This is attributed to the youth and/or wide separation of the binary systems in which the components have not (yet) experienced strong interaction. A clear trend of larger enrichment in higher luminosity objects is observed, consistent with what evolutionary models with rotation predict for a population of O stars at a given age. We confirm the weakness of winds in late O dwarfs. In general, mass loss rates derived from UV lines are lower than mass loss rates obtained from Hα. The UV mass loss rates are even lower than the single line driving limit in the latest type dwarfs. These issues are discussed in the context of the structure of massive stars winds. The evolutionary and spectroscopic masses are in agreement above 25 $M_{\odot}$ but the uncertainties are large. Below this threshold, the few late–type O stars studied here indicate that the mass discrepancy still seems to hold.

Key words. Stars: early-type - Stars: fundamental parameters - Stars: winds, outflows - ISM: H regions

1. Introduction

Massive stars play key roles in various fields of astrophysics due to their strong ionizing fluxes, powerful winds and extreme stellar properties. They have been recognized as the precursors of long–soft gamma–ray bursts. Population III stars are thought to be made of very massive stars with exceptionally hard UV luminosity. As they live rapidly, they are excellent tracers of star formation. But they also trigger the formation of new generations of stars through their feedback effects. The heavy elements produced in their cores are injected in the interstellar medium by stellar winds and supernovae ejecta, contributing to the chemical evolution of galaxies. Constraining their properties and understanding quantitatively their evolution and feedback effects is thus of interest for fields well beyond pure stellar physics.

In addition to their mass, the evolution of massive stars is governed by two main parameters: mass loss (Chiosi & Maeder 1986) and rotation (Maeder & Meynet 2000). The accurate determination of mass–loss rates relies mainly on two types of methods. First, the infrared-millimeter-radio excess emission is measured and converted to mass–loss rate (Wright & Barlow 1975; Barlow & Cohen 1977; Leitherer & Robert 1991). This method suffers from little approximations but requires stars to be relatively nearby to be detected with the current generation of instruments. Second, spectroscopic features sensitive to the wind extension (such as P–Cygni profiles or emission lines) are fitted by atmosphere models (Puls et al. 1996; Hillier & Miller 1999). This method allows the analysis of larger samples of massive stars, but relies on the physics and approximations included in atmosphere models. The main uncertainty in mass–loss rate determinations (which affects both types of methods) is the non–homogeneity of massive stars winds (clumping). Direct (Eversberg et al. 1998) and indirect (e.g. Hillier 1991; Bouret et al. 2005) evidence exists for the presence of inhomogeneities in O and Wolf–Rayet stars winds. Although theoretically expected (MacGregor et al. 1979; Owocki & Rybicki 1984, 1985; Runacres & Owocki 2002), clumping is currently not fully understood and characterized, although work is in progress (e.g. Puls et al. 2006; Sundqvist et al. 2010). This is a severe problem for stellar evolution since mass loss is a key parameter. Hence, having as many stars as possible studied quantitatively is desirable in order to understand their outflows. In this context, the late O-type main–sequence stars represent a puzzle of their own, since they display very weak winds with mass–loss rates down to a few 10^{-10} $M_{\odot}$ yr^{-1} (Martins et al. 2004, 2005b; Marcolino et al. 2009). The origin of such a weakness is not understood.

Rotation has several effects on the appearance and evolution of massive stars. In addition to shaping the surface of the star and modifying the surface temperature (poles being hotter than

Send offprint requests to: F. Martins

the equator), it triggers internal mixing processes (mainly meridional circulation and shear turbulence) which affect the transport of angular momentum and chemical species. Consequently, the timescales (such as main–sequence lifetime) and surface abundances depend on the rotation rate (Maeder & Meynet 2000). Hunter et al. (2008, 2009) have questioned the role of rotational mixing in the surface chemical enrichment of B stars in the Magellanic Clouds and the Galaxy. They found both slowly rotating N–rich and rapidly rotating non enriched stars that, according to the authors, cannot be accounted for by single star evolution with rotation. However, Maeder et al. (2009) argued that when care is taken in disentangling the various parameters on which the surface nitrogen content depends, 80% of the population of B stars is explained by normally rotating single stars. Of particular importance is the age of the population: it is crucial to build samples of stars of the same age to avoid too large a spread in nitrogen surface abundances. So far, the relation between chemical enrichment and rotation has not been looked at in more massive O stars. Since they evolve more rapidly and produce a larger enrichment than B stars, they are important objects to analyze.

The region of the Rosette nebula is especially interesting in this context. It harbors the ionizing cluster NGC2244 at the core of the nebula itself, as well as several more widely spread massive stars in the MonOB2 association. NGC2244 contains seven O stars covering the entire range of spectral types, from O4 to O9. All of them have main–sequence luminosity classes (see Table 1). The stars of MonOB2 have similar spectral types. Hence, this region contains a homogeneous sample of O stars with different masses and luminosities but most likely of the same age. Binaries are also present (Mahy et al. 2009). As such, this sample is well suited to investigate the effects of rotation on massive stars surface abundances. The Rosette nebula is also famous for the numerous young stellar objects and embedded clusters in the so-called Rosette molecular cloud (Phelps & Lada 1997; di Francesco et al. 2010). Triggered star formation is thought to be at work in this region, due to the ionizing radiation and powerful winds of the NGC2244 O stars. Recent results obtained by the *Herschel Space Observatory* reveal the presence of younger objects further away from the HII region center, as well as temperature gradients (di Francesco et al. 2010; Motte et al. 2010; Schneider et al. 2010). Constraining the mechanical energy release and ionizing flux of the massive star population is thus important in order to quantitatively study the process of star formation triggering.

In this paper, we analyze nine O stars and one supposed B star in the Rosette nebula region. Seven are located in NGC2244, three in MonOB2. Our study encompasses six out of the seven O stars powering the Rosette HII region[1]. Two confirmed binaries (HD46149 and HD46573) and one binary candidate (HD46150) are included. This work complements and extends the analysis of HD48099 (Mahy et al. 2010), also a binary member of the MonOB2 association. In Sect. 2 we present the observations of the targets. Their analysis by means of atmosphere models is described in Sect. 3. The results are given in Sect. 4 and discussed in Sect. 5. Finally, our conclusions are drawn in Sect. 6.

2. Observations and data reduction

Table 1 summarizes the main observational properties of our sample stars. Photometry is taken from the Galactic O star Catalog of Maíz-Apellániz et al. (2004). We have adopted a distance of 1.55±0.15 kpc for the Mon OB2 association and NGC2244. Photometric distances range between 1.4 and 1.7 kpc according to the summary of Hensberge et al. (2000). We simply adopt the average of these values in the present work (see also Mahy et al. 2009).

Spectroscopic data were obtained at the Observatoire de Haute-Provence (OHP, France) with the Aurélie spectrograph mounted on the 1.52m telescope. Several observing runs from 2006 to 2008 allowed us to collect spectra in two different wavelength domains: [4450–4900] and [5500-5920]Å. In the adopted configuration, the Aurélie spectrograph offers a resolving power of about $R = 8\,000$ in the blue domain whilst $R = 10\,000$ is reached in the red band. The exposure times, necessary to reach a signal-to-noise ratio higher than 150, were typically 10 to 45 min. We also retrieved 13 spectra from the Elodie ($R = 42\,000$) archives taken from November 1999 to November 2005 with the 1.93m telescope at the OHP. The exposure times of these data ranged from 10 min to 1h.

In April 2007 and March 2008, another set of spectra was obtained at Observatorio Astronómico Nacional of San Pedro Màrtir (SPM) in Mexico with the Espresso spectrograph mounted on the 2.10m telescope ($R = 27\,000$). This échelle spectrograph covers the wavelength domain [3780–6950]Å with 27 orders. We used a typical exposure time from 5 to 15 min. Several consecutive spectra of a given night were added to improve the signal-to-noise ratio of our data.

We have also retrieved 11 spectra from the ESO archives (PI: Casassus, run 076.C-0431(A) and PI: Lo Curto, run 076.C-0164(A)) taken with the Fiber-fed Extended Range Optical Spectrograph (FEROS) mounted on the ESO/MPG 2.20m telescope at La Silla (Chile). The wavelength region covered by this instrument is [3550–9200]Å and the spectral resolution is about $R = 48\,000$. The data reduction was done with an improved version of the FEROS pipeline as described in Sana (2009).

Finally, to model the winds of the O-type stars with more accuracy, we have retrieved a total of 40 high-resolution *IUE* spectra (SWP with a dispersion of 0.2Å). Such data are available for all targets of our sample, except HD 46573. These data were taken between September 1978 and February 1987 with exposure times between 539 and 18000 s. These spectra cover the [1200–1800]Å spectral band, which is particularly interesting for the UV P-Cygni profiles (C IV1548 – 1550 and N V1240).

A full description of the optical instruments used as well as the reduction procedure was given in Mahy et al. (2009). Tables 2 and 3 present the main characteristics of the observational data. For the single stars, we have selected the spectra of Mahy et al. (2009) with the widest wavelength coverage, highest spectral resolution and highest signal–to–noise ratio.

3. Modelling

We have used the code CMFGEN (Hillier & Miller 1998) for the quantitative analysis of the optical and UV spectra. CMFGEN provides non–LTE atmosphere models including winds and line–blanketing. An exhaustive description can be found in Hillier & Miller (1998) and a summary of the main characteristics is given in Hillier et al. (2003). CMFGEN needs as input an estimate of the hydrodynamical structure that we constructed from TLUSTY models (taken from the OSTAR2002 grid of Lanz & Hubeny 2003) connected to a β velocity law of the form $v = v_\infty(1 - R/r)^\beta$ where v_∞ is the wind terminal velocity. We adopted $\beta = 0.8$ since this is the typical value for

[1] Only the O9V star HD258691 is not included due to the lack of spectroscopic data.

Table 1. Sample stars and photometry.

Source	ST	U	B	V	J	H	K	A_V	M_V
				NGC2244					
HD 46223	O4V((f))	6.712	7.484	7.266	6.742	6.684	6.693	1.54	−5.22
HD 46150	O5V((f))z	6.043	6.875	6.745	6.446	6.451	6.453	1.27	−5.48
HD 46485	O7Vn	7.876	8.563	8.243	7.565	7.492	7.463	1.86	−4.57
HD 46056	O8Vn	7.705	8.445	8.245	7.837	7.816	7.837	1.49	−4.20
HD 46149-1	O8V	6.982	7.774	7.602	7.245	7.232	7.268	1.40	−4.13
HD 46149-2	O8.5–9V	–	–	–	–	–	–	1.40	−3.84
HD 46202	O9.5V	7.623	8.360	8.183	7.784	7.760	7.737	1.42	−4.19
				Mon OB2					
HD 46573	O7V((f))z	7.613	8.273	7.933	7.197	7.148	7.145	1.92	−4.94
HD 48279	ON8.5V	7.254	8.047	7.910	7.650	7.681	7.710	1.29	−4.33
HD 46966	O8.5IV	5.910	6.827	6.877	6.919	6.951	7.035	0.71	−4.78
HD 48099-1	O5.5V((f))	5.387	6.323	6.366	6.445	6.490	6.512	0.73	−5.39
HD 48099-2	O9V	–	–	–	–	–	–	0.73	−3.89

Notes. Spectral types are from Sota et al. (2011) and Mahy et al. (2009). Magnitudes are from Maíz-Apellániz et al. (2004). The extinction A_V is $3.1 \times E(B-V)$. The absolute magnitude assumes a distance of 1.55 kpc. For binary stars, we give the observed magnitudes of the system on the row of the primary star. For binary systems, the absolute V magnitudes of each component are computed assuming the V–band flux ratio typical for stars of the same spectral type (see Sect. 4).

Table 2. Journal of optical observations.

Star	Instrument	Resolution	Spectral range [Å]	S/N	Obs Date	HJD [d]	Exposure time [s]
HD 46056	ESPRESSO	18000	[3950 – 6700]	269	20 Mar 2008	2454545.6733	2700
HD 46149	disentangled spectrum – see data in Mahy et al. (2009)						
HD 46150	FEROS	48000	[4000 – 7100]	310	06 Feb 2006	2453772.5895	3600
HD 46202	FEROS	48000	[4000 – 7100]	154	05 Jan 2006	2453740.6191	600
HD 46223	FEROS	48000	[4000 – 7100]	194	08 Feb 2006	2453774.5460	3600
HD 46485	FEROS	48000	[4000 – 7100]	166	05 Jan 2006	2453740.6290	600
HD 46573	FEROS	48000	[4000 – 7100]	268	07 Feb 2006	2453773.5904	3600
HD 46966	FEROS	48000	[4000 – 7100]	200	03 Jan 2006	2453738.7201	600
HD 48099	disentangled spectrum - see Mahy et al. (2010)						
HD 48279	ELODIE	42000	[4000 – 6800]	214	25 Jan 2000	2451569.5028	2700

Table 3. List of IUE UV spectra.

Star	data ID	Obs. Date	HJD [d]	Exposure time [s]
HD 46056	SWP06949	22 Oct 1979	2444168.92297	5100
HD 46149	SWP28151	11 Apr 1986	2446532.40344	2640
HD 46150	SWP10758	05 Dec 1980	2444578.86527	1200
HD 46202	SWP30299	12 Feb 1987	2446839.37549	5100
HD 46223	SWP10757	05 Dec 1980	2444578.81523	1980
HD 46485	SWP28196	19 Apr 1986	2446539.98248	10800
HD 46966	SWP24196	18 Oct 1984	2445991.75211	540
	SWP27918	15 Mar 1986	2446505.35266	540
HD 48099	disentangled spectrum - see Mahy et al. (2010)			
HD 48279	SWP06504	14 Sep 1979	2444130.71788	7200

Notes. IUE UV spectra retrieved from the archive and used for the analysis. The wavelength range is 1150–1975 Å and the spectral resolution 0.2 Å (R=7500 at 1500 Å) for all spectra. For HD 48279, we used the average of the two spectra listed in the table since they were obtained in the same mode (high aperture), with the same exposure time and do not show any variability. For the other stars, we chose the spectra with the highest exposure time in the high aperture mode.

O dwarfs (e.g. Repolust et al. 2004). Once the model was reasonably converged, the radiative acceleration was computed and used to iterate on the initial hydrodynamical structure in the inner atmosphere. The radiation field and level populations were then converged once again. Two to five of these global hydrodynamical iterations were performed before the atmosphere model finally converged.

Our final models include H, He, C, N, O, Ne, Mg, Si, S, Fe with the solar composition of Grevesse et al. (2007) unless otherwise stated. The super–level approach is used to reduce the amount of memory requirements. On average, we include 1600 super levels for a total of 8000 levels. For the formal solution of the radiative transfer equation leading to the emergent spectrum,

a microturbulent velocity varying linearly (with velocity) from 10 km s^{-1} to 0.1 × v_∞ was used.

We included X–ray emission in the wind since this can affect the ionization balance and the strength of key UV diagnostic lines. In practice, we adopted a temperature of 3 million degrees and adjusted the flux level so that the X–ray flux effectively coming out of the atmosphere matches the observed $L_X/L_{\rm bol}$ ratio. This ratio was computed from the observed X–ray fluxes of Wang et al. (2008) and our derived luminosities. In case no X–ray flux was detected, we simply adopted the canonical value $L_X/L_{\rm bol} = 10^{-7}$ (Sana et al. 2006; Nazé 2009).

In practice we proceeded as follows to derive the stellar and wind parameters:

- *Effective temperature*: we used the classical ratio of He to He lines to constrain $T_{\rm eff}$. The main indicators were He 4471 and He 4542. Additional diagnostics are He 4026 (blended with He 4026), He 4388, He 4713, He 4921, He 5876, He 4200, He 5412. The typical uncertainty on the $T_{\rm eff}$ determination is 1000 K.
- *Gravity*: The wings of the Balmer lines Hβ, Hγ and Hδ are the main $\log g$ indicators. An accuracy of about 0.1 dex on $\log g$ is achieved.
- *Luminosity*: We fitted the flux calibrated IUE spectra and UBVJHK fluxes to derive both the luminosity and the extinction. For this, we adopted a distance of 1.55±0.15 kpc (see discussion in Mahy et al. 2009). The Galactic extinction law of Seaton (1979) and Howarth (1983) was used. We adjusted the stellar luminosity and E(B−V) to reproduce the UV-optical-infrared SED. In those cases where no UV spectra were available, we simply derived the extinction from E(B−V) and adjusted the luminosity to reproduce the V magnitude.
- *Wind terminal velocity*: the blueward extension of P–Cygni lines observed in the UV provides v_∞ with an accuracy of 100 km s^{-1}.
- *Mass–loss rate*: We used two diagnostic lines to constrain the mass loss rate: the UV P–Cygni profiles and Hα. In principle, a single value of $\dot{M}$ should allow a good fit of both types of lines. However in practice, several recent studies have shown that this was not the case. In order to be as complete as possible, we thus provide both values: the "UV mass loss rate" ($\dot{M}_{\rm UV}$, given in Table 4) and the "Hα mass loss rates" ($\dot{M}_{\rm H\alpha}$, given in Table 5).

The projected rotational velocities were derived by direct comparison of our synthetic spectra to observed line profiles for fast rotating stars (i.e., those with $V \sin i \geq 150$ km s^{-1}). The rotationally broadened synthetic line profiles usually provided a good match to the observed profile. In the case of moderately to slowly rotating objects, some amount of macroturbulence had to be introduced to correctly reproduce the line profiles of several features (e.g., He 4713, C 5812, He 5876). The need for extra broadening is well documented (Howarth et al. 1997; Ryans et al. 2002; Howarth et al. 2007; Nieva & Przybilla 2007; Martins et al. 2010; Fraser et al. 2010) but its origin is unclear. Aerts et al. (2009) recently suggested that non–radial pulsations could trigger large–scale motions (hence macroturbulence), but this needs to be confirmed by a study covering a wider parameter space. A recent study by Simón-Díaz et al. (2010) showed that the amplitude of macroturbulence was correlated to the amplitude of line profile variability in a sample of OB supergiants. In practice, we introduced macroturbulence by convolving our (rotationally broadened) synthetic spectra with a Gaussian profile ($\propto e^{-\frac{v^2}{2v_{mac}^2}}$ where v_{mac} is the macroturbulent velocity), thus mimicking isotropic turbulence. This is obviously a very simple approach, but it significantly improves the quality of the fits. Given the present limitations, we restricted ourselves to rough estimates of the amount of macroturbulence by judging the fit quality by eye. In practice, we used He 4713 as the main indicator of macroturbulence since it is present with sufficient SNR in all our sample stars. Secondary indicators were the C doublet at 5801–5812 Å and He 5876. $V \sin i$ was also obtained from the Fourier transform method (Simón-Díaz & Herrero 2007). In practice, for the moderately to slowly rotating stars, we obtained upper limits from the absence of zero and the position of the noise level in the FT.

We also determined the nitrogen content of our sample stars. We relied mainly on the N lines between 4500 and 4520 Å. They are present in absorption in all the stars. They are not affected by winds and are strong enough for abundance determination. The uncertainties are of the order of 50%. They were estimated from the comparison of the selected N lines to models with various N content. The errors do not take into account any systematics related to atomic data.

When possible, the degree of inhomogeneities of the winds of our sample stars was determined. Clumping is implemented in CMFGEN by means of a volume filling factor f following the law $f = f_\infty + (1 - f_\infty)e^{-v/v_{cl}}$ where f_∞ is the maximum clumping factor at the top of the atmosphere and v_{cl} a parameter indicating the position where the wind starts to be significantly clumped. As shown by Bouret et al. (2005), O 1371 and N 1720 are two UV features especially sensitive to wind inhomogeneities in early O stars. We have used these lines to constrain f_∞ in the earliest O stars of our sample. In mid to late O stars, no UV clumping diagnostic has been identified. This is confirmed by our study. For the O7–O9 stars of our sample, we computed models with several values of f_∞ (scaling $\dot{M}$ so that $\dot{M}/\sqrt{f}$ is constant) and found no difference in the UV wind sensitive lines. Hence, we decided to adopt $f_\infty = 1$ (i.e. homogeneous model). Our mass–loss rates for those objects should thus be regarded as upper limits.

4. Results

The derived stellar and wind parameters of the sample stars are gathered in Table 4. The values of the Hα mass loss rates are given in Table 5. We show the best optical fits for HD 46223 and HD 48279 in Figs. 1. The optical fits for the other stars are gathered in Appendix A. The fits to the UV spectra for all stars are shown in Fig. 2. Below, we briefly comment on each star.

HD 46223: a clumped wind (f=0.1) is required to fit O 1371. The nitrogen content is difficult to estimate given the weakness of the N 4500–4520 features. A value of N/H=7.0 × 10^{-4} is preferred. It also provides a good fit to the N 1720 feature. The parameters are similar to those of Martins et al. (2005b) within the uncertainties. The better quality and wider wavelength coverage of the present optical spectra explains the refined effective temperature estimate.

HD 46150: this is a binary candidate. We thus derive upper limits on the luminosity and mass loss rate. A clumping factor of 0.1 is necessary to correctly reproduce the O 1371 Å line profile. Models with higher (lower) clumping factor yield a too strong (weak) absorption in the blue part of the profile. See also Sect. 5.2 for further discussion.

HD 46485: this is the second fastest rotator of our sample, with $V \sin i$ = 300 km s^{-1}. The fit of the optical and UV spec-

Table 4. Derived stellar properties of the sample stars.

Source	ST	$T_{\rm eff}$ [kK]	$\log \frac{L}{L_\odot}$	log(g)	log($M_{\rm UV}$)	f_∞	v_∞ [km s^{-1}]	$V \sin i$ [km s^{-1}]	v_{mac} [km s^{-1}]	M$_{evol}$ [$M_\odot$]	M$_{spec}$ [$M_\odot$]	N/H [$\times 10^4$]	log(Q$_0$)
NGC2244													
HD 46223	O4V((f))	43.0	5.60±0.11	4.01	−7.17	0.1	2800	100	32	$52.1^{+6.2}_{-5.9}$	48.3 ± 19.3	7.0±2.0	49.40
HD 46150	O5V((f))z	42.0	<5.65	4.01	−7.30	0.1	2800	100	37	< 53.6	59.5 ± 23.7	3.0±2.0	49.36
HD 46485	O7Vn	36.0	5.05±0.11	3.85	−7.80	1.0	1850	300	–	$28.6^{+3.3}_{-4.3}$	19.5 ± 7.9	≤1.2	48.62
HD 46056	O8Vn	34.5	4.85±0.12	3.89	−8.50	1.0	1500	330	–	$23.1^{+2.4}_{+1.9}$	15.8 ± 6.7	≤0.6	48.32
HD 46149-1	O8V	37.0	4.90±0.12	4.25	< −9.0		1300	∼0	24	$25.9^{+3.5}_{+3.1}$	30.9 ± 21.6	0.8±0.5	48.42
HD 46149-2	O8.5–9V	35.0	4.65±0.16	4.01	–	–	–	100	27	$20.6^{+4.1}_{-3.4}$	12.5 ± 10.1	0.8±0.5	48.10
HD 46202	O9.5V	33.5	4.85±0.12	4.10	−9.0	1.0	1200	20	17	$22.7^{+2.0}_{-2.4}$	29.0 ± 12.4	1.0±0.5	48.19
Mon OB2													
HD 46573	O7V((f))z	36.5	<5.20	3.75	–	–	–	20	43	< 32.5	20.6 ± 8.3	3.0±1.0	48.84
HD 48279	ON8.5V	34.5	4.95±0.11	3.77	−8.8	1.0	1300	125	22	$24.4^{+2.5}_{-1.9}$	15.2 ± 6.1	5.0±3.0	48.47
HD 46966	O8.5IV	35.0	5.20±0.11	3.75	−8.0	1.0	2300	50	27	$30.9^{+4.1}_{-3.8}$	24.5 ± 9.9	1.2±0.5	48.70
HD 48099-1[a]	O5.5V((f))	44.0	5.65±0.07	4.50	−7.60	0.01	2800	91	0	$55.3^{+7.3}_{-5.0}$	155.0 ± 98.7	5.0±2.5	49.36
HD 48099-2[a]	O9V	32.0	4.60±0.06	3.51	–	–	–	51	0	$18.5^{+2.2}_{-1.7}$	5.0 ± 3.5	0.6±0.3	47.93

Notes. The columns give: name, spectral type, effective temperature (uncertainty 1000K except for HD 46149–1 / HD 48099–1, 2000K and HD 46149–2 / HD 48099–2, 3000K), luminosity, effective gravity (uncertainty 0.1 dex, except for HD 46149 and HD 48099, 0.2 dex), UV mass–loss rate, terminal velocity, projected rotational velocity, macroturbulent velocity, evolutionary mass, spectroscopic mass, nitrogen content, ionizing flux. Spectroscopic masses are computed from the true gravity (i.e. $\log g$ corrected from the effect of centrifugal force).
[(a)] from Mahy et al. (2010), except that the error bars on $T_{\rm eff}$ and $\log g$ are similar to HD 46149 (see text for discussion).

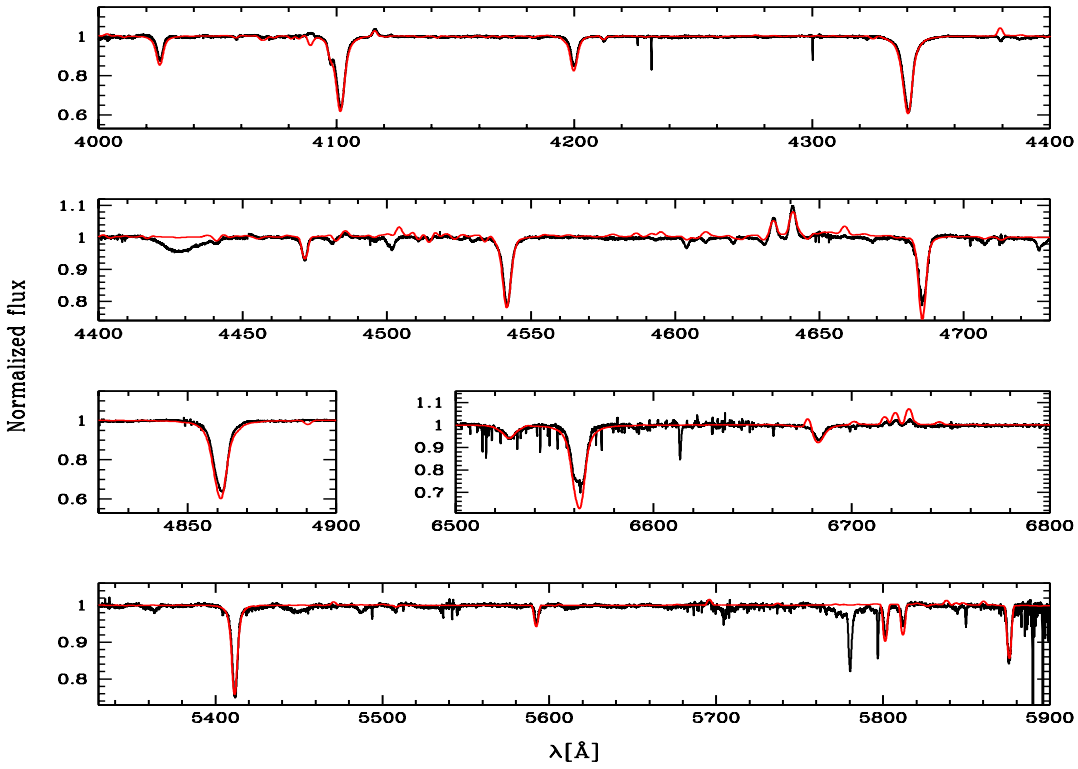

(a) HD 46223

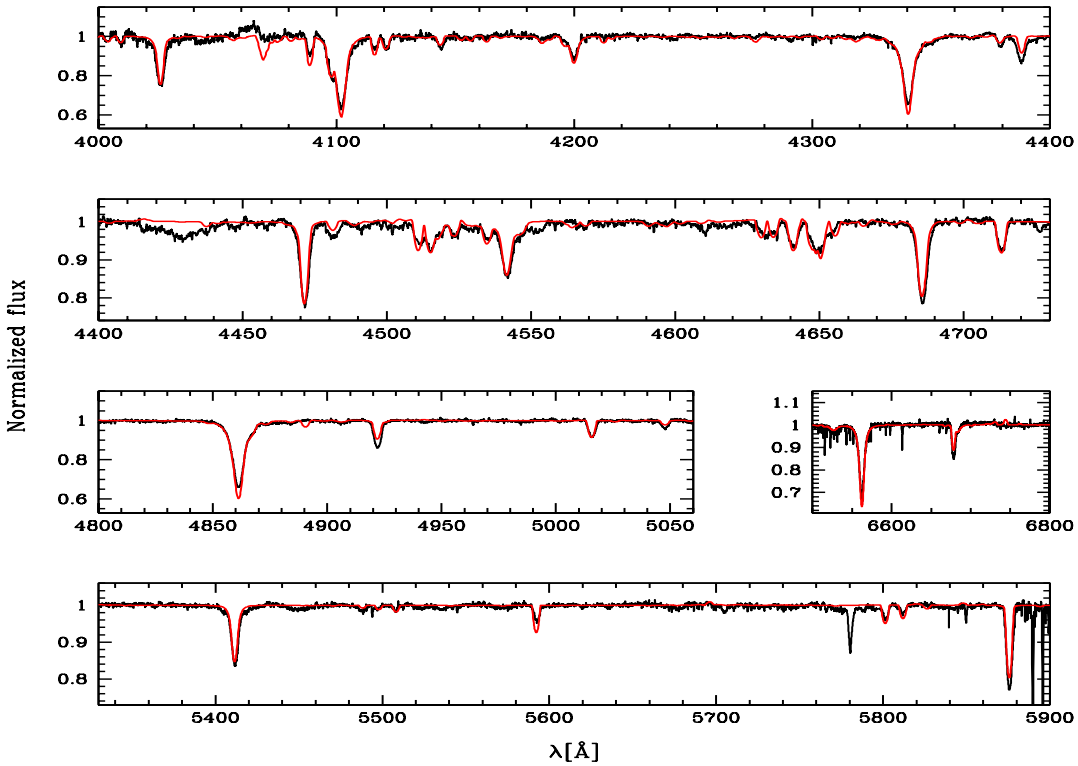

(b) HD 48279

Fig. 1. Best CMFGEN fits (red) of the optical spectra (black) of stars HD46223 (top), HD48279 (bottom). The models have the mass loss rate best reproducing the UV features. The unfitted feature around 4425 Å is a DIB.

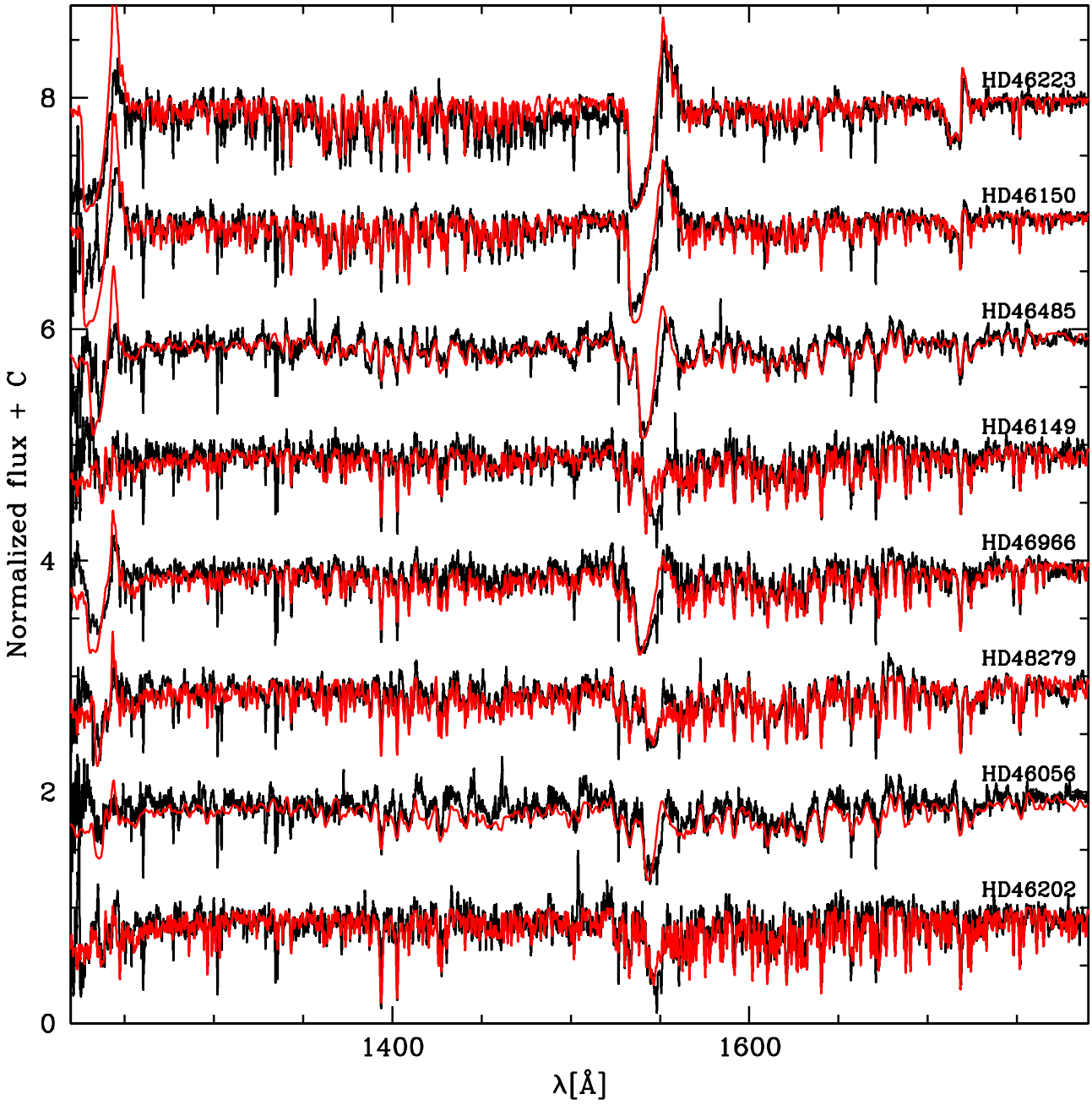

Fig. 2. Best CMFGEN fits (red) of the UV spectra (black) of the sample stars.

tra is of excellent quality. The only notable exceptions are the C III line complex at 4640 Å, C 5801–5812 Å and He 5876 Å. The C 4650 line complex is slightly too weak in our best fit model. However, we found out that this transition is sensitive to detailed line–blanketing effects. The lower level of these transitions is connected to the C ground level by a transition at 538Å. This transition is blended with Fe transitions. The interaction between these UV lines thus affects the strength of the C 4650 lines, in a manner similar to that described by Najarro et al. (2006) for the He singlet lines.

HD 46056: this is the fastest rotator of our sample and no macroturbulence is necessary to reproduce the line profiles. The fit is good with the exception of the C 4650 line complex which is underpredicted. The C 4650 lines suffer from the same problem as for HD 46485.

HD 46149: this is a binary (Mahy et al. 2009). The spectra have been disentangled using the method described in Mahy et al. (2010). They have subsequently been used to classify the two components of the system. The classical diagnostic $\log \frac{EW(HeI4471)}{EW(HeII4542)}$ lead to a spectral type O8 for the primary and O8.5–O9 for the secondary. Similarly, a luminosity class V

was assigned based on the values of log $\frac{EW(SiIV4088)}{EW(HeI4143)}$ (Conti & Alschuler 1971). These classifications are slightly different from those derived by Mahy et al (2009) although for the primary it remains in the error range. However, such a discrepancy for the secondary could come from the disentangling process, making the disentangled spectra uncertain. Indeed, they were computed from a sample of observed spectra taken essentially at similar phases where the separation between the radial velocities of both components ($RV_S - RV_P$) are of about −30, 0 and +140 km s^{-1}. Moreover, the orientation and the large eccentricity of the orbit imply an asymmetric excursion in radial velocity which could also affect the accuracy of the broadest lines. We thus caution that the disentangling process does not provide perfect results and should be refined in the future when more data taken at different phases will be obtained. This is especially true for the wings of broad lines which need to be correctly sampled and fully separated in the observed spectrum (at maximum separation) to be reconstructed correctly (see below – HD 48099). Consequently, the gravity and spectroscopic masses in Table 4 are highly uncertain. The effective temperature and nitrogen content have also larger error bars than the other stars of our sample: 2000 K (3000 K) on $T_{\rm eff}$ for the primary (secondary) and ∼70% on N/H. In addition, given the poor quality of the spectrum of the secondary, we adopted $\log g = 4.0$. Using the calibrations of Martins & Plez (2006), we find that the V–band flux ratio between a O8V and a O9V star is ≈ 1.3. Optical photometry of HD 46149 indicates E(B−V)= 0.45, leading to $A_{\rm V} = 1.40$. For the adopted distance, the absolute V–band magnitude of the system is thus $M_V = -4.75$. Given the V–band flux ratio of the two components, we have $M_{\rm V}^{\rm primary} = -4.13$ and $M_{\rm V}^{\rm secondary} = -3.84$.

HD 46202: the parameters derived for HD 46202 are very similar to those of Martins et al. (2005b). The fit to the optical spectrum is of excellent quality. A combination of a low rotation rate (20 km s^{-1}) and a macroturbulent velocity of 17 km s^{-1} correctly reproduces the photospheric line profiles. See also Sect. 5.2 for further discussion.

HD 46573: this is a binary candidate. No UV spectra are available for that star, so that our analysis is restricted to the optical range. A very good fit is achieved. Only the core of the Balmer lines is too deep in our synthetic spectra. The line profiles show that macroturbulence is important. We found that a combination of V sin$i$ in the range 40–60 km s^{-1} with a macroturbulent velocity of 40 to 50 km s^{-1} leads to much better fits compared to purely rotationally broadened profiles.

HD 48279: our synthetic spectrum provides a good fit of most optical and UV lines. The singlet lines He 4388 Å and He 4921 Å are too weak in our spectrum. They are known to be sensitive to details of line blanketing (Najarro et al. 2006).

HD 46966: the fit of the optical and UV spectra is one of the best of the present work. The only problem is observed in He 4686 Å for which our synthetic profile is too deep. A projected rotational velocity of the order 40–50 km s^{-1} combined with a macroturbulent velocity ∼ 30–40 km s^{-1} provided better fits than models with only rotationally broadened profiles.

HD 48099: this star is a binary and has been studied by Mahy et al. (2010). We have not re-analyzed the two components and we have simply adopted the parameters derived by Mahy et al. However, we add a few words of caution. The spectra used in the disentangling process of this binary system sample the full orbital cycle and hence do not suffer from the same limitations as in the case of HD46149. But whilst we expect narrow spectral features to be reliably reconstructed in the disentangled spectra of both the primary and secondary star, the reconstruction of the broad features is more uncertain. Indeed, given the rather low orbital inclination of HD48099 (Mahy et al. 2010), the maximum radial velocity excursions of the stars remain small ($RV_P^{max} - RV_S^{max} \sim 155$ km s^{-1} – RV_P^{max} and RV_S^{max} being the maximum radial velocities of the primary and secondary components) compared to the possible widths of broad Balmer lines (±950km s^{-1} for Hγ). This poor sampling of the broadest lines can lead to a poor reconstruction of the wings of the Balmer lines especially for the fainter secondary component. Hence, the gravity of the latter is very likely underestimated. There is unfortunately no way to remedy to this situation and as a result, the spectroscopic masses for this system are unreliable as becomes clear for instance when comparing the spectroscopic mass ratio from Table 4 ($M_1/M_2 \sim 30$) with the dynamical mass ratio ($M_1/M_2 = 1.77$) from the orbital solution of Mahy et al. (2010). In view of this discussion, we chose to adopt the same error bars on $T_{\rm eff}$ and $\log g$ as for HD 46149 (i.e. 2000 K on $T_{\rm eff}$ – 3000 K for the secondary– and 0.2 dex on $\log g$). The error bars are thus larger than in Mahy et al. (2010). They are also realistic, since reducing $\log g$ by 0.25 dex, we find that we need an effective temperature lower by 1000-2000 K to correctly reproduce the He and He lines of the primary.

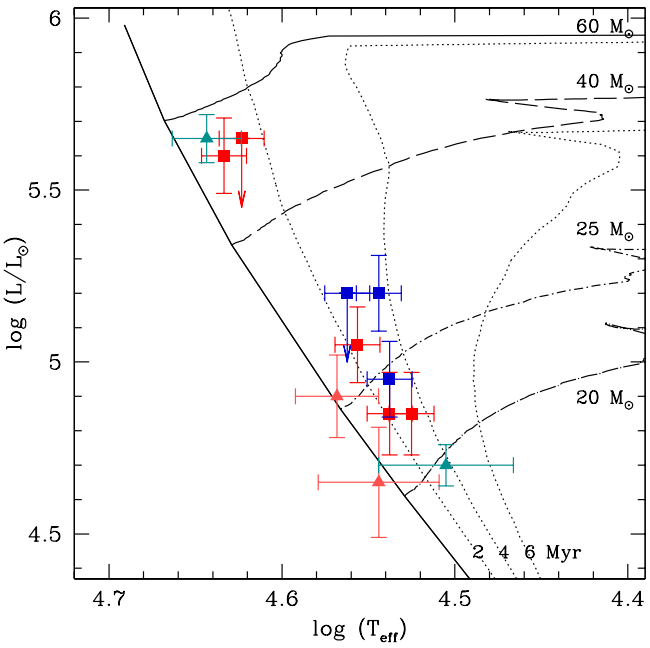

Fig. 3. HR diagram of NGC2244. The evolutionary tracks and isochrones are from Meynet & Maeder (2003). They are computed for an initial rotational velocity of 300 km s^{-1}. Triangles are the components of the binaries HD48099 (cyan) and HD46149 (pink). Stars belonging to NGC2244 are shown in red/pink and stars from the Mon OB2 association are shown in blue/cyan. Arrows indicate upper limits on luminosities for SB1 and binary candidates.

5. Discussion

5.1. HR diagram and evolutionary status

The HR diagram of the stars analyzed in the present study is shown in Fig. 3. Red/pink (blue/cyan) colors are used for the stars of NGC2244 (Mon OB2 respectively).

The stars of NGC 2244 have an age less than 5 Myr. The most massive stars of the cluster, namely HD 46223 and

HD 46150, are less than 2 Myr old. There is no significant age difference between these two stars, contrary to what Wang et al. (2008) suspected. Whether the trend for the most massive stars being younger than the lower mass O stars is real or an artifact of the parameter determination is unclear. It is known that the stellar parameters of an average early O star indicate a younger age than that of late–type O stars (e.g. Fig. 12 of Martins et al. 2005a). An explanation to this trend is that late-type O stars have lower ionizing fluxes and weaker winds than early–type O stars. Consequently, they remain hidden in their parental cloud for a longer time, so that on average late–type O stars appear older. In the present case, since both early and late–type stars are visible at the same time, one needs another explanation. A possibility is that the most massive stars were the last to form. Alternatively, there might be a bias in the determination of the effective temperature of the hottest O stars. It would have to be 2000-3000 K lower in order to lead to an age similar to the late–type O stars. Such a reduction is difficult to explain. Line–blanketing, when included in model atmospheres, leads to a downward revision of effective temperatures by several thousands K. But as shown by Martins et al. (2002), C, N, O, Si, S and Fe are the main contributors to opacities in O stars atmospheres. Since our present models include all these elements and additional ones, it is unlikely that we overestimate $T_{\rm eff}$ by 2000–3000 K. Since we are using clumped models for the hottest stars and homogeneous winds for the coolest ones, one might wonder whether this affects the temperature determination. However the photospheric lines used to constrain $T_{\rm eff}$ are unaffected by clumping since they form deep in the atmosphere where the wind is still homogeneous even in clumped models. Another speculative hypothesis is that the most massive O stars have, on average, larger rotation rates. If so, the use of the same set of evolutionary tracks (i.e., computed with the same initial rotational velocity) for early and late–type O stars is inappropriate. Indeed for faster rotation, the main–sequence lifetime is increased. Maeder & Meynet (2000) concluded that the use of non–rotating tracks could lead to an underestimate of the actual age of stars by about 25%. Brott et al. (2011a) show the effect of rotation on isochrones (see their Fig. 7) and confirm fast rotating massive stars stay closer to the zero-age main sequence compared to moderately rotating lower mass stars of the same age. This could partly explain the age difference we observe between early and late O stars. But this relies on the assumption that rotation is faster for larger masses among O stars. So far, there is no detailed study of the evolution of rotational velocities with spectral type among O stars. An average $V \sin i$ of 129±82 km s^{-1} results from the work of Penny (1996), consistent with the more recent result of Penny et al. (2004) – 131±93 km s^{-1}. Howarth et al. (1997) found a distribution of $V \sin i$ peaked at about 100 km s^{-1}. Concerning B stars, Abt et al. (2002) found values of 100–130 km s^{-1}for B0–B5V stars. It is thus not clear whether there is a trend of larger rotation rate between B and O stars (and consequently not clear whether such a trend continues within the O class).

The stars in the Mon OB2 association appear to have an age of about 1–5 Myr, with a preferred value between 2 and 4 Myr. The only exception is the primary of the binary system HD 48099. As already discussed by Mahy et al. (2010), several factors can explain the apparent younger age of this star: rapid rotation, mass and angular momentum transfer, inappropriate evolutionary tracks. Rapid rotation was the favored explanation. The present study confirms that the secondary star has an age similar to the other stars of the association, making the primary peculiar. It is thus very likely that the position of the primary in the HR diagram is due to a rapid rotation and that comparison with normal (i.e. moderate rotation) evolutionary tracks is not appropriate.

5.2. Wind properties

In Table 5, we gather the mass loss rates derived from our quantitative analysis ($\dot{M}_{\rm UV}$ and $\dot{M}_{\rm H\alpha}$) as well as the theoretical mass loss rates of Vink et al. (2001) and the values L/c^2. The latter corresponds to the mass loss rates obtained if the driving is due to a single line located at the emission peak of the SED. They are thus a lower limit to the mass loss rate expected by the radiation-driven wind theory. From Table 5 we can draw the following conclusions:

1. All stars have $\dot{M}_{\rm UV} < \dot{M}_{\rm H\alpha}$. The difference is between a factor of 10 and a factor of a few 100!
2. The theoretical mass loss rates of Vink et al. (2001) are systematically larger than the UV mass loss rates. The discrepancy reaches 2 orders of magnitudes in the latest type O stars, as usually seen (Martins et al. 2005b; Marcolino et al. 2009). The Hα mass loss rates are usually in rather good agreement with the theoretical predictions (when comparisons are made for unclumped $\dot{M}$ for the early O dwarfs).
3. For all late type O dwarfs, the UV mass loss rates are *lower* than the single line driving limit. This is a serious puzzle. If the UV mass loss rates are the correct ones, this implies that line driving is less efficient than thought. It could mean that the line absorbs only at discrete values of velocities in the range 0–v_∞ (i.e., that absorbing material is present only at specific velocities, see below). For the earliest O dwarfs, the UV mass loss rates are only a factor 3–4 larger than this limit.

The results of Table 5 raise the question of the validity of our mass loss rate determinations. We list a few reasons why they could be biased:

– The mass-loss rates are based on a few features, and sometimes based on only a single line (although the absence of other wind features provides upper limits).
– The inferred mass-loss requires that the wind ionization structure derived by CMFGEN is accurate. Since CMFGEN provides a good fit to the photospheric spectrum, there is no a priori reason that CMFGEN should get the ionization structure dramatically wrong. Studies of H regions generally find that the far UV spectrum predicted by CMFGEN is globally consistent with that required to ionize the nebulae (Morisset et al. 2004; Simón-Díaz & Stasińska 2008).
– CMFGEN does not compute the wind properties from first principles (see Sect. 3). The mass loss rate and velocity law are adopted as input to compute the atmosphere structure and the emerging spectra. However, the results can be used to check the consistency between the adopted mass-loss rate/velocity law and the momentum absorbed by the wind (the knowledge of the atmospheric structure allows the computation of the radiative forces).
– Recent developments in the understanding of the clumping properties of O stars have shown that porosity (and its effect on the velocity structure, called vorosity) could alter the shape of key diagnostic lines (e.g. Sundqvist et al. 2010). Neglecting this effect could thus bias our determination.

In the following we investigate in more detail the last two points. To check the hydrodynamics of our models, we have

Table 5. Summary of various mass loss rates for our sample stars.

Star	ST	$\log(\dot{M}_{\rm UV})$	$\log(\frac{L}{c^2})$	$\log(\dot{M}_{\rm H\alpha})$	$\log(\dot{M}_{Vink})$
HD 46223	O4V((f))	−7.17	−7.57	−6.20	−5.75
HD 46150	O5V((f))z	−7.30	−7.52	−6.40	−5.68
HD 46485	O7Vn	−7.80	−8.12	−6.45	−6.50
HD 46056	O8Vn	−8.50	−8.32	–	−6.80
HD 46149-1	O8V	< −9.0	−8.27	–	−6.74
HD 46202	O9.5V	−9.00	−8.32	−7.10	−6.72
HD 46573	O7V((f))z	–-	−7.97	−6.30	−6.25
HD 48279	ON8.5V	−8.80	−8.22	−6.80	−6.64
HD 46966	O8.5IV	−8.00	−7.97	−6.40	−6.45
HD 48099-1	O5.5V((f))	−7.60	−7.52	–	−5.66

Notes. The columns give: name; spectral type; derived UV mass loss rate; mass loss rate expected for driving by a single line located at the SED emission peak in the single scattering condition; Hα mass loss rate; theoretical mass loss rates of Vink et al. (2001). The filling factor f_∞ (see Sect. 3) is 0.1 for HD 46223 and HD 46150, 0.01 for HD 48099–1, and 1.0 (i.e. no clumping included) for all other stars.

run several tests on HD 46202 which is typical of the late type O stars with only weak evidence for winds in C 1548–1550 (and perhaps N 1240). We derive a UV mass-loss rate of 1.0 $\times 10^{-9}$ $M_\odot$ yr^{-1}. This is a factor of 5 lower than the single-line limit (4.8 $\times 10^{-9}$ $M_\odot$ yr^{-1}), and a factor of 190 lower than that derived using Vink's prescription for estimating the mass-loss rate (which gives $\dot{M}$=1.9 $\times 10^{-7}$ $M_\odot$ yr^{-1}), and is primarily based on the strength of the absorption associated with the C 1548–1550 doublet. As noted previously, the single line limit is larger than the derived UV mass loss rate. To check the hydrodynamics, we ran additional models with as many elements/lines as allowed by our computational resources (the models include H, He, C, N, O, Ne, Mg, Si, S, Ar, Ca, Fe, Ni and a total of about 10 000 atomic levels) to be able to calculate the radiative force as accurately as possible.

The momentum equation can be written as:

$$V\frac{dV}{dr} = \frac{-1}{\rho}\frac{dP}{dr} - g + g_r \quad (1)$$

where

$$g = GM/r^2 \quad (2)$$

and, g_r, the radiative acceleration, is given by

$$g_r = \frac{4\pi}{c}\rho \int \chi_\nu H_\nu d\nu \,. \quad (3)$$

Once g_r is computed, we can thus check whether Eq. 1 is satisfied or not.

When clumping is important we utilize the same equation, however this is only an approximation. First we note that the presence of clumps implies a dynamic flow, but the above equation is for a steady flow. Second, it is unclear how to handle the pressure term when clumping is important – in practice this is not crucial for O stars since we assume the clumping to be initiated close to, or above the sonic point where the gas pressure term can be neglected. The expression for g_r, ρ and χ_ν are evaluated in the clumps.

In our best fit model to the UV lines, the radiation field exceeds that required to drive the wind everywhere – at most locations by over an order of magnitude. This result is not unexpected, since our derived mass-loss rate is lower than the single-line limit. As a check of the consistency of the calculations we computed a model using a mass loss rate of 4.0 $\times 10^{-8}$ $M_\odot$ yr^{-1}– this is a factor five below Vink's estimate, but a factor of 40 above what we derived. As shown in Fig. 4 (right panel), the predicted UV spectrum shows some crucial disagreements with observation. Particularly noteworthy is the presence of a saturated C profile, and two high-velocity wind features due to Si . In the observed spectrum, Si shows only photospheric components[2]. The high mass loss rate model shown has no X-rays — when we include X-rays N 1240, unlike the observations, shows a strong P Cygni profile. The weakness of the N profile relative to C is consistent with the late spectral class of HD 46202, and argues against a shift of the wind to high ionization stages.

For a mass-loss rate of 4 $\times 10^{-8}$ $M_\odot$ yr^{-1}, the wind momentum deposited is close to that needed to drive the wind for velocities in excess of 700 km s^{-1}, and for a standard β = 1 velocity law. Below 700 km s^{-1} there is insufficient line force, sometimes by a large factor, to drive the flow. This is an important issue — for a steady flow the momentum balance must be satisfied at all depths, not just globally. Clearly we have an inconsistency. Either the derived UV mass-loss rate is wrong or there is an additional retarding force that needs to be included in the momentum balance equation.

For early type O dwarfs, mass loss rates are larger and closer to the theoretical predictions. However, problems still occur. We take HD 46150 as an illustrative case. For that star, we derive a mass-loss of 5.0×10^{-8} $M_\odot$ yr^{-1} from UV diagnostics. This gives a C profile in reasonable agreement with observation, but the N doublet is overestimated. Surprisingly both the C and N profile do not reach zero intensity (C has a residual intensity of 15% while the residual intensity for N is 35%).

On the other hand, the mass-loss derived from Hα (assuming f=0.1, V_{cl}=100 km/s) is nearly an order of magnitude larger – 4.0×10^{-7} $M_\odot$ yr^{-1}. This mass–loss rate also provides a better fit to the cores of Hβ and Hδ. The optically derived mass-loss is inconsistent with the O 1339,1343 and O 1371 lines – the theoretical spectra show noticeable perturbations by the wind whereas the observed profiles are photospheric only (see Fig. 4). The fit to C is somewhat worse although definitive statements are impossible since C shows a strong P Cygni profile that is insensitive to $\dot{M}$.

Clumping, and more precisely porosity, might be a way to partly solve the issues mentioned above. Porosity comes in two flavors — spatial and velocity. Spatial porosity has been invoked to help explain the observed X-ray profiles, which tend to show

[2] If we adopted a lower $T_{\rm eff}$ for HD 46202, the disagreement with Si would be even more striking

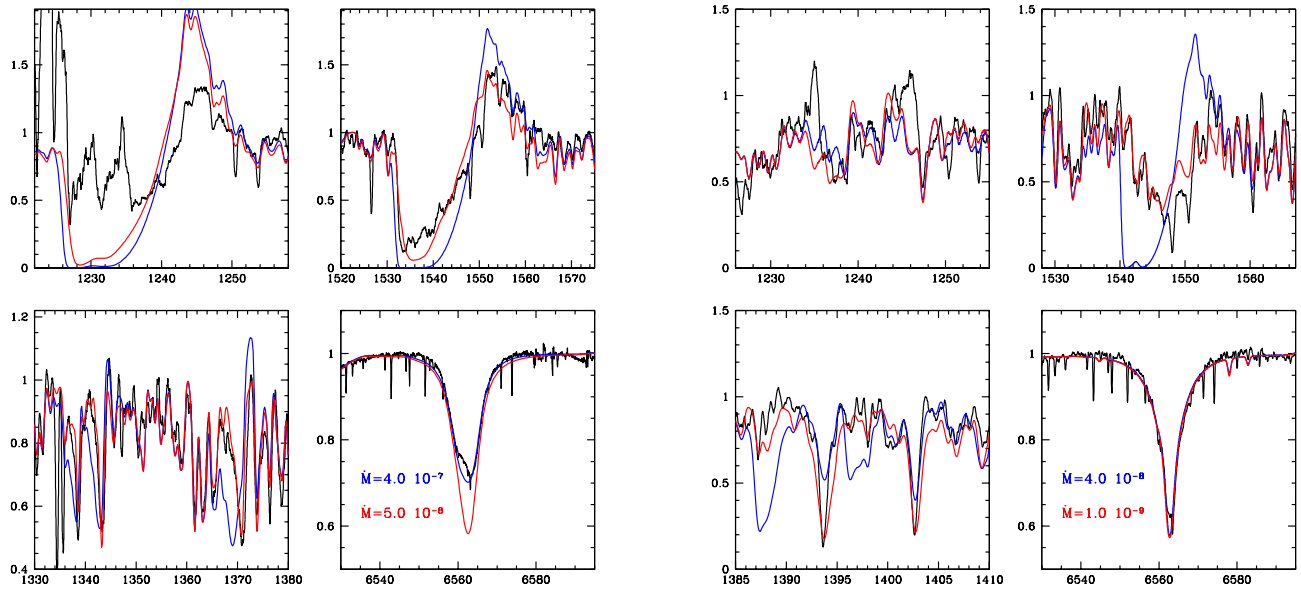

(a) HD 46150 (b) HD 46202

Fig. 4. Comparison between the best fit models of the UV spectrum (red lines) and models with higher mass loss rates (blue lines). The solid lines are the observed spectra. The left panel shows the comparison for HD 46150, the right panel for HD 46202. The narrow absorption features in the C 1548–1550 profiles are of interstellar nature.

much more symmetric profiles than expected on the basis of Hα derived mass-loss rates (Oskinova et al. 2007). An alternative explanation is that Hα mass-loss rates are too high — by a factor of a few (Cohen et al. 2010). The need for spatial porosity, and its importance, is controversial. Cohen et al. (2010) argue that the the X-ray profiles in ζ Pup are much better explained by a simple reduction in mass-loss. In addition, Owocki & Cohen (2006) have argued that the wind clumping structure is inconsistent with that required to give rise to a significant porosity effect.

Vorosity (i.e. porosity in velocity space) can arise in a clumped medium because the clump velocities are discrete – along a given sight line not all velocities may be present. Since continuum transfer is unaffected by the presence of velocity fields, vorosity, unlike spatial porosity, only affects line profiles.[3] As shown by Prinja & Massa (2010), vorosity could explain that the ratio of optical depth in the two components of Si 1393,1403 in B supergiants is not equal to the ratio of oscillator strengths, as expected in the case of homogeneous flows.

Recent simulations by Sundqvist et al. (2010, 2011) have highlighted the importance of vorosity (among others) on the formation of strong UV lines. They show that accounting for vorosity, UV line profiles can be strongly reduced for a given mass loss rate. At the same time, Hα is less affected. This tends to bring the optical and UV mass loss rates into better agreement when fitting oberved spectra. But these results also indicate that if vorosity is important, it implies that the winds are clumped. Consequently the Hα mass loss rates derived using homogeneous models (such as most values in Table 5) are upper limits. These computations are still exploratory (there is no detailed radiative transfer nor feedback on the atmosphere structure) but they appear to be a way to solve the issues presented above.

[3] For the X-ray lines vorosity is not important – it is the continuum opacity which primarily affects the shape of these lines.

Aside from this, the effect of porosity and vorosity on theoretical mass-loss rates is unclear. If it begins beyond the critical point we would expect a reduction in the line force, and hence a reduction in the terminal velocity of the wind, with no change in the mass-loss rate. The reduction in line force occurs because thick lines would absorb less continuum flux, due to the presence of absorbing material only at specific velocities and not all over the entire 0–v_∞ velocity range. The radiation force from thin lines would not alter since only the column density, not the velocity field, is important. Of course the definition of which lines are thin and which are optically thick may be affected by the wind structure. If vorosity is important below the critical point we might expect a reduction in the mass-loss rate.

Clearly, the structure, properties and dynamics of O star winds is complex and requires improvements in both spectroscopic analysis and theoretical predictions. But vorosity appears as a valid way of solving (at least partly) some of the issues raised above.

Whatever the exact nature of these winds, some qualitative features can be obtained directly from the observations. This is what we show in Fig. 5. Most of the results presented above rely directly or indirectly on atmosphere models. In Fig. 5 we show a direct comparison between the observed spectra of two stars: HD46966 and HD48279. According to Table 4, they have very similar $T_{\rm eff}$ and gravities. This is mirrored in Fig. 5 by the perfect match of the He and He features and the wings of Balmer lines. However, N 1240 and C 1548–1550 show a smaller blueward extent in HD48279 indicating a lower terminal velocity. In addition, C 1548–1550 is clearly weaker in HD48279 while the N 1240 profile are of similar strength (slightly weaker in HD48279 though). The Hα profiles are barely differenciated. From the C optical features, we tentatively estimate the carbon abundance (C/H) of HD48279 (respectively HD 46966) to be 1.0×10^{-4} (resp. 2.0×10^{-4}).

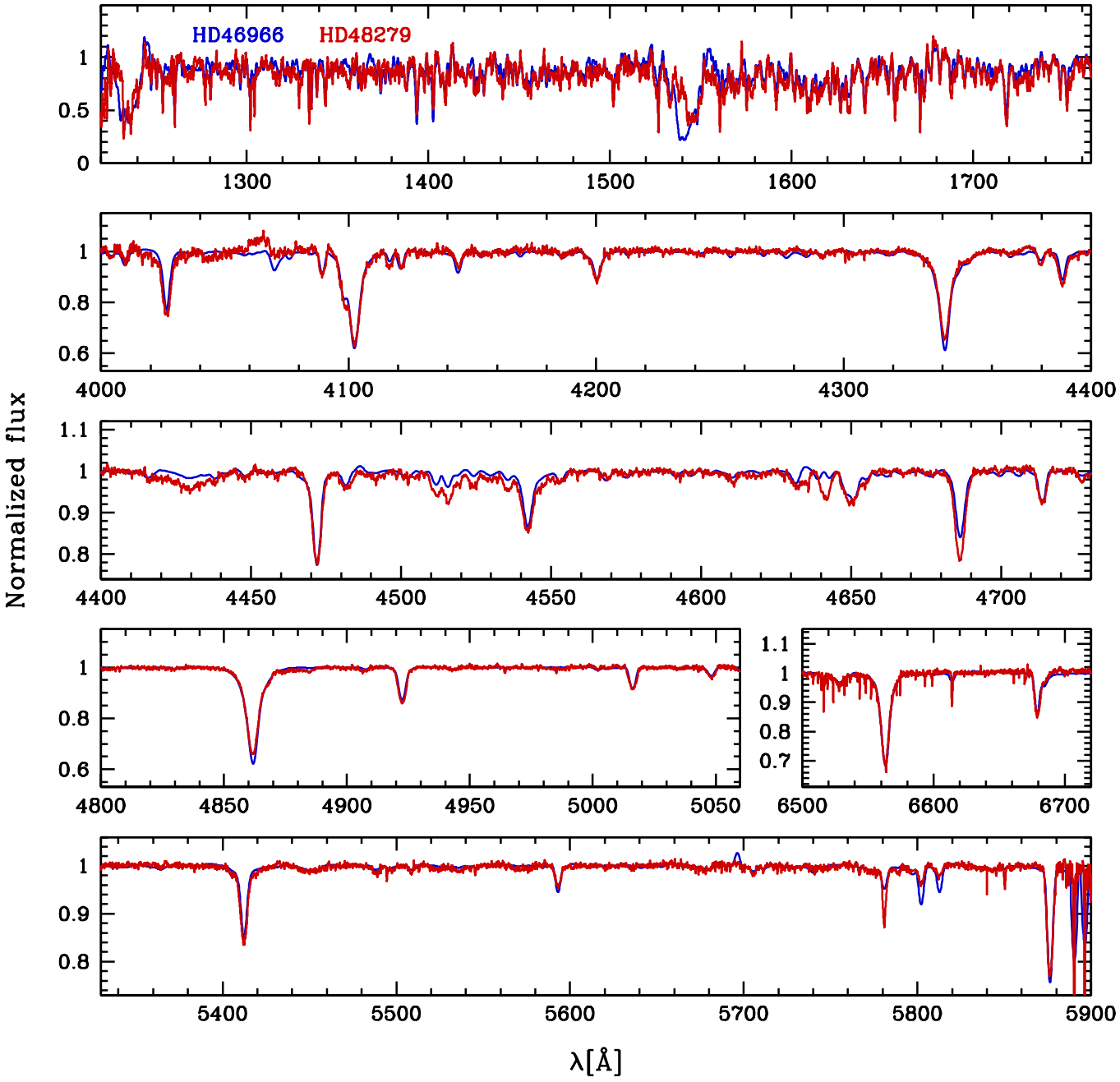

Fig. 5. Comparison between the observed spectra of HD46966 (blue) and HD48279 (red). The spectra of HD46966 have been convolved to the same rotational velocity as HD48279. The similar effective temperature and gravity in both stars is obvious from the He , He and Balmer lines. On the contrary, HD46966 presents a stronger C 1548–1550 line (but a similar Hα profile) and a lower N/C ratio as clearly seen from the C 4070, C 4634–4640, C 5696, C 5801–5812 and N 4500–4520 lines.

Consequently, HD 48279 exhibits a larger N/C ratio compared to HD46966. If the mass loss rate were the same in both stars, one would expect a weaker C 1548–1550 line but also a much stronger N 1240 line (the profile is not saturated) since the nitrogen overabundance in HD48279 is much larger than its carbon depletion (see Table 4 and above). This is not what we see. We thus conclude that the wind of HD48279 is weaker than that of HD46966. The value of the mass loss rate is low enough that the Hα profiles are photospheric in both stars, and thus similar since $T_{\rm eff}$ and $\log g$ are the same. HD46966 has a luminosity $L = 10^{5.20} L_{\odot}$ while for HD48279, $L = 10^{4.95} L_{\odot}$. It is thus natural to have a weaker wind in HD48279. This is what both the UV diagnostics and Hα indicate. We note however the difference in mass loss rate between the two stars is 0.8 dex if the former are used, while it is only 0.4 dex in the case of Hα. This raises once again the question of the origin of the differences between the UV and optical wind sensitive lines. Whatever the reason, we see that two stars with very similar effective temperature and

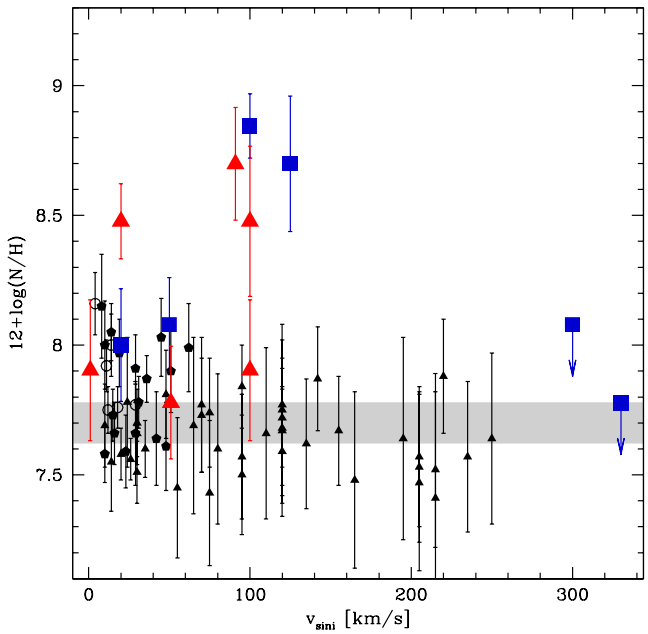

Fig. 6. Nitrogen surface abundance (in units of 12+log(N/H)) as a function of projected rotational velocity. Single O stars are the blue squares and binaries the red triangles. The small black triangles (pentagons, open circles) are the Galactic B stars of Hunter et al. (2009) (Morel et al. 2008; Przybilla et al. 2010) with $\log g$ larger than 3.5 (i.e. comparable to our sample). The grey area corresponds to the range of solar values from studies of the Sun, B stars and HII regions (see Table 3 of Hunter et al. 2009).

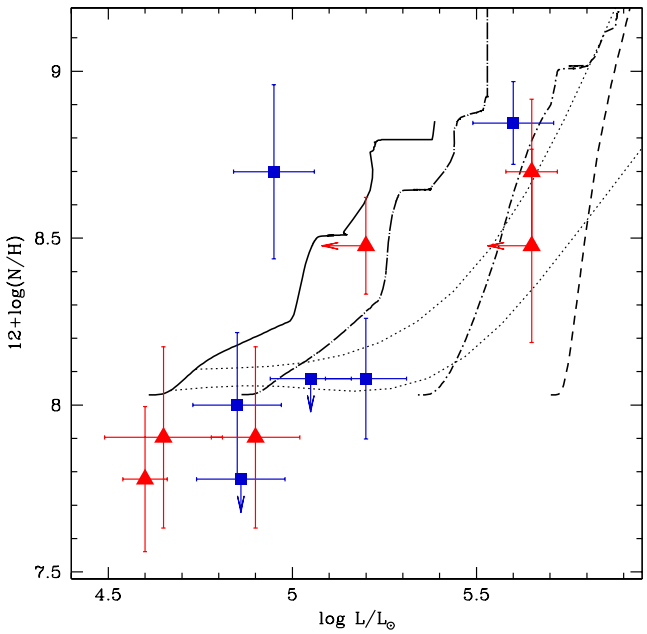

Fig. 7. Nitrogen surface abundance (in units of 12+log(N/H)) as a function of luminosity. Single O stars are the blue squares and binaries the red triangles. Evolutionary tracks – shown by the solid, dot-long dashed, dot-dashed, dashed lines for M=15, 20, 25 and 40 $M_{\odot}$ – are from Meynet & Maeder (2003). The dotted lines are isochrones for 2 and 4 Myr.

gravity can have different wind properties with only a difference in luminosity by less than a factor of two.

5.3. Chemical evolution and rotation

Rotation is known to affect the angular momentum and chemical elements transport through mixing processes (meridional circulation and shear turbulence, see Maeder & Meynet 2000). The first analysis of surface CNO abundances of O stars and B supergiants tends to confirm qualitatively the theoretical predictions: more evolved stars have a higher N content as a result of CNO processing and mixing (Hillier et al. 2003; Heap et al. 2006; Crowther et al. 2006). However, the role of rotation in explaining the chemical patterns of B stars in the Magellanic Clouds has been questioned by the results of the first ESO/VLT Large Programme dedicated to massive stars (Evans et al. 2005, 2006). Hunter et al. (2008) showed that 60% of their sample of B main–sequence stars in the Large Magellanic Cloud displayed nitrogen surface abundances expected by evolutionary models including rotational mixing, but the remaining 40% escaped such an agreement. These outliers are divided in two groups with approximately the same number of members: one with highly enriched but slowly rotating stars; the other with barely enriched fast rotators. The former group was also identified in the SMC (Hunter et al. 2009). In the Galaxy, the results of Hunter et al. (2009) point to a lack of surface nitrogen enrichment in all main–sequence objects, probably due to the relatively unevolved status of most stars. In contrast, Morel et al. (2006, 2008) reported the detection of N-rich non-supergiant Galactic B stars with low rotation rates, lending support to the idea that rotational mixing cannot explain the surface abundances of a significant number of massive stars also in the Galaxy.

However, Maeder et al. (2009) argued that surface chemical enrichment is a multivariate function and does not depend only on projected rotational velocity. The higher the mass of a star, the larger the nitrogen enrichment. Similarly, lower metallicity stars have larger surface enrichment at a given evolutionary state. In addition, more evolved stars show larger N/H ratios. Hence, a combination of ages, masses, metallicities and rotational velocities can lead to various surface enrichments. It is important to disentangle the different effects to draw reliable conclusions. According to Maeder et al. (2009), if this is done, rotational mixing explains most of the observed abundance patterns. 20% of the sample of Hunter et al. (2008) might escape this scenario due to binary evolution. Brott et al. (2011b) built population synthesis models to take all these effects into account. They investigated the properties of a population of 7–60 $M_{\odot}$ stars (with a Salpeter IMF) formed continuously for the last 30 Myr and with rotational velocities drawn from the distribution of Hunter et al. (2008). They confirm that about 35% of the stars observed by Hunter et al. (2008) cannot be explained by single star evolutionary models with rotation. But the remaing – and majority – of the population is well accounted for by rotating evolutionary models. Przybilla et al. (2010) also confirm the role of rotational mixing by showing a tight correlation between N/C and N/O in main sequence and supergiants stars. However, the theoretical enrichments are too large compared to observations.

Most of the results summarized above have been obtained from the analysis of surface abundances of B main–sequence stars. In this paper, we present results for main–sequence O stars. Our sample is smaller than those of Morel et al. (2008) or Hunter et al. (2008) but it allows to identify some trends, and extend their work to the most massive stars. Fig. 6 shows the nitrogen

surface abundance as a function of rotational velocity. The results of Morel et al. (2008), Hunter et al. (2008) and Przybilla et al. (2010) have been added for comparison (small symbols). The following comments can be made:

- up to about 120 km s^{-1} a possible trend of larger N/H with larger V sin$i$ is emerging among O stars, although a significant scatter exists and more stars are definitely needed to draw firm conclusions. We note that our sample is relatively homogeneous in age and metallicity. On the other hand it covers a relatively wide mass range (15–60 $M_{\odot}$). Both binaries and single stars seem to follow this trend.
- the components of the binaries studied in this paper have surface N/H values consistent with those of single stars. This conclusion applies only to the binaries studied here and should not be generalized.
- the two fastest rotators show very little enrichment if any.
- on the main–sequence, in the Galaxy, O stars show on average larger values of N/H than B stars.

These results confirm some of the expectations of stellar evolution with rotation. First, more massive stars display larger surface nitrogen enrichment. This is even more clearly illustrated on Fig. 7 where the ratio N/H is shown as a function of luminosity. A clear trend of higher N content for more luminous stars is observed. At a given age, this is what evolutionary models predict. The dotted lines show isochrones for 2 and 4 Myr, typical of the age of our sample stars. They indicate faster evolution and consequently faster chemical enrichment for more luminous and thus more massive stars. Interestingly, the two fast rotators do not appear as outliers in this plot, but fall perfectly in the sequence followed by most of the stars. This means that given their mass, these objects are too young to have experienced a strong enrichment in spite of their large rotational velocity. This confirms the conclusion of Maeder et al. (2009) that it is important to disentangle the various effects at work in the surface enrichment of massive stars to pin down the true role of rotation.

Our sample includes binaries. In Fig. 6 and 7 they do not show any peculiar property in terms of chemical enrichment compared to single O stars. This does not mean that binarity has no effect on the history of surface enrichment, but that it depends on the binary properties. In particular, not all binaries have experienced mass transfer which would affect both the rotational speed and surface composition (Linder et al. 2008; de Mink et al. 2009). With the exception of HD 48099, all the binaries of our sample have orbital periods larger than 3 days. According to de Mink et al. (2011), it takes more than 8 Myr for Roche–lobe overflow to occur in such systems. This result is valid for binaries of about 20 $M_{\odot}$ and obviously depends on masses and mass ratios. The binaries of our sample are thus most likely too young and/or too separated to have experienced significant mass transfer. This conclusion only applies to the systems included in our sample and should not be generalized to all binary stars. Once mass transfer has occured, it is likely that additional mixing processes take place and affect the surface composition. Further analysis of such interacting systems should shed more light on the exact role of binarity on the chemical appearance of O stars.

In Fig. 7, the only clear outlier is star HD48279 with a very strong enrichment in spite of a moderate luminosity. To a lesser extent, HD46573 can also be considered rather enriched compared to the expectations of single star evolutionary models due to the upper limit on its luminosity. For HD48279 it does not seem possible that rotation only can explain the large N content. According to Fig. 1 of Maeder et al. (2009), an increase of the rotational velocity from 150 km s^{-1} to 300 km s^{-1} leads to an extra enrichment of the order 0.5 dex. HD48279 is 0.7 dex more N rich than the other stars of the same luminosity in Fig. 7. Binarity is excluded for that object (Mahy et al. 2009). The only possible explanation to the strong N enrichment is that HD48279 was member of a binary system in the past and experienced mass transfer and/or tidal interaction. Either the binary has been disrupted (by supernova kick for instance) or the companion is a low–mass compact object rendering any radial velocity variation undetectable (see de Mink et al. 2011). In the case of HD46573, a large initial velocity or binarity can explain the possible slightly larger N/H ratio compared to stars of the same luminosity range (HD46573 has been classified as SB1 by Mahy et al. 2009). Finally, HD46150 also only has an upper limit on its luminosity. But even accounting for an extreme reduction by 0.3 dex, the N/H content would still be consistent with single star evolutionary tracks.

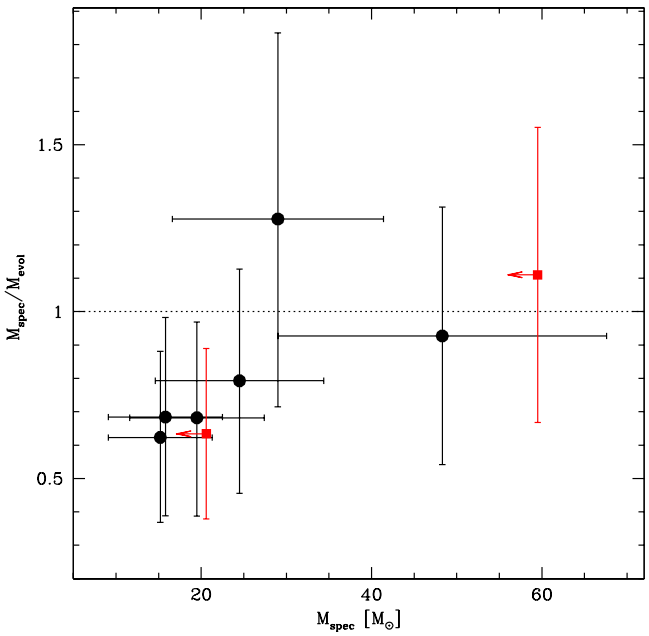

Fig. 8. Ratio of spectroscopic to evolutionary masses versus spectroscopic masses for the sample stars. The dotted line is the one to one relation. Black circles are single stars, red squares are members of binary systems. The insert shows the position of the primary component of HD48099.

5.4. Stellar masses

The determination of stellar masses is a long–standing problem. The so-called "mass discrepancy" (Groenewegen et al. 1989; Herrero et al. 1992) refers to the systematic overestimate of evolutionary masses compared to spectroscopic masses. The former are masses derived from the HR diagram and evolutionary tracks. The latter are the masses resulting from the knowledge of the gravity and radius obtained from spectroscopic analysis with atmosphere models. The revision of the effective temperature scale of O stars (Martins et al. 2002) has lead to improvements (see Gies 2003). However, differences of up to a factor of three still exist in some cases. Massey et al. (2005) and Mokiem et al. (2007) reported a mass discrepancy for LMC stars. The latter indicate that part of the discrepancy could be caused by fast rotation in He-rich stars. Fast rotating stars tend to evolve towards

larger luminosities for the same initial mass as non rotating stars. Consequently, using non rotating tracks to analyze them leads to overestimates of their evolutionary masses. However, even non enriched objects (hence not likely to rotate rapidly) show the mass discrepancy.

In Fig. 8 we show the ratio between spectroscopic (M_{spec}) and evolutionary (M_{ev}) masses for our sample of Galactic stars. Black circles are single stars and red squares the components of binary systems. The spectroscopic masses have been computed from the effective gravity (that we determine through line fitting) corrected from the effect of centrifugal forces. However, because of the high uncertainty on the gravity of the SB2 systems, we do not include the components of HD 46149 and HD48099 in this discussion. In spite of the small number of object, the trend for a mass discrepancy at low masses ($M < 25\ M_{\odot}$) is present. At higher masses, a good agreement is observed, but the error bars are large. These results are qualitatively consistent with those of Repolust et al. (2004) who showed that stars with masses lower than about 50 $M_{\odot}$ seemed to follow a relation parallel to the 1:1 relation in the M_{ev} versus M_{spec} diagram.

Recently, Weidner & Vink (2010) conducted a study of a sample of Galactic O stars and concluded that the mass discrepancy was solved. In their analysis, they mainly focused on binary components. They established the evolutionary masses of their stars by using a spectral type - mass relation. They used the $T_{\rm eff}$–scale of Martins et al. (2005a) to determine an effective temperature and luminosity for each star and subsequently used the evolutionary tracks of Meynet & Maeder (2003) to assign an evolutionary mass. They then compared these estimates to dynamical masses resulting from fits to velocity and light curves of binary systems. They found a good agreement between both types of masses (see their Fig. 3). However, the comparison with spectroscopic masses (not shown directly by Weidner & Vink but available from their Table 3) still reveals that evolutionary masses are larger. Hence, it seems that at least part of the origin of the discrepancy is rooted in an underestimate of gravities.

6. Conclusion

We have analyzed ten OB stars (nine O stars and one B star) in the NGC2244 cluster and MonOB2 association, including two bona-fide binaries and one candidate. Optical and UV spectroscopy have been obtained. Atmosphere models computed with the code CMFGEN have been used to derive the main stellar and wind parameters of the target stars. The main results are the following:

- all stars have an age between 1 and 5 Myr, with a trend of lower age for the most massive stars. Whether this is a real effect or an artifact of the method used to derive the stellar parameters is not clear at present.
- we confirm the existence of weak winds in the latest type stars of our sample. For those stars, UV mass loss rates are lower than the single line driving limit. UV mass loss rates are systematically lower than Hα mass loss rates. Vorosity might be a solution to these issues, although its effects on dynamics are still unclear.
- nitrogen surface abundances in O stars indicate a larger range of enrichment compared to B stars. A clear trend of larger enrichment in higher mass stars is observed, consistent with the prediction of evolutionary models for a population of stars of the same age. There is no clear difference between single and binary stars in our sample, most likely because the latter have not (yet) experienced mass transfer or too severe tidal effects. Fast rotating non enriched O stars are understood as too young to have had time to bring enough fresh nitrogen to their surface.
- the so–called "mass discrepancy" still exists for the latest type O dwarfs. Above 25 $M_{\odot}$, evolutionary and spectroscopic masses are in agreement, within the uncertainties. Part of the discrepancy seems related to underestimates of the spectroscopic masses.

We need to analyze more stars of the same age to confirm the trends observed, especially concerning the surface nitrogen enrichment. Winds of massive stars are complex, and a better understanding of clumping, both observationally and theoretically, is necessary to quantify their properties.

Acknowledgements. We thank the referee, Artemio Hererro, for useful comments. LM and GR are supported by the FNRS (Belgium), by a PRODEX XMM/Integral contract (Belspo) and by the Communauté Française de BelgiqueAction de recherche concertée (ARC)Académie WallonieEurope. LM and GR acknowledge the Ministère de lEnseignement Supérieur et de la Recherche de la Communauté Française for supporting their travels to O.H.P. DJH acknowledges support from STScI theory grant HST-AR-11756.01.A. We also thank the staff of Observatoire de Haute-Provence and of La Silla ESO Observatory for their technical support.

References

Abt, H. A., Levato, H., & Grosso, M. 2002, ApJ, 573, 359
Aerts, C., Puls, J., Godart, M., & Dupret, M. 2009, A&A, 508, 409
Barlow, M. J. & Cohen, M. 1977, ApJ, 213, 737
Bouret, J.-C., Lanz, T., & Hillier, D. J. 2005, A&A, 438, 301
Brott, I., de Mink, S. E., Cantiello, M., et al. 2011a, A&A, 530, A115
Brott, I., Evans, C. J., Hunter, I., et al. 2011b, A&A, 530, A116
Chiosi, C. & Maeder, A. 1986, ARA&A, 24, 329
Cohen, D. H., Leutenegger, M. A., Wollman, E. E., et al. 2010, MNRAS, 405, 2391
Conti, P. S. & Alschuler, W. R. 1971, ApJ, 170, 325
Crowther, P. A., Lennon, D. J., & Walborn, N. R. 2006, A&A, 446, 279
de Mink, S. E., Cantiello, M., Langer, N., et al. 2009, A&A, 497, 243
de Mink, S. E., Langer, N., & Izzard, R. G. 2011, Bulletin de la Societe Royale des Sciences de Liege, 80, 543
di Francesco, J., Sadavoy, S., Motte, F., et al. 2010, A&A, 518, L91
Evans, C. J., Lennon, D. J., Smartt, S. J., & Trundle, C. 2006, A&A, 456, 623
Evans, C. J., Smartt, S. J., Lee, J., et al. 2005, A&A, 437, 467
Eversberg, T., Lepine, S., & Moffat, A. F. J. 1998, ApJ, 494, 799
Fraser, M., Dufton, P. L., Hunter, I., & Ryans, R. S. I. 2010, MNRAS, 404, 1306
Gies, D. R. 2003, in IAU Symposium, Vol. 212, A Massive Star Odyssey: From Main Sequence to Supernova, ed. K. van der Hucht, A. Herrero, & C. Esteban (University Press, Cambridge), 91
Grevesse, N., Asplund, M., & Sauval, A. J. 2007, Space Science Reviews, 130, 105
Groenewegen, M. A. T., Lamers, H. J. G. L. M., & Pauldrach, A. W. A. 1989, A&A, 221, 78
Heap, S. R., Lanz, T., & Hubeny, I. 2006, ApJ, 638, 409
Hensberge, H., Pavlovski, K., & Verschueren, W. 2000, A&A, 358, 553
Herrero, A., Kudritzki, R. P., Vilchez, J. M., et al. 1992, A&A, 261, 209
Hillier, D. J. 1991, A&A, 247, 455
Hillier, D. J., Lanz, T., Heap, S. R., et al. 2003, ApJ, 588, 1039
Hillier, D. J. & Miller, D. L. 1998, ApJ, 496, 407
Hillier, D. J. & Miller, D. L. 1999, ApJ, 519, 354
Howarth, I. D. 1983, MNRAS, 203, 301
Howarth, I. D., Siebert, K. W., Hussain, G. A. J., & Prinja, R. K. 1997, MNRAS, 284, 265
Howarth, I. D., Walborn, N. R., Lennon, D. J., et al. 2007, MNRAS, 381, 433
Hunter, I., Brott, I., Langer, N., et al. 2009, A&A, 496, 841
Hunter, I., Lennon, D. J., Dufton, P. L., et al. 2008, A&A, 479, 541
Lanz, T. & Hubeny, I. 2003, ApJS, 146, 417
Leitherer, C. & Robert, C. 1991, ApJ, 377, 629
Linder, N., Rauw, G., Martins, F., et al. 2008, A&A, 489, 713
MacGregor, K. B., Hartmann, L., & Raymond, J. C. 1979, ApJ, 231, 514
Maeder, A. & Meynet, G. 2000, ARA&A, 38, 143
Maeder, A., Meynet, G., Ekström, S., & Georgy, C. 2009, Communications in Asteroseismology, 158, 72
Mahy, L., Nazé, Y., Rauw, G., et al. 2009, A&A, 502, 937

Mahy, L., Rauw, G., Martins, F., et al. 2010, ApJ, 708, 1537
Maíz-Apellániz, J., Walborn, N. R., Galué, H. Á., & Wei, L. H. 2004, ApJS, 151, 103
Marcolino, W. L. F., Bouret, J., Martins, F., et al. 2009, A&A, 498, 837
Martins, F., Donati, J., Marcolino, W. L. F., et al. 2010, MNRAS, 407, 1423
Martins, F. & Plez, B. 2006, A&A, 457, 637
Martins, F., Schaerer, D., & Hillier, D. J. 2002, A&A, 382, 999
Martins, F., Schaerer, D., & Hillier, D. J. 2005a, A&A, 436, 1049
Martins, F., Schaerer, D., Hillier, D. J., & Heydari-Malayeri, M. 2004, A&A, 420, 1087
Martins, F., Schaerer, D., Hillier, D. J., et al. 2005b, A&A, 441, 735
Massey, P., Puls, J., Pauldrach, A. W. A., et al. 2005, ApJ, 627, 477
Meynet, G. & Maeder, A. 2003, A&A, 404, 975
Mokiem, M. R., de Koter, A., Evans, C. J., et al. 2007, A&A, 465, 1003
Morel, T., Butler, K., Aerts, C., Neiner, C., & Briquet, M. 2006, A&A, 457, 651
Morel, T., Hubrig, S., & Briquet, M. 2008, A&A, 481, 453
Morisset, C., Schaerer, D., Bouret, J., & Martins, F. 2004, A&A, 415, 577
Motte, F., Zavagno, A., Bontemps, S., et al. 2010, A&A, 518, L77
Najarro, F., Hillier, D. J., Puls, J., Lanz, T., & Martins, F. 2006, A&A, 456, 659
Nazé, Y. 2009, A&A, 506, 1055
Nieva, M. F. & Przybilla, N. 2007, A&A, 467, 295
Oskinova, L. M., Hamann, W.-R., & Feldmeier, A. 2007, A&A, 476, 1331
Owocki, S. P. & Cohen, D. H. 2006, ApJ, 648, 565
Owocki, S. P. & Rybicki, G. B. 1984, ApJ, 284, 337
Owocki, S. P. & Rybicki, G. B. 1985, ApJ, 299, 265
Penny, L. R. 1996, ApJ, 463, 737
Penny, L. R., Sprague, A. J., Seago, G., & Gies, D. R. 2004, ApJ, 617, 1316
Phelps, R. L. & Lada, E. A. 1997, ApJ, 477, 176
Prinja, R. K. & Massa, D. L. 2010, A&A, 521, L55
Przybilla, N., Firnstein, M., Nieva, M. F., Meynet, G., & Maeder, A. 2010, A&A, 517, A38
Puls, J., Kudritzki, R.-P., Herrero, A., et al. 1996, A&A, 305, 171
Puls, J., Markova, N., Scuderi, S., et al. 2006, A&A, 454, 625
Repolust, T., Puls, J., & Herrero, A. 2004, A&A, 415, 349
Runacres, M. C. & Owocki, S. P. 2002, A&A, 381, 1015
Ryans, R. S. I., Dufton, P. L., Rolleston, W. R. J., et al. 2002, MNRAS, 336, 577
Sana, H. 2009, A&A, 501, 291
Sana, H., Rauw, G., Nazé, Y., Gosset, E., & Vreux, J. 2006, MNRAS, 372, 661
Schneider, N., Motte, F., Bontemps, S., et al. 2010, A&A, 518, L83
Seaton, M. J. 1979, MNRAS, 187, 73P
Simón-Díaz, S. & Herrero, A. 2007, A&A, 468, 1063
Simón-Díaz, S. & Stasińska, G. 2008, MNRAS, 389, 1009
Simón-Díaz, S., Uytterhoeven, K., Herrero, A., Castro, N., & Puls, J. 2010, Astronomische Nachrichten, 331, 1069
Sota, A., Maíz Apellániz, J., Walborn, N. R., et al. 2011, ApJS, 193, 24
Sundqvist, J. O., Puls, J., & Feldmeier, A. 2010, A&A, 510, A11
Sundqvist, J. O., Puls, J., Feldmeier, A., & Owocki, S. P. 2011, A&A, 528, A64
Vink, J. S., de Koter, A., & Lamers, H. J. G. L. M. 2001, A&A, 369, 574
Wang, J., Townsley, L. K., Feigelson, E. D., et al. 2008, ApJ, 675, 464
Weidner, C. & Vink, J. S. 2010, A&A, 524, A98
Wright, A. E. & Barlow, M. J. 1975, MNRAS, 170, 41

Appendix A: Best fit to the observed spectra.

Figures A.1 to A.4 show the observed spectra in black together with the best fit CMFGEN models in red.

A&A 533, A4 (2011)
DOI: 10.1051/0004-6361/201116949

Astronomy & Astrophysics

Variability in the CoRoT photometry of three hot O-type stars

HD 46223, HD 46150, and HD 46966⋆,⋆⋆

R. Blomme[1], L. Mahy[2], C. Catala[3], J. Cuypers[1], E. Gosset[2,⋆⋆⋆], M. Godart[2], J. Montalban[2], P. Ventura[4], G. Rauw[2], T. Morel[2], P. Degroote[5], C. Aerts[5,6], A. Noels[2], E. Michel[3], F. Baudin[7], A. Baglin[3], M. Auvergne[3], and R. Samadi[3]

[1] Royal Observatory of Belgium, Ringlaan 3, 1180 Brussel, Belgium
e-mail: Ronny.Blomme@oma.be
[2] Institut d'Astrophysique et de Géophysique, University of Liège, Bât. B5C, Allée du 6 Août 17, 4000 Liège, Belgium
[3] LESIA, UMR 8109, Observatoire de Paris, 5 place Jules Janssen, 92195 Meudon Cedex, France
[4] INAF, Osservatorio Astronomico di Roma, via Frascati 33, 00040 Monteporzio Catone (Roma), Italy
[5] Instituut voor Sterrenkunde, K.U. Leuven, Celestijnenlaan 200D, 3001 Leuven, Belgium
[6] Department of Astrophysics, IMAPP, University of Nijmegen, PO Box 9010, 6500 GL Nijmegen, The Netherlands
[7] Institut d'Astrophysique Spatiale (IAS), Bâtiment 121, Université Paris-Sud, 91405 Orsay Cedex, France

Received 24 March 2011 / Accepted 29 June 2011

ABSTRACT

Context. The detection of pulsational frequencies in stellar photometry is required as input for asteroseismological modelling. The second short run (SRa02) of the CoRoT mission has provided photometric data of unprecedented quality and time-coverage for a number of O-type stars.
Aims. We analyse the CoRoT data corresponding to three hot O-type stars, describing the properties of their light curves and search for pulsational frequencies, which we then compare to theoretical model predictions.
Methods. We determine the amplitude spectrum of the data, using the Lomb-Scargle and a multifrequency HMM-like technique. Frequencies are extracted by prewhitening, and their significance is evaluated under the assumption that the light curve is dominated by red noise. We search for harmonics, linear combinations, and regular spacings among these frequencies. We use simulations with the same time sampling as the data as a powerful tool to judge the significance of our results. From the theoretical point of view, we use the MAD non-adiabatic pulsation code to determine the expected frequencies of excited modes.
Results. A substantial number of frequencies is listed, but none can be convincingly identified as being connected to pulsations. The amplitude spectrum is dominated by red noise. Theoretical modelling shows that all three O-type stars can have excited modes, but the relation between the theoretical frequencies and the observed spectrum is not obvious.
Conclusions. The dominant red noise component in the hot O-type stars studied here clearly points to a different origin than the pulsations seen in cooler O stars. The physical cause of this red noise is unclear, but we speculate on the possibility of sub-surface convection, granulation, or stellar wind inhomogeneities being responsible.

Key words. stars: variables: general – stars: early-type – stars: oscillations – stars: individual: HD 46223 – stars: individual: HD 46150 – stars: individual: HD 46966

1. Introduction

Even though the O-type stars are located in the Hertzsprung-Russell (HR) diagram inside a zone where pulsations are expected, no asteroseismological modelling of these stars could be performed prior to the CoRoT (Convection, Rotation and planetary Transits, Baglin et al. 2006; Auvergne et al. 2009) mission. Indeed, few examples of variability have been identified. The most obvious ones are the O9.5 V stars ζ Oph (Kambe et al. 1997) and HD 93521 (Howarth & Reid 1993; Rauw et al. 2008), whose variability is likely related to non-radial pulsations with periods of a few hours. However, the majority of these detections were made spectroscopically. The reason is that the amplitudes of the pulsations are too low to be measured from ground-based photometry. Furthermore, these pulsations can be contaminated by variable stellar winds.

The second short run (SRa02) of the CoRoT satellite in the asteroseismologic channel was partly devoted to the investigation of the photometric variability of O-type stars. Pointing towards the anti-centre of the Galaxy, this instrument observed objects belonging to the young open cluster NGC 2244 inside the Rosette nebula and to the surrounding association Mon OB2. The CoRoT data of three O-type stars that are part of this run have been analysed in previous papers: HD 46149 by Degroote et al. (2010), HD 47129 by Mahy et al. (2011), and HD 46202 by Briquet et al. (2011), the latter paper containing the only forward modelling in terms of seismic data of an O star so far.

In the present paper we study the three remaining O-type stars that are part of the SRa02 run. One of the targets is HD 46223, the hottest member of NGC 2244. Situated at about 1.4–1.7 kpc (Hensberge et al. 2000), this star was previously

⋆ The CoRoT space mission was developed and is operated by the French space agency CNES, with participation of ESA's RSSD and Science Programmes, Austria, Belgium, Brazil, Germany and Spain.
⋆⋆ Tables 2–4 are available at the CDS via anonymous ftp to cdsarc.u-strasbg.fr (130.79.128.5) or via http://cdsarc.u-strasbg.fr/viz-bin/qcat?J/A+A/533/A4
⋆⋆⋆ Senior Research Associate F.R.S.-FNRS.

quoted in the literature as having a spectral type O5 V (Hiltner 1956; Bisiacchi et al. 1982), O5 ((f)) (Conti & Leep 1974), O4 ((f)) (Massey et al. 1995) and O4 V((f$^+$)) (Mahy et al. 2009). The nine-year spectroscopic campaign by Mahy et al. to investigate multiplicity did not reveal any significant variation of the radial velocity related to the presence of a companion. In addition, Chandra mosaic observations of NGC 2244 (Wang et al. 2008) detect no strong clustering of X-ray sources around HD 46223, leading to the conclusion that there is also no lower-mass neighbour present. According to Wang et al., the small number of close-by X-ray sources could indicate that this star is younger compared to the population of the central part of the cluster.

The next target is HD 46150, the second hottest star in NGC 2244. Literature values for the spectral type are between O5 V((f)) (Underhill & Gilroy 1990; Maíz-Apellániz et al. 2004) and O5.5 V((f)) (Conti & Ebbets 1977; Garmany et al. 1980). The detailed study of Mahy et al. (2009) confirms the O5.5 V((f)) spectral type. Radial velocity variations have been detected in this star, but it is not clear if these are caused by binarity or motions in the stellar atmosphere (see Mahy et al. 2009, and references therein). Mahy et al. monitored this star but could not find any significant period in their data. They note the lack of spectral variability over short timescales (~7 days).

The third target studied in the present paper is the late O-type star HD 46966, belonging to the Mon OB2 association. The spectral classification generally agrees on O8.5 V (Conti et al. 1977; Garmany et al. 1980; Mahy et al. 2009) or O8 V (Munari & Tomasella 1999; Maíz-Apellániz et al. 2004). Moreover, spectroscopic monitoring reveals no clues on the existence of a secondary component (Mahy et al. 2009).

These three stars are among the youngest (1–6 Myr, Bonatto & Bica 2009) and most massive observed by the CoRoT satellite. They therefore have the potential to extend our knowledge about pulsations into the higher-mass domain. The CoRoT light curves are of unprecedented quality and have a long observational time span (longer than the rotational cycle). They thus provide the ideal data set to reveal the presence or absence of such pulsations.

We first present in Sect. 2 the detailed frequency analysis of the HD 46223 CoRoT light curve. In Sects. 3 and 4 we give the frequency analysis of HD 46150 and HD 46966 respectively. Section 5 is devoted to determining the theoretically expected pulsation frequencies. We discuss the results in Sects. 6, and 7 we provide the conclusions of our research.

2. HD 46223

2.1. CoRoT data

The data we used here were obtained during the CoRoT second short run (SRa02) made from 08 Oct. to 12 Nov. 2008. We started from the level N2 data (Samadi et al. 2007), which for each observation list the time, flux, error on the flux, and flagging information. The flagging indicates whether these data are contaminated by instrumental and environmental conditions of the CoRoT satellite such as, e.g., the South Atlantic Anomaly (SAA) and other Earth orbit perturbations (see Auvergne et al. 2009). In our analysis, we discarded all flagged points, as well as those few points that are listed with a negative flux error.

2.2. Spectral window

The spectral window for the HD 46223 observations below 10 d^{-1} (Fig. 1) is characterised by a first peak at $f = 2.007$ d^{-1} and its double at about $f = 4.011$ d^{-1}. This is related to the passage of the satellite, twice in a sidereal day, through the SAA. The relative amplitude of these two peaks is 3.5% and 1.1%, respectively. In addition, owing to the orbital period of the satellite (6184 s) there are gaps in the data set, which generate other structures with peaks around $f = 13.972$ d^{-1} and their harmonics.

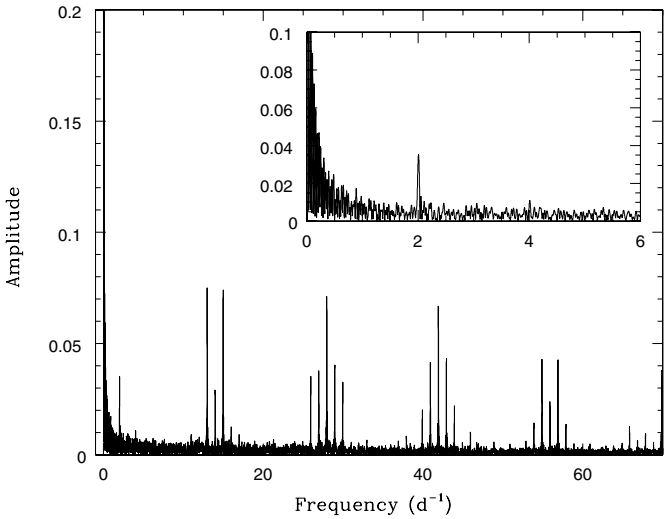

Fig. 1. Spectral window of the HD 46223 observations. The inset zooms in on the low-frequency region.

The spectral window also exhibits a peak at $f = 2699.76$ d^{-1}, corresponding to the sampling regularity of about 32.003 s. As a consequence, the pseudo-Nyquist frequency is located at about 1350 d^{-1}. The word "pseudo" emphasizes that the sampling is not ideally regular. In addition, because of the discarded flagged data, the duty cycle of the observations is only 86.75%. Because the data for all three stars were collected simultaneously with the same instrument, the spectral window properties for the other stars are very similar (see Table 1).

2.3. Detrending

In common with almost all CoRoT targets, there is a long-term trend visible in the data. This decreasing slope is likely caused by the CCD ageing (Auvergne et al. 2009). To remove this trend we divided the flux counts by the best-fit linear slope to the data.

The final version of the CoRoT light curve covers $T \approx 34.3$ days. The exact start and end times, duration, number of points, and frequency resolution are listed in Table 1. We did not convert the fluxes to magnitudes.

2.4. Frequency-by-frequency prewhitening

The range of variations observed in the HD 46223 CoRoT light curve (Fig. 2, top) is of the order of 16 000 counts, corresponding to 8 mmag. No clear pattern in the variations is visible. To better understand the variability of the CoRoT light curve, we applied a Fourier analysis based on the Lomb-Scargle method (Lomb 1976; Scargle 1982).

The amplitude spectrum (Fig. 3, top) exhibits many peaks and appears to be noisy. The highest peak is located at about $f = 0.75$ d^{-1} and the second one at about $f = 0.25$ d^{-1}, but no high-significance peaks are clearly detected, nor does there appear to be systematics, such as a constant spacing between peaks. A plot

Table 1. CoRoT data and results from the analysis for the three stars.

Parameter	HD 46223	HD 46150	HD 46966
CoRoT data			
number of raw data, N_R	92687	92695	92688
number of non-flagged data, N	80403	80282	82273
duty cycle (N/N_R, in %)	86.75	86.61	88.76
start date non-flagged data (HJD – 2 450 000)	4748.488547	4748.485591	4748.488454
end date non-flagged data (HJD – 2 450 000)	4782.819650	4782.819657	4782.805898
duration, T (d)	34.331103	34.334066	34.317444
freq resolution (d^{-1})	0.029128	0.029126	0.029140
Spectral window			
window peak (%) at 2.0 d^{-1}	3.5	3.8	3.9
window peak (%) at 4.0 d^{-1}	1.1	1.0	1.1
Stopping criterion: number of frequencies			
AIC_c	860	821	595
BIC	491	444	277
HQC	662	625	427
Number of red-noise significant frequencies			
	59	50	53
Number of red-noise significant frequencies present in both halves of the observing run			
	10	7	3
Red noise – fit parameters			
α_0 (counts)	442 ± 31	430 ± 65	416 ± 85
τ (d)	0.09 ± 0.01	0.08 ± 0.02	0.17 ± 0.05
γ	0.96 ± 0.02	0.96 ± 0.03	0.91 ± 0.02

of the spectrum up to the pseudo-Nyquist frequency shows very little power at high frequencies. In the subsequent analysis, we therefore limited the frequency domain to 0–100 d^{-1}.

For a more detailed analysis, we performed a traditional prewhitening. We started by subtracting the average from the fluxes. We then determined the amplitude spectrum using the Lomb-Scargle method. We selected the frequency corresponding to the highest peak in the amplitude spectrum and fitted a sine function ($A_j \sin(2\pi f_j t_i + \phi_j)$) to the fluxes as a function of time (t_i). In the fitting procedure, the semi-amplitude (A_j) and phase (ϕ_j) are free parameters, while the frequency (f_j) was allowed to vary within a range of $\pm 0.1/T$ from its peak value[1] (where $1/T$ is the frequency resolution and $0.1/T$ the step size in our frequency grid). The fitted sine function was then subtracted from the data and the amplitude spectrum was re-computed from these prewhitened data. This procedure was continued until we reached the noise level in the observations. After the prewhitening, the observed variability, whatever its nature, is thus described (down to the noise level) as a sum of terms, with each term being a sine function at a particular frequency.

2.5. Stopping criteria

To judge when we had reached the noise level, we explored three stopping criteria that have been discussed in the literature (Hannan & Quinn 1979; Hannan 1980; Liddle 2007). The information content of the fit is given by

$$c_N(m) = -2\ln(L_N(m)) + \begin{cases} 2m + \dfrac{2m(m+1)}{(N-m-1)} & \text{Akaike, corrected } (AIC_c) \\ m\ \ln(N) & \text{Bayesian (BIC)} \\ 2m\ \ln(\ln(N)) & \text{Hannan – Quinn (HQC),} \end{cases} \quad (1)$$

[1] The $\pm 0.1/T$ value turns out to be quite close to (slightly higher than) the formal errors we obtained on the frequencies (see Eqs. (3–5) and Tables 2–4).

where N is the number of observations, m is the number of parameters and $L_N(m)$ is the likelihood function. To within a constant, $-2\ln(L_N(m))$ can be written as (Press et al. 1992, Sect. 15.1)

$$\sum_{i=1}^{N} \frac{(y_i - F(t_i, \mathbf{\Theta}_m))^2}{\sigma_i^2}, \quad (2)$$

where y_i are the fluxes observed at times t_i, and $\mathbf{\Theta}_m$ is the vector containing the m fit-parameters. For the value of σ_i we took the error bars listed with each observed flux. We stopped the prewhitening process when $c_N(m)$ had reached a minimum. This is very similar to least-squares minimization, but the additional terms in Eq. (1) correct for the improving of the model fit with an increasing number of parameters. We set $m = 3k$, counting three parameters (frequency, amplitude, phase) for each of the k sine functions we fit. Note that we subtracted the average from the observed fluxes before starting the prewhitening procedure (Sect. 2.4), which could lead to a bias.

Applying this to the HD 46223 data, we found that the minimum of AIC_c is reached at 860 terms, BIC at 491 and HQC at 662. To judge the reliability of these stopping criteria, we ran a number of simulations where we constructed artificial light curves with a given number of sine functions. We used the same time sampling as for the observations and attributed to it the same noise level and flagging (this approach is used in all simulated light curves discussed in this paper). For the amplitudes and frequencies we took either values from the analysis of the observations, or randomly drawn values distributed according to the statistics of the observed spectrum. Noise was added to the simulation using a Gaussian random variable (with mean zero and standard deviation unity) multiplied by the listed error on the observed flux. We then applied our prewhitening procedure to the simulations and compared the results of the stopping criteria with the known number of terms we introduced. It turns out that BIC gives the best value, which is always within a factor 1.5 of the correct result. Degroote et al. (2009b) also used BIC in

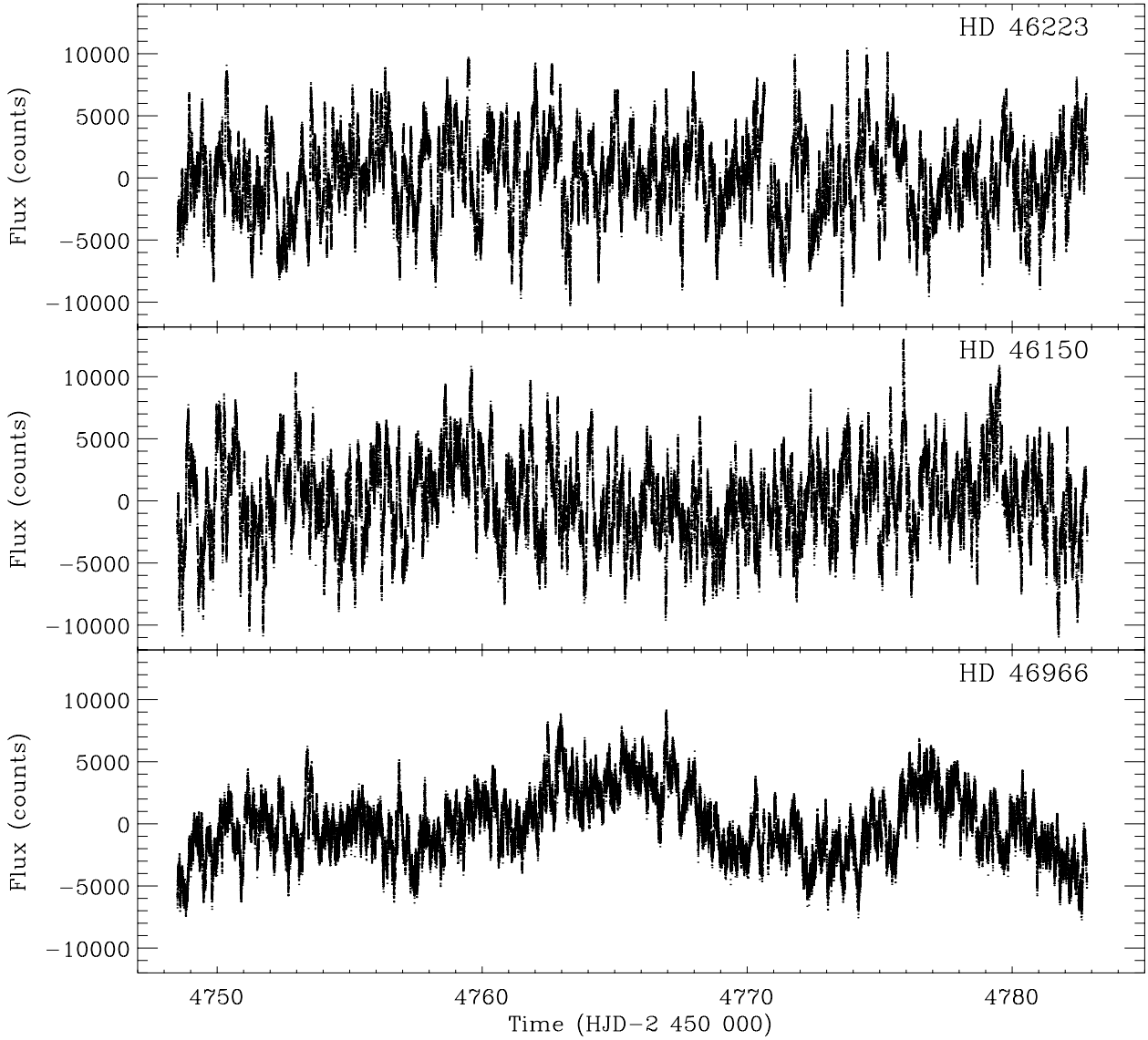

Fig. 2. Detrended CoRoT light curves, covering the full 34.3 days of the observing run. Each observation is represented by a dot. Flagged data are not plotted. *Top*: HD 46223, *middle*: HD 46150, *bottom*: HD 46966.

preference over the (uncorrected) AIC as a stopping criterion in their study of the β Cep star HD 180642.

As an additional test, we also repeated the analysis on the observed data after rebinning over a number of points (up to 32 points, i.e. 17 min), but found approximately the same results. This is consistent with the fact that there is little power at higher frequencies. Based on the above, we took the BIC rounded-off value of 500 terms as the stopping criterion. The final 500 frequencies and corresponding semi-amplitudes and phases are listed in Table 2. The phases are defined with respect to $t = 0$ corresponding to the first non-flagged data point (as listed in Table 1).

New frequencies found during the prewhitening procedure can be quite close to previously found frequencies. The resolution criterion for this is that frequencies should be separated by at least $1.5/T$ to be considered unique (Loumos & Deeming 1978). Applying this to our list of 500 frequencies, we find that 276 of them are unique.

The canonical errors estimated on these frequencies (f), and their corresponding semi-amplitudes (A_f) and phases (ϕ_f) are given by the expressions of Lucy & Sweeney (1971) and Montgomery & O'Donoghue (1999):

$$\epsilon(f) = \sqrt{\frac{6}{N}}\,\frac{1}{\pi T}\,\frac{\sigma_f}{A_f} \tag{3}$$

$$\epsilon(A_f) = \sqrt{\frac{2}{N}}\,\sigma_f \tag{4}$$

$$\epsilon(\phi_f) = \sqrt{\frac{2}{N}}\,\frac{\sigma_f}{A_f}, \tag{5}$$

with σ_f the standard deviation on the light curve at the current stage of prewhitening. These formal errors are also listed in Table 2.

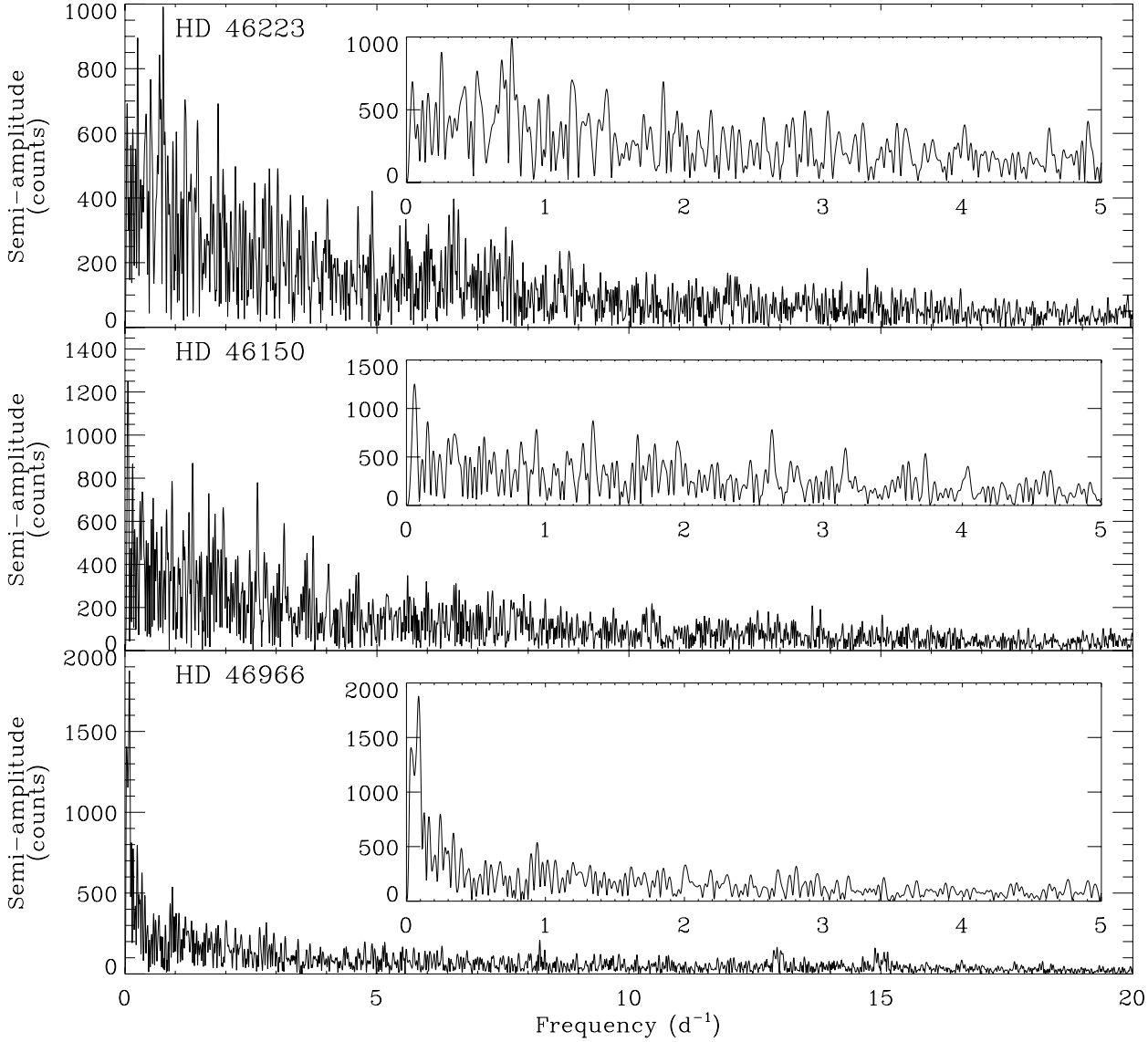

Fig. 3. Amplitude spectrum of the CoRoT light curves computed by the Lomb-Scargle method. The insets show a zoom-in of the amplitude spectrum on the low-frequencies domain. *Top*: HD 46223, *middle*: HD 46150, *bottom:* HD 46966.

2.6. Multifrequency fitting

The Lomb-Scargle-based iterative prewhitening consists in a one-by-one determination of the sine functions and in their removal from the light curve. In a gapped or unevenly sampled data set, the height of peaks depends on the height of other peaks in the periodogram. A more general procedure should therefore determine all sine function terms simultaneously.

To be more reliable in the detection of the frequencies, we also used a multifrequency algorithm introduced by Gosset et al. (2001, their Eqs. (A13) to (A19)), which was developed from the Heck et al. (1985, hereafter HMM) method. We note that this multifrequency algorithm is not based on the Lomb-Scargle technique. However, for CoRoT data we found that the amplitude spectrum computed from Lomb-Scargle and from HMM agree very well. The multifrequency algorithm takes into account the mutual influence of peaks by fitting them all together, and is therefore in principle an improvement on the one-by-one prewhitening procedure used in Sect. 2.4. Similarly to the prewhitening procedure, the present method refines the value of each frequency (allowing it to vary within the natural width of the individual peaks).

We applied this method to the non-flagged data of the HD 46223 CoRoT light curves, but the great number of data points involves an excessive computation time. Accordingly, we had to deal with a limited number of terms at the same time. We found that the values of the frequencies fitted by the multifrequency programme are very similar to those determined by the prewhitening procedure and show only small differences in the amplitudes. We therefore do not list these results.

2.7. Significance levels

Although the quality of the CoRoT curve is unparalleled, it is still important to check whether peaks detected in the amplitude spectrum might result from a random variation rather than representing a periodic signal. To do this, we used the statistical criterion presented by Gosset (2007), which was quoted in Mahy et al. (2011). The probability that at least one of the

Table 2. List of sine function terms for HD 46223.

ID	Freq. (d^{-1})	Freq. Error (d^{-1})	Semi-ampl. (counts)	Semi-ampl. Error (counts)	Phase (rad)	Phase Error (rad)	Standard Deviation (counts)	Sig. Red-noise	Red-noise Significant	Half-run Test
1	0.7548	0.0050	989.095	305.732	-2.500	0.309	3296.681	1.0000		*
2	0.2493	0.0068	882.119	371.151	-1.830	0.421	3221.288	1.0000		*
3	0.5102	0.0067	772.225	323.271	1.476	0.419	3160.377	1.0000		*
4	0.6858	0.0063	752.212	296.426	-0.497	0.394	3112.720	1.0000		*
5	1.1944	0.0056	699.589	244.181	0.676	0.349	3067.088	1.0000		*
6	1.8456	0.0046	691.462	199.852	-2.537	0.289	3026.889	1.0000		*
7	0.0395	0.0091	681.390	385.046	-1.697	0.565	2986.975	1.0000		*
8	0.4251	0.0077	650.217	312.906	-0.054	0.481	2948.151	1.0000		*
9	0.9477	0.0064	636.137	251.785	-1.726	0.396	2912.468	1.0000		*
10	1.4370	0.0053	642.207	212.699	-1.822	0.331	2877.663	1.0000		*
...	...	...	...	...	...	...	...	...	...	...
59	7.5519	0.0027	303.826	51.957	0.500	0.171	1913.541	0.0080	R	
...	...	...	...	...	...	...	...	...	...	...

Notes. This is an excerpt of Table 2. The full table is available in electronic form at the CDS. We list the first ten terms as well as the first term that is significant under the assumption of red noise (indicated with "R"). Terms that are found in both halves of the observing run are indicated with "*" in the last column.

semi-amplitudes of an extended set of frequencies exceeds a threshold z under the null hypothesis of a stochastic process of variance σ_f^2 is given by

$$\mathrm{Prob}[Z_{\max} > z] = 1 - \mathrm{e}^{-\mathrm{e}^{-0.93z + \ln(0.8N)}}, \quad (6)$$

where $Z_{\max} = \max_{f<f_{\mathrm{Ny}}} Z(f)$, N is the number of points in the data set and $Z(f) = A_f^2 N/(4\sigma_f^2)$ with A_f the semi-amplitude of the frequency f and σ_f the standard deviation on the light curve at the current stage of prewhitening.

We also explored a different version of this criterion, which uses (Degroote et al. 2009a)

$$\mathrm{Prob}[Z_{\max} > z] = 1 - (1 - \exp(-z))^{N_i}, \quad (7)$$

where N_i is the number of independent frequencies. Degroote et al. show that the CoRoT data are sufficiently well equally-spaced that we can take $N_i = 2N$. In our work, the first criterion (given by Eq. (6)) turns out to be slightly stricter, and we therefore discuss only results obtained with that one.

In applying this criterion, the simplest approach is to assume white noise, i.e. σ_f is independent of frequency and its value is given by the standard deviation on the light curve at the current stage of prewhitening. Under that assumption all 500 sine function terms are highly significant.

2.8. Red noise

It is quite clear from the amplitude spectrum (Fig. 3) that the power increases substantially towards lower frequencies. This strongly suggests the presence of red noise. We stress that the word "noise" does not imply an instrumental origin but rather points to predominantly stochastic behaviour: in Sect. 6.2 we discuss the possible physical cause of the red noise.

In the present section, we determine the observed properties of this red noise. Stanishev et al. (2002) suggest to describe the amplitude spectrum $\alpha(f)$ by using the following fit-function:

$$\alpha(f) = \frac{\alpha_0}{1 + (2\pi\tau f)^\gamma}, \quad (8)$$

with α_0 the scaling factor, γ the slope of the linear part (in a log-log plot) and τ an estimation of the mean duration of the dominant structures in the light curve. We fitted this profile to the amplitude spectrum of HD 46223 (Fig. 4, top) to quantify the information about the red noise contained in the periodogram. We applied a least-squares fit to the logarithm of both frequency and semi-amplitude, limiting the frequencies used to 0–100 d^{-1}. The resulting fit parameters and their 1-sigma error bars are listed in Table 1.

To re-evaluate the significance of the peaks under the hypothesis of red noise, we need to determine its $\sigma_{f,\mathrm{red}}$. We did this by first converting the fit-function for amplitude (Eq. (8)) into power. We then re-scaled that function so that its integral over frequency (up to the pseudo-Nyquist frequency of ~1350 d^{-1}) is the same as the variance on the flux multiplied by the pseudo-Nyquist frequency.

We then repeated the prewhitening procedure and determined for each frequency the significance of the peak by using Eq. (6) with $Z(f) = A_f^2 N/(4\sigma_{f,\mathrm{red}}^2)$. It is important to realise that in doing so, we still select the highest peak at each step in the prewhitening process, not the one that is most significant under red-noise conditions. If we were to select the most significant peak, it would correspond to a small-amplitude contribution to the light curve. In the prewhitening procedure (Sect. 2.4) we would then need to fit a sine function with this frequency to the light curve, and subtract it. The fitting procedure will not succeed, because in attempting to fit only a minor contribution to the light curve, it will be led astray by the much higher-amplitude contributions (which have not been removed yet). It will therefore give an incorrect result, or will fail to converge.

Applying this procedure, we found 59 significant sine functions with a significance level below 0.01; we indicate them with an "R" in Table 2.

2.9. Split into two halves

We next applied an additional method to determine the reliability of the sine function terms we found. We split the data set into two halves, and repeated the analysis separately on each half. We then checked how many of the original terms can also be found in both halves. We considered two frequencies (f_1 and f_2) to be the same if $|f_1 - f_2| < \sqrt{\epsilon^2(f_1) + \epsilon^2(f_2)}$, where the errors are defined in Eq. (3). Simulations with artificial data confirm that

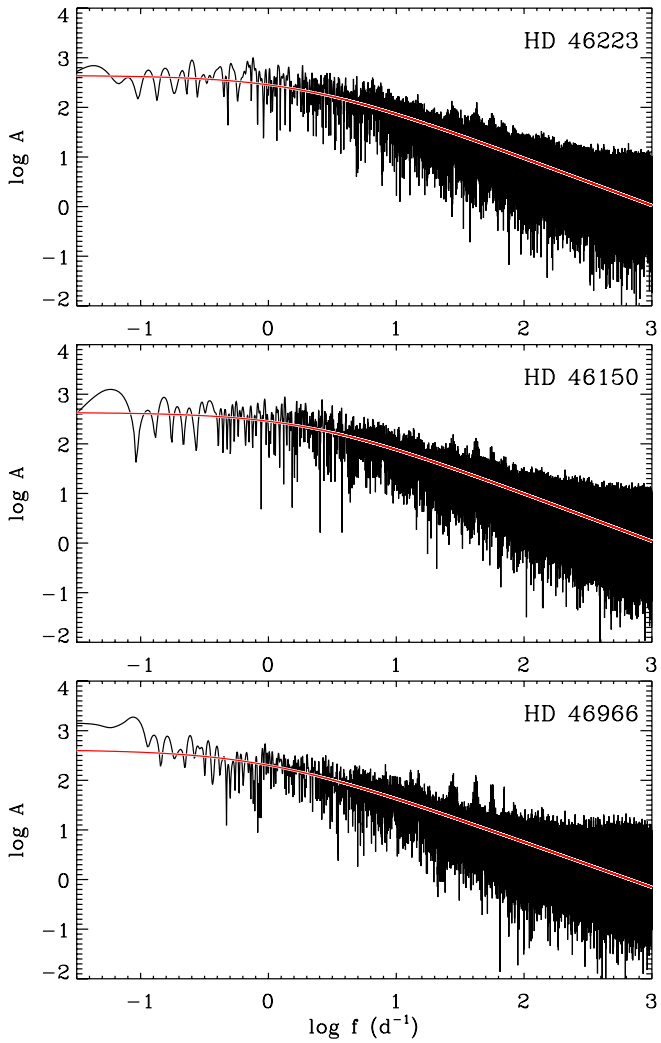

Fig. 4. Fit-function (Eq. 8, red line) to the amplitude spectra as a function of frequency, in a log–log plot. *Top*: HD 46223, *middle*: HD 46150, *bottom*: HD 46966.

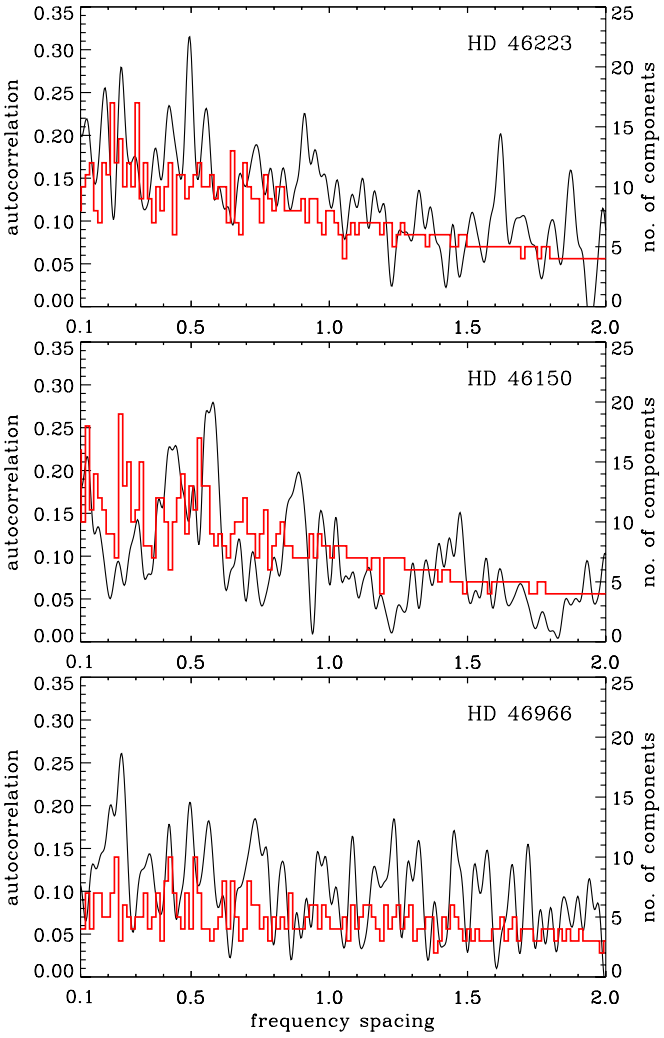

Fig. 5. Autocorrelation functions (black curve) of the power periodograms and number of components in a chain with a given frequency spacing (red curve). *Top*: HD 46223, *middle*: HD 46150, *bottom*: HD 46966.

this is the appropriate criterion to use. We could of course relax it by considering equality to within 2 or 3 times the 1-sigma error bar, but this would considerably increase the number of false coincidences.

If we first look at the terms determined assuming white noise, we find that of the 500 terms extracted from the full run, 202 are present in both halves. This is substantially less than the 282 terms we find if we construct an artificial, noisy, light curve from the first 100 observed terms of HD 46223. Other simulations with frequencies drawn randomly according to the observed distribution also find a significantly larger number of terms in both halves.

If we limit ourselves to the 59 red-noise significant terms listed in Table 2, we find that only 10 are present in both halves of the data set.

2.10. Frequency combinations and spacings

We next searched for the presence of low-order harmonics (up to order 10) in the list of 500 frequencies. With the usual criterion that frequencies should be equal to within the square root of the sum of the squares of the individual 1-sigma errors, we found 983 such harmonics. However, simulations as in Sect. 2.5 show a factor 2–3 more harmonics. Our findings must therefore be attributed to coincidences, not to true harmonics.

A similar search for linear combinations of the type $f_1 + f_2 = f_3$ among the 500 frequencies revealed 45 412 results. But, again, simulations showed these to be spurious. If we limit our search to frequencies significant assuming the red-noise hypothesis, we find no harmonics and only one linear combination. The reason we found so few of these is that most of our red-noise frequencies are between 10 and 20 d^{-1}; harmonics and sums of these are then outside the 10–20 d^{-1} range. Because of the limited value of these results, we do not list them.

In addition to these linear combinations, we investigated the frequency spacing for HD 46223. Degroote et al. (2010) found such spacing for the O8 V star HD 46149. Following their work, we looked at both the autocorrelation function of the power periodogram and the number of components we find in a chain (f_0, $f_0 + \Delta f$, $f_0 + 2\Delta f$, ...) with an assumed frequency spacing Δf. In both the chain and autocorrelation test, we started from the 500 frequencies, but eliminated those outside the 3.0–12.0 d^{-1} domain. The lower limit is taken to avoid the stronger peaks, the upper limit to avoid effects from the satellite orbital period (13.972 d^{-1}). To determine the number of components in a chain

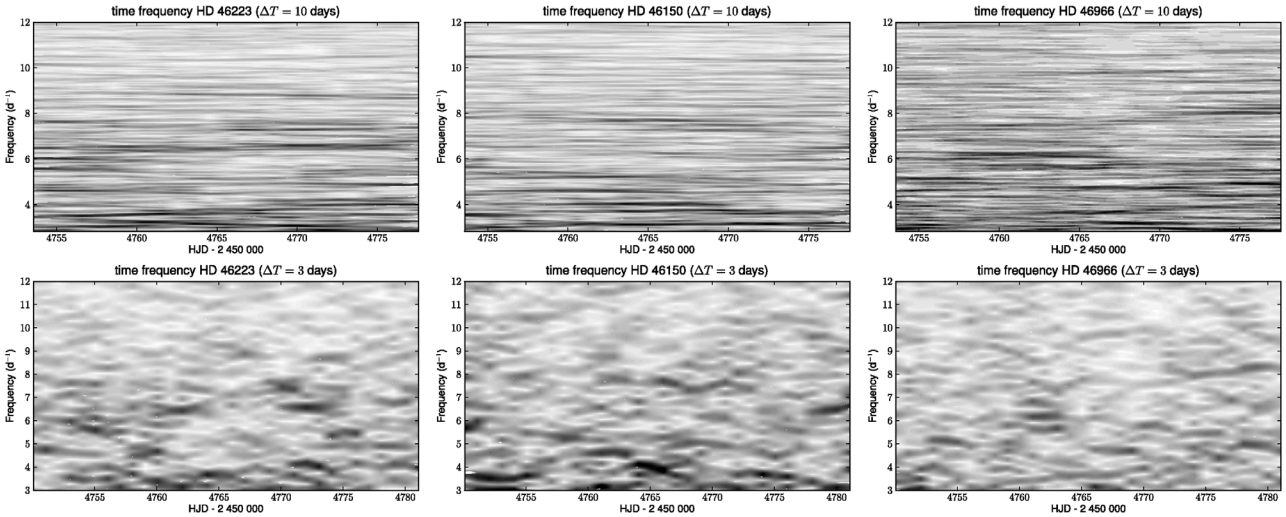

Fig. 6. Time-frequency analysis of the light curves. The top row uses a sliding window of 10 days, the bottom row one of 3 days. *Left panels*: HD 46223, *middle*: HD 46150, *right*: HD 46966. The grey scale indicates the semi-amplitude of the frequencies. Clearly the frequencies do not have long lifetimes.

at a given frequency, we considered that $f_0 + n\Delta f$ equals a listed frequency if both differ by less than the step size we used in the figure, which is 0.015 d^{-1}. For Δf, we considered only the range of 0.1 to 2.0 d^{-1}, because this is where both the autocorrelation and chain-test function have their highest values.

Figure 5 (top) shows the results for HD 46223. The autocorrelation function has a peak at $\Delta f = 0.5$ d^{-1}, but the number of components does not confirm this peak. We therefore conclude that we do not detect significant frequency spacings in HD 46223.

2.11. Time-frequency analysis

We also performed a time-frequency analysis (Fig. 6) to detect variations in the amplitude of frequencies or in the frequencies themselves as a function of time.

For this purpose, a sliding window with lengths of 10 and 3 days was applied to the light curve and shifted with a step of one day. Then we applied a Fourier analysis on each frame by using the HMM method (for further details on this time-frequency analysis method, see Huat et al. 2009). A plot of all frequencies in the 3–12 d^{-1} range detected on a sliding window of 10 and 3 days is shown in Fig. 6. This figure confirms what we already found from the test where we split the data into two halves. The frequencies are clearly not stable over the ~34-day timescale of the observation. The figures do not show many frequencies that have a lifetime longer than the duration of the sliding window. This behaviour is compatible with the dominant presence of red noise.

The limited lifetime also raises doubts about the applicability of the $1.5/T$ criterion (Loumos & Deeming 1978) to resolve frequencies (see Sect. 2.5). A limited lifetime translates into a broadening of the frequency. This will reduce the number of unique frequencies found in our analysis.

3. HD 46150

For the analysis of HD 46150 we applied a similar detrending as for HD 46223. The range of variations observed in the HD 46150 CoRoT light curve (Fig. 2, middle) is of the order of 16 000 counts, corresponding to 8 mmag. More details are listed in Table 1. No clear pattern in the variations is visible. The amplitude spectrum (Fig. 3, middle) is noisy and has its highest peak at 0.055 d^{-1}. Because there is little power at high frequencies, we limited the frequency domain to 0–100 d^{-1} in the subsequent analysis.

We next applied our standard prewhitening procedure and checked the stopping criteria (Eq. (1)). From the values found (Table 1) we decided to limit the number of terms to 500. This list of frequencies and corresponding semi-amplitudes and phases is given in Table 3 (this table is only available in electronic form at CDS). Applying the significance criterion (Eq. (6)) with the assumption of white noise results in all 500 terms being significant. The Loumos & Deeming (1978) test shows 296 of these to be unique. Multifrequency fitting (see Sect. 2.6) gives basically the same set of terms, though with slightly different amplitudes.

However, it is again clear that there is a substantial red-noise component present in the spectrum, which we fit with the fit-function of Eq. (8) (see Table 1 and Fig. 4, middle). Judging the significance of peaks with respect to this red noise, we found 50 significant terms (indicated with "R" in Table 3), using a 0.01 cut-off.

When we split the observed data set into two, we found that 195 of the 500 terms occur in both halves, but this is less than the simulations of Sect. 2.9 show. Under the red-noise hypothesis, only seven of the 50 terms are present in both halves. We also explored the linear combinations of all 500 frequencies, but simulations show these to be not significant, as for HD 46223 (see Sect. 2.10). We found no linear combinations among the red-noise frequencies unless we relaxed the criterion we had implemented for considering two frequencies to be equal. This shows that there are no significant linear combinations.

We next applied a similar frequency spacing test as for HD 46223. A peak in the autocorrelation function was found at $\Delta f = 0.58$ d^{-1}, but it was not confirmed by the plot with the number of components in a chain (Fig. 5, middle). Finally, a time-frequency analysis (Fig. 6, middle) showed short "lifetimes" for the frequencies, which is again consistent with red noise.

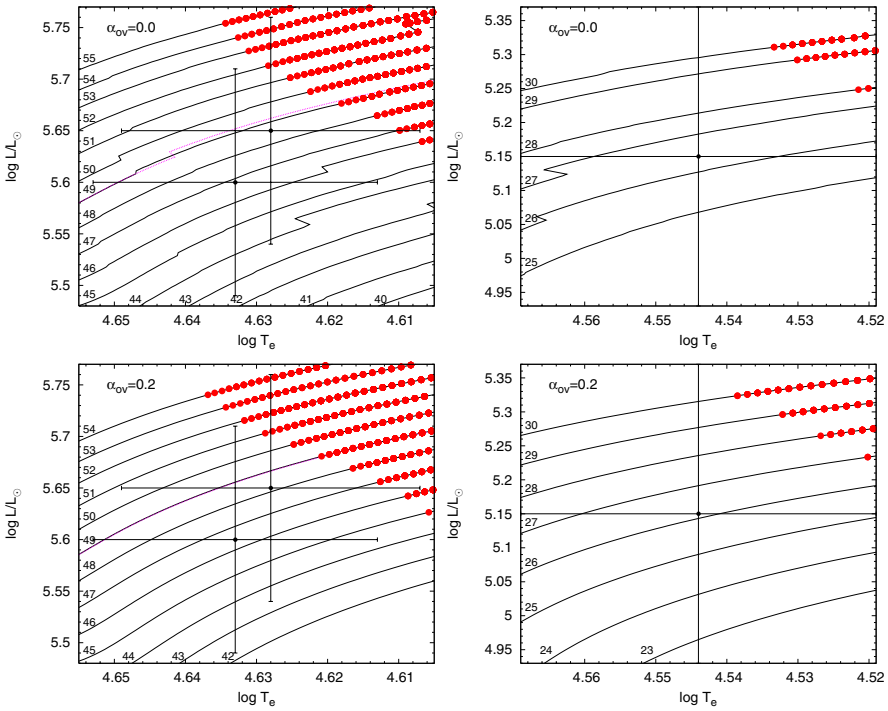

Fig. 7. Evolutionary tracks relevant for our three stars. The models in the bottom figures include overshooting, the ones at the top do not. *Left*: tracks of 40 to 55 $M_\odot$ computed with a mass-loss rate of 6.0×10^{-8} $M_\odot\,\mathrm{yr}^{-1}$. The error boxes of HD 46223 (the hotter star) and HD 46150 (the cooler star) are also displayed. To show that both stars can be modelled by the same mass-loss rate without affecting the excited frequency domain, we also plot a 49 $M_\odot$ track computed with $\dot{M} = 6.8 \times 10^{-8}$ $M_\odot\,\mathrm{yr}^{-1}$ (magenta-coloured line). *Right*: same, but for HD 46966 computed with a mass-loss rate of $5.0 \times 10^{-9} M_\odot\,\mathrm{yr}^{-1}$. The full circles indicate positions along the tracks that have excited frequencies.

4. HD 46966

The treatment of the data of HD 46966 was similar to that of HD 46223 and HD 46150 and details are listed in Table 1. The CoRoT curve of HD 46966 (Fig. 2, bottom) exhibits an almost regular oscillation with an approximate period of 10 days, but only about three cycles are covered by the observations. In addition, we detected variability on shorter timescales. The peak-to-peak variation amplitudes correspond to about 6 mmag.

Because there is little power at high frequencies, we limited the frequency domain to 0–100 d^{-1}. We applied our standard prewhitening procedure and checked the stopping criteria (Eq. (1)). From the values found (Table 1), we decided to limit the number of terms to 300. The list of frequencies and corresponding semi-amplitudes and phases is given in Table 4 (this table is only available in electronic form at CDS). The Loumos & Deeming (1978) criterion shows 196 of these to be unique. The amplitude spectrum (Fig. 3, bottom) is characterised by a first peak that is three times larger than the second one. This peak, at $f = 0.084\ \mathrm{d}^{-1}$, i.e. 12 days, corresponds to the observed almost regular oscillation.

It is, however, better to consider red noise, described by the fit-function from Eq. (8). Applying this, we found 53 significant terms, with a cut-off of 0.01. They are indicated with an "R" in Table 4. Note that in this analysis the $f = 0.084\ \mathrm{d}^{-1}$ frequency discussed above is no longer considered significant. Table 4 shows that it has a false-alarm probability of 0.997, which is too high compared to our 0.01 cut-off. Multifrequency fitting (see Sect. 2.6) gives basically the same set of frequencies, though with slightly different amplitudes.

The test where we split the observed data set into two showed that only 77 of the 300 terms were found in both halves. For the terms that are significant under the red-noise hypothesis, only three were found in both halves. Simulations as in Sect. 2.9 show that these numbers are not significant.

We also explored the linear combinations between the 300 frequencies, but simulations show that these are not significant, as for the two other stars. Limiting ourselves to the 53 red-noise frequencies, we found no linear combinations. Only when we increase the criterion that we employ for equality of frequencies by a factor of three did we begin to find linear combinations. The result is therefore not significant.

We also applied a similar frequency spacing test as for HD 46223. Again, a peak in the autocorrelation function was found, at $\Delta f = 0.25\ \mathrm{d}^{-1}$. The plot with the number of frequencies in a chain peaks at a different value of $\Delta f = 0.43\ \mathrm{d}^{-1}$, however (Fig. 5, bottom), showing the result to be not significant. As for the two other stars, the time-frequency analysis (Fig. 6, bottom) shows short lifetimes for the frequencies; this again indicates the presence of red noise.

5. Theoretical pulsations

An important goal of the CoRoT photometry is to detect radial or non-radial pulsation modes in massive stars. To predict which modes can be expected, we computed a grid of models by using the Rome stellar evolution code ATON (Ventura et al. 2008). In these calculations, we assumed a metallicity of $Z = 0.015$ and the metal mixture of Grevesse & Noels (1993). We also used the MAD non-adiabatic pulsation code (Dupret et al. 2003) to determine the frequencies of excited modes. The computations were made on the basis of preliminary stellar and wind parameters derived from the atmosphere code CMFGEN (Hillier & Miller 1998) by Martins et al. (in prep.). These parameters are listed in Table 5. We note, however, that we used the same value for the mass-loss rate for HD 46223 as for HD 46150 to compute the evolutionary tracks. The difference between the value used and those listed in Table 5 does not significantly affect our results. Additionally, we considered models both with and without overshooting.

HD 46223 and HD 46150 are in very similar positions in the HR diagram, whilst HD 46966 is cooler and more evolved. All three stars lie just at the boundary of the instability strip of the κ-mechanism. Theoretical excited frequencies for that mechanism are generally in the range of 2–5 d^{-1} for $l = 0$ to $l = 4$ and

Table 5. Stellar parameters for the three stars.

Parameter	HD 46223	HD 46150	HD 46966
$\log T_{\rm eff}$(K)	4.633 ± 0.020	4.628 ± 0.021	4.544 ± 0.025
$\log g$ (cgs)	4.00	4.00	3.75
$\log L/L_\odot$	5.60 ± 0.11	5.65 ± 0.11	5.15 ± 0.22
$R/R_\odot$	11.39	12.35	10.24
$\log \dot{M}$ ($M_\odot$ yr^{-1})	−7.20	−7.17	−8.30
$v_{\rm eq} \sin i$ (km s^{-1})	100	100	50
$v_{\rm macro}$ (km s^{-1})	32	37	27

Notes. Preliminary stellar and wind parameters derived by Martins et al. (in prep.).

a non-radial mode is also excited around 12 d^{-1}. The theoretical frequencies from our model calculations are shown in Fig. 8 for 30 and 52 $M_\odot$ (without overshooting): models with these masses present the largest number of excited modes. Models computed with overshooting give similar results.

For HD 46223 we considered stellar evolution models with an initial mass ranging from 45 to 53 $M_\odot$ (Fig. 7, left panel). On these tracks, models with a mass greater than 47 $M_\odot$ show excited modes. For this mass range, the excited modes all have frequencies around 4 d^{-1}. However, if we look at the observed amplitude spectrum of HD 46223 (Fig. 3, top), no outstanding peak is situated close to 4 d^{-1}, which means that this star probably does not present pulsations, neither radial nor non-radial. For HD 46150 a similar conclusion can be drawn. There are low-amplitude peaks around 4 d^{-1}, but the peaks are not strong and they could be the result of noise.

The amplitude spectrum of HD 46966 is clearly dominated by peaks at the frequencies f = 0.084 and 0.039 d^{-1}. The time coverage of the CoRoT observations is too short to know if these are regular variations. Furthermore, it is unlikely that these two frequencies are caused by excited modes (Fig. 8, bottom) because those modes are predicted to be between 2.5 and 4 d^{-1}. Even though the amplitude spectrum has peaks situated in this frequency region, these peaks are weak.

It is important to emphasize that the results presented in this section depend on the stellar parameters determined by Martins et al. (in prep.). These parameters are still under investigation and should therefore be considered as preliminary. Nonetheless, the present work shows that even with the unprecedented quality of the CoRoT light curves, we do not convincingly detect the predicted excited modes. This suggests that they are only weakly excited, or perhaps, not at all. On the other hand, a number of stronger peaks are observed, but at frequencies that are so different from the theoretical ones that we cannot attribute them to the expected excited modes, at least not within the framework of current theoretical models. It is thus not possible to conclude with certainty that these three stars are pulsating. Moreover, we also explored the possibility of solar-like oscillations because Degroote et al. (2010) found such oscillations in the OB binary system HD 46149. But the existence of these oscillations was rejected in HD 46150, HD 46223, and HD 46966 because no regular spacings were found in the amplitude spectra.

6. Discussion

6.1. Radius and rotational frequency

In a presumably single star, large-scale photometric variations can have a frequency compatible with the rotational frequency

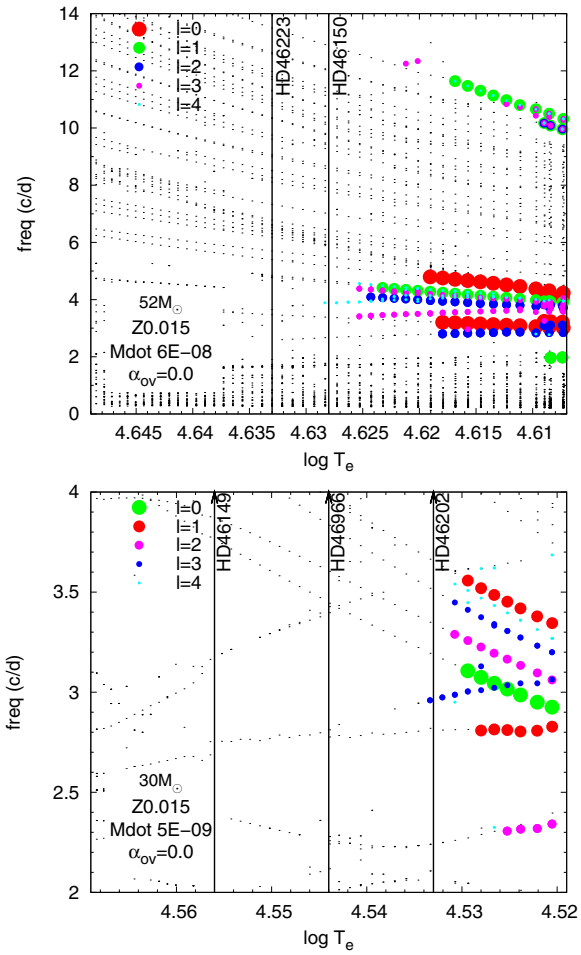

Fig. 8. Theoretical oscillation frequencies (for the κ-mechanism) computed with the MAD non-adiabatic code, as a function of the effective temperature. The results shown here do not include overshooting. *Top*: 52 $M_\odot$ track. *Bottom*: 30 $M_\odot$ track. The black points indicate models that do not show pulsations, the coloured full circles stand for those models with the excited frequencies. The l-value is colour-coded (see legend). We also indicate with vertical lines the effective temperatures of the three stars studied here, as well as HD 46149 (Degroote et al. 2010) and HD 46202 (Briquet et al. 2011).

of the star. Their exact origin could be attributed to the existence of a spot on the star or be associated with the stellar wind.

The first low frequency detected in the amplitude spectrum of HD 46223 is f = 0.249 d^{-1}, corresponding to 4.02 days. With this period and the parameters from Table 5, we derived an equatorial velocity $v_{\rm eq}$ of about 140 km s^{-1}, which is higher than the $v_{\rm eq} \sin i$ value of 100 km s^{-1} measured by Mahy et al. (2009) and Martins et al. (in prep.). Consequently, the frequency f = 0.249 d^{-1} could be associated with the rotational cycle of the star, implying a rotational period of about ∼4 days and an inclination of 43−45°.

For HD 46150 the amplitude spectrum exhibits a strong peak at f = 0.055 d^{-1}, corresponding to 18 days. The derived equatorial velocity is 34 km s^{-1}, which is too low compared to the $v_{\rm eq} \sin i$. The frequency corresponding to the equatorial velocity found by Mahy et al. (2009) or Martins et al., should be close to or higher than 0.16 d^{-1}. The list of frequencies (Table 3) shows that the third frequency (f = 0.144 d^{-1}) in Table 3 is quite close. It corresponds to an equatorial velocity of 90 km s^{-1}, which is

within acceptable range of the Mahy et al. and Martins et al. value, but would require an inclination of 90°.

The amplitude spectrum of HD 46966 is marked by a strong peak at $f = 0.084\ \mathrm{d}^{-1}$, representing a period of 12 days. With the stellar parameters mentioned in Table 5, we estimate the equatorial velocity to be close to 44 km s^{-1}. This velocity is just below the 1-sigma error bar on the $v_{\mathrm{eq}} \sin i$ determined by Mahy et al. (2009). Martins et al. (in prep.), on the other hand, clearly show that the $v_{\mathrm{eq}} \sin i$ is lower than 50 km s^{-1}. Consequently, the frequency $f = 0.084\ \mathrm{d}^{-1}$ could be associated with the rotational cycle of the star, implying a rotational period of about 12 days.

6.2. Pulsations and red noise

For the three O-type stars studied here, a substantial number of sine function terms are found. However, it is unclear how many of those – if any – can be classified as true independent modes. They do not show the linear combinations or frequency spacings that may be expected in pulsators. If these terms were interpreted as pulsational modes, then their lifetimes would be very short. The amplitude spectra for these three stars are therefore unlike any of those of known pulsators in that part of the HR diagram (Aerts et al. 2010, Chap. 2).

This is clearly illustrated by comparing the periodogram of these hot O stars (spectral types O4–O8) to that of the cooler star HD 46202 (O9 V). This star behaves like a classical pulsator, with clear β Cep-like pulsations that dominate the power spectrum (Briquet et al. 2011). Various causes for what we see in our periodograms can be eliminated: rotational effects on pulsation can be excluded because our periodograms are very different from those of Be stars (e.g. Diago et al. 2009). Spots on the surface of the star would give clearly isolated frequencies (and linear combinations between them). A power excess due to stochastic modes would occur at higher frequencies.

The interpretation that ascribes most of the power in the periodogram to red noise therefore seems more appropriate. We stress again that this red noise is caused by a physical mechanism in the star. It is not an instrumental effect, because its behaviour is different from star to star in these simultaneous observations. The parameters of the fit-function (Table 1) show that HD 46966 has a somewhat lower α_0 and a somewhat longer τ than the other two stars. Compared with Plaskett's Star (HD 47129) a clearer difference is seen: especially the γ value is different ($\gamma = 2.3$, Mahy et al. 2011). We also fitted the red-noise component of HD 46149 (Degroote et al. 2010). This star has a $\tau = 29.5 \pm 12$ and $\gamma = 0.55 \pm 0.01$, which are substantially different from the stars studied in this paper. All this points to an origin for the red noise that is intrinsic to the star.

To see how convincing the red-noise description is, we simulated light curves containing only red noise (according to the fit-function – Eq. (8)), and analysed them in the same way as the real data. We followed the prescription by Timmer & Koenig (1995) to generate the red noise. In the simulated data, the number of significant red-noise frequencies found is somewhat higher (by a factor less than two) than in the real data. Only one or two of these significant red-noise frequencies can be found in both halves of the light curve (somewhat less than for the real data). The number of linear combinations found is higher than for the real data, but this is presumably related to the higher number of significant red-noise frequencies. It therefore seems that the observed data can largely be described as red noise, though a few pulsational frequencies might be present.

The presence of red noise in the stellar signal indicates stochastic, chaotic, or quasiperiodic effects. It occurs in a number of astrophysical contexts, such as the light curves of Mira variables (Templeton & Karovska 2009) and red supergiants (Kiss et al. 2006), and the X-ray light curves of active galaxies (Vaughan et al. 2003), dwarf novae (Hakala et al. 2004) and high-mass X-ray binaries (Burderi 1994).

The physical cause of this red noise in early-type stars is not clear. Below we discuss three possibilities: sub-surface convection, granulation, and inhomogeneities in the stellar wind. We stress that all three are highly speculative and that as yet no modelling exists to see if they would give the correct quantitative behaviour.

A link between red noise and convection was already pointed out by Schwarzschild (1975). For early-type stars, Cantiello et al. (2009) show the existence of a sub-surface convection zone caused by the opacity peak due to iron ionization. The authors show that stars in the HR diagram where this zone is present also show microturbulence, non-radial pulsations, wind clumping, and line-profile variability, suggesting that these are caused by the convection zone. We speculate that the red noise detected in the early-type stars studied here is also a consequence of this convection zone, and could be associated with any of the above observational indicators. The position of our stars in the HR diagram shows that they should have a fairly weak convection zone (see Cantiello et al. 2009, their Fig. 9). This suggests that the high quality of the CoRoT data allows us to see a more subtle effect than Cantiello et al. considered. Instead of attributing the red noise to convection only, there could also be an interaction between pulsation and convection. Perdang (2009) shows that this can result in red-noise dominated light curves.

We also explored if the physical cause of the red noise could be described as granulation. Kallinger & Matthews (2010) show that in the two δ Scuti stars they study, the many hundreds of peaks in the amplitude spectrum can also be interpreted as being caused by granulation. Their Fig. 3 relates the typical frequency of granulation (i.e. the inverse of the timescale) to a specific combination of mass, radius, and effective temperature. Although this relation is based on cooler stars, we nevertheless used it to predict the granulation frequency in our stars. The value we found is $\sim$35 d^{-1}, but this cannot be linked to any significant frequency or inverse timescale of the observations discussed in this paper. If granulation is the cause of the red noise in these hot O stars, it would therefore need to have properties that cannot simply be extrapolated from granulation in cooler-type stars.

Finally, the red noise could be caused by inhomogeneities in the stellar wind. There are various observational indicators showing that the stellar winds of early-type stars are clumped (see review by Puls et al. 2008, and references therein). The exact cause of this clumping is not clear. Intrinsic instabilities in the radiative driving mechanism have been proposed (Owocki & Rybicki 1984), but the onset of clumping seems to happen very close to the stellar surface (Puls et al. 2006). The red noise could therefore be related to the onset of clumping at the stellar surface.

The behaviour of the early-type O stars (spectral types O4–O8) is considerably different from that of later-type stars. When taking out the dominant binary signature of HD 47129 (O8 III/I + O7.5 V/III), a series of frequencies is found that might be caused by pulsations, but a clear red-noise component is present as well (Mahy et al. 2011). HD 46149 (O8,

Degroote et al. 2010) does have significant frequency spacing. HD 46202 (O9 V) shows clear β Cep-like pulsations (Briquet et al. 2011). Observations with the *MOST (Microvariability and Oscillations of Stars)* satellite of the O9.5 V star ζ Oph also show β Cep-type pulsations (Walker et al. 2005). Among the early B-type stars, pulsation frequencies are easily found: Degroote et al. (2009a) present a study of 358 candidate B-star pulsators, showing numerous classical SPBs (slowly-pulsating B stars). We also note that a red-noise component is present in their spectra, but it is much more limited in frequency range than for the stars discussed here (see their Fig. 2).

The present data combined with information from the literature permit a first attempt at empirically mapping the hottest part of the instability strip for β Cep and SPB stars. We can compare the position in the HR diagram of our stars, HD 47129 (Mahy et al. 2011), HD 46149 (Degroote et al. 2010), HD 46202 (Briquet et al. 2011) and ζ Oph (Walker et al. 2005) to theoretical predictions of the β Cep and SPB instability strip. Zdravkov & Pamyatnykh (2008) present the theoretical strip for models up to 40 $M_{\odot}$ for a metallicity $Z = 0.02$. Most of the stars in our list fall into their theoretical β Cep instability strip, but outside the SPB one. Because only a few of these stars actually show β Cep pulsations, this suggests either that the strip is much narrower, or that the pulsations are excited for only a small fraction of the stars in the strip. Especially constraining is a group of three stars (HD 46966, HD 46202 and ζ Oph) that are close to one another in the HR diagram, with HD 46202 and ζ Oph showing β Cep pulsations, but HD 46966 not.

A number of O-type β Cep pulsators have also been detected in ground-based observations (e.g. Telting et al. 2006; De Cat et al. 2007; Pigulski & Pojmański 2008). These are all late O-type stars and therefore close to the three-star group. A detailed knowledge of their astrophysical parameters would allow a better mapping of the instability strip in that part of the HR diagram. In the hotter part, we note the absence of β Cep pulsations in the main-sequence stars discussed here. The theoretical β Cep strip extends to the terminal age main sequence (TAMS), however, and stars more evolved than those studied here could therefore show β Cep pulsations.

7. Conclusions

The CoRoT light curves of the hot O-type stars HD 46223, HD 46150 and HD 46966 were analysed using standard methods to search for pulsation frequencies. The detection of these frequencies would allow an asteroseismological interpretation. However, the results show that most of the variations of these stars are of a stochastic nature. The only significant exception to the above is the possible rotation period detected for HD 46223 and HD 46966, although these conclusions are not strong and still require confirmation. Evidence for a rotation period in the HD 46150 data is even less strong.

The periodogram of these three stars is clearly different from that of a classical pulsator such as HD 46202. Most of the power in our periodograms is not caused by pulsation, but is more correctly described by red noise. Based on the limited number of stars studied so far, a trend is suggested: the earliest O stars show red noise, while the later O-types have pulsational frequencies of the β Cep type. The switch-over occurs around spectral type O8.

The specific physical cause of this noise in O-type stars is at present unclear. We point out the possibilities of subsurface convection, granulation or inhomogeneities in the wind. All three options are highly speculative and therefore await confirmation by detailed modelling. The CoRoT data of these three hot stars present interesting challenges for our understanding of the outer photosphere and inner wind of early-type stars.

Acknowledgements. We thank the CoRoT team for the acquisition and the reduction of the CoRoT data. We also thank F. Martins for making the preliminary results of his analysis available to us. We thank the anonymous referee for his/her constructive comments. L.M., E.G. and G.R. are grateful to the F.N.R.S (Belgium), the PRODEX XMM/Integral contract (Belspo), GAIA DPAC Prodex and the Communauté française de Belgique – Action de recherche concertée – A.R.C. – Académie Wallonie-Europe for their support. P.D. and C.A. acknowledge the financial support of the European Research Council under the European Community's Seventh Framework Programme (FP7/2007–2013)/ERC grant agreement No 227224 (PROSPERITY), from the Research Council of K.U. Leuven (GOA/2008/04), and from the Belgian federal science policy office (C90309: CoRoT Data Exploitation).

References

Aerts, C., Christensen-Dalsgaard, J., & Kurtz, D. W. 2010, Asteroseismology (Dordrecht: Springer)
Auvergne, M., Bodin, P., Boisnard, L., et al. 2009, A&A, 506, 411
Baglin, A., Auvergne, M., Barge, P., et al. 2006, in The CoRoT Mission Pre-Launch Status – Stellar Seismology and Planet Finding, ed. M. Fridlund, A. Baglin, J. Lochard, & L. Conroy (ESA, Noordwijk), ESA SP, 1306, 33
Bisiacchi, G. F., Lopez, J. A., & Firmani, C. 1982, A&A, 107, 252
Bonatto, C., & Bica, E. 2009, MNRAS, 394, 2127
Briquet, M., Aerts, C., Baglin, A., et al. 2011, A&A, 527, A112
Burderi, L. 1994, in Astronomical Society of the Pacific Conf. Ser., Vol. 61, Astronomical Data Analysis Software and Systems III, ed. D. R. Crabtree, R. J. Hanisch, & J. Barnes (California: ASP), 353
Cantiello, M., Langer, N., Brott, I., et al. 2009, A&A, 499, 279
Conti, P. S., & Ebbets, D. 1977, ApJ, 213, 438
Conti, P. S., & Leep, E. M. 1974, ApJ, 193, 113
Conti, P. S., Leep, E. M., & Lorre, J. J. 1977, ApJ, 214, 759
De Cat, P., Briquet, M., Aerts, C., et al. 2007, A&A, 463, 243
Degroote, P., Aerts, C., Ollivier, M., et al. 2009a, A&A, 506, 471
Degroote, P., Briquet, M., Catala, C., et al. 2009b, A&A, 506, 111
Degroote, P., Briquet, M., Auvergne, M., et al. 2010, A&A, 519, A38
Diago, P. D., Gutiérrez-Soto, J., Auvergne, M., et al. 2009, A&A, 506, 125
Dupret, M.-A., De Ridder, J., De Cat, P., et al. 2003, A&A, 398, 677
Garmany, C. D., Conti, P. S., & Massey, P. 1980, ApJ, 242, 1063
Gosset, E. 2007, Le calcul du niveau de signification du plus haut pic dans les périodogrammes de type Fourier par la formule de Horne-Baliunas est contreindiqué, Thèse d'Agrégation de l'Enseignement Supérieur, Seconde Thèse Annexe, University of Liège, Liège
Gosset, E., Royer, P., Rauw, G., Manfroid, J., & Vreux, J. 2001, MNRAS, 327, 435
Grevesse, N., & Noels, A. 1993, in Perfectionnement de l'Association Vaudoise des Chercheurs en Physique, AVCP, Lausanne, 205
Hakala, P., Ramsay, G., Wheatley, P., Harlaftis, E. T., & Papadimitriou, C. 2004, A&A, 420, 273
Hannan, E. J. 1980, Ann. Stat., 8, 1071
Hannan, E. J., & Quinn, B. 1979, J. Roy. Stat. Soc. Ser. B, 41, 190
Heck, A., Manfroid, J., & Mersch, G. 1985, A&AS, 59, 63, (HMM)
Hensberge, H., Pavlovski, K., & Verschueren, W. 2000, A&A, 358, 553
Hillier, D. J., & Miller, D. L. 1998, ApJ, 496, 407
Hiltner, W. A. 1956, ApJS, 2, 389
Howarth, I. D., & Reid, A. H. N. 1993, A&A, 279, 148
Huat, A.-L., Hubert, A.-M., Baudin, F., et al. 2009, A&A, 506, 95
Kallinger, T., & Matthews, J. M. 2010, ApJ, 711, L35
Kambe, E., Hirata, R., Ando, H., et al. 1997, ApJ, 481, 406
Kiss, L. L., Szabó, G. M., & Bedding, T. R. 2006, MNRAS, 372, 1721
Liddle, A. R. 2007, MNRAS, 377, L74
Lomb, N. R. 1976, Ap&SS, 39, 447
Loumos, G. L., & Deeming, T. J. 1978, Ap&SS, 56, 285
Lucy, L. B., & Sweeney, M. A. 1971, AJ, 76, 544
Mahy, L., Nazé, Y., Rauw, G., et al. 2009, A&A, 502, 937
Mahy, L., Gosset, E., Baudin, F., et al. 2011, A&A, 525, A101
Maíz-Apellániz, J., Walborn, N. R., Galué, H. Á., & Wei, L. H. 2004, ApJS, 151, 103
Massey, P., Johnson, K. E., & Degioia-Eastwood, K. 1995, ApJ, 454, 151
Montgomery, M. H., & O'Donoghue, D. 1999, Delta Scuti Star Newsletter, 13, 28
Munari, U., & Tomasella, L. 1999, A&AS, 137, 521
Owocki, S. P., & Rybicki, G. B. 1984, ApJ, 284, 337

Perdang, J. 2009, in EAS Pub. Ser., 38, ed. M. Goupil, Z. Koláth, N. Nardetto, & P. Kervella (Les Ulis, France: EDP), 43
Pigulski, A., & Pojmański, G. 2008, A&A, 477, 917
Press, W. H., Teukolsky, S. A., Vetterling, W. T., & Flannery, B. P. 1992, Numerical recipes in FORTRAN. The art of scientific computing, 2nd edn. (Cambridge: University Press)
Puls, J., Markova, N., Scuderi, S., et al. 2006, A&A, 454, 625
Puls, J., Vink, J. S., & Najarro, F. 2008, A&ARv, 16, 209
Rauw, G., De Becker, M., van Winckel, H., et al. 2008, A&A, 487, 659
Samadi, R., Fialho, F., Costa, J. E. S., et al. 2007 [arXiv:astro-ph/0703354]
Scargle, J. D. 1982, ApJ, 263, 835
Schwarzschild, M. 1975, ApJ, 195, 137
Stanishev, V., Kraicheva, Z., Boffin, H. M. J., & Genkov, V. 2002, A&A, 394, 625
Telting, J. H., Schrijvers, C., Ilyin, I. V., Uytterhoeven, K., et al. 2006, A&A, 452, 945
Templeton, M. R., & Karovska, M. 2009, ApJ, 691, 1470
Timmer, J. & Koenig, M. 1995, A&A, 300, 707
Underhill, A. B., & Gilroy, K. K. 1990, ApJ, 364, 626
Vaughan, S., Edelson, R., Warwick, R. S., & Uttley, P. 2003, MNRAS, 345, 1271
Ventura, P., D'Antona, F., & Mazzitelli, I. 2008, Ap&SS, 316, 93
Walker, G. A. H., Kuschnig, R., Matthews, J. M., et al. 2005, ApJ, 623, L145
Wang, J., Townsley, L. K., Feigelson, E. D., et al. 2008, ApJ, 675, 464
Zdravkov, T., & Pamyatnykh, A. A. 2008, J. Phys. Conf. Ser., 118, 012079

Appendix B

Frequency lists derived from the CoRoT photometry

Table B.1: Lists of frequencies extracted from the CoRoT light curves.

n	Frequency (d^{-1})	Error on the frequency (d^{-1})	Semi-ampl. (counts)	Error on the semi-ampl. (counts)	Phase (radians)	Error on the phase (radians)	Variance	Significance level under whitenoise	Significance level under rednoise
				Plaskett					
1	0.823	0.000	65390.288	527.361	-1.220	0.008	11109771401.078	0.000	0.000
2	1.646	0.000	93015.317	467.349	-0.622	0.005	8725245792.296	0.000	0.000
3	2.469	0.000	18497.051	334.051	-0.747	0.018	4457787741.458	0.000	0.000
4	3.292	0.001	8644.425	327.459	0.220	0.038	4283587618.761	0.748	0.000
5	4.115	0.003	2057.559	326.032	-0.037	0.158	4246357810.141	1.000	0.000
6	4.938	0.003	1636.017	325.953	-0.965	0.199	4244285611.435	1.000	0.000
7	5.761	0.002	3388.720	325.900	0.982	0.096	4242909187.673	1.000	0.000
8	0.069	0.000	38907.662	325.691	-1.084	0.008	4237473433.108	0.000	0.000
9	0.139	0.000	24156.572	290.653	1.335	0.012	3375059701.254	0.000	0.000
10	0.208	0.004	1196.440	281.284	-1.284	0.235	3160703096.832	1.000	1.000
11	0.370	0.000	32074.725	279.935	-1.213	0.009	3154152042.999	0.000	0.000
12	0.648	0.000	19199.730	260.150	1.264	0.014	2703557776.892	0.000	0.000
13	0.399	0.000	16520.039	245.528	0.230	0.015	2408203329.473	0.000	0.016
14	0.887	0.000	20771.107	234.128	-0.513	0.011	2189759667.949	0.000	0.000
15	0.935	0.000	19778.638	224.062	-0.309	0.011	2005508930.832	0.000	0.000
16	0.441	0.000	18829.569	215.765	-1.337	0.011	1859730204.625	0.000	0.000
17	0.543	0.000	15522.473	207.592	-0.173	0.013	1721510453.475	0.000	0.007
18	0.800	0.000	16470.149	199.731	-1.020	0.012	1593596913.339	0.000	0.000
19	0.270	0.000	12368.277	191.653	-0.856	0.015	1467308611.359	0.000	1.000
20	0.606	0.000	15554.667	184.259	0.687	0.012	1356274256.302	0.000	0.001
21	0.572	0.000	13579.510	177.776	1.521	0.013	1262507929.097	0.000	0.157
22	1.214	0.000	13854.300	171.629	-1.481	0.012	1176711693.751	0.000	0.000
23	1.185	0.000	10179.754	165.549	0.573	0.016	1094818712.747	0.000	0.000
24	0.233	0.000	12974.596	159.937	1.442	0.012	1021848553.838	0.000	1.000
25	1.056	0.000	10659.468	154.223	0.991	0.014	950144514.945	0.000	0.000
26	1.267	0.000	12313.703	149.339	-0.424	0.012	890920021.428	0.000	0.000
27	0.495	0.000	9796.200	144.671	-0.468	0.015	836090683.693	0.000	1.000
28	1.000	0.000	9862.043	139.414	0.124	0.014	776435003.885	0.000	0.010
29	0.113	0.000	10070.317	134.864	-0.958	0.013	726581194.733	0.000	1.000
30	0.857	0.000	10647.324	129.873	0.601	0.012	673792838.275	0.000	0.081
31	1.334	0.000	10051.436	125.318	-0.956	0.012	627354793.089	0.000	0.000
32	1.360	0.000	9568.077	120.750	0.470	0.013	582459610.569	0.000	0.000
33	1.559	0.000	8377.653	115.775	-0.885	0.014	535445834.817	0.000	0.000

Table B.1 – continued

n	Frequency (d^{-1})	Error on the frequency (d^{-1})	Semi-ampl. (counts)	Error on the semi-ampl. (counts)	Phase (radians)	Error on the phase (radians)	Variance	Significance level under whitenoise	Significance level under rednoise
34	0.037	0.000	8117.545	112.128	1.098	0.014	502250766.334	0.000	1.000
35	0.717	0.000	8501.412	108.446	0.375	0.013	469806420.275	0.000	1.000
36	0.179	0.000	8208.499	104.776	0.185	0.013	438547576.895	0.000	1.000
37	0.911	0.000	8518.063	100.675	-0.829	0.012	404887670.094	0.000	0.980
38	0.342	0.000	7677.982	97.087	0.479	0.013	376539636.705	0.000	1.000
39	1.889	0.000	6861.751	93.606	0.256	0.014	350024755.555	0.000	0.000
40	1.145	0.000	6352.882	90.426	0.893	0.014	326646851.361	0.000	1.000
41	1.685	0.000	5146.177	87.804	-1.263	0.017	307977784.458	0.000	0.010
42	0.472	0.000	4802.539	85.474	0.043	0.018	291849665.366	0.000	1.000
43	1.410	0.000	4830.456	83.265	-0.638	0.017	276960669.570	0.000	1.000
44	0.295	0.000	4981.728	81.200	1.231	0.016	263389766.548	0.000	1.000
45	1.623	0.000	4678.823	79.188	-1.422	0.017	250498216.947	0.000	0.409
46	0.761	0.000	5179.399	77.187	-1.512	0.015	238002289.323	0.000	1.000
47	0.975	0.000	4691.224	75.177	0.784	0.016	225768630.433	0.000	1.000
48	1.865	0.000	4007.611	72.981	1.068	0.018	212767367.542	0.000	0.184
49	2.085	0.000	4705.696	70.863	1.434	0.015	200596118.523	0.000	0.000
50	1.783	0.000	4676.150	68.570	-0.424	0.015	187829629.120	0.000	0.016
51	0.693	0.000	4023.876	66.936	-1.499	0.017	178980860.939	0.000	1.000
52	0.018	0.000	2333.130	65.265	1.245	0.028	170156969.312	0.004	1.000
53	1.308	0.000	3806.768	63.946	1.467	0.017	163348354.892	0.000	1.000
54	0.519	0.000	3752.534	62.391	-0.892	0.017	155501775.912	0.000	1.000
55	1.948	0.000	4365.908	60.836	-1.129	0.014	147844333.049	0.000	0.003
56	0.627	0.000	3534.168	59.330	1.333	0.017	140615752.746	0.000	1.000
57	2.313	0.000	2970.519	57.794	-1.323	0.019	133432495.191	0.000	0.143
58	1.591	0.000	3602.858	56.378	0.348	0.016	126972131.902	0.000	1.000
59	2.045	0.000	3982.436	54.973	0.795	0.014	120723343.712	0.000	0.006
60	1.090	0.000	3429.068	53.639	0.250	0.016	114936598.753	0.000	1.000
61	2.824	0.000	3248.987	52.418	-0.652	0.016	109759934.845	0.000	0.000
62	1.119	0.000	2954.676	51.277	-1.548	0.017	105035041.261	0.000	1.000
63	2.446	0.000	3051.276	50.160	0.096	0.016	100509266.792	0.000	0.007
64	0.088	0.000	2838.638	49.046	0.030	0.017	96095918.322	0.000	1.000
65	1.521	0.000	2903.890	47.944	-0.275	0.017	91823730.538	0.000	1.000
66	2.009	0.000	3036.131	46.852	0.941	0.015	87690536.840	0.000	1.000
67	2.504	0.000	2909.505	45.710	1.433	0.016	83465514.046	0.000	0.010
68	1.024	0.000	2856.375	44.616	-1.116	0.016	79518353.757	0.000	1.000

Table B.1 – continued

n	Frequency (d^{-1})	Error on the frequency (d^{-1})	Semi-ampl. (counts)	Error on the semi-ampl. (counts)	Phase (radians)	Error on the phase (radians)	Variance	Significance level under whitenoise	Significance level under rednoise
69	3.313	0.000	2213.980	43.476	-1.373	0.020	75505696.961	0.000	0.000
70	1.816	0.000	2638.933	42.452	0.402	0.016	71993798.103	0.000	1.000
71	1.489	0.000	2433.128	41.508	-0.874	0.017	68826214.088	0.000	1.000
72	2.273	0.000	2070.906	40.567	0.013	0.020	65739808.892	0.000	1.000
73	3.060	0.000	2119.165	39.732	1.176	0.019	63063586.753	0.000	0.019
74	1.446	0.000	2086.090	38.937	-0.744	0.019	60564369.389	0.000	1.000
75	1.242	0.000	2025.352	38.249	-1.111	0.019	58441741.259	0.000	1.000
76	1.737	0.000	2027.004	37.614	-1.484	0.019	56517387.022	0.000	1.000
77	3.031	0.000	1835.180	36.923	-0.468	0.020	54461662.272	0.000	0.671
78	2.137	0.000	1619.716	36.324	-0.705	0.022	52706680.216	0.000	1.000
79	0.421	0.000	1794.400	35.757	0.793	0.020	51074292.276	0.000	1.000
80	2.365	0.000	1664.916	35.189	-0.077	0.021	49466676.564	0.000	1.000
81	2.683	0.000	1686.050	34.656	0.046	0.021	47979800.724	0.000	1.000
82	3.220	0.000	2113.893	34.132	-0.893	0.016	46539524.871	0.000	0.002
83	3.001	0.000	1638.319	33.596	1.146	0.021	45088286.688	0.000	1.000
84	2.584	0.000	1710.263	33.084	0.369	0.019	43724605.604	0.000	1.000
85	3.968	0.000	1604.845	32.586	-1.440	0.020	42416941.417	0.000	0.000
86	2.735	0.000	1561.932	32.110	-1.216	0.021	41188039.140	0.000	1.000
87	3.266	0.000	1727.239	31.628	0.641	0.018	39960700.313	0.000	0.292
88	2.212	0.000	1560.072	31.101	-0.193	0.020	38639831.833	0.000	1.000
89	0.052	0.000	1438.252	30.641	1.090	0.021	37505428.447	0.000	1.000
90	0.591	0.000	1503.947	30.199	-1.043	0.020	36432138.498	0.000	1.000
91	0.720	0.000	1535.807	29.742	-0.378	0.019	35336408.416	0.000	1.000
92	4.508	0.000	1455.464	29.262	-0.680	0.020	34206052.255	0.000	0.000
93	4.709	0.000	1261.282	28.843	-1.330	0.023	33233514.117	0.000	0.000
94	2.416	0.000	1227.078	28.467	-0.033	0.023	32372602.736	0.000	1.000
95	0.156	0.000	1275.219	28.099	-1.528	0.022	31539668.847	0.000	1.000
96	1.657	0.000	1219.299	27.727	-0.585	0.023	30711182.747	0.000	1.000
97	0.658	0.000	1320.984	27.368	0.645	0.021	29920835.211	0.000	1.000
98	2.759	0.000	1182.523	27.003	0.801	0.023	29128631.864	0.000	1.000
99	3.675	0.000	1301.685	26.649	0.870	0.020	28368975.031	0.000	0.971
100	4.094	0.000	1235.193	26.300	-0.610	0.021	27631665.574	0.000	0.275
101	1.281	0.000	1122.343	25.961	-1.187	0.023	26922908.680	0.000	1.000
102	1.556	0.000	1164.499	25.635	-0.305	0.022	26252166.363	0.000	1.000
103	1.921	0.000	1205.536	25.297	0.534	0.021	25564929.207	0.000	1.000

Table B.1 – continued

n	Frequency (d^{-1})	Error on the frequency (d^{-1})	Semi-ampl. (counts)	Error on the semi-ampl. (counts)	Phase (radians)	Error on the phase (radians)	Variance	Significance level under whitenoise	Significance level under rednoise
104	4.881	0.000	1078.664	24.954	-0.610	0.023	24875598.358	0.000	0.009
105	0.946	0.000	1133.389	24.618	0.352	0.022	24209699.734	0.000	1.000
106	3.816	0.000	879.204	24.277	-0.523	0.028	23543968.025	0.003	1.000
107	3.177	0.000	1113.278	23.935	0.061	0.021	22885626.292	0.000	1.000
108	0.248	0.000	1081.325	23.619	-0.287	0.022	22285079.141	0.000	1.000
109	4.337	0.000	1055.367	23.312	0.147	0.022	21709493.715	0.000	0.800
110	3.413	0.000	1043.092	23.004	0.902	0.022	21138703.735	0.000	1.000
111	4.441	0.000	993.938	22.701	-0.325	0.023	20585967.200	0.000	0.930
112	2.945	0.000	1134.356	22.393	-0.478	0.020	20032177.133	0.000	1.000
113	2.171	0.000	1087.776	22.108	0.188	0.020	19524592.804	0.000	1.000
114	2.630	0.000	967.827	21.829	1.547	0.023	19035273.559	0.000	1.000
115	2.476	0.000	1009.935	21.543	0.512	0.021	18539960.101	0.000	1.000
116	0.448	0.000	882.688	21.297	-0.867	0.024	18118433.588	0.000	1.000
117	2.845	0.000	832.509	21.076	1.057	0.025	17745139.626	0.000	1.000
118	3.730	0.000	928.248	20.851	-0.742	0.022	17367611.489	0.000	1.000
119	0.793	0.000	882.502	20.622	-1.480	0.023	16988062.954	0.000	1.000
120	4.216	0.000	864.742	20.389	-0.984	0.024	16606943.595	0.000	1.000
121	3.130	0.000	873.663	20.174	0.505	0.023	16259003.015	0.000	1.000
122	1.066	0.000	823.940	19.954	1.092	0.024	15904789.189	0.000	1.000
123	3.536	0.000	841.120	19.740	-0.961	0.023	15566990.439	0.000	1.000
124	6.593	0.000	842.502	19.529	1.127	0.023	15234967.807	0.000	0.000
125	7.410	0.000	824.895	19.318	1.537	0.023	14907505.746	0.000	0.000
126	3.602	0.000	813.049	19.108	-0.311	0.024	14584973.269	0.000	1.000
127	3.445	0.000	889.144	18.888	-1.098	0.021	14252015.932	0.000	1.000
128	8.228	0.000	792.539	18.677	-0.077	0.024	13934902.634	0.000	0.000
129	3.366	0.000	860.704	18.469	-1.218	0.021	13626726.468	0.000	1.000
130	3.926	0.000	842.820	18.258	-0.001	0.022	13316059.732	0.000	1.000
131	5.644	0.000	772.225	18.047	-0.720	0.023	13010973.543	0.000	0.207
132	2.879	0.000	758.868	17.862	1.557	0.024	12745530.873	0.000	1.000
133	3.771	0.000	809.116	17.668	1.167	0.022	12469300.319	0.000	1.000
134	1.151	0.000	705.235	17.458	-0.101	0.025	12174764.772	0.000	1.000
135	4.020	0.000	720.901	17.275	0.221	0.024	11921442.624	0.000	1.000
136	9.056	0.000	694.998	17.093	-0.467	0.025	11671750.491	0.000	0.000
137	5.352	0.000	701.701	16.916	-0.675	0.024	11431352.726	0.000	1.000
138	5.698	0.000	699.734	16.740	-1.071	0.024	11194079.292	0.000	0.802

Table B.1 – continued

n	Frequency (d^{-1})	Error on the frequency (d^{-1})	Semi-ampl. (counts)	Error on the semi-ampl. (counts)	Phase (radians)	Error on the phase (radians)	Variance	Significance level under whitenoise	Significance level under rednoise
139	2.532	0.000	679.924	16.558	1.130	0.024	10952406.658	0.000	1.000
140	4.366	0.000	664.335	16.385	-1.007	0.025	10724758.612	0.000	1.000
141	4.785	0.000	721.302	16.219	-0.507	0.022	10508244.994	0.000	1.000
142	4.662	0.000	756.173	16.048	1.176	0.021	10288570.990	0.000	1.000
143	2.796	0.000	622.839	15.877	0.885	0.025	10069448.127	0.000	1.000
144	5.850	0.000	656.677	15.720	-1.239	0.024	9871993.211	0.000	0.929
145	4.557	0.000	599.555	15.568	1.011	0.026	9681909.510	0.001	1.000
146	2.605	0.000	581.758	15.410	0.149	0.026	9486076.033	0.001	1.000
147	0.396	0.000	578.153	15.260	-0.097	0.026	9302248.022	0.001	1.000
148	4.167	0.001	471.776	15.113	-0.279	0.032	9123895.806	0.085	1.000
149	3.483	0.000	586.280	14.963	-0.475	0.026	8944380.192	0.000	1.000
150	3.636	0.000	566.320	14.831	0.726	0.026	8787099.625	0.001	1.000
151	4.250	0.000	638.914	14.698	0.840	0.023	8629820.911	0.000	1.000
152	2.985	0.000	552.041	14.567	1.081	0.026	8476720.412	0.001	1.000
153	0.824	0.000	522.104	14.436	-0.189	0.028	8325508.809	0.003	1.000
154	1.716	0.000	520.401	14.309	-1.261	0.027	8178877.547	0.003	1.000
155	5.019	0.000	514.891	14.193	1.062	0.028	8046606.997	0.003	1.000
156	4.127	0.000	567.874	14.075	-0.787	0.025	7914331.474	0.000	1.000
157	3.884	0.000	494.194	13.952	-1.301	0.028	7775827.240	0.006	1.000
158	2.340	0.000	456.024	13.833	-0.183	0.030	7643755.880	0.029	1.000
159	6.685	0.000	511.147	13.716	-1.306	0.027	7515554.189	0.001	0.999
160	0.553	0.000	498.068	13.608	-0.114	0.027	7397274.604	0.002	1.000
161	3.335	0.000	483.892	13.500	1.474	0.028	7280282.754	0.004	1.000
162	6.312	0.000	515.170	13.392	1.361	0.026	7163962.121	0.001	1.000
163	2.246	0.000	456.322	13.286	0.200	0.029	7051221.041	0.012	1.000
164	4.617	0.000	516.357	13.179	0.135	0.026	6938696.890	0.000	1.000
165	5.597	0.000	464.465	13.068	1.432	0.028	6821506.825	0.005	1.000
166	5.081	0.000	436.982	12.958	-0.231	0.030	6707587.067	0.017	1.000
167	2.066	0.000	466.130	12.857	-1.204	0.028	6603534.670	0.003	1.000
168	4.062	0.000	460.687	12.760	-1.142	0.028	6504196.708	0.003	1.000
169	4.304	0.000	466.558	12.659	1.485	0.027	6401768.435	0.002	1.000
170	0.197	0.000	431.888	12.557	-0.527	0.029	6298905.271	0.011	1.000
171	1.192	0.000	417.609	12.462	0.545	0.030	6204116.538	0.020	1.000
172	5.271	0.000	462.724	12.368	0.810	0.027	6110676.326	0.001	1.000
173	5.229	0.000	413.073	12.277	0.182	0.030	6021019.810	0.018	1.000

Table B.1 – continued

n	Frequency (d^{-1})	Error on the frequency (d^{-1})	Semi-ampl. (counts)	Error on the semi-ampl. (counts)	Phase (radians)	Error on the phase (radians)	Variance	Significance level under whitenoise	Significance level under rednoise
174	1.981	0.000	393.923	12.189	0.383	0.031	5934629.731	0.043	1.000
175	5.414	0.000	412.857	12.105	1.416	0.029	5853533.816	0.014	1.000
176	6.412	0.000	387.686	12.022	0.619	0.031	5773162.409	0.045	1.000
177	4.486	0.000	402.408	11.937	0.026	0.030	5691980.445	0.018	1.000
178	0.279	0.000	410.298	11.851	0.450	0.029	5610471.416	0.010	1.000
179	2.558	0.000	388.493	11.767	-0.179	0.030	5531151.942	0.028	1.000
180	0.915	0.000	388.058	11.681	-0.249	0.030	5450511.469	0.024	1.000
181	4.912	0.000	403.907	11.601	0.568	0.029	5376257.511	0.008	1.000
182	5.946	0.000	400.811	11.519	-0.787	0.029	5300949.346	0.009	1.000
183	6.020	0.000	413.277	11.438	-0.757	0.028	5225995.612	0.003	1.000
184	6.055	0.000	400.051	11.356	0.492	0.028	5151958.718	0.006	1.000
185	7.134	0.000	379.247	11.271	-1.009	0.030	5075129.394	0.018	1.000
186	11.523	0.000	364.877	11.192	0.979	0.031	5003875.314	0.036	0.000
187	0.327	0.000	382.380	11.116	-0.561	0.029	4936430.903	0.011	1.000
188	3.097	0.000	370.066	11.039	-0.826	0.030	4867571.314	0.020	1.000
189	5.791	0.000	364.671	10.963	1.098	0.030	4800791.307	0.024	1.000
190	5.506	0.000	360.304	10.890	1.554	0.030	4737173.602	0.027	1.000
191	6.520	0.001	337.790	10.815	0.801	0.032	4672832.311	0.084	1.000
192	1.386	0.000	367.227	10.742	0.407	0.029	4609725.293	0.013	1.000
193	1.462	0.000	360.505	10.670	0.559	0.030	4547861.170	0.017	1.000
194	0.748	0.000	365.363	10.593	-0.215	0.029	4482720.793	0.010	1.000
195	4.194	0.001	330.731	10.520	-1.441	0.032	4421310.489	0.074	1.000
196	3.297	0.000	355.308	10.449	-1.496	0.029	4361746.523	0.015	1.000
197	1.895	0.000	356.112	10.379	1.410	0.029	4303516.636	0.012	1.000
198	1.012	0.001	314.048	10.311	0.114	0.033	4247416.176	0.131	1.000
199	8.610	0.001	319.444	10.243	0.347	0.032	4191515.903	0.086	1.000
200	3.510	0.000	334.846	10.177	0.810	0.030	4137051.683	0.030	1.000
					HD 46223				
1	0.754	0.000	932.705	16.442	0.340	0.018	10867991.663	0.000	0.000
2	0.248	0.000	850.467	16.066	-1.061	0.019	10376696.081	0.000	0.000
3	0.506	0.000	791.205	15.762	1.152	0.020	9987655.255	0.000	0.000
4	0.684	0.000	775.321	15.519	1.433	0.020	9682337.183	0.000	0.000
5	1.192	0.000	712.818	15.286	-1.122	0.021	9393499.721	0.000	0.000
6	1.846	0.000	690.853	15.083	0.435	0.022	9146256.867	0.000	0.000
7	0.422	0.000	674.664	14.883	0.253	0.022	8905162.705	0.000	0.000

Table B.1 – continued

n	Frequency (d^{-1})	Error on the frequency (d^{-1})	Semi-ampl. (counts)	Error on the semi-ampl. (counts)	Phase (radians)	Error on the phase (radians)	Variance	Significance level under whitenoise	Significance level under rednoise
8	0.039	0.000	697.285	14.696	-0.798	0.021	8682974.272	0.000	0.000
9	0.794	0.000	728.438	14.499	-0.795	0.020	8451220.700	0.000	0.000
10	1.436	0.000	662.771	14.319	-0.407	0.022	8242135.942	0.000	0.000
11	0.946	0.000	649.054	14.145	-0.788	0.022	8044018.627	0.000	0.000
12	0.715	0.000	719.815	13.973	-0.290	0.019	7849607.928	0.000	0.000
13	0.643	0.000	575.829	13.801	-0.268	0.024	7657130.046	0.000	0.000
14	0.155	0.000	610.610	13.633	1.265	0.022	7471315.511	0.000	0.000
15	0.544	0.000	573.062	13.464	0.011	0.023	7287367.341	0.000	0.000
16	0.387	0.000	557.141	13.314	-0.974	0.024	7126500.889	0.000	0.000
17	1.269	0.000	584.844	13.169	-1.136	0.023	6971603.086	0.000	0.000
18	2.861	0.000	483.492	13.035	0.087	0.027	6830315.492	0.002	0.008
19	2.190	0.000	508.787	12.912	1.570	0.025	6702159.130	0.000	0.002
20	0.311	0.000	501.725	12.795	0.358	0.026	6581210.958	0.000	0.003
21	1.012	0.000	473.009	12.677	-0.517	0.027	6460270.501	0.002	0.014
22	2.776	0.000	489.600	12.566	-1.368	0.026	6348261.703	0.000	0.006
23	3.031	0.000	479.696	12.451	-0.841	0.026	6232578.826	0.001	0.010
24	1.311	0.000	491.625	12.337	-0.633	0.025	6118742.008	0.000	0.005
25	0.214	0.000	469.661	12.220	-1.554	0.026	6003448.599	0.001	0.016
26	1.708	0.000	443.590	12.115	0.349	0.027	5900220.326	0.003	0.054
27	2.569	0.000	424.125	12.013	0.977	0.028	5801459.061	0.006	0.123
28	1.944	0.000	424.748	11.915	-1.057	0.028	5707125.250	0.005	0.120
29	4.901	0.000	428.811	11.817	-1.366	0.028	5613667.137	0.003	0.101
30	1.107	0.000	414.545	11.718	0.393	0.028	5520321.327	0.006	0.180
31	0.111	0.000	431.158	11.627	0.812	0.027	5434745.694	0.002	0.092
32	3.284	0.000	404.410	11.532	-1.104	0.029	5346712.873	0.008	0.262
33	1.753	0.000	399.134	11.444	-1.417	0.029	5264827.147	0.009	0.315
34	3.526	0.000	431.595	11.356	0.869	0.026	5183979.583	0.001	0.090
35	3.594	0.000	411.518	11.267	-0.057	0.027	5103276.193	0.003	0.202
36	2.345	0.000	414.205	11.175	-0.193	0.027	5020274.238	0.002	0.182
37	1.400	0.000	411.030	11.085	1.471	0.027	4939896.518	0.002	0.206
38	0.841	0.000	470.893	10.996	-0.525	0.023	4860559.817	0.000	0.015
39	0.880	0.000	445.968	10.906	-1.298	0.024	4781420.660	0.000	0.048
40	0.343	0.000	397.063	10.801	-1.342	0.027	4690244.869	0.002	0.338
41	4.016	0.000	393.236	10.709	1.418	0.027	4610417.557	0.002	0.382
42	6.521	0.000	389.377	10.621	-1.128	0.027	4535336.787	0.002	0.430

Table B.1 – continued

n	Frequency (d^{-1})	Error on the frequency (d^{-1})	Semi-ampl. (counts)	Error on the semi-ampl. (counts)	Phase (radians)	Error on the phase (radians)	Variance	Significance level under whitenoise	Significance level under rednoise
43	3.101	0.000	375.931	10.534	-0.603	0.028	4460846.668	0.005	0.615
44	1.505	0.000	390.969	10.450	-0.458	0.027	4390252.283	0.001	0.410
45	4.621	0.000	376.927	10.367	0.088	0.028	4320835.116	0.003	0.600
46	0.604	0.000	366.338	10.282	0.000	0.028	4250387.365	0.005	0.747
47	2.097	0.000	353.613	10.201	1.283	0.029	4183317.392	0.010	0.889
48	1.629	0.000	345.899	10.125	1.422	0.029	4120962.334	0.014	0.945
49	1.979	0.000	344.166	10.051	0.245	0.029	4061320.442	0.013	0.954
50	6.610	0.000	341.682	9.978	-1.427	0.029	4002530.158	0.013	0.966
51	6.429	0.000	339.444	9.907	0.926	0.029	3945703.977	0.013	0.974
52	1.365	0.000	324.909	9.836	1.354	0.030	3889126.994	0.029	0.997
53	6.018	0.000	327.063	9.768	-0.848	0.030	3835861.406	0.022	0.996
54	2.726	0.000	331.801	9.699	-1.046	0.029	3781689.221	0.014	0.991
55	2.395	0.000	325.198	9.631	-0.486	0.030	3728590.511	0.018	0.997
56	5.455	0.000	312.549	9.562	-1.271	0.031	3675678.860	0.037	1.000
57	5.569	0.000	309.725	9.498	-1.423	0.031	3626954.676	0.038	1.000
58	6.759	0.000	306.086	9.435	0.813	0.031	3578715.751	0.043	1.000
59	7.553	0.000	314.445	9.373	-1.448	0.030	3532117.282	0.021	1.000
60	3.218	0.000	309.335	9.310	0.067	0.030	3484774.868	0.026	1.000
61	1.214	0.000	304.599	9.250	0.005	0.030	3439933.775	0.031	1.000
62	2.910	0.000	298.603	9.188	0.995	0.031	3393567.481	0.041	1.000
63	7.257	0.001	292.691	9.127	-0.808	0.031	3348509.123	0.054	1.000
64	3.782	0.001	290.860	9.068	0.758	0.031	3305614.187	0.054	1.000
65	2.279	0.000	297.633	9.010	-0.291	0.030	3263305.869	0.029	1.000
66	2.474	0.001	283.558	8.952	-0.174	0.032	3221321.740	0.068	1.000
67	3.150	0.000	295.115	8.894	-1.406	0.030	3180016.826	0.027	1.000
68	7.683	0.000	289.415	8.836	0.512	0.031	3139052.044	0.035	1.000
69	6.357	0.000	283.659	8.779	-0.940	0.031	3098276.204	0.046	1.000
70	2.143	0.000	282.640	8.722	-1.193	0.031	3058352.086	0.044	1.000
71	7.335	0.001	271.973	8.666	-0.026	0.032	3018891.341	0.081	1.000
72	3.455	0.001	257.428	8.612	-0.339	0.033	2981754.306	0.188	1.000
73	3.406	0.001	266.930	8.564	1.271	0.032	2948775.056	0.092	1.000
74	4.929	0.001	257.349	8.516	0.058	0.033	2915250.076	0.157	1.000
75	0.067	0.001	241.549	8.468	1.116	0.035	2882875.721	0.367	1.000
76	3.733	0.001	251.767	8.423	0.694	0.033	2852335.270	0.188	1.000
77	5.937	0.001	261.831	8.377	1.128	0.032	2820918.717	0.088	1.000

Table B.1 – continued

n	Frequency (d^{-1})	Error on the frequency (d^{-1})	Semi-ampl. (counts)	Error on the semi-ampl. (counts)	Phase (radians)	Error on the phase (radians)	Variance	Significance level under whitenoise	Significance level under rednoise
78	6.077	0.001	250.268	8.329	0.334	0.033	2789202.015	0.173	1.000
79	8.802	0.001	234.099	8.284	1.552	0.035	2758709.695	0.411	1.000
80	1.667	0.001	233.376	8.242	1.460	0.035	2731079.572	0.401	1.000
81	3.825	0.001	236.110	8.201	-0.317	0.035	2703943.213	0.325	1.000
82	7.007	0.001	238.776	8.161	-1.357	0.034	2677291.949	0.260	1.000
83	5.259	0.001	230.816	8.121	-0.279	0.035	2651444.818	0.383	1.000
84	2.657	0.001	228.771	8.082	0.959	0.035	2625716.760	0.403	1.000
85	5.651	0.001	226.523	8.042	1.272	0.036	2599766.472	0.427	1.000
86	4.055	0.001	218.920	8.002	1.260	0.037	2574457.553	0.580	1.000
87	7.141	0.001	220.696	7.965	-1.075	0.036	2550717.440	0.512	1.000
88	8.835	0.001	216.957	7.928	0.202	0.037	2527010.401	0.578	1.000
89	3.952	0.000	254.623	7.891	1.175	0.031	2503451.345	0.048	1.000
90	3.995	0.001	232.264	7.855	0.385	0.034	2480187.906	0.222	1.000
91	3.629	0.001	212.494	7.812	-0.341	0.037	2453129.741	0.610	1.000
92	4.400	0.001	206.964	7.776	1.038	0.038	2431017.173	0.723	1.000
93	6.272	0.001	203.822	7.741	0.112	0.038	2409112.815	0.775	1.000
94	9.103	0.001	204.453	7.707	0.937	0.038	2387861.468	0.739	1.000
95	4.787	0.001	204.102	7.673	0.477	0.038	2366933.109	0.726	1.000
96	1.870	0.001	201.715	7.640	0.960	0.038	2346276.467	0.762	1.000
97	8.627	0.001	198.848	7.606	-1.301	0.038	2325975.007	0.806	1.000
98	5.983	0.001	204.250	7.574	-0.110	0.037	2306178.229	0.656	1.000
99	5.618	0.001	205.121	7.541	-1.119	0.037	2286291.834	0.611	1.000
100	2.016	0.001	203.157	7.508	-0.820	0.037	2266409.107	0.639	1.000
101	7.622	0.001	198.839	7.475	-0.133	0.038	2246557.394	0.726	1.000
102	0.450	0.001	198.847	7.443	-1.208	0.037	2226912.586	0.704	1.000
103	4.217	0.001	220.955	7.410	-1.307	0.034	2207595.355	0.195	1.000
104	4.142	0.001	203.719	7.378	-1.176	0.036	2188473.189	0.530	1.000
105	4.724	0.001	201.399	7.344	0.126	0.036	2168053.405	0.566	1.000
106	2.511	0.001	188.220	7.312	1.181	0.039	2149338.883	0.867	1.000
107	6.890	0.001	198.824	7.281	-1.390	0.037	2130964.123	0.589	1.000
108	7.895	0.001	188.128	7.250	1.072	0.039	2112924.085	0.837	1.000
109	7.287	0.001	189.756	7.219	0.934	0.038	2094985.294	0.782	1.000
110	4.301	0.001	195.803	7.188	0.491	0.037	2077248.217	0.603	1.000
111	4.489	0.001	207.021	7.158	-0.672	0.035	2059570.773	0.305	1.000
112	4.648	0.001	200.885	7.125	-1.554	0.035	2040579.182	0.422	1.000

Table B.1 – continued

n	Frequency (d^{-1})	Error on the frequency (d^{-1})	Semi-ampl. (counts)	Error on the semi-ampl. (counts)	Phase (radians)	Error on the phase (radians)	Variance	Significance level under whitenoise	Significance level under rednoise
113	2.937	0.001	192.421	7.090	-0.923	0.037	2020841.821	0.622	1.000
114	7.431	0.001	191.588	7.059	0.368	0.037	2003334.324	0.622	1.000
115	5.852	0.001	189.538	7.028	-1.081	0.037	1985891.252	0.656	1.000
116	5.507	0.001	184.235	6.998	-1.213	0.038	1968818.470	0.775	1.000
117	6.049	0.001	186.616	6.968	-1.363	0.037	1951986.979	0.692	1.000
118	4.818	0.001	183.891	6.938	-0.975	0.038	1935160.304	0.744	1.000
119	2.596	0.001	183.020	6.908	-0.451	0.038	1918641.774	0.746	1.000
120	6.547	0.001	181.953	6.879	-0.477	0.038	1902138.715	0.753	1.000
121	1.334	0.001	187.512	6.849	0.712	0.037	1885679.055	0.575	1.000
122	1.545	0.001	180.242	6.819	0.221	0.038	1869301.060	0.757	1.000
123	0.970	0.001	174.766	6.791	0.013	0.039	1853789.699	0.867	1.000
124	5.180	0.001	176.532	6.763	-0.585	0.038	1838485.608	0.813	1.000
125	2.760	0.001	174.488	6.734	-0.337	0.039	1823055.110	0.843	1.000
126	0.686	0.001	174.089	6.706	-0.720	0.039	1807978.893	0.835	1.000
127	7.396	0.001	174.597	6.678	-1.368	0.038	1792960.587	0.806	1.000
128	7.062	0.001	173.948	6.651	-0.322	0.038	1778435.792	0.805	1.000
129	0.366	0.001	168.768	6.623	-0.049	0.039	1763342.634	0.899	1.000
130	8.872	0.001	164.399	6.596	1.213	0.040	1749032.159	0.952	1.000
131	8.341	0.001	168.171	6.569	0.023	0.039	1734737.488	0.885	1.000
132	5.693	0.001	167.909	6.543	1.058	0.039	1720976.145	0.877	1.000
133	2.310	0.001	165.701	6.516	-0.851	0.039	1707068.707	0.905	1.000
134	3.378	0.001	166.415	6.490	-0.038	0.039	1693300.153	0.880	1.000
135	10.514	0.001	164.547	6.464	1.190	0.039	1679554.321	0.902	1.000
136	9.433	0.001	164.431	6.438	0.877	0.039	1666016.632	0.892	1.000
137	5.335	0.001	160.471	6.411	-0.028	0.040	1652517.733	0.944	1.000
138	1.931	0.001	172.127	6.386	0.893	0.037	1639532.381	0.659	1.000
139	6.117	0.001	163.002	6.361	-0.739	0.039	1626569.664	0.882	1.000
140	1.577	0.001	159.437	6.335	-1.515	0.040	1613377.005	0.932	1.000
141	8.660	0.001	162.656	6.310	-0.144	0.039	1600502.754	0.862	1.000
142	1.798	0.001	159.652	6.284	-0.946	0.039	1587705.539	0.908	1.000
143	4.549	0.001	158.026	6.259	-0.219	0.040	1575046.331	0.924	1.000
144	8.289	0.001	157.285	6.235	1.528	0.040	1562723.498	0.926	1.000
145	8.155	0.001	164.926	6.210	-1.018	0.038	1550351.217	0.734	1.000
146	11.253	0.001	168.156	6.183	-1.102	0.037	1536803.890	0.611	1.000
147	11.329	0.001	159.467	6.159	-0.692	0.039	1524946.716	0.845	1.000

Table B.1 – continued

n	Frequency (d^{-1})	Error on the frequency (d^{-1})	Semi-ampl. (counts)	Error on the semi-ampl. (counts)	Phase (radians)	Error on the phase (radians)	Variance	Significance level under whitenoise	Significance level under rednoise
148	6.653	0.001	152.675	6.134	0.340	0.040	1512438.513	0.954	1.000
149	0.516	0.001	153.490	6.110	-0.139	0.040	1500923.156	0.936	1.000
150	6.476	0.001	156.520	6.087	-0.516	0.039	1489476.328	0.870	1.000
151	7.707	0.001	149.787	6.063	-1.102	0.040	1477972.544	0.966	1.000
152	1.414	0.001	149.745	6.040	1.480	0.040	1466837.728	0.961	1.000
153	5.590	0.001	148.208	6.017	0.709	0.041	1455659.632	0.970	1.000
154	1.186	0.001	142.631	5.996	1.253	0.042	1445163.341	0.995	1.000
155	9.539	0.001	143.386	5.974	-1.206	0.042	1434737.469	0.991	1.000
156	4.254	0.001	161.556	5.953	0.583	0.037	1424460.142	0.622	1.000
157	4.179	0.001	160.260	5.931	0.630	0.037	1414242.279	0.646	1.000
158	3.899	0.001	145.713	5.906	0.779	0.041	1402238.132	0.967	1.000
159	5.309	0.001	143.713	5.884	-1.373	0.041	1391847.331	0.979	1.000
160	3.004	0.001	140.179	5.862	-1.258	0.042	1381434.109	0.993	1.000
161	11.743	0.001	137.727	5.841	-0.613	0.042	1371617.703	0.997	1.000
162	5.093	0.001	139.023	5.821	-0.528	0.042	1362073.570	0.993	1.000
163	9.799	0.001	147.918	5.800	0.545	0.039	1352519.524	0.897	1.000
164	10.107	0.001	144.523	5.780	-0.947	0.040	1343133.839	0.946	1.000
165	9.142	0.001	146.027	5.759	-0.750	0.039	1333163.485	0.913	1.000
166	9.587	0.001	137.272	5.738	-0.466	0.042	1323459.816	0.992	1.000
167	9.307	0.001	136.349	5.717	-0.780	0.042	1314033.980	0.994	1.000
168	4.090	0.001	132.901	5.697	-0.025	0.043	1304801.482	0.998	1.000
169	6.306	0.001	133.141	5.678	-1.063	0.043	1295950.927	0.998	1.000
170	0.573	0.001	132.270	5.658	-1.170	0.043	1286957.056	0.998	1.000
171	14.048	0.001	133.960	5.639	1.107	0.042	1278203.862	0.995	1.000
172	7.777	0.001	132.960	5.619	-0.243	0.042	1269461.378	0.996	1.000
173	0.401	0.001	132.085	5.600	1.223	0.042	1260777.668	0.997	1.000
174	14.889	0.001	131.789	5.581	-1.532	0.042	1252140.699	0.997	1.000
175	12.002	0.001	132.145	5.562	0.484	0.042	1243524.509	0.995	1.000
176	5.397	0.001	129.524	5.542	-0.107	0.043	1234842.533	0.998	1.000
177	1.128	0.001	127.927	5.523	1.324	0.043	1226467.658	0.999	1.000
178	12.148	0.001	131.482	5.505	-0.902	0.042	1218188.351	0.993	1.000
179	2.824	0.001	130.769	5.486	1.018	0.042	1209975.581	0.994	1.000
180	10.454	0.001	129.076	5.467	1.129	0.042	1201483.695	0.997	1.000
181	5.133	0.001	127.707	5.448	-0.936	0.043	1193158.984	0.998	1.000
182	5.769	0.001	127.231	5.429	1.439	0.043	1185098.886	0.998	1.000

Table B.1 – continued

n	Frequency (d^{-1})	Error on the frequency (d^{-1})	Semi-ampl. (counts)	Error on the semi-ampl. (counts)	Phase (radians)	Error on the phase (radians)	Variance	Significance level under whitenoise	Significance level under rednoise
183	12.411	0.001	126.675	5.411	-0.982	0.043	1177105.998	0.998	1.000
184	8.523	0.001	125.763	5.393	-0.188	0.043	1169141.727	0.998	1.000
185	6.389	0.001	125.815	5.374	0.590	0.043	1161220.807	0.998	1.000
186	3.123	0.001	126.469	5.356	-0.125	0.042	1153344.405	0.997	1.000
187	5.361	0.001	123.223	5.338	1.014	0.043	1145537.448	0.999	1.000
188	8.690	0.001	122.465	5.320	0.667	0.043	1137881.334	0.999	1.000
189	13.051	0.001	122.941	5.302	1.272	0.043	1130324.308	0.999	1.000
190	10.342	0.001	121.897	5.285	1.075	0.043	1122845.435	0.999	1.000
191	9.965	0.001	121.868	5.267	0.071	0.043	1115422.044	0.999	1.000
192	6.854	0.001	121.225	5.250	-0.193	0.043	1108024.421	0.999	1.000
193	6.932	0.001	126.079	5.232	0.466	0.042	1100677.558	0.989	1.000
194	4.364	0.001	130.547	5.213	-0.776	0.040	1092541.021	0.943	1.000
195	11.185	0.001	122.422	5.196	1.371	0.042	1085232.338	0.997	1.000
196	7.513	0.001	123.664	5.178	-0.069	0.042	1077969.703	0.993	1.000
197	8.606	0.001	121.311	5.161	0.115	0.043	1070625.981	0.997	1.000
198	0.173	0.001	120.862	5.143	1.040	0.043	1063395.428	0.997	1.000
199	3.238	0.001	119.456	5.126	0.728	0.043	1056229.403	0.999	1.000
200	10.862	0.001	119.571	5.108	0.324	0.043	1049098.508	0.998	1.000
201	11.960	0.001	114.763	5.091	0.050	0.044	1041980.028	1.000	1.000
202	3.758	0.001	117.595	5.074	-1.368	0.043	1035001.512	0.999	1.000
203	8.257	0.001	117.794	5.057	-0.803	0.043	1028213.441	0.999	1.000
204	8.951	0.001	116.251	5.041	1.344	0.043	1021480.573	0.999	1.000
205	0.644	0.001	113.417	5.024	-0.257	0.044	1014753.841	1.000	1.000
206	13.983	0.001	114.341	5.008	0.745	0.044	1008214.391	1.000	1.000
207	9.686	0.001	113.294	4.992	-0.600	0.044	1001749.735	1.000	1.000
208	10.137	0.001	112.296	4.976	-1.548	0.044	995485.070	1.000	1.000
209	4.515	0.001	112.598	4.960	0.588	0.044	989185.119	1.000	1.000
210	4.859	0.001	114.252	4.945	-0.925	0.043	983083.458	0.999	1.000
211	10.776	0.001	110.774	4.929	0.070	0.044	976834.739	1.000	1.000
212	2.252	0.001	110.436	4.914	0.000	0.044	970673.002	1.000	1.000
213	6.578	0.001	109.813	4.898	0.698	0.045	964510.244	1.000	1.000
214	9.188	0.001	111.701	4.883	0.496	0.044	958473.632	1.000	1.000
215	5.878	0.001	110.776	4.867	0.357	0.044	952409.720	1.000	1.000
216	8.007	0.001	108.074	4.852	-1.010	0.045	946286.914	1.000	1.000
217	7.172	0.001	110.299	4.837	1.162	0.044	940454.457	1.000	1.000

Table B.1 – continued

n	Frequency (d^{-1})	Error on the frequency (d^{-1})	Semi-ampl. (counts)	Error on the semi-ampl. (counts)	Phase (radians)	Error on the phase (radians)	Variance	Significance level under whitenoise	Significance level under rednoise
218	7.309	0.001	106.601	4.822	-1.371	0.045	934586.133	1.000	1.000
219	2.220	0.001	111.178	4.807	-1.412	0.043	928757.972	0.999	1.000
220	2.432	0.001	110.292	4.792	0.981	0.043	922991.000	0.999	1.000
221	8.433	0.001	105.522	4.776	0.029	0.045	916970.541	1.000	1.000
222	13.957	0.001	105.342	4.761	-1.076	0.045	911392.184	1.000	1.000
223	11.921	0.001	107.599	4.747	-1.203	0.044	905872.313	1.000	1.000
224	12.290	0.001	105.260	4.732	0.497	0.045	900309.225	1.000	1.000
225	12.242	0.001	112.936	4.718	-0.318	0.042	894758.167	0.992	1.000
226	12.339	0.001	104.654	4.703	-0.146	0.045	889171.289	1.000	1.000
227	9.026	0.001	102.785	4.688	-0.615	0.046	883574.869	1.000	1.000
228	13.495	0.001	102.983	4.674	1.283	0.045	878161.717	1.000	1.000
229	8.764	0.001	101.843	4.660	-0.749	0.046	872901.011	1.000	1.000
230	6.787	0.001	103.040	4.646	1.258	0.045	867662.472	1.000	1.000
					HD 46150				
1	0.057	0.000	1251.651	16.827	0.585	0.013	11365207.101	0.000	0.000
2	1.341	0.000	867.291	16.233	-0.078	0.019	10577441.603	0.000	0.000
3	0.146	0.000	859.512	15.946	0.909	0.019	10206544.453	0.000	0.288
4	0.931	0.000	797.426	15.684	1.346	0.020	9873859.498	0.000	0.000
5	2.627	0.000	783.450	15.429	1.138	0.020	9555825.228	0.000	0.000
6	0.344	0.000	809.566	15.174	-0.964	0.019	9242356.762	0.000	0.085
7	1.661	0.000	757.900	14.938	-0.060	0.020	8956820.377	0.000	0.000
8	0.558	0.000	740.387	14.694	-1.277	0.020	8667070.541	0.000	0.051
9	0.822	0.000	649.148	14.459	-1.032	0.022	8391433.532	0.000	0.078
10	1.947	0.000	623.497	14.255	0.555	0.023	8157315.261	0.000	0.000
11	3.156	0.000	610.665	14.069	1.349	0.023	7945649.734	0.000	0.000
12	0.297	0.000	598.559	13.906	-1.317	0.023	7762740.530	0.000	1.000
13	1.267	0.000	559.358	13.757	-1.051	0.025	7596383.872	0.000	0.059
14	1.785	0.000	578.773	13.609	1.570	0.024	7434617.522	0.000	0.000
15	0.321	0.000	552.708	13.460	0.428	0.024	7272435.130	0.000	1.000
16	0.725	0.000	535.862	13.330	-1.308	0.025	7132934.979	0.000	1.000
17	3.731	0.000	525.087	13.196	-0.735	0.025	6990426.283	0.000	0.000
18	0.240	0.000	498.664	13.068	-1.297	0.026	6855271.116	0.001	1.000
19	0.527	0.000	501.764	12.950	-1.039	0.026	6731468.973	0.001	1.000
20	0.850	0.000	489.608	12.832	0.329	0.026	6609948.494	0.001	1.000
21	1.852	0.000	456.507	12.721	0.296	0.028	6495289.800	0.004	0.163

Table B.1 – continued

n	Frequency (d^{-1})	Error on the frequency (d^{-1})	Semi-ampl. (counts)	Error on the semi-ampl. (counts)	Phase (radians)	Error on the phase (radians)	Variance	Significance level under whitenoise	Significance level under rednoise
22	1.413	0.000	450.168	12.617	-0.460	0.028	6389657.662	0.005	0.969
23	2.763	0.000	454.032	12.514	-0.303	0.028	6286556.179	0.003	0.001
24	2.472	0.000	448.417	12.412	-0.180	0.028	6183846.352	0.004	0.006
25	0.628	0.000	473.409	12.311	-0.487	0.026	6083534.102	0.001	1.000
26	0.586	0.000	451.658	12.211	0.951	0.027	5985680.665	0.002	1.000
27	1.747	0.000	418.221	12.109	0.791	0.029	5885460.372	0.011	0.911
28	2.195	0.000	425.801	12.013	1.106	0.028	5792547.931	0.006	0.131
29	0.114	0.000	414.652	11.919	-1.287	0.029	5702959.945	0.009	1.000
30	1.153	0.000	420.141	11.828	-1.454	0.028	5615578.937	0.005	1.000
31	3.611	0.000	411.347	11.736	-0.024	0.029	5528760.030	0.007	0.000
32	1.181	0.000	387.115	11.647	0.390	0.030	5444947.958	0.025	1.000
33	2.006	0.000	381.348	11.567	-1.091	0.030	5370655.293	0.030	0.987
34	3.017	0.000	379.670	11.488	0.308	0.030	5297230.710	0.028	0.044
35	4.037	0.000	370.519	11.409	1.340	0.031	5224781.590	0.041	0.001
36	1.511	0.000	364.556	11.334	-0.048	0.031	5156505.428	0.049	1.000
37	4.585	0.001	360.458	11.261	-1.559	0.031	5090356.700	0.054	0.000
38	2.653	0.001	356.068	11.189	-0.603	0.031	5025696.978	0.061	0.674
39	2.238	0.001	348.017	11.120	0.013	0.032	4963620.789	0.084	1.000
40	0.029	0.001	345.153	11.052	0.780	0.032	4902726.314	0.087	1.000
41	0.363	0.001	347.238	10.984	1.085	0.032	4843339.967	0.069	1.000
42	1.071	0.001	343.337	10.918	-0.503	0.032	4784985.523	0.076	1.000
43	1.899	0.001	338.143	10.851	-1.181	0.032	4726253.239	0.090	1.000
44	2.150	0.001	333.307	10.785	0.595	0.032	4668871.705	0.105	1.000
45	3.228	0.001	340.064	10.718	-0.112	0.032	4611338.269	0.065	0.283
46	5.607	0.001	336.331	10.652	-0.336	0.032	4554528.465	0.071	0.000
47	2.819	0.001	331.153	10.585	-0.662	0.032	4497575.018	0.084	0.935
48	1.622	0.001	322.190	10.520	0.232	0.033	4442542.367	0.123	1.000
49	4.002	0.001	315.434	10.459	0.445	0.033	4390702.006	0.159	0.124
50	3.488	0.001	314.753	10.397	0.110	0.033	4338869.551	0.150	0.551
51	1.980	0.001	314.623	10.336	0.120	0.033	4288270.204	0.137	1.000
52	2.567	0.001	311.734	10.276	1.270	0.033	4238836.496	0.145	1.000
53	0.782	0.001	309.438	10.216	0.426	0.033	4189633.244	0.149	1.000
54	5.978	0.001	307.892	10.158	-1.161	0.033	4142215.284	0.147	0.000
55	6.528	0.001	305.075	10.099	1.494	0.033	4094224.871	0.155	0.000
56	2.330	0.001	305.126	10.041	0.854	0.033	4047330.439	0.141	1.000

Table B.1 – continued

n	Frequency (d^{-1})	Error on the frequency (d^{-1})	Semi-ampl. (counts)	Error on the semi-ampl. (counts)	Phase (radians)	Error on the phase (radians)	Variance	Significance level under whitenoise	Significance level under rednoise
57	1.478	0.001	313.466	9.983	-0.506	0.032	4000782.636	0.079	1.000
58	0.674	0.001	293.555	9.925	1.251	0.034	3954169.447	0.217	1.000
59	4.531	0.001	294.878	9.868	-0.704	0.033	3908480.898	0.185	0.129
60	3.054	0.001	297.730	9.812	-0.207	0.033	3864845.070	0.144	1.000
61	0.463	0.001	285.639	9.758	-1.418	0.034	3822183.367	0.253	1.000
62	4.634	0.001	282.469	9.706	0.213	0.034	3781743.008	0.275	0.261
63	3.569	0.001	281.762	9.655	-0.682	0.034	3742231.628	0.265	0.998
64	5.193	0.001	277.567	9.605	0.514	0.035	3703185.981	0.304	0.093
65	4.916	0.001	276.766	9.555	1.159	0.035	3664652.115	0.294	0.204
66	3.116	0.001	266.727	9.507	1.196	0.036	3628171.454	0.441	1.000
67	2.373	0.001	269.346	9.460	-0.257	0.035	3592597.573	0.369	1.000
68	2.099	0.001	264.367	9.415	0.665	0.036	3558063.409	0.436	1.000
69	2.899	0.001	261.317	9.369	0.018	0.036	3523403.683	0.470	1.000
70	6.630	0.001	279.280	9.323	0.423	0.033	3488823.283	0.178	0.001
71	8.338	0.001	267.430	9.277	1.242	0.035	3454694.336	0.314	0.000
72	3.657	0.001	257.856	9.229	1.156	0.036	3419289.623	0.462	1.000
73	1.824	0.001	254.185	9.185	-0.530	0.036	3386144.567	0.511	1.000
74	2.788	0.001	252.194	9.140	-1.443	0.036	3353188.950	0.527	1.000
75	7.202	0.001	257.037	9.095	-1.208	0.035	3320432.724	0.404	0.005
76	7.287	0.001	258.181	9.050	-0.590	0.035	3287513.591	0.360	0.003
77	7.911	0.001	253.424	9.005	0.789	0.036	3255285.488	0.425	0.001
78	0.193	0.001	252.795	8.961	0.071	0.035	3222977.862	0.413	1.000
79	4.140	0.001	250.056	8.916	1.337	0.036	3191185.044	0.443	1.000
80	1.435	0.001	247.092	8.873	0.932	0.036	3160292.963	0.479	1.000
81	7.517	0.001	248.595	8.830	0.619	0.036	3129872.616	0.423	0.006
82	6.298	0.001	245.396	8.788	-0.375	0.036	3099885.262	0.464	0.144
83	4.283	0.001	241.435	8.746	-0.750	0.036	3070520.335	0.525	1.000
84	0.908	0.001	272.582	8.705	-0.593	0.032	3041701.088	0.083	1.000
85	0.979	0.001	261.622	8.664	-0.417	0.033	3012895.216	0.156	1.000
86	6.750	0.001	234.440	8.616	-1.352	0.037	2979904.697	0.602	0.172
87	8.645	0.001	232.757	8.576	-0.898	0.037	2952412.134	0.616	0.004
88	0.416	0.001	228.388	8.537	-0.659	0.037	2925608.083	0.691	1.000
89	5.660	0.001	223.501	8.499	0.819	0.038	2899463.688	0.775	0.990
90	8.044	0.001	236.957	8.460	-0.996	0.036	2873171.935	0.449	0.009
91	1.697	0.001	224.789	8.422	0.789	0.037	2847127.569	0.703	1.000

Table B.1 – continued

n	Frequency (d^{-1})	Error on the frequency (d^{-1})	Semi-ampl. (counts)	Error on the semi-ampl. (counts)	Phase (radians)	Error on the phase (radians)	Variance	Significance level under whitenoise	Significance level under rednoise
92	6.566	0.001	223.979	8.384	0.845	0.037	2821767.600	0.698	0.556
93	4.404	0.001	213.908	8.347	-1.359	0.039	2796540.895	0.878	1.000
94	7.707	0.000	277.016	8.311	-0.232	0.030	2772380.861	0.024	0.000
95	7.666	0.000	274.304	8.275	-0.250	0.030	2748727.069	0.027	0.000
96	4.457	0.001	217.911	8.221	-0.135	0.038	2713216.276	0.738	1.000
97	7.010	0.001	219.756	8.186	-0.016	0.037	2689702.704	0.673	0.422
98	6.012	0.001	220.905	8.150	-0.946	0.037	2666243.479	0.622	0.953
99	6.372	0.001	216.063	8.115	0.389	0.038	2643127.030	0.715	0.918
100	3.284	0.001	218.276	8.079	0.308	0.037	2620057.601	0.640	1.000
101	1.213	0.001	211.391	8.044	-1.461	0.038	2597410.050	0.778	1.000
102	5.130	0.001	212.076	8.010	0.194	0.038	2575129.525	0.742	1.000
103	4.830	0.001	211.067	7.975	0.407	0.038	2553007.814	0.745	1.000
104	2.947	0.001	208.880	7.940	1.042	0.038	2530712.342	0.773	1.000
105	9.691	0.001	201.808	7.906	1.257	0.039	2508928.115	0.890	0.045
106	2.125	0.001	205.510	7.873	-1.033	0.038	2487920.811	0.807	1.000
107	8.594	0.001	205.137	7.840	-0.535	0.038	2467174.106	0.797	0.166
108	3.443	0.001	201.686	7.807	-0.884	0.039	2446504.305	0.849	1.000
109	1.047	0.001	201.275	7.774	0.705	0.039	2425866.629	0.841	1.000
110	3.876	0.001	200.523	7.742	0.178	0.039	2405867.634	0.839	1.000
111	12.551	0.001	199.489	7.709	-0.860	0.039	2385708.207	0.843	0.001
112	10.457	0.001	199.442	7.677	0.521	0.038	2365782.659	0.827	0.018
113	5.275	0.000	261.300	7.645	-1.416	0.029	2345899.068	0.013	0.307
114	5.231	0.001	240.509	7.613	1.513	0.032	2326479.235	0.070	0.922
115	5.379	0.001	221.521	7.570	-1.359	0.034	2300138.232	0.254	1.000
116	8.293	0.001	196.641	7.533	-0.690	0.038	2278060.252	0.808	0.556
117	5.541	0.001	197.254	7.502	-1.160	0.038	2258841.524	0.775	1.000
118	6.975	0.001	195.227	7.469	1.029	0.038	2239361.228	0.802	0.999
119	2.419	0.001	187.108	7.437	-1.561	0.040	2220315.665	0.930	1.000
120	0.086	0.001	182.657	7.408	-0.235	0.041	2202679.228	0.966	1.000
121	9.532	0.001	201.754	7.379	-0.253	0.037	2185613.356	0.576	0.058
122	5.442	0.001	193.620	7.350	1.308	0.038	2168543.968	0.767	1.000
123	5.635	0.001	186.947	7.320	-0.881	0.039	2151080.146	0.889	1.000
124	5.465	0.001	195.079	7.292	-0.058	0.037	2134618.042	0.691	1.000
125	5.931	0.001	177.759	7.263	1.003	0.041	2117201.171	0.975	1.000
126	9.232	0.001	178.046	7.235	-1.531	0.041	2101154.348	0.969	0.849

Table B.1 – continued

n	Frequency (d^{-1})	Error on the frequency (d^{-1})	Semi-ampl. (counts)	Error on the semi-ampl. (counts)	Phase (radians)	Error on the phase (radians)	Variance	Significance level under whitenoise	Significance level under rednoise
127	3.794	0.001	177.843	7.208	1.118	0.041	2085287.485	0.966	1.000
128	3.194	0.001	176.973	7.180	-0.759	0.041	2069631.838	0.967	1.000
129	2.307	0.001	175.827	7.153	-0.804	0.041	2053928.159	0.971	1.000
130	10.273	0.001	175.476	7.127	0.396	0.041	2038787.519	0.968	0.500
131	8.758	0.001	173.368	7.100	0.124	0.041	2023677.462	0.978	0.997
132	6.198	0.001	205.725	7.075	0.027	0.034	2009161.607	0.279	1.000
133	6.239	0.001	202.623	7.049	-0.770	0.035	1994499.116	0.326	1.000
134	1.380	0.001	170.405	7.015	-0.898	0.041	1975214.917	0.983	1.000
135	1.577	0.001	169.628	6.989	-0.256	0.041	1960738.563	0.983	1.000
136	5.070	0.001	169.030	6.963	1.034	0.041	1946440.297	0.983	1.000
137	4.697	0.001	176.294	6.938	1.077	0.039	1932170.847	0.904	1.000
138	6.698	0.001	172.639	6.913	-0.278	0.040	1918061.779	0.945	1.000
139	0.862	0.001	172.186	6.887	-0.125	0.040	1903664.752	0.943	1.000
140	1.315	0.001	168.288	6.861	0.929	0.041	1889559.296	0.973	1.000
141	10.343	0.001	169.177	6.835	-1.331	0.040	1875320.322	0.961	0.761
142	7.442	0.001	163.908	6.810	-0.241	0.042	1861405.930	0.989	1.000
143	7.875	0.001	183.519	6.784	0.009	0.037	1847536.516	0.633	0.998
144	7.949	0.001	174.174	6.759	0.254	0.039	1833871.329	0.858	1.000
145	1.011	0.001	164.399	6.732	-1.415	0.041	1818948.340	0.978	1.000
146	2.606	0.001	160.945	6.707	-0.978	0.042	1805581.732	0.991	1.000
147	11.163	0.001	157.303	6.682	0.890	0.042	1792421.236	0.997	0.928
148	6.474	0.001	162.149	6.659	-0.028	0.041	1779890.146	0.981	1.000
149	12.761	0.001	155.742	6.635	0.065	0.043	1767388.518	0.997	0.466
150	13.642	0.001	153.878	6.612	0.863	0.043	1755164.164	0.999	0.286
					HD 46966				
1	0.085	0.000	2534.278	13.058	1.459	0.005	7013745.673	0.000	0.000
2	0.039	0.000	1882.840	11.283	-1.517	0.006	5236825.435	0.000	0.000
3	0.234	0.000	643.881	9.601	0.949	0.015	3792244.148	0.000	0.001
4	0.106	0.000	813.800	9.274	-1.355	0.011	3537746.525	0.000	0.000
5	0.935	0.000	517.887	8.991	0.014	0.017	3325094.516	0.000	0.000
6	0.281	0.000	535.826	8.794	-1.564	0.016	3181125.088	0.000	0.144
7	0.192	0.000	574.143	8.598	0.075	0.015	3040746.126	0.000	0.064
8	0.059	0.000	687.741	8.428	0.329	0.012	2922152.695	0.000	0.001
9	0.664	0.000	424.787	8.231	-1.384	0.019	2786799.771	0.000	0.709
10	1.203	0.000	397.039	8.113	-0.525	0.020	2707743.628	0.000	0.112

Table B.1 – continued

n	Frequency (d^{-1})	Error on the frequency (d^{-1})	Semi-ampl. (counts)	Error on the semi-ampl. (counts)	Phase (radians)	Error on the phase (radians)	Variance	Significance level under whitenoise	Significance level under rednoise
11	0.897	0.000	365.620	7.993	-0.240	0.022	2628244.251	0.000	0.996
12	1.615	0.000	365.634	7.893	1.345	0.022	2562706.864	0.000	0.067
13	0.346	0.000	363.507	7.791	0.627	0.021	2497250.248	0.000	1.000
14	0.564	0.000	339.831	7.691	1.524	0.023	2433065.196	0.000	1.000
15	1.014	0.000	335.365	7.602	-1.522	0.023	2377130.339	0.000	1.000
16	2.009	0.000	321.246	7.513	0.089	0.023	2321813.693	0.000	0.202
17	1.315	0.000	325.028	7.429	0.041	0.023	2270208.980	0.000	0.996
18	1.846	0.000	302.775	7.347	1.035	0.024	2220421.733	0.000	0.850
19	2.800	0.000	288.126	7.263	0.597	0.025	2170052.007	0.000	0.095
20	0.390	0.000	356.637	7.184	0.626	0.020	2122979.302	0.000	1.000
21	0.160	0.000	315.860	7.104	1.566	0.022	2075990.977	0.000	1.000
22	0.436	0.000	317.986	7.025	1.233	0.022	2029861.407	0.000	1.000
23	2.185	0.000	287.113	6.940	-1.022	0.024	1981084.054	0.000	0.752
24	2.669	0.000	278.993	6.870	0.787	0.025	1941617.057	0.000	0.320
25	1.080	0.000	273.063	6.801	-0.589	0.025	1902960.291	0.000	1.000
26	1.666	0.000	277.462	6.736	0.065	0.024	1866344.880	0.000	1.000
27	1.262	0.000	283.461	6.672	0.361	0.024	1831227.935	0.000	1.000
28	1.804	0.000	245.785	6.609	-0.028	0.027	1797006.431	0.002	1.000
29	2.295	0.000	249.713	6.554	-0.522	0.026	1767022.506	0.001	1.000
30	2.748	0.000	226.835	6.501	0.629	0.029	1738308.343	0.011	1.000
31	1.228	0.000	242.432	6.449	1.038	0.027	1711060.782	0.002	1.000
32	2.477	0.000	228.423	6.397	-0.837	0.028	1683261.793	0.006	1.000
33	3.174	0.000	206.692	6.346	0.900	0.031	1656559.464	0.048	1.000
34	1.709	0.000	212.064	6.298	-1.151	0.030	1631469.169	0.024	1.000
35	0.604	0.000	214.640	6.255	1.265	0.029	1609315.255	0.016	1.000
36	2.866	0.000	215.472	6.212	-0.873	0.029	1587350.207	0.012	1.000
37	3.436	0.000	213.423	6.169	0.155	0.029	1565341.801	0.013	1.000
38	3.096	0.000	203.681	6.124	-0.635	0.030	1543008.254	0.032	1.000
39	8.229	0.000	199.324	6.084	1.088	0.031	1522490.954	0.043	0.001
40	0.960	0.000	197.476	6.044	-0.639	0.031	1502583.916	0.045	1.000
41	1.115	0.000	198.984	6.004	0.914	0.030	1483065.536	0.034	1.000
42	1.470	0.000	202.188	5.965	1.468	0.030	1463711.700	0.021	1.000
43	3.666	0.000	194.565	5.925	-1.291	0.030	1444037.854	0.041	1.000
44	5.153	0.000	200.625	5.886	0.977	0.029	1425179.670	0.019	0.462
45	4.900	0.000	191.347	5.847	1.344	0.031	1406534.982	0.044	0.948

Table B.1 – continued

n	Frequency (d^{-1})	Error on the frequency (d^{-1})	Semi-ampl. (counts)	Error on the semi-ampl. (counts)	Phase (radians)	Error on the phase (radians)	Variance	Significance level under whitenoise	Significance level under rednoise
46	2.957	0.000	188.683	5.809	0.027	0.031	1388180.002	0.051	1.000
47	1.896	0.001	184.732	5.772	1.561	0.031	1370389.923	0.068	1.000
48	0.527	0.001	181.852	5.736	1.562	0.032	1353344.156	0.081	1.000
49	1.580	0.000	183.419	5.701	1.450	0.031	1336901.330	0.061	1.000
50	4.756	0.001	177.686	5.665	-0.334	0.032	1320350.392	0.099	1.000
51	2.051	0.001	177.661	5.631	0.410	0.032	1304323.708	0.089	1.000
52	5.728	0.001	177.174	5.597	1.201	0.032	1288708.839	0.084	0.944
53	4.389	0.001	173.054	5.563	0.791	0.032	1273124.233	0.115	1.000
54	4.623	0.001	166.235	5.531	-1.516	0.033	1258294.413	0.202	1.000
55	6.291	0.001	166.026	5.501	-1.296	0.033	1244654.324	0.189	0.983
56	5.581	0.001	163.487	5.471	-0.938	0.033	1231264.173	0.221	1.000
57	2.576	0.001	159.697	5.441	-0.213	0.034	1217902.564	0.287	1.000
58	4.961	0.001	156.568	5.411	0.633	0.035	1204605.853	0.348	1.000
59	1.866	0.001	157.157	5.384	-0.181	0.034	1192279.054	0.309	1.000
60	1.351	0.001	164.951	5.356	0.271	0.032	1180160.484	0.136	1.000
61	1.162	0.001	151.967	5.329	1.015	0.035	1168047.093	0.416	1.000
62	0.126	0.001	151.739	5.301	0.994	0.035	1155785.364	0.398	1.000
63	0.802	0.001	151.223	5.274	-0.881	0.035	1144089.443	0.390	1.000
64	3.607	0.001	148.804	5.247	-0.436	0.035	1132626.639	0.444	1.000
65	3.872	0.001	144.580	5.222	0.503	0.036	1121578.322	0.570	1.000
66	2.363	0.001	150.145	5.197	0.210	0.035	1110889.530	0.354	1.000
67	2.231	0.001	157.839	5.173	-0.358	0.033	1100624.129	0.159	1.000
68	2.150	0.001	156.204	5.147	0.502	0.033	1089930.701	0.174	1.000
69	2.900	0.001	140.597	5.120	-0.902	0.036	1078478.269	0.615	1.000
70	5.509	0.001	141.792	5.096	1.545	0.036	1068389.362	0.544	1.000
71	1.535	0.001	139.808	5.072	0.059	0.036	1058337.407	0.594	1.000
72	1.775	0.001	139.960	5.049	0.898	0.036	1048505.737	0.563	1.000
73	6.786	0.001	142.938	5.025	-1.403	0.035	1038775.912	0.429	1.000
74	6.051	0.001	150.557	5.002	1.034	0.033	1029162.508	0.198	1.000
75	5.950	0.001	148.728	4.978	-1.199	0.033	1019376.667	0.222	1.000
76	5.120	0.001	136.987	4.953	-0.843	0.036	1009272.226	0.576	1.000
77	3.939	0.001	139.826	4.930	0.872	0.035	999750.278	0.444	1.000
78	5.325	0.001	137.379	4.906	0.812	0.036	990237.030	0.510	1.000
79	6.595	0.001	136.176	4.883	-1.344	0.036	980745.309	0.531	1.000
80	1.043	0.001	134.300	4.860	-0.645	0.036	971464.635	0.580	1.000

Table B.1 – continued

n	Frequency (d^{-1})	Error on the frequency (d^{-1})	Semi-ampl. (counts)	Error on the semi-ampl. (counts)	Phase (radians)	Error on the phase (radians)	Variance	Significance level under whitenoise	Significance level under rednoise
81	3.766	0.001	133.993	4.837	1.015	0.036	962410.140	0.567	1.000
82	6.198	0.001	121.960	4.815	-0.683	0.039	953885.856	0.940	1.000
83	8.959	0.001	121.581	4.796	-1.171	0.039	946334.731	0.939	1.000
84	4.423	0.001	122.277	4.778	-1.119	0.039	938923.253	0.916	1.000
85	2.698	0.001	119.706	4.759	1.488	0.040	931586.960	0.953	1.000
86	8.326	0.001	120.120	4.740	0.530	0.039	924398.313	0.939	1.000
87	7.501	0.001	124.569	4.722	1.228	0.038	917224.699	0.811	1.000
88	7.307	0.001	120.015	4.703	-0.857	0.039	910050.004	0.924	1.000
89	2.268	0.001	118.668	4.685	1.188	0.039	902879.187	0.940	1.000
90	1.138	0.001	116.777	4.666	-0.400	0.040	895771.268	0.962	1.000
91	2.325	0.001	115.187	4.649	-0.540	0.040	888976.723	0.975	1.000
92	5.775	0.001	114.095	4.631	0.876	0.041	882271.637	0.980	1.000
93	7.809	0.001	112.720	4.614	1.256	0.041	875865.029	0.987	1.000
94	9.685	0.001	112.984	4.598	-1.287	0.041	869594.684	0.983	1.000
95	0.698	0.001	110.947	4.581	0.105	0.041	863312.698	0.992	1.000
96	9.436	0.001	111.144	4.565	0.972	0.041	857141.256	0.989	1.000
97	4.731	0.001	111.308	4.548	0.974	0.041	850970.666	0.986	1.000
98	3.012	0.001	106.724	4.532	1.069	0.042	844781.853	0.999	1.000
99	7.046	0.001	107.370	4.515	-0.843	0.042	838758.104	0.997	1.000
100	1.423	0.001	108.846	4.499	-0.943	0.041	832827.674	0.992	1.000
101	10.157	0.001	107.449	4.484	0.384	0.042	826966.611	0.995	1.000
102	8.005	0.001	105.886	4.468	-0.317	0.042	821265.670	0.998	1.000
103	3.207	0.001	110.915	4.453	-0.609	0.040	815689.022	0.968	1.000
104	3.361	0.001	109.973	4.438	-1.185	0.040	810101.965	0.975	1.000
105	3.254	0.001	109.315	4.421	-1.013	0.040	804085.318	0.977	1.000
106	4.179	0.001	111.800	4.405	0.643	0.039	798194.151	0.936	1.000
107	3.985	0.001	107.065	4.390	-1.385	0.041	792614.860	0.988	1.000
108	9.314	0.001	103.910	4.374	0.940	0.042	786966.067	0.997	1.000
109	1.496	0.001	104.674	4.359	0.425	0.042	781502.853	0.995	1.000
110	2.515	0.001	103.589	4.343	0.609	0.042	776079.184	0.997	1.000
111	9.797	0.001	103.210	4.329	0.490	0.042	770773.332	0.997	1.000
112	4.345	0.001	102.872	4.314	0.958	0.042	765480.424	0.997	1.000
113	7.280	0.001	98.806	4.299	0.797	0.044	760209.877	1.000	1.000
114	5.189	0.001	103.375	4.284	1.351	0.041	754950.001	0.993	1.000
115	7.613	0.001	101.209	4.269	0.455	0.042	749697.671	0.998	1.000

Table B.1 – continued

n	Frequency (d^{-1})	Error on the frequency (d^{-1})	Semi-ampl. (counts)	Error on the semi-ampl. (counts)	Phase (radians)	Error on the phase (radians)	Variance	Significance level under whitenoise	Significance level under rednoise
116	5.833	0.001	101.325	4.255	0.817	0.042	744730.806	0.997	1.000
117	4.656	0.001	99.642	4.241	0.062	0.043	739765.228	0.999	1.000
118	2.108	0.001	98.681	4.226	1.017	0.043	734816.563	0.999	1.000
119	12.021	0.001	97.280	4.213	-1.084	0.043	730015.780	1.000	1.000
120	7.444	0.001	97.643	4.199	-0.619	0.043	725296.473	0.999	1.000
121	5.629	0.001	95.354	4.185	-0.581	0.044	720570.467	1.000	1.000
122	6.914	0.001	95.039	4.172	-0.064	0.044	715907.077	1.000	1.000
123	8.888	0.001	98.272	4.158	-0.218	0.042	711227.599	0.998	1.000
124	0.333	0.001	94.061	4.145	1.140	0.044	706769.789	1.000	1.000
125	6.659	0.001	94.703	4.132	-0.049	0.044	702333.019	1.000	1.000
126	8.577	0.001	94.457	4.119	0.481	0.044	697906.349	1.000	1.000
127	9.518	0.001	97.323	4.106	0.352	0.042	693485.278	0.998	1.000
128	5.462	0.001	96.830	4.093	-1.332	0.042	689172.032	0.998	1.000
129	6.139	0.001	91.429	4.079	1.354	0.045	684534.028	1.000	1.000
130	2.779	0.001	93.073	4.067	1.525	0.044	680318.782	1.000	1.000
131	10.783	0.001	91.725	4.054	-0.595	0.044	676126.841	1.000	1.000
132	2.418	0.001	91.378	4.042	1.260	0.044	671951.884	1.000	1.000
133	6.718	0.001	89.454	4.029	0.813	0.045	667805.983	1.000	1.000
134	5.003	0.001	89.902	4.017	0.183	0.045	663736.941	1.000	1.000
135	0.776	0.001	88.847	4.005	1.318	0.045	659729.356	1.000	1.000
136	8.056	0.001	86.322	3.993	-0.755	0.046	655796.676	1.000	1.000
137	7.194	0.001	86.061	3.981	-0.090	0.046	652069.610	1.000	1.000
138	6.104	0.001	86.302	3.970	0.729	0.046	648337.394	1.000	1.000
139	0.744	0.001	87.500	3.959	-0.633	0.045	644624.722	1.000	1.000
140	1.943	0.001	86.684	3.947	1.272	0.046	640983.245	1.000	1.000
141	0.993	0.001	84.020	3.936	-0.269	0.047	637394.014	1.000	1.000
142	2.925	0.001	85.860	3.925	0.124	0.046	633829.134	1.000	1.000
143	4.497	0.001	85.816	3.914	0.208	0.046	630201.241	1.000	1.000
144	9.136	0.001	84.163	3.903	1.300	0.046	626528.847	1.000	1.000
145	10.596	0.001	84.294	3.892	0.088	0.046	622989.772	1.000	1.000
146	6.996	0.001	84.059	3.880	-0.736	0.046	619431.756	1.000	1.000
147	8.651	0.001	83.848	3.869	1.556	0.046	615930.904	1.000	1.000
148	3.326	0.001	84.124	3.858	-0.223	0.046	612428.825	1.000	1.000
149	4.076	0.001	85.781	3.848	-0.347	0.045	608991.513	1.000	1.000
150	9.901	0.001	85.308	3.837	-0.195	0.045	605493.300	1.000	1.000

Table B.1 – continued

n	Frequency (d^{-1})	Error on the frequency (d^{-1})	Semi-ampl. (counts)	Error on the semi-ampl. (counts)	Phase (radians)	Error on the phase (radians)	Variance	Significance level under whitenoise	Significance level under rednoise
151	6.471	0.001	81.878	3.825	-1.298	0.047	601885.173	1.000	1.000
152	12.081	0.001	81.756	3.814	0.540	0.047	598529.264	1.000	1.000
153	4.804	0.001	81.056	3.804	0.194	0.047	595189.586	1.000	1.000
154	16.602	0.001	80.740	3.793	1.282	0.047	591935.086	1.000	1.000
155	6.261	0.001	83.110	3.783	0.675	0.046	588693.136	1.000	1.000
					HD 46149				
1	0.083	0.000	392.123	3.292	-1.506	0.008	445853.225	0.000	0.001
2	0.173	0.000	319.578	3.031	-0.707	0.009	378063.058	0.000	0.339
3	0.480	0.000	292.040	2.797	-0.713	0.010	321892.792	0.000	0.421
4	0.521	0.000	272.301	2.607	0.724	0.010	279682.784	0.000	0.787
5	0.351	0.000	219.324	2.447	-0.922	0.011	246438.657	0.000	1.000
6	13.970	0.000	159.851	2.335	-0.061	0.015	224328.281	0.000	0.000
7	0.043	0.000	150.542	2.271	-0.699	0.015	212206.309	0.000	1.000
8	0.871	0.000	125.950	2.219	-0.025	0.018	202641.097	0.000	1.000
9	0.562	0.000	138.724	2.175	0.744	0.016	194638.441	0.000	1.000
10	0.686	0.000	118.809	2.128	-0.582	0.018	186360.816	0.000	1.000
11	0.441	0.000	121.138	2.085	-1.443	0.017	178807.505	0.000	1.000
12	0.971	0.000	107.565	2.045	1.260	0.019	172094.252	0.000	1.000
13	0.278	0.000	102.378	2.012	0.064	0.020	166619.727	0.000	1.000
14	0.233	0.000	92.648	1.989	0.550	0.021	162796.235	0.000	1.000
15	0.311	0.000	79.755	1.968	0.817	0.025	159307.295	0.000	1.000
16	1.054	0.000	71.214	1.949	-0.164	0.027	156352.342	0.004	1.000
17	0.144	0.000	65.968	1.933	-1.548	0.029	153788.343	0.018	1.000
18	0.608	0.001	60.878	1.919	-0.002	0.032	151510.710	0.080	1.000
19	1.383	0.000	62.685	1.907	0.219	0.030	149579.637	0.040	1.000
20	0.938	0.001	55.016	1.894	1.420	0.034	147654.139	0.331	1.000
21	2.889	0.001	55.436	1.884	0.589	0.034	146047.503	0.277	0.000
22	1.208	0.001	51.930	1.874	1.339	0.036	144510.318	0.565	1.000
23	0.732	0.001	52.038	1.865	-0.922	0.036	143136.469	0.529	1.000
24	1.124	0.001	48.637	1.857	0.400	0.038	141852.671	0.840	1.000
25	0.465	0.001	48.303	1.849	0.647	0.038	140670.751	0.850	1.000
26	0.377	0.001	44.964	1.842	-0.645	0.041	139589.125	0.987	1.000
27	0.530	0.001	44.951	1.835	1.496	0.041	138582.529	0.985	1.000
28	1.006	0.001	41.914	1.829	0.547	0.044	137695.847	1.000	1.000
29	1.459	0.001	45.402	1.824	-1.315	0.040	136841.651	0.969	1.000

Table B.1 – continued

n	Frequency (d^{-1})	Error on the frequency (d^{-1})	Semi-ampl. (counts)	Error on the semi-ampl. (counts)	Phase (radians)	Error on the phase (radians)	Variance	Significance level under whitenoise	Significance level under rednoise
30	1.500	0.001	42.292	1.818	0.696	0.043	135996.810	0.999	1.000
31	0.661	0.001	37.927	1.813	1.450	0.048	135163.002	1.000	1.000
32	1.096	0.001	36.509	1.808	-0.804	0.050	134459.369	1.000	1.000
33	3.856	0.001	34.503	1.803	-0.439	0.052	133793.223	1.000	0.000
34	1.723	0.001	39.276	1.799	-1.246	0.046	133192.830	1.000	1.000
35	1.828	0.001	35.201	1.795	-1.333	0.051	132608.235	1.000	1.000
36	1.426	0.001	32.202	1.792	-0.004	0.056	132046.016	1.000	1.000
37	1.242	0.001	34.024	1.788	0.627	0.053	131509.689	1.000	1.000
38	2.453	0.001	32.266	1.784	0.932	0.055	130956.373	1.000	1.000
39	3.408	0.001	31.175	1.781	-1.051	0.057	130437.595	1.000	0.003
40	1.644	0.001	31.719	1.777	-0.167	0.056	129951.900	1.000	1.000
41	2.356	0.001	29.979	1.774	-0.699	0.059	129460.169	1.000	1.000
42	5.785	0.001	31.091	1.771	-0.522	0.057	128995.960	1.000	0.000
43	7.230	0.001	29.851	1.768	-0.012	0.059	128529.397	1.000	0.000
44	0.121	0.001	30.386	1.764	-0.163	0.058	128080.664	1.000	1.000
45	4.811	0.001	28.713	1.761	1.058	0.061	127639.062	1.000	0.000
46	0.210	0.001	27.443	1.759	1.089	0.064	127222.787	1.000	1.000
47	6.267	0.001	26.771	1.756	0.090	0.066	126860.981	1.000	0.000
48	1.794	0.001	26.199	1.754	-1.294	0.067	126501.715	1.000	1.000
49	0.908	0.001	29.076	1.751	-0.519	0.060	126158.348	1.000	1.000
50	5.760	0.001	25.273	1.749	0.898	0.069	125815.762	1.000	0.000
51	2.163	0.001	24.834	1.747	-1.322	0.070	125493.928	1.000	1.000
52	0.865	0.001	26.574	1.744	-1.354	0.066	125174.787	1.000	1.000
53	1.560	0.001	25.777	1.742	-1.140	0.068	124841.970	1.000	1.000
54	1.596	0.001	25.379	1.740	0.742	0.069	124551.310	1.000	1.000
55	0.338	0.001	23.805	1.738	-0.000	0.073	124240.099	1.000	1.000
56	6.745	0.001	23.593	1.736	1.218	0.074	123956.686	1.000	0.000
57	2.096	0.001	24.049	1.734	-0.504	0.072	123678.838	1.000	1.000
58	2.042	0.001	22.836	1.732	-1.239	0.076	123409.373	1.000	1.000
59	2.426	0.001	23.313	1.730	-0.923	0.074	123143.103	1.000	1.000
60	1.335	0.001	23.665	1.728	-0.175	0.073	122882.666	1.000	1.000
61	2.604	0.001	22.433	1.726	0.534	0.077	122631.169	1.000	1.000
62	1.167	0.001	22.510	1.725	0.975	0.077	122386.703	1.000	1.000
63	0.505	0.001	21.889	1.723	-0.096	0.079	122146.281	1.000	1.000
64	3.013	0.001	22.023	1.721	0.639	0.078	121906.858	1.000	1.000

Table B.1 – continued

n	Frequency (d^{-1})	Error on the frequency (d^{-1})	Semi-ampl. (counts)	Error on the semi-ampl. (counts)	Phase (radians)	Error on the phase (radians)	Variance	Significance level under whitenoise	Significance level under rednoise
65	5.292	0.001	21.704	1.720	-0.292	0.079	121665.686	1.000	0.000
66	1.919	0.001	22.644	1.718	1.291	0.076	121432.061	1.000	1.000
67	2.281	0.001	21.577	1.716	-0.268	0.080	121196.775	1.000	1.000
68	0.256	0.001	21.475	1.715	-0.933	0.080	120966.429	1.000	1.000
69	3.879	0.001	20.781	1.713	0.981	0.082	120738.337	1.000	0.400
70	0.704	0.001	20.553	1.712	0.972	0.083	120520.091	1.000	1.000
71	0.075	0.001	21.165	1.710	1.147	0.081	120307.315	1.000	1.000
72	1.271	0.001	20.047	1.709	-0.419	0.085	120095.530	1.000	1.000
73	0.775	0.001	19.571	1.707	-0.655	0.087	119894.707	1.000	1.000
74	3.361	0.001	18.793	1.706	0.990	0.091	119707.380	1.000	1.000
75	2.528	0.001	19.654	1.704	-0.778	0.087	119522.475	1.000	1.000
76	13.824	0.001	18.877	1.703	-1.365	0.090	119343.548	1.000	0.000
77	3.611	0.001	18.240	1.702	-0.254	0.093	119166.029	1.000	1.000
78	7.697	0.002	17.935	1.701	-0.434	0.095	119001.699	1.000	0.000
79	1.305	0.002	17.814	1.700	1.036	0.095	118841.822	1.000	1.000
80	2.803	0.002	17.494	1.698	0.893	0.097	118683.515	1.000	1.000
					HD 46202				
1	0.510	0.000	86.264	1.299	-1.411	0.015	68955.343	0.000	
2	4.856	0.000	77.639	1.264	0.722	0.016	65284.843	0.000	
3	4.690	0.000	68.833	1.234	-0.405	0.018	62274.470	0.000	
4	2.289	0.000	65.917	1.211	0.545	0.018	59974.426	0.000	
5	2.643	0.000	58.219	1.189	0.081	0.020	57806.630	0.000	
6	3.004	0.000	50.229	1.171	0.162	0.023	56115.469	0.000	
7	0.038	0.000	38.789	1.158	-0.516	0.030	54841.954	0.027	
8	0.814	0.001	34.714	1.151	-0.435	0.033	54143.530	0.188	
9	2.217	0.001	33.908	1.144	-0.058	0.034	53537.830	0.247	
10	1.459	0.001	31.942	1.138	-1.234	0.036	52953.186	0.492	
11	2.193	0.001	34.499	1.133	-1.477	0.033	52444.345	0.161	
12	2.126	0.001	27.614	1.127	-0.706	0.041	51942.704	0.984	
13	0.218	0.001	26.393	1.123	0.378	0.043	51569.206	0.999	
14	0.843	0.001	24.885	1.119	0.110	0.045	51224.151	1.000	
15	0.544	0.001	24.763	1.116	-0.538	0.045	50914.127	1.000	
16	13.973	0.001	24.024	1.113	-0.633	0.046	50607.037	1.000	
17	2.154	0.001	23.531	1.109	0.799	0.047	50315.236	1.000	
18	0.061	0.001	22.544	1.106	1.382	0.049	50032.695	1.000	

Table B.1 – continued

n	Frequency (d^{-1})	Error on the frequency (d^{-1})	Semi-ampl. (counts)	Error on the semi-ampl. (counts)	Phase (radians)	Error on the phase (radians)	Variance	Significance level under whitenoise	Significance level under rednoise
19	1.118	0.001	22.331	1.103	0.216	0.049	49765.179	1.000	
20	2.490	0.001	22.475	1.100	0.768	0.049	49513.637	1.000	
21	2.355	0.001	22.466	1.098	0.173	0.049	49261.694	1.000	
22	0.435	0.001	21.094	1.095	0.849	0.052	49009.543	1.000	
23	0.380	0.001	21.265	1.092	-0.152	0.051	48792.745	1.000	
24	0.579	0.001	20.176	1.090	1.296	0.054	48584.118	1.000	
25	1.150	0.001	18.288	1.088	0.193	0.059	48383.433	1.000	
26	0.788	0.001	18.154	1.086	0.835	0.060	48215.226	1.000	
27	0.722	0.001	17.579	1.084	-0.593	0.062	48050.564	1.000	
28	3.082	0.001	16.862	1.082	-0.342	0.064	47902.480	1.000	
29	0.992	0.001	18.213	1.081	0.949	0.059	47757.617	1.000	
30	0.964	0.001	16.141	1.079	0.552	0.067	47608.516	1.000	

Appendix C

Journal of observations of the Cygnus region

Table C.1: Journal of observations linked to the Cygnus campaign.

HJD	He I 4471	He II 4542	N III 4634	N III 4641	He II 4686	He I 4713	He I 5876	Na I 5890	Na I 5896
				HD 190864					
2134.4733	−13.0	−5.2	−19.3	−26.3	−4.9	−18.6	−13.9	−19.1	−18.3
4711.3132	−16.4	−7.7	−23.4	−29.5	11.6	−20.9	——	——	——
4712.3000	−15.5	−4.3	−20.5	−24.8	13.4	−11.9	——	——	——
4712.3111	−13.7	−7.2	−30.3	−24.2	18.0	−15.7	——	——	——
4717.2954	−16.0	−6.9	−18.9	−28.4	17.1	−16.6	——	——	——
4718.3637	−15.9	−3.9	−19.7	−35.9	13.4	−14.2	——	——	——
4740.2629	−15.8	−8.5	−20.5	−30.9	10.9	−18.3	——	——	——
4741.3195	−11.0	−5.1	−18.1	−28.3	11.7	−9.6	——	——	——
4743.5116	−12.2	−6.5	−15.7	−28.2	13.0	−13.2	——	——	——
4982.8779	−20.7	−9.2	−28.3	−62.0	−3.5	−25.4	−13.3	−20.1	−18.6
4988.7847	−16.1	−0.8	−10.6	−32.4	−27.7	—	−19.7	−18.4	−18.5
5355.4081	−17.0	−4.0	−16.2	−25.1	1.0	−16.1	——	——	——
5356.4053	−14.3	−7.2	−17.3	−34.0	−1.2	−14.1	——	——	——
5415.3437	−14.0	−5.2	−21.6	−29.5	4.5	−14.8	——	——	——
5416.3784	−18.8	−10.9	−25.0	−33.6	−7.0	−20.2	——	——	——
5417.3323	−18.5	−8.2	−24.3	−34.4	7.6	−16.9	——	——	——
5419.3479	−13.8	−7.1	−20.4	−30.7	0.4	−16.9	——	——	——
				HD 227018					
4711.3323	12.7	23.3	——	——	24.4	15.0	——	——	——
4712.3346	20.2	23.8	——	——	27.6	21.1	——	——	——
4717.3188	16.0	20.9	——	——	25.3	15.0	——	——	——
4718.3862	16.4	22.5	——	——	23.6	13.6	——	——	——
4740.2871	12.1	15.3	——	——	20.6	13.4	——	——	——
4741.3477	12.0	15.8	——	——	16.8	—	——	——	——
4742.2887	11.9	19.5	——	——	22.7	16.4	——	——	——
4744.3032	15.6	21.6	——	——	22.8	13.0	——	——	——
5417.3604	18.2	26.2	——	——	27.1	17.0	——	——	——
5419.3755	20.8	27.7	——	——	26.7	24.5	——	——	——
				HD 193514					
3246.5202	−7.1	2.7	−14.7	−27.4	——	−9.8	−1.1	−15.5	−13.6
3600.4087	−9.9	5.4	−21.1	−30.6	——	−7.5	−4.8	−15.8	−13.7
4711.3635	−19.4	−9.1	−18.4	−28.4	——	−14.9	——	——	——
4712.3753	−26.1	−10.8	−21.4	−30.9	——	−21.8	——	——	——
4717.5446	−19.3	−4.4	−20.0	−31.8	——	−10.7	——	——	——

Table C.1 – continued

HJD	He I 4471	He II 4542	N III 4634	N III 4641	He II 4686	He I 4713	He I 5876	Na I 5890	Na I 5896
4718.5362	−16.2	−5.4	−15.7	−24.1	——	−18.4	——	——	——
4740.3384	−24.8	−9.4	−15.3	−30.0	——	−20.3	——	——	——
4741.2966	−12.4	−4.0	−21.6	−31.5	——	−7.5	——	——	——
4742.2647	−18.4	−6.7	−15.7	−29.5	——	−24.8	——	——	——
4743.2729	−19.2	−4.9	−14.1	−28.3	——	−15.0	——	——	——
4744.4118	−19.8	−2.4	−11.7	−26.0	——	−14.0	——	——	——
4987.8912	−23.1	−15.2	−35.4	−42.1	——	−20.2	−19.2	−13.9	−8.9
5355.5532	−22.1	−11.8	−26.2	−37.0	——	−19.6	——	——	——
5355.5678	−21.1	−8.5	−24.3	−36.0	——	−19.1	——	——	——
5356.4702	−13.1	−9.6	−20.1	−39.5	——	−15.6	——	——	——
5356.4882	−10.7	−2.5	−22.4	−33.6	——	−16.9	——	——	——
5360.4096	−15.3	−6.6	−18.9	−29.3	——	−10.0	——	——	——
5361.3856	−23.6	−12.9	−26.9	−38.5	——	−21.2	——	——	——
5415.5272	−16.3	−10.2	−23.9	−36.5	——	−12.7	——	——	——
5416.5327	−25.3	−12.8	−28.9	−40.0	——	−19.8	——	——	——
5418.6223	−16.2	−6.7	−30.2	−45.0	——	−10.9	——	——	——
5420.4585	−17.3	−9.2	−20.3	−33.3	——	−11.6	——	——	——
HD 193595									
4711.3816	−14.7	−7.9	—-	—-	−4.9	−14.4	——	——	——
4712.4309	−16.1	−9.1	—-	—-	−4.6	−12.7	——	——	——
4717.5141	−10.9	−6.2	—-	—-	−4.9	−12.1	——	——	——
4718.5148	−13.5	−6.4	—-	—-	−3.8	−12.3	——	——	——
4740.3919	−15.5	−9.5	—-	—-	−6.3	−14.7	——	——	——
4741.5279	−10.0	−4.2	—-	—-	1.5	−8.6	——	——	——
4989.8582	−15.9	−14.1	—-	—-	−3.2	−12.5	−9.0	−16.1	−11.4
5417.5197	−14.1	−7.5	—-	—-	−6.4	−13.2	——	——	——
5421.4977	−12.7	−8.2	—-	—-	−7.7	−12.3	——	——	——
HD 193682									
4711.4038	−62.6	−42.6	——	——	−50.3	——	——	——	——
4712.4927	−62.2	−48.8	——	——	−60.2	——	——	——	——
4717.3593	−52.0	−39.8	——	——	−58.8	——	——	——	——
4718.4224	−46.6	−38.4	——	——	−50.2	——	——	——	——
4740.4349	−35.5	−29.2	——	——	−36.6	——	——	——	——
4741.4987	−27.0	−29.8	——	——	−45.0	——	——	——	——
4989.9081	−48.9	−50.0	——	——	−56.8	——	−52.3	−14.0	−6.7
5361.4260	−39.6	−33.2	——	——	−44.1	——	——	——	——

Table C.1 – continued

HJD	He I 4471	He II 4542	N III 4634	N III 4641	He II 4686	He I 4713	He I 5876	Na I 5890	Na I 5896
5415.5474	−48.9	−35.2	——	——	−74.2	——	——	——	——
5417.5457	−57.7	−38.2	——	——	−68.5	——	——	——	——
5418.5280	−50.9	−43.4	——	——	−60.9	——	——	——	——
HD 191978									
3247.4196	−21.5	−14.1	——	——	−14.9	−18.8	−12.4	−17.3	−17.3
3246.3746	−20.8	−15.9	——	——	−15.1	−20.0	−13.6	−18.2	−17.7
4711.4730	−21.5	−11.2	——	——	−10.1	−12.7	——	——	——
4712.5341	−19.5	−12.7	——	——	−9.4	−11.7	——	——	——
4717.4173	−17.0	−11.0	——	——	−7.0	−9.9	——	——	——
4743.2985	−17.6	−9.1	——	——	−6.5	−9.2	——	——	——
4982.9824	−20.4	−16.1	——	——	−10.7	−7.4	−17.9	−22.7	−16.4
4991.9009	−22.5	−14.8	——	——	−17.9	−22.7	−16.6	−21.2	−19.7
5415.3646	−10.8	−1.9	——	——	−0.4	−3.4	——	——	——
5416.4217	−15.7	−6.5	——	——	−5.9	−8.3	——	——	——
5419.4729	−11.9	−1.1	——	——	−6.8	−5.9	——	——	——
HD 191423									
4711.4958	−47.7	−59.4	——	——	——	−57.2	——	——	——
4712.5506	−41.2	−93.2	——	——	——	−51.4	——	——	——
4717.4436	−43.8	−72.6	——	——	——	−63.6	——	——	——
4718.5873	−40.5	−30.5	——	——	——	−53.8	——	——	——
4743.3283	−49.2	−55.8	——	——	——	−62.9	——	——	——
4991.9379	−41.7	−42.0	——	——	——	—	——	−24.5	−23.3
5418.4186	−45.3	−46.2	——	——	——	−55.3	——	——	——
5421.5876	−42.5	−66.0	——	——	——	−50.9	——	——	——
HD 193117									
4711.5245	−26.5	−17.8	——	——	−12.7	−20.5	——	——	——
4712.4647	−31.6	−20.9	——	——	−13.3	−25.3	——	——	——
4718.3403	−25.7	−17.4	——	——	−11.5	−20.3	——	——	——
4743.3577	−23.4	−25.5	——	——	−9.0	−23.2	——	——	——
4986.9239	−27.6	−0.9	——	——	−19.4	−34.2	−17.0	−11.9	−9.5
4991.9784	−27.3	−14.3	——	——	−2.6	−22.8	−12.8	−9.4	−7.0
5417.4239	−25.5	−16.4	——	——	−11.1	−20.6	——	——	——
5420.6211	−25.2	−14.0	——	——	−8.1	−20.8	——	——	——
HD 194334									
4711.5581	−17.4	−7.9	——	——	39.4	−14.3	——	——	——
4718.3065	−22.9	−13.0	——	——	17.8	−23.7	——	——	——

Table C.1 – continued

HJD	He I 4471	He II 4542	N III 4634	N III 4641	He II 4686	He I 4713	He I 5876	Na I 5890	Na I 5896
4745.3411	−15.4	−1.8	——	——	18.7	−7.7	——	——	——
5052.8184	−8.9	3.0	——	——	24.6	−17.8	−10.3	−14.4	−11.6
5053.7053	−19.8	−1.5	——	——	9.8	−22.7	−9.9	−11.7	−10.3
5403.8632	−10.7	−1.9	——	——	——-	−20.4	−11.6	−11.5	−10.5
5404.8888	−15.8	−11.1	——	——	2.1	−10.1	−7.4	−10.8	−10.2
5360.4619	−12.5	−2.2	——	——	35.1	−12.5	——	——	——
5361.5363	−10.4	−2.8	——	——	37.6	−14.2	——	——	——
5416.6210	−18.2	−9.7	——	——	31.4	−13.2	——	——	——
5420.4943	−11.7	−3.7	——	——	33.3	−15.8	——	——	——
HD 195213									
4711.5962	−10.3	2.7	−15.6	−20.7	——	−9.5	——	——	——
4717.5787	−3.4	12.1	−14.6	−16.5	——	−2.0	——	——	——
4718.5593	3.1	14.1	−2.9	−20.0	——	1.5	——	——	——
4743.3856	−4.0	6.1	−18.3	−20.4	——	−3.5	——	——	——
5051.7513	−7.6	11.4	——	——	——	−5.4	−4.7	−18.3	−17.2
5052.7110	−8.6	2.8	——	——	——	−20.9	−11.4	−19.0	−19.4
5402.8624	−5.4	4.1	——	——	——	−8.0	−1.9	−12.3	−11.7
5360.5868	3.4	14.7	−10.9	−19.5	——	2.0	——	——	——
5415.6170	−1.7	9.3	−6.9	−10.7	——	−1.9	——	——	——
5420.5309	−5.2	5.6	−9.1	−13.4	——	−2.8	——	——	——
HD 228841									
4712.3982	−54.4	−25.7	——	——	——	−24.8	——	——	——
4717.4766	−50.3	−19.1	——	——	——	−19.1	——	——	——
4718.4808	−41.0	−18.2	——	——	——	−38.2	——	——	——
4744.2722	−43.8	−27.4	——	——	——	−82.7	——	——	——
4989.8092	−63.2	−36.3	——	——	——	——-	——	−17.3	−15.1
5361.5708	−34.2	−19.8	——	——	——	−57.2	——	——	——
5415.4213	−52.8	−24.9	——	——	——	−70.0	——	——	——
5418.5980	−47.7	−32.3	——	——	——	−22.0	——	——	——
HD 229234									
4717.3892	−56.5	−42.1	——	——	−38.1	−50.0	——	——	——
4718.4482	26..9	41.2	——	——	45.7	36.1	——	——	——
4740.5010	−1.9	19.4	——	——	24.3	10.2	——	——	——
4742.3217	−23.9	−12.3	——	——	−5.2	−10.5	——	——	——
4992.7849	25.4	34.3	——	——	25.3	4.3	24.7	−22.8	−21.0
5051.8116	16.0	46.0	——	——	27.9	17.0	11.1	−23.7	−21.2

Table C.1 – continued

HJD	He I 4471	He II 4542	N III 4634	N III 4641	He II 4686	He I 4713	He I 5876	Na I 5890	Na I 5896
5052.7710	13.9	26.8	——	——	22.2	13.1	10.5	−22.5	−21.3
5403.9302	3.4	10.4	——	——	4.3	−6.7	2.2	−21.0	−18.5
5404.9917	−80.5	−70.5	——	——	−68.5	−65.8	−70.2	−20.1	−19.2
5355.4346	−46.4	−28.3	——	——	−30.3	−34.8	——	——	——
5355.4666	−53.2	−42.4	——	——	−37.0	−44.2	——	——	——
5360.5530	4.5	17.1	——	——	23.6	14.5	——	——	——
5361.4974	19.0	31.9	——	——	38.3	31.5	——	——	——
5415.5786	−60.3	−48.1	——	——	−55.9	−55.8	——	——	——
5416.5599	−6.1	3.3	——	——	8.4	−2.5	——	——	——
5417.5762	28.1	40.3	——	——	42.4	40.3	——	——	——
5418.5637	−48.7	−37.5	——	——	−30.6	−38.9	——	——	——
5420.4096	23.8	28.5	——	——	39.2	31.6	——	——	——
5421.4347	9.6	——	——	——	——	12.8	——	——	——
				HD 227757					
4988.8797	−23.8	−30.2	——	——	−27.1	−26.4	−24.4	−13.0	−10.8
5403.7927	−24.6	−23.4	——	——	−26.6	−35.7	−21.1	−12.4	−11.6
5724.8037	−23.1	−21.2	——	——	−26.2	−30.9	−23.2	−12.0	−10.0
5726.7373	−30.3	−25.3	——	——	−31.6	−28.9	−22.7	−12.4	−11.0
5728.7408	−24.5	−24.0	——	——	−27.7	−24.4	−22.7	−11.7	−10.2
				HD 194094					
4987.9233	−23.5	−7.5	——	——	−21.5	−14.2	−20.0	−15.4	−13.5
4991.8497	−21.9	−13.1	——	——	−15.1	−25.9	−21.2	−17.7	−17.4
5416.5918	−15.1	−11.3	——	——	0.6	−9.7	——	——	——
5421.5321	−13.7	−9.2	——	——	−3.2	−8.3	——	——	——
5820.7063	−18.6	−17.6	——	——	−11.1	−13.4	−16.2	−12.0	−11.0
				HD 227245					
5049.8148	2.2	16.0	——	——	6.5	−10.2	6.3	−15.1	−13.3
5050.6777	5.0	6.9	——	——	20.2	5.2	5.9	−14.4	−11.0
5723.9405	3.8	6.3	——	——	4.3	0.3	6.9	−10.5	−8.0
5725.7942	3.2	11.0	——	——	13.1	6.1	7.4	−13.3	−11.6
5727.7497	15.4	8.7	——	——	9.7	7.8	8.9	−10.3	−8.6
				HD 194280					
3286.3646	−13.2	−23.7	−21.2	−4.3	−16.9	——	——	——	——
3289.4693	−13.9	−20.4	−8.8	−2.1	−12.1	——	——	——	——
3290.4109	−14.0	−21.8	−6.7	−12.8	−13.8	——	——	——	——
3547.5563	12.6	−24.4	−11.8	−6.1	−16.5	——	——	——	——

Table C.1 – continued

HJD	He I 4471	He II 4542	N III 4634	N III 4641	He II 4686	He I 4713	He I 5876	Na I 5890	Na I 5896
3548.5482	12.1	−33.0	−14.4	−8.3	−24.0	——	——	——	——
3550.5544	12.0	−24.4	−8.7	−7.1	−18.9	——	——	——	——
3551.5537	11.8	−27.3	−17.8	−13.6	−28.7	——	——	——	——
3553.5246	11.5	−30.5	−14.8	−8.9	−23.4	——	——	——	——
3554.5746	11.2	−30.4	−13.4	−3.5	−22.4	——	——	——	——
3555.5858	11.0	−30.9	−14.3	−5.4	−21.7	——	——	——	——
3980.3504	−4.5	−29.1	−12.0	−7.7	−20.1	——	——	——	——
3980.4150	−4.6	−27.2	−3.9	−5.1	−12.0	——	——	——	——
3980.4803	−4.7	−24.6	−5.6	1.9	−13.7	——	——	——	——
3981.3906	−4.8	−23.9	−4.6	6.6	−13.0	——	——	——	——
3983.3073	−5.2	−29.9	−9.8	−13.0	−22.4	——	——	——	——
3983.3996	−5.4	−24.4	−14.6	−10.6	−20.5	——	——	——	——
3984.3371	−5.5	−22.2	−3.6	−5.3	−17.0	——	——	——	——
3984.4163	−5.7	−23.6	−16.4	−9.1	−26.0	——	——	——	——
4035.2915	−15.9	−30.0	−18.5	−14.8	−20.7	——	——	——	——
4396.2979	−15.4	−27.9	−11.2	−1.6	−10.1	——	——	——	——
4397.2638	−15.5	−32.2	−11.4	−11.6	−18.5	——	——	——	——
4400.3769	−16.0	−20.9	−14.8	−7.7	−14.0	——	——	——	——
4401.2699	−15.9	−27.7	−18.6	−6.8	−17.8	——	——	——	——
4402.2615	−16.0	−17.5	−19.4	−3.1	−13.0	——	——	——	——
4403.3107	−16.2	−19.8	−31.1	−10.7	−21.5	——	——	——	——
4405.2752	−16.3	−27.6	−8.9	−1.2	−18.4	——	——	——	——
4406.2612	−16.4	−24.4	−6.0	−6.5	−16.8	——	——	——	——
4407.2709	−16.5	−25.5	−6.6	−9.3	−18.2	——	——	——	——
4408.2688	−16.5	−19.2	−5.6	−4.9	−8.1	——	——	——	——
4409.2674	−16.6	−25.2	−13.3	−5.9	−20.1	——	——	——	——
4410.2680	−16.7	−24.6	−5.7	−7.0	−15.1	——	——	——	——
4412.3017	−16.8	−24.4	13.4	1.4	−15.3	——	——	——	——
4413.2761	−16.9	−18.9	−14.9	−2.0	−9.0	——	——	——	——
4414.3143	−17.0	−14.9	0.1	2.6	−10.5	——	——	——	——
4415.2739	−16.9	−28.1	−6.0	−0.4	−8.3	——	——	——	——
4416.2648	−17.0	−19.8	−18.6	−8.1	−20.3	——	——	——	——
4417.3066	−17.0	−27.8	−14.9	7.3	−17.2	——	——	——	——
4418.2530	−17.0	−21.4	−23.5	−0.2	−17.9	——	——	——	——
4419.2956	−17.1	−24.8	−21.0	−3.2	−18.5	——	——	——	——
4421.2507	−17.0	−21.3	−2.4	−4.9	−13.3	——	——	——	——

Table C.1 – continued

HJD	He I 4471	He II 4542	N III 4634	N III 4641	He II 4686	He I 4713	He I 5876	Na I 5890	Na I 5896
4422.2597	−17.0	−27.9	−18.9	−7.7	−19.6	———	———	———	———
4423.2513	−17.0	−22.5	−6.1	−6.5	−13.8	———	———	———	———

Table C.2: Journal of observations of HD 193443.

HJD	Phase	Primary	Secondary
3246.478	0.048	24.5	−106.5
3600.354	0.442	−11.3	−40.8
4711.350	0.238	10.7	−79.7
4712.361	0.373	−13.9	−29.6
4717.342	0.040	9.0	−113.0
4718.411	0.183	11.3	−102.2
4740.316	0.117	41.6	−111.0
4741.272	0.245	25.5	−85.5
4743.482	0.541	−23.8	17.8
5174.265	0.236	19.3	−81.0
5176.238	0.500	−16.9	4.4
5177.227	0.633	−34.8	39.8
5355.377	0.492	−21.1	−4.4
5355.391	0.494	−13.9	−8.6
5356.425	0.632	−41.2	58.7
5356.449	0.636	−34.3	66.6
5360.368	0.161	31.2	−105.4
5360.386	0.163	40.9	−100.6
5361.363	0.294	11.9	−79.8
5370.387	0.502	−13.4	−4.1
5371.364	0.633	−32.9	41.7
5372.367	0.768	−37.9	62.3
5373.395	0.905	−35.6	40.4
5374.396	0.039	26.9	−88.3
5375.360	0.168	34.0	−106.5
5415.450	0.538	−24.7	17.8
5416.448	0.671	−36.0	48.1
5417.403	0.799	−38.8	78.9
5418.443	0.939	−17.6	6.6
5419.518	0.083	36.8	−114.2
5420.348	0.194	25.5	−1.8
5421.388	0.333	5.4	−46.7
5539.234	0.116	29.9	−114.1
5540.234	0.250	14.7	−66.8
5541.241	0.385	−5.5	−48.7
5542.249	0.520	−21.7	−9.5
5543.239	0.652	−41.1	53.9

Table C.3: Journal of observations of HD 228989.

HJD	Phase	Primary	Secondary
5049.952	0.230	196.1	−224.5
5050.752	0.681	−181.5	207.9
5402.935	0.259	198.0	−225.6
5416.490	0.902	−139.1	116.7
5417.471	0.455	46.6	−67.2
5419.600	0.656	−155.3	174.9
5420.580	0.209	191.1	−218.6
5421.620	0.795	−174.1	185.6
5724.883	0.790	−194.4	210.0
5725.868	0.345	155.3	−196.7
5726.812	0.877	−135.7	141.7
5727.833	0.453	50.9	−70.3
5728.818	0.009	8.4	−20.2
5813.661	0.847	−158.3	179.0
5813.895	0.979	−37.2	22.1
5814.666	0.414	81.7	−122.7
5814.885	0.537	−48.3	38.1
5815.646	0.966	−44.8	39.7

Table C.4: Journal of observations of HD 194649.

HJD	Phase	Primary	Secondary
4992.893	0.553	−16.6	20.6
5053.753	0.488	−0.5	−42.9
5355.505	0.415	38.7	−138.3
5360.502	0.887	−80.9	98.8
5361.456	0.168	55.4	−183.7
5415.488	0.092	35.1	−151.2
5417.614	0.718	−85.9	153.0
5724.943	0.288	48.5	−214.6
5725.923	0.577	−45.0	64.4
5726.858	0.853	−81.8	122.8
5727.881	0.154	41.3	−179.7
5728.870	0.445	14.2	−117.6
5816.658	0.317	42.1	−196.3
5817.656	0.611	−61.9	106.5
5818.656	0.905	−64.8	71.6
5818.877	0.971	−25.6	0.0
5820.642	0.491	2.8	−40.1

Bibliography

Abt, H. A. & Biggs, E. S., 1972, *Bibliography of stellar radial velocities*.

Aigrain, S., Favata, F. & Gilmore, G., 2004, Characterising stellar micro-variability for planetary transit searches, *A&A* **414**, 1139–1152.

Auvergne, M., Bodin, P., Boisnard, L. et al., 2009, The CoRoT satellite in flight: description and performance, *A&A* **506**, 411–424.

Baglin, A., Auvergne, M., Barge, P. et al., 2006, Scientific Objectives for a Minisat: CoRoT, in *ESA Special Publication* (M. Fridlund, A. Baglin, J. Lochard, & L. Conroy, ed.), *ESA Special Publication*, vol. 1306, 33–+.

Belkacem, K., Dupret, M. A. & Noels, A., 2010, Solar-like oscillations in massive main-sequence stars. I. Asteroseismic signatures of the driving and damping regions, *A&A* **510**, A6+.

Benaglia, P., Koribalski, B. & Albacete Colombo, J. F., 2006, Radio Detection of Colliding Wind Binaries, *PASA* **23**, 50–63.

Beuther, H., 2011, Formation and early evolution of massive stars, *Bulletin de la Societe Royale des Sciences de Liege* **80**, 200–210.

Bhavya, B., Mathew, B. & Subramaniam, A., 2007, Pre-main sequence stars, emission stars and recent star formation in the Cygnus region, *Bulletin of the Astronomical Society of India* **35**, 383–411.

Blaauw, A., 1961, On the origin of the O- and B-type stars with high velocities (the "run-away" stars), and some related problems, *BAIN* **15**, 265–+.

Blomme, R., 2009, Non-radial pulsations and large-scale structure in stellar winds, *Communications in Asteroseismology* **158**, 131–+.

Blomme, R., Mahy, L., Catala, C. et al., 2011, Variability in the CoRoT photometry of three hot O-type stars. HD 46223, HD 46150, and HD 46966, *A&A* **533**, A4+.

Boeche, C., Munari, U., Tomasella, L. & Barbon, R., 2004, Kinematics and binaries in young stellar aggregates. II. NGC 6913 ≡ M 29, *A&A* **415**, 145–154.

Bonatto, C. & Bica, E., 2009, Probing the age and structure of the nearby very young open clusters NGC2244 and 2239, *MNRAS* **394**, 2127–2140.

Bonnell, I. A., 2001, The Formation of Close Binary Stars, in *The Formation of Binary Stars* (H. Zinnecker & R. Mathieu, ed.), *IAU Symposium*, vol. 200, 23–+.

Bonnell, I. A. & Bate, M. R., 2005, Binary systems and stellar mergers in massive star formation, *MNRAS* **362**, 915–920.

Bonnell, I. A. & Smith, R. J., 2011, The Formation of Massive Stars, in *IAU Symposium* (J. Alves, B. G. Elmegreen, J. M. Girart, & V. Trimble, ed.), *IAU Symposium*, vol. 270, 57–64.

Bonnell, I. A., Smith, R. J., Clark, P. C. & Bate, M. R., 2011, The efficiency of star formation in clustered and distributed regions, *MNRAS* **410**, 2339–2346.

Bosch, G., Terlevich, E. & Terlevich, R., 2009, Gemini/GMOS Search for Massive Binaries in the Ionizing Cluster of 30 Dor, *AJ* **137**, 3437–3441.

Bouret, J.-C., Lanz, T. & Hillier, D. J., 2005, Lower mass loss rates in O-type stars: Spectral signatures of dense clumps in the wind of two Galactic O4 stars, *A&A* **438**, 301–316.

Bozic, H., Harmanec, P., Horn, J. et al., 1995, Toward a consistent model of the B0.5IVe + sdO binary ϕ Persei., *A&A* **304**, 235–+.

Briquet, M., Aerts, C., Baglin, A. et al., 2011, An asteroseismic study of the O9V star HD 46202 from CoRoT space-based photometry, *A&A* **527**, A112+.

Bromm, V. & Larson, R. B., 2004, The First Stars, *Annu. Rev. Astron. Astrophys.* **42**, 79–118.

Brott, I., de Mink, S. E., Cantiello, M. et al., 2011a, Rotating massive main-sequence stars. I. Grids of evolutionary models and isochrones, *A&A* **530**, A115+.

Brott, I., Evans, C. J., Hunter, I. et al., 2011b, Rotating massive main-sequence stars. II. Simulating a population of LMC early B-type stars as a test of rotational mixing, *A&A* **530**, A116+.

Buzug, T., 2008, *Algebraic and Statistical Reconstruction Methods*, Springer Berlin Heidelberg, 10.1007/978-3-540-39408-2_6.

Cantiello, M., Langer, N., Brott, I. et al., 2009, Sub-surface convection zones in hot massive stars and their observable consequences, *A&A* **499**, 279–290.

Cassinelli, J. P., Mathis, J. S. & Savage, B. D., 1981, Central object of the 30 Doradus Nebula, a supermassive star, *Science* **212**, 1497–1501.

Castor, J. I., Abbott, D. C. & Klein, R. I., 1975, Radiation-driven winds in Of stars, *ApJ* **195**, 157–174.

Cohen, D. H., Leutenegger, M. A., Wollman, E. E. et al., 2010, A mass-loss rate determination for ζ Puppis from the quantitative analysis of X-ray emission-line profiles, *MNRAS* **405**, 2391–2405.

Conti, P. S., 1973, Spectroscopic studies of O-type stars. II. Comparison with non-LTE models., *ApJ* **179**, 161–179.

Conti, P. S., 1974, Spectroscopic studies of O-type stars. IV. Lines in the red region., *ApJ* **187**, 539–549.

Conti, P. S. & Alschuler, W. R., 1971, Spectroscopic Studies of O-Type Stars. I. Classification and Absolute Magnitudes, *ApJ* **170**, 325–+.

Conti, P. S. & Ebbets, D., 1977, Spectroscopic studies of O-type stars. VII. Rotational velocities V sin i and evidence for macroturbulent motions., *ApJ* **213**, 438–447.

Conti, P. S., Leep, E. M. & Lorre, J. J., 1977, Spectroscopic studies of O-type stars. VIII - Radial velocities and the K-term, *ApJ* **214**, 759–772.

Crowther, P. A., Schnurr, O., Hirschi, R. et al., 2010, The R136 star cluster hosts several stars whose individual masses greatly exceed the accepted 150$M_{\odot}$ stellar mass limit, *MNRAS* **408**, 731–751.

Cuypers, J., 1987, *The period analysis of variable stars*, Academiae Analecta.

Darcourt, J., Koulibaly, P. & Migneco, O., 1998, Méthodes itératives de reconstruction, *ACOMEN* **4**, 100–107.

De Becker, M., Rauw, G., Manfroid, J. & Eenens, P., 2006, Early-type stars in the young open cluster IC 1805. II. The probably single stars HD 15570 and HD 15629, and the massive binary/triple system HD 15558, *A&A* **456**, 1121–1130.

De Loore, C. & van Rensbergen, W., 2005, The Evolution of Massive Close Binaries, *APSS* **296**, 337–352.

de Mink, S. E., Cantiello, M., Langer, N. et al., 2009, Rotational mixing in massive binaries. Detached short-period systems, *A&A* **497**, 243–253.

de Wit, W. J., Testi, L., Palla, F. & Zinnecker, H., 2005, The origin of massive O-type field stars: II. Field O stars as runaways, *A&A* **437**, 247–255.

Degroote, P., Briquet, M., Auvergne, M. et al., 2010, Detection of frequency spacings in the young O-type binary HD 46149 from CoRoT photometry, *A&A* **519**, A38+.

Delgado, A. J., Alfaro, E. J., Moitinho, A. & Franco, J., 1998, Pre-Main-Sequence Stars in the Young Galactic Cluster IC 4996: A CCD Photometric Study, *AJ* **116**, 1801–1809.

Eggleton, P. P., 1983, Approximations to the radii of Roche lobes, *ApJ* **268**, 368–+.

Evans, C. J., Lennon, D. J., Smartt, S. J. & Trundle, C., 2006, The VLT-FLAMES survey of massive stars: observations centered on the Magellanic Cloud clusters NGC 330, NGC 346, NGC 2004, and the N11 region, *A&A* **456**, 623–638.

Eversberg, T., Lepine, S. & Moffat, A. F. J., 1998, Outmoving Clumps in the Wind of the Hot O Supergiant zeta Puppis, *ApJ* **494**, 799–+.

Feldmeier, A., Oskinova, L. & Hamann, W.-R., 2003, X-ray line emission from a fragmented stellar wind, *A&A* **403**, 217–224.

Ferraz-Mello, S., 1981, Estimation of Periods from Unequally Spaced Observations, *AJ* **86**, 619–+.

Figer, D. F., 2005, The stellar Initial Mass Function in the Galactic Center, in *The Initial Mass Function 50 Years Later* (E. Corbelli, F. Palla, & H. Zinnecker, ed.), *Astrophysics and Space Science Library*, vol. 327, 89–+.

Forbes, D., 1981, The young open clusters Berkeley 62 and Berkeley 86, *PASP* **93**, 441–446.

Frescura, F. A. M., Engelbrecht, C. A. & Frank, B. S., 2008, Significance of periodogram peaks and a pulsation mode analysis of the Beta Cephei star V403Car, *MNRAS* **388**, 1693–1707.

Fullerton, A. W., 2011, Structure in the winds of O-Type stars: observations and inferences, in *IAU Symposium* (C. Neiner, G. Wade, G. Meynet, & G. Peters, ed.), *IAU Symposium*, vol. 272, 136–147.

Fullerton, A. W., Gies, D. R. & Bolton, C. T., 1996, Absorption Line Profile Variations among the O Stars. I. The Incidence of Variability, *ApJS* **103**, 475–+.

García, B. & Mermilliod, J. C., 2001, High-mass binaries in the very young open cluster NGC 6231. Implication for cluster and star formation, *A&A* **368**, 122–136.

Garmany, C. D., Conti, P. S. & Massey, P., 1980, Spectroscopic studies of O type stars. IX - Binary frequency, *ApJ* **242**, 1063–1076.

Garmany, C. D. & Stencel, R. E., 1992, Galactic OB associations in the northern Milky Way Galaxy. I - Longitudes 55 deg to 150 deg, *A&A Supplement Series* **94**, 211–244.

Garmany, C. D. & Vacca, W. D., 1991, New spectral classifications for O-type stars in the Northern Hemisphere, *PASP* **103**, 347–354.

Gies, D. R., 1987a, The kinematical and binary properties of association and field O stars, *ApJS* **64**, 545–563.

Gies, D. R., 1987b, The kinematical and binary properties of association and field O stars, *ApJS* **64**, 545–563.

Gies, D. R., 2004, Doppler tomography of binary stars, in *Spectroscopically and Spatially Resolving the Components of the Close Binary Stars* (R. W. Hilditch, H. Hensberge, & K. Pavlovski, ed.), *Astronomical Society of the Pacific Conference Series*, vol. 318, 61–68.

Gies, D. R., 2008, Binaries in Massive Star Formation, in *Massive Star Formation: Observations Confront Theory* (H. Beuther, H. Linz, & T. Henning, ed.), *Astronomical Society of the Pacific Conference Series*, vol. 387, 93–+.

Godart, M., 2011, *Unveiling the internal structure and evolution of massive stars through their pulsation modes*, Ph.D. thesis, University of Liège.

González, J. F. & Levato, H., 2006, Separation of composite spectra: the spectroscopic detection of an eclipsing binary star, *A&A* **448**, 283–292.

Gosset, E., 2007, *Le calcul du niveau de signification du plus haut pic dans les périodogrammes de type Fourier par la formule de Horne-Baliunas est contre-indiqué, Thèse d'Agrégation de l'Enseignement Supérieur, Seconde Thèse Annexe*, University of Liège.

Gosset, E., Rauw, G., Manfroid, J. et al., 2005, Preliminary results of an observational campaign aiming at the study of the binary system LSS3074, in *Massive Stars and High-Energy Emission in OB Associations* (G. Rauw, Y. Nazé, R. Blomme, & E. Gosset, ed.), 77–80.

Gosset, E., Royer, P., Rauw, G. et al., 2001, A first detailed study of the colliding wind WR+O binary WR 30a, *MNRAS* **327**, 435–451.

Goy, G., 1973, A new general O type stars catalogue, *A&A Supplement Series* **12**, 277–+.

Gräfener, G. & Hamann, W.-R., 2008, Are Wolf-Rayet Winds Driven by Radiation?, in *Mass Loss from Stars and the Evolution of Stellar Clusters* (A. de Koter, L. J. Smith, & L. B. F. M. Waters, ed.), *Astronomical Society of the Pacific Conference Series*, vol. 388, 21–+.

Gray, D. F., 2005, *The Observation and Analysis of Stellar Photospheres*, Cambridge University Press.

Grevesse, N., Asplund, M. & Sauval, A. J., 2007, The Solar Chemical Composition, *Space Science Reviews* **130**, 105–114.

Grundstrom, E. D., Gies, D. R., Hillwig, T. C. et al., 2007, A Spectroscopic Study of Mass Outflows in the Interacting Binary RY Scuti, *ApJ* **667**, 505–519.

Hadrava, P., 2009, Disentangling of spectra - theory and practice, *ArXiv e-prints* .

Harries, T. J., Hilditch, R. W. & Hill, G., 1998, Interacting OB star binaries: LZ Cep, SZ Cam and IU AUR, *MNRAS* **295**, 386–396.

Harvey, J., 1985, High-Resolution Helioseismology, in *Future Missions in Solar, Heliospheric & Space Plasma Physics* (E. Rolfe & B. Battrick, ed.), *ESA Special Publication*, vol. 235, 199–+.

Heber, U., Moehler, S. & Groote, D., 1995, HS 1914+7139: a rapidly rotating massive B-star far away from the galactic plane., *A&A* **303**, L33+.

Heck, A., Manfroid, J. & Mersch, G., 1985, On period determination methods, *A&A Supplement Series* **59**, 63–72.

Hensberge, H. & Pavlovski, K., 2007, Modern Analysis Techniques for Spectroscopic Binaries, in *IAU Symposium* (W. I. Hartkopf, E. F. Guinan, & P. Harmanec, ed.), *IAU Symposium*, vol. 240, 136–147.

Hensberge, H., Pavlovski, K. & Verschueren, W., 2000, The eclipsing binary V578 Mon in the Rosette nebula: age and distance to NGC 2244 using Fourier disentangled component spectra, *A&A* **358**, 553–571.

Herbst, W. & Havlen, R. J., 1977, ARA OB1, NGC 6193 and ARA R1 - an optical study of a very young southern complex, *A&A Supplement Series* **30**, 279–295.

Herrero, A., Kudritzki, R. P., Vilchez, J. M. et al., 1992, Intrinsic parameters of galactic luminous OB stars, *A&A* **261**, 209–234.

Hill, G., 1993, The Measurement of Radial Velocities Using Cross-Correlation Techniques as Applied to Binary Stars, in *New Frontiers in Binary Star Research* (K.-C. Leung & I.-S. Nha, ed.), *Astronomical Society of the Pacific Conference Series*, vol. 38, 127–+.

Hillier, D. J., 2008, What Do We Really Know About the Winds of Massive Stars?, in *IAU Symposium* (F. Bresolin, P. A. Crowther, & J. Puls, ed.), *IAU Symposium*, vol. 250, 89–96.

Hillier, D. J. & Miller, D. L., 1998, The Treatment of Non-LTE Line Blanketing in Spherically Expanding Outflows, *ApJ* **496**, 407–+.

Hillwig, T. C., Gies, D. R., Bagnuolo, W. G., Jr. et al., 2006, Binary and Multiple O-Type Stars in the Cassiopeia OB6 Association, *ApJ* **639**, 1069–1080.

Hiltner, W. A., 1956, Photometric, Polarization, and Spectrographic Observations of O and B Stars., *ApJS* **2**, 389–+.

Høg, E., Fabricius, C., Makarov, V. V. et al., 2000, The Tycho-2 catalogue of the 2.5 million brightest stars, *A&A* **355**, L27–L30.

Hohle, M. M., Neuhäuser, R. & Schutz, B. F., 2010, Masses and luminosities of O- and B-type stars and red supergiants, *Astronomische Nachrichten* **331**, 349–+.

Horne, J. H. & Baliunas, S. L., 1986, A prescription for period analysis of unevenly sampled time series, *ApJ* **302**, 757–763.

Horne, K., 1991, in *Fundamental Properties of Cataclysmic Variable Stars: 12th North American Workshop on Cataclysmic Variables and Low Mass X-ray Binaries* (A. Shafter, ed.), 23, SDSU Press.

Howarth, I. D. & Reid, A. H. N., 1993, UES and IUE observations of the O9.5 V star HD 93521: Non-radial pulsations, wind, and distance, *A&A* **279**, 148–162.

Howarth, I. D., Siebert, K. W., Hussain, G. A. J. & Prinja, R. K., 1997, Cross-correlation characteristics of OB stars from IUE spectroscopy, *MNRAS* **284**, 265–285.

Howarth, I. D., Stickland, D. J., Prinija, R. K. et al., 1991, Spectroscopic binary orbits from ultraviolet radial velocities. VIII - LZ Cephei (HD 209481), *The Observatory* **111**, 167–178.

Humphreys, R. M., 1978, Studies of luminous stars in nearby galaxies. I. Supergiants and O stars in the Milky Way., *ApJS* **38**, 309–350.

Hunter, I., Lennon, D. J., Dufton, P. L. et al., 2008, The VLT-FLAMES survey of massive stars: atmospheric parameters and rotational velocity distributions for B-type stars in the Magellanic Clouds, *A&A* **479**, 541–555.

Ilijić, S., 2003, *Spectral disentangling of close binary stars*, Master's thesis, University of Zagreb.

Irvine, N. J., 1989, HD 93521 - A high-latitude shell star, *ApJ* **337**, L33–L35.

Kaitchuck, R. H., Schlegel, E. M., Honeycutt, R. K. et al., 1994, An atlas of Doppler emission-line tomography of cataclysmic variable stars, *ApJS* **93**, 519–530.

Kak, A. C. & Slaney, M., 2001, *Principles of Computerized Tomographic Imaging (Classics in Applied Mathematics)*, Society of Industrial and Applied Mathematics.

Kallinger, T. & Matthews, J. M., 2010, Evidence for Granulation in Early A-Type Stars, *ApJL* **711**, L35–L39.

Kambe, E., Hirata, R., Ando, H. et al., 1997, Multiperiodicity of zeta Ophiuchi from Multisite Observations, *ApJ* **481**, 406–+.

Kameswara Rao, N., 1972, Light Variations of Three Spectroscopic Binaries, *PASP* **84**, 563–+.

Kennedy, M., Dougherty, S. M., Fink, A. & Williams, P. M., 2010, Modeling the Radio Emission from Cyg OB2 No. 5: A Quadruple System?, *ApJ* **709**, 632–643.

Kennedy, M., Dougherty, S. M., Williams, P. M. & Fink, A., 2011, Cyg OB2 #5: When three stars are just not enough, *Bulletin de la Société Royale des Sciences de Liège* **80**, 572–577.

Kholtygin, A. F. & Kostenko, F. V., 2000, Discrete Absorption Components in OB Star Winds, in *Thermal and Ionization Aspects of Flows from Hot Stars* (H. Lamers & A. Sapar, ed.), *Astronomical Society of the Pacific Conference Series*, vol. 204, 233–+.

Knödlseder, J., Cerviño, M., Le Duigou, J.-M. et al., 2002, Gamma-ray line emission from OB associations and young open clusters. II. The Cygnus region, *A&A* **390**, 945–960.

Kratter, K. M., 2011, The Formation of Binaries, *ArXiv e-prints* .

Kuiper, R., Klahr, H., Beuther, H. & Henning, T., 2010, Circumventing the Radiation Pressure Barrier in the Formation of Massive Stars via Disk Accretion, *ApJ* **722**, 1556–1576.

Lada, C. J. & Lada, E. A., 2003, Embedded Clusters in Molecular Clouds, *Annu. Rev. Astron. Astrophys.* **41**, 57–115.

Lamers, H. J. G. L. M. & Cassinelli, J. P., 1999, *Introduction to Stellar Winds*.

Lamers, H. J. G. L. M. & Leitherer, C., 1993, What are the mass-loss rates of O stars?, *ApJ* **412**, 771–791.

Lanz, T. & Hubeny, I., 2003, A Grid of Non-LTE Line-blanketed Model Atmospheres of O-Type Stars, *ApJS* **146**, 417–441.

Le Duigou, J.-M. & Knödlseder, J., 2002, Characteristics of new star cluster candidates in the Cygnus area, *A&A* **392**, 869–884.

Linder, N., 2008, *A multi-wavelength study of interactions in O+O binary systems*, Phd thesis, University of Liège, Faculté des Sciences.

Linder, N., Rauw, G., Manfroid, J. et al., 2009, A multiwavelength investigation of the massive eclipsing binary Cygnus OB2 #5, *A&A* **495**, 231–241.

Linder, N., Rauw, G., Martins, F. et al., 2008, High-resolution optical spectroscopy of Plaskett's star, *A&A* **489**, 713–723.

Liu, T., Janes, K. A. & Bania, T. M., 1989, Radial-velocity measurements in 20 young open clusters, *AJ* **98**, 626–640.

Lucy, L. B. & Solomon, P. M., 1970, Mass Loss by Hot Stars, *ApJ* **159**, 879–+.

Lucy, L. B. & Sweeney, M. A., 1971, Spectroscopic binaries with circular orbits., *AJ* **76**, 544–556.

Maeder, A., 1992, Stellar yields as a function of initial metallicity and mass limit for black hole formation, *A&A* **264**, 105–120.

Maeder, A. & Meynet, G., 2000, The Evolution of Rotating Stars, *Annu. Rev. Astron. Astrophys.* **38**, 143–190.

Maeder, A. & Meynet, G., 2004, Evolution of Massive Stars with Rotation and Mass Loss (Invited Review), in *Stellar Rotation* (A. Maeder & P. Eenens, ed.), *IAU Symposium*, vol. 215, 500–+.

Mahy, L., Gosset, E., Baudin, F. et al., 2011a, Plaskett's star: analysis of the CoRoT photometric data, *A&A* **525**, A101+.

Mahy, L., Martins, F., Machado, C. et al., 2011b, The two components of the evolved massive binary LZ Cephei. Testing the effects of binarity on stellar evolution, *A&A* **533**, A9+.

Mahy, L., Nazé, Y., Rauw, G. et al., 2009, Early-type stars in the young open cluster NGC 2244 and in the Monoceros OB2 association. I. The multiplicity of O-type stars, *A&A* **502**, 937–950.

Mahy, L., Rauw, G., Martins, F. et al., 2010, A New Investigation of the Binary HD 48099, *ApJ* **708**, 1537–1544.

Mahy, L., Rauw, G., Martins, F. et al., 2011c, The multiplicity of O-type stars in NGC 2244, *Bulletin de la Societe Royale des Sciences de Liege* **80**, 622–627.

Malchenko, S. L. & Tarasov, A. E., 2009, Spectroscopy of B and Be stars in the diffuse stellar clusters NGC 6871 and NGC 6913, *Astrophysics* **52**, 235–250.

Marchenko, S. V., Moffat, A. F. J. & Eenens, P. R. J., 1998, The Wolf-Rayet Binary WR 141 (WN5O + O5 V-III) Revisited, *PASP* **110**, 1416–1422.

Marcolino, W. L. F., Bouret, J.-C., Martins, F. et al., 2009, Analysis of Galactic late-type O dwarfs: more constraints on the weak wind problem, *A&A* **498**, 837–852.

Marsh, T. R. & Horne, K., 1988, Images of accretion discs. II - Doppler tomography, *MNRAS* **235**, 269–286.

Martins, F., 2004, *New atmosphere models for massive stars: line-blanketing effects and wind properties of O stars*, Ph.D. thesis, Université Toulouse III, France.

Martins, F., 2011, UV, optical and near-IR diagnostics of massive stars, *Bulletin de la Société Royale des Sciences de Liège* **80**, 29–41.

Martins, F., Hillier, D. J., Paumard, T. et al., 2008, The most massive stars in the Arches cluster, *A&A* **478**, 219–233.

Martins, F., Mahy, L., Rauw, G. & Hillier, D. J., 2011, A quantitative study of O stars in NGC2244 and the Mon OB2 association, *ArXiv e-prints* .

Martins, F. & Plez, B., 2006, UBVJHK synthetic photometry of Galactic O stars, *A&A* **457**, 637–644.

Martins, F., Schaerer, D. & Hillier, D. J., 2005a, A new calibration of stellar parameters of Galactic O stars, *A&A* **436**, 1049–1065.

Martins, F., Schaerer, D., Hillier, D. J. & Heydari-Malayeri, M., 2004, Puzzling wind properties of young massive stars in SMC-N81, *A&A* **420**, 1087–1106.

Martins, F., Schaerer, D., Hillier, D. J. et al., 2005b, O stars with weak winds: the Galactic case, *A&A* **441**, 735–762.

Mason, B. D., Gies, D. R., Hartkopf, W. I. et al., 1998, ICCD speckle observations of binary stars. XIX - an astrometric/spectroscopic survey of O stars, *AJ* **115**, 821–+.

Mason, B. D., Hartkopf, W. I., Gies, D. R. et al., 2009, The High Angular Resolution Multiplicity of Massive Stars, *AJ* **137**, 3358–3377.

Massey, P., Johnson, K. E. & Degioia-Eastwood, K., 1995, The Initial Mass Function and Massive Star Evolution in the OB Associations of the Northern Milky Way, *ApJ* **454**, 151–+.

Mathys, G., 1988, The upper main sequence of OB associations. I - Spectral types and lines of C and N of southern single-lined O stars, *A&A Supplement Series* **76**, 427–444.

Mathys, G., 1989, The upper main sequence of OB associations. II - The single-lined O stars: Spectral classification of northern stars and lines of C and N, *A&A Supplement Series* **81**, 237–252.

Mermilliod, J.-C., 1995, The database for galactic open clusters (BDA)., in *Information On-Line Data in Astronomy* (D. Egret & M. A. Albrecht, ed.), *Astrophysics and Space Science Library*, vol. 203, 127–138.

Meynet, G. & Maeder, A., 2000, Stellar evolution with rotation. V. Changes in all the outputs of massive star models, *A&A* **361**, 101–120.

Meynet, G. & Maeder, A., 2003, Stellar evolution with rotation. X. Wolf-Rayet star populations at solar metallicity, *A&A* **404**, 975–990.

Milne, E. A., 1926, On the possibility of the emission of high-speed atoms from the sun and stars, *MNRAS* **86**, 459–473.

Montgomery, M. H. & O'Donoghue, D., 1999, A derivation of the errors for least squares fitting to time series data, *Delta Scuti Star Newsletter* **13**, 28–+.

Muller, P., 1954, Double star observations at Lick Observatory, *AJ* **59**, 388–396.

Nazé, Y., Damerdji, Y., Rauw, G. et al., 2010, First Orbital Solution for the Non-thermal Emitter Cyg OB2 No. 9, *ApJ* **719**, 634–641.

Negueruela, I., 2004, A search for luminous Be stars, *Astronomische Nachrichten* **325**, 380–392.

Niemela, V. S. & Gamen, R. C., 2005, The nearest star of spectral type O3: a component of the multiple system HD 150136, *MNRAS* **356**, 974–978.

Oey, M. S. & Clarke, C. J., 2005, Statistical Confirmation of a Stellar Upper Mass Limit, *ApJ* **620**, L43–L46.

Ogura, K. & Ishida, K., 1981, UBV Photometry of NGC2244, *PASJ* **33**, 149–+.

Owocki, S., 2011, Theory of Winds from Hot, Luminous Massive Stars, *Bulletin de la Societe Royale des Sciences de Liege* **80**, 16–28.

Owocki, S. P., 2008, Dynamical simulation of the "velocity-porosity" reduction in observed strength of stellar wind lines, in *Clumping in Hot-Star Winds* (W.-R. Hamann, A. Feldmeier, & L. M. Oskinova, ed.), 121–+.

Pavlovski, K., Tamajo, E., Koubský, P. et al., 2009, Chemical evolution of high-mass stars in close binaries - II. The evolved component of the eclipsing binary V380Cygni, *MNRAS* **400**, 791–804.

Penny, L. R. & Gies, D. R., 2009, A FUSE Survey of the Rotation Rates of Very Massive Stars in the Small and Large Magellanic Clouds, *ApJ* **700**, 844–858.

Penny, L. R., Gies, D. R., Hartkopf, W. I. et al., 1993, The frequency of binary stars in the young cluster Trumpler 14, *PASP* **105**, 588–594.

Puls, J., Kudritzki, R., Herrero, A. et al., 1996, O-star mass-loss and wind momentum rates in the Galaxy and the Magellanic Clouds Observations and theoretical predictions., *A&A* **305**, 171–+.

Puls, J., Markova, N., Scuderi, S. et al., 2006, Bright OB stars in the Galaxy. III. Constraints on the radial stratification of the clumping factor in hot star winds from a combined $H_{\pm}$, IR and radio analysis, *A&A* **454**, 625–651.

Puls, J., Vink, J. S. & Najarro, F., 2008, Mass loss from hot massive stars, *A&A Review* **16**, 209–325.

Rauw, G., 2007, *A multi-wavelength approach to the study of high-energy phenomena associated with early-type stars*, Ph.D. thesis, University of Liège, thèse d'agrégation de l'enseignement supérieur.

Rauw, G., Crowther, P. A., De Becker, M. et al., 2005a, The spectrum of the very massive binary system WR 20a (WN6ha + WN6ha): Fundamental parameters and wind interactions, *A&A* **432**, 985–998.

Rauw, G., Crowther, P. A., De Becker, M. et al., 2005b, The spectrum of the very massive binary system WR 20a (WN6ha + WN6ha): Fundamental parameters and wind interactions, *A&A* **432**, 985–998.

Rauw, G. & De Becker, M., 2004, Early-type stars in the young open cluster IC 1805. I. The SB2 system BD+60°497 and the probably single stars BD +60°501 and BD+60°513, *A&A* **421**, 693–702.

Rauw, G., De Becker, M., van Winckel, H. et al., 2008, Spectroscopic and photometric variability of the O9.5 Vp star HD 93521, *A&A* **487**, 659–670.

Rauw, G., Nazé, Y., Carrier, F. et al., 2001, The strange case of the massive binary HD 149404, *A&A* **368**, 212–224.

Rauw, G., Nazé, Y., Fernández Lajús, E. et al., 2009, Optical spectroscopy of X-Mega targets in the Carina nebula - VII. On the multiplicity of Tr16-112, HD93343 and HD93250, *MNRAS* **398**, 1582–1592.

Rauw, G., Sana, H., Gosset, E. et al., 2000, A new orbital solution for the massive binary system HD 93403, *A&A* **360**, 1003–1010.

Rauw, G., Sana, H. & Nazé, Y., 2011, A spectroscopic investigation of early-type stars in the young open cluster Westerlund 2, *ArXiv e-prints* .

Rauw, G., Vreux, J.-M. & Bohannan, B., 1999, The Interacting Early-Type Binary BD +40 deg4220 (V729 Cyg): Modeling the Colliding Winds Region, *ApJ* **517**, 416–430.

Reed, C., 2005, Photometry and Spectroscopy for Luminous Stars (Reed 2005), *VizieR Online Data Catalog* **5125**, 0–+.

Reimann, H.-G., 1989, UVBY photometry of open clusters. II - NGC 6871, *Astronomische Nachrichten* **310**, 273–280.

Repolust, T., Puls, J. & Herrero, A., 2004, Stellar and wind parameters of Galactic O-stars. The influence of line-blocking/blanketing, *A&A* **415**, 349–376.

Ritchie, B. W., Clark, J. S., Negueruela, I. & Crowther, P. A., 2009, A VLT/FLAMES survey for massive binaries in Westerlund 1. I. First observations of luminous evolved stars, *A&A* **507**, 1585–1595.

Rivero Gonzalez, J. G., Puls, J., Najarro, F. & Brott, I., 2011, Nitrogen line spectroscopy in O-stars – II. Surface nitrogen abundances for O-stars in the Large Magellanic Cloud, *ArXiv e-prints* .

Rudy, R. J. & Herman, L. C., 1978, The variable linear polarization of the O-star binary HD 47129 /Plaskett's star/, *PASP* **90**, 163–166.

Ryans, R. S. I., Dufton, P. L., Rolleston, W. R. J. et al., 2002, Macroturbulent and rotational broadening in the spectra of B-type supergiants, *MNRAS* **336**, 577–586.

Sana, H. & Evans, C. J., 2011, The multiplicity of massive stars **272**, 474–485.

Sana, H., Gosset, E. & Evans, C. J., 2009, The massive star binary fraction in young open clusters - II. NGC6611 (Eagle Nebula), *MNRAS* **400**, 1479–1492.

Sana, H., Gosset, E., Nazé, Y. et al., 2008, The massive star binary fraction in young open clusters - I. NGC 6231 revisited, *MNRAS* **386**, 447–460.

Sana, H., Gosset, E. & Rauw, G., 2006, The OB binary HD152219: a detached, double-lined, eclipsing system, *MNRAS* **371**, 67–80.

Sana, H., James, G. & Gosset, E., 2011a, The massive star binary fraction in young open clusters - III. IC 2944 and the Cen OB2 association, *MNRAS* **416**, 817–831.

Sana, H., Le Bouquin, J.-B., De Becker, M. et al., 2011b, The Non-thermal Radio Emitter HD 93250 Resolved by Long Baseline Interferometry, *ApJL* **740**, L43+.

Scargle, J. D., 1982, Studies in astronomical time series analysis. II - Statistical aspects of spectral analysis of unevenly spaced data, *ApJ* **263**, 835–853.

Schaerer, D., 2002, On the properties of massive Population III stars and metal-free stellar populations, *A&A* **382**, 28–42.

Schaerer, D., 2003, The transition from Population III to normal galaxies: Lyalpha and He II emission and the ionising properties of high redshift starburst galaxies, *A&A* **397**, 527–538.

Schwarzenberg-Czerny, A., 1998, The distribution of empirical periodograms: Lomb-Scargle and PDM spectra, *MNRAS* **301**, 831–840.

Simon, K. P. & Sturm, E., 1994, Disentangling of composite spectra, *A&A* **281**, 286–291.

Simón-Díaz, S. & Herrero, A., 2007, Fourier method of determining the rotational velocities in OB stars, *A&A* **468**, 1063–1073.

Skinner, S. L., Zhekov, S. A., Palla, F. & Barbosa, C. L. D. R., 2005, Chandra X-ray observations of the young stellar cluster NGC 6193 in the Ara OB1 association, *MNRAS* **361**, 191–205.

Slesnick, C. L., Hillenbrand, L. A. & Massey, P., 2002, The Star Formation History and Mass Function of the Double Cluster h and χ Persei, *ApJ* **576**, 880–893.

Slettebak, A., 1956, Line Broadening in the Spectra of o- and Early B-Type Stars., *ApJ* **124**, 173–+.

Sota, A., Maíz Apellániz, J., Barbá, R. H. et al., 2011, The Galactic O-Star Spectral Survey (GOSSS) Project status and first results, *Bulletin de la Société Royale des Sciences de Liège* **80**, 519–523.

Stanishev, V., Kraicheva, Z., Boffin, H. M. J. & Genkov, V., 2002, PX Andromedae: Superhumps and variable eclipse depth, *A&A* **394**, 625–632.

Stickland, D. J., 1996, Spectroscopic binary orbits from ultraviolet radial velocities. Paper 22: HD 48099, *The Observatory* **116**, 294–297.

Sundqvist, J. O., Owocki, S. P. & Puls, J., 2011a, The nature and consequences of clumping in hot, massive star winds, *ArXiv e-prints* .

Sundqvist, J. O., Puls, J. & Feldmeier, A., 2010, Mass loss from inhomogeneous hot star winds. I. Resonance line formation in 2D models, *A&A* **510**, A11+.

Sundqvist, J. O., Puls, J., Feldmeier, A. & Owocki, S. P., 2011b, Mass loss from inhomogeneous hot star winds. II. Constraints from a combined optical/UV study, *A&A* **528**, A64+.

Tadross, A. L., Werner, P., Osman, A. & Marie, M., 2002, Morphological analysis of open clusters' propertiesII. Relationships projected onto the galactic plane, *New Astronomy* **7**, 553–575.

Turner, D. G., 1976, The value of R in Monoceros, *ApJ* **210**, 65–75.

Turner, N. H., ten Brummelaar, T. A., Roberts, L. C. et al., 2008, Adaptive Optics Photometry and Astrometry of Binary Stars. III. a Faint Companion Search of O-Star Systems, *AJ* **136**, 554–565.

Underhill, A. B., 1995, A Study of the Spectra of Seven Of Stars. II. Line Profiles and Equivalent Widths, *ApJS* **100**, 461–+.

Uyanıker, B., Fürst, E., Reich, W. et al., 2001, The Cygnus superbubble revisited, *A&A* **371**, 675–697.

Vanbeveren, D., 2011, Signatures of binary evolution processes in massive stars, *Bulletin de la Société Royale des Sciences de Liège* **80**, 530–542.

Vanbeveren, D., De Loore, C. & Van Rensbergen, W., 1998, Massive stars, *Annu. Rev. Astron. Astrophys.* **9**, 63–152.

Ventura, P., D'Antona, F. & Mazzitelli, I., 2008, The ATON 3.1 stellar evolutionary code. A version for asteroseismology, *APSS* **316**, 93–98.

Vink, J. S., de Koter, A. & Lamers, H. J. G. L. M., 2000, New theoretical mass-loss rates of O and B stars, *A&A* **362**, 295–309.

Walborn, N. R., 1971, Some Spectroscopic Characteristics of the OB Stars: an Investigation of the Space Distribution of Certain OB Stars and the Reference Frame of the Classification, *ApJS* **23**, 257–+.

Walborn, N. R., 2003, CNO Morphology in OB Spectra, in *Astronomical Society of the Pacific Conference Series* (C. Charbonnel, D. Schaerer, & G. Meynet, ed.), *Astronomical Society of the Pacific Conference Series*, vol. 304, 29–+.

Walborn, N. R. & Howarth, I. D., 2000, Digital Spectroscopy of O3-O5 and ON/OC Supergiants in Cygnus, *PASP* **112**, 1446–1454.

Walborn, N. R., Howarth, I. D., Lennon, D. J. et al., 2002, A New Spectral Classification System for the Earliest O Stars: Definition of Type O2, *AJ* **123**, 2754–2771.

Wang, J., Townsley, L. K., Feigelson, E. D. et al., 2008, A Chandra Study of the Rosette Star-forming Complex. I. The Stellar Population and Structure of the Young Open Cluster NGC 2244, *ApJ* **675**, 464–490.

Wang, J.-J. & Hu, J.-Y., 2000, Spectral classification and reddening in the young open cluster NGC 6913, *A&A* **356**, 118–126.

Weigelt, G., Albrecht, R., Barbieri, C. et al., 1991, First results from the faint object camera - High-resolution observations of the central object R136 in the 30 Doradus nebula, *ApJ* **378**, L21–L23.

Wichmann, R., 1998, *Nightfall User Manual*, http://www.hs.uni-hamburg.de/DE/Ins/Per/Wichmann/Nightfall.html.

Wolfe, R. H., Jr., Horak, H. G. & Storer, N. W., 1967, *The machine computation of spectroscopic binary elements*, 251, New York: Gordon & Breach.

Zinnecker, H. & Yorke, H. W., 2007, Toward Understanding Massive Star Formation, *Annu. Rev. Astron. Astrophys.* **45**, 481–563.